Walter Steurer
Sofia Deloudi

Crystallography of Quasicrystals

Concepts, Methods and Structures

Springer

Springer Series in
MATERIALS SCIENCE   126

Springer Series in
MATERIALS SCIENCE

Editors: R. Hull   R. M. Osgood, Jr.   J. Parisi   H. Warlimont

The Springer Series in Materials Science covers the complete spectrum of materials physics, including fundamental principles, physical properties, materials theory and design. Recognizing the increasing importance of materials science in future device technologies, the book titles in this series reflect the state-of-the-art in understanding and controlling the structure and properties of all important classes of materials.

Please view available titles in *Springer Series in Materials Science*
on series homepage http://www.springer.com/series/856

Walter Steurer
Sofia Deloudi

Crystallography of Quasicrystals

Concepts, Methods and Structures

With 177 Figures

Springer

Professor Dr. Walter Steurer
Dr. Sofia Deloudi
ETH Zürich, Department of Materials, Laboratory of Crystallography
Wolfgang-Pauli-Str. 10, 8093 Zürich, Switzerland
E-mail: steurer@mat.ethz.ch, deloudi@mat.ethz.ch

Series Editors:

Printed on acid-free paper

Preface

The quasicrystal community comprises mathematicians, physicists, chemists, materials scientists, and a handful of crystallographers. This diversity is reflected in more than 10,000 publications reporting 25 years of quasicrystal research. Always missing has been a monograph on the "Crystallography of Quasicrystals," a book presenting the main concepts, methods and structures in a self-consistent unified way; a book that translates the terminology and way of thinking of all these specialists from different fields into that of crystallographers, in order to look at detailed problems as well as at the big picture from a structural point of view.

Once Albert Einstein pointed out: "As far as the laws of mathematics refer to reality, they are not certain; as far as they are certain, they do not refer to reality." Accordingly, this book is aimed at bridging the gap between the ideal mathematical and physical constructs and the real quasicrystals of intricate complexity, and, last but not the least, providing a toolbox for tackling the structure analysis of real quasicrystals.

The book consists of three parts. The part "Concepts" treats the properties of tilings and coverings. If decorated by polyhedral clusters, these can be used as models for quasiperiodic structures. The higher-dimensional approach, central to the crystallography of quasicrystals, is also in the center of this part.

The part "Methods" discusses experimental techniques for the study of real quasicrystals as well as power and limits of methods for their structural analysis. What can we know about a quasicrystal structure and what do we want to know, why, and what for, this is the guideline.

The part "Structures" presents examples of quasicrystal structures, followed by a discussion of phase stability and transformations from a microscopical point of view. It ends with a chapter on soft quasicrystals and artificially fabricated macroscopic structures that can be used as photonic or phononic quasicrystals.

   This book is intended for researchers in the field of quasicrystals and all scientists and graduate students who are interested in the crystallography of quasicrystals.

Zürich,   *Walter Steurer*
June 2009   *Sofia Deloudi*

Contents

Part II Methods

Acronyms

AC	Approximant crystal(s)
ADP	Atomic displacement parameter(s)
AET	Atomic environment type(s)
AFM	Atomic force microscopy
AT	Ammann tiling
bcc	Body-centered cubic
BZ	Brillouin Zone
CBED	Convergent-beam electron diffraction
ccp	Cubic close packed
CF	Charge flipping
CN	Coordination number
CS	Composite structure(s)
*d*D	*d*-dimensional
D_m	Mass density
D_p	Point density
fcc	Face-centered cubic
EXAFS	Extended X-ray absorption fine structure spectroscopy
FS	Fibonacci sequence
FT	Fourier transform
FWHM	Full width at half maximum
HAADF-STEM	High-angle annular dark-field scanning transmission electron microscopy
hcp	Hexagonal close packed
HRTEM	High-resolution transmission electron microscopy
HT	High temperature
IUCr	International union of crystallography
IMS	Incommensurately modulated structure(s)
K^{3D}	3D point group
LEED	Low-energy electron diffraction
LDE	Low-density elimination
LT	Low temperature

MC	Metacrystal(s)
ME	Mössbauer effect
MEM	Maximum-entropy method
nD	n-dimensional
ND	Neutron diffraction
NMR	Nuclear magnetic resonance
NS	Neutron scattering
PAS	Periodic average structure(s)
PC	Periodic crystal(s)
pdf	probability density function
PDF	Pair distribution function
PDS	Phason diffuse scattering
PF	Patterson function
PNC	Phononic crystal(s)
PT	Penrose tiling
PTC	Photonic crystal(s)
PNQC	Phononic quasicrystal(s)
PTQC	Photonic quasicrystal(s)
PV	Pisot-Vijayaraghavan
QC	Quasicrystal(s)
QG	Quiquandon-Gratias
SAED	Selected area electron diffraction
STM	Scanning tunneling microscopy
TDS	Thermal diffuse scattering
TM	Transition metal(s)
TEM	Transmission Electron microscopy
XRD	X-ray diffraction

Symbols

$F(\mathbf{H})$	Structure factor
$f_k\left(\lvert\mathbf{H}\rvert\right)$	Atomic scattering factor
F_n	Fibonacci number
G	Metric tensor of the direct lattice
G^*	Metric tensor of the reciprocal lattice
$\Gamma(R)$	Point group operation
$g_k\left(\mathbf{H}^\perp\right)$	Geometrical form factor
$\gcd(k, n)$	Greatest common divisor
$h_1\,h_2\ldots h_n$	Miller indices of a Bragg reflection (reciprocal lattice node) from the set of parallel lattice planes $(h_1\,h_2\ldots h_n)$
$(h_1\,h_2\ldots h_3)$	Miller indices denoting a plane (crystal face or single lattice plane)
M	Set of direct space vectors
M^*	Set of reciprocal space vectors
M_{F}^*	Set of Structure factor weighted reciprocal space vectors, i.e. Fourier spectrum
M_{I}^*	Set of intensity weighted reciprocal space vectors, i.e. diffraction pattern
λ_i	Eigenvalues
P_n	Pell number
$\rho(\mathbf{r})$	Electron density distribution function
S	Substitution and/or scaling matrix
σ	Substitution rule
Σ	nD Lattice
Σ^*	nD Reciprocal lattice
τ	Golden mean
$T_k\left(\mathbf{H}^\parallel\right)$	Temperature factor or atomic displacement factor
$[u_1\,u_2\ldots u_n]$	Indices denoting a direction
V	Vector space
$V^\parallel$	Parallel space (par-space)
$V^\perp$	Perpendicular space (perp-space)
W	Embedding matrix
w_n	nth word of a substitutional sequence

1

Tilings and Coverings

A packing is an arrangement of non-interpenetrable objects touching each other. The *horror vacui* of Mother Nature leads to the densest possible packings of structural units (atoms, ions, molecules, coordination polyhedra, atomic clusters, etc.) under constraints such as directional chemical bonding or charge balance. Of course, in the case of real crystals, the structural units are not hard spheres or rigid entities but usually show some flexibility. Consequently, the real packing density, i.e. the ratio of the volume filled by the atoms to the total volume, may differ considerably from that calculated for rigid spheres. For instance, the packing density $D_p = \pi\sqrt{3}/16 = 0.34$ of the diamond structure is very low compared to $D_p = \pi/\sqrt{18} = 0.74$ of the dense sphere packing. However, this low number does not reflect the high density and hardness of diamond, it just reflects the inappropriateness of the hard sphere model due to the tetrahedrally oriented, strong covalent bonds. Dense packing can be entropically disfavored at high temperatures. The *bcc* structure type, for instance, with $D_p = \pi\sqrt{3}/8 = 0.68$, is very common for high-temperature (HT) phases due to its higher vibrational entropy compared to *hcp* or *ccp* structures.

If the packing density equals one, the objects fill space without gaps and voids and the packing can be described as tiling. nD periodic tilings can always be reduced to a packing of copies of a single unit cell, which corresponds to a nD parallelotope (parallelepiped in 3D, parallelogram in 2D). In case of quasiperiodic tilings at least two unit cells are needed.

Quasiperiodic tilings can be generated by different methods such as the (i) substitution method, (ii) tile assembling guided by matching rules, (iii) the higher-dimensional approach, and (iv) the generalized dual-grid method [3, 6]. We will discuss the first three methods.

Contrary to packings and tilings, coverings fill the space without gaps but with partial overlaps. There is always a one-to-one correspondence between coverings and tilings. Every covering can be represented by a (decorated) tiling. However, not every tiling can be represented by a covering based on a finite number of covering clusters. Usually, certain patches of tiles are taken for the construction of covering clusters.

In this chapter, we will discuss examples of basic tilings and coverings, which are crucial for the description and understanding of the quasicrystal structures known so far. Consequently, the focus will be on tilings with pentagonal, octagonal, decagonal, dodecagonal, and icosahedral diffraction symmetry. They all have in common that their scaling symmetries are related to quadratic irrationalities. This is also the case for the 1D Fibonacci sequence, which will also serve as an easily accessible and illustrative example for the different ways to generate and describe quasiperiodic tilings. The heptagonal (tetrakaidecagonal) tiling, which is based on cubic irrationalities, is discussed as an example of a different class of tilings. No QC are known yet with this symmetry, only approximants such as particular borides (see Sect. 8.1).

The reader who is generally interested in tilings is referred to the comprehensive book on *Tilings and Patterns* by Grünbaum and Shephard [9], which contains a wealth of tilings of all kinds. A few terms used for the description of tilings are explained in the following [19, 23, 34, 35].

Local isomorphism (LI) Two tilings are locally isomorphic if and only if *every* finite region contained in either tiling can also be found, in the same orientation, in the other. In other words, locally isomorphic tilings have the same *R*-atlases for all *R*, where the *R*-atlas of a tiling consists of all its tile patches of radius *R*. The LI class of a tiling is the set of all locally isomorphous tilings. Locally isomorphic structures have the same autocorrelation (Patterson) function, i.e. they are homometric. This means they also have the same diffraction pattern. Tilings, which are self-similar, have matching rules and an Ammann quasilattice are said to belong to the *Penrose local isomorphism* (PLI) class.

Orientational symmetry The tile edges are oriented along the set of star vectors defining the orientational (rotational) symmetry *N*. While there may be many points in regular tilings reflecting the orientational symmetry locally, there is usually no point of global symmetry. This is the case for exceptionally singular tilings. Therefore, the point-group symmetry of a tiling is better defined in reciprocal space. It is the symmetry of the structure factor (amplitudes and phases) weighted reciprocal (quasi)lattice. It can also be defined as the symmetry of the LI class.

Self-similarity There exists a mapping of the tiling onto itself, generating a tiling with larger tiles. In the case of a substitution tiling, this mapping is called *inflation* operation since the size of the tiles is distended. The inverse operation is *deflation* which shrinks the tiling in a way that each old tile of a given shape is decorated in the same way by a patch of the new smaller tiles. Self-similarity operations must respect matching rules. Sometimes the terms *inflation* (*deflation*) are used just in the opposite way referring to the increased (decreased) number of tiles generated.

Matching rules These constitute a construction rule forcing quasiperiodicity, which can be derived either from substitution (deflation) rules or

based on the nD approach. Matching rules can be coded either in the decoration of the tiles or in their shape. A tiling is said to admit *perfect* matching rules of radius R, if all tilings with the same R-atlas are locally isomorphic to it. A set of matching rules is said to be *strong*, if all tilings admitted are quasiperiodic, but not in a single LI class. *Weak* matching rules are the least restrictive ones which guarantee quasiperiodicity. They allow bounded departures from a perfect quasiperiodic tiling. The diffraction pattern will show diffuse scattering beside Bragg diffraction. Non-local matching rules need some global information on the tiling. They rather allow to check whether a tiling is quasiperiodic than to be used as a growth rule.

Ammann lines Tilings of the PLI class have the property that, if their unit tiles are properly decorated by line segments, these join together in the tiling and form sets of continuous lines (Ammann lines). According to the orientational symmetry, N sets of parallel, quasiperiodically spaced lines form, which are called Amman N-grid or Ammann quasilattice. Contrary to a periodic N grid with non-crystallographic symmetry, it has a finite number of Voronoi cell shapes.

Remark The explanations, definitions, and descriptions in the gray boxes are intended to give a simple and intuitive understanding of the concepts. Therefore, they are not always written in a mathematically rigorous style.

1.1 1D Substitutional Sequences

Besides several quasiperiodic sequences, examples of other kinds of non-periodic substitutional sequences will also be discussed, showing what they have in common and what clearly distinguishes them. The quasiperiodic sequences treated here are the Fibonacci sequence, which plays an important role in tilings with 5-fold rotational symmetry, and the Octonacci sequence, also known as Pell sequence, which is related to tilings with 8-fold symmetry.

The non-quasiperiodic sequences discussed here are the almost periodic squared Fibonacci sequence and the critical Thue–Morse sequence. The squared Fibonacci sequence has a fractal atomic surface and a pure point Fourier spectrum of infinite rank, while the Thue–Morse sequence shows a singular continuous spectrum. Both are mainly of interest for artificial structures such as photonic or phononic crystals. Finally, the properties of a randomized Fibonacci sequence will be shortly discussed.

1.1.1 Fibonacci Sequence (FS)

The Fibonacci sequence, a 1D quasiperiodic substitutional sequence (see, e.g., [26]), can be obtained by iterative application of the substitution rule $\sigma : L \mapsto LS, S \mapsto L$ to the two-letter alphabet $\{L, S\}$. The substitution rule can be alternatively written employing the substitution matrix S

$$\sigma : \begin{pmatrix} L \\ S \end{pmatrix} \mapsto \underbrace{\begin{pmatrix} 1 & 1 \\ 1 & 0 \end{pmatrix}}_{=S} \begin{pmatrix} L \\ S \end{pmatrix} = \begin{pmatrix} LS \\ L \end{pmatrix}. \qquad (1.1)$$

The substitution matrix does not give the order of the letters, just their relative frequencies in the resulting words w_n, which are finite strings of the two kinds of letters. Longer words can be created by multiple action of the substitution rule. Thus, $w_n = \sigma^n(L)$ means the word resulting from the n-th iteration of σ (L): $L \mapsto LS$. The action of the substitution rule is also called inflation operation as the number of letters is inflated by each step. The FS can as well be created by recursive concatenation of shorter words according to the concatenation rule $w_{n+2} = w_{n+1}w_n$. The generation of the first few words is shown in Table 1.1.

The frequencies $\nu_n^L = F_{n+1}, \nu_n^S = F_n$ of letters L, S in the word $w_n = \sigma^n(L)$, with $n \geq 1$, result from the $(n-1)$th power of the transposed substitution matrix to

$$\begin{pmatrix} \nu_n^L \\ \nu_n^S \end{pmatrix} = (S^T)^{n-1} \begin{pmatrix} 1 \\ 1 \end{pmatrix}. \qquad (1.2)$$

The Fibonacci numbers $F_{n+2} = F_{n+1} + F_n$, with $n \geq 0$ and $F_0 = 0, F_1 = 1$, form a series with $\lim_{n\to\infty} F_n/F_{n-1} = \tau = 1.618\ldots$, which is called the *golden ratio*. Arbitrary Fibonacci numbers can be calculated directly by Binet's formula

Table 1.1. Generation of words $w_n = \sigma^n(L)$ of the Fibonacci sequence by repeated action of the substitution rule $\sigma(L) = LS$, $\sigma(S) = L$. ν_n^L and ν_n^S denote the frequencies of L and S in the words w_n; F_n are the Fibonacci numbers

n	$w_{n+2} = w_{n+1}w_n$	ν_n^L	ν_n^S
0	L	1	0
1	LS	1	1
2	LSL	2	1
3	LSLLS	3	2
4	LSLLSLSL	5	3
5	LSLLSLSLLSLLS	8	5
6	$\underbrace{\text{LSLLSLSLLSLLS}}_{w_5}\underbrace{\text{LSLLSLSL}}_{w_4}$	13	8
$\vdots$	$\vdots$	$\vdots$	$\vdots$
n		F_{n+1}	F_n
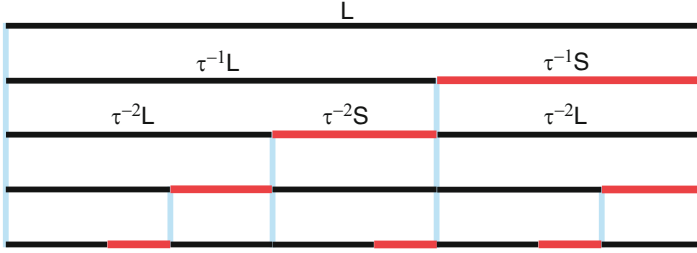
Fig. 1.1. Graphical representation of the substitution rule σ of the Fibonacci sequence. Rescaling by a factor $1/\tau$ at each step keeps the total length constant. Shown is a deflation of the line segment lengths corresponding to an inflation of letters

$$F_n = \frac{(1+\sqrt{5})^n - (1-\sqrt{5})^n}{2^n\sqrt{5}}. \tag{1.3}$$

The number τ If a line segment is divided in the *golden ratio*, then this *golden section* has the property that the larger subsegment is related to the smaller as the whole segment is related to the larger subsegment (Fig. 1.1). This way of creating harmonic proportions has been widely used in art and architecture for millenniums. The symbol τ is derived from the Greek noun $\tau o\mu\acute{\eta}$ which means cut, intersection. Alternatively, the symbol ϕ is used frequently. τ can be represented by the simplest possible continued fraction expansion

$$\tau = 1 + \cfrac{1}{1 + \cfrac{1}{1 + \cfrac{1}{1 + \cdots}}}. \tag{1.4}$$

Since it only contains the numeral one, it is the irrational number with the worst truncated continued fraction approximation. The convergents c_i are just ratios of two successive Fibonacci numbers

$$c_1 = 1, \quad c_2 = 1 + \frac{1}{1} = 2, \quad c_3 = 1 + \frac{1}{1 + \frac{1}{1}} = \frac{3}{2}, \ldots, c_n = \frac{F_{n+1}}{F_n}. \tag{1.5}$$

This poor convergence is the reason that τ is sometimes called the "most irrational number." The strong irrationality may impede the lock-in of incommensurate (quasiperiodic) into commensurate (periodic) systems such as rational approximants.

The scaling properties of the FS can be derived from the eigenvalues λ_i of the substitution matrix S. For this purpose, the eigenvalue equation

$$\det|S - \lambda I| = 0, \tag{1.6}$$

with the unit matrix I, has to be solved. The evaluation of the determinant yields the characteristic polynomial

$$\lambda^2 - \lambda - 1 = 0 \tag{1.7}$$

with the eigenvalues $\lambda_1 = (1 + \sqrt{5})/2 = 2\cos\pi/5 = 1.618\ldots = \tau$, $\lambda_2 = (1 - \sqrt{5})/2 = -2\cos 2\pi/5 = -0.618\ldots = 1 - \tau = -1/\tau$ and the eigenvectors

$$\mathbf{v}_1 = \begin{pmatrix} \tau \\ 1 \end{pmatrix}, \quad \mathbf{v}_2 = \begin{pmatrix} -1/\tau \\ 1 \end{pmatrix}. \tag{1.8}$$

We can now explicitly write the eigenvalue equation $\mathsf{S}\mathbf{v}_i = \lambda_i\mathbf{v}_i$ for the first eigenvalue, for instance,

$$\begin{pmatrix} 1 & 1 \\ 1 & 0 \end{pmatrix}\begin{pmatrix} \tau \\ 1 \end{pmatrix} = \begin{pmatrix} \tau + 1 \\ \tau \end{pmatrix} = \tau\begin{pmatrix} \tau \\ 1 \end{pmatrix}. \tag{1.9}$$

If we assign long and short line segments, respectively, to the letters L and S we get the 1D Fibonacci tiling (Fig. 1.1). Relating the eigenvector $\begin{pmatrix} \tau \\ 1 \end{pmatrix}$ to $\begin{pmatrix} \mathrm{L} \\ \mathrm{S} \end{pmatrix}$ shows that an infinite Fibonacci tiling $s(\mathbf{r})$ is invariant under scaling with the eigenvalue τ, $s(\tau\mathbf{r}) = s(\mathbf{r})$.

The scaling operation maps each tiling vector $\mathbf{r}$ to an already existing tiling vector $\tau\mathbf{r}$. Consequently, the ratio of patches of the Fibonacci tiling, which correspond to words w_n and w_{n+1} created by successive application of the substitution matrix S, is given by the ratio of the eigenvector components

$$\frac{w_{n+1}}{w_n} = \frac{\mathrm{L}}{\mathrm{S}} = \frac{\mathrm{LS}}{\mathrm{L}} = \frac{\mathrm{LSL}}{\mathrm{LS}} = \frac{\mathrm{LSLLS}}{\mathrm{LSL}} = \cdots = \frac{\tau}{1}. \tag{1.10}$$

The length of a word $\ell(w_n)$ can be easily calculated to $\ell(w_n) = \tau^n\mathrm{L}$. The mean vertex distance, d_{av}, results to

$$d_{\mathrm{av}} = \lim_{n\to\infty}\frac{F_{n+1}\mathrm{L} + F_n\mathrm{S}}{F_{n+1} + F_n} = \left\{\frac{F_{n+1}}{F_{n+2}}\tau + \frac{F_n}{F_{n+2}}\right\}\mathrm{S} = (3 - \tau)\mathrm{S}, \tag{1.11}$$

yielding a vertex point density $D_{\mathrm{p}} = 1/d_{\mathrm{av}}$. $d_{\mathrm{av}} = a_{\mathrm{PAS}}$ is also the period of the periodic average structure (PAS) of the FS (see section 3.3). The total length of the Fibonacci tiling for n line segments reads, in units of S,

$$x_n = (n + 1)(3 - \tau) - 1 - \frac{1}{\tau}\left\{\left[\frac{n + 1}{\tau}\right] \mod 1\right\}. \tag{1.12}$$

Periodic lattices scale with integer factors, thus the eigenvalues are integers. In case of quasiperiodic "lattices" (*quasilattices*), the eigenvalues are *algebraic numbers* (*Pisot numbers*), which have the *Pisot–Vijayaraghavan (PV) property*:

$$\lambda_1 > 1, \quad |\lambda_i| < 1 \quad \forall i > 1. \tag{1.13}$$

Thus, a Pisot number is a real algebraic number larger than one and its conjugates have an absolute value less than one. Tilings satisfy the PV property if they have point Fourier spectra. The PV property connected to this is that the n-th power of a Pisot number approaches integers as n approaches infinity. The PV property is a necessary condition for a pure point Fourier spectrum, however, it is not sufficient. The Thue–Morse sequence, for instance, has the PV property, but it has a singular continuous Fourier spectrum (see Sect. 1.1.4).

1.1.2 Octonacci Sequence

The Octonacci sequence, in mathematics better known as Pell sequence, describes the sequence of spacings of the Ammann quasilattice (8-grid) of the octagonal Ammann–Beenker tiling (see Sect. 1.2.5). The name Octonacci is composed from "Octo-" for octagonal and "-acci" from the Fibonacci sequence. It can be generated in analogy to the Fibonacci sequence by a substitution rule $\sigma : \mathrm{L} \mapsto \mathrm{LLS}, \mathrm{S} \mapsto \mathrm{L}$ to the two-letter alphabet $\{\mathrm{L}, \mathrm{S}\}$ [42]. It can also be created by recursive concatenation of shorter words according to the concatenation rule $w_{n+2} = w_{n+1}w_{n+1}w_n$. The generation of the first few words is shown in Table 1.2. The substitution matrix S reads

$$\sigma : \begin{pmatrix} \mathrm{L} \\ \mathrm{S} \end{pmatrix} \mapsto \underbrace{\begin{pmatrix} 2 & 1 \\ 1 & 0 \end{pmatrix}}_{=\mathsf{S}} \begin{pmatrix} \mathrm{L} \\ \mathrm{S} \end{pmatrix} = \begin{pmatrix} \mathrm{LLS} \\ \mathrm{L} \end{pmatrix}. \tag{1.14}$$

The evaluation of the determinant of the eigenvalue equation yields the characteristic polynomial

$$\lambda^2 - 2\lambda - 1 = 0 \tag{1.15}$$

Table 1.2. Generation of words $w_n = \sigma^n(\mathrm{S})$ of the Octonacci sequence by repeated action of the substitution rule $\sigma(\mathrm{L}) = \mathrm{LLS}$, $\sigma(\mathrm{S}) = \mathrm{L}$. ν_n^{L} and ν_n^{S} denote the frequencies of L and S, f_n are the Pell numbers

n	$w_{n+2} = w_{n+1}w_{n+1}w_n$	ν_n^{L}	ν_n^{S}	$\nu_n^{\mathrm{L}} + \nu_n^{\mathrm{S}}$
0	S	0	1	1
1	L	1	0	1
2	LLS	2	1	3
3	LLSLLSL	5	2	7
4	LLSLLSLLLSLLSLLLS	12	5	17
5	$\underbrace{\mathrm{LLSLLSLLLSLLSLLLS}}_{w_4} \underbrace{\mathrm{LLSLLSLLLSLLSLLLS}}_{w_4} \underbrace{\mathrm{LLSLLSL}}_{w_3}$	29	12	41
$\vdots$	$\vdots$	$\vdots$	$\vdots$	$\vdots$
n		f_n	$g_n - f_n$	g_n

with the eigenvalues $\lambda_1 = 1 + \sqrt{2} = (2 + \sqrt{8})/2 = 2.41421\ldots = \omega$, $\lambda_2 = 1 - \sqrt{2} = -0.41421\ldots$, which satisfy the PV property. The eigenvalue ω can be represented by the continued fraction expansion

$$\omega = 2 + \cfrac{1}{2 + \cfrac{1}{2 + \frac{1}{2 + \ldots}}}. \tag{1.16}$$

The frequencies $\nu_n^{\mathrm{L}} = f_n, \nu_n^{\mathrm{S}} = g_n - f_n$ of letters L, S in the word $w_n = \sigma^n(\mathrm{S})$, with $n \geq 1$, result to

$$\begin{pmatrix} \nu_n^{\mathrm{L}} + \nu_n^{\mathrm{S}} \\ \nu_n^{\mathrm{L}} - \nu_n^{\mathrm{S}} \end{pmatrix} = (\mathsf{S}^T)^{n-1} \begin{pmatrix} 1 \\ 1 \end{pmatrix}. \tag{1.17}$$

The Pell numbers $f_{n+2} = 2f_{n+1} + f_n$, with $n \geq 0$ and $f_0 = 0$ and $f_1 = 1$, form a series with $\lim_{n \to \infty} f_{n+1}/f_n = 1 + \sqrt{2} = 2.41421\ldots$, which is called the *silver ratio* or *silver mean*. They can be calculated as well by the following equation

$$f_n = \frac{\omega^n - \omega^{-n}}{\omega - \omega^{-1}} \tag{1.18}$$

The 2D analogue to the Octonacci sequence, a rectangular quasiperiodic 2-grid, can be constructed from the Euclidean product of two tilings that are each based on the Octonacci sequence. If only even or only odd vertices are connected by diagonal bonds then the so called Labyrinth tilings L_m and their duals L_m^*, respectively, result [42].

1.1.3 Squared Fibonacci Sequence

By squaring the substitution matrix S of the Fibonacci sequence, the squared FS can be obtained

$$\sigma : \begin{pmatrix} \mathrm{L} \\ \mathrm{S} \end{pmatrix} \mapsto \underbrace{\begin{pmatrix} 2 & 1 \\ 1 & 1 \end{pmatrix}}_{=\mathsf{S}^2} \begin{pmatrix} \mathrm{L} \\ \mathrm{S} \end{pmatrix} = \begin{pmatrix} \mathrm{LLS} \\ \mathrm{SL} \end{pmatrix}. \tag{1.19}$$

This operation corresponds to the substitution rule $\sigma : \mathrm{L} \mapsto \mathrm{LLS}, \mathrm{S} \mapsto \mathrm{SL}$ applied to the two-letter alphabet $\{\mathrm{L}, \mathrm{S}\}$.

The scaling properties of the squared FS can be derived from the eigenvalues λ_i of the substitution matrix S^2. For this purpose, the eigenvalue equation

$$\det |\mathsf{S}^2 - \lambda \mathsf{I}| = 0, \tag{1.20}$$

with the unit matrix I, has to be solved. The evaluation of the determinant yields the characteristic polynomial

$$\lambda^2 - 3\lambda + 1 = 0 \tag{1.21}$$

with the eigenvalues $\lambda_1 = \tau^2$, $\lambda_2 = 1/\tau^2 = 2 - \tau$, which satisfy the PV property, and the same eigenvectors as for the FS. The generation of the first few words is shown in Table 1.3.

Table 1.3. Generation of words $w_n = \sigma^n(L)$ of the squared Fibonacci sequence by repeated action of the substitution rule $\sigma(L) = LLS$, $\sigma(S) = SL$ or by concatenation. ν_n^L and ν_n^S denote the frequencies of L and S in the words w_n, F_n are the Fibonacci numbers

n	$w_n = w_{n-1}w_{n-1}\overline{w}_{n-1}$, $\overline{w}_n = \overline{w}_{n-1}w_{n-1}$ with $w_0 = L$ and $\overline{w}_0 = S$	ν_n^L	ν_n^S
0	L	1	0
1	LLS	2	1
2	LLSLLSSL	5	3
3	LLSLLSSLLLSLLSSLSLLLS	13	8
4	$\underbrace{\text{LLSLLSSLLLSLLSSLSLLLS}}_{w_3}\,\underbrace{\text{LLSLLSSLLLSLLSSLSLLLS}}_{w_3}\,\underbrace{\text{SLLLSLLSLLSSL}}_{\overline{w}_3}$	34	21
$\vdots$ $\vdots$		$\vdots$	$\vdots$
n		F_{2n+1}	F_{2n}

Table 1.4. Generation of words $w_n = \sigma^n(A)$ of the Thue–Morse sequence by repeated action of the substitution rule $\sigma(A) = AB$, $\sigma(B) = BA$ or by concatenation

n	$w_n = w_{n-1}\overline{w}_{n-1}$, $\overline{w}_n = \overline{w}_{n-1}w_{n-1}$ with $w_0 = A$ and $\overline{w}_0 = B$
0	A
1	AB
2	ABBA
3	ABBABAAB
4	ABBABAABBAABABBA
5	$\underbrace{\text{ABBABAABBAABABBA}}_{w_4}\,\underbrace{\text{BAABABBAABBABAAB}}_{\overline{w}_4}$
$\vdots$	$\vdots$

1.1.4 Thue–Morse Sequence

The (Prouhet-)Thue–Morse sequence results from the multiple application of the substitution rule $\sigma : A \mapsto AB, B \mapsto BA$ to the two-letter alphabet $\{A, B\}$. The substitution rule can be alternatively written employing the substitution matrix S

$$\sigma : \begin{pmatrix} A \\ B \end{pmatrix} \mapsto \underbrace{\begin{pmatrix} 1 & 1 \\ 1 & 1 \end{pmatrix}}_{=\mathsf{S}} \begin{pmatrix} A \\ B \end{pmatrix} = \begin{pmatrix} AB \\ BA \end{pmatrix}. \tag{1.22}$$

The frequencies in the sequence of the letters A and B are equal. The length of the sequence after the n-th iteration is 2^n. The Thue–Morse sequence can also be generated by concatenation: $w_{n+1} = w_n\overline{w}_n$, $\overline{w}_{n+1} = \overline{w}_n w_n$ with $w_0 = A$ and $\overline{w}_0 = B$ (Table 1.4).

The characteristic polynomial $\lambda^2 - 2\lambda = 0$ leads to the eigenvalues $\lambda_1 = 2$ and $\lambda_2 = 0$. Although these numbers show the PV property, the Fourier spectrum of the TMS can be singular continuous without any Bragg peaks. If we assign intervals of a given length to the letters A and B, then every other vertex belongs to a periodic substructure of period A+B. This is also the size of the unit cell of the PAS, which contains two further vertices at distances A and B, respectively, from its origin. All vertices of the PAS are equally weighted. The Bragg peaks, which would result from the PAS, are destroyed for special values of A and B by the special order of the Thue–Morse sequence leading to a singular continuous Fourier spectrum. The broad peaks split into more and more peaks if the resolution is increased. In the generic case, however, a Fourier module exists beside the singular continuous spectrum. Depending on the decoration, the Thue–Morse sequence will show Bragg peaks besides the singular continuous spectrum (see Fig. 6.2).

1.1.5 1D Random Sequences

It is not possible to say much more about general 1D random sequences than that their Fourier spectra will be absolutely continuous. However, depending on the parameters (number of prototiles, frequencies, correlations), the spectra can show rather narrow peaks for particular reciprocal lattice vectors. General formulas have been derived for different cases of 1D random sequences [15].

The diffraction pattern of a FS, decorated with Al atoms and randomized by a large number of phason flips, is shown in Fig. 1.2. Although the Fourier spectrum of such a random sequence is absolutely continuous, it is peaked for reciprocal space vectors of the type m/L and n/S with $m \approx n\tau$, with m and n two successive Fibonacci numbers.

The continuous diffuse background under the peaked spectrum of the randomized FS can be described by the relation $I_{\text{diff}} \sim f(h)[1 - \cos(2\pi h(L - S)]$ ($f_{\text{Al}}(h)$ is the atomic form factor of Al, L, and S are the long and short interatomic distances in the Al decorated FS).

1.2 2D Tilings

The symmetry of periodic tilings, point group and plane group (2D space group), can be given in a straightforward way (see, e.g., Table 1.7). In case of general quasiperiodic tilings, there is no 2D space or point group symmetry at all. Some tilings show scaling symmetry. In case of singular tilings, there is just one point of global point group symmetry other than 1. The orientational order of equivalent tile edges ("bond-orientational order"), however, is clearly defined and can be used as one parameter for the classification of tilings. This means, one takes one type of tile edge, which may be arrowed or not, in all orientations occurring in the tiling and forms a star. The point symmetry group of that star is then taken for classifying the symmetry of the tiling.
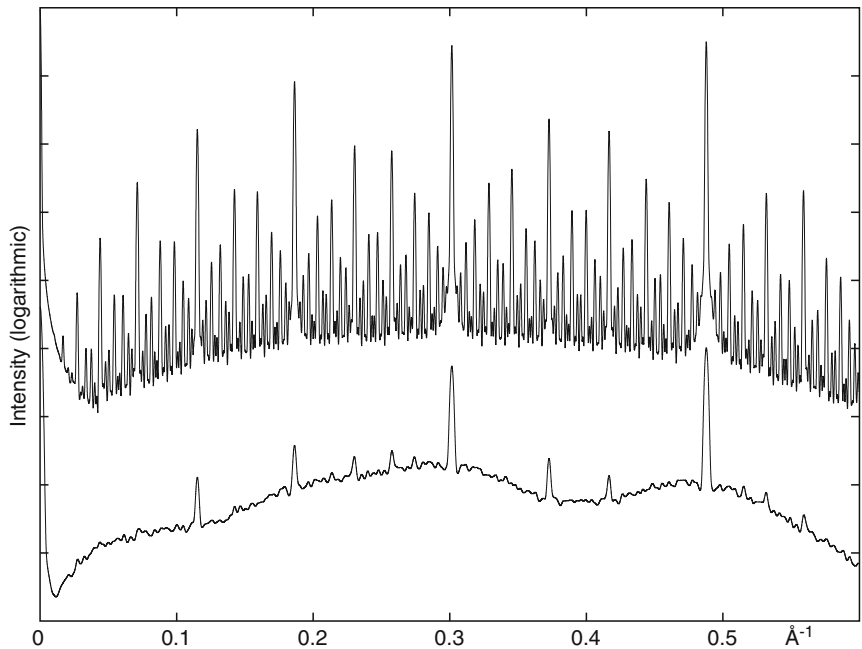
Fig. 1.2. Diffraction patterns of a Fibonacci sequence before (*top*) and after (*bottom*) partial randomization ($\approx 25\%$ of all tiles have been flipped). The vertices of the Fibonacci sequence are decorated by Al atoms with the short distance S = 2.4 Å; the diffraction patterns have been convoluted with a Gaussian with FWHM = 0.001 Å^{-1} to simulate realistic experimental resolution (courtesy of Th. Weber)

Table 1.5. Point groups of 2D quasiperiodic structures (tilings) (based on [13]). Besides the general case with n-fold rotational symmetry, a few practically relevant special cases are given. k denotes the order of the group

Point group type	k	Conditions	$n = 5$	$n = 7$	$n = 8$	$n = 10$	$n = 12$	$n = 14$
nmm	$2n$	n even			$8mm$	$10mm$	$12mm$	$14mm$
nm	$2n$	n odd	$5m$	$7m$				
n	n		5	7	8	10	12	14

This is related to the autocorrelation (Patterson) function. In Table 1.5, the possible point symmetry groups of 2D quasiperiodic structures (tilings) are given.

The general space group symmetries possible for 2D quasiperiodic structures with rotational symmetry $n \leq 15$ are listed in Table 1.6.

By taking the symmetry of the Patterson function for the tiling symmetry, it is not possible to distinguish between centrosymmetric and non-centrosymmetric tilings. This means that in the case of 2D tilings only

Table 1.6. Space groups of 2D quasiperiodic structures (tilings) (based on [32]). Besides the general case with n-fold rotational symmetry, a few practically relevant special cases are given. The lattice symmetry is $2n$ for n odd

Point group	Conditions	$n = 5$	$n = 7$	$n = 8$	$n = 10$	$n = 12$	$n = 14$
nmm	n even			$p8mm$	$p10mm$	$p12mm$	$p14mm$
	$n = 2^p$			$p8gm$			
$nm1$	n odd	$5m1$	$7m1$				
$n1m$	n odd	$51m$	$71m$				
n		$p5$	$p7$	$p8$	$p10$	$p12$	$p14$

even rotational symmetries could be discriminated, both pentagonal and decagonal tilings have decagonal Patterson symmetry, for instance. The same is true for the Laue symmetry, which is the symmetry of the intensity weighted reciprocal space, i.e. of the Bragg intensity distribution.

The symmetry can also be defined for the local isomorphism (LI) class of a tiling. Then a tiling is said to admit a certain point symmetry, if this symmetry maps the tiling onto another tiling in the same LI class. The transformed tiling cannot be distinguished from the original one by any local means, since tilings of the same LI class are locally indistinguishable from each other. In this sense, the concept of point symmetry differs for quasiperiodic structures from periodic ones. The point group of a tiling here is the point group of its LI class. For a periodic tiling, the LI class consists of only one element, and the definition of point symmetry reduces to the usual one.

Perhaps the best approach is based on the symmetry of the structure-factor-weighted reciprocal lattice, which even allows to derive a kind of space group symmetry. The full equivalence of such a Fourier space approach to a derivation of space groups in direct space has been demonstrated for periodic structures by [5] and applied to quasiperiodic structures by [32]. This kind of space group symmetry corresponds to that which can be obtained from the higher-dimensional approach (see Chap. 3).

1.2.1 Archimedean Tilings

The Archimedean tilings, which are all periodic, have been derived by Kepler in analogy to the Archimedean solids (see Sect. 2.1). Three of them are regular, i.e. consist of congruent regular polygons and show only one type of vertex configuration. The regular tilings are the triangle tiling 3^6, the square tiling 4^4 and the hexagon tiling 6^3. A vertex configuration n^m is defined by the kind of polygons along a circuit around a vertex. For instance, 6^3 means that at a vertex 3 hexagons meet.

The eight semiregular tilings are uniform, i.e. have only one type of vertex (vertex transitive), and consist of two or more regular polygons as tiles.
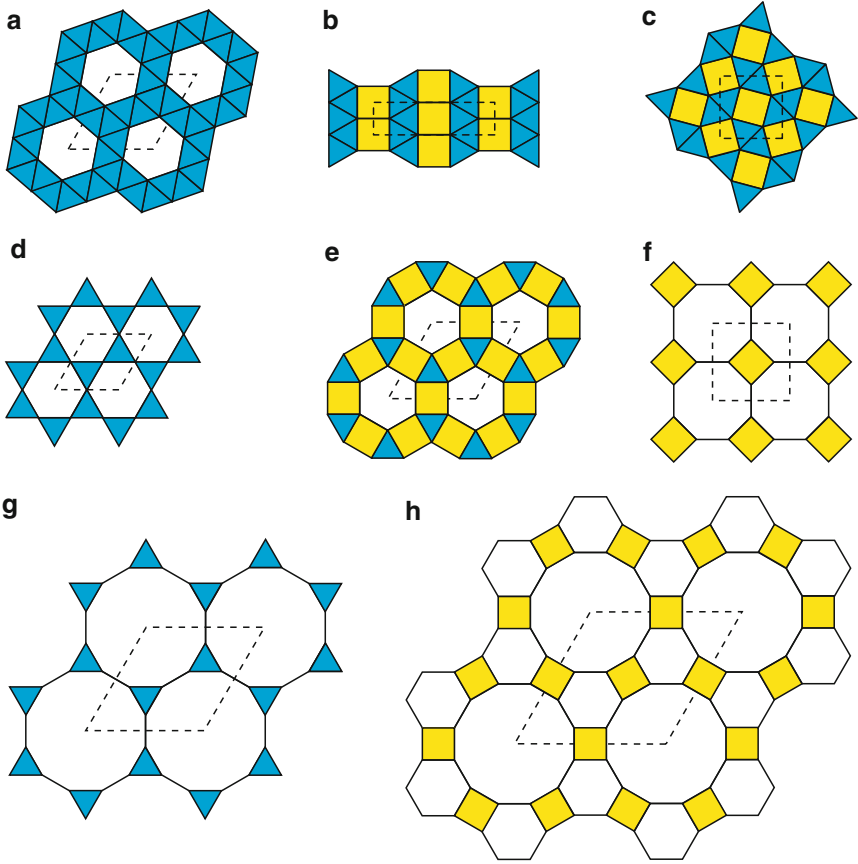
Fig. 1.3. The eight semiregular Archimedean tilings: (**a**) Snub hexagonal tiling $3^4.6$, (**b**) elongated triangular tiling $3^3.4^2$, (**c**) snub square tiling $3^2.4.3.4$, (**d**) trihexagonal tiling 3.6.3.6, (**e**) small rhombitrihexagonal tiling 3.4.6.4, (**f**) truncated square tiling 4.8^2, (**g**) truncated hexagonal tiling 3.12^2, and (**h**) great rhombitrihexagonal tiling 4.6.12. The unit cells are outlined by dashed lines

The Archimedean tilings are discussed here since they are quite common in structures of intermetallic phases and soft QC approximants. Particularly interesting for QC approximants are the tilings 4.8^2 with octagonal tiles, and 3.12 and 4.6.12, which contain dodecagonal tiles. Some characteristic data of the semiregular tilings that are depicted in Fig. 1.3 are listed in Table 1.7.

1.2.2 Square Fibonacci Tiling

The square Fibonacci tiling is a simple example of a 2D quasiperiodic tiling with crystallographic point symmetry (4mm) [24]. It can be generated, for instance, by superposition of two Fibonacci line grids, which are orthogonal

Table 1.7. Characteristic data for the eight semiregular Archimedean tilings. The number of vertices n_V per unit cell is given; the density is calculated for a close packing of equal circles at the vertices. In the second lines, the lattice parameter a is given for a tile edge length of 1 and the Wyckoff positions occupied are listed [28]

Name	Vertex Configuration	n_V	Plane Group a	Density Wyckoff position
Snub hexagonal tiling[a]	$3^4.6$	6	$p6$ $a = \sqrt{7}$	$\pi\sqrt{3}/7 = 0.7773$ $6(d)\ x = 3/7, y = 1/7$
Elongated triangular tiling	$3^3.4^2$	4	$c2mm$ $a = 1$ $b = 2 + \sqrt{3}$	$\pi/(2 + \sqrt{3}) = 0.8418$ $4(e)\ y = (1 + \sqrt{3})/(4 + 2\sqrt{3})$
Snub square tiling	$3^2.4.3.4$	4	$p4gm$ $a = (2 + \sqrt{3})^{1/2}$	$\pi/(2 + \sqrt{3}) = 0.8418$ $4(c)\ x = 1 - -1/4$ $[(2 - \sqrt{3})(2 + \sqrt{3})]^{1/2}$
Trihexagonal tiling[b]	$3.6.3.6$	3	$p6mm$ $a = 2$	$\pi\sqrt{3}/8 = 0.6802$ $3(c)$
Small rhombitri-hexagonal tiling	$3.4.6.4$	6	$p6mm$ $a = 1 + \sqrt{3}$	$\pi\sqrt{3}/(4 + 2\sqrt{3}) = 0.7290$ $6(e)\ x = 1/(3 + \sqrt{3})$
Truncated square tiling	4.8^2	4	$p4mm$ $a = 1 + \sqrt{2}$	$\pi/(3 + 2\sqrt{2}) = 0.5390$ $4(e)\ x = 1/(2 + 2\sqrt{2})$
Truncated hexagonal tiling	3.12^2	6	$p6mm$ $a = 2 + \sqrt{2}$	$\pi\sqrt{3}/(7 + 4\sqrt{3}) = 0.3907$ $6(e)\ x = (1 - 1/\sqrt{3})$
Great rhombitri-hexagonal tiling	$4.6.12$	12	$p6mm$ $a = 3 + \sqrt{3}$	$\pi/(3 + 2\sqrt{3}) = 0.4860$ $12(f)\ x = 1/(3\sqrt{3} + 3),$ $y = x + 1/3$

[a] Two enantiomorphs
[b] Kagome net; quasiregular tiling because all edges are shared by equal polygons

to each other (Fig. 1.4). The substitution rule, also depicted in Fig. 1.4, can be written employing the substitution matrix S

$$\mathsf{S} = \begin{pmatrix} 1\ 1\ 1 \\ 1\ 0\ 0 \\ 2\ 0\ 1 \end{pmatrix}, \tag{1.23}$$

with the characteristic polynom $-x^3 + 2x^2 + 2x - 1 = -(1 + x)(1 - 3x + x^2)$ and the eigenvalues $\lambda_1 = \tau^2$ and $\lambda_2 = \tau^{-2}$ for the irreducible component $(1 - 3x + x^2)$. Therefore, the PV property is fulfilled. The tile frequencies are τ^{-2} for the large squares, τ^{-4} for the small squares and $2\tau^{-3}$ for the rectangles (independent from their orientation).

The square Fibonacci tiling is quasiperiodic, if based on prototiles of different sizes. In case the FS results from a quasiperiodic distribution of two types of atoms, or atoms and vacancies on a periodic lattice, then one periodic direction can result. In the example shown in Fig. 1.5, a square lattice is decorated
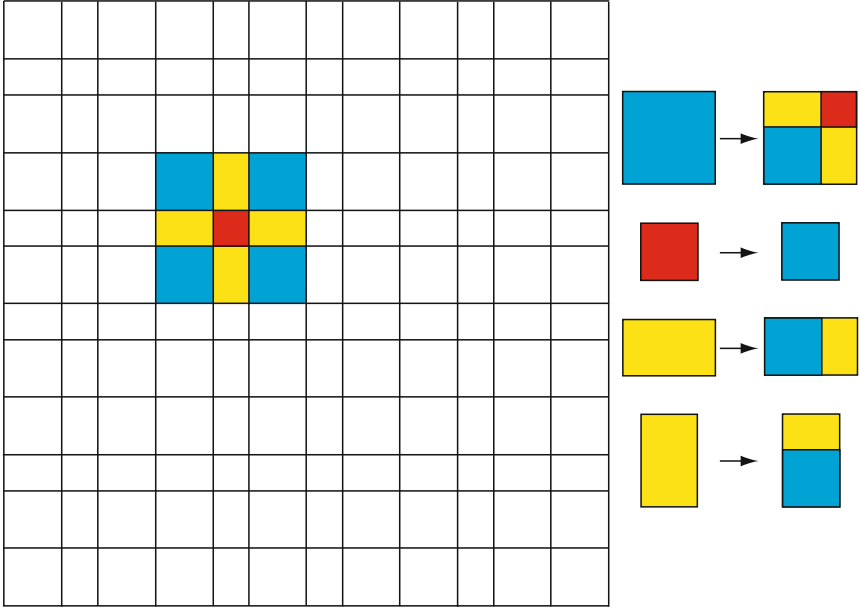
Fig. 1.4. The square Fibonacci tiling generated by superposition of two, to each other orthogonal, Fibonacci line grids. The minimum covering cluster is marked in the tiling, the inflation rule is shown at right

by full circles (L) and vacancies (S) like a FS in two orthogonal directions and with one mirror line along one diagonal. One of the two diagonal directions of the underlying lattice then results to be periodic. This pattern has the property that vacancies are never closer to each other than one square diagonal and that they are fully surrounded by the filled circles with the distance of one square edge.

Analogously, the 3D cube Fibonacci tiling can be created, which may be of interest for vacancy ordered structures.

1.2.3 Penrose Tiling (PT)

The Penrose tiling was discovered by Roger Penrose [30] and popularized by Martin Gardner in the popular scientific journal *Scientific American* [8]. There are several versions of the PT presented in the book *Tilings and Patterns* by Grünbaum and Shephard [9]: a pentagon based tiling (P1), a kite and dart version of it (P2) and a rhomb tiling (P3). All three of them are mutually locally derivable and belong to the Penrose local isomorphism (PLI) class. According to its reciprocal space symmetry, the PT is a decagonal quasiperiodic tiling. The PLI class tilings possess matching rules that force quasiperiodicity. If the matching rules are relaxed other tilings become possible, which may be quasiperiodic, periodic, or all kinds of non-periodic up to
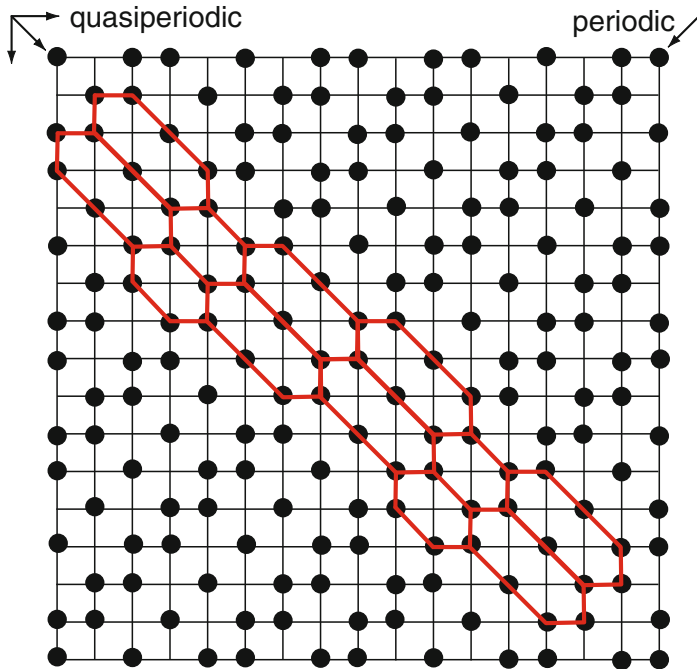
Fig. 1.5. Substitutional square Fibonacci tiling. The vertices of a square lattice are either occupied (*full circles*) or unoccupied. Along the horizontal and vertical axes as well as along one diagonal the substitutional sequence (distances between occupied vertices) is the Fibonacci sequence. Along the other diagonal, the pattern is periodic

fully random. The binary tiling will be discussed as an example, which may have some importance for the description of real quasicrystals.

1.2.3.1 Rhomb Penrose Tiling

The rhomb PT [29, 30] can be constructed from two unit tiles: a skinny (acute angle $\alpha = \pi/5$) and a fat rhomb (acute angle $\alpha = 2\pi/5$) with equal edge lengths a_r and areas $a_r^2 \sin \pi/5$ and $a_r^2 \sin 2\pi/5$, respectively. Their areas and frequencies in the PT are both in the ratio $1 : \tau$. The construction has to obey matching rules, which can be derived from the scaling properties of the PT (Fig. 1.6). The local matching rules are perfect, that means that they force quasiperiodicity. However, there are no growth rules, which restrain the growing tiling from running into dead ends.

The eight different vertex configurations and their relative frequencies in the regular PT are shown in Fig. 1.7. The letter in the symbols indicates the topology, the upper index gives the number of linkages and the lower index the number of double arrows [16, 29].

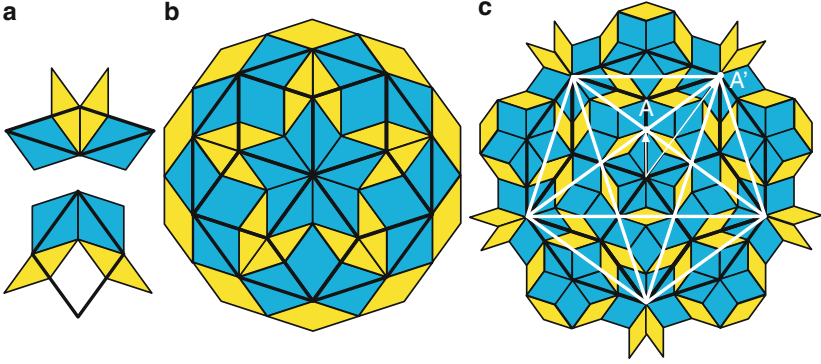**Fig. 1.6.** Scaling properties of the Penrose tiling. (**a**) The substitution (inflation) rule for the rhomb prototiles. In (**b**) a PT (*thin lines*) is superposed by another PT (*thick lines*) scaled by S, in (**c**) scaling by S^2 is shown. A subset of the vertices of the scaled tilings are the vertices of the original tiling. The rotoscaling operation S^2 is also a symmetry operation of a pentagram (*white lines*), mapping each vertex of a pentagram onto another one. This is demonstrated in (**c**) on the example of the vertex A which is mapped onto A′ by S^2

The set of vertices of the PT, M_{PT}, is a subset of the vector module $M = \left\{ \mathbf{r} = \sum_{i=0}^{4} n_i a_r \mathbf{e}_i \,\middle|\, \mathbf{e}_i = (\cos 2\pi i/5, \sin 2\pi i/5) \right\}$. M_{PT} consists of five subsets

$$M_{\mathrm{PT}} = \cup_{k=0}^{4} M_k \quad \text{with} \quad M_k = \left\{ \pi^{\|}(\mathbf{r}_k) \,\middle|\, \pi^{\perp}(\mathbf{r}_k) \in T_{ik}, i = 0, \dots, 4 \right\} \quad (1.24)$$

and $\mathbf{r}_k = \sum_{j=0}^{4} \mathbf{d}_j \, (n_j + k/5)$, $n_j \in Z$ (for the definition of d_j see Sect. 3.1). The i-th triangular subdomain T_{ik} of the k-th pentagonal occupation domain corresponds to

$$T_{ik} = \left\{ \mathbf{t} = x_i \mathbf{e}_i + x_{i+1} \mathbf{e}_{i+1} \,\middle|\, x_i \in [0, \lambda_k], x_{i+1} \in [0, \lambda_k - x_i] \right\} \quad (1.25)$$

with λ_k the radius of a pentagonally shaped occupation domain: $\lambda_0 = 0$, for $\lambda_{1,\dots,4}$ see Eq. (3.138). Performing the scaling operation $\mathsf{S}M_{\mathrm{PT}}$ with the matrix

$$\mathsf{S} = \begin{pmatrix} 0 & 1 & 0 & \bar{1} \\ 0 & 1 & 1 & \bar{1} \\ \bar{1} & 1 & 1 & 0 \\ \bar{1} & 0 & 1 & 0 \end{pmatrix}_D = \left(\begin{array}{cc|cc} \tau & 0 & 0 & 0 \\ 0 & \tau & 0 & 0 \\ \hline 0 & 0 & -\frac{1}{\tau} & 0 \\ 0 & 0 & 0 & -\frac{1}{\tau} \end{array} \right)_V = \begin{pmatrix} \mathsf{S}^{\|} & 0 \\ 0 & \mathsf{S}^{\perp} \end{pmatrix}_V \quad (1.26)$$

yields a tiling dual to the original PT, enlarged by a factor τ. The subscript D refers to the 4D crystallographic basis (D-basis), while subscript V indicates that the vector components refer to a Cartesian coordinate system (V-basis) (see Sect. 3.1). Here S is applied to the projected 4D crystallographic basis (D-basis), i.e. the star of four rationally independent basis
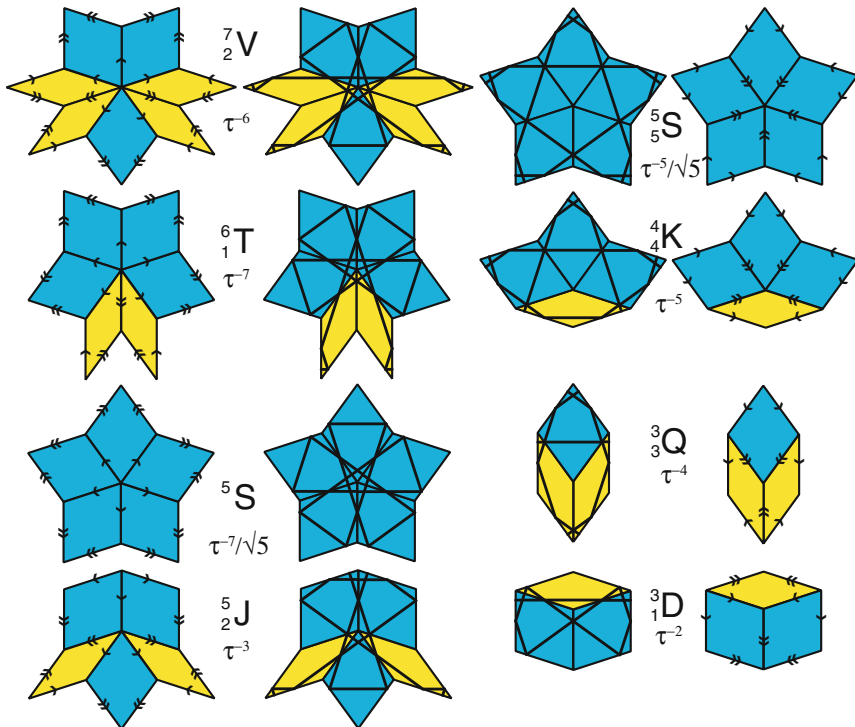
Fig. 1.7. The eight different vertex configurations of the regular Penrose tiling shown for decorations by *arrows* (*single* and *double*) and by Ammann line segments. The relative vertex frequencies are given below the vertex symbols. The configurations $^5_5$S, $^4_4$K, and $^3_3$Q transform into star (S), boat (B), and hexagon (H) tiles of the HBS tiling if those vertices are omitted where only double-arrowed edges meet (see Sect. 1.2.3.2)

vectors $\mathbf{a}_i = a_r \mathbf{e}_i$, $i = 1, \ldots, 4$. If a 2D Cartesian coordinate system is used, then the submatrix $\mathsf{S}^{\parallel}$ has to be applied.

Only scaling by S^{4n} results in a PT (increased by a factor τ^{4n}) of original orientation. Then the relationship $\mathsf{S}^{4n} M_{\mathrm{PT}} = \tau^{4n} M_{\mathrm{PT}}$ holds. S^2 maps the vertices of an inverted and by a factor τ^2 enlarged PT upon the vertices of the original PT. This operation corresponds to a hyperbolic rotation in superspace [20]. The rotoscaling operation $\Gamma(10)\mathsf{S}^2$ leaves the subset of vertices of a PT forming a pentagram invariant (Fig. 1.6).

By a particular decoration of the unit tiles with line segments, infinite lines (Ammann lines) are created forming a Fibonacci penta-grid (5-grid, "Ammann quasilattice" [23]) (Fig. 1.8). The line segments can act as matching rules forcing strict quasiperiodicity. In case of simpleton flips, the Ammann lines are broken (see Fig. 1.8). The dual of the Ammann quasilattice is the deflation of the original PT.
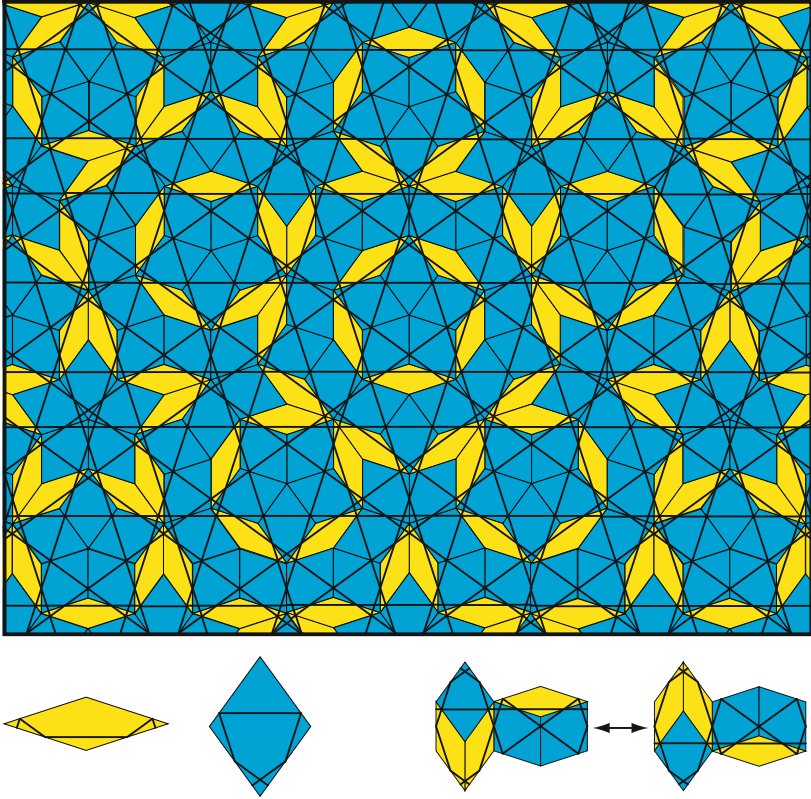
Fig. 1.8. The Penrose tiling with Amman lines drawn in. The decoration of the unit tiles by Ammann line segments and the action of simpleton flips are shown at the bottom

The third variant of the PT is the kite and dart tiling, denoted P2 tiling in the book by Grünbaum and Shephard [9]. Its relationship to the rhomb PT (P3) tiling is shown in Fig. 1.9. Starting with the kite and dart tiling (Fig. 1.9(a)), we cut the tiles into large acute and small obtuse isosceles triangles as shown in Fig. 1.9(b) and obtain the Robinson triangle tiling. The edge lengths of the triangles are in the ratio τ. While the black dots form a sufficient matching rule for the kites and darts, the isosceles triangles need, additionally, an orientation marker along the edges marked by two filled circles. In case of the acute triangle, this is an arrow pointing away from the corner where the isosceles edges meet; in case of the obtuse triangle, it is just the opposite.

If we fuse now all pairs of baseline connected acute triangles to skinny rhombs, and pairs of long-edge connected acute triangles together with pairs of short-edge linked obtuse triangles to fat rhombs, then we end up with a rhomb PT (Fig. 1.9(c)). The rhomb edge from the marked to the unmarked vertex also gets an orientation, which is usually marked by a double arrow.

Fig. 1.9. The interrelations between the (**a**) kite and dart tiling (P2), the (**b**) triangle tiling and (**c**) the rhomb Penrose tiling (P3). The *full circles* form a matching rule for the kites and darts
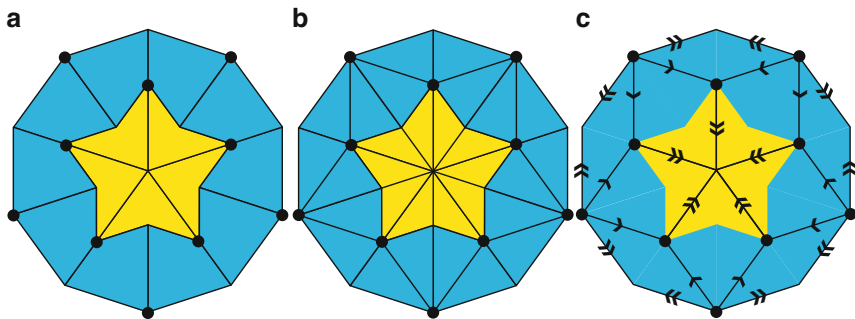
The remaining color decoration of the fat rhombs marks the position of the one disappeared vertex, which was present in the kite and dart tiling.

1.2.3.2 Pentagon PT and the Dual Hexagon-Boat-Star (HBS) Tiling

The pentagon Penrose tiling (P1) consists of pentagons, skinny rhombs, boats, and stars (Fig. 1.10). The pentagons have three different decorations with Amman bars and inflation/deflation rules [27]. There exists a one-to-one relationship to the Penrose rhomb tiling (P3 tiling) [16]. Note that the pentagons show five different decorations with rhombs.

If we connect the centers of the pentagons then we obtain the HBS tiling, which is dual to the P1 tiling. In the P1 tiling, all spiky tiles are fully surrounded by pentagon tiles. Consequently, the vertices of the H tile correspond to the centers of pentagons surrounding a rhomb tile. Analogously, the vertices of a B tile are the centers of pentagons surrounding a boat tile of the P1 tiling, and those of an S tile the centers of pentagons framing a star tile of the P1 tiling. The prototile frequencies are in a ratio $n_H : n_B : n_S = \sqrt{5}\tau : \sqrt{5} : 1$ [25].

The interrelations between the HBS tiling and the P3 tiling are as follows. As shown in Fig. 1.10, the H tile consists of one fat and two skinny rhombs, the B tile of three fat and one skinny rhomb, and the S tile of five fat rhombs. These prototile decorations with rhomb tiles correspond to the vertex configurations $^5_5$S, $^4_4$K, and $^3_3$Q of Fig. 1.7. If those vertices are omitted, where only double-arrowed edges meet, the star, boat and hexagon tiles of the HBS tiling are obtained.

1.2.3.3 The Binary Rhomb Tiling

If we relax the matching rules of the rhomb PT to the condition that at each vertex only tile angles meet which are all odd or all even multiples of $\pi/5$, then we obtain a binary tiling [22]. There are seven different vertex surroundings possible. The binary tiling is a substitution tiling without the PV property
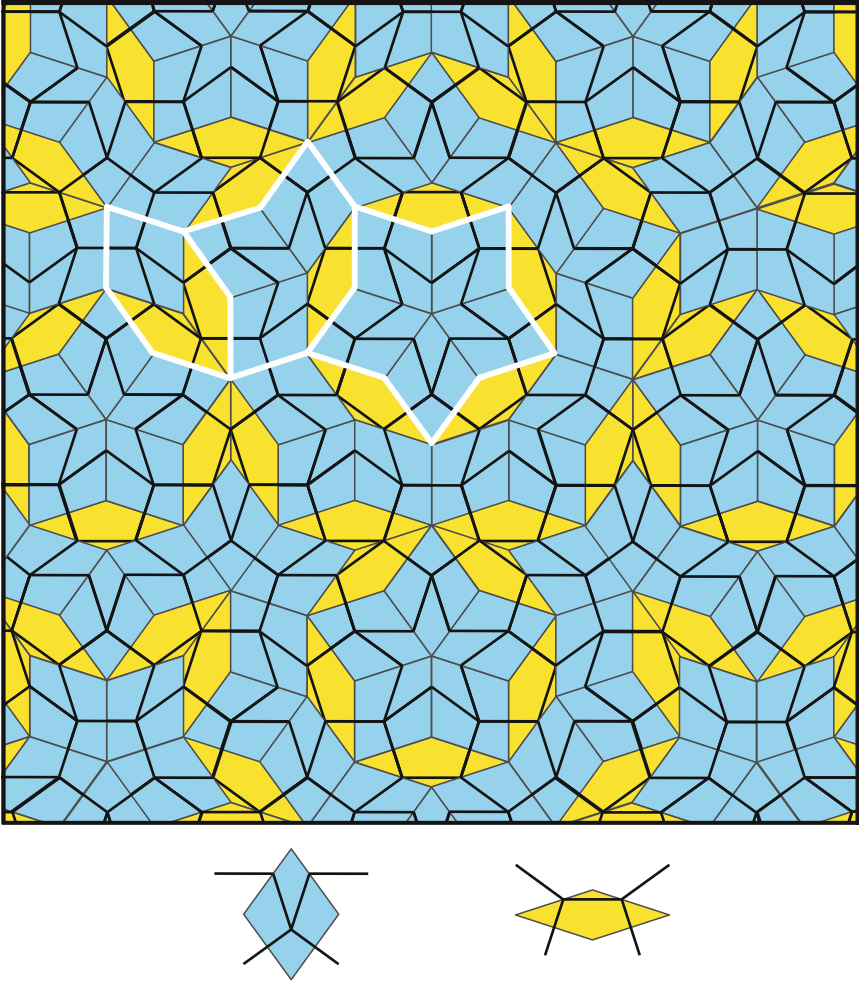
Fig. 1.10. Penrose pentagon tiling (P1 tiling, *black lines*) with underlying Penrose rhomb tiling (P3 tiling). At the bottom, the decoration of the rhomb prototiles is shown that produces the pentagon tiling. Hexagon, boat, and star supertiles are outlined by a thick white line

[33]. Its substitution rule is shown in (Fig. 1.11). The first substitution of the fat rhomb gives a boat tile, that of the skinny rhomb creates a hexagon tile. In further generations also star tiles appear showing the relationship to HBS tilings. The matching rules are in agreement but do not enforce the substitution rule. However, it is possible to define non-local matching rules which force quasiperiodicity. This can be done, for instance, by a particular decoration of τ^2 inflated Penrose rhombs which then acts as perfect local matching rule [4].
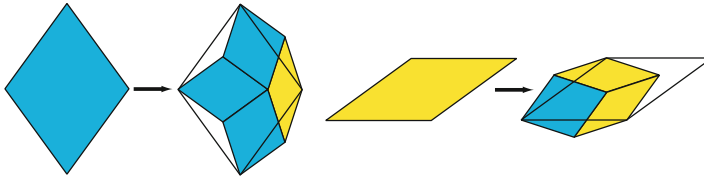
Fig. 1.11. The substitution rule of the binary rhomb tiling. The first substitution leads to a boat and a hexagon tile

1.2.3.4 Gummelt Covering

Particular quasiperiodic tilings, including some with 8-, 10-, and 12-fold symmetry that are relevant for real QC, can be fully covered by one or more covering clusters. By covering cluster we mean a patch of tiles of the respective tiling. In Fig. 1.12, the decoration of the Gummelt decagon with patches of the kite and dart tiling, the Robinson triangle tiling, the rhomb PT, and the pentagon PT are shown together with the (in size) inflated tilings.

The Gummelt decagon is a single, mirror-symmetrical, decagonal cluster with overlap rules that force perfectly ordered structures of the PLI class [10] (Fig. 1.13). There are different ways of marking the overlap rules. In Fig. 1.13 (a)–(e), the rocket decoration is used, in (h) directed overlap lines are shown. For the rocket decoration, the colors of the overlap areas of two Gummelt decagons must agree. The overlap lines in (h) form a fat Penrose tile, which is marked by arrows (matching rule for the perfect PT) in (h) and unmarked in (i). There are nine different allowed coordinations of a central Gummelt decagon by other decagons possible so that all decagon edges are fully covered. The coordination numbers are 4, 5 or 6.

The centers of the decagons form a pentagon PT (marked pentagons, rhomb, boat, star) when the overlap rules are obeyed (Fig. 1.14). The dual to it is the so-called τ^2-HBS supertiling. The H tiles contain 4 Gummelt decagon centers, the B tiles 7 and the S tiles 10. The HBS tile edge length is τ^2 times that of the decagon, which itself is equal to τ times the edge length of the underlying rhomb PT (Fig. 1.12(c)).

It is also possible to assign an HBS tiling to a Gummelt decagon covering where the tiling edge length is equal to that of the decagon [41]. A decagon is decomposed in two hexagon tiles (containing the rockets) and one boat tile. Depending on the kind of overlap, H, B and S tiles result from merging the original tiles. By relaxing the overlap rules (Fig. 1.13(i)) one can obtain random decagon coverings [12] (Fig. 1.13(f) and (g)). The decagon centers now form a random pentagon tiling and the pentagon centers a random HBS supertiling, called two-level random PT. In Fig. 1.13(i) a fully relaxed overlapping rule is shown. If only the single arrows in Fig. 1.13(h) are abandoned, then we get an intermediate overlap rule [7]. The resulting tilings are related to random rhomb PT, which still satisfy the double-arrow condition, and are called four-level random PT.
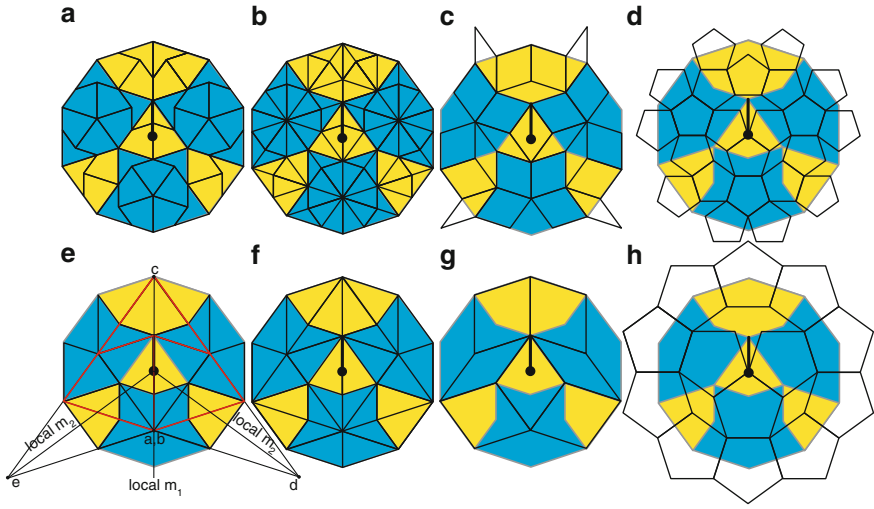
Fig. 1.12. Gummelt-decagon covering patches. (**a**) Kite and dart tiling, (**b**) Robinson triangle tiling, (**c**) rhomb PT, (**d**) pentagon PT, and the in size by a factor τ inflated tilings in (**e**)–(**h**) (after [11]). In (**e**), the decoration with an ace is shown, which consists of two kites and one dart, all of them inflated in size by a factor τ. There are also the local mirror planes drawn in as well as the rotation points a–e
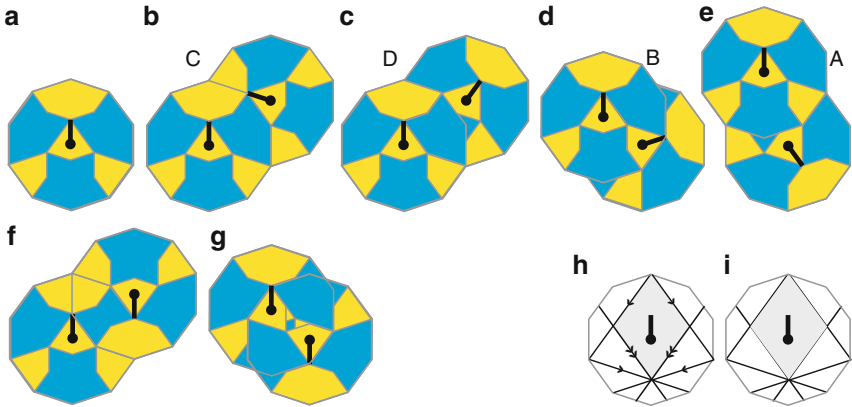
Fig. 1.13. Gummelt-decagon (**a**) and its overlap rules for the construction of perfect tilings of the PLI class (**b**–**e**, **h**). Pairs of overlapping Gummelt decagons are related by one of the following rotations around the points marked a–e in Fig. 1.12(**e**). A: $4\pi/5$ around the points a, b; B: $2\pi/5$ around a, b; C: $2\pi/5$ around c; D: $\pi/5$ around d. With relaxed (unoriented) overlap rules random decagonal coverings can be obtained (**f**, **g**, **i**). A fat Penrose rhomb tile is marked gray in (**h**, **i**)
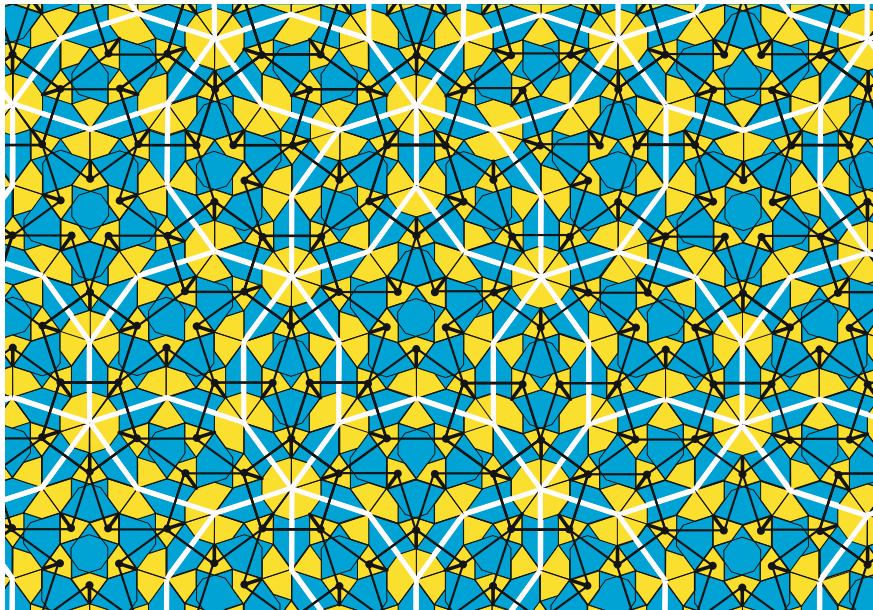
Fig. 1.14. Gummelt-decagon covering. The centers of the decagons of the type shown in Fig. 1.13(a) form a marked Penrose pentagon tiling (P1 tiling). Connecting the pentagon centers leads to a HBS supertiling (*white lines*)

Lord and Ranganathan [25] derived rules for the decoration of Gummelt decagons that are consistent with a strictly quasiperiodic pattern (G pattern) of these decagons. They identified the regions in the cartwheel pattern inscribed in the decagon that can be equally decorated throughout a G pattern. These regions are the dark-gray (online: blue) kites (K) and darts (D) of Fig. 1.12(a) and the τ-inflated light-gray (online: yellow) kites (L) of Fig. 1.12(e), which result from merging the small light-gray (online: yellow) kites and darts of Fig. 1.12(a). The G patterns resulting from decagons decorated with these prototiles are called DKL tilings. The prototile frequencies are in a ratio $n_D : n_K : n_L = \tau : \sqrt{5} : 1$. DKL tilings, and therewith G patterns as well, scale with a τ^2 inflation rule.

Pairs of overlapping Gummelt decagons are related by one of the following rotations around the points marked a–e in Fig. 1.12(e). A: $4\pi/5$ around the points a, b; B: $2\pi/5$ around a, b; C: $2\pi/5$ around c; D: $\pi/5$ around d; E: $\pi/5$ around e. Within the overlapping regions there are local symmetries, which can be used to classify 2D G patterns or 3D G-pattern based columnar coverings. There are just three types of 2D G patterns, which are listed in Table 1.8.

The number of symmetry types of 3D G patterns, where Gummelt decagons are replaced by Gummelt columns, which are periodic along the column axis, amounts to 165 (Table 1.9). Along the periodic directions,

Table 1.8. Local symmetries of the overlap regions in 2D G patterns (from [25]). The symbols m refer to the local mirror planes marked in 1.12(e), and B–E to the rotations B: $2\pi/5$ around a, b; C: $2\pi/5$ around c; D: $\pi/5$ around d; E: $\pi/5$ around e. The points a–e are marked in 1.12(e). The symbol p denotes primitive translations

	m_1	m_2	D, E	B, C
p 10	-	-	10	5
p 5m	-	m	5m	5
p 10m	m	m	10m	5m

there are screw axes and local glide planes possible similar as in the well known rod groups. Based on these symmetries, which are compatible with strictly quasiperiodic G patterns, proper decorations of columnar structures of quasicrystals can be derived. On the other hand, experimentally obtained structure models can be tested on whether or not they admit one of the allowed symmetries.

1.2.4 Heptagonal (Tetrakaidecagonal) Tiling

By heptagonal (tetrakaidecagonal) tiling we refer to tilings with 14-fold diffraction symmetry. The tilings have three rhombic prototiles with acute angles of $\pi/7$, $2\pi/7$, and $3\pi/7$ (Fig. 1.15). The global rotational symmetry of singular tilings of this kind can be 7- or 14-fold. Heptagonal symmetry is the lowest that is associated with a cubic irrational number, and shows, therefore, unusual properties.

A number λ is called a Pisot number, if it is a real algebraic number (a root of an irreducible polynomial) greater than 1, and all its conjugates have absolute values less than 1. The tilings shown here satisfy this condition as the eigenvalues of the reducible 7D scaling matrix S are 4.04892, 1, -0.69202, and -0.35680. The eigenvalue 1 corresponds to one redundant dimension, and can be discarded for the 6D irreducible representation of S in 6D. The three remaining eigenvalues are the solutions of the irreducible polynomial

$$x^3 - 3x^2 - 4x - 1 = 0, \tag{1.27}$$

related to S. According to a basis as defined in Fig. 1.16 where the scaling symmetry is visualized, the scaling matrix can be written in 7D as

$$\mathsf{S} = \begin{pmatrix} 1 & 1 & 0 & \bar{1} & \bar{1} & 0 & 1 \\ 1 & 1 & 1 & 0 & \bar{1} & \bar{1} & 0 \\ 0 & 1 & 1 & 1 & 0 & \bar{1} & \bar{1} \\ \bar{1} & 0 & 1 & 1 & 1 & 0 & \bar{1} \\ \bar{1} & \bar{1} & 0 & 1 & 1 & 1 & 0 \\ 0 & \bar{1} & \bar{1} & 0 & 1 & 1 & 1 \\ 1 & 0 & \bar{1} & \bar{1} & 0 & 1 & 1 \end{pmatrix}_D . \tag{1.28}$$

Table 1.9. Local symmetries of the overlap volumes in 3D G patterns (adapted from [25]). The symbols m, c refer to the directions of local mirror planes marked in 1.12(e), and B, C, D, E to the rotations B: $2\pi/5$ around a, b; C: $2\pi/5$ around c; D: $\pi/5$ around d; E: $\pi/5$ around e. The points a–e are marked in 1.12(e). The symbol P denotes primitive translations along the periodic axis. Where C and E are empty, they are the same as B and D, respectively. 5_p and 10_q are screw axes; $p = 0$ and $q = 0$ refer to simple rotations

Rod symmetry	m_1	m_2	D	B	C	E
$P10_q(p)$	-	-	10_q	5_p	5_p	10_{2p-q}
$P10/m$	-	-	$10/m$	$\overline{10}(=5/m)$		
$P\overline{5}(p)$	-	-	$\overline{5}$	5_p	5_{2p}	$\overline{5}(z=p)$
$P10_5/m$	-	-	$10_5/m$	$\overline{10}(=5/m)$		
$P5_r2(p)$	-	2	5_r2	5_p	5_p	$5_{-r}2$
$P\overline{10}c2$	-	2	$\overline{10}c2$	$\overline{10}$		
$P5c(p)$	-	c	$5c$	5_p	5_{2p}	$5c$
$P10/mc$	-	c	$10/mc$	$\overline{10}(=5/m)$		
$P5m(p)$	-	m	$5m$	5_p	5_{2p}	$5m$
$P\overline{10}m2$	-	m	$\overline{10}m2$	$\overline{10}$		
$P10_q22(p)$	2	2	10_q22	5_p2	5_p2	$10_{2p-q}22$
$P10/mcc$	2	2	$10/mcc$	$\overline{10}c2$		
$P\overline{5}1m(p)$	2	m	$\overline{5}1m$	5_p2	5_{2p}	$\overline{5}1m$
$P10_5/mcm$	2	m	$10_5/mcm$	$\overline{10}c2$		
$P\overline{5}1c(p)$	2	c	$\overline{5}1c$	5_p2	5_{2p}	$\overline{5}1c$
$P\overline{5}m1$	m	2	$\overline{5}m1$	$5m$		
$P10_5/mmc$	m	2	$10_5/mmc$	$\overline{10}m2$		
$P10mm$	m	m	$10mm$	$5m$		
$P10/mmm$	m	m	$10/mmm$	$\overline{10}m2$		
$P10_5mc$	m	c	10_5mc	$5m$		
$P\overline{5}c1$	c	2	$\overline{5}c1$	$5c$		
$P10cm$	c	m	$10cm$	$5c$		
$P10cc$	c	c	$10cc$	$5c$		

The indices shown in Fig. 1.16 give the columns of the scaling matrix. This scaling symmetry corresponds to the planar heptagrammal form of the star heptagon with Schläfli symbol {7/3}. The irreducible representation of the scaling symmetry is 6D and is given by

$$
\mathsf{S} = \begin{pmatrix}
0 & 1 & 1 & 0 & \overline{1} & \overline{1} \\
0 & 1 & 2 & 1 & \overline{1} & \overline{2} \\
\overline{1} & 1 & 2 & 2 & 0 & \overline{2} \\
\overline{2} & 0 & 2 & 2 & 1 & \overline{1} \\
\overline{2} & \overline{1} & 0 & 2 & 1 & 0 \\
\overline{1} & \overline{1} & 0 & 1 & 1 & 0
\end{pmatrix}_D .
\tag{1.29}
$$
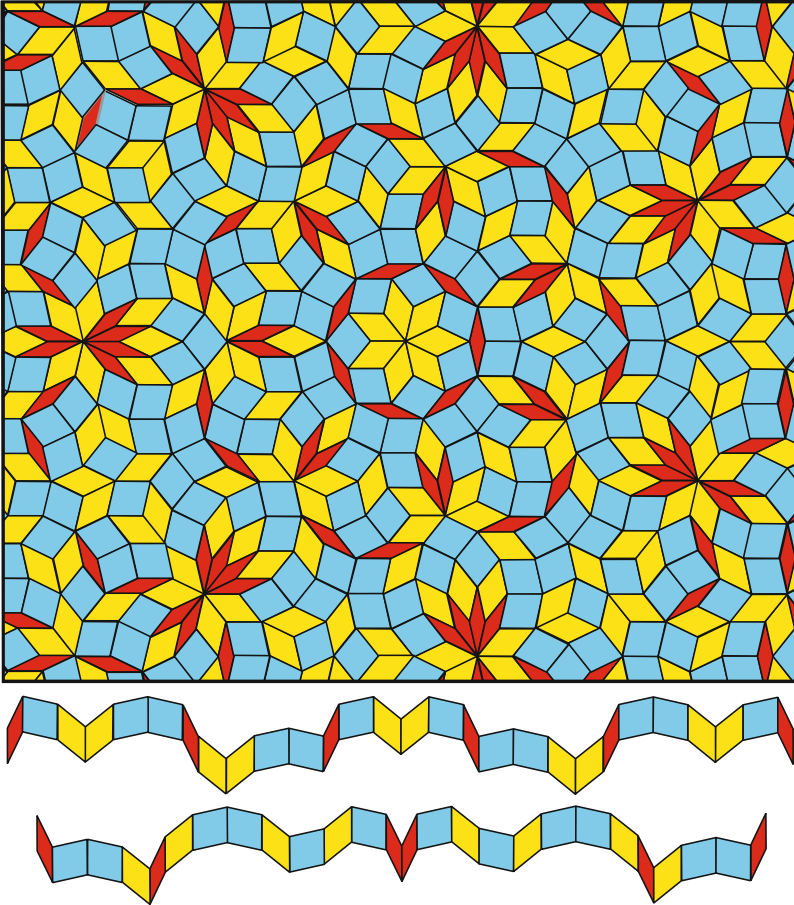
Fig. 1.15. Heptagonal (tetrakaidecagonal) rhomb tiling. The alternation condition applies and is illustrated by the lane of tiles shown below the tiling. It requires that the three types of rhomb tiles, which are related by mirror symmetry, have to alternate along the lane

Schläfli symbol   The Schläfli symbol is a notation of the form $\{p, q, r, ...\}$ that defines regular polygons, polyhedra, and polytopes. It describes the number of edges of each polygon meeting at a vertex of a regular or semi-regular tiling or solid. For a Platonic solid, it is written $\{p, q\}$, where p is the number of edges each face has, and q is the number of faces that meet at each vertex. Its reversal gives the symbol of the dual polygon, polyhedron, or polytope.

The symbol $\{p\}$ denotes a regular polygon with p edges for integer p, or a star polygon for rational p. For example, a regular pentagon is represented

Fig. 1.16. Scaling symmetry of a heptagonal tiling (*top*) which corresponds to the planar heptagrammal form of a {7/3} heptagon (*bottom*). The reference basis is shown by the black vectors, while the gray (online: *red*) indices give the columns of the scaling matrix. The eigenvalues are: 4.04892, 1, −0.692021, and −0.356896
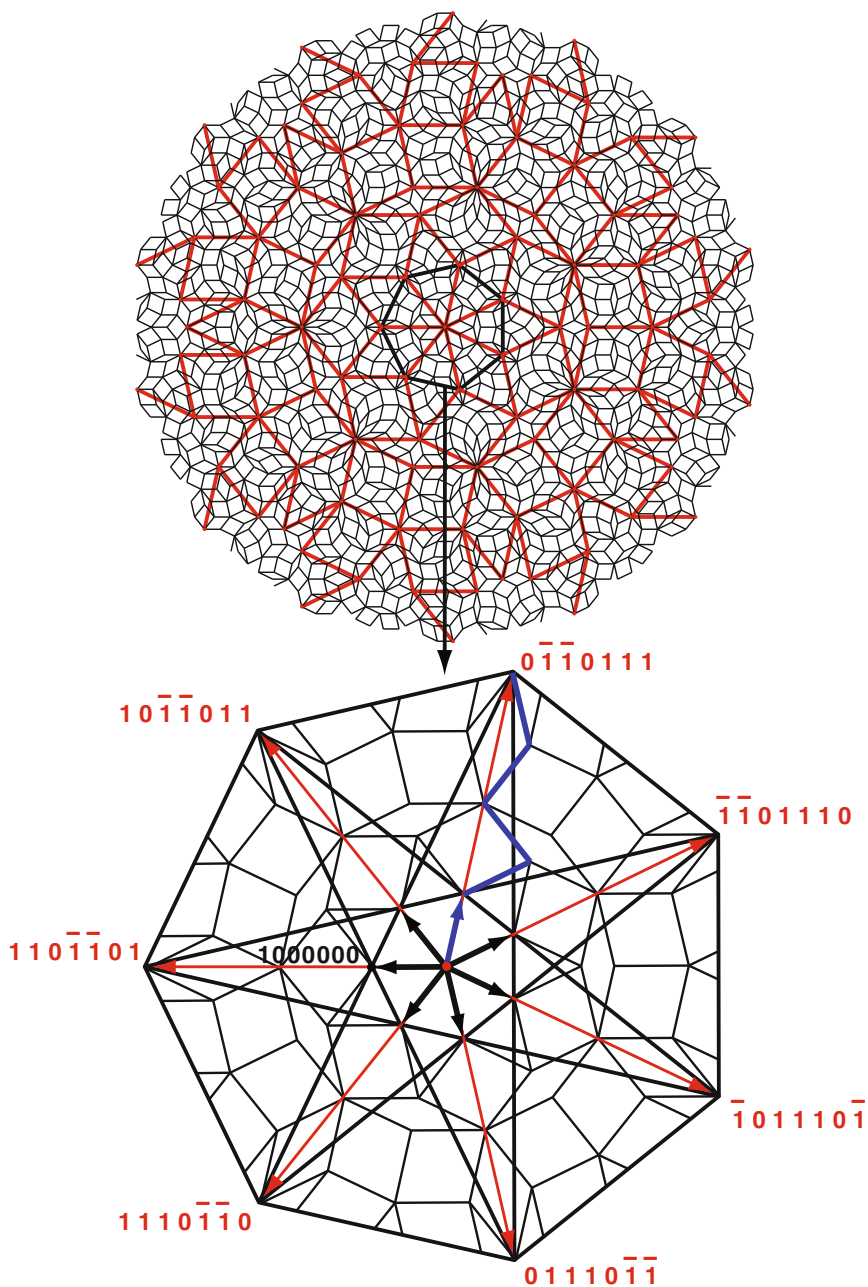
by {5} (convex regular polygon), and a pentagram by {5/2} (nonconvex star polygon). In case of rational $p = m/n$, m means a 2D object with m vertices where every n-th vertex is connected giving an n-gram. n is also the number of different polygons in an n-gram.

Heptagonal (tetrakaidecagonal) tilings can be generated either based on the nD approach or by substitution rules. In the first case it can have the PV property, in the second case it cannot. Finite atomic surfaces and, consequently, a pure point Fourier spectrum on one hand, and a substitution rule on the other hand mutually exclude each other for axial symmetries 7, 9, 11, or greater than 12. If generated based on the nD approach, a heptagonal tiling does not exhibit perfect matching rules, it just obeys the alternation condition, which is a kind of weak matching rule (Fig. 1.15). In Fig. 1.17, it is illustrated that the alternation condition does not apply to approximants.

Generally speaking, canonical projection tilings with a substitution rule, cannot have rotational symmetry of order 7, 9, 11, or greater than 12, because their scaling would have to be an algebraic number of rank at least 3, while canonical projection tilings with a substitution rule have quadratic scaling [14]. It has been shown, that a PV rhomb substitution rule with cubic or greater scaling will not have a polytope window [31].

Pisot scaling factor and the diffraction pattern   If a tiling is a primitive substitution tiling, it has a non-trivial Bragg diffraction spectrum only if the scaling factor (the largest eigenvalue of the substitution matrix) is a Pisot number. That implies that wave vectors exist for which the structure factor does not converge to zero for an infinite volume tiling (constructive
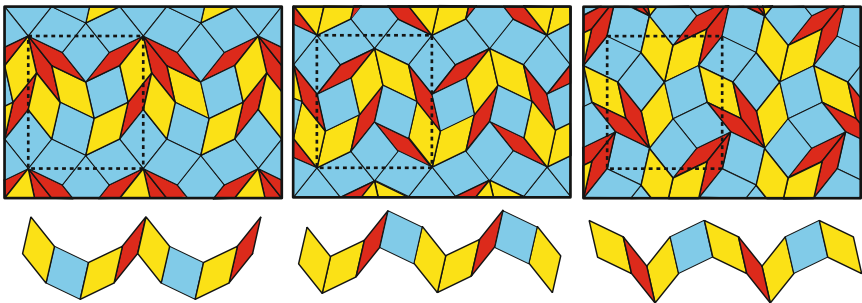

Fig. 1.17. The alternation condition does not apply in the case of approximants. Three different approximants to the heptagonal tiling with one and the same unit cell size (*dashed line*) are shown. Below the tilings, the violation of the alternation rule is demonstrated on one lane for each case

interference). For an infinite tiling one needs n substitutions with n approaching infinity. The structure factor is then the product of n iterations. The n-th substitution contributes its Fourier transform to the structure factor, with the n-th power of the scaling factor in the exponential function. This product does not converge to zero for n approaching infinity and we have constructive interference only if the n-th power of the scaling factor converges to an integer, as is the case for Pisot numbers. Else, every substitution leads to differently phased waves leading to destructive interference.

All canonical projection tilings are self-similar with a Pisot scaling factor and well defined, finite atomic surfaces. They have, therefore, always nontrivial Bragg diffraction spectra.

All heptagonal (tetrakaidecagonal) tilings considered in this book are canonical projection tilings and can equally be generated by the cut-and-project method (see Chap. 3.6.2). They have Pisot scaling factors as required for finite (non-fractal) atomic surfaces and a pure-point Fourier spectrum.

1.2.5 Octagonal Tiling

The octagonal (8-fold) tiling was first studied independently by R. Ammann in 1977 and F. P. M. Beenker in 1981, at that time a student of the Dutch mathematician N. G. de Bruijn. Beenker discovered an octagonal tiling with substitution rule and derived a way to obtain octagonal tilings by the strip-projection method [1]. The octagonal tiling shown in Fig. 1.18, called Ammann–Beenker tiling, has perfect matching rules and belongs to the PLI class.

It can be obtained as dual to two periodic 4-grids rotated by $\pi/4$ against each other. If the prototiles are decorated with line segments, quasiperiodically spaced straight lines result when assembled to a tiling. They have been classified as primary and secondary Ammann lines. The dual to the primary Ammann quasilattice is the tiling itself. The ratio of the long to the short intervals between the primary Ammann lines amounts to $1+1/\omega = 1 + \sqrt{2}/2 = 1.707$. The secondary Ammann lines extend over the tile boundaries and correspond to a perfect matching rule [34]. They can also be obtained by local decoration of the tiles with line segments leading to 4 different rhombs, 5 squares, and their enantiomorphs. The secondary Ammann quasilattice is locally isomorphic to the primary one, rotated by $\pi/8$ and scaled down by a factor $\sqrt{2}$. The alternation condition is only a weak matching rule for the octagonal tiling and enforces rather quasiperiodic tilings with only 4-fold symmetry.

The set of vertices of the octagonal Ammann–Beenker tiling M_{OT} is a subset of the vector module $M = \left\{ \mathbf{r} = \sum_{i=0}^{3} n_i a_r \mathbf{e}_i \middle| \mathbf{e}_i = (\cos 2\pi i/8, \sin 2\pi i/8) \right\}$, with the tile edge length a_r. Scaling by the matrix S yields an isomorphic tiling enlarged by a factor $\delta_s = 1 + \sqrt{2}$

$$\mathsf{S} \cdot \mathsf{M}_{OT} = (1 + \sqrt{2})\mathsf{M}_{OT} \tag{1.30}$$
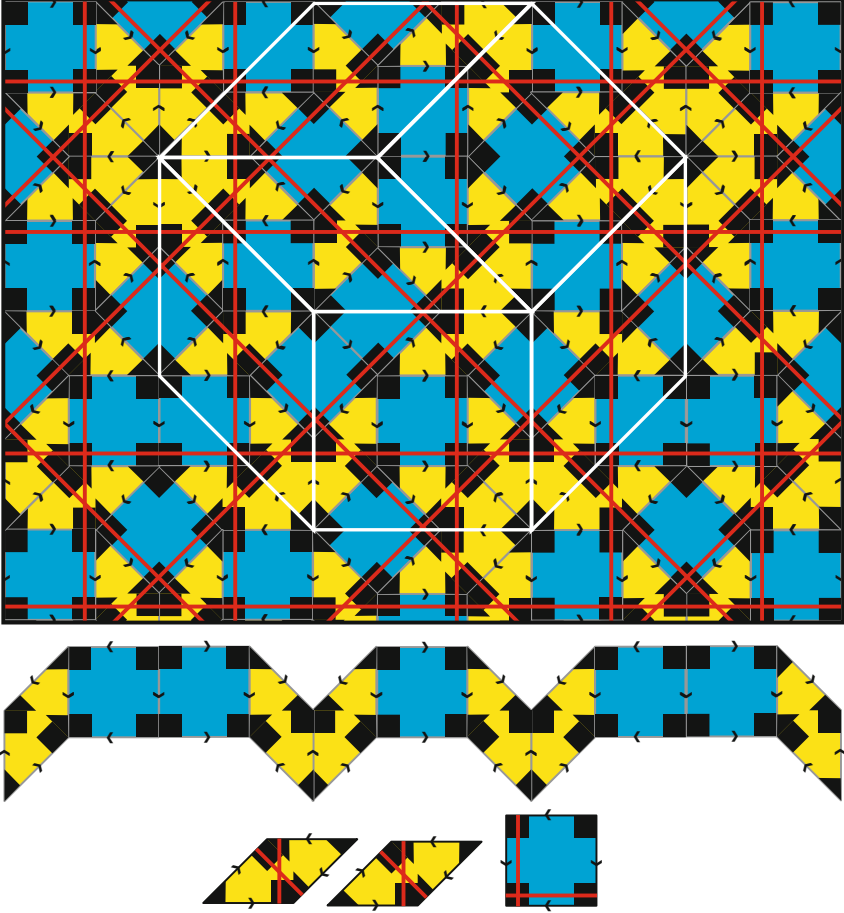
Fig. 1.18. The octagonal Ammann–Beenker tiling with matching rules, primary Ammann-line decoration [34] and a patch of supertiles (*white*) forming a covering cluster (cf. [2]). The covering cluster exists in two different copies which are mirror-symmetric along the long diagonal of the overlapping rhomb tile. The alternation condition is illustrated by the lane of tiles shown below the tiling. It requires that the two types of rhomb tiles, which are related by mirror symmetry, have to alternate along the lane

with

$$
\mathsf{S} = \begin{pmatrix} 1\ 1\ 0\ \bar{1} \\ 1\ 1\ 1\ 0 \\ 0\ 1\ 1\ 1 \\ \bar{1}\ 0\ 1\ 1 \end{pmatrix}_D = \left(\begin{array}{cc|cc} 1+\sqrt{2} & 0 & 0 & 0 \\ 0 & 1+\sqrt{2} & 0 & 0 \\ \hline 0 & 0 & 1-\sqrt{2} & 0 \\ 0 & 0 & 0 & 1-\sqrt{2} \end{array} \right)_V
$$

$$
= \left(\begin{array}{c|c} \mathsf{S}^{\parallel} & 0 \\ \hline 0 & \mathsf{S}^{\perp} \end{array} \right)_V . \tag{1.31}
$$

Diagonalisation of S, defined on the vector star $a_r \mathbf{e}_i$ (D basis), yields the eigenvalues of the scaling matrix on the cartesian (V) basis, the quadratic Pisot numbers

$$\lambda_1 = 1 + 2 \cos 2\pi/8 = 1 + \sqrt{2} = 2.41421,$$
$$\lambda_2 = 1 + 2 \cos 6\pi/8 = 1 - \sqrt{2} = -0.41420. \tag{1.32}$$

The first eigenvalue is called silver mean or silver ratio δ_s, in analogy to the golden mean τ.

The silver mean (ratio) δ_s   The silver ratio $\delta_s = 1 + \sqrt{2}$, can be represented by the continued fraction expansion

$$\delta_s = 2 + \cfrac{1}{2 + \cfrac{1}{2 + \frac{1}{2 + \dots}}}. \tag{1.33}$$

The convergents c_i are just ratios of two successive Pell numbers, with $P_0 = 0$, $P_1 = 1, P_n = 2P_{n-1} + P_{n-2}$,

$$c_1 = 2/1, \quad c_2 = 5/2, \quad c_3 = 12/5, \dots, c_n = \frac{P_{n+1}}{P_n}. \tag{1.34}$$

The ratio of the frequencies of the square to the rhomb tiles in the tiling is $1 : \sqrt{2}$, and that of the two mirror symmetrical rhombs is the same. The ratio of the areas of a square to a rhomb tile is $\sqrt{2} : 1$. Consequently, the total area of the tiling covered by squares equals that covered by rhombs.

An octagonal patch of two corner-linked squares plus four rhomb tiles can be used as covering cluster [2]. If the edges are properly arrowed than the Ammann–Beenker tiling can be obtained if the number of octagon clusters is maximized at the same time. An alternative to arrowing is using the inflated (concerning the number of tiles) unarrowed octagonal patch, which has the same overlapping constraints.

In Fig. 1.19, we show an octagonal tiling generated by the nD approach (see Chap. 3.6.3). The alternation condition is fulfilled in the tiling, as is shown exemplarily on two lanes below the tiling in the figure.

1.2.6 Dodecagonal Tiling

Many different dodecagonal (12-fold) tilings have been studied so far. One of the best investigated is the Socolar tiling. It is composed of three prototiles, a regular hexagon (H), a square (S), and a $\pi/6$ rhomb (R), which appear in two enantiomorphic (mirror-symmetric) forms concerning the matching rules [34] (Fig. 1.20). It belongs to the PLI class of tilings. The tilings scale with the factor $\xi = 2 + \sqrt{3} = 3.73205$. The ratios of tile frequencies are H : S : R = $1 : \sqrt{3} : \sqrt{3}$ for both enantiomorphs.

Fig. 1.19. Octagonal tiling generated by the nD approach. The alternation condition is illustrated by the lanes of tiles shown below the tiling. It requires that the two types of rhomb tiles related by mirror symmetry alternate along the lane

By proper decoration of the tiles with line segments, a primary and a secondary Ammann quasilattice can be obtained. The ratio of the long to the short intervals between the primary Ammann lines amounts to $1 + 1/\xi = 1.26795$. The dual of the primary Ammann quasilattice is just the original tiling itself. The secondary Amman quasilattice can only be obtained either by non-local decoration of the prototiles with line segments or by local decoration of 3 rhomb tiles, 5 squares, and 5 hexagons plus their enantiomorphs. The secondary Ammann quasilattice is locally isomorphic to the primary one rotated by $\pi/12$ and scaled down by a factor $2\cos\pi/12 = 1.93185$. The dodecagonal Socolar tiling can also be obtained as the dual of two superimposed periodic 3-grids rotated by $\pi/6$ against each other. The ordering of tiles along each lane of tiles satisfies the alternation condition. However, this weak matching rule enforces only quasiperiodic tilings with at least hexagonal symmetry.
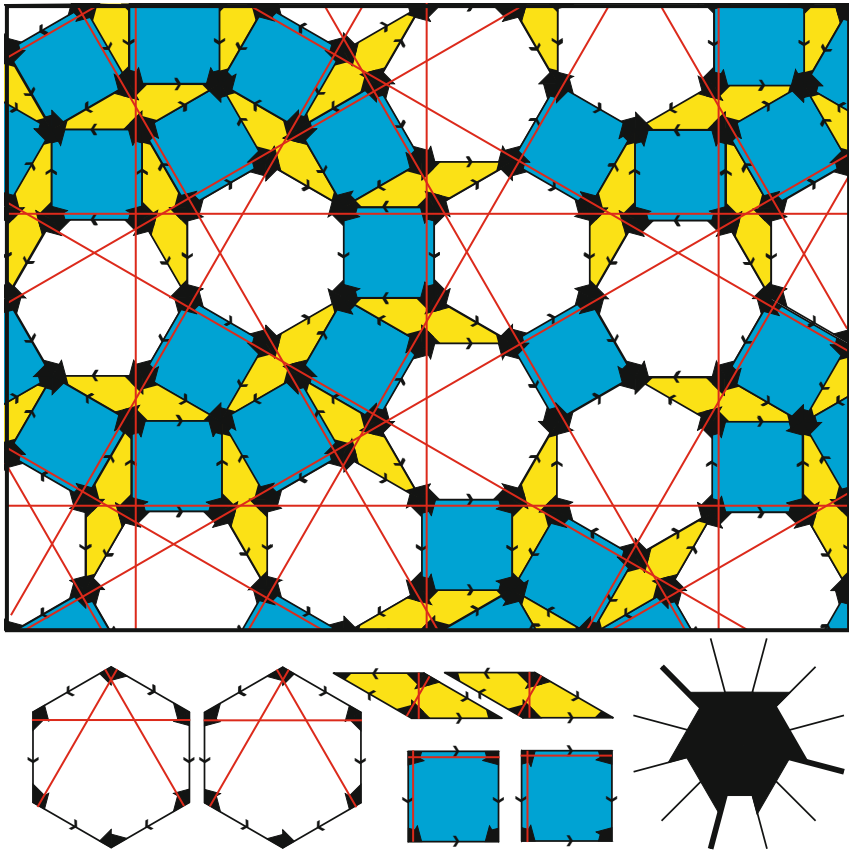
Fig. 1.20. Dodecagonal Socolar tiling with primary Ammann lines (*cf.* [34]). The prototiles are shown in their two enantiomorphic forms. The matching rule is defined by arrows as well as a key, which is shown enlarged at bottom right

An example for a dodecagonal rhomb tiling is shown in Fig. 1.21. This tiling can be generated using the *n*D approach (see Chap. 3.6.5) and is a canonical projection tiling. The dodecagonal rhomb tiling satisfies the alternation condition, as visualized in Fig. 1.21.

Like the Socolar tiling, the dodecagonal rhomb tiling is also composed of three prototiles. Two of them, the square and the $\pi/6$ rhomb are also building units of the Socolar tiling, while the third tile, the hexagon, is substituted in the dodecagonal rhomb tiling by a $\pi/3$ rhomb. The eigenvalues are the quadratic Pisot numbers

$$\begin{aligned}
\lambda_1 &= 1 + 2\cos 2\pi/12 = 1 + \sqrt{3} = 2.73205, \\
\lambda_2 &= 1 - 2\cos 2\pi/12 = 1 - \sqrt{3} = -0.73205.
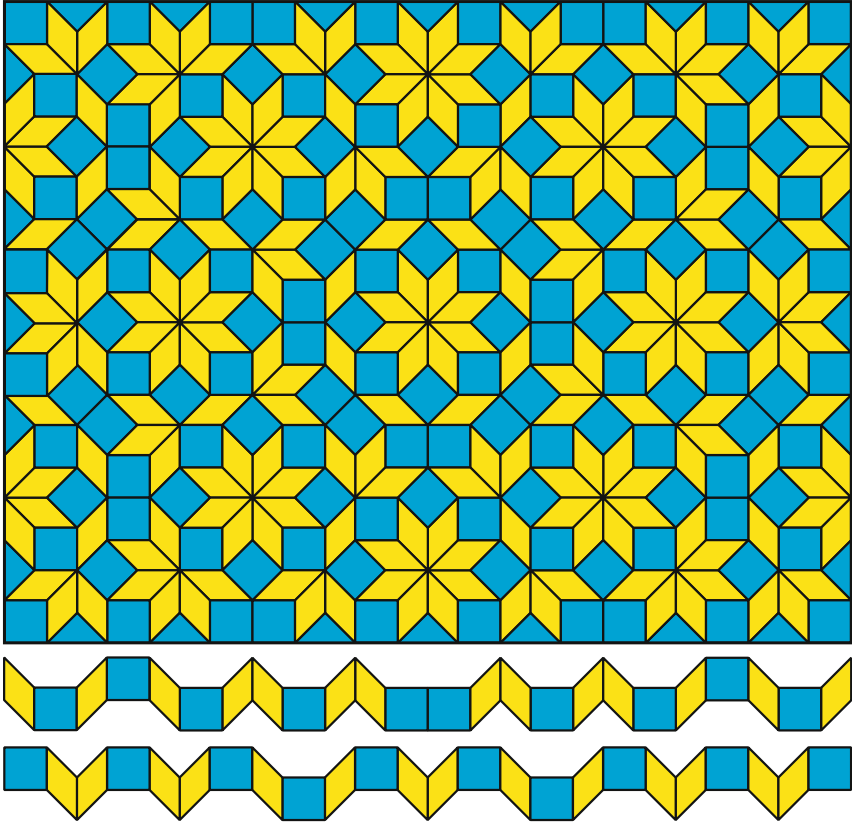\end{aligned} \tag{1.35}$$
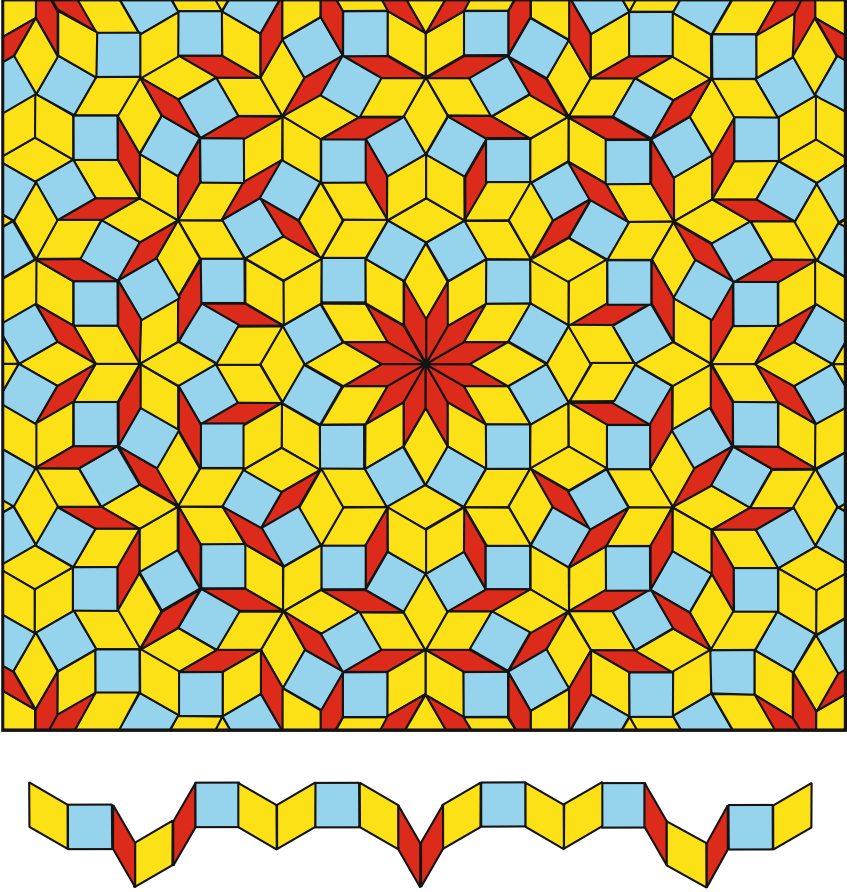
Fig. 1.21. Dodecagonal tiling generated by the nD approach. The alternation condition is illustrated by the lane of tiles shown below the tiling. It requires that the three types of rhomb tiles alternate along the lane in a mirror symmetric way

They are the eigenvalues of the scaling matrix

$$\mathsf{S} = \begin{pmatrix} 1\ 2\ 0\ \bar{1} \\ 1\ 1\ 1\ 0 \\ 0\ 1\ 1\ 1 \\ \bar{1}\ 0\ 2\ 1 \end{pmatrix}_D \tag{1.36}$$

according to a basis as defined in Fig. 1.22, where the scaling symmetry is visualized. The indices shown in Fig. 1.22 give the columns of the scaling matrix. This scaling symmetry corresponds to the planar dodecagrammal form of the star dodecagon with Schläfli symbol $\{12/5\}$.
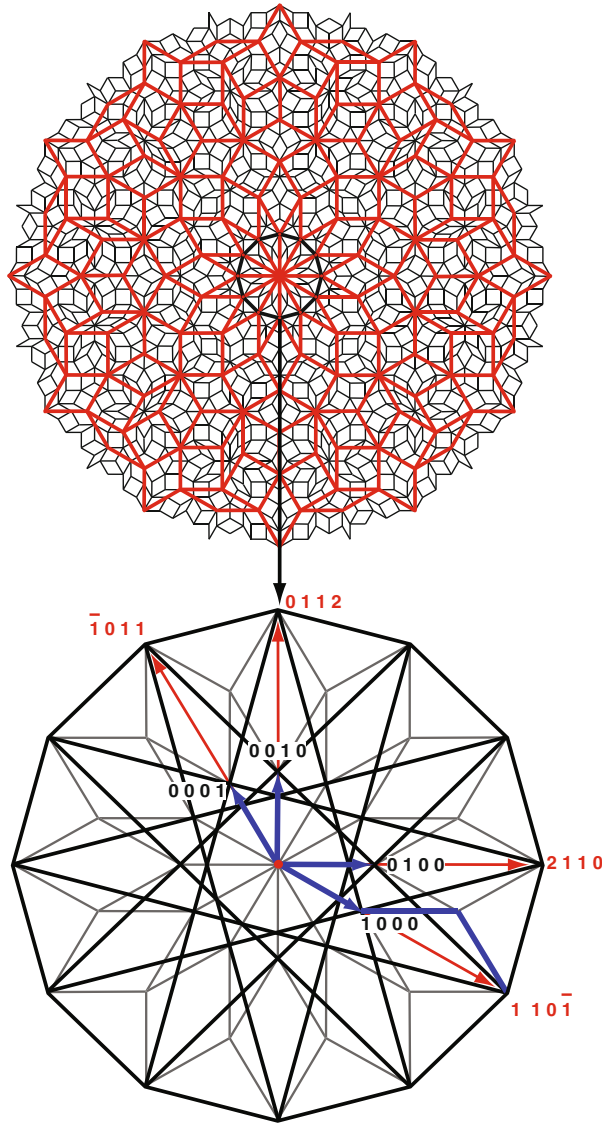
Fig. 1.22. Scaling symmetry of a tiling (*top*) which corresponds to the planar dodecagrammal form of a {12/5} dodecagon (*bottom*). The reference basis is shown by the black vectors, while the gray (online: *red*) indices give the columns of the scaling matrix. The eigenvalues are 2.73205 and −0.73205

1.2.7 2D Random Tilings

Two-dimensional random tilings can be obtained by randomizing strictly quasiperiodic tilings, particularly via phason flips. This has been performed

in several studies, for instance [38, 40]. Generally, the non-geometrical constraints forcing an on-average quasiperiodic tiling in combination with the maximization the configurational entropy have to be much stronger than in the 3D case.

For instance, by relaxing the overlap rules of the Gummelt covering (Fig. 1.13(i)) one can obtain random decagon coverings [12] (Fig. 1.13(f), (g)). The decagon centers form a random pentagon tiling and the pentagon centers a random HBS supertiling, called two-level random PT. In Fig. 1.13(i) a fully relaxed overlapping rule is shown. If only the single arrows in Fig. 1.13(h) are abandoned, then we get an intermediate overlap rule [7]. The resulting tilings are related to random rhomb PT, which still satisfy the double-arrow condition, and are called four-level random PT.

1.3 3D Tilings

There is just a single 3D tiling relevant for serving as quasilattice of real quasicrystals. This is the 3D Penrose or Ammann tiling, which underlies icosahedral QC as it is known so far. Another useful tiling for model calculations is the 3D cube Fibonacci tiling, which is just an extension of the 2D square FS (see Sect. 1.1.3).

1.3.1 3D Penrose Tiling (Ammann Tiling)

The 3D analogue to the Penrose tiling is called 3D Penrose tiling (3D PT) or Ammann tiling [21, 23, 35, 37]. It consists of two kinds of unit tiles: a prolate and an oblate rhombohedron with equal edge lengths a_r (Fig. 1.23).

The acute angles of the rhombs covering these rhombohedra amount to $\alpha_r = \theta = \arctan(2) = 63.44°$. The volumes of the unit tiles are given by

$$V_p = \frac{4}{5}a_r^3 \sin\frac{2\pi}{5}, \quad V_o = \frac{4}{5}a_r^3 \sin\frac{\pi}{5} = \frac{V_p}{\tau} \tag{1.37}$$
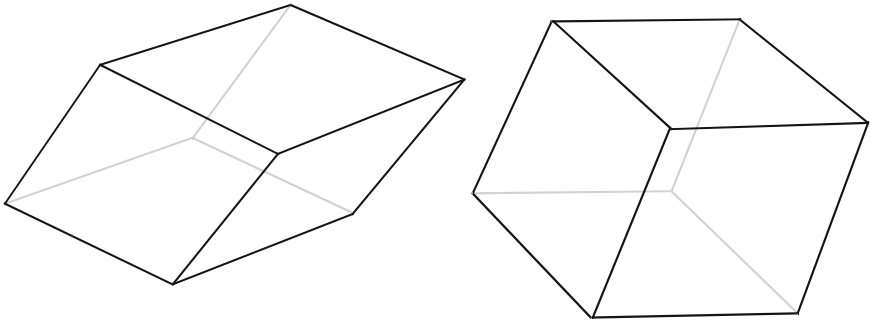

Fig. 1.23. The two unit tiles of the Ammann tiling: a prolate (*left*) and an oblate (*right*) rhombohedron with equal edge lengths a_r

and their relative frequencies in the Ammann tiling are $\tau : 1$. Therefrom the point density D_{p} results to

$$D_{\mathrm{p}} = \frac{\tau + 1}{\tau V_p + V_o} = \frac{\tau}{a_r^3} \, \sin \frac{2\pi}{5} \; . \tag{1.38}$$

The set of vertices of the Ammann tiling M_{AT} is

$$M_{AT} = \left\{ \pi^{\|}(\mathbf{r}) \middle\| \pi^{\perp}(\mathbf{r}) \in T_i, i = 1, \ldots, 60 \right\} \tag{1.39}$$

with $\mathbf{r} = \sum_{j=1}^{6} n_j \mathbf{d}_j, n_j \in Z$. The 60 trigonal pyramidal subdomains T_i of the triacontahedron correspond to

$$T_i = \left\{ \mathbf{t} = \sum_{j=1}^{3} x_j \mathbf{e}_j \middle\| x_1 \in [0, \lambda], x_2 \in [0, \lambda - x_1], x_3 \in [0, \lambda - x_1 - x_2] \right\} \tag{1.40}$$

with λ the central distance of the vertices and $\mathbf{e}_j$ vectors pointing to adjacent vertices of the triacontahedron.

There are several sets of matching rules known for the 3D Penrose tiling. The perhaps most relevant one for the growth of real icosahedral quasicrystals have been derived by [35]. They are not based on the two prototiles, the oblate and the prolate rhombohedron, but on four zonohedra: (a) a triacontahedron (10 oblate + 10 prolate tiles), (b) a rhombic icosahedron (5 oblate + 5 prolate tiles) (c) a rhombic dodecahedron (2 oblate + 2 prolate tiles), (d) a single prolate rhombohedron (see Fig. 2.6). These new prototiles, properly decorated by segments of planes, produce infinite, quasiperiodically spaced planes that run throughout the tiling. In analogy to the Ammann lines in the case of the 2D Penrose tiling, these planes are called *Ammann planes*. This matching rule produces just a single LI class, which is different from that obtained from the 6D approach.

1.3.2 3D Random Tilings

Due to geometrical constraints, 3D random tilings can be on average quasiperiodic. However, the stabilization by high configurational entropy is only possible at high temperatures. Geometrically, random tilings can be obtained by starting from a strictly ordered tiling and subsequent randomization of the tiling by phason flips (Fig. 1.24). This can be performed by Monte Carlo simulations flipping the interior of rhombic dodecahedra consisting of two prolate and two oblate rhombohedra. The diffraction pattern of a 3D random tiling, constituted by the right ratio of Penrose rhombohedra without matching rules, was shown to exhibit sharp Bragg-like peaks and strong phason diffuse scattering [39].

Geometrically, the average structure of a random tiling can be described to some extent by the nD approach, if the sharp reflections are taken for Bragg
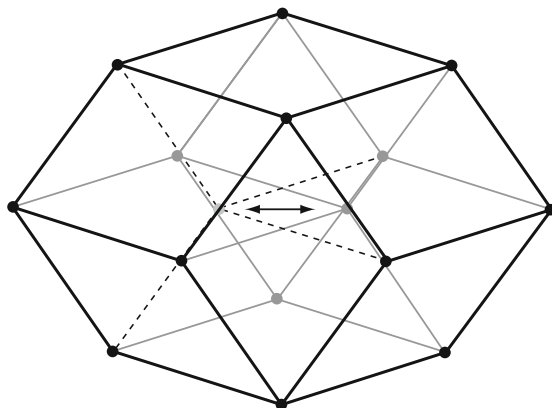
Fig. 1.24. Characteristic dodecahedron of two prolate and two oblate Penrose rhombohedra illustrating the action of a phason flip

reflections. Then the resulting atomic surface will not be dense and will not obey the closeness condition. For the consequences for structure analysis see [18]. For a general discussion of random tiling models see [17].

References

1. F.P.M. Beenker, Algebraic Theory of Non-periodic Tilings of the Plane by Two Simple Building Blocks: a Square and a Rhombus. Eindhoven Technical University of Technology, TH-Report, 82-WSK04 (1982)
2. S.I. Ben-Abraham, F. Gähler, Covering cluster description of octagonal MnSiAl quasicrystals. Phys. Rev. B **60**, 860–864 (1999)
3. N.G.D. Bruijn, Dualization of Multigrids. J. Phys. (France) **47**, 9–18 (1986)
4. F. Gähler, M. Baake, M. Schlottmann, Binary tiling quasicrystals and matching rules. Phys. Rev. B. **50**, 12458–12467 (1994)
5. A. Bienenstock, P.P. Ewald, Symmetry of Fourier Space. Acta Crystallogr. **15**, 1253–1261 (1962)
6. F. Gähler, J. Rhyner, Equivalence of the Generalized Grid and Projection Methods for the Construction of Quasi-Periodic Tilings. J. Phys. A: Math. Gen. **19**, 267–277 (1986)
7. F. Gähler, M. Reichert, Cluster models of decagonal tilings and quasicrystals. J. Alloys Comp. **342**, 180–185 (2002)
8. M. Gardner, Mathematical Games. Sci. Amer. **236**, 110–121 (1977)
9. B. Grünbaum, G.C. Shephard, Tilings and Patterns. W.H. Freeman and Company, New York (1987)
10. P. Gummelt, Penrose tilings as coverings of congruent decagons. Geom. Dedic. **62**, 1–17 (1996)
11. P. Gummelt, Decagon clusters in perfect and random decagonal structures. In: Quasicrystals. Ed. H.-R. Trebin, pp. 90–104, VCH Wiley (2003)
12. P. Gummelt, C. Bandt, A cluster approach to random Penrose tilings. Mater. Sci. Eng. A **294**, 250–253 (2000)

13. T. Hahn, H. Klapper, Point groups and crystal classes. In: International Tables for Crystallography, vol. A, Kluwer Academic Publishers, Dordrecht/Boston/London, pp. 761–808 (2002)
14. E.O. Harriss, Non-periodic rhomb substitution tilings that admit order n rotational symmetry. Discr. Comp. Geom. **34**, 523–536 (2005)
15. S. Hendricks, E. Teller, X-ray Interference in Partially Ordered Layer Lattices. J. Chem. Phys. **10**, 147–167 (1942)
16. C.L. Henley, Sphere Packings and Local Environments in Penrose Tilings. Phys. Rev. B **34**, 797–816 (1986)
17. C.L. Henley, Random tiling models. In: Quasicrystals. The state of the art. Eds.: D.P. Di Vicenzo and P.J. Steinhardt. World Scientific, Singapore, pp. 459–560 (1999)
18. C.L. Henley, V. Elser, M. Mihalkovic, Structure determinations for random-tiling quasicrystals. Z. Kristall. **215**, 553–568 (2000)
19. K. Ingersent, in: Quasicrystals. The state of the art. D.P. Vincenzo and P.J. Steinhardt (eds.), World Scientific, Singapore, pp. 197–224 (1999)
20. A. Janner, Decagrammal Symmetry of Decagonal $Al_{78}Mn_{22}$ Quasicrystal. Acta Crystallogr. A **48**, 884–901 (1992)
21. T. Janssen, Aperiodic Crystals: a Contradictio in Terminis? Phys. Rep. **168**, 55–113 (1988)
22. F. Lançon, L. Billard, Two-dimensional system with a quasicrystalline ground state. J. Phys. (France) **49**, 249–256 (1988)
23. D. Levine, P.J. Steinhardt, Quasicrystals. I. Definition and Structure. Phys. Rev. B **34**, 596–616 (1986)
24. R. Lifshitz, The square Fibonacci tiling. J. Alloys Comp. **342**, 186–190 (2002)
25. E.A. Lord, S. Ranganathan, The Gummelt decagon as a 'quasi unit cell'. Acta Crystallogr. A **57**, 531–539 (2001)
26. J.M. Luck, C. Godrèche, A. Janner, T. Janssen, The Nature of the Atomic Surfaces of Quasiperiodic Self-similar Structures. J. Phys. A: Math. Gen. **26**, 1951–1999 (1997)
27. R. Lueck, Basic Ideas of Ammann Bar Grids. Int. J. Mod. Phys. B **7**, 1437–1453 (1993)
28. M. O'Keeffe, B.G. Hyde, Plane Nets in Crystal Chemistry. Phil. Trans. Roy. Soc. (London) A **295**, 553–618 (1980)
29. A. Pavlovitch, M. Kléman, Generalized 2D Penrose Tilings: Structural Properties. J. Phys. A: Math. Gen. **20**, 687–702 (1987)
30. R. Penrose, The Rôle of Aesthetics in Pure and Applied Mathematical Research. Bull. Inst. Math, Appl. **10**, 266–271 (1974)
31. P.A.B. Pleasants, Designer quasicrystals: cut-and-project sets with pre-assigned properties. Amer. Math. Soc., Providence (2000)
32. D.S. Rokhsar, D.C. Wright, N.D. Mermin, The Two-Dimensional Quasicrystallographic Space-Groups with Rotational Symmetries Less Than 23-Fold. Acta Crystallogr. Sect. A **44**, 197–211 (1988)
33. M. Senechal, Quasicrystals and Geometry. Cambridge University Press, Cambridge (1995)
34. J.E.S. Socolar, Simple Octagonal and Dodecagonal Quasicrystals. Phys. Rev. B **39**, 10519–10551 (1989)
35. J.E.S. Socolar, P.J. Steinhardt, Quasicrystals. II., Unit Cell Configurations. Phys. Rev. B **34**, 617–647 (1986)

36. J.E.S. Socolar, Weak matching rules for quasicrystals. Commun. Math. Phys. **129**, 599–619 (1990)
37. W. Steurer, T. Haibach, Reciprocal Space Images of Aperiodic Crystals. International Tables for Crystallography, vol. B Kluwer Academic Publishers: Dordrecht, pp. 486–518 (2001)
38. K.J. Strandburg, Random-Tiling Quasicrystal. Phys. Rev. B **40**, 6071–6084 (1989)
39. L.H. Tang, Random-Tiling Quasi-Crystal in 3 Dimensions. Phys. Rev. Lett. **64**, 2390–2393 (1990)
40. T.R. Welberry, Optical Transform and Monte-Carlo Study of Phason Fluctuations in Quasi-Periodic Tilings. J. Appl. Crystallogr. **24**, 203–211 (1991)
41. R. Wittmann, Comparing different approaches to model the atomic structure of a ternary decagonal quasicrystal. Z. Kristallogr. **214**, 501–505 (1999)
42. H.Q. Yuan, U. Grimm, P. Repetowicz, M. Schreiber, Energy spectra, wave functions, and quantum diffusion for quasiperiodic systems. Phys. Rev. B **62**, 15569–15578 (2000)

2

Polyhedra and Packings

Ideal crystal structures are characterized by their space group, metrics of the unit cell and the kind of atoms occupying the Wyckoff (equipoint) positions. Depending on the structure type, it may be useful to describe a structure as packing of atoms or larger structural units such as chains, columns, bands, layers, or polyhedra. We will focus in this chapter on polyhedra and their space-filling packings. This can be very useful for analyzing and understanding the geometry of quasiperiodic structures. One has to keep in mind, however, that these polyhedra may just be geometrical units and not necessarily crystal-chemically well-defined entities (atomic clusters; for a detailed discussion see Sect. 10.3).

In physical space, the geometry of quasiperiodic structures can be likewise discussed based on tilings or coverings, which are decorated by atoms or by larger structural subunits (clusters). All quasicrystal structures known so far can be well described based on polyhedral clusters. Whether these clusters are more than just structural subunits is not clear yet. Anyway, a discussion of the most important polyhedra and their space-filling properties will be crucial for understanding the structures of quasicrystals and their approximants.

The group–subgroup relationships between polyhedra and their packings with icosahedral and those with cubic point group symmetry are shown in Fig. 2.1. The first obvious but remarkable property of icosahedral clusters is that they are invariant under the action of the cubic point groups 23 or $2/m\bar{3}$, depending on whether or not they are centrosymmetric. Consequently, from a geometrical point of view, there is no need to distort an icosahedral cluster for fitting it into a cubic unit cell without breaking the cubic symmetry. Distortions may only be necessary if we consider the densest packings of icosahedral clusters on a periodic (cubic) lattice.
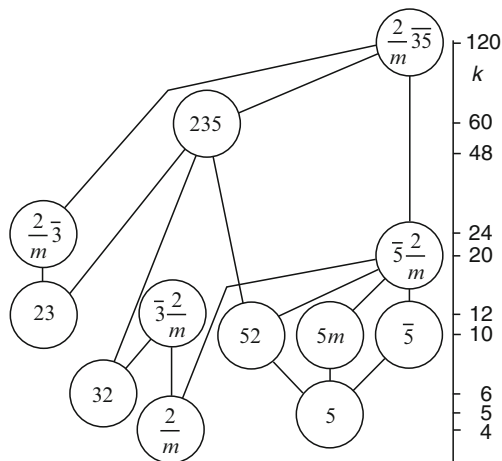
Fig. 2.1. Group-subgroup relationships between the holohedral icosahedral point group $2/m\bar{3}\bar{5}$ and some of its subgroups arranged according to the group order k

In the following sections, we present the well known regular and semiregular polyhedra and discuss their packings.[1]

2.1 Convex Uniform Polyhedra

A convex polyhedron is called *regular* if its faces are all equal and regular (equilateral and equiangular) surrounding all vertices (corners) in the same way (with the same solid angles). In other words, regular polyhedra are *face-transitive* and *vertex-transitive*. Without the second condition, one obtains the non-uniform *face-regular* (face-transitive) polyhedra, such as the rhombic dodecahedron, triacontahedron, or the pentagonal bipyramid. In 3D, there are exactly five regular polyhedra, the *Platonic solids* (Fig. 2.2). These are the tetrahedron, $\bar{4}3m$: {3,3}; the octahedron, $4/m\bar{3}2/m$: {3,4}; the hexahedron (cube), $4/m\bar{3}2/m$: {4,3}; the icosahedron, $2/m\bar{3}\bar{5}$: {3,5}; and the dodecahedron, $2/m\bar{3}\bar{5}$: {5,3}. The orientational relationship to the cubic symmetry is indicated by a cubic unit cell in each case (Fig. 2.2). The Schläfli symbol {p, q} denotes the type of face (p-gon), where p is its number of edges and q the number of faces surrounding each vertex. A polyhedron can also be characterized by its *vertex configuration*, which just gives the kind of polygons along a circuit around a vertex. A polyhedron {p, q} has the vertex configuration p^q.

---

[1] We will use the notion introduced by Lord, E. A., Mackay, A. L., Ranganathan, S.: New Geometries for New Materials. Cambridge University Press, Cambridge (2006)
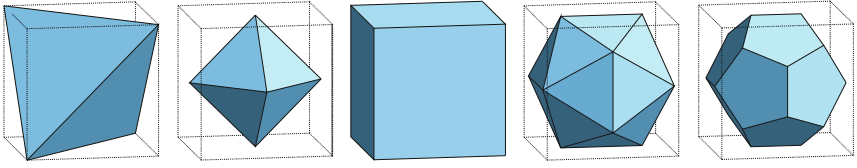
Fig. 2.2. The five Platonic solids inscribed in cubic unit cells to show their orientational relationships to the 2- and 3-fold axes of the cube: tetrahedron, $\{3,3\}$ 3^3, octahedron, $\{3,4\}$ 3^4, hexahedron (cube), $\{4,3\}$ 4^3, icosahedron, $\{3,5\}$ 3^5, dodecahedron, $\{5,3\}$ 5^3

The dual $\{q, p\}$ of any of the Platonic solids $\{p, q\}$ is a Platonic solid again. The tetrahedron is its own dual, cube and octahedron are duals of each other, and so are the icosahedron and the dodecahedron. The circumspheres of the Platonic solids pass through all vertices, the midspheres touch all edges and the inspheres all faces.

The other kind of convex uniform polyhedra, i.e. with one type of vertex surrounding only (vertex-transitive), are the *semi-regular* polyhedra. Their characteristic is that their faces are all regular polygons, however, of at least two kinds, i.e. they are facially regular but not face-transitive. They include the 13 *Archimedean solids* (Table 2.1 and Fig. 2.3) and infinitely many prisms and antiprisms with n-fold symmetry.

The prisms consist of two congruent n-gons plus n squares, $4^2.n$, and have point symmetry N/mmm. The antiprisms consist of two twisted congruent n-gons plus n equilateral triangles, $3^3.n$, with point symmetry $\overline{2N}m2$. Consequently, the only antiprism with crystallographic symmetry is the octahedron, 3^4. The square antiprism, $3^3.4$, has point symmetry $\bar{8}m2$ and the hexagonal antiprism, $3^3.6$, $\overline{12}m2$.

The Archimedean solids can all be inscribed in a sphere and in one of the Platonic solids. In Table 2.1 some characteristic values of the Archimedean polyhedra are listed. The snub cube and the snub dodecahedron can occur in two enantimorphic forms each. The cuboctahedron and the icosidodecahedron are edge-uniform as well and called *quasi-regular* polyhedra. The truncated cuboctahedron and the icosidodecahedron are also called great rhombicuboctahedron and great rhombicosidodecahedron, respectively. The syllable *rhomb* indicates that one subset of faces lies in the planes of the rhombic dodecahedron and rhombic triacontahedron, respectively.

The duals of the Archimedean solids are the *Catalan solids*. Their faces are congruent but not regular, i.e. they are face-transitive but not vertex-transitive. While the Archimedan solids have circumspheres, their duals have inspheres. The midspheres, touching the edges are common to both of them. The two most important cases for quasiperiodic structures are the rhombic dodecahedron $V(3.4)^2$, i.e. the dual of the cuboctahedron, and the rhombic triacontahedron $V(3.5)^2$, i.e. the dual of the icosidodecahedron (Fig. 2.3 (n) and (o)). The *face configuration* is used for the description of face-transitive polyhedra. It corresponds to a sequential count of the number of faces that exist

Table 2.1. Characteristic data for the thirteen Archimedean solids and of two of their duals (below the horizontal line). Faces are abbreviated tri(angle), squ(are), pen(tagon), hex(agon), oct(agon), dec(agon), rho(mb). In the last column, the ratio of the edge length a_s of the faces to the edge length of the circumscribed polyhedron (Platonic solid) a_p is given, where $p = c$(ubic), t(etrahedron), o(ctahedron), i(cosahedron), d(odecahedron), m(idsphere radius)

Name	Vertex Config- uration	Faces	Edges	Vertices	Point Group	Typical Ratios $p : a_s/a_p$
Truncated tetrahedron	3.6^2	4 tri, 4 hex	18	12	$\bar{4}3m$	$t : 1/3$
Cuboctahedron	$(3.4)^2$	8 tri, 6 squ	24	12	$m\bar{3}m$	$c : 1/\sqrt{2}$
Truncated cube	3.8^2	8 tri, 6 oct	36	24	$m\bar{3}m$	$c : \sqrt{2} - 1$
Rhombicuboctahedron	3.4^3	8 tri, 18 squ	48	24	$m\bar{3}m$	$c : \sqrt{2} - 1$
Truncated cubo-ctahedron	$4.6.8$	12 squ, 8 hex, 6 oct	72	48	$m\bar{3}m$	$c : 2/7(\sqrt{2} - 1)$
Truncated octahedron	4.6^2	8 tri, 6 oct	36	24	$m\bar{3}m$	$c : 1/2\sqrt{2}$
Snub cube[a]	$3^4.4$	32 tri, 6 squ	60	24	432	$c : 0.438$
Icosidodecahedron	$(3.5)^2$	20 tri, 12 pen	60	30	$m\bar{3}\bar{5}$	$i : 1/2$
Truncated dodecahedron	3.10^2	20 tri, 12 dec	90	60	$m\bar{3}\bar{5}$	$d : 1/\sqrt{5}$
Truncated icosahedron	5.6^2	12 pen, 20 hex	90	60	$m\bar{3}\bar{5}$	$i : 1/3$
Rhombicosi-dodecahedron	$3.4.5.4$	20 tri, 30 squ, 12 pen	120	60	$m\bar{3}\bar{5}$	$d : \sqrt{5} + 1/6$
Truncated icosidodecahedron	$4.6.10$	30 squ, 20 hex, 12 dec	180	120	$m\bar{3}\bar{5}$	$d : \sqrt{5} + 1/10$
Snub dodecahedron[a]	$3^4.5$	80 tri, 12 pen	150	60	235	$i : 0.562$
Rhombic dodecahedron	$V(3.4)^2$	12 rho	24	14	$m\bar{3}m$	$m : 3\sqrt{2}/4$
Rhombic triaconta-hedron	$V(3.5)^2$	30 rho	60	32	$m\bar{3}\bar{5}$	$m : (5 - \sqrt{5})/4$

[a]Two enantiomorphs

at each vertex around a face. For instance, $V(3.4)^2$ means that at the vertices of the 4-gon, which is a rhomb in this case, 3 or 4 faces, respectively, meet.
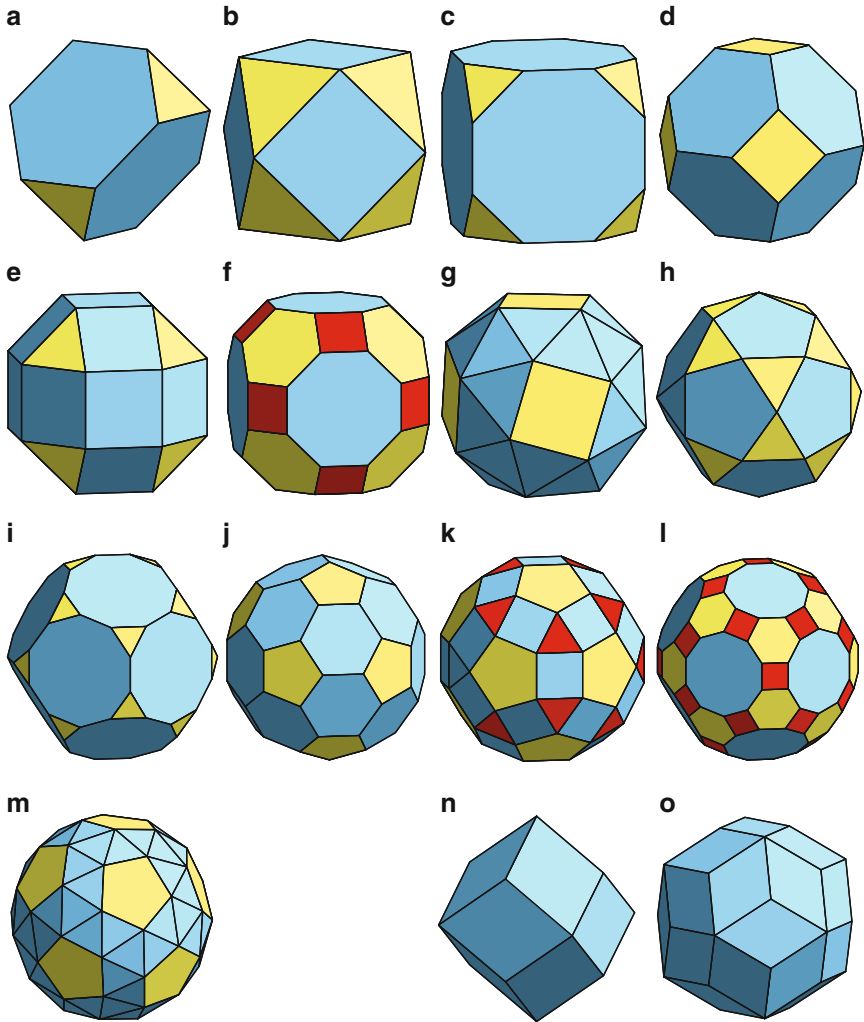
Fig. 2.3. The 13 Archimedean solids: (**a**) truncated tetrahedron, 3.6^2, (**b**) cuboctahedron, $(3.4)^2$, (**c**) truncated cube, 3.8^2, (**e**) (small) rhombicuboctahedron, 3.4^3, (**f**) truncated cuboctahedron (great rhombicuboctahedron), 4.6.8, (**d**) truncated octahedron, 4.6^2, (**g**) snub cube, $3^4.4$, only one enantiomorph shown, (**h**) icosidodecahedron, $(3.5)^2$, (**i**) truncated dodecahedron, 3.10^2, (**j**) truncated icosahedron, 5.6^2, (**k**) (small) rhombicosidodecahedron, 3.4.5.4, (**l**) truncated icosidodecahedron (great rhombicosidodecahedron), 4.6.10, (**m**) snub dodecahedron, $3^4.5$, only one enantiomorph shown. The rhombic dodecahedron, $V(3.4)^2$ (**n**), and the rhombic triacontahedron, $V(3.5)^2$ (**o**), are duals of the cuboctahedron (**b**) and the icosidodecahedron (**h**) and belong to the Catalan solids

2.2 Packings of Uniform Polyhedra with Cubic Symmetry

The cube is the only regular polyhedron that can tile 3D space without gaps and overlaps. The space group symmetry of the resulting tesselation is just that of a cubic lattice and denoted as $P4/m\bar{3}2/m : 4^3$. The truncated octahedron (Kelvin polyhedron, Voronoi cell of the *bcc* lattice), $Im\bar{3}m : 4.6^2$, is the only semi-regular polyhedron which can be packed space-filling, i.e. without gaps and overlaps, yielding a body-centered cubic (*bcc*) tiling. In all other cases, at least two types of (semi-)regular polyhedra are needed for space filling (Table 2.2).

Truncated cubes can be packed sharing the octagonal faces, the remaining voids are filled by octahedra (Fig. 2.4(b)). Octahedra are also needed to make the packing of square-sharing cuboctahedra space filling (Fig. 2.4(c)). The gaps left in an edge connected framework of octahedra can be filled by tetrahedra (Fig. 2.4(d)). The same is true for a packing of hexagon sharing truncated tetrahedra (Fig. 2.4(e)).

A *bcc* packing of truncated cuboctahedra, which touch each other with their hexagonal faces, need octagonal prisms for filling the gaps (Fig. 2.4(f)). Three polyhedra are needed for the following six packings. Square-sharing

Table 2.2. Space-filling packings of regular and semi-regular polyhedra with cubic symmetry

Polyhedra	Fig. 2.4	Space group: Symbols
Truncated octahedra	(a)	$Im\bar{3}m : 4.6^2$
Truncated cubes + octahedra	(b)	$Pm\bar{3}m : 3.8^2 + 3^4$
Cuboctahedra + octahedra	(c)	$Pm\bar{3}m : 3.4.3.4 + 3^4$
Octahedra + tetrahedra	(d)	$Fm\bar{3}m : 3^3 + 3^4$
Truncated tetrahedra + tetrahedra	(e)	$Fd\bar{3}m : 3.6^2 + 3^3$
Truncated cuboctahedra + octagonal prisms	(f)	$Im\bar{3}m : 4.6.8 + 4^2.8$
Rhombicuboctahedra + cuboctahedra + cubes	(g)	$Pm\bar{3}m : 3.4^3 + 3.4.3.4 + 4^3$
Rhombicuboctahedra + cubes + tetrahedra	(h)	$Fm\bar{3}m : 3.4^3 + 4^3 + 3^3$
Truncated cuboctahedra + truncated octahedra + cubes	(i)	$Pm\bar{3}m : 4.6.8 + 4.6^2 + 4^3$
Truncated octahedra + cuboctahedra + truncated (Friauf) tetrahedra	(j)	$Fm\bar{3}m : 4.6^2 + 3.4.3.4 + 3.6^2$
Truncated cuboctahedra + truncated cubes + truncated tetrahedra	(k)	$Fm\bar{3}m : 4.6.8 + 3.8^2 + 3.6^2$
Rhombicuboctahedra + truncated cubes + octagonal prisms + cubes	(l)	$Pm\bar{3}m : 3.4^3 + 3.8^2 + 4^2.8 + 4^3$
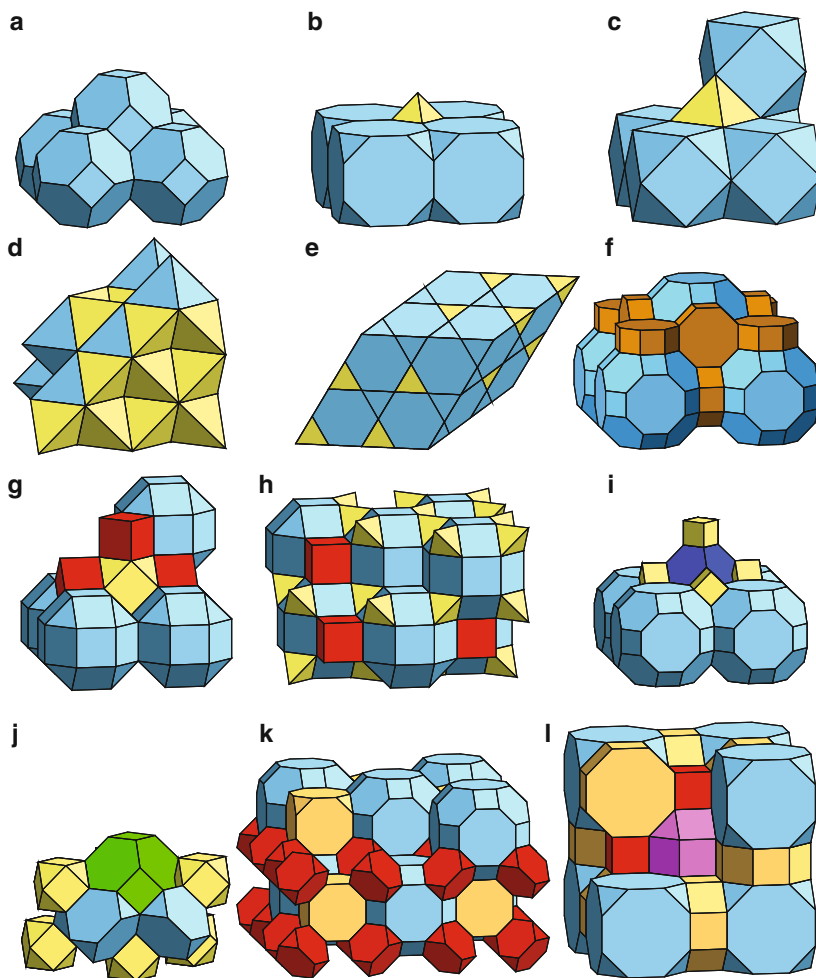
Fig. 2.4. Packings of regular and semi-regular polyhedra with resulting cubic symmetry (see also Table 2.2). (**a**) Truncated octahedra, (**b**) truncated cubes + octahedra, (**c**) cuboctahedra + octahedra, (**d**) octahedra + tetrahedra, (**e**) truncated tetrahedra + tetrahedra, (**f**) truncated cuboctahedra + octagonal prisms, (**g**) rhombicuboctahedra + cuboctahedra + cubes, (**h**) rhombicuboctahedra + truncated cubes + octagonal prisms + cubes, (**i**) truncated cuboctahedra + truncated octahedra + cubes, (**j**) truncated octahedra + cuboctahedra + truncated tetrahedra, (**k**) truncated cuboctahedra + truncated cubes + truncated tetrahedra (**l**) rhombicuboctahedra + truncated cubes + octagonal prisms + cubes

rhombicuboctahedra in a primitive cubic arrangement leave holes which can be filled by cubes and cuboctahedra in the ratio 1:3:1 (Fig. 2.4(g)). The gaps in a face-centered cubic packing of square sharing rhombicuboctahedra can be filled by cubes and tetrahedra (Fig. 2.4(h)).

Truncated cuboctahedra, in contact with their octagonal faces, form gaps to be filled with cubes and truncated octahedra (Fig. 2.4(i)). Truncated octahedra are fully surrounded by cuboctahedra, sharing the square faces, and by truncated tetrahedra linked by the hexagonal faces (Fig. 2.4(j)). This compound can be packed without gaps. Square-sharing truncated cuboctahedra form a *fcc* packing with voids, which can be filled with truncated cubes and truncated tetrahedra (Fig. 2.4(k)). Finally, a packing that needs four types of uniform polyhedra to be space filling: Truncated cubes linked via octagonal prisms form a primitive cubic tiling with rhombicuboctahedra in the center of the cubic unit cell and cubes filling the residual gaps (Fig. 2.4(l)).

2.3 Packings and Coverings of Polyhedra with Icosahedral Symmetry

There is no way to pack semi-regular polyhedra with icosahedral symmetry in a space-filling way, neither periodically nor quasiperiodically. However, allowing slight distortions (a few degrees) opens the way to numerous packings. For instance, four slightly deformed face-sharing pentagondodecahedra can form a tetrahedral cluster. Such clusters can be arranged in a diamond-structure-type network. Slightly distorted face-sharing pentagondodecahedra can also decorate the vertices and mid-edge positions of prolate and oblate Penrose rhombohedra forming the basic units of hierarchical (quasi)periodic structures.

Due to their group-subgroup relationship to cubic symmetry, edge or face-sharing icosahedra or pentagondodecahedra can be arranged on the vertices of cubic lattices in a non-space-filling way. It is also possible to create helical structures by face-sharing icosahedra or pentagondodecahedra.

3D coverings are gapless space-filling decorations of 3D tilings with partially overlapping polyhedra. The simplest case is a covering with tetrahedra. The tetrahedra overlap in small tetrahedral regions close to the corners. In other words, this covering corresponds to the packing of truncated tetrahedra and tetrahedra (Fig. 2.4(e)).

Triacontahedra can overlap by sharing a part of their vertices and volumes in two ways. Along the 5-fold direction, their shared volume corresponds to a rhombic icosahedron (Fig. 2.5(a)), and along the 3-fold direction just to an oblate golden rhombohedron (Fig. 2.5(b)). The vertices inside of two triacontrahedra interpenetrating along the 2-fold direction form a rhombic dodecahedron (Fig. 2.5(c)). The shared volume, however, is larger. Two faces of the rhombic dodecahedron are capped due to two additional vertices generated at the intersection of two edges each (Fig. 2.5(c)). The triacontahedron, as well as the rhombic icosahedron and dodecahedron are zonohedra. The edges of zonohedra are oriented in n directions. The number of faces equals $n(n-1)$. Starting with the triacontahedron (Fig. 2.6(a)), with $n = 6$, and removing one zone of faces, we get the rhombic icosahedron (Fig. 2.6(b)). Again removing one zone yields the rhombic dodecahedron (Fig. 2.6(c)), although a
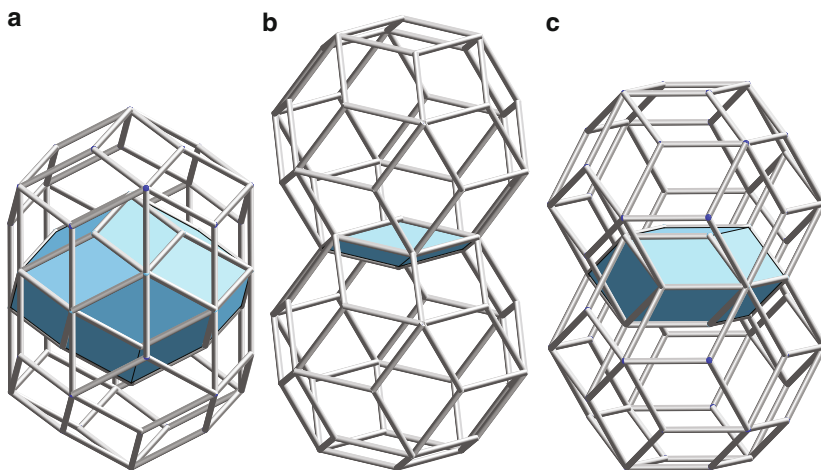
Fig. 2.5. Triacontahedra overlapping along the (**a**) 5-, (**b**) 3- and (**c**) 2-fold directions. The shared volumes, a rhombic icosahedron (**a**), an oblate golden rhombohedron and a rhombic dodecahedron (**c**), respectively, are marked
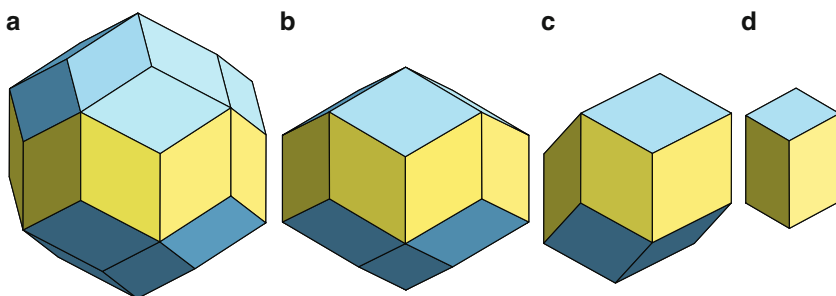
Fig. 2.6. The sequence of zonohedra resulting after repeated removal of zones (marked yellow): (**a**) Triacontahedron, (**b**) rhombic icosahedron, (**c**) rhombic dodecahedron, and (**d**) prolate golden rhombohedron

zonohedron as well, it is different from the one resulting as the dual of the cuboctahedron. While the first one is oblate, the latter one is more isometric. Finally, we obtain the prolate golden rhombohedron, one of the two prototiles of the 3D Penrose tiling (Ammann tiling) (Fig. 2.6(d)).

The rhombic triacontahedron is an edge- and face-transitive zonohedron (Catalan solid), dual to the icosidodecahedron. It is composed of 30 golden rhombs which are joined at 60 edges and 32 vertices, twelve 5-fold, and twenty 3-fold ones. The short diagonals of the rhombs form the edges of a pentagon-dodecahedron, the long diagonals an icosahedron. The faces of the triaconta-

hedron are rhombs with edge length a_r and with acute angle α_r

$$\alpha_r = \arccos(\frac{1}{\sqrt{5}}). \tag{2.1}$$

The long and short diagonals are

$$d_{\text{long}} = 2a_r\sqrt{\frac{5+\sqrt{5}}{10}} = \tau d_{\text{short}}, \quad d_{\text{short}} = 2a_r\sqrt{\frac{5-\sqrt{5}}{10}}. \tag{2.2}$$

The volume of the triacontahedron amounts to $V = 4a^3\sqrt{5+2\sqrt{5}}$, the surface to $A = 12a^2\sqrt{5}$. The dihedral angle between two faces is $2\pi/5$. The rhombic triacontahedron forms the hull of the projection of a 6D hypercube to 3D. A cube can be inscribed sharing 8 vertices of the subset of 20 of the dodecahedron. The edge length of the cube equals the long diagonal of the golden rhomb and any of the dodecahedron. The radius of the circumsphere is τa_r.

The icosahedral cluster shell is the optimum polyhedron for 12-fold coordination and a size ratio of 0.902 of the central atom to the coordinating atoms. In case of uniform spheres (size ratio 1), there is 12-fold coordination as well, leading to a cuboctahedron in the *ccp* case and to an anticuboctahedron (triangular orthobicupola) in the *hcp* case. Larger clusters that are typical for quasicrystals and their approximants, usually contain icosahedral and dodecagonal shells which then form triacontahedral clusters. Therefore, it is important to know the way such clusters can be packed periodically as well as quasiperiodically.

Packing triacontahedra along their 2-fold axes by sharing one face leads to a primitive cubic packing (Fig. 2.7(a)). In the center, between eight triacontrahedra, there is an empty space left with the shape of a dimpled triacontahedron. The vertices in the centers of the dimples form a cube (see Fig. 2.7(a)). This packing can also be seen as covering of triacontahedra located at the vertices of a *bcc* lattice. The triacontahedra share an oblate rhombohedron along each space diagonal (3-fold axis) of the cubic unit cell.

Since icosahedral quasicrystals show close resemblance to cluster-decorated Ammann tilings, it is worthwhile to discuss the way the prototiles can be decorated by triacontahedra. Along the face diagonals of the golden rhombs as well as along the edges, the tricontahedra share one face, along the 3-fold diagonals one oblate rhombohedron. Face sharing triacontahedra decorating the 30 vertices of an icosidodecahedron and the 12 vertices of an icosahedron form a cluster, the envelope of which is again a rhombic triacontahedron.[2]

[2] Sándor Kabai: 30+12 Rhombic Triacontahedra. The Wolfram Demonstrations Project http://demonstrations.wolfram.com/3012RhombicTriacontahedra/
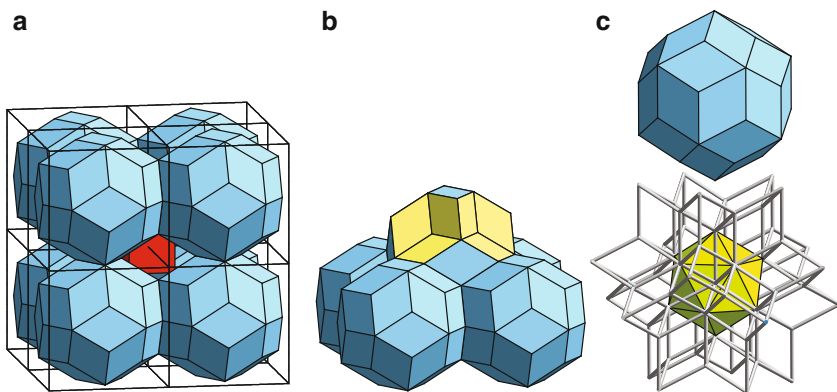
Fig. 2.7. (**a**) Packing of triacontahedra by sharing a face along each of the eight 2-fold directions. (**b**) The remaining empty space has the shape of a dimpled triacontahdron, i.e. a triacontahedron with eight oblate rhombohedra removed. (**c**) Packing of a triacontahedron into one of the twelve pentagonal dimples of a rhombic hexecontahedron

The formation of a compound of a triacontahedron with a stellated triacontahedron is shown in Fig. 2.7(c). The stellated triacontahedron, called rhombic hexecontahedron, consists of 20 prolate golden rhombohedra. The 12 vertices closest to the center of the star-polyhedron form an icosahedron.

3

Higher-Dimensional Approach

The nD approach elegantly restores hidden symmetries and correlations of quasiperiodic structures. Since it is based on reciprocal space information, it is directly accessible from experimental diffraction data. nD crystallography is an extension of the well developed 3D crystallography and many well-established powerful 3D methods can be adapted for nD structure analysis. The nD approach is also a prerequisite for understanding phason modes and the structural relationships between quasicrystals and their approximants. In this chapter, the nD embedding of 1D, 2D and 3D quasiperiodic tilings presented in Chap. 1 will be discussed.

Aperiodic crystals such as quasicrystals lack lattice periodicity in par-space. Their Fourier spectrum $M_\mathrm{F}^* = \{F(\mathbf{H})\}$ consists of δ-peaks on a $\mathbb{Z}$-module (an additive Abelian group)

$$
M^* = \left\{ \mathbf{H} = \sum_{i=1}^{n} h_i \mathbf{a}_i^* \,\middle|\, h_i \in \mathbb{Z} \right\}, \tag{3.1}
$$

of rank n ($n > d$) with basis vectors $\mathbf{a}_i^*$, $i = 1, \ldots, n$. In the embedding approach, n determines the minimal dimension of the embedding space and d that of the aperiodic crystal. In our considerations, the dimension d of the aperiodic crystal usually equals the dimension of 3D par-space $V^\parallel$.

The dimension of the space in which n-fold rotational symmetry gets compatible with mD lattice periodicity is shown in Table 3.1. Only even dimensions open up new possibilities. For existing quasiperiodic structures with 5-, 8-, 10- and 12-fold symmetry, embedding space dimensions up to four are sufficient. For the description of artificial quasiperiodic structures, which may be of interest for photonics, for instance, higher symmetries can be beneficial. Then, embedding spaces with even higher dimensions will be needed.

With increasing number of dimensions, the number of symmetry groups grows drastically (Table 3.2). Fortunately, only a rather small number of symmetry groups is needed for the description of quasicrystals. The restriction that the projection of the nD point symmetry group onto 3D par-space has to

Table 3.1. Dimension m of the space in which n-fold rotational symmetry gets compatible with mD lattice periodicity ([12], [14])

m	n
0	1
1	2
2	3, 4, 6
4	5, 8, 10, 12
6	7, 9, 14, 15, 18, 20, 24, 30
8	16, 21, 28, 36, 40, 42, 60
10	11, 22, 35, 45, 48, 56, 70, 72, 84, 90, 120

Table 3.2. Numbers of symmetry groups in dimensions up to $D = 6$ [41]. The number of enantiomorphic groups to be added for the total number of symmetry groups are given in parentheses

Symmetry group	1	2	3	4	5	6
Crystal systems	1	4	7	33 (+7)	59	251
Bravais lattices	1	5	14	64 (+10)	189	841
Point groups	2	10	32	227 (+44)	955	7 104
Space groups	2	17	219 (+11)	4783 (+111)	222 018 (+79)	28 927 922 (+7 052)

be isomorphous to the point group of the 3D quasiperiodic structure decreases the number of relevant symmetry groups drastically. The point groups for axial quasiperiodic structures for the general and a few special cases are listed in Table 3.3. The orientation of the symmetry elements in nD space is defined by the isomorphism of the 3D and the nD point groups. One has to keep in mind, however, that the action of an n-fold rotation can be different in the two orthogonal subspaces $V^{\parallel}$ and $V^{\perp}$. There are only two point groups for quasicrystals with icosahedral diffraction symmetry $m\bar{3}\bar{5}$, of order $k = 120$, and 235, of order 60.

What is the physics behind the nD approach? A crystal structure can be fully described by its lattice parameters, space group, and the content of the asymmetric unit. Of course, the symmetry of a structure is the consequence and not the origin of its order. The existence of a lattice is the usual consequence of packing copies of a finite number of structural building units as dense as possible. For instance, the densest packing of a single layer of uniform spheres automatically obeys the 2D space group symmetry $p6mm$.

Table 3.3. 3D Point symmetry groups of axial quasicrystals [36]. Besides the general case with n-fold rotational symmetry, a few practically relevant special cases are given. k denotes the order of the group. Under 'Type' the corresponding periodic crystal symmetry type is given

Point Group Type	k	Conditions	$n=5$ trigonal	$n=7$ trigonal	$n=8$ tetragonal	$n=10$ hexagonal	$n=12$ dodecagonal
$\dfrac{n}{m}\dfrac{2}{m}\dfrac{2}{m}$	$4n$	n even			$\dfrac{8}{m}\dfrac{2}{m}\dfrac{2}{m}$	$\dfrac{10}{m}\dfrac{2}{m}\dfrac{2}{m}$	$\dfrac{12}{m}\dfrac{2}{m}\dfrac{2}{m}$
$\bar{n}\,2m$	$2n$	n even			$\bar{8}\,2m$	$\overline{10}\,2m$	$\overline{12}\,2m$
$\bar{n}\dfrac{2}{m}$	$4n$	n odd	$\bar{5}\dfrac{2}{m}$	$\bar{7}\dfrac{2}{m}$			
nmm	$2n$	n even			$8mm$	$10mm$	$12mm$
nm	$2n$	n odd	$5m$	$7m$			
$n\,2\,2$	$2n$	n even			$8\,2\,2$	$10\,2\,2$	$12\,2\,2$
$n\,2$	$2n$	n odd	$5\,2$	$7\,2$			
$\dfrac{n}{m}$	$2n$	n even			$\dfrac{8}{m}$	$\dfrac{10}{m}$	$\dfrac{12}{m}$
$\bar{n}$	$2n$	n even			$\bar{8}$	$\overline{10}$	$\overline{12}$
$\bar{n}$	n	n odd	$\bar{5}$	$\bar{7}$			
n	n		5	7	8	10	12

The same is true for quasicrystals. Let us assume that a quasiperiodic structure can be described as covering based on one or more clusters with non-crystallographic symmetry. Then, the cluster centers form a subset of a $\mathbb{Z}$ module. A $\mathbb{Z}$ module can be seen as proper projection of an nD lattice onto physical space. The hard constraint, to have a minimum distance between cluster centers, means that only a part of the nD lattice is to be projected onto physical space. This bounded region is called strip or window ($\Rightarrow$ strip-projection method) (see Fig. 3.3).

This means that the condition of a minimum distance is the only physics hidden in the nD approach. Thus, it is just a brilliant visualization of geometrical constraints. Some physical interactions in quasiperiodic structures, however, may be more vividly described based in the nD approach.

3.1 nD Direct and Reciprocal Space Embedding

The nD embedding space V can be separated into two orthogonal subspaces both preserving the point group symmetry according to the nD space group

$$V = V^{\parallel} \oplus V^{\perp}, \tag{3.2}$$

with the par(allel) space $V^{\parallel} = \mathrm{span}(\mathbf{v}_1, \mathbf{v}_2, \mathbf{v}_3)$ and the perp(endicular) space $V^{\perp} = \mathrm{span}(\mathbf{v}_4, \ldots, \mathbf{v}_n)$. If not indicated explicitly, the basis defined by the vectors $\mathbf{v}_i$ (V-basis) will refer to a Cartesian coordinate system. The n-star of rationally independent vectors defining the $\mathbb{Z}$-module M^* can be considered as appropriate *projection* $\mathbf{a}_i^* = \pi^{\parallel}(\mathbf{d}_i^*)$ ($i = 1, \ldots, n$) of the basis vectors $\mathbf{d}_i^*$ (D-basis) of an nD reciprocal lattice Σ^* with

$$M^* = \pi^{\parallel}(\Sigma^*) \ . \tag{3.3}$$

As simple illustration of the nD embedding, the relationship between the 1D reciprocal space of the Fibonacci sequence and its 2D embedding space is shown in Fig. 3.1(c). For comparison, the ways of embedding other kinds of aperiodic crystals such as incommensurately modulated structures (IMS) (Fig. 3.1(a)) and composite structures (CS) (Fig. 3.1(b)) are shown as well (for a more in-depth description see [48]). Additionally, beside the standard way of embedding a quasiperiodic structure (QC-setting), an alternative way, the IMS-setting is shown (Fig. 3.1(d)). The latter one can be particularly
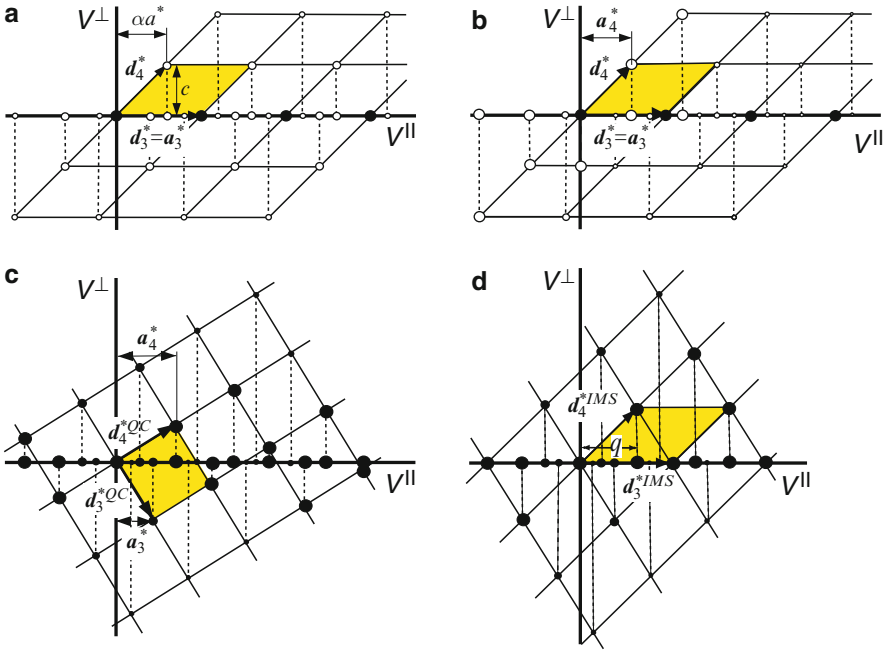

Fig. 3.1. Reciprocal space embedding of the 3D aperiodic structures shown in Fig. 3.2. (**a**) Incommensurately modulated structure (IMS), (**b**) composite structure (CS), (**c**) Fibonacci sequence in the standard QC-setting and in the (**d**) IMS-setting. Dashed lines indicate the projections, vectors $\mathbf{d}_i^*$ refer to the nD reciprocal basis (D-basis), a^* and a_i^* are the lattice parameters in reciprocal par-space, $q = \alpha a^*$ is the modulus of the wave vector of an incommensurate modulation

useful for the study of structural phase transitions of QC. The IMS-setting can also be seen as approximant structure in perp-space contrary to the usual approximants in par-space.

Characteristic features of quasicrystals are their non-crystallographic point group symmetry and their reciprocal-space scaling symmetry $\mathsf{S}M^* = sM^*$. S denotes a scaling symmetry matrix acting on a Fourier module and s is its eigenvalue. In the case of quasiperiodic structures with crystallographic point symmetry, the structures may be described either as quasicrystals or as IMS or CS, respectively. In practice, the embedding technique applied will depend on the intensity distribution. If large Fourier coefficients exist on a subset $\Lambda^* \subset M^*$, the description as IMS may be preferable. However, if the major Fourier coefficients are related by scaling, the quasicrystal will be the more appropriate description.

The hyperspace decomposition equation (3.2) has to keep the orthogonal subspaces invariant under the symmetry operations $\Gamma(R)$ of the nD point group $K^{n\mathrm{D}}$ of Σ^*. These restrictions have the important consequence that only a small subset of all nD symmetry groups is necessary to describe the symmetry of aperiodic crystals in the nD approach.

The two invariant subspaces are defined by the eigenvectors of the symmetry operations. The reduced symmetry operations are obtained by the similarity transformation

$$\mathsf{W}\Gamma(R)\mathsf{W}^{-1} = \Gamma^{\mathrm{red}}(R) = \Gamma^{\parallel}(R) \oplus \Gamma^{\perp}(R),\ R \in K^{n\mathrm{D}}\ . \qquad (3.4)$$

The reduced symmetry matrix is block-diagonal consisting of the symmetry operations of each subspace. The columns of W are the vectors $\mathbf{d}_i^*$, with components given on the V-basis, spanning the reciprocal space, while the blocks of rows can be considered as projectors $\pi^{\parallel}$ and $\pi^{\perp}$ onto $V^{\parallel}$ and $V^{\perp}$, respectively. The rows of W^{-1} are the components, defined on the V-basis, of the vectors $\mathbf{d}_i$ spanning the direct space.

In direct space, the aperiodic crystal structure results from a *cut* of a periodic nD *hypercrystal* with dD physical (parallel) space $V^{\parallel}$ [17] (Fig. 3.2). An nD hypercrystal corresponds to an nD lattice Σ decorated with nD *hyperatoms*. The basis vectors of Σ are obtained via the orthogonality condition of direct and reciprocal space

$$\mathbf{d}_i \mathbf{d}_j^* = \delta_{ij}\ . \qquad (3.5)$$

The atomic positions in par-space thus depend on the embedding and the shape of the *atomic surfaces* (*occupation domains*). Atomic surfaces are the components of hyperatoms in $(n - d)$D complementary (perpendicular) space $V^{\perp}$ (Fig. 3.2). Cutting a hypercrystal structure with par-space at different perp-space positions will result in different par-space structures. This is a consequence of the irrational slope of the par-space section with respect to the n-dimensional lattice. All sections with different perp-space components belong to the same *local isomorphism class* (i.e. they are homometric)
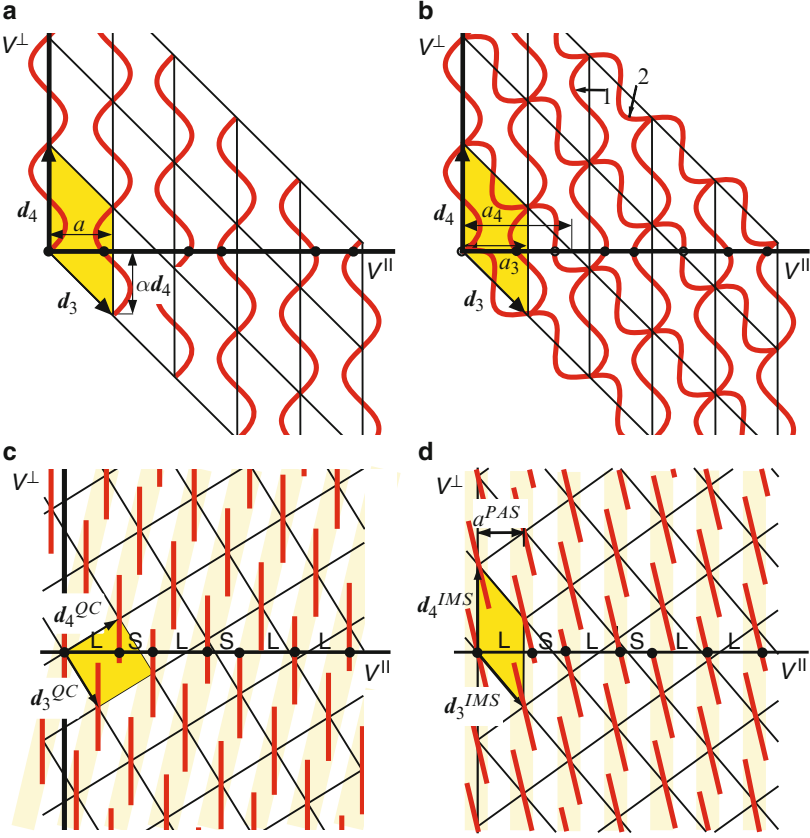
Fig. 3.2. Direct-space embedding of the three fundamental types of 3D aperiodic structures: (**a**) modulated structure, (**b**) composite structure with modulated subsystems (marked 1 and 2), and quasiperiodic sequences in the (**c**) QC-setting and (**d**) IMS-setting. Vectors $\mathbf{d}_i$ mark the nD basis vectors while a and a^{PAS} refer to the lattice parameters of the average structures. L and S denote the long and short unit tiles of the Fibonacci sequence

and will show identical diffraction patterns. Consequently, only quasicrystals belonging to different local isomorphism classes can be distinguished by diffraction experiments.

The various types of aperiodic crystals differ from each other by the characteristics of their atomic surfaces. Quasicrystals show *discrete* atomic surfaces (which may also be of fractal shape) while those of IMS and CS are essentially *continuous*. Essentially continuous means that they may consist also of discrete segments in the presence of a density modulation. However, their atomic surfaces can always be described by modulation functions. With the amplitudes of the modulation function going to zero, a continuous transition to a

periodic structure (basis structure) will be performed. Composite structures consist of two or more substructures which themselves may be modulated. In reciprocal space, the characteristics of IMS and CS are the crystallographic point symmetry of their Fourier modules M^* and the existence of large Fourier coefficients on a distinct subset $\Lambda^* \subset M^*$ related to the reciprocal lattice of their *periodic average structures (PAS)* (see Sect. 3.3).

The embedding method discussed so far is called *cut-and-project method*. The par-space cut through the *n*D hypercrystal corresponds to a reciprocal space projection onto the par-space. This is a consequence of the mathematical relationship between direct and reciprocal space, i.e. the Fourier transform. This *n*D approach has originally been introduced by de Wolff for the description of IMS and has been later extended for CS ([16] and references therein) and, eventually, adopted and adapted for the description of QC [16].

Originally, Nicolaas G. de Bruijn [5] laid the foundation of the *n*D approach for quasicrystals by defining vertex selection rules (occupation domains) for the Penrose tiling. Embedding his occupation domains (windows) in 4D space, he created the method later called *strip-projection* method. Thereby, the window (strip, occupation domain) cuts selected points out of a lattice which then are projected onto the boundary of the window. In reciprocal space, the Fourier transform results as the convolution of the Fourier transform of the lattice, which is a point lattice again, with the Fourier transform of the window (Fig. 3.3). If the embedding is performed in a way that the resulting *n*D lattice is hypercubic and the projection of the *n*D unit cell onto $V^\perp$ gives the acceptance window, it is called *canonical embedding* and the generated tiling is denoted as canonical projection tiling.
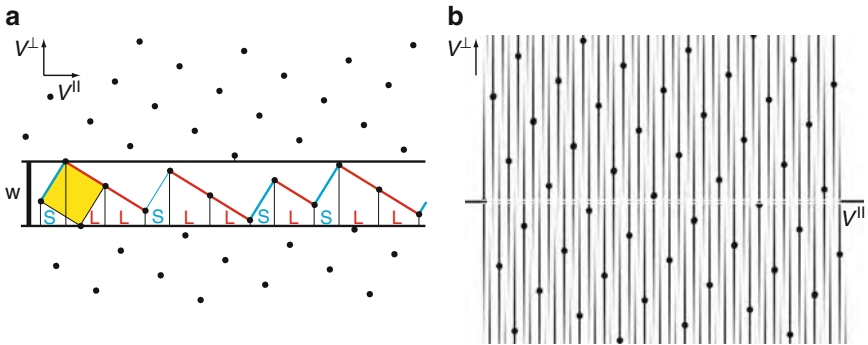

Fig. 3.3. 2D embedding of the 1D Fibonacci sequence according to the strip-projection method. (**a**) A strip with the irrational slope $1/\tau$ relative to the 2D lattice acts as window with width w. The lattice points inside the strip projected onto its boundary, the par-space, yield the Fibonacci sequence. (**b**) In reciprocal space, each lattice point is convoluted with the Fourier transform (FT) of the strip (indicated as density plot). The Fourier transform of the 1D FS is obtained by cutting the FT of the window (indicated by the white double line)

Hyperatom An ideal nD hypercrystal is an nD periodic arrangement of nD objects, the hyperatoms. The 3D par-space component of a hyperatom is described in the same way as an atom for a 3D periodic crystal structure. The $(n-3)$D perp-space component is called atomic surface or occupation domain.

Atomic surface An atomic surface is a kind of probability density distribution function. Each point on an atomic surface gives the probability to find an atom in the respective par-space intersection. It contains information on the atomic species and other atomic parameters as well. Atomic surfaces can be partitioned into subdomains.

Atomic surface partition An atomic surface is partitioned into subdomains that contain all vertices with the same coordination (atomic environment type, AET). Equal AET means equal Wigner–Seitz cell (Voronoi domain) and, with some restrictions, the same local physical (e.g., magnetic moment) and chemical (e.g., bonding) properties.

3.2 Rational Approximants

The nD approach allows an illustrative representation of the relationships between aperiodic crystals and their *rational approximants* [9, 10]. The analogue to the lock-in transition of an IMS to a commensurately modulated structure (superstructure) is the transition of a quasicrystal to a rational approximant (Fig. 3.4). While in the case of an IMS the modulation vector changes from an irrational to a rational value, for a QC the number of n rationally independent reciprocal basis vectors changes to d, i.e. the dimension of the par-space. In hyperspace, the irrational slope of the cut of the nD lattice with par-space turns into a rational one. This means, that the corresponding lattice nodes lie exactly in the par-space and determine the lattice parameters of the three-dimensional periodic approximant.

This transition can be described by a shear deformation (linear phason strain) of the hypercrystal parallel to $V^\perp$ [10]. Thereby, a position vector $\mathbf{r}$ of the nD hypercrystal is transformed to the vector $\mathbf{r}'$ of the approximant:

$$\mathbf{r}' = \mathsf{A}^\perp \mathbf{r} \tag{3.6}$$

with the shear matrix

$$\mathsf{A}^\perp = \left(\begin{array}{ccc|ccc} 1 & & 0 & 0 & \cdots & 0 \\ & \ddots & & \vdots & \ddots & \vdots \\ 0 & & 1 & 0 & \cdots & 0 \\ \hline A_{41} & \cdots & A_{43} & 1 & & 0 \\ \vdots & \ddots & \vdots & & \ddots & \\ A_{n1} & \cdots & A_{n3} & 0 & & 1 \end{array}\right)_V = \left(\begin{array}{c|c} 1 & 0 \\ \hline (\tilde{A}^{-1})^T & 1 \end{array}\right)_V . \tag{3.7}$$
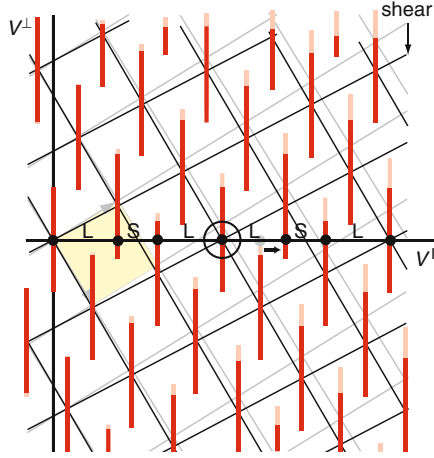
Fig. 3.4. Embedded Fibonacci chain ...LSLSLL... (semi-opaque in the background) and its rational (LSL) approximant. The encircled lattice node is shifted to par-space by shearing the 2D lattice along the perp-space. Thereby, one par-space cut disappears in the drawing and a new one appears changing locally SL into LS (phason flip marked by a horizontal arrow)
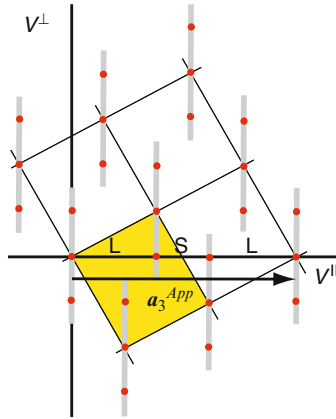

Fig. 3.5. Embedding of a FS approximant (LSL) with discrete atomic surfaces (online: red dots) overlaid the atomic surfaces of the sheared FS (gray). The size of the par-space unit cell is marked by an arrow

The determinant of A is equal to one. Thus, the volume of the nD unit cell does not change during the transformation. However, due to the rational slope of par-space the atomic surfaces are not dense anymore but consist of discrete points (Fig. 3.5). The point density of quasicrystals and their approximants differ and shifting par-space parallel to $V^\perp$ can change the structure of the approximant. The symmetry group of the approximant is a subgroup of the

symmetry group of the quasicrystal. The eliminated symmetry elements can appear as twin laws [25], as observed, e.g., in 10-fold twinned orthorhombic approximants of decagonal $Al_{70}Co_{15}Ni_{15}$ [24].

In reciprocal space, the phason strain leads to a shift of the diffraction vectors $\mathbf{H}$ as a function of their perp-space components:

$$\mathbf{H}^{\parallel\prime} = \mathbf{H}^{\parallel} + \tilde{A}\mathbf{H}^{\perp} . \tag{3.8}$$

The nD reciprocal lattice vectors transform according to

$$\mathbf{H}' = (A^{-1})^T\mathbf{H} \tag{3.9}$$

with

$$(A^{-1})^T = \begin{pmatrix} 1 & & 0 & -A_{41} & \cdots & -A_{n1} \\ & \ddots & & \vdots & \ddots & \vdots \\ 0 & & 1 & -A_{43} & \cdots & -A_{n3} \\ \hline 0 \cdots 0 & & & 1 & & 0 \\ \vdots \ddots \vdots & & & & \ddots & \\ 0 \cdots 0 & & & 0 & & 1 \end{pmatrix}_V = \begin{pmatrix} 1 & \tilde{A} \\ \hline 0 & 1 \end{pmatrix}_V . \tag{3.10}$$

Since the approximant structure results from a rational cut of the nD lattice with par-space, its diffraction pattern corresponds to a projection of nD reciprocal space along rational reciprocal lattice lines. Consequently, the Fourier coefficients of the approximant correspond to the sum of the Fourier coefficients (structure factors) that project onto one and the same diffraction vector of the approximant, $\mathbf{H}^{Ap}$, in physical reciprocal space.

3.3 Periodic Average Structure (PAS)

The PAS of an IMS can be obtained by orthogonal projection of the modulation function onto par-space (see Fig. 3.2(a)). In case of QC, this would give a dense structure. To obtain the PAS of a QC in the usual setting, an oblique projection in a proper direction has to be performed (see Fig. 3.2(c)) ([45], and references therein). The reciprocal-space point group symmetry of the PAS of an IMS is equal or higher to that of the IMS while it is equal or lower in case of a quasiperiodic structure.

The oblique projection is not the only way to obtain a PAS. As shown in Figs. 3.1 and 3.2, quasiperiodic structures can be embedded in different ways. The standard way, denoted by QC-setting, is the symmetry adapted way of embedding. The alternative embedding, called IMS-setting, selects a subset of reflections on a 3D point lattice as main reflections and deals with all others

as satellite reflections. Since main reflections lie in par-space by definition, the reciprocal hyperlattice has to be sheared parallel to the perp-space, $\Sigma^*_{\mathrm{IMS}} = \mathsf{A}^\perp \Sigma^*_{\mathrm{QC}}$, to achieve this condition. In direct space, this corresponds to a shear of the hyperlattice parallel to par-space, $\Sigma_{\mathrm{IMS}} = \mathsf{A}^\parallel \Sigma_{\mathrm{QC}}$, $\mathsf{A}^\parallel = (\tilde{\mathsf{A}}^\perp)^{-1}$, leaving the par-space intersection with the hyperstructure invariant.

Once the unit cell parameters of the PAS of a quasiperiodic structure are known, the PAS can as well be obtained by taking the structure modulo the unit cell. All atomic positions are mapped into the projected atomic surfaces. This means that the boundaries of the projected atomic surfaces give the maximum distance of an atom of the quasiperiodic structure from the next atomic site of the PAS.

The point-group symmetry of the PAS, which always is a crystallographic one, is necessarily lower than that of the QC with its non-crystallographic symmetry (except for 1D QC). Therefore, a one-to-one mapping of the atoms of a quasiperiodic structure to the projected atomic surfaces of the PAS is not possible due to topological reasons. This means that some of the projected atomic surfaces may contain none, or more than one atomic position if one superposes the quasiperiodic structure with its PAS.

Since for a single quasiperiodic structure an infinite number of different PAS is possible, one needs to find the most relevant one. This will be the PAS with the smallest possible projected atomic surfaces which have occupancy factors closest to one. The total Bragg intensity in the respective reciprocal space section is a direct measure for this property. By using the set of strongest Bragg reflections as reciprocal basis of the PAS, one usually obtains the most representative PAS.

The occupancy factor can be calculated comparing the point densities of the quasiperiodic structure and its PAS. It is also related to the ratio of the total area of the projected atomic surfaces in one unit cell of the PAS to the area of this unit cell. The relevance of a PAS can be estimated by the ratio of the total intensity of the reflections related to the PAS to the total intensity of all reflections.

The size of the projected atomic surface is a measure for the maximum displacement of an atom on a PAS site that is necessary to move it to its position in the quasiperiodic structure. This can be seen as the amplitude of a displacive modulation which transforms the PAS into the respective QC. Since the occupancy factor cannot be exactly one for topological reasons, except in the 1D case, this displacive modulation is always accompanied by a substitutional (density) modulation.

These concepts are of particular interest for the study of geometrical aspects of quasicrystal-to-crystal phase transformations, growth of quasicrystal–crystal interfaces, as well as the intrinsic band-gap behavior of photonic or phononic quasicrystals. The PAS allows to (loosely) classify quasiperiodic structures regarding their "degree of quasiperiodicity," depending on how close their structures are to periodicity.

3.4 Structure Factor

The structure factor $F(\mathbf{H})$ of a periodic structure is defined as the Fourier transform (FT) of the electron density distribution function $\rho(\mathbf{r})$ of the m atoms within its unit cell (UC)

$$F(\mathbf{H}) = \int_{\text{UC}} \rho(\mathbf{r}) \, e^{2\pi i \mathbf{Hr}} \, d\mathbf{r} = \sum_{k=1}^{m} T_k(\mathbf{H}) \, f_k(|\mathbf{H}|) \, e^{2\pi i \mathbf{Hr}_k} . \qquad (3.11)$$

For discretely distributed atoms, the FT can be performed for each atom separately yielding the atomic scattering factors $f_k(|\mathbf{H}|)$. The same is true for the average displacements of the atoms from their equilibrium positions due to phonons (thermal vibrations). The FT of the probability density function to find an atom in a given volume gives the temperature factor $T_k(\mathbf{H})$. This allows to replace the Fourier integral by a sum over the n atoms in the unit cell.

The temperature factor is called Debye–Waller (DW) factor if it describes the effect of thermal vibrations of atoms (due to phonons) on the intensities of Bragg reflections. In the course of structure refinements, however, this factor subsumes also contributions from static displacements (due to disorder) of the atoms from their equilibrium positions. Consequently, the more general term "atomic displacement factor (ADF)" should be used, and instead of "atomic thermal parameters" rather the term "atomic displacement parameters (ADP)" should be used.

3.4.1 General Formulae

In a similar way, the structure factor of a quasicrystal can be calculated within the nD approach. In case of a dD quasiperiodic structure, the FT of the electron density distribution function $\rho(\mathbf{r})$ of the m hyperatoms within the nD unit cell can be separated into the contributions of the dD par- and $(n-d)$D perp-space components and we obtain

$$F(\mathbf{H}) = \sum_{k=1}^{m} T_k\left(\mathbf{H}^{\|}, \mathbf{H}^{\perp}\right) f_k\left(|\mathbf{H}^{\|}|\right) g_k\left(\mathbf{H}^{\perp}\right) e^{2\pi i \mathbf{Hr}_k} . \qquad (3.12)$$

In par-space one gets the conventional atomic scattering factor $f_k\left(|\mathbf{H}^{\|}|\right)$ and the atomic displacement (temperature) factor $T_k\left(\mathbf{H}^{\|}\right)$. In perp-space, the FT of the atomic surfaces, called geometrical form factor $g_k\left(\mathbf{H}^{\perp}\right)$, results to

$$g_k\left(\mathbf{H}^{\perp}\right) = \frac{1}{A_{\text{UC}}^{\perp}} \int_{A_k} e^{2\pi i \mathbf{H}^{\perp} \mathbf{r}^{\perp}} \, d\mathbf{r}^{\perp}, \qquad (3.13)$$

with $A_{\text{UC}}^{\perp}$ the volume of the nD unit cell projected onto $V^{\perp}$, and A_k the volume of the k-th atomic surface. For polygonal, polyhedral, or polychoral domains, which can be decomposed into triangles, tetrahedra, or pentachora,

the geometrical form factor is calculated from their unique parts using the site symmetry. Since the Fourier integral is linear, the geometrical form factor results from the summation of the Fourier integrals of these fundamental units.

The perp-space component $T_k\left(\mathbf{H}^\perp\right)$ of the atomic displacement (temperature) factor describes the effect of phason fluctuations along the perp-space. These fluctuations, originate either from phason modes or from random phason flips. Assuming harmonic (static or dynamic) displacements in nD space one obtains in analogy to the usual expression [50]

$$T_k\left(\mathbf{H}\right) = T_k\left(\mathbf{H}^\|, \mathbf{H}^\perp\right) = \mathrm{e}^{-2\pi^2 \mathbf{H}^{\|T}\langle \mathbf{u}^\| \mathbf{u}^{\|T}\rangle \mathbf{H}^\|}\mathrm{e}^{-2\pi^2 \mathbf{H}^{\perp T}\langle \mathbf{u}^\perp \mathbf{u}^{\perp T}\rangle \mathbf{H}^\perp}, \quad (3.14)$$

with

$$\langle \mathbf{u}_i^\| \mathbf{u}_j^{\|T}\rangle = \begin{pmatrix} \langle u_1^2\rangle & \langle u_1 u_2\rangle & \langle u_1 u_3\rangle \\ \langle u_2 u_1\rangle & \langle u_2^2\rangle & \langle u_2 u_3\rangle \\ \langle u_3 u_1\rangle & \langle u_3 u_2\rangle & \langle u_3^2\rangle \end{pmatrix}_V \quad (3.15)$$

and

$$\langle \mathbf{u}_i^\perp \mathbf{u}_j^{\perp T}\rangle = \begin{pmatrix} \langle u_4^2\rangle & \cdots & \langle u_4 u_n\rangle \\ \vdots & \ddots & \vdots \\ \langle u_n u_4\rangle & \cdots & \langle u_n^2\rangle \end{pmatrix}_V. \quad (3.16)$$

The elements of type $\langle u_i u_j\rangle$ represent the mean displacements of the hyperatoms along the i-th axis times the displacements of the atoms along the j-th axis on the V-basis. This model excludes phonon–phason interactions as no coupling is defined.

3.4.2 Calculation of the Geometrical Form Factor

In the following, the calculation of the geometrical form factor is illustrated for the most important classes of quasicrystals. In case of pentagonal, octagonal, decagonal, and dodecagonal structures, the FT has to be performed for 2D atomic surfaces, in case of icosahedral structures for 3D atomic surfaces, and in the case of heptagonal and tetrakaidecagonal structures 4D atomic surfaces have to be Fourier transformed. As already mentioned, this problem is essentially reduced to the calculation of the FT of triangles, tetrahedra, and pentachora, respectively.

Although the general solution for this problem is well known [13], some special cases, leading to singularities in these general formulae have to be calculated explicitly. In the following, the formulae for the different cases are given.

3.4.2.1 2D Atomic Surfaces

The FT of a triangle defined by two vectors $\mathbf{e}_1, \mathbf{e}_2$, can be calculated based on an oblique coordinate system: $\mathbf{x} = x_1 \mathbf{e}_1 + x_2 \mathbf{e}_2$ and $2\pi\mathbf{q} = q_1 \mathbf{e}_1^* + q_2 \mathbf{e}_2^*$, where $q_j = 2\pi\mathbf{H}\,\mathbf{e}_j$ and $\mathbf{e}_i \mathbf{e}_j^* = \delta_{ij}$. With

$$F_0(\mathbf{H}) = \int \exp(2\pi\mathrm{i}\mathbf{q} \cdot \mathbf{x})\mathrm{d}V \quad (3.17)$$

and $dV = V \, dx_1 \, dx_2$, where V is the volume of the parallelogram defined by $\mathbf{e}_1, \mathbf{e}_2$, $V = |\mathbf{e}_1 \times \mathbf{e}_2|$, it follows for the Fourier integral:

$$F_0(\mathbf{H}) = V \int_0^1 \exp(iq_1 x_1) dx_1 \int_0^{1-x_1} \exp(iq_2 x_2) dx_2. \tag{3.18}$$

The direct calculation of the above integral leads to

$$F_0(\mathbf{H}) = V(q_1(\exp(iq_2) - 1) - q_2(\exp(iq_1) - 1))/(q_1 q_2 (q_1 - q_2)). \tag{3.19}$$

To avoid singularities in (3.19), a case differentiation must be done before integration of (3.18). In the following, the special cases and the corresponding formulae are given.

Case 1 $q_1 = 0, q_2 = 0$: $F_0(\mathbf{H}) = \frac{1}{2}V$.
Case 2 $q_1 = 0, q_2 = q/q_1 = q, q_2 = 0$: $F_0(\mathbf{H}) = V(1 + iq - \exp(iq))/q^2$.
Case 3 $q_1 = q, q_2 = q$: $F_0(\mathbf{H}) = V(\exp(iq)(1 - iq) - 1)/q^2$.

3.4.2.2 3D Atomic Surfaces

The FT of a tetrahedron defined by three vectors $\mathbf{e}_1, \mathbf{e}_2, \mathbf{e}_3$, can be calculated based on an oblique coordinate system: $\mathbf{x} = x_1 \mathbf{e}_1 + x_2 \mathbf{e}_2 + x_3 \mathbf{e}_3$ and $2\pi \mathbf{q} = q_1 \mathbf{e}_1^* + q_2 \mathbf{e}_2^* + q_3 \mathbf{e}_3^*$, where $q_j = 2\pi \mathbf{H} \, \mathbf{e}_j$ and $\mathbf{e}_i \mathbf{e}_j^* = \delta_{ij}$. With

$$F_0(\mathbf{H}) = \int \exp(2\pi i \mathbf{q} \cdot \mathbf{x}) dV \tag{3.20}$$

and $dV = V dx_1 \, dx_2 \, dx_3$, where V is the volume of the parallelepiped defined by $\mathbf{e}_1, \mathbf{e}_2, \mathbf{e}_3$, $V = \mathbf{e}_1 \cdot |\mathbf{e}_2 \times \mathbf{e}_3|$, it follows for the Fourier integral

$$F_0(\mathbf{H}) = V \int_0^1 \exp(iq_1 x_1) dx_1 \int_0^{1-x_1} \exp(iq_2 x_2) dx_2$$
$$\cdot \int_0^{1-x_1-x_2} \exp(iq_3 x_3) dx_3. \tag{3.21}$$

The direct calculation of the above integral leads to

$$F_0(\mathbf{H}) = -iV(q_2 q_3 q_4 \exp(iq_1) + q_3 q_1 q_5 \exp(iq_2) + q_1 q_2 q_6 \exp(iq_3)$$
$$+ q_4 q_5 q_6)/(q_1 q_2 q_3 q_4 q_5 q_6) \tag{3.22}$$

with $q_j = 2\pi \mathbf{H} \, \mathbf{e}_j, (j = 1, 2, 3)$, $q_4 = q_2 - q_3, q_5 = q_3 - q_1$, and $q_6 = q_1 - q_2$.

To avoid singularities in (3.22), a case differentiation must be done before integration of (3.21). In the following, the special cases and the corresponding formulae are given.

`Case 1` $q_1 = 0, q_2 = 0, q_3 = 0$: $F_0(\mathbf{H}) = \frac{1}{6}V$.

`Case 2` $q_1 = 0, q_2 = 0, q_3 = q/q_1 = 0, q_2 = q, q_3 = 0/q_1 = q, q_2 = 0, q_3 = 0$:

$$F_0(\mathbf{H}) = V(q(1 + \frac{1}{2}\mathrm{i}q) + \mathrm{i}\exp(\mathrm{i}q) - \mathrm{i})/q^3. \tag{3.23}$$

`Case 3` $q_1 = q, q_2 = q, q_3 = 0/q_1 = q, q_2 = 0, q_3 = q/q_1 = 0, q_2 = q, q_3 = q$:

$$F_0(\mathbf{H}) = V(2\mathrm{i} - q - \exp(\mathrm{i}q)(2\mathrm{i} + q))/q^3. \tag{3.24}$$

`Case 4` $q_1 = q, q_2 = q', q_3 = 0/q_1 = q, q_2 = 0, q_3 = q'/q_1 = 0, q_2 = q, q_3 = q'$:

$$F_0(\mathbf{H}) = V((-1 + \exp(\mathrm{i}q))\,\mathrm{i}q'^2 + qq'^2$$
$$+ (1 - \exp(\mathrm{i}q')) + \mathrm{i}q')\,\mathrm{i}q^2)/(q^2q'^2(q - q')) \tag{3.25}$$

`Case 5` $q_1 = q, q_2 = q, q_3 = q$:

$$F_0(\mathbf{H}) = V(\mathrm{i}\exp(\mathrm{i}q)(1 + \mathrm{i}q(\frac{1}{2}\mathrm{i}q - 1)) - \mathrm{i})/(q^3). \tag{3.26}$$

`Case 6` $q_1 = q, q_2 = q, q_3 = q'/q_1 = q, q_2 = q', q_3 = q/q_1 = q', q_2 = q, q_3 = q$:

$$F_0(\mathbf{H}) = V((\exp(\mathrm{i}q) - 1)\,\mathrm{i}q'^2 + (\exp(\mathrm{i}q') + \exp(\mathrm{i}q)\,\mathrm{i}q' - 1)\,\mathrm{i}q^2$$
$$- (\exp(\mathrm{i}q)(2 + \mathrm{i}q') - 2) \cdot \mathrm{i}qq')/(q^2q'(q - q')^2). \tag{3.27}$$

3.4.2.3 4D Atomic Surfaces

The FT of a pentachoron defined by four vectors $\mathbf{e}_1, \mathbf{e}_2, \mathbf{e}_3, \mathbf{e}_4$, can be calculated based on an oblique coordinate system: $\mathbf{x} = x_1\mathbf{e}_1 + x_2\mathbf{e}_2 + x_3\mathbf{e}_3 + x_4\mathbf{e}_3$ and $2\pi\mathbf{q} = q_1\mathbf{e}_1^* + q_2\mathbf{e}_2^* + q_3\mathbf{e}_3^* + q_4\mathbf{e}_4^*$, where $q_j = 2\pi\mathbf{H}\,\mathbf{e}_j$ and $\mathbf{e}_i\mathbf{e}_j^* = \delta_{ij}$. With

$$F_0(\mathbf{H}) = \int \exp(2\pi\mathrm{i}\mathbf{q} \cdot \mathbf{x})\mathrm{d}V \tag{3.28}$$

and $\mathrm{d}V = V\,\mathrm{d}x_1\,\mathrm{d}x_2\,\mathrm{d}x_3\,\mathrm{d}x_4$, where V is the Volume of the parallelotope defined by $\mathbf{e}_1, \mathbf{e}_2, \mathbf{e}_3, \mathbf{e}_4$, $V = \sqrt{\det(\mathsf{G})}$, and G the metric tensor, which is the symmetric matrix of inner products of the set of vectors $\mathbf{e}_1, \cdots, \mathbf{e}_4$, and whose entries are given by $G_{ij} = \mathbf{e}_i \cdot \mathbf{e}_j$. It follows for the Fourier integral

$$F_0(\mathbf{H}) = V \int_0^1 \exp(\mathrm{i}q_1x_1)\mathrm{d}x_1 \int_0^{1-x_1} \exp(\mathrm{i}q_2x_2)\mathrm{d}x_2$$
$$\cdot \int_0^{1-x_1-x_2} \exp(\mathrm{i}q_3x_3)\mathrm{d}x_3 \int_0^{1-x_1-x_2-x_3} \exp(\mathrm{i}q_4x_4)\mathrm{d}x_4. \tag{3.29}$$

The direct calculation of the above integral leads to:

$$
\begin{aligned}
F_0(\mathbf{H}) = {} & V\,(q_3 q_4 \exp(iq_1)(q_1(q_1 - q_2)(q_1 - q_3)(q_1 - q_4))^{-1} \\
& + q_3 q_4 \exp(iq_2)(q_2(q_2 - q_1)(q_2 - q_3)(q_2 - q_4))^{-1} \\
& + q_4 \exp(iq_3)((q_3 - q_1)(q_3 - q_2)(q_3 - q_4))^{-1} \\
& + q_3 \exp(iq_4)((q_4 - q_1)(q_4 - q_2)(q_4 - q_3))^{-1} + (q_1 q_2)^{-1})(q_3 q_4)^{-1} \quad (3.30)
\end{aligned}
$$

with $q_j = 2\pi \mathbf{H}\,\mathbf{e}_j$, $(j = 1, 2, 3, 4)$. To avoid singularities in (3.30) a case differentiation must be done before integration of (3.29). In the following, the special cases and the corresponding formulae are given.

Case 1 $q_1 = 0, q_2 = 0, q_3 = 0, q_4 = 0$: $F_0(\mathbf{H}) = \frac{1}{24} V$.

Case 2 $q_1 = 0, q_2 = 0, q_3 = 0, q_4 = q / q_1 = 0, q_2 = 0, q_3 = q, q_4 = 0 / q_1 = 0,$
$q_2 = q, q_3 = 0, q_4 = 0 / q_1 = q, q_2 = 0, q_3 = 0, q_4 = 0$:

$$
F_0(\mathbf{H}) = V\,(\exp(iq) - 1 - iq + \frac{1}{2}q^2 + \frac{1}{6}iq^3)/q^4. \quad (3.31)
$$

Case 3 $q_1 = 0, q_2 = 0, q_3 = q, q_4 = q / q_1 = 0, q_2 = q, q_3 = q, q_4 = 0 / q_1 = q,$
$q_2 = q, q_3 = 0, q_4 = 0 / q_1 = q, q_2 = 0, q_3 = q, q_4 = 0 / q_1 = q, q_2 = 0, q_3 = 0,$
$q_4 = q / q_1 = 0, q_2 = q, q_3 = 0, q_4 = q$:

$$
F_0(\mathbf{H}) = V\,(3 + 2iq - \frac{1}{2}q^2 + i\,\exp(iq)(3i + q))/q^4 \quad (3.32)
$$

Case 4 $q_1 = 0, q_2 = q, q_3 = q, q_4 = q / q_1 = q, q_2 = 0, q_3 = q, q_4 = q / q_1 = q,$
$q_2 = q, q_3 = 0, q_4 = q / q_1 = q, q_2 = q, q_3 = q, q_4 = 0$:

$$
F_0(\mathbf{H}) = -V\,(iq + 3 + \exp(iq)(2iq - 3 + \frac{1}{2}q^2))/q^4 \quad (3.33)
$$

Case 5 $q_1 = q, q_2 = q, q_3 = q, q_4 = q$:

$$
F_0(\mathbf{H}) = V\,(1 + \exp(iq)(-1 + iq + \frac{1}{2}q^2 - \frac{1}{6}iq^3))/q^4 \quad (3.34)
$$

Case 6 $q_1 = 0, q_2 = 0, q_3 = q, q_4 = q' / q_1 = 0, q_2 = q, q_3 = q', q_4 = 0 / q_1 = q,$
$q_2 = q', q_3 = 0, q_4 = 0 / q_1 = q, q_2 = 0, q_3 = q', q_4 = 0 / q_1 = q, q_2 = 0,$
$q_3 = 0, q_4 = q' / q_1 = 0, q_2 = q, q_3 = 0, q_4 = q'$:

$$
\begin{aligned}
F_0(\mathbf{H}) = {} & V\,((\exp(iq) - 1)q'^{\,3} - iqq'^{\,3} + \frac{1}{2}q^2 q'^{\,3} - \\
& q^3(\exp(iq') - 1 - iq' + \frac{1}{2}q'^{\,2}))/(q^3 q'^{\,3}(q - q')) \quad (3.35)
\end{aligned}
$$

Case 7 $q_1 = 0, q_2 = q, q_3 = q', q_4 = q'' / q_1 = q, q_2 = 0, q_3 = q', q_4 = q'' /$
$q_1 = q, q_2 = q', q_3 = 0, q_4 = q'' / q_1 = q, q_2 = q', q_3 = q'', q_4 = 0$:

$$F_0(\mathbf{H}) = V(-1 - \mathrm{i}q - q(q^2((-1 + \exp(\mathrm{i}q''))q'^{\,2} -$$
$$(-1 + \exp(\mathrm{i}q'))q''^{\,2}) + (-1 + \exp(\mathrm{i}q))q''\,(q'^{\,3} - q'\,q''^{\,2}) +$$
$$q((1 - \exp(\mathrm{i}q''))q'^{\,3} + (1 - \exp(\mathrm{i}q))q'^{\,2}q'' +$$
$$(-1 + \exp(\mathrm{i}q))q'\,q''^{\,2} + (-1 + \exp(\mathrm{i}q'))q''^{\,3})))$$
$$/(q^2q'\,q''\,(((q - q')q'\,(q - q'')q''\,(q'' - q')) - \mathrm{i}\exp(q)))\quad(3.36)$$

Case 8 $q_1 = 0, q_2 = q, q_3 = q, q_4 = q'/q_1 = 0, q_2 = q, q_3 = q'\ q_4 = q/q_1 = 0,$
$q_2 = q'\ q_3 = q, q_4 = q/q_1 = q, q_2 = 0, q_3 = q, q_4 = q'/q_1 = q, q_2 = 0,$
$q_3 = q'q_4 = q/q_1 = q'\ q_2 = 0, q_3 = q, q_4 = q/q_1 = q, q_2 = q, q_3 = 0,$
$q_4 = q'/q_1 = q, q_2 = q'\ q_3 = 0, q_4 = q/q_1 = q'\ q_2 = q, q_3 = q, q_4 = 0/$
$q_1 = q, q_2 = q, q_3 = q, q_4 = 0/q_1 = q, q_2 = q'\ q_3 = q, q_4 = 0/q_1 = q'\ q_2 = q,$
$q_3 = q, q_4 = 0$:

$$F_0(\mathbf{H}) = V(q^3(-1 + \exp(\mathrm{i}q') - \mathrm{i}q'') + \mathrm{i}(2 + \exp(\mathrm{i}q))q^2q'^{\,2} +$$
$$q(3 + \exp(\mathrm{i}q)(-3 - \mathrm{i}q') - \mathrm{i}q')q'^{\,2} + 2(-1 + \exp(\mathrm{i}q))q'^{\,3})$$
$$/(q'^{\,2}q^3(q - q')^2)\quad(3.37)$$

Case 9 $q_1 = q, q_2 = q, q_3 = q, q_4 = q'/q_1 = q, q_2 = q, q_3 = q'\,, q_4 = q/q_1 = q,$
$q_2 = q'\,, q_3 = q, q_4 = q/q_1 = q'\,, q_2 = q, q_3 = q, q_4 = q$:

$$F_0(\mathbf{H}) = V(\exp(\mathrm{i}q)q^2(q - q')^{-1} + (q - q')^2q^{-1} -$$
$$\exp(\mathrm{i}q)(q - q')^2q^{-1} + \exp(\mathrm{i}q')q^2(q' - q)^{-1} +$$
$$\frac{1}{2}\exp(\mathrm{i}q)q'\,(-q^2 + 2\mathrm{i}q' + q(-4\mathrm{i} + q')))/(q'\,q^2(q - q')^2)\quad(3.38)$$

Case 10 $q_1 = q, q_2 = q, q_3 = q'\,, q_4 = q''/q_1 = q, q_2 = q'\,, q_3 = q, q_4 = q''/q_1 = q'\,, q_2 = q, q_3 = q, q_4 = q''/q_1 = q'\,, q_2 = q, q_3 = q'', q_4 = q/q_1 = q'\,, q_2 = q'', q_3 = q, q_4 = q/q_1 = q, q_2 = q'\,, q_3 = q'', q_4 = q$:

$$F_0(\mathbf{H}) = V((\exp(\mathrm{i}q) + \exp(\mathrm{i}q''))q(q - q')q'\,(q - q'')^{-1}$$
$$+ (1 - \exp(\mathrm{i}q))(q - q')(q - q'')(q' - q'')q^{-1} + (\exp(\mathrm{i}q) - \exp(\mathrm{i}q'))$$
$$q(q - q'')q''\,(q' - q)^{-1} - \mathrm{i}\exp(\mathrm{i}q)q'\,q''\,(q'' - q'))$$
$$/(qq'\,q''\,(q - q')(q - q'')(q' - q''))\quad(3.39)$$

Case 11 $q_1 = q, q_2 = q, q_3 = q'\,, q_4 = q'/q_1 = q, q_2 = q'\,, q_3 = q'\,, q_4 = q/q_1 = q, q_2 = q'\,, q_3 = q, q_4 = q'$:

$$F_0(\mathbf{H}) = V(q(3 + \exp(\mathrm{i}q)(-3 - \mathrm{i}q'))q'^{\,2} + (-1 + \exp(\mathrm{i}q))q'^{\,3} +$$
$$q^2q'\,(-3 + \exp(\mathrm{i}q')(3 - \mathrm{i}q') + \mathrm{i}\exp(\mathrm{i}q)q') +$$
$$q^3(1 + \mathrm{i}\exp(\mathrm{i}q')(\mathrm{i} + q')))/(q^2q'^{\,2}(q - q')^3)\quad(3.40)$$

3.5 1D Quasiperiodic Structures

Structures with 1D quasiperiodic order and 2D hyperlattice periodicity (1D quasicystals) are the simplest representatives of QC. A few phases of this structure type have been observed experimentally ([43] and references therein).

A fundamental model of a 1D quasiperiodic structure is the Fibonacci sequence (FS). Since its embedding space is only 2D, it is frequently used to illustrate the principles of the nD approach. However, since in 1D there is only crystallographic point symmetry possible (1 and $\bar{1}$), it can be described as IMS as well. One has to keep in mind, however, that 1D quasiperiodic structures exist which need an embedding space of dimension $n > d + 1$. These are, for instance, all quasiperiodic sequences formed by substitution rules based on n letters with $n > d + 1$ [29].

Generally, 1D quasiperiodic structures are on the borderline between quasiperiodic structures and IMS. They can be described in either of the two approaches. The description as quasiperiodic structure (QC-setting) is advantageous if some kind of scaling symmetry is present or if there is a close structural relationship with 2D or 3D QC. This is the case for 1D QC occurring as intermediate states during quasicrystal-to-crystal transformations. The description as IMS (IMS-setting) may be helpful in the course of structure analysis. The diffraction pattern can then be separated into a set of main reflections and a set of satellite reflections. The main reflections are related to the 3D periodic average structure, which can be determined with conventional methods. However, indexing a typical 1D quasicrystal as IMS may be difficult as the intensity distribution does not allow main reflections to be determined easily (see Sect. 3.1).

In the following, the FS will be used as an example to describe the quasiperiodic direction of 3D structures with 1D quasiperiodic stacking of periodic atomic layers. We discuss the general triclinic case and define the z-direction as the quasiperiodic direction with $\mathbf{a}_3^*$ aligned parallel to it.

3.5.1 Reciprocal Space

The electron density distribution function $\rho(\mathbf{r})$ of a 1D quasicrystal is given by the Fourier series

$$\rho(\mathbf{r}) = \frac{1}{V} \sum_{\mathbf{H}} F(\mathbf{H}) e^{-2\pi i \mathbf{H} \mathbf{r}} \ . \tag{3.41}$$

The Fourier coefficients (structure factors) $F(\mathbf{H})$ are functions of the scattering vectors $\mathbf{H} = \sum_{i=1}^{3} h_i^{\parallel} \mathbf{a}_i^*$ with $h_1^{\parallel}, h_2^{\parallel} \in \mathbb{Z}$, $h_3^{\parallel} \in \mathbb{R}$. Introducing four reciprocal basis vectors, all scattering vectors can be indexed with integer components: $\mathbf{H} = \sum_{i=1}^{4} h_i \mathbf{a}_i^*$ with $\mathbf{a}_4^* = \alpha \mathbf{a}_3^*$, α an irrational algebraic number and $h_i \in \mathbb{Z}$. The set M^* of all diffraction vectors $\mathbf{H}$ forms a vector module

(Z-module) of rank four. The vectors $\mathbf{a}_i^*$ can be considered as par-space projections of the basis vectors $\mathbf{d}_i^*$ of the corresponding 4D reciprocal lattice Σ^* with

$$\mathbf{d}_1^* = |\mathbf{a}_1^*| \begin{pmatrix} x_1 \\ y_1 \\ z_1 \\ 0 \end{pmatrix}_V , \quad \mathbf{d}_2^* = |\mathbf{a}_2^*| \begin{pmatrix} x_2 \\ y_2 \\ z_2 \\ 0 \end{pmatrix}_V , \quad \mathbf{d}_3^* = |\mathbf{a}_3^*| \begin{pmatrix} 0 \\ 0 \\ 1 \\ -c\alpha \end{pmatrix}_V , \quad \mathbf{d}_4^* = |\mathbf{a}_3^*| \begin{pmatrix} 0 \\ 0 \\ \alpha \\ c \end{pmatrix}_V . \tag{3.42}$$

The subscript V indicates that the vector components refer to a Cartesian coordinate system (V-basis). The direct 4D basis vectors, spanning the 4D lattice Σ, result from the orthogonality condition (3.5), i.e. as the columns of $(W^{-1})^T$

$$\mathbf{d}_1 = \frac{1}{(x_1 y_2 - x_2 y_1)|\mathbf{a}_1^*|} \begin{pmatrix} y_2 \\ -x_2 \\ 0 \\ 0 \end{pmatrix}_V , \quad \mathbf{d}_2 = \frac{1}{(x_1 y_2 - x_2 y_1)|\mathbf{a}_2^*|} \begin{pmatrix} -y_1 \\ x_1 \\ 0 \\ 0 \end{pmatrix}_V ,$$

$$\mathbf{d}_3 = \frac{1}{(1+\alpha^2)|\mathbf{a}_3^*|} \begin{pmatrix} \frac{y_1 z_2 - y_2 z_1}{x_1 y_2 - x_2 y_1} \\ \frac{x_2 z_1 - x_1 z_2}{x_1 y_2 - x_2 y_1} \\ 1 \\ -\frac{\alpha}{c} \end{pmatrix}_V , \quad \mathbf{d}_4 = \frac{1}{(1+\alpha^2)|\mathbf{a}_3^*|} \begin{pmatrix} \frac{\alpha(y_1 z_2 - y_2 z_1)}{x_1 y_2 - x_2 y_1} \\ \frac{\alpha(x_2 z_1 - x_1 z_2)}{x_1 y_2 - x_2 y_1} \\ \alpha \\ \frac{1}{c} \end{pmatrix}_V , \tag{3.43}$$

with $x_i^2 + y_i^2 + z_i^2 = 1$. The vectors $\mathbf{a}_i = \pi^{\parallel} \mathbf{d}_i, i = 1 \ldots 3$, span the reciprocal basis of the periodic average structure and the basis structure. The basis vectors $\mathbf{d}_i$ determine the 4D metric tensor G defined as

$$\mathsf{G} = W^{-1}(W^{-1})^T = \begin{pmatrix} \mathbf{d}_1\mathbf{d}_1 & \mathbf{d}_1\mathbf{d}_2 & \mathbf{d}_1\mathbf{d}_3 & \mathbf{d}_1\mathbf{d}_4 \\ \mathbf{d}_2\mathbf{d}_1 & \mathbf{d}_2\mathbf{d}_2 & \mathbf{d}_2\mathbf{d}_3 & \mathbf{d}_2\mathbf{d}_4 \\ \mathbf{d}_3\mathbf{d}_1 & \mathbf{d}_3\mathbf{d}_2 & \mathbf{d}_3\mathbf{d}_3 & \mathbf{d}_3\mathbf{d}_4 \\ \mathbf{d}_4\mathbf{d}_1 & \mathbf{d}_4\mathbf{d}_2 & \mathbf{d}_4\mathbf{d}_3 & \mathbf{d}_4\mathbf{d}_4 \end{pmatrix} \tag{3.44}$$

and the volume of the 4D unit cell results to $V = \sqrt{\det \mathsf{G}}$. The point density D_p in par-space, the reciprocal of the mean atomic volume, is determined by the size of the atomic surfaces A_i

$$D_{\mathrm{p}} = \frac{1}{V} \sum_{i=1}^{n} A_i . \tag{3.45}$$

Weighting each atomic surface in (3.45) with its atomic weight M_{A_i}, the mass density D_{m} can be expressed as

$$D_{\mathrm{m}} = \frac{1}{V} \sum_{i=1}^{n} A_i M_{A_i} . \tag{3.46}$$

3.5.2 Symmetry

The possible Laue symmetry group K^{3D} of the intensity weighted Fourier module (diffraction pattern)

$$M_I^* = \left\{ I(\mathbf{H}) = |F(\mathbf{H})|^2 \;\middle|\; \mathbf{H} = \sum_{i=1}^{4} h_i a_i^*, h_i \in \mathbb{Z} \right\} \qquad (3.47)$$

results from the direct product $K^{3D} = K^{2D} \otimes K^{1D} \otimes \bar{1}$. K^{2D} is one of the ten crystallographic 2D point groups, $K^{1D} = 1$ or $\bar{1}$. Consequently, all 3D crystallographic Laue groups except the two cubic ones (they would mix periodic and aperiodic directions) are permitted: $\bar{1}$, $2/m$, mmm, $4/m$, $4/mmm$, $\bar{3}$, $\bar{3}m$, $6/m$, $6/mmm$. If one distinguishes between symmetry operations $R \in K^{2D}$ and $R' \in K^{1D}$ the Laue group $2/m$ can occur in two different orientations with regard to the unique axis $[0010]_V$: $2'/m$ and $2/m'$. Thus, there are 10 different Laue groups.

Thirty-one point groups result from the direct products $K^{3D} = K^{2D} \otimes K^{1D}$ and their subgroups of index 2. These are all twenty-seven 3D crystallographic point groups except the five cubic point groups. Four additional point groups are obtained by considering the different settings in 2, $2'$, m, m', $2/m'$, $2'/m$, $2'mm'$ and $2mm$. The necessity to distinguish between primed and non-primed operations is based on reduced tensor symmetries of physical properties. A table of the eighty 3D space groups compatible with 1D quasiperiodicity has been derived by [49]. These space groups contain no symmetry operations with translation components along the unique direction $[0010]_V$. The 80 symmetry groups leaving the 4D hypercrystal structure invariant are a subset of the (3+1)D space groups (superspace groups) given by [21]. This subset corresponds to all superspace groups with the basis space group being one of the eighty 3D space groups mentioned above marked by the bare symbols (00γ), $(\alpha\beta 0)$, or $(\alpha\beta\gamma)$. In the last two cases, only one of the coefficients α, β, γ is allowed to be irrational.

According to the scaling symmetry the choice of the basis vectors $\mathbf{d}_3$, $\mathbf{d}_4$, and therewith the indexing of the quasiperiodic axis is not unique. Even if all Bragg peaks can be indexed, a set of α^n-times (in case of the FS $\alpha = \tau$) enlarged or decreased basis vectors will again describe their positions equivalently well. A first attempt to solve the problem of indexing was given by [8]. In the case of a primitive QC having a simple atomic surface the intensity distribution is a simple function of the geometrical form factor (3.13) and consequently a monotonically decreasing function of $|\mathbf{H}^\perp|$. If the intensity of scaled scattering vectors decreases monotonically in the same way as predicted the proper basis has been selected. However, given a more complicated structure this approach may fail. It has been shown by [4] that a detailed analysis of the Patterson function (autocorrelation function) depending on perp-space components allows the basis vectors of more complex structures to be determined properly.

3.5.3 Example: Fibonacci Structure

If the Fibonacci sequence (see Sect. 1.1.1) is chosen for the quasiperiodic direction of a 1D quasicrystal, it may simply be called a Fibonacci structure. In the following, the Fibonacci structure is geometrically defined as layer structure: layers with 2D lattice periodicity in the (110) plane are stacked quasiperiodically in the [001] direction. The distances between the layers follow the Fibonacci sequence ... LSLLS .... Based on the scaling symmetry matrix in (1.1), the 4D reciprocal lattice Σ^* is spanned by basis vectors according to (3.43) with $\alpha = \tau$. Without loss of generality we can further set $c = 1$. For clarity we choose a 4D hypercubic basis. Then, the embedding matrix $\mathsf{W} = (\mathbf{d}_1^*, \mathbf{d}_2^*, \mathbf{d}_3^*, \mathbf{d}_4^*)$ (see (3.4)) and its transposed inverse one, $(\mathsf{W}^{-1})^\mathrm{T} = (\mathbf{d}_1, \mathbf{d}_2, \mathbf{d}_3, \mathbf{d}_4)$, read

$$\mathsf{W} = |\mathbf{a}^*| \begin{pmatrix} 1 & 0 & 0 & 0 \\ 0 & 1 & 0 & 0 \\ 0 & 0 & 1 & \tau \\ 0 & 0 & -\tau & 1 \end{pmatrix}, \quad (\mathsf{W}^{-1})^\mathrm{T} = \frac{|\mathbf{a}|}{2+\tau} \begin{pmatrix} 1 & 0 & 0 & 0 \\ 0 & 1 & 0 & 0 \\ 0 & 0 & 1 & \tau \\ 0 & 0 & -\tau & 1 \end{pmatrix}. \tag{3.48}$$

According to the strip-projection method, the par-space structure ("quasilattice") of the Fibonacci structure is a subset M^{FS} of the vector module M defined by the window A

$$M = \left\{ \mathbf{r} = \sum_{i=1}^{4} n_i \pi^{\|}(\mathbf{d}_i), n_i \in \mathbb{Z} \right\},$$

$$M^{FS} = \left\{ \mathbf{r} = \pi^{\|}(\sum_{i=1}^{4} m_i \mathbf{d}_i) \Big| m_i \in Z, |\pi^{\perp}(\sum_{i=3}^{4} m_i \mathbf{d}_i)| \leq \frac{A}{2} = \frac{(1+\tau)|\mathbf{a}|}{2(2+\tau)} \right\}. \tag{3.49}$$

In the cut-and-project method, the Fibonacci structure can be obtained in the par-space section of a decorated 4D hyperlattice Σ spanned by the basis vectors according to (3.43)

$$\mathbf{d}_1 = |\mathbf{a}| \begin{pmatrix} 1 \\ 0 \\ 0 \\ 0 \end{pmatrix}_V, \quad \mathbf{d}_2 = |\mathbf{a}| \begin{pmatrix} 0 \\ 1 \\ 0 \\ 0 \end{pmatrix}_V,$$

$$\mathbf{d}_3 = \frac{|\mathbf{a}|}{(2+\tau)|} \begin{pmatrix} 0 \\ 0 \\ 1 \\ -\tau \end{pmatrix}_V, \quad \mathbf{d}_4 = \frac{|\mathbf{a}|}{(2+\tau)|} \begin{pmatrix} 0 \\ 0 \\ \tau \\ 1 \end{pmatrix}_V \tag{3.50}$$

The volume of the 4D unit cell amounts to $V = \sqrt{\det \mathsf{G}} = |\mathbf{a}|^4/(2+\tau)$. The point density D_{p} in par-space, i.e. the reciprocal of the mean atomic volume, equals

$$D_{\mathrm{p}} = \frac{A}{V} = \frac{\tau^2}{|\mathbf{a}|^3} \, \text{Å}^{-3}. \tag{3.51}$$

This value can also be obtained as the reciprocal of the average distance $d_{av} = (3-\tau)\mathsf{S}$ of the vertices (see (1.11)), where $\mathsf{S} = \pi^{\parallel}\mathbf{d}_3 = |\mathbf{a}|/(2+\tau)$.

The 4D hyperlattice is decorated with 4D hyperatoms. The atomic surfaces along the 1D perp-space are line segments of length $(1+\tau)|\mathbf{a}|/(2+\tau)$. They are centered at positions $x_1, x_2, 0, 0$ relative to the origin of the 4D unit cell (see Fig. 3.6). The atomic surface can be decomposed into sections, which show the same local environment (Voronoi domains) in par-space. Projecting all nearest neighbors of the hyperatom of interest onto $V^{\perp}$ encodes all different environments as shown in Fig. 3.6.

If the par-space $V^{\parallel}$ cuts the hyperatom, e.g. in the region marked **a**, the central atom is coordinated by one atom at a distance S on the left side and another one at distance L on the right side. Consequently, all hyperatoms that share a distinct region of the atomic surface in the projection onto perp-space determine all bond distances and angles in par-space.
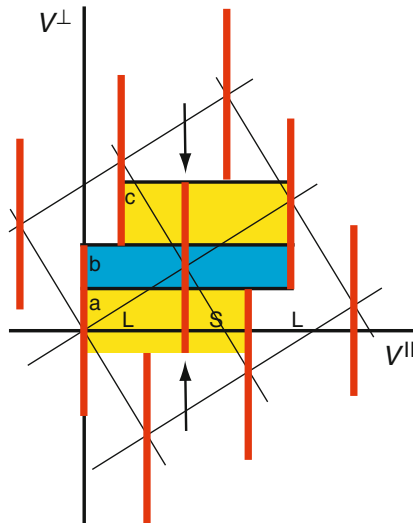
Fig. 3.6. By projecting all nearest neighbors along $V^{\parallel}$ onto one hyperatom (marked by arrows), the segments (partitions) with the three different coordinations can be obtained. Cutting the hyperatom in the light-gray (online: yellow) area **a** leads to vertices at distances L to the left and S to the right, in the dark-gray (online:blue) area **b** to L and L, and in the other light-gray (online: yellow) area **c** to S and L. The lengths of the segments give the frequencies of these coordinations. The nearest neighbors of the hyperatom show the closeness condition

The point density has to be invariant for any shift of par-space along the perp-space. This leads to the *closeness condition*: when the atomic surfaces are projected onto perp-space each boundary of an atomic surface has to fit exactly to another one (the uppermost and lowest hyperatoms in Fig. 3.6 fit exactly to the central one). The structures resulting from par-space cuts at different perp-space positions all belong to the same local isomorphism class.

3.5.3.1 Scaling Symmetry

The point and space group symmetry of the Fibonacci structure is as described for the general case in Sect. 3.5.2. The scaling symmetry has been already discussed and the scaling matrix S shown in (1.1). If we block-diagonalize this matrix, we obtain the scaling factors acting on par- as well as on perp-space

$$
\mathsf{W} \cdot \mathsf{S} \cdot \mathsf{W}^{-1} = |\mathbf{a}^*|
\begin{pmatrix}
1 & 0 & 0 & 0 \\
0 & 1 & 0 & 0 \\
0 & 0 & 1 & \tau \\
0 & 0 & -\tau & 1
\end{pmatrix}
\cdot
\begin{pmatrix}
1 & 0 & 0 & 0 \\
0 & 1 & 0 & 0 \\
0 & 0 & 0 & 1 \\
0 & 0 & 1 & 1
\end{pmatrix}
\cdot
\frac{|\mathbf{a}|}{2 + \tau}
\begin{pmatrix}
1 & 0 & 0 & 0 \\
0 & 1 & 0 & 0 \\
0 & 0 & 1 & -\tau \\
0 & 0 & \tau & 1
\end{pmatrix}
=
$$

$$
=
\left(
\begin{array}{ccc|c}
1 & 0 & 0 & 0 \\
0 & 1 & 0 & 0 \\
0 & 0 & \tau & 0 \\
\hline
0 & 0 & 0 & \tau^{-1}
\end{array}
\right)
=
\left(
\begin{array}{c|c}
\mathsf{S}^{\|} & 0 \\
\hline
0 & \mathsf{S}^{\perp}
\end{array}
\right).
\tag{3.52}
$$

The loci of the scaled lattice points lie on hyperbolae of the type $x_4 = \pm c/x_3$ (Fig. 3.7). Consequently, the scaling operation can be seen as hyperbolic rotation by multiples of $\phi = \operatorname{arcsinh} 1/2 = 0.4812$, $n \in \mathbb{Z}$ (see [15] and references therein)

$$
\begin{bmatrix} x_1 \\ x_2 \\ x_3 \\ x_4 \end{bmatrix}
=
\begin{bmatrix}
x_1 \\
x_2 \\
\cosh n\phi + \sinh n\phi \\
-\sinh n\phi + \cosh n\phi
\end{bmatrix}.
\tag{3.53}
$$

Scaling the diffraction vector $\mathsf{S}^n\mathbf{H}$, with $\mathbf{H} = \sum_{i=1}^{4} h_i \mathbf{d}_i^*$ yields

$$
\begin{pmatrix}
1 & 0 & 0 & 0 \\
0 & 1 & 0 & 0 \\
0 & 0 & 0 & 1 \\
0 & 0 & 1 & 1
\end{pmatrix}^n
\cdot
\begin{pmatrix} h_1 \\ h_2 \\ h_3 \\ h_4 \end{pmatrix}
=
\begin{pmatrix}
1 & 0 & 0 & 0 \\
0 & 1 & 0 & 0 \\
0 & 0 & F_n & F_{n+1} \\
0 & 0 & F_{n+1} & F_{n+2}
\end{pmatrix}
\cdot
\begin{pmatrix} h_1 \\ h_2 \\ h_3 \\ h_4 \end{pmatrix}
=
\begin{pmatrix}
h_1 \\
h_2 \\
F_n h_3 + F_{n+1} h_4 \\
F_{n+1} h_3 + F_{n+2} h_4
\end{pmatrix}
\tag{3.54}
$$

with the Fibonacci numbers F_n. For $n \geq 0$, the perp-space component of the diffraction vector is continuously decreased leading to increased norms of the structure factors due to the shape of $g_k\left(\mathbf{H}^{\perp}\right)$ (see Sect. 3.5.3.2)

$$
|F(\mathsf{S}^n\mathbf{H})| > |F(\mathsf{S}^{n-1}\mathbf{H})| > \cdots > |F(\mathsf{S}\mathbf{H})| > |F(\mathbf{H})|.
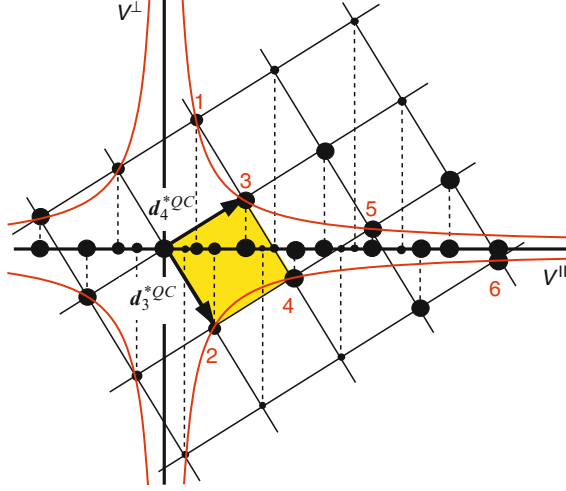\tag{3.55}
$$

Fig. 3.7. Scaling the reciprocal lattice of the Fibonacci sequence by S corresponds to a hyperbolic rotation. Reflection $1\,00\bar{1}1$ is mapped to the reciprocal lattice points $2\,0010 \mapsto 3\,0001 \mapsto 4\,0011 \mapsto 5\,0012 \mapsto 6\,1123$

3.5.3.2 Structure Factor

The structure factor of the Fibonacci structure can be obtained by substituting the value for $g_k\left(\mathbf{H}^\perp\right)$ (3.8) into (3.12). Since there is only one atomic surface per unit cell, a line segment of length $(1+\tau)|\mathbf{a}|/(2+\tau)$ centered at $x_1, x_2, 0, 0$ (see Fig. 3.2(c)), we obtain by Fourier transformation

$$g_k\left(\mathbf{H}^\perp\right) = \frac{2+\tau}{\pi\tau^2\left(-\tau h_3 + h_4\right)} \sin\left(\frac{\pi\tau^2\left(-\tau h_3 + h_4\right)}{2+\tau}\right) \tag{3.56}$$

Thus, the geometrical form factor $g_k(\mathbf{H}^\perp)$ is of the form $\sin x^\perp / x^\perp$. The upper and lower envelopes of this function are hyperbolae $\pm 1/x^\perp$. Hence, the envelope of the diffracted intensity is proportional to $(1/x^\perp)^2$ and convergent. In Fig. 3.8, the structure factors as function of the par- and perp-space component of the diffraction vector are shown. Since the FS is centrosymmetric, the structure amplitudes can adopt phases 0 and π, i.e. the signs $+$ and $-$, only.

The intensity statistics for the basically experimentally accessible reciprocal space has been calculated for total 161,822 reflections along the quasiperiodic direction $[00h_3h_4]$ with $-1000 \leq h_3, h_4 \leq 1000$ and $0 \leq \sin\theta/\lambda \leq 2\,\text{Å}^{-1}$, i.e. a resolution of $1\,\text{Å}$ (Table 3.4). It turns out that the strongest 44 reflections add up to 92.57% of the total diffracted intensity, and the strongest 425 reflections total 99.25%.

The scaling symmetry, $s(\tau x) = \tau s(x)$, can be used for the derivation of phase relationships between structure factors. If $s(x)$ is the 1D par-space Fibonacci structure then we can write the structure factor as
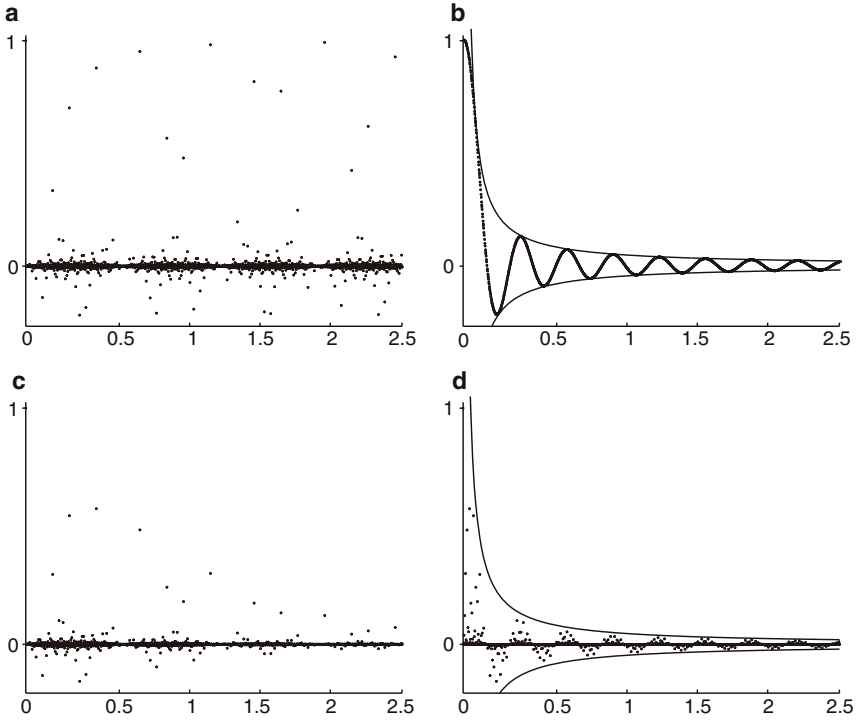
Fig. 3.8. Structure factors of a Fibonacci structure as function of (**a**), (**c**) the par- and (**b**), (**d**) perp-space components of the diffraction vectors. In (**a**), (**b**) the vertices are decorated with equal point atoms. In (**c**), (**d**) the vertices were occupied by aluminum atoms with an overall ADP of $\langle u^2 \rangle^{\parallel} = 0.005\,\text{Å}^2$. Short distance S $= 2.5\,\text{Å}$, all structure factors within $0 \leq |\mathbf{H}| \leq 2.5\,\text{Å}^{-1}$ have been calculated and normalized to $F(\mathbf{0}) = 1$

$$F(h) = \sum_k e^{2\pi i h x_k}, \quad x_k = m_k S + n_k L. \tag{3.57}$$

The set of coordinates x_k, defining the vertices of the FS $s(x)$, multiplied by a factor τ coincides with a subset of vectors defining the vertices of the original sequence (Fig. 1.1). The residual vertices correspond to a particular decoration of the scaled sequence $\tau^2 s(x)$. We obtain the original sequence $s(x)$ by merging the sequence $\tau s(x)$ with the sequence $\tau^2 s(x)$ shifted by the distance L. By Fourier transform is obtained

$$\sum_k e^{2\pi i h x r_k} = \sum_k e^{2\pi i h \tau x_k} + \sum_k e^{2\pi i h \tau^2 (x_k + L)}. \tag{3.58}$$

This can be reformulated in terms of structure factors as

$$F(h) = F(\tau h) + e^{2\pi i h L}\, F(\tau^2 h). \tag{3.59}$$

Table 3.4. Intensity statistics for the Fibonacci structure with the vertices decorated by aluminum atoms ($\langle u^2 \rangle^{\parallel} = 0.0127$ Å^2) for a short distance S = 2.5 Å S (from [42]). In the upper lines, the number of reflections in the respective intervals is given, in the lower lines the partial sums $\sum I(\mathbf{H})$ are given as percentage of the total diffracted intensity (without $I(\mathbf{0})$)

$I(\mathbf{H})/I(\mathbf{H})_{\max}$	≥ 0.1	≥ 0.01 and < 0.1	≥ 0.001 and < 0.01	< 0.001
$0.0 \leq \sin\theta/\lambda \leq 0.2$ Å^{-1}	17	148	1505	14 511
$\sum I(\mathbf{H})$	52.53%	2.56%	0.27%	0.03%
$0.2 \leq \sin\theta/\lambda \leq 0.4$ Å^{-1}	11	107	1066	14 998
$\sum I(\mathbf{H})$	27.03%	2.03%	0.19%	0.02%
$0.4 \leq \sin\theta/\lambda \leq 0.6$ Å^{-1}	9	64	654	15 456
$\sum I(\mathbf{H})$	9.84%	0.96%	0.12%	0.01%
$0.6 \leq \sin\theta/\lambda \leq 0.8$ Å^{-1}	6	27	326	15 823
$\sum I(\mathbf{H})$	2.94%	0.34%	0.07%	0.01%
$0.8 \leq \sin\theta/\lambda \leq 2.0$ Å^{-1}	1	35	338	96 720
$\sum I(\mathbf{H})$	0.23%	0.79%	0.06%	0.01%

3.5.3.3 The Fibonacci Structure in the IMS Description

The nD embedding of quasiperiodic structures is not unique. On one side, the absolute perp-space scale is arbitrary (factor c in (3.42) and (3.43)), on the other side, the atomic surfaces do not necessarily need to be parallel to perp-space. They may have a par-space component making them similar to modulation functions of incommensurately modulated structures (IMS). In the following, the standard embedding will be called QC-setting and the alternative one IMS-setting. The two variants are shown in Fig. 3.1(c) and (d) for the reciprocal space and in Fig. 3.2(c), and (d) for the direct space.

The transformation from the QC- to the IMS-setting is performed by a shear operation. In direct space, the hyperstructure is sheared parallel to the par-space leaving the par-space structure invariant. The goal is to orient the vector $\mathbf{d}_4^{\mathrm{IMS}}$ parallel to the perp-space. In reciprocal space, the shear direction is parallel to the perp-space bringing $\mathbf{d}_3^{\mathrm{IMS}}$ parallel to the par-space. While in the QC-setting the set of reflections cannot be separated into main and satellite reflections, this is possible in the IMS setting. Reflections of type $h_1 h_2 h_3 h_4$ are main reflections for $h_4 = 0$ and satellite reflections else with the satellite vector $\mathbf{q} = \pi^{\parallel} \mathbf{d}_4^{IMS}$.

There are infinitely many ways to embed the Fibonacci structure in the IMS-setting; however, only a very few make sense from a crystal-chemical point of view. The criterion is the intensity ratio between main and satellite reflections. The higher the total intensity is of main reflections compared to that of satellite reflections, the more physical relevance has the IMS-setting for the description of structure and properties. The best choice for the Fibonacci structure is to apply the shear transformation $A^{\parallel}$ (3.60) to a basis with one newly defined vector $\mathbf{d}_4^{'\mathrm{QC}} = \mathbf{d}_3^{\mathrm{QC}} + \mathbf{d}_4^{\mathrm{QC}}$.

$$A^{\parallel} = \begin{pmatrix} 1 & 0 & 0 & 0 \\ 0 & 1 & 0 & 0 \\ 0 & 0 & 1 & \tau^{-3} \\ 0 & 0 & 0 & 1 \end{pmatrix}_V \tag{3.60}$$

Then we obtain the following new direct and reciprocal basis

$$\mathbf{d}_1^{\mathrm{IMS}} = \mathbf{d}_1^{\mathrm{QC}}, \mathbf{d}_2^{\mathrm{IMS}} = \mathbf{d}_2^{\mathrm{QC}}, \mathbf{d}_3^{\mathrm{IMS}} = \frac{|\mathbf{a}|}{2+\tau} \begin{pmatrix} 0 \\ 0 \\ 3-\tau \\ -\tau \end{pmatrix}_V, \quad \mathbf{d}_4^{\mathrm{IMS}} = \frac{|\mathbf{a}|}{2+\tau} \begin{pmatrix} 0 \\ 0 \\ 0 \\ \tau^2 \end{pmatrix}_V$$

$$\mathbf{d}_1^{*\mathrm{IMS}} = \mathbf{d}_1^{*\mathrm{QC}}, \mathbf{d}_2^{*\mathrm{IMS}} = \mathbf{d}_2^{*\mathrm{QC}}, \mathbf{d}_3^{*\mathrm{IMS}} = |\mathbf{a}^*| \begin{pmatrix} 0 \\ 0 \\ \tau^2 \\ 0 \end{pmatrix}_V, \quad \mathbf{d}_4^{*\mathrm{IMS}} = |\mathbf{a}^*| \begin{pmatrix} 0 \\ 0 \\ \tau \\ 3-\tau \end{pmatrix}_V$$

$$\tag{3.61}$$

3.5.3.4 Periodic Average Structure

As mentioned above, 1D quasicrystals can equivalently be treated as IMS showing a periodic average structure (PAS). The PAS of a Fibonacci structure can also be derived by an oblique projection onto par-space $V^{\parallel}$ (Fig. 3.9) as demonstrated in [46].
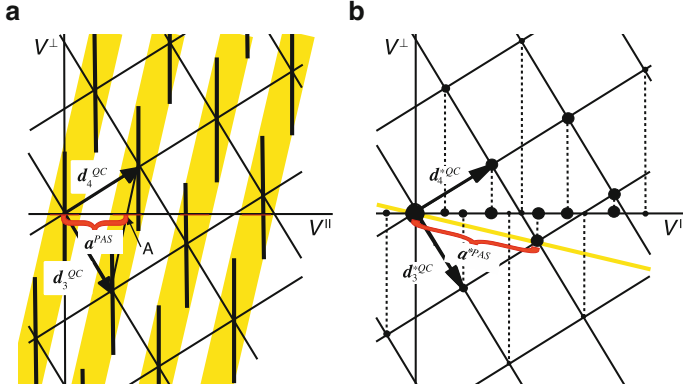
Fig. 3.9. (**a**) Oblique projection (marked gray, online: yellow) onto reciprocal space leads to the average structure of the Fibonacci sequence. The bold (online: red) horizontal bars represent the projected atomic surfaces. The unit cell length a^{PAS} of the average structure is marked with a brace. (**b**) An oblique section (marked gray, online: yellow) of par-space leads to the diffraction pattern of the PAS of the FS

Based on the projection with

$$\pi^{\parallel}(\mathbf{r}) = \begin{pmatrix} 1 & 0 & 0 & 0 \\ 0 & 1 & 0 & 0 \\ 0 & 0 & 1 & 3-2\tau \end{pmatrix}_V \mathbf{r}_V = \begin{pmatrix} 1 & 0 & 0 & 0 \\ 0 & 1 & 0 & 0 \\ 0 & 0 & \tau^{-2} & \tau^{-2} \end{pmatrix}_D \mathbf{r}_D \qquad (3.62)$$

the basis vectors of the average periodic structure result to $\mathbf{a}_1^{\mathrm{PAS}} = \mathbf{a}_1$, $\mathbf{a}_2^{\mathrm{PAS}} = \mathbf{a}_2$, $\mathbf{a}_3^{\mathrm{PAS}} = \tau^{-2}\mathbf{a}_3$ and $\mathbf{a}_1^{*\mathrm{PAS}} = \mathbf{a}_1^*$, $\mathbf{a}_2^{*\mathrm{PAS}} = \mathbf{a}_2^*$, $\mathbf{a}_3^{*\mathrm{PAS}} = \tau^2\mathbf{a}_3^*$. The oblique projection in par-space results in an oblique section in reciprocal space (Fig. 3.9). Consequently, all reflections of type $(h_1 h_2 h_3 h_3)_D$ are main reflections. Of course, there is an infinite number of different PAS possible [3], only a few of them are of physical relevance, however.

3.5.3.5 Superstructures of the Fibonacci Structure

Real quasicrystal structures consist of more than one kind of atoms. This means that they can be described in terms of a decoration of a basic quasiperiodic structure (tiling). In the nD description this can be a decoration (partition) of an atomic surface, of the unit cell or the formation of a supercell. Therefore, in the following the principle of superstructure formation is discussed on three examples of 2-color superstructures of the FS (Fig. 3.10). Only substitutional superstructures are considered, i.e. there are no additional vertices created, there is only a "chemical" ordering on the existing vertices of the FS.

While the structures shown in Fig. 3.10(a) and (c) are proper superstructures in the sense that they obey the chemical closeness condition between
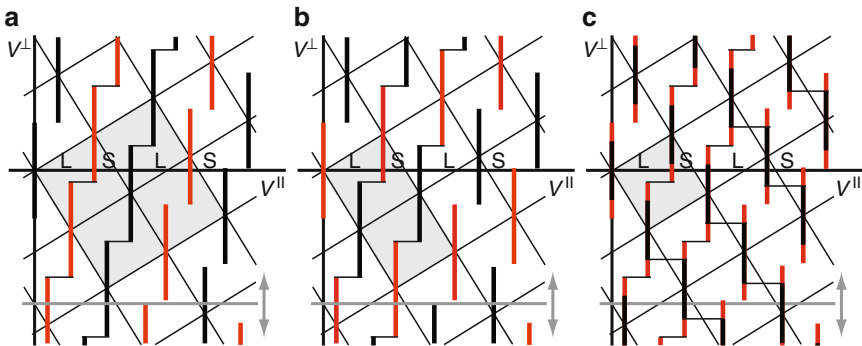
Fig. 3.10. Two-color superstructures of the FS. (**a**) and (**c**) are proper superstructures, which obey the chemical closeness condition between like atoms. In case (**b**) a par-space shift along the perp-space would transform via phason flips black into gray (online: red) atoms and vice versa

like atoms, that depicted in (b) is not. A par-space shift along the perp-space would, via phason flips, transform black into gray (online: red) atoms and vice versa. However, from a chemical point of view it is more physical than the example shown in Fig. 3.10(a), where A–B distances can be both, L and S, and no A–A and B–B neighbors exist. On the contrary, in Fig. 3.10(b), the atomic distances between like atoms, A–A or B–B, are of length L and between unlike atoms, A–B, of length S. The structure, with composition AB, is just a 2-fold superstructure of the FS. This 2-color FS can be generated by the substitution rule

$$\sigma : L^{AA} \mapsto L^{AA}S^{AB}L^{BB}L^{BB}S^{BA}, L^{BB} \mapsto L^{BB}S^{BA}L^{AA}L^{AA}S^{AB}, \quad (3.63)$$

$$S^{AB} \mapsto L^{AA}S^{AB}L^{BB}, S^{BA} \mapsto L^{BB}S^{BA}L^{AA}, \quad (3.64)$$

applied to the two-letter alphabet {L, S}. If the short distance $S = S^{AB} = S^{BA}$ links L^{AA} and L^{BB} independently from their order, then the substitution rule can be alternatively written employing the substitution matrix S

$$\underbrace{\begin{pmatrix} 1\,2\,2 \\ 2\,1\,2 \\ 1\,1\,1 \end{pmatrix}}_{=\mathsf{S}} \begin{pmatrix} L^{AA} \\ L^{BB} \\ S \end{pmatrix} = \begin{pmatrix} L^{AA} + 2L^{BB} + 2S \\ 2L^{AA} + L^{BB} + 2S \\ L^{AA} + L^{BB} + S \end{pmatrix}. \quad (3.65)$$

The characteristic polynom $1 + 5x + 3x^2 - x^3$ can be reduced to $-1 - 4x + x^2$. The resulting eigenvalues τ^3 and $-\tau^{-3}$ fulfill the PV property. Consequently, a pure point Fourier spectrum results on the $\mathbb{Z}$ module of rank 2

$$M^* = \left\{ \mathbf{H}^{\|} = \sum_{i=1}^{2} h_i \mathbf{a}_i^*, |\mathbf{a}_2^* = \frac{1}{2}\tau \mathbf{a}_1^*, h_i \in \mathbb{Z} \right\}. \quad (3.66)$$

Compared to the diffraction pattern of the FS, there appear superstructure reflections of the type $h_2 = n/2$ referring to the original unit cell of the FS. According to (3.65), the 2-color FS scales with a factor of τ^3.

Concerning the example shown in Fig. 3.10(a), all next neighbors are of different kind and a 4-fold centered supercell is needed for the 2D description. This gives rise to a reflection condition of the type $h_1h_2 : h_1 + h_2 = 2n$ based on the supercell lattice parameters.

In the example depicted in Fig. 3.10(c), the composition is AB_τ (A corresponds to red atoms, B to green ones). The closeness condition is fulfilled for the gray (online: red) atoms with a flip distance S/τ and for the black ones with S. There are no neighboring A atoms. A–B and B–B distances can be of length S or L. Since no supercell is needed in the 2D description, no additional reflections appear compared to the basic FS.

3.5.3.6 Approximant Structures

The $\langle m, n \rangle$-approximant $(m, n \in N)$ of a Fibonacci structure can be obtained applying the shear matrix of (3.7) with $A_{43} \neq 0$ to $\mathbf{r}$

$$\mathbf{r} = m\mathbf{d}_3 + n\mathbf{d}_4 = \frac{|\mathbf{a}_3^*|}{2 + \tau} \begin{pmatrix} 0 \\ 0 \\ m + n\tau \\ n - m\tau \end{pmatrix}_V . \tag{3.67}$$

From the condition that the perp-space component of the approximant basis vector has to vanish

$$A\mathbf{r} = \frac{|\mathbf{a}_3^*|}{2 + \tau} \begin{pmatrix} 0 \\ 0 \\ m + n\tau \\ A_{43}(m + n\tau)n - m\tau \end{pmatrix}_V \stackrel{!}{=} \frac{|\mathbf{a}_3^*|}{2 + \tau} \begin{pmatrix} 0 \\ 0 \\ m + n\tau \\ 0 \end{pmatrix}_V , \tag{3.68}$$

the shear matrix coefficient results to

$$A_{43} = \frac{m\tau - n}{n\tau + m} . \tag{3.69}$$

The basis vectors $\mathbf{a}_i^{\mathrm{Ap}}, i = 1, \cdots, 3$ of the $\langle m, n \rangle$-approximant result to

$$\mathbf{a}_i^{\mathrm{Ap}} = \mathbf{a}_i, i = 1, 2, \ \mathbf{a}_3^{\mathrm{Ap}} = \frac{(m + n\tau)}{2 + \tau} \mathbf{a}_3. \tag{3.70}$$

All peaks are shifted according to (3.8). Projecting the 4D reciprocal space onto par-space results in a periodic reciprocal lattice. Thus, all reflection indices $h_1 h_2 h_3 h_4$ of the quasicrystal are transformed to $h_1 h_2 (mh_3 + nh_4) = h_1^{\mathrm{Ap}} h_2^{\mathrm{Ap}} h_3^{\mathrm{Ap}}$ on the basis of the $\langle m, n \rangle$-approximant. Consequently, all structure factors $F(\mathbf{H})$ for reflections with $h_1 h_2 (h_3 - on)(h_4 + om)$, $o \in Z$ are projected onto each other.

3.5.3.7 The *Klotz* construction

The *Klotz* construction [26] is an alternative way for the generation of tilings and their approximants. In case of the Fibonacci tiling, two squares, called *Klötze* (plural of the German word *Klotz*), are arranged to a fundamental domain, the copies of which form a 2D uniform, dihedral, periodic tiling under translation (Fig. 3.11).

The set of all translations constitutes a 2D square lattice. The edge lengths of the squares define the lengths of the prototiles resulting from the cut along $V^{\parallel}$. The extension of the fundamental domain along $V^{\perp}$ defines the window,
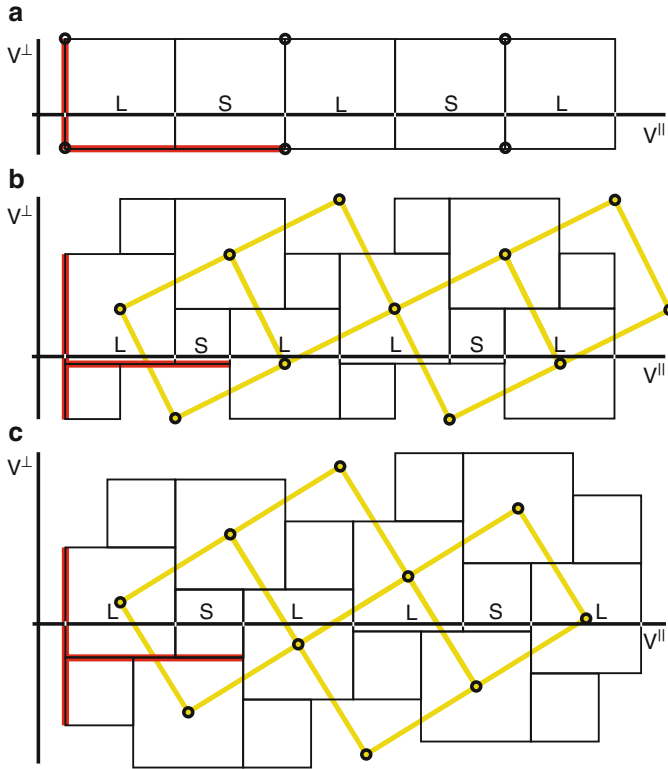
Fig. 3.11. *Klotz* construction based on two fundamental domains (*squares*). The ratio of their edge lengths is 1 in (**a**), 2 in (**b**) and τ in (**c**). Along the cutting line $V^{\parallel}$, this corresponds to 1D periodic approximant sequences (LS), (LSL), and the quasiperiodic FS, respectively. The thick (online: red) lines mark the projections of the unit cell of the 2D lattice upon $V^{\parallel}$ and $V^{\perp}$. This gives the Delone cluster (LS) and the window, respectively. Vertices of 2D rectangular or square lattices are marked by *open circles*

which will be relevant for the nD description (see Sect. 3.5.3). The projection of the 2D unit cell onto $V^{\parallel}$ defines the Delone cluster (LS), which is a covering cluster for the Fibonacci tiling. It covers the Fibonacci tiling, with sometimes overlapping S, in the following way

$$\ldots (\text{L(S)L})(\text{LS})(\text{L(S)L})(\text{L(S)L})(\text{LS})\ldots \tag{3.71}$$

The ratios of the edge lengths of the squares and the window give the relative frequencies of the prototiles in the tiling. The ratio of the areas of the squares gives the fraction of the Fibonacci tiling covered by the one and by the other prototile. If the edge lengths of the two squares are chosen in the

ratio of successive Fibonacci numbers then rational approximants result from the cut. In Fig. 3.11, the 1/1- and the 2/1-approximants are shown beside the Fibonacci tiling.

If $V^{\parallel}$ runs through a lattice point then the resulting Fibonacci tiling will have an inversion center since the whole Klotz tiling itself is centrosymmetric. A symmetric sequence can also be obtained from the words w_n generated by the substitution rule (1.1) by just removing the last two letters [23].

3.6 2D Quasiperiodic Structures

The 3D structures to be discussed in this section are quasiperiodic in two dimensions. They can be subsumed under the category of axial quasiperiodic structures, which can be seen, only geometrically (!), as periodic stackings of 2D quasiperiodic layers. The examples gone through in the following are mainly based on the 2D tilings presented in Chap. 1. The derivation of the proper nD embedding is best performed in reciprocal space.

The first step is to define a symmetry adapted set of reciprocal basis vectors $\mathbf{a}_i^*$, $i = 1 \ldots, n$. The vector components are given on a 3D Cartesian basis (V-basis). The set of all diffraction vectors $\mathbf{H} = \sum_{i=1}^{n} h_i \mathbf{a}_i^*$ forms a $\mathbb{Z}$-module M^* of rank n. The vectors $\mathbf{a}_i^*$, $i = 1, \ldots, n$ can be considered as par-space projections of the basis vectors $\mathbf{d}_i^*$, $i = 1, \ldots, n$ of the nD reciprocal lattice Σ^*. These vectors span the nD D-basis. The par-space components of the nD vectors $\mathbf{d}_i^* = (x_1, x_2, \cdots, x_n)_V$ are x_1, x_2, x_3, with x_3 the periodic direction. The n-fold axis ($n > 2$) is always oriented along $[0\ 0\ 1\ 0\ \cdots\ 0]_V$.

The second step is to decompose the, in 3D reducible, symmetry-adapted representation of the n-fold rotation into its irreducible representations. This can be done using the property that the trace of a transformation matrix is independent from the basis used. Then the proper irreducible representations can be identified in the character tables of the respective symmetry groups. For our purpose it is sufficient to consider the point groups of type Nm (C_{Nv}) with the generating elements $\alpha = N$, with N an N-fold rotation, and $\beta = m$, with m the reflection on a vertical mirror plane. With the identity operation $\varepsilon = 1$ the following relations hold: $\alpha^N = \beta^2 = \varepsilon$ and $\alpha\beta = \beta\alpha^{-1}$. The general form of the character table is given in Table 3.5 for odd orders p of N and in Table 3.6 for even orders.

The 2D irreducible representations can be written without loss of generality in the form

$$\alpha^r \mapsto \begin{vmatrix} \cos(r\frac{2\pi}{p}) & -\sin(r\frac{2\pi}{p}) \\ \sin(r\frac{2\pi}{p}) & \cos(r\frac{2\pi}{p}) \end{vmatrix}, \quad \beta \mapsto \begin{vmatrix} 0 & 1 \\ 1 & 0 \end{vmatrix}. \tag{3.72}$$

Based on the decomposition of the reducible representation of the N-fold rotation operation, the perp-space components of the nD basis can be derived. The matrix $\mathsf{W} = (\mathbf{d}_1^*, \ldots, \mathbf{d}_p^*)_V$ contains the nD reciprocal basis vectors as columns. Consequently, the columns of the transposed inverse matrix

Table 3.5. General form of the character table for point groups of type $Nm(C_{Nv})$ for odd order p of N (see, e.g., [2]). ε denotes the identity operation, α^n the rotation around $2n\pi/N$, and β the reflection on a vertical mirror plane (i.e., the normal to the mirror plane is perpendicular to the N-fold rotation axis)

Elements	ε	α	$\ldots$	$\alpha^{\frac{p-1}{2}}$	$\frac{p-1}{2}\beta$
Γ_1	1	1	$\ldots$	1	1
Γ_2	1	1	$\ldots$		-1
Γ_3	2	$2\cos(\frac{2\pi}{p})$	$\ldots$	$2\cos(\frac{p-1}{2}\frac{2\pi}{p})$	0
Γ_4	2	$2\cos(2\frac{2\pi}{p})$	$\ldots$	$2\cos((p-1)\frac{2\pi}{p})$	0
$\vdots$	$\vdots$	$\vdots$	$\ldots$	$\vdots$	$\vdots$
$\Gamma_{(p+3)/2}$	2	$2\cos(\frac{p-1}{2}\frac{2\pi}{p})$	$\ldots$	$2\cos((\frac{p-1}{2})^2\frac{2\pi}{p})$	0

Table 3.6. General form of the character table for point groups of type $Nm(C_{Nv})$ for even order p of N (see, e.g., [2]). ε denotes the identity operation, α^n the rotation around $2n\pi/N$, β and $\beta\prime$ the reflection on vertical mirror planes with the normal to the mirror plane along or between 3D reciprocal basis vectors and perpendicular to the N-fold axis

Elements	ε	α	$\ldots$	$\alpha^{\frac{p}{2}}$	$\frac{p}{2}\beta$	$\frac{p}{2}\beta'$
Γ_1	1	1	$\ldots$	1	1	1
Γ_2	1	1	$\ldots$	1	-1	-1
Γ_3	-1	1	$\ldots$	$(-1)^{\frac{p}{2}}$	1	-1
Γ_4	-1	1	$\ldots$	$(-1)^{\frac{p}{2}}$	-1	1
Γ_5	2	$2\cos(\frac{2\pi}{p})$	$\ldots$	$2\cos(\frac{p}{2}\frac{2\pi}{p})$	0	0
Γ_6	2	$2\cos(2\frac{2\pi}{p})$	$\ldots$	$2\cos(p\frac{2\pi}{p})$	0	0
$\vdots$	$\vdots$	$\vdots$	$\ldots$	$\vdots$	$\vdots$	$\vdots$
$\Gamma_{(p+6)/2}$	2	$2\cos((\frac{p}{2}-1)\frac{2\pi}{p})$	$\ldots$	$2\cos(\frac{p}{2}(\frac{p}{2}-1)\frac{2\pi}{p})$	0	0

$(W^{-1})^T = (\mathbf{d}_1,\ldots,\mathbf{d}_p)_V$ are made up by the nD direct basis vectors. Denoting the matrix W for short by its coefficients w_{ij}, its inverse by W_{ij}, their transposed matrices by w_{ji} and W_{ji}, and using the Einstein summation convention the transformation between D- and V-bases of basis vectors, coordinates and indices can be performed as following:

$$(\mathbf{d}_i^*)_V = w_{ij}(\mathbf{d}_j^*)_D, \quad (\mathbf{d}_i^*)_D = W_{ij}(\mathbf{d}_j^*)_V, \quad (h_i)_V = W_{ji}(h_j)_D, \quad (h_i)_D = w_{ji}(h_j)_V$$
$$(\mathbf{d}_i)_V = W_{ji}(\mathbf{d}_j)_D, \quad (\mathbf{d}_i)_V = w_{ji}(\mathbf{d}_j)_D, \quad (x_i)_V = w_{ij}(x_j)_D, \quad (x_i)_D = W_{ij}(x_j)_V$$
$$(3.73)$$

For the 2D quasiperiodic substructure, there is a minimum embedding dimension n given by the condition that the N-fold rotational symmetry has to leave the nD lattice invariant (see Table 3.1). n equals 4 in case of 5-, 8-,

10- and 12-fold symmetry, and 6 for 7- and 14-fold, for instance. It may be helpful, however, to use the canonical hypercubic description which is based on the full star of basis vectors. The embedding dimension n results to $n = N$ if N is odd and $n = N/2$ for N even. In the hypercubic case, the derivation of atomic surfaces may be simpler.

3.6.1 Pentagonal Structures

There are two ways of embedding pentagonal tilings, which can be used as basic quasilattices for pentagonal structures. The 4D minimum embedding dimension leads to a hyperrhombohedral unit cell, the 5D canonical embedding to a hypercubic unit cell. Adding a third, periodic dimension allows to model axial quasicrystal structures.

3.6.1.1 (4+1)D Embedding

Here, the case is described where only the four rationally independent reciprocal basis vectors out of the five related to the 2D quasiperiodic substructure are used for embedding. Each of the five reciprocal basis vectors can be described as linear combination of the four other ones, for instance, $\mathbf{a}_0^* = -(\mathbf{a}_1^* + \mathbf{a}_2^* + \mathbf{a}_3^* + \mathbf{a}_4^*)$. This minimum-dimensional embedding leads to a hyperrhombohedral unit cell of the quasiperiodic substructure.

The embedding matrix is derived from the reducible representation $\Gamma(\alpha)$ of the 5-fold rotation, $\alpha = 5$, which can be written as 5×5 matrix with integer coefficients acting on the reciprocal space vectors $\mathbf{H}$. The 5D representation can be composed from the irreducible representations Γ_1, Γ_3, and Γ_4 shown in the character table below (Table 3.7).

The 2D representation Γ_3 describes the component of the 5D rotation in the 2D quasiperiodic physical subspace, the 2D representation Γ_4 the component of the rotation in perp-space, and the 1D representation Γ_1 that along the 5-fold axis (Fig. 3.12). The sum of the corresponding characters $1+\tau-1-\tau = 0$ equals the trace of the reducible rotation matrix given in (3.74). Based thereon, the 5-fold rotation matrix can be block-diagonalised in the following way

Table 3.7. Character table for the pentagonal group $5m$ (C_{5v}) [20]. ε denotes the identity operation, α^n the rotation around $2n\pi/5$, and β the reflection on a vertical mirror plane

Elements	ε	α	α^2	β
Γ_1	1	1	1	1
Γ_2	1	1	1	-1
Γ_3	2	τ	$-1-\tau$	0
Γ_4	2	$-1-\tau$	τ	0
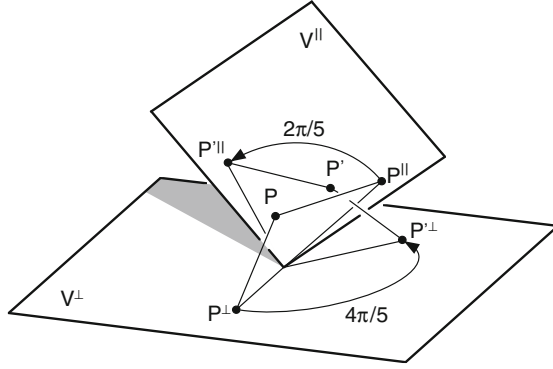
Fig. 3.12. Illustration of a 4D 5-fold rotation by the par- and perp-space projections of the trajectory of the point P during its rotation to P′

$$
\Gamma(5) =
\begin{pmatrix}
0 & 0 & 0 & \bar{1} & 0 \\
1 & 0 & 0 & \bar{1} & 0 \\
0 & 1 & 0 & \bar{1} & 0 \\
0 & 0 & 1 & \bar{1} & 0 \\
0 & 0 & 0 & 0 & 1
\end{pmatrix}_{D^*}
=
\left(
\begin{array}{ccc|cc}
\cos\frac{2\pi}{5} & -\sin\frac{2\pi}{5} & 0 & 0 & 0 \\
\sin\frac{2\pi}{5} & \cos\frac{2\pi}{5} & 0 & 0 & 0 \\
0 & 0 & 1 & 0 & 0 \\
\hline
0 & 0 & 0 & \cos\frac{4\pi}{5} & -\sin\frac{4\pi}{5} \\
0 & 0 & 0 & \sin\frac{4\pi}{5} & \cos\frac{4\pi}{5}
\end{array}
\right)_{V^*}
=
$$

$$
=
\left(
\begin{array}{c|c}
\Gamma^{\parallel}(5) & 0 \\
\hline
0 & \Gamma^{\perp}(5)
\end{array}
\right)_{V^*}.
\tag{3.74}
$$

3.6.1.2 Reciprocal Space

The electron density distribution function $\rho(\mathbf{r})$ of a 3D quasicrystal can be represented by the Fourier series given in (3.41). All Fourier coefficients, i.e. the structure factors $F(\mathbf{H})$, can be indexed with integer indices based on five reciprocal space vectors: $\mathbf{H} = \sum_{i=1}^{5} h_i \mathbf{a}_i^*$ with $\mathbf{a}_i^* = a^* \left(\cos(2\pi i/5), \sin(2\pi i/5), 0 \right), i = 1, \ldots, 4$, $a^* = |\mathbf{a}_1^*| = |\mathbf{a}_2^*| = |\mathbf{a}_3^*| = |\mathbf{a}_4^*|, \mathbf{a}_5^* = |\mathbf{a}_5^*| (0,0,1)$ and $h_i \in \mathbb{Z}$ (Fig. 3.13).

The vector components refer to a Cartesian coordinate system in par-space $V^{\parallel}$. The set of all diffraction vectors $\mathbf{H}$ forms a $\mathbb{Z}$-module M^* of rank five. The vectors $\mathbf{a}_i^*$, $i = 1, \ldots, 5$ can be considered as par-space projections of the basis vectors $\mathbf{d}_i^*$, $i = 1, \ldots, 5$ of the 5D reciprocal lattice Σ^* with

$$
\mathbf{d}_i^* = a^* \sqrt{\frac{2}{5}}
\begin{pmatrix}
\cos\frac{2\pi i}{5} \\
\sin\frac{2\pi i}{5} \\
0 \\
c \cos\frac{4\pi i}{5} \\
c \sin\frac{4\pi i}{5}
\end{pmatrix}_{V^*}
, \quad i = 1, \ldots, 4; \quad
\mathbf{d}_5^* = a_5^*
\begin{pmatrix}
0 \\
0 \\
1 \\
0 \\
0
\end{pmatrix}_{V^*}
. \tag{3.75}
$$

c is an arbitrary constant which is usually set to 1 (as it is also done in the following). The subscript V denotes components referring to a 5D Cartesian
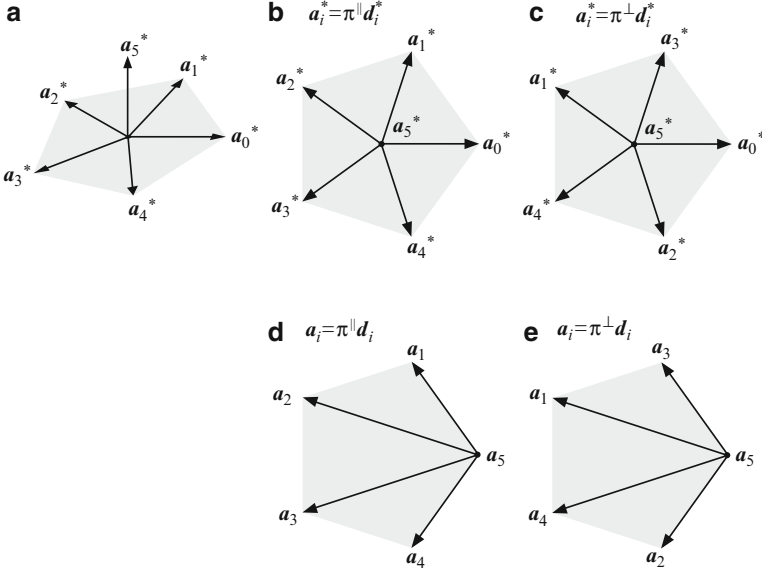
Fig. 3.13. Reciprocal basis of the pentagonal phase shown in perspective view (**a**) as well as in projections upon the parallel (**b**) and the perp-space (**c**). The vector $\mathbf{a}_0^* = -(\mathbf{a}_1^* + \mathbf{a}_2^* + \mathbf{a}_3^* + \mathbf{a}_4^*)$ is linear dependent. The corresponding projections of the direct basis are depicted in (**d**) and (**e**)

coordinate system (V-basis), while subscript D refers to the 5D crystallographic basis (D-basis). The embedding matrix W (3.76), which contains the reciprocal space vectors $\mathbf{d}_i^*$, $i = 1, \ldots, 5$ as columns, results to

$$\mathsf{W} = \sqrt{\frac{2}{5}} \begin{pmatrix} \cos\frac{2\pi}{5} & \cos\frac{4\pi}{5} & \cos\frac{6\pi}{5} & \cos\frac{8\pi}{5} & 0 \\ \sin\frac{2\pi}{5} & \sin\frac{4\pi}{5} & \sin\frac{6\pi}{5} & \sin\frac{8\pi}{5} & 0 \\ 0 & 0 & 0 & 0 & \sqrt{\frac{5}{2}} \\ \cos\frac{4\pi}{5} & \cos\frac{8\pi}{5} & \cos\frac{12\pi}{5} & \cos\frac{16\pi}{5} & 0 \\ \sin\frac{4\pi}{5} & \sin\frac{8\pi}{5} & \sin\frac{12\pi}{5} & \sin\frac{16\pi}{5} & 0 \end{pmatrix}_{V^*} . \qquad (3.76)$$

The direct 5D basis is obtained from the orthogonality condition (3.5) as column vectors of the transpose $(\mathsf{W}^{-1})^T$ of the inverse embedding matrix W

$$\mathbf{d}_i = \frac{1}{a^*}\sqrt{\frac{2}{5}} \begin{pmatrix} \cos\frac{2\pi i}{5} - 1 \\ \sin\frac{2\pi i}{5} \\ 0 \\ \cos\frac{4\pi i}{5} - 1 \\ \sin\frac{4\pi i}{5} \end{pmatrix}_V , \quad i = 1, \ldots, 4; \quad \mathbf{d}_5 = \frac{1}{a_5^*} \begin{pmatrix} 0 \\ 0 \\ 1 \\ 0 \\ 0 \end{pmatrix}_V . \qquad (3.77)$$

The metric tensors G and G^* are of type

$$
\begin{pmatrix}
A & B & B & B & 0 \\
B & A & B & B & 0 \\
B & B & A & B & 0 \\
B & B & B & A & 0 \\
0 & 0 & 0 & 0 & C
\end{pmatrix}
\tag{3.78}
$$

with $A = 4/5a^{*2}$, $B = -1/5a^{*2}$, $C = a_5^{*2}$, for reciprocal space and $A = 2/a^{*2}$, $B = 1/a^{*2}$, $C = 1/a_5^{*2}$ for direct space. Therefrom, the direct and reciprocal lattice parameters can be derived as

$$
d_i^* = \frac{2}{\sqrt{5}}a^*, \quad d_5^* = a_5^*, \quad \alpha_{ij} = 104.48°, \quad \alpha_{i5} = 90°, \quad i,j = 1,\ldots,4 \tag{3.79}
$$

and

$$
d_i = \frac{2}{\sqrt{5}a^*}, \quad d_5 = \frac{1}{a_5^*}, \quad \alpha_{ij} = 60°, \quad \alpha_{i5} = 90°, \quad i,j = 1,\ldots,4 . \tag{3.80}
$$

The volume of the 5D unit cell results to

$$
V = \sqrt{\det(\mathsf{G})} = \frac{\sqrt{5}}{a^{*4}a_5^*} = \frac{25\sqrt{5}}{16}d^4 d_5. \tag{3.81}
$$

3.6.1.3 Symmetry

The diffraction symmetry of pentagonal phases, i.e., the point symmetry group leaving invariant the intensity weighted Fourier module (diffraction pattern) M_I^*, is one of the two Laue groups $\bar{5}2/m$ or $\bar{5}$. The space groups leaving the 5D hypercrystal structure invariant are that subset of all 5D space groups, the point groups of which are isomorphous to the 3D pentagonal point groups (Table 3.8).

The orientation of the symmetry elements of the 5D space groups is defined by the isomorphism of the 3D and 5D point groups. The 5-fold axis defines the unique direction $[00100]_V$ or $[00001]_D$, which is the periodic direction. The 5D reflection and inversion operations m and $\bar{1}$ reflect and invert in both subspaces $V^\parallel$ and $V^\perp$ in the same way. The 5-fold rotation has the component $2\pi/5$ in $V^\parallel$ and $4\pi/5$ in $V^\perp$ (Fig. 3.13) as already found in (3.74). The same decomposition can be obtained from $\mathsf{W} \cdot \Gamma(5) \cdot \mathsf{W}^{-1}$.

The symmetry matrices for the reflections on mirror planes, with normals along and between reciprocal basis vectors, respectively, read for the examples with the normal of the mirror plane m_2 along $\mathbf{a}_2^*$ and of the mirror plane m_{14} along $\mathbf{a}_1^* - \mathbf{a}_4^*$:

$$
\Gamma(m_2) = \begin{pmatrix}
0 & 0 & \bar{1} & 1 & 0 \\
0 & \bar{1} & 0 & 1 & 0 \\
\bar{1} & 0 & 0 & 1 & 0 \\
0 & 0 & 0 & 1 & 0 \\
0 & 0 & 0 & 0 & 1
\end{pmatrix}_{V^*}, \quad
\Gamma(m_{14}) = \begin{pmatrix}
0 & 0 & 0 & \bar{1} & 0 \\
0 & 0 & \bar{1} & 0 & 0 \\
0 & \bar{1} & 0 & 0 & 0 \\
\bar{1} & 0 & 0 & 0 & 0 \\
0 & 0 & 0 & 0 & 1
\end{pmatrix}_{V^*}, \tag{3.82}
$$

Table 3.8. The five 3D pentagonal point groups of order k and the twenty-two corresponding 5D pentagonal space groups with extinction conditions [36]. The notation is analogous to that of trigonal space groups. The first position in the point group and the second position in the space group symbols refer to generating symmetry elements oriented along the periodic direction, the second position to the symmetry elements oriented along reciprocal space basis vectors and the third position to those oriented between them. S means staggered lattice in analogy to R in the trigonal case

3D Point Group	k	5D Space Group	Reflection Conditions
$\bar{5}\dfrac{2}{m}$	20	$P\bar{5}\dfrac{2}{m}1$	No condition
		$P\bar{5}\dfrac{2}{c}1$	Odd layers along
		$P\bar{5}1\dfrac{2}{m}$	No condition
		$P\bar{5}1\dfrac{2}{c}$	Odd layers between
		$S\bar{5}\dfrac{2}{m}$	No condition
		$S\bar{5}\dfrac{2}{c}$	Odd layers between
$5m$	10	$P5m1$	No condition
		$P5c1$	Odd layers along
		$P51m$	No condition
		$P51c$	Odd layers between
		$S5m$	No condition
		$S5c$	Odd layers between
52	10	$P512$	No condition
		$P5_j12$	$0000h_j : jh_5 = 5n$
		$P521$	No condition
		$P5_j21$	$0000h_j : jh_5 = 5n$
		$S52$	No condition
$\bar{5}$	5	$P\bar{5}$	No condition
		$S\bar{5}$	No condition
5	5	$P5$	No condition
		$P5_j$	$0000h_j : jh_5 = 5n$
		$S5$	No condition

The five possible 3D point groups and the twenty-two 5D space groups of pentagonal quasiperiodic structures are listed in Table 3.8. The translation components of the 5-fold screw axes and the c-glide planes are along the periodic direction. The capital letter S marks staggered lattice types in analogy to the rhombohedral Bravais lattice in the trigonal case.

A typical property of the reciprocal space of quasiperiodic structures is its scaling symmetry (Fig. 3.14). The scaling operation is represented by the matrix S^*, which can be diagonalized by $\mathsf{W} \cdot \mathsf{S}^* \cdot W^{-1}$
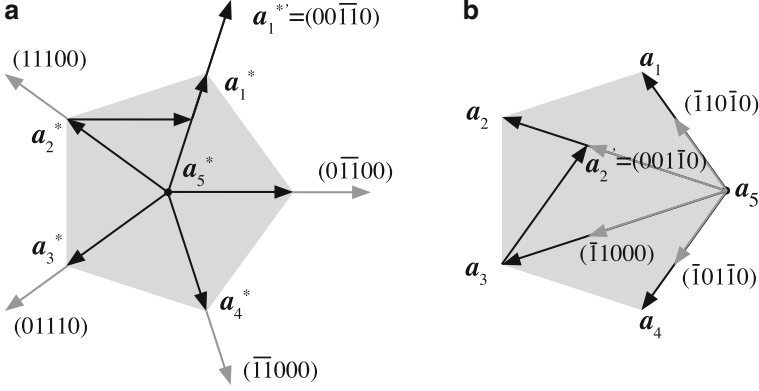
Fig. 3.14. Reciprocal and direct space scaling by the matrices S^* (**a**) and S (**b**), respectively. The scaled basis vectors (marked gray) keep their orientation and are increased or decreased in length by a factor τ (**a**) or $1/\tau$ (**b**). Explicitly shown is the scaling of the vectors $\mathbf{a}_1^*$ and $\mathbf{a}_2$: $\mathbf{a}_1^{*\prime} = \mathbf{a}_2^* + \mathbf{a}_0^* + \mathbf{a}_1^*$ with $\mathbf{a}_0^* = -\sum_{i=1}^{4}\mathbf{a}_i^*$, and $\mathbf{a}_2' = \mathbf{a}_3 - \mathbf{a}_4$

$$
\mathsf{S}^* = \begin{pmatrix} 0\,1\,0\,\bar{1}\,0 \\ 0\,1\,1\,\bar{1}\,0 \\ \bar{1}\,1\,1\,0\,0 \\ \bar{1}\,0\,1\,0\,0 \\ 0\,0\,0\,0\,1 \end{pmatrix}_{D^*} = \left(\begin{array}{ccc|cc} \tau & 0 & 0 & 0 & 0 \\ 0 & \tau & 0 & 0 & 0 \\ 0 & 0 & 1 & 0 & 0 \\ \hline 0 & 0 & 0 & -1/\tau & 0 \\ 0 & 0 & 0 & 0 & -1/\tau \end{array}\right)_{V^*} = \left(\begin{array}{c|c} \Gamma^{\parallel}\,(\mathsf{S}^*) & 0 \\ \hline 0 & \Gamma_1^{\perp}\,(\mathsf{S}^*) \end{array}\right)_{V*}.
$$

(3.83)

The eigenvalues of the scaling matrix are the Pisot numbers $\lambda_1 = 1 + 2\cos\pi/5 = \tau = 1.61803$, $\lambda_2 = 1 + 2\cos 4\pi/5 = -1/\tau = -0.61803$, which are the solutions of the characteristic polynomial $1 + x - 3x^2 - x^3 + 3x^4 - x^5 = (1-x)(-1-x+x^2)^2$. The scaling symmetry matrix for the direct space basis vectors and the reflection indices $\mathsf{S} = [(\mathsf{S}^*)^{-1}]^{\mathsf{T}}$ results to

$$
\mathsf{S} = \begin{pmatrix} \bar{1}\,0\,\bar{1}\,\bar{1}\,0 \\ 1\,0\,1\,0\,0 \\ 0\,1\,0\,1\,0 \\ \bar{1}\,\bar{1}\,0\,\bar{1}\,0 \\ 0\,0\,0\,0\,1 \end{pmatrix}_{D} = \left(\begin{array}{ccc|cc} 1/\tau & 0 & 0 & 0 & 0 \\ 0 & 1/\tau & 0 & 0 & 0 \\ 0 & 0 & 1 & 0 & 0 \\ \hline 0 & 0 & 0 & -\tau & 0 \\ 0 & 0 & 0 & 0 & -\tau \end{array}\right)_{V} = \left(\begin{array}{c|c} \Gamma^{\parallel}\,(\mathsf{S}) & 0 \\ \hline 0 & \Gamma_1^{\perp}\,(\mathsf{S}) \end{array}\right)_{V}.
$$

(3.84)

3.6.1.4 (5+1)D Embedding

The following nD description is based on the full set of five reciprocal basis vectors related to the quasiperiodic substructure plus one in the periodic direction. The 5-fold reducible 6×6 rotation matrix can be block-diagonalised in the following way

$$
\Gamma(5) = \begin{pmatrix} 0\,0\,0\,0\,1\,0 \\ 1\,0\,0\,0\,0\,0 \\ 0\,1\,0\,0\,0\,0 \\ 0\,0\,1\,0\,0\,0 \\ 0\,0\,0\,1\,0\,0 \\ 0\,0\,0\,0\,0\,1 \end{pmatrix}_{D^*} = \left(\begin{array}{ccc|cc} \cos\frac{2\pi}{5} & -\sin\frac{2\pi}{5} & 0 & 0 & 0 \\ \sin\frac{2\pi}{5} & \cos\frac{2\pi}{5} & 0 & 0 & 0 \\ 0 & 0 & 1 & 0 & 0 \\ \hline 0 & 0 & 0 & \cos\frac{4\pi}{5} & -\sin\frac{4\pi}{5} \\ 0 & 0 & 0 & \sin\frac{4\pi}{5} & \cos\frac{4\pi}{5} \\ 0 & 0 & 0 & 0 & 0 & 1 \end{array} \right)_{V^*} =
$$

$$
= \left(\begin{array}{c|c} \Gamma^{\|}(5) & 0 \\ \hline 0 & \Gamma^{\perp}(5) \end{array} \right)_{V^*} . \tag{3.85}
$$

Both par- and perp-subspaces are 3D in this case. The set of all diffraction vectors $\mathbf{H}$ forms a $\mathbb{Z}$-module M^* of rank six. The vectors $\mathbf{a}_i^*$, $i = 1, \ldots, 6$, with $a^* = a_1^* = a_2^* = a_3^* = a_4^* = a_5^*$ ($a_0^* = a_5^*$), can be considered as par-space projections of the basis vectors $\mathbf{d}_i^*$, $i = 1, \ldots, 6$ of the 6D reciprocal lattice Σ^* with

$$
\mathbf{d}_i^* = a_i^* \sqrt{\frac{2}{5}} \begin{pmatrix} \cos\frac{2\pi i}{5} \\ \sin\frac{2\pi i}{5} \\ 0 \\ c\cos\frac{4\pi i}{5} \\ c\sin\frac{4\pi i}{5} \\ \frac{c}{\sqrt{2}} \end{pmatrix}_{V^*} , \quad i = 1, \ldots, 5; \quad \mathbf{d}_6^* = a_6^* \begin{pmatrix} 0 \\ 0 \\ 1 \\ 0 \\ 0 \\ 0 \end{pmatrix}_{V^*} . \tag{3.86}
$$

Without loss of generality c can be set to 1. Then the W matrix for 6D reciprocal space reads

$$
\mathsf{W} = \sqrt{\frac{2}{5}} \begin{pmatrix} \cos\frac{2\pi}{5} & \cos\frac{4\pi}{5} & \cos\frac{6\pi}{5} & \cos\frac{8\pi}{5} & 1 & 0 \\ \sin\frac{2\pi}{5} & \sin\frac{4\pi}{5} & \sin\frac{6\pi}{5} & \sin\frac{8\pi}{5} & 0 & 0 \\ 0 & 0 & 0 & 0 & 0 & \sqrt{\frac{5}{2}} \\ \cos\frac{4\pi}{5} & \cos\frac{8\pi}{5} & \cos\frac{12\pi}{5} & \cos\frac{16\pi}{5} & 1 & 0 \\ \sin\frac{4\pi}{5} & \sin\frac{8\pi}{5} & \sin\frac{12\pi}{5} & \sin\frac{16\pi}{5} & 0 & 0 \\ \frac{1}{\sqrt{2}} & \frac{1}{\sqrt{2}} & \frac{1}{\sqrt{2}} & \frac{1}{\sqrt{2}} & \frac{1}{\sqrt{2}} & 0 \end{pmatrix}_{V^*} . \tag{3.87}
$$

The direct 6D basis is obtained from the orthogonality condition (3.5) as column vectors of the transpose $(\mathsf{W}^{-1})^T$ of the inverse embedding matrix W

$$
\mathbf{d}_i = \frac{1}{a^*}\sqrt{\frac{2}{5}} \begin{pmatrix} \cos\frac{2\pi i}{5} \\ \sin\frac{2\pi i}{5} \\ 0 \\ \cos\frac{4\pi i}{5} \\ \sin\frac{4\pi i}{5} \\ 1/\sqrt{2} \end{pmatrix}_{V} , \quad i = 1, \ldots, 5; \quad \mathbf{d}_6 = \frac{1}{a_6^*} \begin{pmatrix} 0 \\ 0 \\ 1 \\ 0 \\ 0 \\ 0 \end{pmatrix}_{V} . \tag{3.88}
$$

The metric tensors G and G^* are of type

$$
\begin{pmatrix}
A & 0 & 0 & 0 & 0 & 0 \\
0 & A & 0 & 0 & 0 & 0 \\
0 & 0 & A & 0 & 0 & 0 \\
0 & 0 & 0 & A & 0 & 0 \\
0 & 0 & 0 & 0 & A & 0 \\
0 & 0 & 0 & 0 & 0 & B
\end{pmatrix},
\tag{3.89}
$$

with $A = a^{*2}$, $B = a_6^{*2}$, for reciprocal space and $A = 1/a^{*2}$, $B = 1/a_6^{*2}$ for direct space. Therefrom, the direct and reciprocal lattice parameters can be derived as $d_i^* = a_i^*, d_i = 1/a_i^*, \alpha_{ij}^* = \alpha_{ij} = 90°, i, j = 1, \ldots, 6$. The volume of the 6D unit cell results, with $d = d_1 = d_2 = d_3 = d_4 = d_5$, to

$$
V = \sqrt{\det(\mathsf{G})} = \frac{1}{a^{*5}a_6^*} = d^5 d_6.
\tag{3.90}
$$

3.6.1.5 Example: Pentagonal Quasicrystal

The 6D hyperlattice Σ of the pentagonal structure possesses decagonal symmetry. The symmetry can be lowered to pentagonal by a proper decoration with atomic surfaces breaking the decagonal lattice symmetry. For instance, if an atomic surface with just pentagonal symmetry is put at the origin of the 5D subunit cell. This can be a superstructure of the pentagonal Penrose tiling, when the decagonal atomic surface is decorated in a proper way. Basically, the description of a pentagonal structure is analogous to that of the decagonal case and will be treated in Sect. 3.6.4, consequently.

3.6.2 Heptagonal Structures

Axial quasicrystals with heptagonal diffraction symmetry, i.e., with Laue groups $\bar{7}2/m$ or $\bar{7}$, possess heptagonal structures. So far, there are only a few approximants known and no quasicrystals. The embedding matrix can be derived from the reducible representation $\Gamma(\alpha)$ of the 7-fold rotation, $\alpha = 7$, which can be written as 7×7 matrix with integer coefficients acting on the reciprocal space vectors $\mathbf{H}$. The 7D representation is reducible to par- and perp-space components, which can be combined from the irreducible representations $\Gamma_3, \Gamma_1, \Gamma_4$, and Γ_5 shown in the character table below (Table 3.9).

Consequently, a $2\pi/7$ rotation in $V^\parallel$ around the 7-fold axis has component rotations of $4\pi/7$ and $6\pi/7$ in the two 2D orthogonal $V^\perp$ subspaces (Fig. 3.15). The decomposition of the reducible symmetry matrix α yields (3.91)

Table 3.9. Character table for the heptagonal group $7m$ (C_{7v}). ε denotes the identity operation, α^n the rotation around $2n\pi/7$, and β the reflection on a mirror plane

Elements	ε	α	α^2	α^3	β
Γ_1	1	1	1	1	1
Γ_2	1	1	1	1	-1
Γ_3	2	$2\cos 2\pi/7$	$2\cos 4\pi/7$	$2\cos 6\pi/7$	0
Γ_4	2	$2\cos 4\pi/7$	$2\cos 8\pi/7$	$2\cos 12\pi/7$	0
Γ_5	2	$2\cos 6\pi/7$	$2\cos 12\pi/7$	$2\cos 4\pi/7$	0

Fig. 3.15. 7D reciprocal (**a**–**c**) and direct (**d**–**f**) space bases $\mathbf{d}_i^*$ and $\mathbf{d}_i, i = 1, \ldots, 7$, respectively, projected onto the par-space (**a**, **d**) and the two 2D perp-subspaces (**b**, **e**) and (**c**, **f**). The vectors $\mathbf{a}_7^*$ and $\mathbf{a}_7$ along the periodic direction are perpendicular to the plane spanned by the vectors $\mathbf{a}_i^*, i = 1, \ldots, 6$ and $\mathbf{a}_i, i = 1, \ldots, 6$, respectively

$$
\Gamma(\alpha) = \begin{pmatrix} 0\ 0\ 0\ 0\ 0\ \bar{1}\ 0 \\ 1\ 0\ 0\ 0\ 0\ \bar{1}\ 0 \\ 0\ 1\ 0\ 0\ 0\ \bar{1}\ 0 \\ 0\ 0\ 1\ 0\ 0\ \bar{1}\ 0 \\ 0\ 0\ 0\ 1\ 0\ \bar{1}\ 0 \\ 0\ 0\ 0\ 0\ 1\ \bar{1}\ 0 \\ 0\ 0\ 0\ 0\ 0\ 0\ 1 \end{pmatrix}_{D^*} = \left(\begin{array}{ccc|cc|cc} \cos\frac{2\pi}{7} & -\sin\frac{2\pi}{7} & 0 & 0 & 0 & 0 & 0 \\ \sin\frac{2\pi}{7} & \cos\frac{2\pi}{7} & 0 & 0 & 0 & 0 & 0 \\ 0 & 0 & 1 & 0 & 0 & 0 & 0 \\ \hline 0 & 0 & 0 & \cos\frac{4\pi}{7} & -\sin\frac{4\pi}{7} & 0 & 0 \\ 0 & 0 & 0 & \sin\frac{4\pi}{7} & \cos\frac{4\pi}{7} & 0 & 0 \\ \hline 0 & 0 & 0 & 0 & 0 & \cos\frac{6\pi}{7} & -\sin\frac{6\pi}{7} \\ 0 & 0 & 0 & 0 & 0 & \sin\frac{6\pi}{7} & \cos\frac{6\pi}{7} \end{array} \right)_{V}
$$

$$
= \begin{pmatrix} \begin{array}{c|c|c} \Gamma^{\parallel}(7) & 0 & 0 \\ \hline 0 & \Gamma_1^{\perp}(7) & 0 \\ \hline 0 & 0 & \Gamma_2^{\perp}(7) \end{array} \end{pmatrix}_V
\tag{3.91}
$$

3.6.2.1 Reciprocal Space

The electron density distribution function $\rho(\mathbf{r})$ of a 3D quasicrystal can be represented by the Fourier series given in (3.41). All Fourier coefficients, i.e., the structure factors $F(\mathbf{H})$, can be indexed based on seven reciprocal basis vectors with integers: $\mathbf{H} = \sum_{i=1}^{7} h_i \mathbf{a}_i^*$ with $\mathbf{a}_i^* = a^*(\cos(2\pi i/7), \sin(2\pi i/7), 0)$, $a^* = |\mathbf{a}_i^*|, i = 1, \ldots, 6, \mathbf{a}_7^* = |\mathbf{a}_7^*|(0, 0, 1)$ and $h_i \in \mathbb{Z}$ (Fig. 3.15).

The vector components refer to a Cartesian coordinate system in par-space $V^{\parallel}$. The set of all diffraction vectors $\mathbf{H}$ forms a $\mathbb{Z}$-module M^* of rank seven. The vectors $\mathbf{a}_i^*$, $i = 1, \ldots, 7$ can be considered as par-space projections of the basis vectors $\mathbf{d}_i^*$, $i = 1, \ldots, 7$ of the 7D reciprocal lattice Σ^* with

$$
\mathbf{d}_i^* = a^* \begin{pmatrix} \cos\frac{2\pi i}{7} \\ \sin\frac{2\pi i}{7} \\ 0 \\ c\cos\frac{4\pi i}{7} \\ c\sin\frac{4\pi i}{7} \\ c\cos\frac{6\pi i}{7} \\ c\sin\frac{6\pi i}{7} \end{pmatrix}_V, \quad i = 1, \ldots, 6, \quad \mathbf{d}_7^* = a_7^* \begin{pmatrix} 0 \\ 0 \\ 1 \\ 0 \\ 0 \\ 0 \\ 0 \end{pmatrix}_V.
\tag{3.92}
$$

The coupling factor between par- and perp-space rotations equals 2 and 3, respectively, for the two 2D perpendicular subspaces, c is an arbitrary constant which is usually set to 1 (as it is also done in the following). The subscript V denotes components referring to a 7D Cartesian coordinate system (V-basis), while subscript D refers to the 7D crystallographic basis (D-basis). The embedding matrix W (3.93) results to

$$
\mathsf{W} = \begin{pmatrix}
\cos\frac{2\pi}{7} & \cos\frac{4\pi}{7} & \cos\frac{6\pi}{7} & \cos\frac{8\pi}{7} & \cos\frac{10\pi}{7} & \cos\frac{12\pi}{7} & 0 \\
\sin\frac{2\pi}{7} & \sin\frac{4\pi}{7} & \sin\frac{6\pi}{7} & \sin\frac{8\pi}{7} & \sin\frac{10\pi}{7} & \sin\frac{12\pi}{7} & 0 \\
0 & 0 & 0 & 0 & 0 & 0 & 1 \\
\cos\frac{4\pi}{7} & \cos\frac{8\pi}{7} & \cos\frac{12\pi}{7} & \cos\frac{16\pi}{7} & \cos\frac{20\pi}{7} & \cos\frac{24\pi}{7} & 0 \\
\sin\frac{4\pi}{7} & \sin\frac{8\pi}{7} & \sin\frac{12\pi}{7} & \sin\frac{16\pi}{7} & \sin\frac{20\pi}{7} & \sin\frac{24\pi}{7} & 0 \\
\cos\frac{6\pi}{7} & \cos\frac{12\pi}{7} & \cos\frac{18\pi}{7} & \cos\frac{24\pi}{7} & \cos\frac{30\pi}{7} & \cos\frac{36\pi}{7} & 0 \\
\sin\frac{6\pi}{7} & \sin\frac{12\pi}{7} & \sin\frac{18\pi}{7} & \sin\frac{24\pi}{7} & \sin\frac{30\pi}{7} & \sin\frac{36\pi}{7} & 0
\end{pmatrix}.
\tag{3.93}
$$

The direct 7D basis is obtained from the orthogonality condition (3.5)

$$
\mathbf{d}_i = \frac{2}{7a_i^*}
\begin{pmatrix}
\cos\frac{2\pi i}{7} - 1 \\
\sin\frac{2\pi i}{7} \\
0 \\
\cos\frac{4\pi i}{7} - 1 \\
\sin\frac{4\pi i}{7} \\
\cos\frac{6\pi i}{7} - 1 \\
\sin\frac{6\pi i}{7}
\end{pmatrix}_V
, \quad i = 1,\ldots,6, \quad
\mathbf{d}_7 = \frac{1}{a_7^*}
\begin{pmatrix}
0 \\
0 \\
1 \\
0 \\
0 \\
0 \\
0
\end{pmatrix}_V .
\tag{3.94}
$$

The metric tensors G and G^* are of type

$$
\begin{pmatrix}
A & B & B & B & B & B & 0 \\
B & A & B & B & B & B & 0 \\
B & B & A & B & B & B & 0 \\
B & B & B & A & B & B & 0 \\
B & B & B & B & A & B & 0 \\
B & B & B & B & B & A & 0 \\
0 & 0 & 0 & 0 & 0 & 0 & C
\end{pmatrix}
\tag{3.95}
$$

with $A = 3a^{*2}$, $B = -1/2a^{*2}$, $C = a_7^{*2}$, for reciprocal space and $A = 4/7a^{*2}$, $B = 2/7a^{*2}$, $C = 1/a_7^{*2}$ for direct space. Therefrom the direct and reciprocal lattice parameters can be derived as

$$
d_i^* = \sqrt{3}a^*, \quad dd_7^* = a_7^*, \quad \alpha_{ij} = \arccos 1/6 = 99.59°, \quad \alpha_{i7} = 90°, \quad i,j = 1,\ldots,6
\tag{3.96}
$$

and

$$
d_i = \frac{2}{\sqrt{7}a^*}, \quad i = 1,\ldots,6, \quad d_7 = \frac{1}{a_7^*}, \quad \alpha_{ij} = 60°, \quad \alpha_{i5} = 90°, \quad i,j = 1,\ldots,4 .
\tag{3.97}
$$

This means that the 6D subspace orthogonal to the periodic direction has hyperrhombohedral symmetry. The volume of the 7D unit cell results to

$$
V = \sqrt{\det(\mathsf{G})} = \frac{8}{49\sqrt{7}a^{*6}a_7^*} .
\tag{3.98}
$$

3.6.2.2 Symmetry

The diffraction symmetry of heptagonal phases, i.e., the point symmetry group leaving the intensity weighted Fourier module (diffraction pattern) M_I^* invariant, is one of the two Laue groups $\bar{7}2/m$ or $\bar{7}$. The space groups leaving the 7D hypercrystal structure invariant are that subset of all 7D space groups, the point groups of which are isomorphous to the 3D heptagonal point groups (Table 3.10). The orientation of the symmetry elements of the 7D space groups

Table 3.10. The five 3D heptagonal point groups of order k and the twenty-two corresponding 7D heptagonal space groups with reflection conditions [36]. The notation is analogous to that of trigonal space groups. The first position in the point and space group symbols refers to generating symmetry elements oriented along the periodic direction, the second position to the symmetry elements oriented along reciprocal space basis vectors and the third position to those oriented between them. S means staggered lattice in analogy to R in the trigonal case

3D Point Group	k	7D Space Group	Reflection Conditions
$\bar{7}\dfrac{2}{m}$	28	$P\bar{7}\dfrac{2}{m}1$	No condition
		$P\bar{7}\dfrac{2}{c}1$	Odd layers along
		$P\bar{7}1\dfrac{2}{m}$	No condition
		$P\bar{7}1\dfrac{2}{c}$	Odd layers between
		$S\bar{7}\dfrac{2}{m}$	No condition
		$S\bar{7}\dfrac{2}{c}$	Odd layers between
$7m$	14	$P7m1$	No condition
		$P7c1$	Odd layers along
		$P71m$	No condition
		$P71c$	Odd layers between
		$S7m$	No condition
		$S7c$	Odd layers between
72	14	$P712$	No condition
		$P7_j12$	$0000h_j : jh_7 = 7n$
		$P721$	No condition
		$P7_j21$	$0000h_j : jh_7 = 7n$
		$S72$	No condition
$\bar{7}$	7	$P\bar{7}$	No condition
		$S\bar{7}$	No condition
7	7	$P7$	No condition
		$P7_j$	$0000h_j : jh_7 = 7n$
		$S7$	No condition

is defined by the isomorphism of the 3D and 7D point groups. The 7-fold axis defines the unique direction $[0010000]_V$ or $[0000001]_D$, which is the periodic direction. The 7D reflection and inversion operations m and $\bar{1}$ reflect and invert in both subspaces $V^{\parallel}$ and $V^{\perp}$ in an analogous manner. The 7-fold rotation has the component $2\pi/7$ in $V^{\parallel}$ and $4\pi/7$, $6\pi/7$ in the two 2D subspaces of $V^{\perp}$ (Fig. 3.15) as already described in (3.91). The same decomposition can be obtained from $\mathsf{W} \cdot \Gamma(7) \cdot W^{-1}$.

The symmetry matrices for the reflections on mirror planes with normals along and between reciprocal basis vectors, respectively, read for the examples with the normal of the mirror plane m_1 along $\mathbf{a}_1^*$ and of the mirror plane m_{15} along $\mathbf{a}_1^* - \mathbf{a}_5^*$:

$$\Gamma(m_1) = \begin{pmatrix} \bar{1} & 1 & 0 & 0 & 0 & 0 & 0 \\ 0 & 1 & 0 & 0 & 0 & 0 & 0 \\ 0 & 1 & 0 & 0 & 0 & \bar{1} & 0 \\ 0 & 1 & 0 & 0 & \bar{1} & 0 & 0 \\ 0 & 1 & 0 & \bar{1} & 0 & 0 & 0 \\ 0 & 1 & \bar{1} & 0 & 0 & 0 & 0 \\ 0 & 0 & 0 & 0 & 0 & 0 & 1 \end{pmatrix}_{D^*} , \quad \Gamma(m_{15}) = \begin{pmatrix} 0 & 0 & 0 & 0 & 1 & \bar{1} & 0 \\ 0 & 0 & 0 & 1 & 0 & \bar{1} & 0 \\ 0 & 0 & 1 & 0 & 0 & \bar{1} & 0 \\ 0 & 1 & 0 & 0 & 0 & \bar{1} & 0 \\ 1 & 0 & 0 & 0 & 0 & \bar{1} & 0 \\ 0 & 0 & 0 & 0 & 0 & \bar{1} & 0 \\ 0 & 0 & 0 & 0 & 0 & 0 & 1 \end{pmatrix}_{D^*} \quad (3.99)$$

The five possible 3D point groups and twenty-two 7D space groups of heptagonal quasiperiodic structures are listed in Table 3.10. The translation components of the 7-fold screw axes and the c-glide planes are along the periodic direction. The capital letter S marks staggered lattice types in analogy to the rhombohedral Bravais lattice in the trigonal case.

The scaling symmetry leaving the reciprocal space lattice invariant (Fig. 3.16) is represented by the matrix S^*
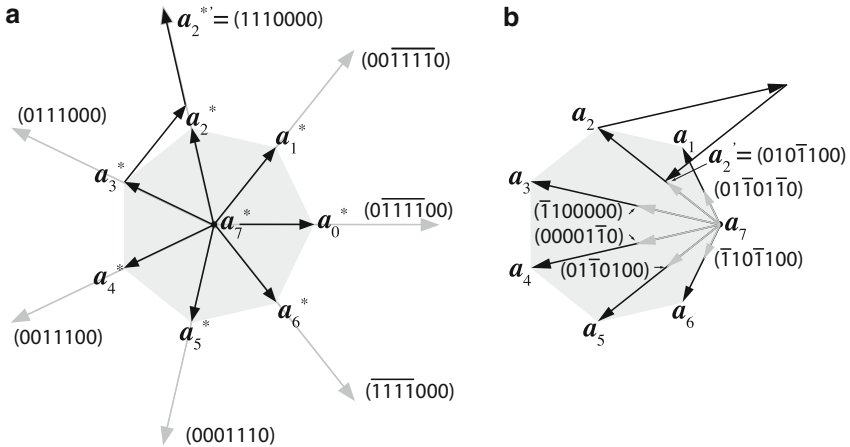
Fig. 3.16. Reciprocal (**a**) and direct (**b**) space scaling by the matrices S^* and S, respectively. The scaled basis vectors (marked *gray*) keep their orientation and are scaled by a factor $1 + 2\cos 2\pi/7 = 2.24698$ in (**a**) or by $-2\cos 4\pi/7 = 0.44504$. The examples shown explicitly are $\mathbf{a}_2^{*\prime} = \mathbf{a}_3^* + \mathbf{a}_1^* + \mathbf{a}_2^*$ with $\mathbf{a}_0^* = -\sum_{i=1}^{6} \mathbf{a}_i^*$ in (**a**) and $\mathbf{a}_2' = \mathbf{a}_2 - \mathbf{a}_4 + \mathbf{a}_5$ in (**b**)

$$\mathsf{S}^* = \begin{pmatrix} 0 & 1 & 0 & 0 & 0 & \bar{1} & 0 \\ 0 & 1 & 1 & 0 & 0 & \bar{1} & 0 \\ \bar{1} & 1 & 1 & 1 & 0 & \bar{1} & 0 \\ \bar{1} & 0 & 1 & 1 & 1 & \bar{1} & 0 \\ \bar{1} & 0 & 0 & 1 & 1 & 0 & 0 \\ \bar{1} & 0 & 0 & 0 & 1 & 0 & 0 \\ 0 & 0 & 0 & 0 & 0 & 0 & 1 \end{pmatrix}_{D^*}$$

$$= \left(\begin{array}{ccc|cc|cc} 1+2\cos\frac{2\pi}{7} & 0 & 0 & 0 & 0 & 0 & 0 \\ 0 & 1+2\cos\frac{2\pi}{7} & 0 & 0 & 0 & 0 & 0 \\ 0 & 0 & 1 & 0 & 0 & 0 & 0 \\ \hline 0 & 0 & 0 & 1+2\cos\frac{4\pi}{7} & 0 & 0 & 0 \\ 0 & 0 & 0 & 0 & 1+2\cos\frac{4\pi}{7} & 0 & 0 \\ \hline 0 & 0 & 0 & 0 & 0 & 1+2\cos\frac{8\pi}{7} & 0 \\ 0 & 0 & 0 & 0 & 0 & 0 & 1+2\cos\frac{8\pi}{7} \end{array} \right)_{V^*}$$

$$= \left(\begin{array}{c|c|c} \Gamma^{\parallel}(\mathsf{S}^*) & 0 & 0 \\ \hline 0 & \Gamma_1^{\perp}(\mathsf{S}^*) & 0 \\ \hline 0 & 0 & \Gamma_2^{\perp}(\mathsf{S}^*) \end{array} \right)_{V^*} . \tag{3.100}$$

The eigenvalues of the scaling matrix are the cubic Pisot numbers

$$\lambda_1 = 1 + 2\cos 2\pi/7 = 2.24698, \quad \lambda_2 = 1 + 2\cos 4\pi/7 = 0.55496,$$
$$\lambda_3 = 1 + 2\cos 8\pi/7 = -0.80194 \tag{3.101}$$

which are the solutions of the characteristic polynomial $1 - 3x - x^2 + 9x^3 - 4x^4 - 6x^5 + 5x^6 - x^7 = (1-x)(1-x-2x^2+x^3)^2$. The scaling symmetry matrix for the direct space basis vectors and the reflection indices, $\mathsf{S} = [(\mathsf{S}^*)^{-1}]^{\mathsf{T}}$, results to

$$\mathsf{S} = \begin{pmatrix} 0 & 0 & \bar{1} & 0 & 0 & \bar{1} & 0 \\ 1 & 1 & 1 & 0 & 1 & 1 & 0 \\ \bar{1} & 0 & 0 & 0 & \bar{1} & 0 & 0 \\ 0 & \bar{1} & 0 & 0 & 0 & \bar{1} & 0 \\ 1 & 1 & 0 & 1 & 1 & 1 & 0 \\ \bar{1} & 0 & 0 & \bar{1} & 0 & 0 & 0 \\ 0 & 0 & 0 & 0 & 0 & 0 & 1 \end{pmatrix}_D$$

$$= \left(\begin{array}{ccc|cc|cc} -2\cos\frac{4\pi}{7} & 0 & 0 & 0 & 0 & 0 & 0 \\ 0 & -2\cos\frac{4\pi}{7} & 0 & 0 & 0 & 0 & 0 \\ 0 & 0 & 1 & 0 & 0 & 0 & 0 \\ \hline 0 & 0 & 0 & -2\cos\frac{6\pi}{7} & 0 & 0 & 0 \\ 0 & 0 & 0 & 0 & -2\cos\frac{6\pi}{7} & 0 & 0 \\ \hline 0 & 0 & 0 & 0 & 0 & -2\cos\frac{2\pi}{7} & 0 \\ 0 & 0 & 0 & 0 & 0 & 0 & -2\cos\frac{2\pi}{7} \end{array} \right)_V =$$

$$= \left(\begin{array}{c|c|c} \Gamma^{\parallel}(\mathsf{S}) & 0 & 0 \\ \hline 0 & \Gamma_1^{\perp}(\mathsf{S}) & 0 \\ \hline 0 & 0 & \Gamma_2^{\perp}(\mathsf{S}) \end{array} \right)_V . \tag{3.102}$$

3.6.3 Octagonal Structures

Axial quasicrystals with octagonal diffraction symmetry possess octagonal structures. There are only a few examples known, all of them metastable. The embedding matrix can be derived from the reducible representation $\Gamma(\alpha)$ of the 8-fold rotation, $\alpha = 8$, which can be written as 5×5 matrix with integer coefficients acting on the reciprocal space vectors $\mathbf{H}$. The 5D representation The 5D representation is reducible to a par- and a perp-space component. It can be composed from the irreducible representations Γ_5, Γ_1, and Γ_7 shown in the character table (Table 3.11) under the condition that the trace of the 5D matrix does not change.

The 8-fold rotation α can be described in its action by the reducible matrix with trace 1. If we consider the 8-fold rotation taking place in 5D space (D-basis) then we can also represent it on a Cartesian basis (V-basis). By this transformation the trace must not change. Since the characters correspond to the traces of the respective symmetry matrices we can identify the characters $\Gamma_5(\alpha) = \sqrt{2}$ and $\Gamma_7(\alpha) = -\sqrt{2}$ as traces of the symmetry matrices

$$
\begin{aligned}
\begin{pmatrix} \cos \frac{2\pi}{8} & -\sin \frac{2\pi}{8} \\ \sin \frac{2\pi}{8} & \cos \frac{2\pi}{8} \end{pmatrix}_V &= \tfrac{1}{2} \begin{pmatrix} \sqrt{2} & -\sqrt{2} \\ \sqrt{2} & \sqrt{2} \end{pmatrix}_V, \\
\begin{pmatrix} \cos \frac{6\pi}{8} & -\sin \frac{6\pi}{8} \\ \sin \frac{6\pi}{8} & \cos \frac{6\pi}{8} \end{pmatrix}_V &= -\tfrac{1}{2} \begin{pmatrix} \sqrt{2} & -\sqrt{2} \\ \sqrt{2} & \sqrt{2} \end{pmatrix}_V.
\end{aligned}
\tag{3.103}
$$

Consequently, in 5D space the then irreducible integer representation of $\Gamma(\alpha)$ (3.104) can be composed of the two 2D representations $\Gamma_5(\alpha)$ and $\Gamma_7(\alpha)$ plus $\Gamma_1(\alpha)$, for the periodic direction.

Table 3.11. Character table of the octagonal group $8mm$ (C_{8v}). ε denotes the identity operation, α^n the rotation around $2n\pi/8$, and β the reflection on a mirror plane

Elements	ε	α	α^2	α^3	α^4	β
Γ_1	1	1	1	1	1	1
Γ_2	1	1	1	1	1	-1
Γ_3	1	-1	1	-1	1	1
Γ_4	1	-1	1	-1	1	-1
Γ_5	2	$\sqrt{2}$	0	$-\sqrt{2}$	-2	0
Γ_6	2	0	$\bar{2}$	0	2	0
Γ_7	2	$-\sqrt{2}$	0	$\sqrt{2}$	-2	0

$$
\Gamma(8) = \begin{pmatrix} 0\,0\,0\,\bar{1}\,0 \\ 1\,0\,0\,0\,0 \\ 0\,1\,0\,0\,0 \\ 0\,0\,1\,0\,0 \\ 0\,0\,0\,0\,1 \end{pmatrix}_D = \left(\begin{array}{ccc|cc} \frac{1}{\sqrt{2}} & -\frac{1}{\sqrt{2}} & 0 & 0 & 0 \\ \frac{1}{\sqrt{2}} & \frac{1}{\sqrt{2}} & 0 & 0 & 0 \\ 0 & 0 & 1 & 0 & 0 \\ 0 & 0 & 0 & -\frac{1}{\sqrt{2}} & -\frac{1}{\sqrt{2}} \\ 0 & 0 & 0 & \frac{1}{\sqrt{2}} & -\frac{1}{\sqrt{2}} \end{array} \right)_V = \left(\begin{array}{c|c|c} \Gamma_5(8) & 0 & 0 \\ \hline 0 & \Gamma_2(8) & 0 \\ \hline 0 & 0 & \Gamma_7(8) \end{array} \right)_V
$$

$$(3.104)$$

3.6.3.1 Reciprocal Space

The electron density distribution function $\rho(\mathbf{r})$ of a 3D quasicrystal can be represented by the Fourier series given in (3.41). All Fourier coefficients, i.e., the structure factors $F(\mathbf{H})$, can be integer indexed based on five reciprocal basis vectors: $\mathbf{H} = \sum_{i=1}^{4} h_i \mathbf{a}_i^*$ with $\mathbf{a}_i^* = a^* \left(\cos 2\pi i/8, \sin 2\pi i/8, 0 \right)$, $i = 1, \dots, 4$, $a^* = |\mathbf{a}_1^*| = |\mathbf{a}_2^*| = |\mathbf{a}_3^*| = |\mathbf{a}_4^*|$, $\mathbf{a}_5^* = |\mathbf{a}_5^*| \, (0, 0, 1)$, and $h_i \in \mathbb{Z}$ (Fig. 3.17).

The vector components refer to a Cartesian coordinate system in par-space $V^{\parallel}$. The set of all diffraction vectors $\mathbf{H}$ forms a $\mathbb{Z}$-module M^* of rank five. The vectors $\mathbf{a}_i^*$, $i = 1, \dots, 5$ can be considered as par-space projections of the basis vectors $\mathbf{d}_i^*$, $i = 1, \dots, 5$ of the 5D reciprocal lattice Σ^* with

$$
\mathbf{d}_i^* = a^* \begin{pmatrix} \cos \frac{2\pi i}{8} \\ \sin \frac{2\pi i}{8} \\ 0 \\ c \cos \frac{6\pi i}{8} \\ c \sin \frac{6\pi i}{8} \end{pmatrix}_V , \quad i = 1, \dots, 4; \quad \mathbf{d}_5^* = a_5^* \begin{pmatrix} 0 \\ 0 \\ 1 \\ 0 \\ 0 \end{pmatrix}_V . \tag{3.105}
$$

The coupling factor between par- and perp-space rotations equals 3, c is an arbitrary constant which is usually set to 1 (as it is also done in the following). The subscript V denotes components referring to a 5D Cartesian coordinate
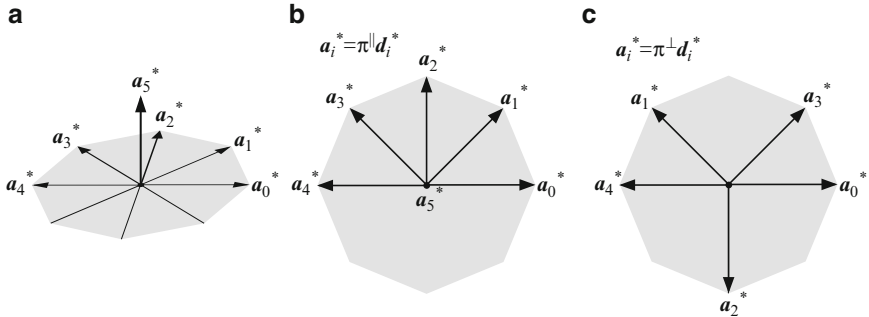
Fig. 3.17. 5D reciprocal space basis $\mathbf{d}_i^*$, $i = 1, \dots, 5$ projected onto the (**a**, **b**) par- and (**c**) perp-space. The basis vectors spanning the hyperlattice in direct space have the same orientation

system (V-basis), while subscript D refers to the 5D crystallographic basis (D-basis). The embedding matrix W (3.4) results to

$$\mathsf{W} = \begin{pmatrix} \cos\frac{2\pi}{8} & \cos\frac{4\pi}{8} & \cos\frac{6\pi}{8} & \cos\frac{8\pi}{8} & 0 \\ \sin\frac{2\pi}{8} & \sin\frac{4\pi}{8} & \sin\frac{6\pi}{8} & \sin\frac{8\pi}{8} & 0 \\ 0 & 0 & 0 & 0 & 1 \\ \cos\frac{6\pi}{8} & \cos\frac{2\pi}{8} & \cos\frac{8\pi}{8} & \cos\frac{4\pi}{8} & 0 \\ \sin\frac{6\pi}{8} & \sin\frac{2\pi}{8} & \sin\frac{8\pi}{8} & \sin\frac{4\pi}{8} & 0 \end{pmatrix} = \begin{pmatrix} \frac{1}{\sqrt{2}} & 0 & -\frac{1}{\sqrt{2}} & \bar{1} & 0 \\ \frac{1}{\sqrt{2}} & 1 & \frac{1}{\sqrt{2}} & 0 & 0 \\ 0 & 0 & 0 & 0 & 1 \\ -\frac{1}{\sqrt{2}} & 0 & \frac{1}{\sqrt{2}} & \bar{1} & 0 \\ \frac{1}{\sqrt{2}} & \bar{1} & \frac{1}{\sqrt{2}} & 0 & 0 \end{pmatrix}. \qquad (3.106)$$

The direct 5D basis is obtained from the orthogonality condition (3.5) as column vectors of $(\mathsf{W}^{-1})^T$

$$\mathbf{d}_i = \frac{1}{2a_i^*}\begin{pmatrix} \cos\frac{2\pi i}{8} \\ \sin\frac{2\pi i}{8} \\ 0 \\ \cos\frac{6\pi i}{8} \\ \sin\frac{6\pi i}{8} \end{pmatrix}_V, \quad i=1,\ldots,4; \quad \mathbf{d}_5 = \frac{1}{a_5^*}\begin{pmatrix} 0 \\ 0 \\ 1 \\ 0 \\ 0 \end{pmatrix}_V. \qquad (3.107)$$

The metric tensors G and G^* are of type

$$\begin{pmatrix} A & 0 & 0 & 0 & 0 \\ 0 & A & 0 & 0 & 0 \\ 0 & 0 & A & 0 & 0 \\ 0 & 0 & 0 & A & 0 \\ 0 & 0 & 0 & 0 & B \end{pmatrix} \qquad (3.108)$$

with $A = 2a_1^{*2}$, $B = a_5^{*2}$, for reciprocal space and $A = 1/2a^{*2}$, $B = 1/a_5^{*2}$ for direct space. Therefrom, the direct and reciprocal lattice parameters can be derived as

$$d_i^* = \sqrt{2}a_1^*, \quad d_5^* = a_5^*, \quad \alpha_{ij} = 90°, \quad i,j = 1,\ldots,5 \qquad (3.109)$$

and

$$d_i = \frac{1}{\sqrt{2}a^*}, \ i,j = 1,\ldots,4, \quad d_5 = \frac{1}{a_5^*}, \quad \alpha_{ij} = 90°, \quad \alpha_{i5} = 90°, \ i,j = 1,\ldots,4. \qquad (3.110)$$

This means that the unit cell has hypertetragonal symmetry and the 4D subspace orthogonal to the periodic direction is hypercubic. The volume of the 5D unit cell results to

$$V = \sqrt{\det(\mathsf{G})} = \frac{1}{4a^{*4}a_5^*} = d^4 d_5. \qquad (3.111)$$

3.6.3.2 Symmetry

The diffraction symmetry of octagonal phases, i.e., the point symmetry group leaving the intensity weighted Fourier module (diffraction pattern) M_I^* invariant, is one of the two Laue groups $8/mmm$ or $8/m$. The 62 space groups [36]

leaving the 5D hypercrystal structure invariant are that subset of the 5D space groups, the point groups of which are isomorphous to the seven 3D octagonal point groups (Table 3.12). The orientation of the symmetry elements of the 5D space groups is fixed by the isomorphism of the 3D and 5D point groups. The 8-fold axis defines the unique direction $[00100]_V$ or $[00001]_D$, which is the periodic direction. There are two different orientations of mirror planes and 2-fold axes possible with respect to the phys-space star of reciprocal basis vectors. If the normal to the mirror plane, or the 2-fold axis, is oriented along a reciprocal basis vector it gets the symbol m, or d, and it is denoted "along", otherwise it is "between" and the symbols get primed, m' and d'. Examples for the action of these two types of mirror planes are shown in eqs. 3.112 and 3.113. The normal to the mirror plane m_2 is along to $\mathbf{a}_2^*$, that of m_{12} is between $\mathbf{a}_1^*$ and $\mathbf{a}_2^*$.

The reflection and inversion operations are equivalent in both subspaces $V^\parallel$ and $V^\perp$. $\Gamma(8)$, a $2\pi/8$ rotation in $V^\parallel$ around the 8-fold axis corresponds to a $6\pi/8$ rotation in $V^\perp$ (Fig. 3.17):

$$\Gamma(m_2) = \begin{pmatrix} 0 & 0 & \bar{1} & 0 & 0 \\ 0 & \bar{1} & 0 & 0 & 0 \\ \bar{1} & 0 & 0 & 0 & 0 \\ 0 & 0 & 0 & 1 & 0 \\ 0 & 0 & 0 & 0 & 1 \end{pmatrix}_D = \left(\begin{array}{ccc|cc} 1 & 0 & 0 & 0 & 0 \\ 0 & \bar{1} & 0 & 0 & 0 \\ 0 & 0 & 1 & 0 & 0 \\ \hline 0 & 0 & 0 & 1 & 0 \\ 0 & 0 & 0 & 0 & \bar{1} \end{array}\right)_V \tag{3.112}$$

$$\Gamma(m_{12}) = \begin{pmatrix} 0 & \bar{1} & 0 & 0 & 0 \\ \bar{1} & 0 & 0 & 0 & 0 \\ 0 & 0 & 0 & 1 & 0 \\ 0 & 0 & 1 & 0 & 0 \\ 0 & 0 & 0 & 0 & 1 \end{pmatrix}_D = \left(\begin{array}{ccc|cc} \frac{1}{\sqrt{2}} & -\frac{1}{\sqrt{2}} & 0 & 0 & 0 \\ -\frac{1}{\sqrt{2}} & -\frac{1}{\sqrt{2}} & 0 & 0 & 0 \\ 0 & 0 & 1 & 0 & 0 \\ \hline 0 & 0 & 0 & -\frac{1}{\sqrt{2}} & -\frac{1}{\sqrt{2}} \\ 0 & 0 & 0 & -\frac{1}{\sqrt{2}} & \frac{1}{\sqrt{2}} \end{array}\right)_V \tag{3.113}$$

$$\Gamma(\bar{1}) = \left(\begin{array}{ccc|cc} \bar{1} & 0 & 0 & 0 & 0 \\ 0 & \bar{1} & 0 & 0 & 0 \\ 0 & 0 & \bar{1} & 0 & 0 \\ \hline 0 & 0 & 0 & \bar{1} & 0 \\ 0 & 0 & 0 & 0 & \bar{1} \end{array}\right)_V \quad . \tag{3.114}$$

The translation components of the 8-fold screw axis and the c-glide planes are along the periodic direction.

The set of reciprocal space vectors M^* is invariant under scaling with the matrix S^*, $\mathsf{S}^{*m}M^* = s^{*m}M^*$, with $s^* = 1 \pm \sqrt{2}$ (Fig. 3.18). This scaling matrix also applies to the direct space coordinates. It reads

$$\mathsf{S}^* = \begin{pmatrix} 1 & 1 & 0 & \bar{1} & 0 \\ 1 & 1 & 1 & 0 & 0 \\ 0 & 1 & 1 & 1 & 0 \\ \bar{1} & 0 & 1 & 1 & 0 \\ 0 & 0 & 0 & 0 & 1 \end{pmatrix}_{D^*} = \left(\begin{array}{ccc|cc} 1+\sqrt{2} & 0 & 0 & 0 & 0 \\ 0 & 1+\sqrt{2} & 0 & 0 & 0 \\ 0 & 0 & 1 & 0 & 0 \\ \hline 0 & 0 & 0 & 1-\sqrt{2} & 0 \\ 0 & 0 & 0 & 0 & 1-\sqrt{2} \end{array}\right)_{V^*} \quad . \tag{3.115}$$

Table 3.12. The seven 3D octagonal point groups of order k and the sixty-two corresponding 5D octagonal space groups with extinction conditions [36]. The notation is analogous to that of tetragonal space groups. The first position in the point and space group symbols refers to generating symmetry elements oriented along the periodic direction, the second and third position to the symmetry elements oriented along and between reciprocal space basis vectors, respectively

3D Point Group	k	5D Space Group	Reflection Conditions
$\dfrac{8}{m}\dfrac{2}{m}\dfrac{2}{m}$	32	$P\dfrac{8}{m}\dfrac{2}{m}\dfrac{2}{m}$	No condition
		$P\dfrac{8}{m}\dfrac{2_1}{b}\dfrac{2}{m}$	All layers, odd parity, along
		$P\dfrac{8}{m}\dfrac{2}{c}\dfrac{2}{c}$	Odd layers, along and between
		$P\dfrac{8}{m}\dfrac{2_1}{n}\dfrac{2}{c}$	Odd layers, even parity, along; Even layers, odd parity, along; Odd layers, between
		$P\dfrac{8}{m}\dfrac{2_1}{m}\dfrac{2}{m}$	Zero layer, odd parity
		$P\dfrac{8}{m}\dfrac{2}{b}\dfrac{2}{m}$	All layers, odd parity, along; Zero layer, odd parity
		$P\dfrac{8}{m}\dfrac{2_1}{c}\dfrac{2}{c}$	Odd layers, along and between; Zero layer, odd parity
		$P\dfrac{8}{m}\dfrac{2}{n}\dfrac{2}{c}$	Odd layers, even parity, along; Even layers, odd parity, along; Odd layers, between; Zero layer, odd parity
		$P\dfrac{8_4}{m}\dfrac{2}{m}\dfrac{2}{c}$	Odd layers between
		$P\dfrac{8_4}{m}\dfrac{2_1}{b}\dfrac{2}{c}$	Odd layers between; All layers, odd parity, along
		$P\dfrac{8_4}{m}\dfrac{2}{c}\dfrac{2}{m}$	Odd layers along
		$P\dfrac{8_4}{m}\dfrac{2_1}{n}\dfrac{2}{m}$	Odd layers, even parity, along; Even layers, odd parity, along
		$P\dfrac{8_4}{m}\dfrac{2_1}{m}\dfrac{2}{c}$	Odd layers, between; Zero layer, odd parity
		$P\dfrac{8_4}{n}\dfrac{2}{b}\dfrac{2}{c}$	Odd layers, between; All layers, odd parity, along; Zero layer, odd parity
		$P\dfrac{8_4}{n}\dfrac{2_1}{c}\dfrac{2}{m}$	Odd layers, along; Zero layer, odd parity
		$P\dfrac{8_4}{n}\dfrac{2}{n}\dfrac{2}{m}$	Odd layers, even parity along; Even layers, odd parity, along; Zero layer, odd parity
		$S\dfrac{8}{m}\dfrac{2}{m}\dfrac{2}{m}$	No extinctions

Table 3.12. (continued)

3D Point Group	k	5D Space Group	Reflection Conditions
		$S\dfrac{8}{m}\dfrac{2}{m}\dfrac{2}{c}$	Odd layers, between
		$S\dfrac{8_4}{m}\dfrac{2}{d}\dfrac{2}{m}$	2 mod 4 layers, even parity, along 0 mod 4 layers, odd parity, along Zero layer, odd parity
		$S\dfrac{8_4}{m}\dfrac{2}{d}\dfrac{2}{c}$	2 mod 4 layers, even parity, along 0 mod 4 layers, odd parity, along Odd layers, between Zero layer, odd parity
$\dfrac{8}{m}$	16	$P\dfrac{8}{m}$	No extinctions
		$P\dfrac{8}{n}$	Zero layer, odd parity
$\dfrac{8}{m}$	16	$P\dfrac{8_4}{m}$	kz when k odd
		$P\dfrac{8_4}{n}$	Zero layer, odd parity kz when k odd
		$S\dfrac{8}{m}$	No extinctions
		$S\dfrac{8_2}{n}$	Zero layer, odd parity $2kz$ when k odd
$8\,2\,2$	16	$P\,8\,2\,2$ $P\,8\,2_1\,2$ $P\,8_j\,2\,2$	No extinctions Zero layer, odd parity, along kz when jk not a multiple of 8
		$P\,8_j\,2_1\,2$	Zero layer, odd parity, along kz when jk not a multiple of 8
		$S\,8\,2\,2$ $S\,8_j\,2\,2$	No extinctions $2kz$ when $2jk$ not a multiple of 8
$8\,mm$	16	$P\,8\,mm$ $P\,8\,bm$ $P\,8\,cc$	No extinctions All layers, odd parity, along Odd layers, along and between
		$P\,8\,nc$	Odd layers, even parity, along Even layers, odd parity, along Odd layers, between
		$P\,8_4\,mc$	Odd layers between
		$P\,8_4\,bc$	Odd layers between All layers, odd parity, along
		$P\,8_4\,cm$	Odd layers along
		$P\,8_4\,nm$	Odd layers, even parity, along Even layers, odd parity, along
		$S\,8\,mm$	No extinctions

Table 3.12. (continued)

3D Point Group	k	5D Space Group	Reflection Conditions
		$S\,8\,mc$	Odd layers between
		$S\,8_2\,dm$	2 mod 4 layers, even parity, along 0 mod 4 layers, odd parity, along
		$S\,8_2\,dc$	2 mod 4 layers, even parity, along 0 mod 4 layers, odd parity, along Odd layers, between
$\bar{8}\,m\,2$	16	$P\,\bar{8}\,m\,2$	No extinctions
		$P\,\bar{8}\,b\,2$	All layers, odd parity, along
		$P\,\bar{8}\,c\,2$	Odd layers along
		$P\,\bar{8}\,n\,2$	Even layers, odd parity, along Odd layers, even parity, along
		$P\,\bar{8}\,2\,m$	No extinctions
		$P\,\bar{8}\,2_1\,m$	Zero layer, odd parity, along
		$P\,\bar{8}\,2\,c$	Odd layers between
		$P\,\bar{8}\,2_1\,c$	Odd layers between Zero layer, odd parity, along
		$S\,\bar{8}\,m\,2$	No extinctions
		$S\,\bar{8}\,d\,2$	2 mod 4 layers, even parity, along 0 mod 4 layers, odd parity, along
		$S\,\bar{8}\,2\,m$	No extinctions
		$S\,\bar{8}\,2\,c$	Odd layers between
$\bar{8}$	8	$P\,\bar{8}$	No extinctions
		$S\,\bar{8}$	No extinctions
8	8	$P\,8$	No extinctions
		$P\,8_j$	kz when jk not a multiple of 8
		$S\,8$	No extinctions
		$S\,8_j$	$2kz$ when $2jk$ not a multiple of 8

The scaling symmetry matrix for the direct space basis vectors and the reflection indices $\mathsf{S} = [(\mathsf{S}^*)^{-1}]^{\mathsf{T}}$ results to

$$
\mathsf{S} = \begin{pmatrix} \bar{1}\ 1\ 0\ \bar{1}\ 0 \\ 1\ \bar{1}\ 1\ 0\ 0 \\ 0\ 1\ \bar{1}\ 1\ 0 \\ \bar{1}\ 0\ 1\ \bar{1}\ 0 \\ 0\ 0\ 0\ 0\ 1 \end{pmatrix}_{D^*} = \left(\begin{array}{ccc|cc} -1+\sqrt{2} & 0 & 0 & 0 & 0 \\ 0 & -1+\sqrt{2} & 0 & 0 & 0 \\ 0 & 0 & 1 & 0 & 0 \\ \hline 0 & 0 & 0 & -1-\sqrt{2} & 0 \\ 0 & 0 & 0 & 0 & -1-\sqrt{2} \end{array}\right)_V .
$$

$$(3.116)$$
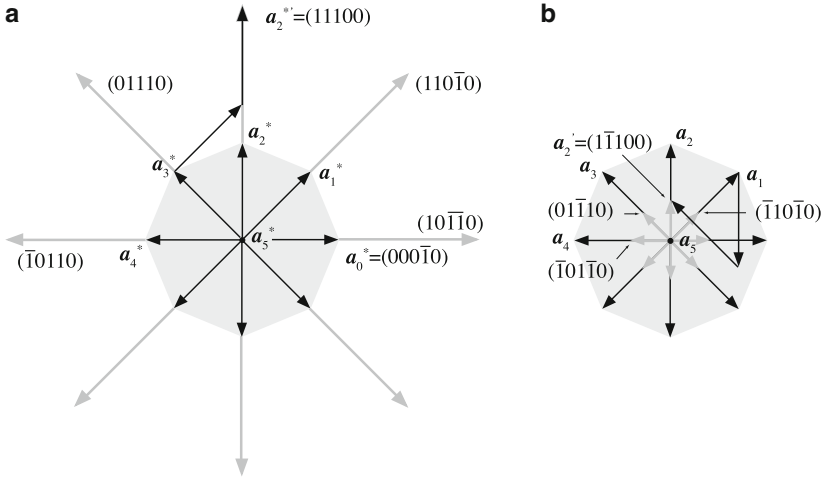
Fig. 3.18. Reciprocal (**a**) and direct (**b**) space scaling by the matrices S^* and S. The scaled basis (marked gray) vectors keep their orientation and are scaled by a factor $1 + 2\cos 2\pi/8 = 1 + \sqrt{2} = 2.4142$ in reciprocal space (**a**) and by a factor $-1 + 2\cos 2\pi/8 = -1 + \sqrt{2} = 0.4142$ in direct space (**b**). The examples shown explicitly are $\mathbf{a}_2^{*\prime} = \mathbf{a}_3^* + \mathbf{a}_1^* + \mathbf{a}_2^*$ in (**a**) and $\mathbf{a}_2' = \mathbf{a}_1 - \mathbf{a}_2 + \mathbf{a}_3$ in (**b**)

3.6.3.3 Example: Octagonal Quasicrystal

A characteristic section through the 5D unit cell of an octagonal structure, with a single octagonal atomic surface in the origin, together with its projections onto par- and perp-space is shown in Fig. 3.19. The closeness condition between the atomic surfaces is fulfilled along the [1 1 0 0 0] direction and its permutations. The relationship between the different types of vertices of the octagonal tiling and the partitioning of the atomic surface is shown below (Fig. 3.20).

3.6.3.4 Periodic Average Structure

In the following, different PAS are discussed on the example of a 2D octagonal tiling, omitting the third dimension for clarity. The embedding space is 4D and consists of the two 2D orthogonal subspaces $V^{\parallel}$ and $V^{\perp}$. The atomic surfaces are of regular octagonal shape and occupy the nodes of the 4D hypercubic lattice.

The 4D basis $\mathbf{d}_i$ for the octagonal tiling is hypercubic and defined by

$$\mathbf{d}_i = \frac{1}{2a_i^*}\begin{pmatrix} \cos\frac{2\pi i}{8} \\ \sin\frac{2\pi i}{8} \\ \cos\frac{6\pi i}{8} \\ \sin\frac{6\pi i}{8} \end{pmatrix}_V , \quad i = 1,\ldots,4 , \tag{3.117}$$
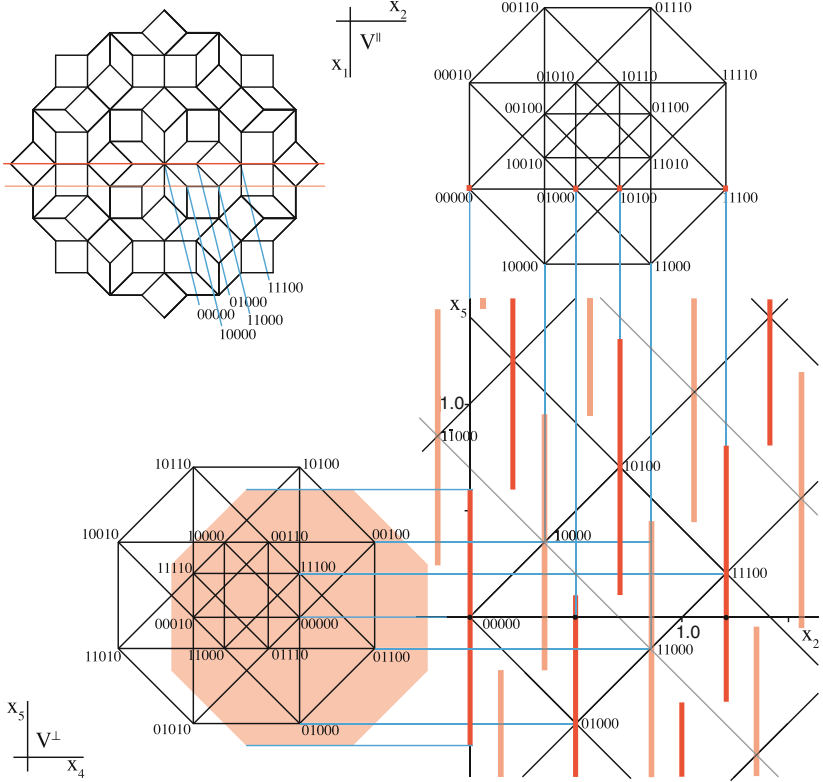
Fig. 3.19. Characteristic $(0x_200x_5)$ section through the 5D unit cell (*lower right*) together with its projections onto par- (*lower left*) and perp-space (*upper right*). The 16 corners of the unit cell are indexed on the D-basis. The atomic surface is just the projected 4D subunit cell (gray, online: pink shaded octagon) in cases of a canonical tiling. The light-gray atomic surfaces belong to the section $(\sqrt{2}\,x_2\,0 - \sqrt{2}\,x_5)$. The vertices generated along x_2 are marked on the octagonal tiling (*upper left*)

with par-space spanned by the vectors $\{(1,0,0,0),\ (0,1,0,0)\}_V$. The length of the 2D reciprocal basis vectors a^* is related to the unit tile's edge length a_r by $a^* = 1/2a_r$. The reciprocal basis can be obtained by the condition $\mathbf{d}_i \cdot \mathbf{d}_j^* = \delta_{ij}$. The atomic surface is defined by the perp-space vectors

$$\mathbf{a}_i^{AS} = a_r\sqrt{1 + \frac{1}{\sqrt{2}}}\begin{pmatrix} 0 \\ 0 \\ \cos\frac{(2i-1)\pi}{8} \\ \sin\frac{(2i-1)\pi}{8} \end{pmatrix}_V, \quad i = 1,\ldots,8 . \tag{3.118}$$

The octagonal tiling generated in this way is depicted in Fig. 3.20, with vertices colored according to their coordination. At the bottom of Fig. 3.20 the atomic surface is shown of the tiling embedded in 4D space. The partition of
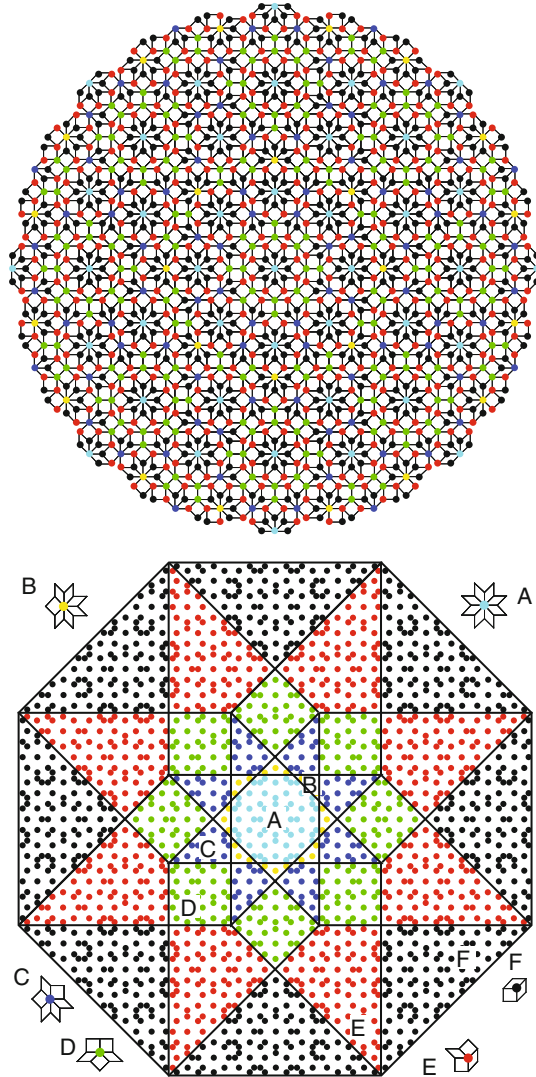
Fig. 3.20. Octagonal tiling with the six different vertex types, A–F, which are color coded. Below the tiling, the partitioning of the atomic surface is shown together with the six vertex configurations. The colored filled circles on the atomic surface correspond to the lifted vertices of the tiling

the atomic surface is made visible by keeping the color code of the tiling. The tiling shown corresponds to that described by [39].

As discussed in Sect. 3.3, the reciprocal lattice of a PAS of a 2D quasiperiodic tiling is best defined by the origin and two strong reflections (cut plane). In direct space, this corresponds to a projection of the hyperstructure onto

par-space, along the directions perpendicular to the cut plane in reciprocal space. The lattice parameters of the PAS are given by the selected reflections. The PAS can be easily obtained sticking to par-space by taking the quasiperiodic tiling modulo the unit cell of the PAS.

Figure 3.21 shows the structure factors as a function of $|\mathbf{H}^{\perp}|$, and of the intensities as a function of $\mathbf{H}^{\parallel}$. The reflections chosen for the derivation of the different PAS shown in Figs. 3.22 and 3.23 are indexed in 3.21. Letters
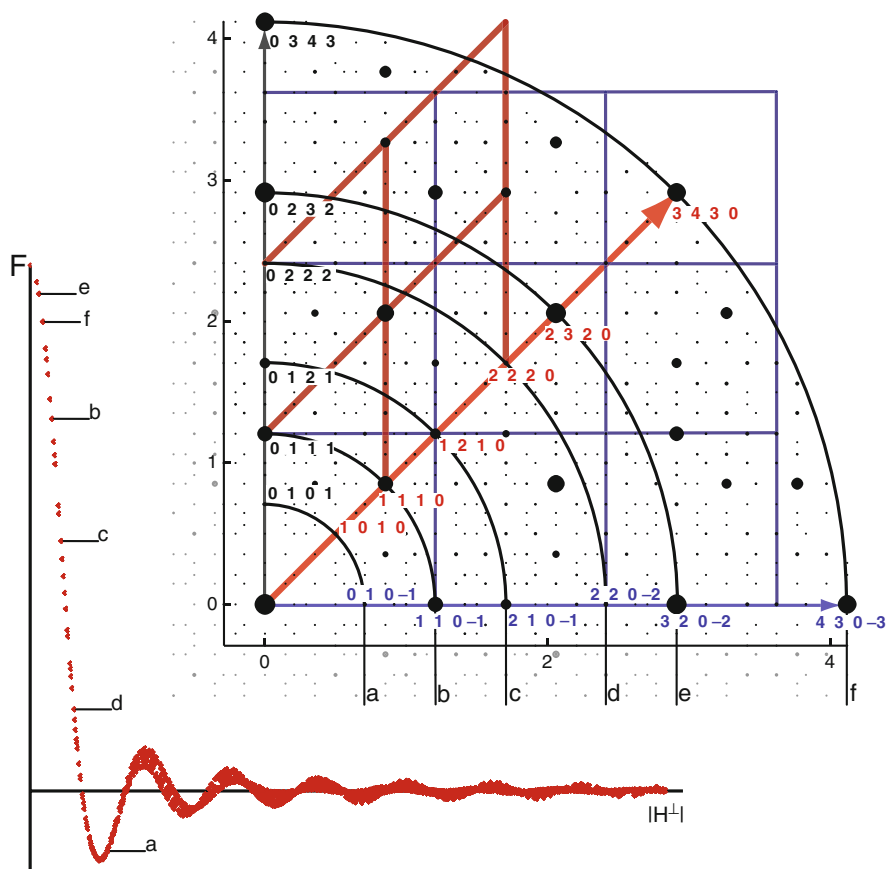
Fig. 3.21. Structure factors $F(|\mathbf{H}^{\perp}|)$ of the octagonal tiling as a function of $|\mathbf{H}^{\perp}|$ (*lower left part*) and diffraction pattern in par-space (*upper right part*). The absolute value of $F(|\mathbf{H}^{\perp}|)$ decreases with increasing $|\mathbf{H}^{\perp}|$ and oscillates around zero. There is only one branch as expected for a atomic surface positioned on the origin of the hypercrystal structure. On the diffraction pattern, the reflections of the PAS shown are denoted. Symmetrically equivalent Bragg reflections are marked by letters a–f. For reflections of type b, the linear combinations of two chosen reflections are marked on grids (online: red and blue). Reflections on these grids lie on the corresponding cut-planes in nD reciprocal space
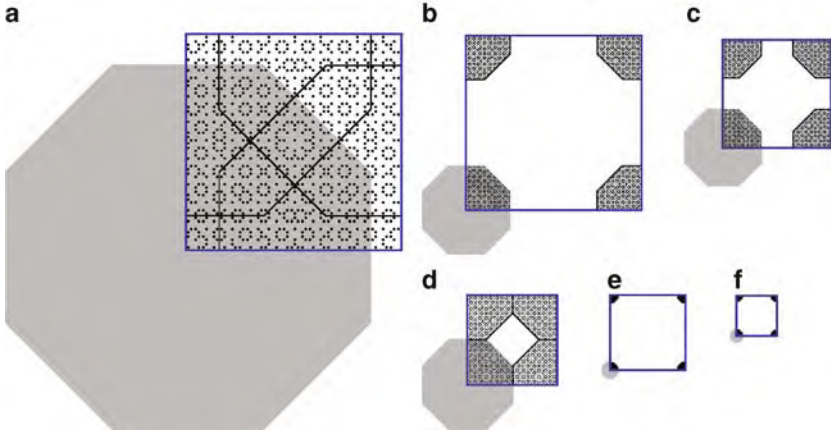
Fig. 3.22. Vertices of the octagonal tiling modulo one unit cell of the different PAS denoted with black and (online: blue) indices (i.e., along the horizontal and vertical directions) in Fig. 3.21, lying on circles a–f (indicated in the *upper right* corner of each unit cell). The projected atomic surfaces are shown as well as the vertices of the tiling that have been projected into the unit cell by the modulo operation. For each PAS, the lattice parameter/occupancy factor is a, 1.4142/2.4142; b, 0.8284/0.8284; c, 0.5858/0.4142; d, 0.4142/0.2071; e, 0.3431/0.1421; f, 0.2426/0.0711
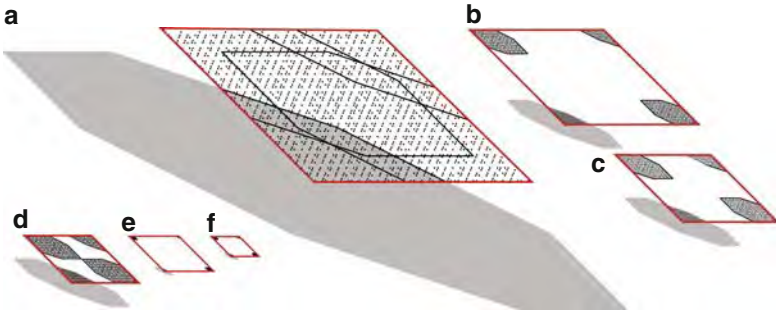
Fig. 3.23. Vertices of the octagonal tiling, modulo one unit cell of the PAS denoted with black and gray (online: *red*) indices (i.e., along the diagonal and vertical directions) in Fig. 3.21, lying on circles a–f (indicated in the *upper right* corner of each unit cell). The projected atomic surfaces are shown as well as the vertices of the tiling that have been projected into the unit cell by the modulo operation. For each PAS, the lattice parameter/occupancy factor is a, 2/3.4142; b, 1.1716/1.1716; c, 0.8284/0.5858; d, 0.5850/0.2929; e, 0.4853/0.2010; f, 0.3431/0.1005

a–f denote symmetrically equivalent reflections on a circle with a given radius $|\mathbf{H}^{\parallel}|$ in par-space. They all have the same intensity and $|\mathbf{H}^{\perp}|$. There are two non-equivalent ways of choosing the pairs of reflections. One leads to a rhombic unit cell of the PAS, the other to a quadratic one. The reflection indices defining each PAS are given in Fig. 3.21.

The reflections are denoted by two letters, the first one corresponds to one of the circles a–f, the second to the unit cell, with r for rhombic (online: red) and s for square (online:blue). For one case (br/bs) a (online: red/blue) reciprocal lattice is drawn in the figure. All the PAS that are denoted in Fig. 3.21, are shown in Figs. 3.22 and 3.23.

While a PAS is unambiguously defined by the cut-space that is spanned by the two chosen reflections in higher dimensions, this is not the case for a PAS that is generated remaining in par-space only. Here, each choice of two reflections which all lie in the same cut-space, will result in a PAS with the same size and shape of projected atomic surfaces, but different edge lengths and occupancy factors.

The fact, that PAS exist with exactly the same maximal deviation of the tiling vertices from the lattice nodes of the PAS (size of the projected atomic surfaces) but different corresponding occupancy factors demonstrates how important it is to select the most reasonable PAS to a given tiling. In general, a quasiperiodic tiling has infinitely many possible PAS [3]. The best PAS will have lattice parameters comparable to the edge length of the unit tiles and occupancy factors close to one. The best PAS for our octagonal tiling is defined by the strong reflections br/bq, consequently. The relationship between the PAS and the tilings is illustrated in Figs. 3.24 and 3.25 for these cases.
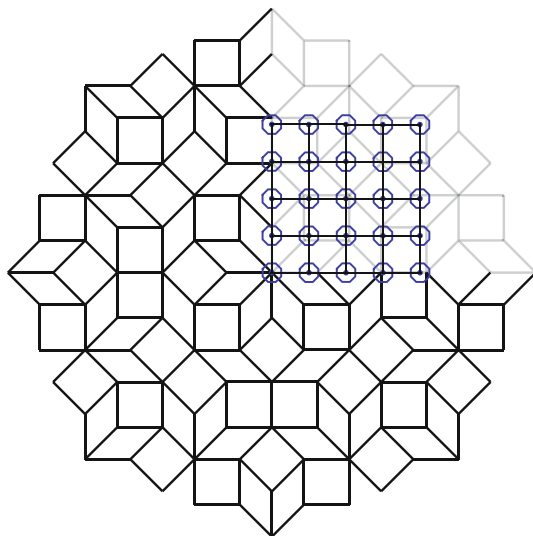
Fig. 3.24. Octagonal tiling with overlaid PAS of type bq, defined by the reflections 0111 and $110\bar{1}$ (Fig. 3.21). The small (online: blue) octagons on the square grid correspond to projected atomic surfaces. Every vertex of the octagonal tiling lies within such an octagon, but 17% of the octagons are not occupied. The PAS lattice parameter amounts to $2/(\sqrt{2}+1)*a_r$, with a_r the edge length of the octagonal tiling
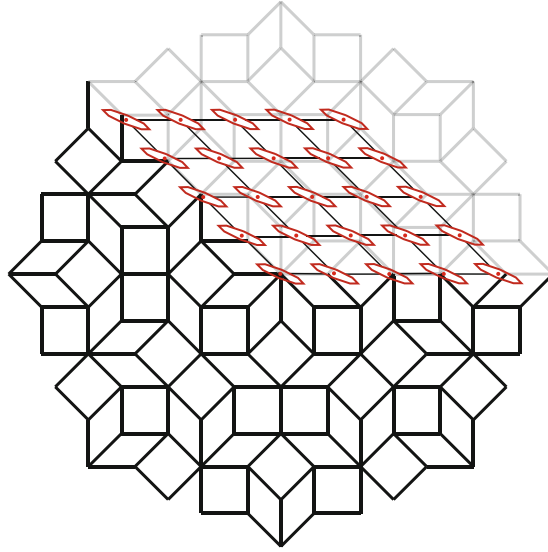
Fig. 3.25. Octagonal tiling, with overlaid PAS of type br, defined by the reflections 0111 and 1110 (Fig. 3.21). The small (online: red) octagons positioned on each lattice node of the periodic grid, correspond to projected atomic surfaces. Every vertex of the octagonal tiling lies within such an octagon. The occupancy factor of this PAS amounts to 1.1716

3.6.4 Decagonal Structures

Quasicrystals that exhibit decagonal diffraction symmetry are called decagonal phases. Many stable and metastable representatives of this class of quasicrystals have been observed experimentally ([44] and references therein). The Penrose tiling will be used as an example for the 2D quasiperiodic atomic layers in a decagonal structure. The embedding matrix can be derived from the reducible representation $\Gamma(\alpha)$ of the 10-fold rotation, $\alpha = 10$, which can be written as 5×5 matrix with integer coefficients acting on the reciprocal space vectors $\mathbf{H}$. The 5D representation can be composed from the irreducible representations Γ_1, Γ_5, and Γ_7 shown in the character table below (Table 3.13).

The 2D representation $\Gamma_5 = \tau$ describes the component of the 5D rotation in the 2D quasiperiodic physical subspace, the 2D representation $\Gamma_7 = 1 - \tau$ the component of the rotation in perp-space, and the 1D representation $\Gamma_1 = 1$ that along the 5-fold axis. The sum of the corresponding characters $\tau + 1 - \tau + 1 = 2$ equals the trace of the reducible rotation matrix given in (3.119). Based thereon, the 10-fold rotation matrix can be block-diagonalised in the following way

Table 3.13. Character table for the decagonal group $10mm$ (C_{10v}). ε denotes the identity operation, α^n the rotation around $2n\pi/10$, and β, β' the reflection on the two different types of mirror planes

Elements	ε	α	α^2	α^3	α^4	α^5	5β	$5\beta'$
Γ_1	1	1	1	1	1	1	1	1
Γ_2	1	1	1	1	1	1	-1	-1
Γ_3	1	-1	1	-1	1	-1	1	-1
Γ_4	1	-1	1	-1	1	-1	-1	1
Γ_5	2	τ	$-1+\tau$	$1-\tau$	$-\tau$	-2	0	0
Γ_6	2	$-1+\tau$	$-\tau$	$-\tau$	$-1+\tau$	2	0	0
Γ_7	2	$1-\tau$	$-\tau$	τ	$-1+\tau$	-2	0	0
Γ_8	2	$-\tau$	$-1+\tau$	$-1+\tau$	$-\tau$	2	0	0

$$
\Gamma(10) = \begin{pmatrix} 0\,0\,0\,\bar{1}\,0 \\ 1\,0\,0\,1\,0 \\ 0\,1\,0\,\bar{1}\,0 \\ 0\,0\,1\,1\,0 \\ 0\,0\,0\,0\,1 \end{pmatrix}_{D^*}
= \left(\begin{array}{ccc|cc} \cos\frac{2\pi}{5} & -\sin\frac{2\pi}{10} & 0 & 0 & 0 \\ \sin\frac{2\pi}{5} & \cos\frac{2\pi}{10} & 0 & 0 & 0 \\ 0 & 0 & 1 & 0 & 0 \\ \hline 0 & 0 & 0 & \cos\frac{6\pi}{10} & -\sin\frac{4\pi}{10} \\ 0 & 0 & 0 & \sin\frac{4\pi}{10} & \cos\frac{6\pi}{10} \end{array} \right)_{V^*}
=
$$

$$
= \left(\begin{array}{c|c} \Gamma^{\parallel}(10) & 0 \\ \hline 0 & \Gamma^{\perp}(10) \end{array} \right)_{V^*} . \tag{3.119}
$$

The 5D decagonal lattice can be fully equivalently described on a pentagonal basis as well (*pentagonal setting*) (see Sect. 3.6.1.1). This can be seen in analogy to the usual description of hexagonal lattices on a trigonal (rhombohedral) basis. Then the matrix for the 10-fold rotation and the unitary matrix M_{dp} for the transformation of direct and reciprocal basis vectors as well as of coordinates and indices from the decagonal basis to the pentagonal basis read

$$
\Gamma(10)_{\text{pent}} = \begin{pmatrix} 0\,1\,\bar{1}\,0\,0 \\ 0\,1\,0\,\bar{1}\,0 \\ 0\,1\,0\,0\,0 \\ \bar{1}\,1\,0\,0\,0 \\ 0\,0\,0\,0\,1 \end{pmatrix}, \quad M_{dp} = \begin{pmatrix} 0\,1\,0\,0\,0 \\ 0\,0\,0\,1\,0 \\ \bar{1}\,0\,0\,0\,0 \\ 0\,0\,\bar{1}\,0\,0 \\ 0\,0\,0\,0\,1 \end{pmatrix}. \tag{3.120}
$$

3.6.4.1 Reciprocal Space

The electron density distribution function $\rho(\mathbf{r})$ of a 3D quasicrystal can be represented by the Fourier series given in (3.41). All Fourier coefficients, i.e., the structure factors $F(\mathbf{H})$, can be integer indexed based on

a

b

c

d

$a_i = \pi^\parallel d_i$

e

$a_i = \pi^\perp d_i$
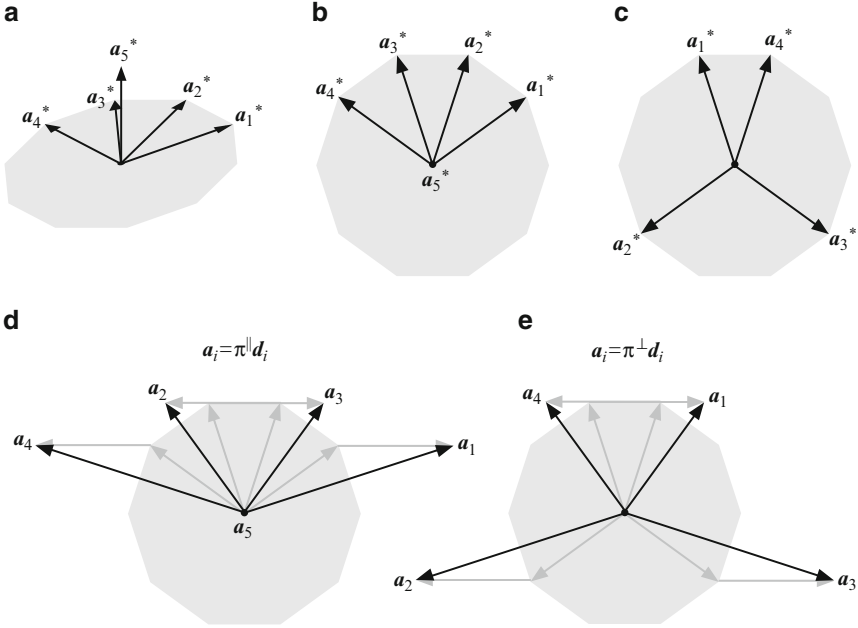
Fig. 3.26. Reciprocal basis of the decagonal phase. The projections upon the parallel (**a**, **b**, **d**) and the perp-space (**c**, **e**) are shown. The gray vectors illustrate how the direct space vectors are composed of unit vectors $\mathbf{e}_i$

five reciprocal basis vectors: $\mathbf{H} = \sum_{i=1}^{5} h_i \mathbf{a}_i^*$ with $\mathbf{a}_i^* = a^* \mathbf{e}_i = a^*$ $(\cos(2\pi i/10), \sin(2\pi i/10), 0)$, $i = 1, \ldots, 4$, $a^* = |\mathbf{a}_1^*| = |\mathbf{a}_2^*| = |\mathbf{a}_3^*| = |\mathbf{a}_4^*|$, $\mathbf{a}_5^* = |\mathbf{a}_5^*| (0, 0, 1)$ and $h_i \in \mathbb{Z}$ (Fig. 3.26).

The vector components refer to a Cartesian coordinate system in par-space $V^\parallel$. The set of all diffraction vectors $\mathbf{H}$ forms a $\mathbb{Z}$-module M^* of rank five. The vectors $\mathbf{a}_i^*$, $i = 1, \ldots, 5$ can be considered as par-space projections of the basis vectors $\mathbf{d}_i^*$, $i = 1, \ldots, 5$ of the 5D reciprocal lattice Σ^* with

$$\mathbf{d}_i^* = a^* \begin{pmatrix} \cos \frac{2\pi i}{10} \\ \sin \frac{2\pi i}{10} \\ 0 \\ c \cos \frac{6\pi i}{10} \\ c \sin \frac{6\pi i}{10} \end{pmatrix}_V \ , \ i = 1, \ldots, 4; \quad \mathbf{d}_5^* = a_5^* \begin{pmatrix} 0 \\ 0 \\ 1 \\ 0 \\ 0 \end{pmatrix}_V \ . \tag{3.121}$$

c is an arbitrary constant which is usually set to 1 (as it is also done in the following). The subscript V denotes components referring to a 5D Cartesian coordinate system (V-basis), while subscript D refers to the 5D crystallographic basis (D-basis). The embedding matrix W results to

$$\mathsf{W} = \begin{pmatrix} \cos\frac{2\pi}{10} & \cos\frac{4\pi}{10} & \cos\frac{6\pi}{10} & \cos\frac{8\pi}{10} & 0 \\ \sin\frac{2\pi}{10} & \sin\frac{4\pi}{10} & \sin\frac{6\pi}{10} & \sin\frac{8\pi}{10} & 0 \\ 0 & 0 & 0 & 0 & 1 \\ \cos\frac{6\pi}{10} & \cos\frac{12\pi}{10} & \cos\frac{18\pi}{10} & \cos\frac{24\pi}{10} & 0 \\ \sin\frac{6\pi}{10} & \sin\frac{12\pi}{10} & \sin\frac{18\pi}{10} & \sin\frac{24\pi}{10} & 0 \end{pmatrix}. \qquad (3.122)$$

The direct 5D basis is obtained from the orthogonality condition (3.5)

$$\mathbf{d}_i = \frac{2}{5a^*} \begin{pmatrix} \cos\frac{2\pi i}{10} + (-1)^{i-1} \\ \sin\frac{2\pi i}{10} \\ 0 \\ \cos\frac{6\pi i}{10} + (-1)^{i-1} \\ \sin\frac{6\pi i}{10} \end{pmatrix}_V, \quad i = 1,\ldots,4; \quad \mathbf{d}_5 = \frac{1}{a_5^*} \begin{pmatrix} 0 \\ 0 \\ 1 \\ 0 \\ 0 \end{pmatrix}_V. \qquad (3.123)$$

The metric tensors G and G^* are of type

$$\begin{pmatrix} A & B & -B & B & 0 \\ B & A & B & -B & 0 \\ -B & B & A & B & 0 \\ B & -B & B & A & 0 \\ 0 & 0 & 0 & 0 & C \end{pmatrix} \qquad (3.124)$$

with $A = 2a^{*2}$, $B = -1/2a^{*2}$, $C = a_5^{*2}$, for reciprocal space and $A = 4/(5a^{*2})$, $B = -2/(5a^{*2})$, $C = 1/a_5^{*2}$ for direct space. Therefrom the direct and reciprocal lattice parameters can be derived as

$$d_i^* = a^*\sqrt{2}, \quad d_5^* = a_5^*, \quad \alpha_{ij} = 104.5°, \quad \alpha_{i5} = 90°, \quad i,j = 1,\ldots,4 \qquad (3.125)$$

and

$$d_i = d = \frac{2}{a^*\sqrt{5}}, \quad d_5 = \frac{1}{a_5^*}, \quad \alpha_{ij} = 60°, \quad \alpha_{i5} = 90°, \quad i,j = 1,\ldots,4 . \qquad (3.126)$$

The volume of the 5D unit cell results to

$$V = \sqrt{\det(\mathsf{G})} = \frac{4}{5\sqrt{5}a^{*4}a_5^*} = \frac{\sqrt{5}d^4 d_5}{4} . \qquad (3.127)$$

3.6.4.2 Symmetry

The diffraction symmetry of decagonal phases, i.e., the point symmetry group leaving the intensity weighted Fourier module (diffraction pattern) M_I^* invariant, is one of the two Laue groups $10/mmm$ or $10/m$. The 18 space groups leaving the 5D hypercrystal structure invariant are that subset of the 5D space groups, the point groups of which are isomorphous to the 7 possible 3D decagonal point groups (Table 3.14). The orientation of the symmetry elements of the 5D space groups is defined by the isomorphism of the 3D and

Table 3.14. The seven 3D decagonal point groups of order k and the nineteen corresponding 5D decagonal space groups with reflection conditions [36]. The notation is analogous to that of hexagonal space groups. The first (second) position in the point (space) group symbols refers to generating symmetry elements oriented along the periodic direction, the second (third) position to the symmetry elements oriented along reciprocal space basis vectors and the third (fourth) position to those oriented between them

3D Point Group	k	5D Space Group	Reflection Conditions
$\dfrac{10}{m}\dfrac{2}{m}\dfrac{2}{m}$	40	$P\dfrac{10}{m}\dfrac{2}{m}\dfrac{2}{m}$	No condition
		$P\dfrac{10}{m}\dfrac{2}{c}\dfrac{2}{c}$	$h_1h_2h_2h_1h_5 : h_5 = 2n$ $h_1h_2\bar{h}_2\bar{h}_1h_5 : h_5 = 2n$
		$P\dfrac{10_5}{m}\dfrac{2}{m}\dfrac{2}{c}$	$h_1h_2\bar{h}_2\bar{h}_1h_5 : h_5 = 2n$
		$P\dfrac{10_5}{m}\dfrac{2}{c}\dfrac{2}{m}$	$h_1h_2h_2h_1h_5 : h_5 = 2n$
$\overline{10}m2$	20	$P\overline{10}m2$	No condition
		$P\overline{10}c2$	$h_1h_2h_2h_1h_5 : h_5 = 2n$
		$P\overline{10}2m$	No condition
		$P\overline{10}2c$	$h_1h_2\bar{h}_2\bar{h}_1h_5 : h_5 = 2n$
$10mm$	20	$P10mm$	No condition
		$P10cc$	$h_1h_2h_2h_1h_5 : h_5 = 2n$ $h_1h_2\bar{h}_2\bar{h}_1h_5 : h_5 = 2n$
		$P10_5mc$	$h_1h_2\bar{h}_2\bar{h}_1h_5 : h_5 = 2n$
		$P10_5cm$	$h_1h_2h_2h_1h_5 : h_5 = 2n$
$10\,2\,2$	20	$P10\,2\,2$	No condition
		$P10_j\,2\,2$	$0000h_j : jh_5 = 10n$
$\dfrac{10}{m}$	20	$P\dfrac{10}{m}$	No condition
		$P\dfrac{10_5}{m}$	$0000h_5 : h_5 = 2n$
$\overline{10}$	10	$P\overline{10}$	No condition
10	10	$P10$	No condition
		$P10_j$	$0000h_j : jh_5 = 10n$

5D point groups. The 10-fold axis defines the unique direction $[00100]_V$ or $[00001]_D$, which is the periodic direction. The reflection and inversion operations $\Gamma(m)$ and $\Gamma(\bar{1})$ are equivalent in both subspaces $V^\parallel$ and $V^\perp$. $\Gamma(10)$, a $2\pi/10$ rotation in $V^\parallel$ around the 10-fold axis corresponds to a $6\pi/10$ rotation in $V^\perp$ (c.f. (3.119) and Fig. 3.13). The translation components of the 10-fold screw axes and the c-glide planes are along the periodic direction.

The symmetry matrices for the reflections on mirror planes with normals along and between reciprocal basis vectors, respectively, read for the examples
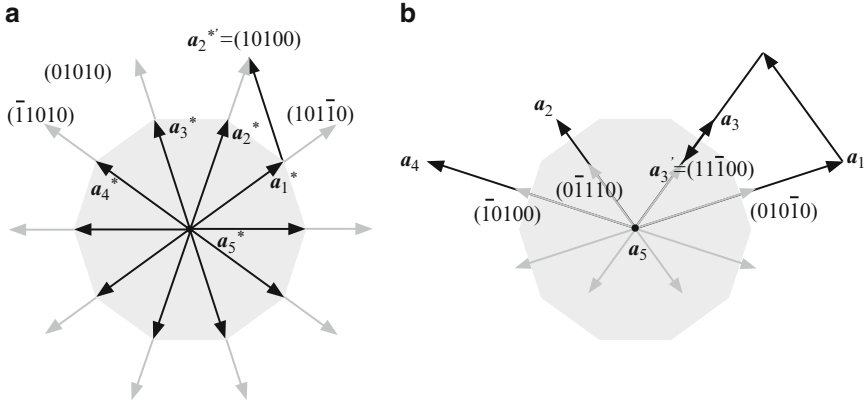
Fig. 3.27. Reciprocal and direct space scaling by the matrices S^* (**a**) and S (**b**), respectively. The scaled basis vectors (marked gray) keep their orientation and are changed in length by a factor τ (**a**) or $1/\tau$ (**b**). Explicitly shown is the scaling of the vectors $\mathbf{a}_2^*$ and $\mathbf{a}_3$: $\mathbf{a}_2^{*\prime} = \mathbf{a}_1^* + \mathbf{a}_3^*$ and $\mathbf{a}_3^\prime = \mathbf{a}_1 + \mathbf{a}_2 - \mathbf{a}_3$

with the normal of the mirror plane m_2 along $\mathbf{a}_2^*$ and of the mirror plane m_{12} along $\mathbf{a}_1^* - \mathbf{a}_2^*$:

$$
\Gamma\left(m_2\right) = \begin{pmatrix} 0 & 0 & \bar{1} & \bar{1} & 0 \\ 0 & \bar{1} & 0 & 1 & 0 \\ \bar{1} & 0 & 0 & \bar{1} & 0 \\ 0 & 0 & 0 & 1 & 0 \\ 0 & 0 & 0 & 0 & 1 \end{pmatrix}_{V^*} , \quad \Gamma\left(m_{12}\right) = \begin{pmatrix} 0 & \bar{1} & \bar{1} & 0 & 0 \\ \bar{1} & 0 & 1 & 0 & 0 \\ 0 & 0 & \bar{1} & 0 & 0 \\ 0 & 0 & 1 & 1 & 0 \\ 0 & 0 & 0 & 0 & 1 \end{pmatrix}_{V^*} . \tag{3.128}
$$

A typical property of the reciprocal space of quasiperiodic structures is its scaling symmetry (Fig. 3.27).

The scaling operation is represented by the matrix S^*, which can be diagonalized by $\mathsf{W} \cdot \mathsf{S}^* \cdot \mathsf{W}^{-1}$

$$
\mathsf{S}^* = \begin{pmatrix} 1 & 1 & 0 & \bar{1} & 0 \\ 0 & 0 & 1 & 1 & 0 \\ 1 & 1 & 0 & 0 & 0 \\ \bar{1} & 0 & 1 & 1 & 0 \\ 0 & 0 & 0 & 0 & 1 \end{pmatrix}_{D^*} = \left(\begin{array}{ccc|cc} \tau & 0 & 0 & 0 & 0 \\ 0 & \tau & 0 & 0 & 0 \\ 0 & 0 & 1 & 0 & 0 \\ \hline 0 & 0 & 0 & -1/\tau & 0 \\ 0 & 0 & 0 & 0 & -1/\tau \end{array} \right)_{V^*} = \left(\begin{array}{c|c} \Gamma^\parallel\left(\mathsf{S}^*\right) & 0 \\ \hline 0 & \Gamma_1^\perp\left(\mathsf{S}^*\right) \end{array} \right)_{V^*} .
$$

$$
\tag{3.129}
$$

The eigenvalues of the scaling matrix are the Pisot numbers $\lambda_1 = 1 + 2\cos \pi/5 = \tau = 1.61803$, $\lambda_2 = 1 + 2\cos 4\pi/5 = -1/\tau = -.61803$, which are the solutions of the characteristic polynomial $1 + x - 3x^2 - x^3 + 3x^4 - x^5 = (1-x)(-1-x+x^2)^2$. The scaling symmetry matrix for the direct space basis vectors and the reflection indices $\mathsf{S} = [(\mathsf{S}^*)^{-1}]^\mathsf{T}$ results to

$$
S = \begin{pmatrix} 0\,0\,1\,\bar{1}\,0 \\ 1\,\bar{1}\,1\,0\,0 \\ 0\,1\,\bar{1}\,1\,0 \\ \bar{1}\,1\,0\,0\,0 \\ 0\,0\,0\,0\,1 \end{pmatrix}_D = \left(\begin{array}{ccc|cc} 1/\tau & 0 & 0 & 0 & 0 \\ 0 & 1/\tau & 0 & 0 & 0 \\ 0 & 0 & 1 & 0 & 0 \\ \hline 0 & 0 & 0 & -\tau & 0 \\ 0 & 0 & 0 & 0 & -\tau \end{array} \right)_V = \left(\begin{array}{c|c} \Gamma^\parallel(S) & 0 \\ \hline 0 & \Gamma_1^\perp(S) \end{array} \right)_V .
$$

$$(3.130)$$

Invariance of tilings under scaling of the basis and atomic surfaces
The embedding space for a given tiling is unique only up to scaling, which results in scaled and permutated atomic surfaces while leaving the tiling unchanged.

The Penrose tiling, for instance, can be generated by four pentagons of two sizes and two orientations positioned at $i/5$, $i = 1, \ldots, 4$, of the 4D hypercrystal diagonal. We denote these pentagons according to their positions and sizes as s_1 (small pentagon at $i = 1$), l_2 (large pentagon at $i = 2$), l_3 and s_4. Their orientations and relative sizes are as defined in (3.138), and we start with a tiling that is generated by this classical embedding. Now we keep the metrics of the tiling unchanged, but embed it on a 4D basis which is scaled by a factor τ. Then the circumradius r of the corresponding atomic surfaces is scaled by a factor τ^2 and their positions are permutated along the diagonal from $s_1 - l_2 - l_3 - s_4$ to $l_3 - s_1 - s_4 - l_2$. Scaling the 4D basis by τ^2 instead, scales r by τ^4 and we get the arrangement $s_4 - l_3 - l_2 - s_1$. For scaling by τ^3, r scales with τ^6 and we get $l_2 - s_4 - s_1 - l_3$, while for τ^4 r scales with τ^8 and the atomic surfaces are back to their original positions. The closeness condition is fulfilled in all these cases, but in different ways. Since the tiling is invariant under the described scaling, this is also the case for its periodic average structures and its Fourier transform (diffraction pattern).

3.6.4.3 Example: Decagonal Quasicrystal Built From Layers of Penrose Tilings

In the following the frequently used pentagonal setting is employed. The Penrose tiling, PT, (see Sect. 1.2.3.1) [33, 34] can be constructed from two unit tiles: a skinny (acute angle $\alpha = \pi/5$) and a fat rhomb (acute angle $\alpha = 2\pi/5$) with equal edge lengths a_r and areas $a_r^2 \sin \pi/5$ and $a_r^2 \sin 2\pi/5$, respectively. Their areas and frequencies in the PT are both in a ratio $1 : \tau$. The construction has to obey matching rules, which can be derived from the scaling properties of the PT (Fig. 3.28).

The set of vertices of the PT M_{PT} is a subset of the vector module $M = \left\{ \mathbf{r} = \sum_{i=0}^{4} n_i a_r \mathbf{e}_i \,\middle|\, \mathbf{e}_i = (\cos 2\pi i/5, \sin 2\pi i/5, 0) \right\}$. M_{PT} consists of five subsets

$$
M_{\mathrm{PT}} = \cup_{k=0}^{4} M_k \quad \text{with} \quad M_k = \left\{ \pi^\parallel(\mathbf{r}_k) \,\middle|\, \pi^\perp(\mathbf{r}_k) \in T_{ik}, i = 0, \ldots, 4 \right\} \quad (3.131)
$$

and $\mathbf{r}_k = \sum_{j=0}^{4} \mathbf{d}_j \left(n_j + k/5 \right), n_j \in \mathbb{Z}$. The i-th triangular subdomain T_{ik} of the k-th pentagonal atomic surface corresponds to
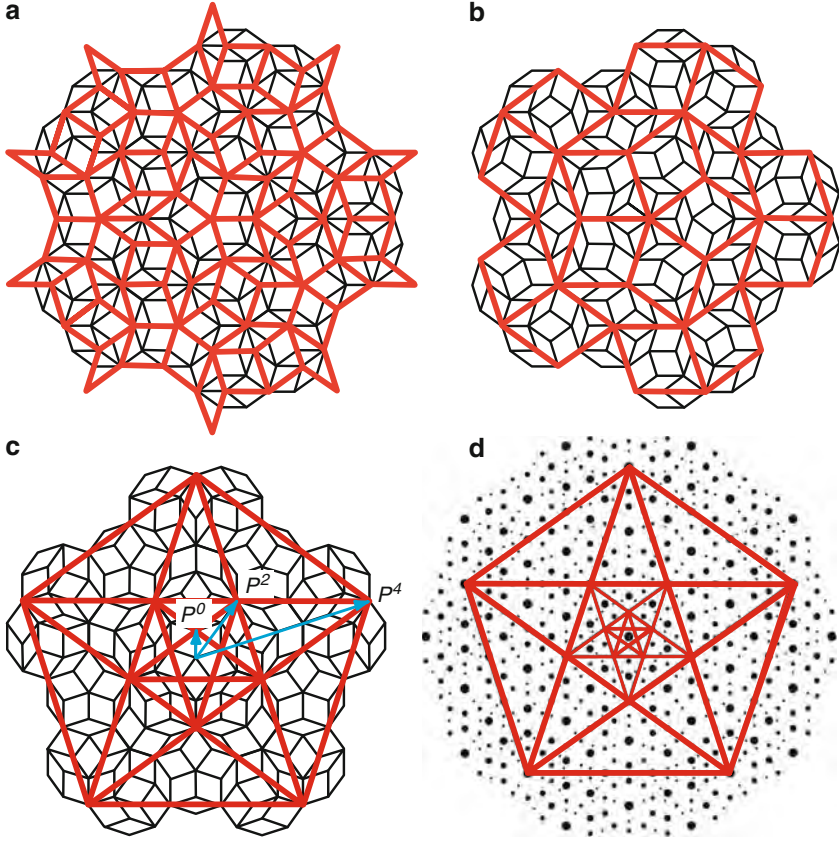
Fig. 3.28. Scaling properties of the Penrose tiling. In (**a**), a PT (*thin lines*) is superposed by a PT (thick lines), which is dual to the original PT and results from scaling by S. In (**b**), the scaling by S^2 is shown, which yields a PT congruent to the original one but enlarged by a factor τ^2 and rotated by $2\pi/10$. The scaling operation by S^{2n} leaves a pentagramm invariant, mapping P^0 to P^2 to P^4 in (**c**). (**d**) Pentagrammal scaling applied to the diffraction pattern of the PT decorated with point atoms

$$T_{ik} = \left\{ \mathbf{t} = x_i \mathbf{e}_i + x_{i+1} \mathbf{e}_{i+1} \Big| x_i \in [0, \lambda_k], x_{i+1} \in [0, \lambda_k - x_i] \right\} \qquad (3.132)$$

with λ_k the radius of a pentagonally shaped atomic surface: $\lambda_0 = 0$, for $\lambda_{1,\cdots,4}$ see (3.138). Performing the scaling operation $\mathsf{S}^* M_{\mathrm{PT}}$ with the matrix

$$\mathsf{S}^* = \begin{pmatrix} 0 & 1 & 0 & \bar{1} & 0 \\ 0 & 1 & 1 & \bar{1} & 0 \\ \bar{1} & 1 & 1 & 0 & 0 \\ \bar{1} & 0 & 1 & 0 & 0 \\ 0 & 0 & 0 & 0 & 1 \end{pmatrix}_{D^*} = \left(\begin{array}{ccc|cc} \tau & 0 & 0 & 0 & 0 \\ 0 & \tau & 0 & 0 & 0 \\ 0 & 0 & 1 & 0 & 0 \\ \hline 0 & 0 & 0 & -1/\tau & 0 \\ 0 & 0 & 0 & 0 & -1/\tau \end{array}\right)_{V^*} = \left(\begin{array}{c|c} \Gamma^{\parallel}(\mathsf{S}^*) & 0 \\ \hline 0 & \Gamma_1^{\perp}(\mathsf{S}^*) \end{array}\right)_{V_*}.$$

$$(3.133)$$
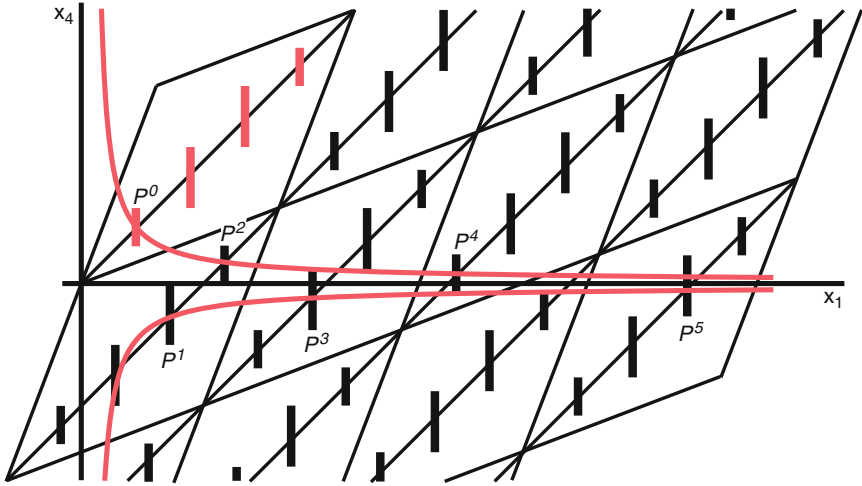
Fig. 3.29. Hyperbolic rotation in superspace. A given point P^0 of the first atomic surface is successively mapped upon the sites marked by P^1, P^2, P^3, P^4, P^5. In each step its x_4-component is decreased by a factor $-1/\tau$ and its x_1-component is increased by a factor τ. The drawing corresponds to the characteristic $(10010)_V$ section of the Penrose tiling

yields a tiling dual to the original PT and enlarged by a factor τ. Only scaling by S^{4n} results in a PT (increased by a factor τ^{4n}) of original orientation (Fig. 3.28). Then the relationship $S^{4n}M_{\mathrm{PT}} = \tau^{4n}M_{\mathrm{PT}}$ holds. S^2 maps the vertices of an inverted and by a factor τ^2 enlarged PT upon the vertices of the original PT. This operation corresponds to a hyperbolic rotation in superspace [15] (Fig. 3.29).

The rotoscaling operation $\Gamma(10)S^2$ leaves the subset of vertices of a PT forming a pentagram invariant [15] (Fig. 3.28(c)).

Characteristic sections and projections of the embedded decagonal structure are shown in Figs. 3.30 and 3.31. In Fig. 3.30 the direction of oblique projection is shown for obtaining the most important PAS.

In the (5+1)D description, the atomic surfaces of the PT correspond to four equidistant planes. These are cut out of the 3D polytope, which results from the projection of the 5D hypercubic subunit cell onto 3D perp-space (Fig. 3.32). The long diagonal of this rhombicosahedron runs along $[000010]_V$, from 000000 to the vertex 111110 (D-basis). By projection of the (5+1)D lattice onto the (4+1)D one, the atomic surfaces can be obtained in the minimum embedding space. This has to be done so that the vertex 111110, with the coordinates $(0000\sqrt{5}\,0)$ (V-basis), is mapped onto 11110, with the coordinates $-\sqrt{5/2}(20020)$ (V-basis). The projection matrix reads
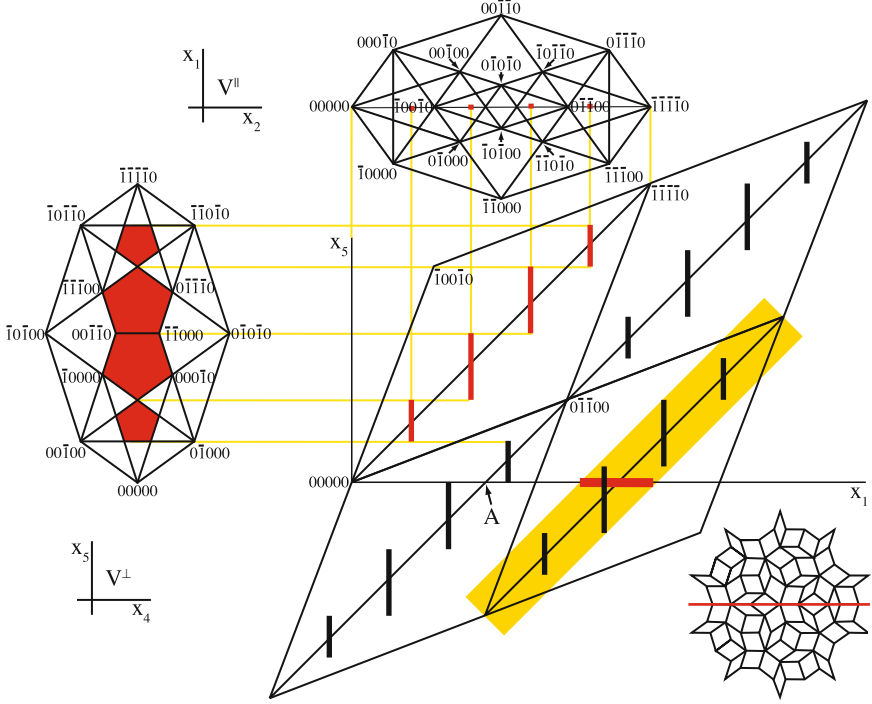
Fig. 3.30. Characteristic $(10010)_V$ section of the Penrose tiling together with the parallel (*above*) and perp-space (*left*) projections of one 5D unit cell. In the lower right unit cell, the oblique projection direction [11110] is highlighted. The PT in the bottom right corner indicates the orientation of the characteristic section

$$
\pi^{6D \to 5D} =
\begin{pmatrix}
1\,0\,0\,0\,0 & -\sqrt{2} \\
0\,1\,0\,0\,0 & 0 \\
0\,0\,1\,0\,0 & 0 \\
0\,0\,0\,1\,0 & -\sqrt{2} \\
0\,0\,0\,0\,1 & 0
\end{pmatrix}_V .
\tag{3.134}
$$

3.6.4.4 Structure Factor

The structure factor of a decagonal phase with Penrose tilings as layers can be calculated according to (3.12). The geometrical form factors g_k for the PT correspond to the Fourier transforms of four pentagonally shaped atomic surfaces (3.13) with the volume of the projected unit cell

$$
A_{\mathrm{UC}}^{\perp} = \frac{4}{25a^{*2}} \left[(7 + \tau) \sin \frac{2\pi}{5} + (2 + \tau) \sin \frac{4\pi}{5} \right] .
\tag{3.135}
$$
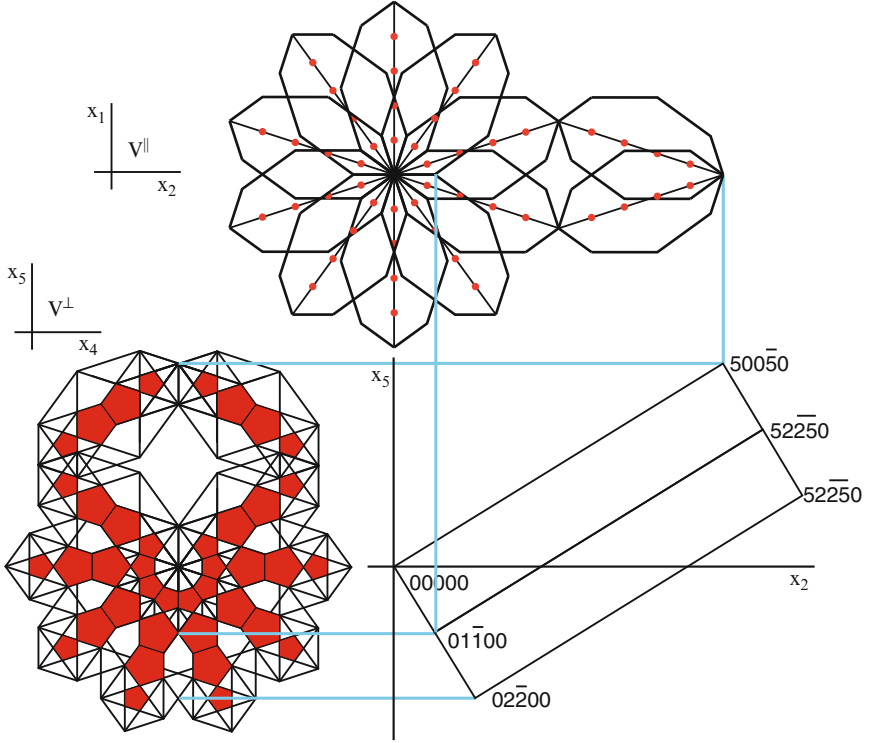
Fig. 3.31. Characteristic $(01010)_V$ section of the Penrose tiling together with the parallel (*above*) and perp-space (*left*) projections showing the surrounding of vertices lying in the section. In the perp-space projection, two out of the 10 symmetrically equivalent projected 5D unit cells have been omitted for the sake of clarity

Integrating the pentagons by triangularisation yields

$$g_k\left(\mathbf{H}^\perp\right) = \frac{1}{A_{\mathrm{UC}}^\perp} \sin\left(\frac{2\pi}{5}\right) \times$$
$$\sum_{j=0}^{4} \frac{A_j\left(\mathrm{e}^{\mathrm{i}A_{j+1}\lambda_k} - 1\right) - A_{j+1}\left(\mathrm{e}^{\mathrm{i}A_j\lambda_k} - 1\right)}{A_j A_{j+1}\left(A_j - A_{j+1}\right)} \qquad (3.136)$$

with j running over five triangles of a pentagon with radius λ_k, $A_j = 2\pi\mathbf{H}^\perp\mathbf{e}_j$ and

$$\mathbf{H}^\perp = \pi^\perp\left(\mathbf{H}\right) = a^* \sum_{j=0}^{4} h_j \begin{pmatrix} 0 \\ 0 \\ 0 \\ \cos\frac{6\pi j}{5} \\ \sin\frac{6\pi j}{5} \end{pmatrix}_V . \qquad (3.137)$$
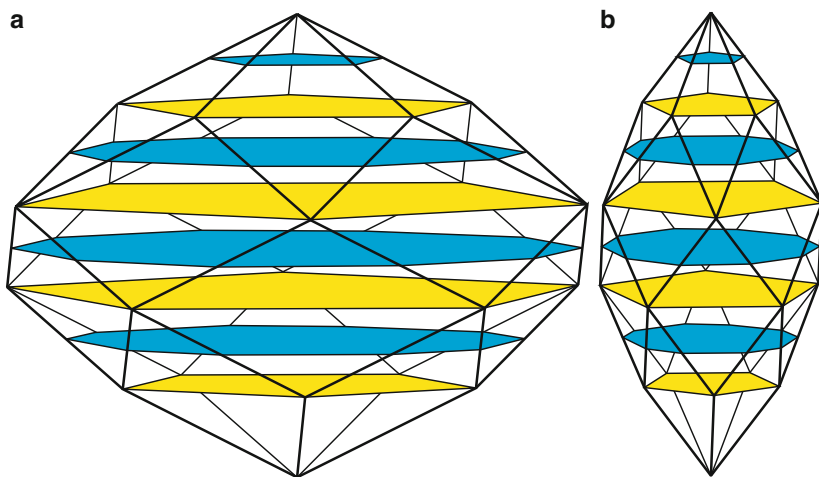
Fig. 3.32. (**a**) 5D hypercubic subunit cell of the Penrose tiling in the (5+1)D embedding projected onto the 3D perp-space gives a rhombicosahedron. Since the (5+1)D embedding uses a redundant basis vector, the atomic surfaces of the Penrose tiling are just a subset of this rhombicosahedron, i.e. five equidistant pentagonal planes (light-gray, online:yellow). The fifth plane intersects the polytope in the origin in just one point. Shifting the set of cutting planes along the long diagonal gives another set of atomic surfaces corresponding to one of the generalized Penrose tilings (dark-gray, online: blue) [33]. In (**b**), the set of atomic surfaces is scaled by a factor τ^{-2} which inflates the corresponding Penrose tiling by a factor τ^2

The radii of the pentagons are

$$\lambda_{1,4} = \frac{2}{5\tau^2 a^*}, \quad \lambda_{2,3} = \frac{2}{5\tau a^*} . \tag{3.138}$$

The edge length a_r of the rhombic unit tiles is for this size of the atomic surfaces $a_r = 2\tau^2/(5a^*)$. The point density D_{p} of the PT in par-space is according to 3.45

$$D_{\mathrm{p}} = \frac{1}{V} \sum_{i=1}^{n} A_i = \frac{5a^{*2}}{2\tau^4} \tan \frac{2\pi}{5} = \tau^2/\{a_r^2 \left[\sin\left(\pi/5\right) + \tau \sin\left(2\pi/5\right)\right]\}. \tag{3.139}$$

The atomic surfaces of the Penrose tiling can be partitioned into sections that correspond to vertices with the same local coordination in par-space. Projecting all nearest neighbors of a hyperatom onto $V^\perp$ determines all different Voronoi polyhedra in par-space (Fig. 3.33).

Any point within a special region is determined by the neighboring hyperatoms that share this region. The central small pentagon, for instance, is related to atoms in par-space with five neighbors located at the vertices of a
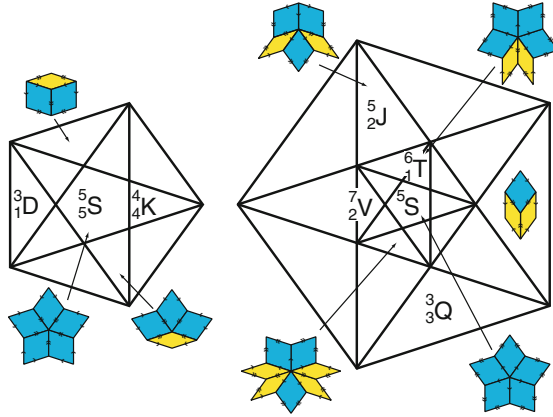
Fig. 3.33. Partitioning of the atomic surfaces corresponding to the eight different vertex coordinations of the PT. The atomic surfaces in $p(11110)_D$ with $p = 1/5$ and $p = 2/5$ are depicted. Those in $p = 3/5$ and $p = 4/5$ are related by an inversion center [33]

pentagon. Depending on the atomic surface, the edges originating from the vertex are single or double arrowed.

Schematic diffraction patterns of the centrosymmetric PT decorated with point atoms in par- and perp-space as well as the radial distribution functions of the structure factors as a function of $H^{\parallel}$ and $H^{\perp}$ are shown in Fig. 3.34. The number of weak reflections increases with the power of 4, that of strong reflections quadratically (strong reflections always have small $H^{\perp}$ components). It is remarkable that the phases of strong reflections are mostly zero (sign +). Three branches of reflections are clearly seen (Fig. 3.34(d)), which result from particular phase relationships of the four atomic surfaces.

To illustrate the origin of the branches, several cases of centrosymmetric structures are shown in Fig. 3.35. According to (3.12), we can write the structure factor for a centrosymmetric structure with one hyperatom in the asymmetric unit located on the body diagonal of the 4D unit cell, $F(\mathbf{H}) = f(|\mathbf{H}^{\parallel}|) g(\mathbf{H}^{\perp}) \cos 2\pi \mathbf{Hr}$. Since we use point atoms, $f(|\mathbf{H}^{\parallel}|) = 1$, and $\mathbf{Hr}$ can be replaced by $k(h_1 + h_2 + h_3 + h_4)$.

In Fig. 3.35(a), there is a decagonal atomic surface in the origin, $k = 0$; therefore, the phase factor equals one, and just one branch results. If the decagon is located at the inversion center at $k = 1/2$, two branches with opposite phase result for the reflection classes with $(h_1 + h_2 + h_3 + h_4)$ even or odd (d). For $k = 1/5$, the phase term can adopt the values 1, $\cos 2\pi i/5$, $i = 1, 2$ (b) corresponding to three branches. Analogously, the number of branches in the other cases can be derived. It should be kept in mind, that in the cases (b), (c), (e) and (f) the number of hyperatoms is always two, sitting in positions related by a center of symmetry. The number of branches
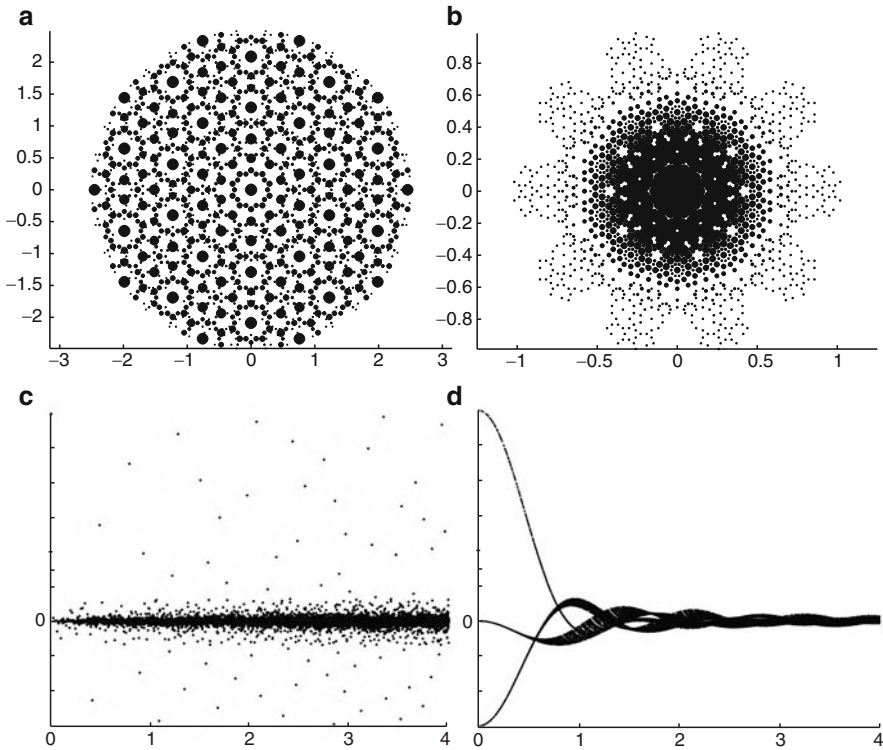
Fig. 3.34. Schematic diffraction patterns of the Penrose tiling decorated with point atoms ($a_r = 4.04\,\text{Å}$) in (**a**) par- and (**b**) perp-space. The radial distribution functions of the structure factors are shown as a function of $H^\parallel$ (**c**) and $H^\perp$ (**d**). Three branches of reflections are clearly seen, which result from particular phase relationships of the four atomic surfaces. All reflections are depicted within $10^{-2}I(\mathbf{0}) < I(\mathbf{H}) < I(\mathbf{0})$ and $0 \leq H^\parallel \leq 2.5\,\text{Å}^{-1}$. The axes in (**a**) and (**b**) are lettered in Å^{-1}

is not directly related to the number of hyperatoms, it mainly depends on the positions, if there are at least two hyperatoms per unit cell.

3.6.4.5 The Penrose Tiling in the *IMS* Description

Alternative to the QC embedding discussed above, the IMS setting can be used. This can be quite useful for the geometrical description of phase transitions or for the derivation of periodic average structures (PAS) of the PT. For that purpose, the 5D hyperstructure has to be sheared parallel to the par-space in a way that the structure along the par-space cut remains invariant (Fig. 3.36). This can be done applying the shear matrix $\mathsf{A}^\parallel$ to the basis $\mathbf{d}_i^{\mathrm{QC}}$, $i = 1\ldots 5$
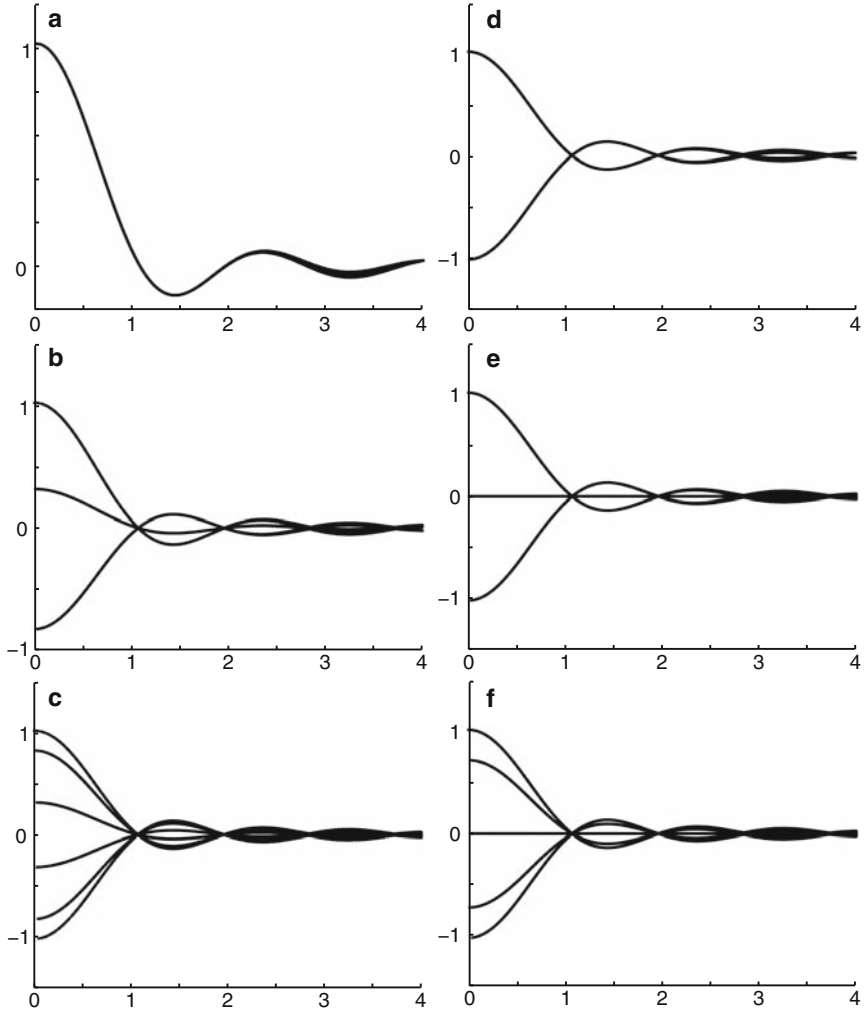
Fig. 3.35. Radial distribution functions of structure factors of different tilings as a function of $H^\perp$. The same 4D lattice parameters have been used as in Fig. 3.34. In (**a**) one decagonal atomic surface is placed on the origin, in (**d**) at $1/2(1\ 1\ 1\ 1)$. One small pentagonal atomic surface is placed each at $k(1\ 1\ 1\ 1)$ and the respective centrosymmetric position; (**b**) $k = 1/5$, (**c**) $k = 1/10$, and (**e**) $k = 1/4$, (**f**) $1/8$. All reflections are depicted within $10^{-2}I(\mathbf{0}) < I(\mathbf{H}) < I(\mathbf{0})$ and $0 \le H^\| \le 2.5\,\text{Å}^{-1}$. The axes in (**a**) and (**b**) are lettered in Å^{-1}

$$
\mathsf{A}^\| = \begin{pmatrix} 1 & 0 & 0 & 0 & 0 \\ 0 & 1 & 0 & -\tau^{-2} & 0 \\ 0 & 0 & 1 & 0 & -\tau \\ 0 & 0 & 0 & 1 & 0 \\ 0 & 0 & 0 & 0 & 1 \end{pmatrix}_V \tag{3.140}
$$

The new basis $\mathbf{d}_i^{\text{IMS}}$, $i = 1 \ldots 5$, of the sheared lattice Σ^{IMS} reads

$$
\mathbf{d}_1^{\text{IMS}} = -\mathsf{A}^{\parallel}(\mathbf{d}_2^{\text{QC}} + \mathbf{d}_3^{\text{QC}}) = \frac{2}{5a^*}\begin{pmatrix} 5\tau^{-1} \\ 0 \\ 0 \\ 3 - \tau \\ 0 \end{pmatrix}_V ,
$$

$$
\mathbf{d}_2^{\text{IMS}} = -\mathsf{A}^{\parallel}(\mathbf{d}_3^{\text{QC}} - \mathbf{d}_2^{\text{QC}}) = \frac{2}{5a^*}\begin{pmatrix} 0 \\ 5(3 - \tau)^{-1/2} \\ 0 \\ 0 \\ -\sqrt{2 + \tau} \end{pmatrix}_V ,
$$

$$
\mathbf{d}_3^{\text{IMS}} = -\mathsf{A}^{\parallel}(\mathbf{d}_1^{\text{QC}} + \mathbf{d}_4^{\text{QC}}) = \frac{2}{5a^*}\begin{pmatrix} 0 \\ 0 \\ 0 \\ 2 + \tau \\ 0 \end{pmatrix}_V ,
$$

$$
\mathbf{d}_4^{\text{IMS}} = \mathsf{A}^{\parallel}(\mathbf{d}_1^{\text{QC}} - \mathbf{d}_4^{\text{QC}}) = \frac{2}{5a^*}\begin{pmatrix} 0 \\ 0 \\ 0 \\ 0 \\ \sqrt{3 - \tau} \end{pmatrix}_V , \tag{3.141}
$$

with $\mathbf{d}_5^{\text{IMS}} = \mathbf{d}_5^{\text{QC}}$. The vectors $\mathbf{d}_3^{\text{IMS}}$ and $\mathbf{d}_4^{\text{IMS}}$ have only perp-space components unequal to zero.

The par-space projection of the sheared 5D hyperstructure gives one of the infinitely many possible periodic average structures (PAS). The 16 corners of the 4D subcell related to the quasiperiodic plane project onto the four corners of a rhombic unit cell, which are part of an orthorhombic C-centered lattice. The C face is perpendicular to $[00100]^V$ and the basis vectors $\mathbf{a}_i^{\text{av}}$, $i = 1 \ldots 3$, read

$$
\mathbf{a}_1^{\text{av}} = \pi^{\parallel}(\mathbf{d}_1^{\text{IMS}}) = \frac{2}{a^*}\begin{pmatrix} \tau^{-1} \\ 0 \\ 0 \end{pmatrix}_V ,
$$

$$
\mathbf{a}_2^{\text{av}} = \pi^{\parallel}(\mathbf{d}_2^{\text{IMS}}) = \frac{2}{a^*}\begin{pmatrix} 0 \\ (3 - \tau)^{-1/2} \\ 0 \end{pmatrix}_V ,
$$

$$
\mathbf{a}_3^{\text{av}} = \pi^{\parallel}(\mathbf{d}_5^{\text{IMS}}) = \frac{1}{a^*}\begin{pmatrix} 0 \\ 0 \\ 1 \end{pmatrix}_V . \tag{3.142}
$$
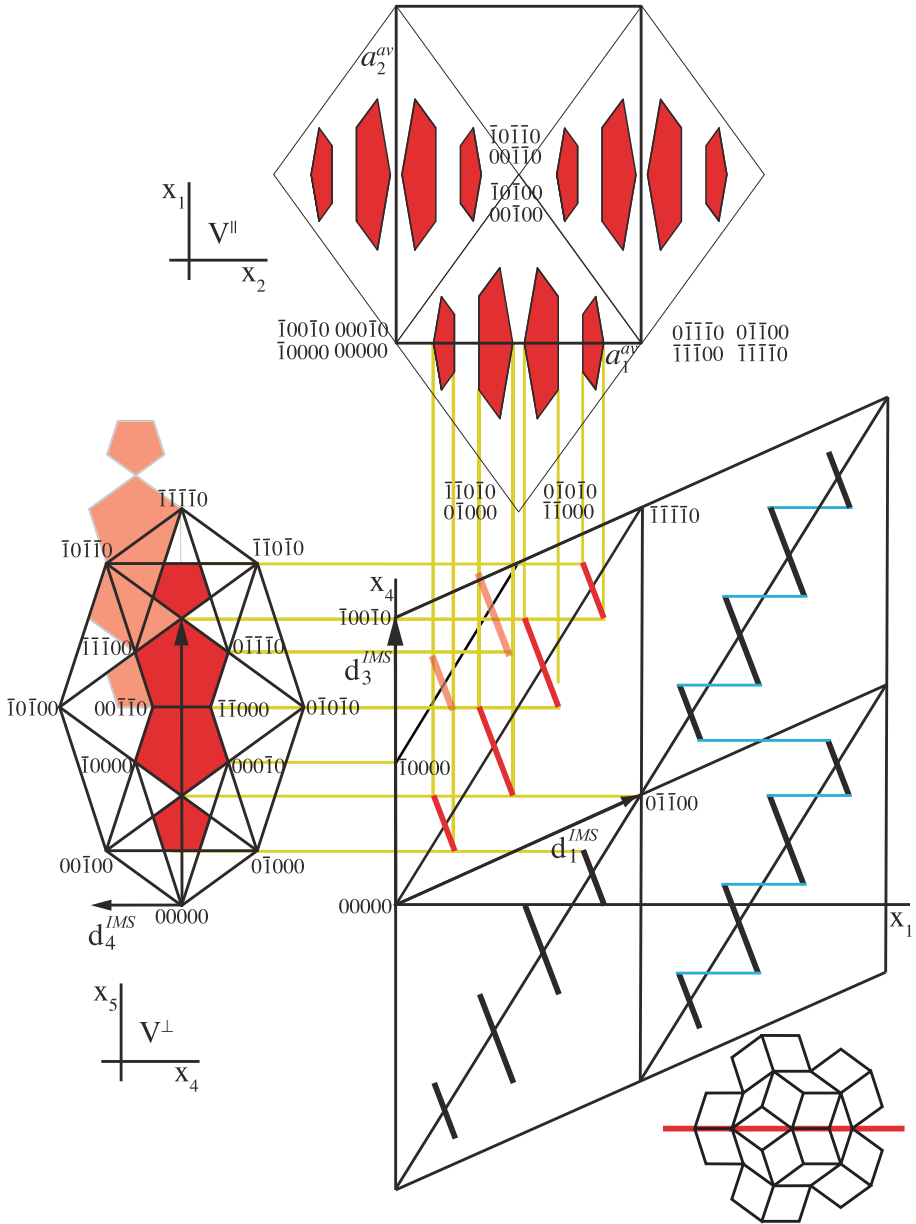
Fig. 3.36. The PT in the IMS setting. The 5D hyperstructure set up in the QC setting (Fig. 3.30) has been sheared by the shear matrix $\mathsf{A}^{\parallel}$ (3.140). The indexing of vertices corresponds to that of the QC setting

3.6.4.6 Periodic Average Structure from the QC-Setting

Fully equivalently, a periodic average structure can be directly obtained from the QC-setting by oblique projection. In the following example, the 5D hyper-structure is projected along $[11110]_D$ and $[\bar{4}1110]_D$ onto $V^\parallel$ (Figs. 3.30 and 3.37) [45].

The projector $\pi^\parallel$ can be easily obtained from a transformation of the basis $\mathbf{d}_i$, $i = 1,\ldots,5$ to a new basis spanned by the vectors $\mathbf{d}_1' = (11110)_D$, $\mathbf{d}_2' = \mathbf{d}_2$, $\mathbf{d}_3' = (\bar{4}1110)_D$, and $\mathbf{d}_4' = \mathbf{d}_4$. The projector

$$\pi^\parallel = \begin{pmatrix} 1\ 0\ 0\ \bar{1} & -\tau\sqrt{3-\tau} \\ 0\ 1\ 0\ 0 & -\tau \\ 0\ 0\ 1\ 0 & 0 \end{pmatrix}_V = \frac{2\sqrt{5}}{5a^*} \begin{pmatrix} 0 & \frac{\tau-1}{2} & -\frac{\tau+1}{2} & 1\ 0 \\ 0 & \cos\frac{\pi}{10} & -\cos\frac{\pi}{10} & 0\ 0 \\ 0 & 0 & 0 & 0\ 1 \end{pmatrix}_D \quad , \quad (3.143)$$

maps the basis of the 5D hyperlattice $\mathbf{d}_i$, $i = 1,\ldots,5$, onto a monoclinic reference lattice spanned by the vectors $\mathbf{a}_i^{\mathrm{av}}$, $i = 1,\ldots,3$,

$$\mathbf{a}_1^{\mathrm{av}} = \pi^\parallel(\mathbf{d}_4) = \frac{2}{\sqrt{5}a^*}\begin{pmatrix}1\\0\\0\end{pmatrix}_V \quad , \quad \mathbf{a}_2^{\mathrm{av}} = \pi^\parallel(\mathbf{d}_2) = \frac{2}{\sqrt{5}a^*}\begin{pmatrix}\sin\frac{\pi}{10}\\\cos\frac{\pi}{10}\\0\end{pmatrix}_V \quad ,$$

$$\mathbf{a}_3^{\mathrm{av}} = \pi^\parallel(\mathbf{d}_5) = \frac{1}{a_5^*}\begin{pmatrix}0\\0\\1\end{pmatrix}_V \quad , \quad \pi^\parallel(\mathbf{d}_1) = \begin{pmatrix}0\\0\\0\end{pmatrix}_V \quad , \quad \pi^\parallel(\mathbf{d}_3) = -\pi^\parallel(\mathbf{d}_2 + \mathbf{d}_4).$$

$$(3.144)$$

Thus, the lattice parameters of the PAS result to $a_1^{\mathrm{av}} = a_2^{\mathrm{av}} = \frac{2}{5a^*}(2\tau - 1) = a_r(3-\tau)/\tau$, and $a_3^{\mathrm{av}} = 1/a_5$, $\alpha_3 = \frac{2\pi}{5}$ (Fig. 3.37). Since the true symmetry of
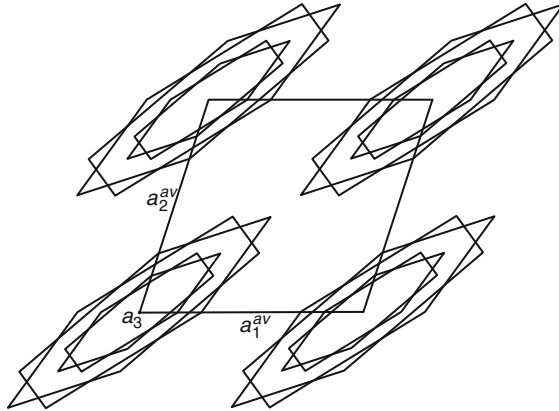
Fig. 3.37. Unit cell of the PAS of the Penrose tiling. All vertices of a PT project into the projected atomic surfaces. By the projection, the pentagons are scaled by factor τ^2 $(1/\tau)$ along the long (short) diagonal of the unit cell. The boundaries of the projected atomic surfaces give the maximum distance of a tiling vertex from the reference lattice node

the PAS is orthorhombic, the monoclinic unit cell should be transformed to a C centered orthorhombic unit cell with lattice parameters

$$\mathbf{a}_1^{\mathrm{av}} = \pi^{\|}(\mathbf{d}_3) = -\frac{2}{\sqrt{5}a^*} \begin{pmatrix} \sin\frac{\pi}{10} + 1 \\ \cos\frac{\pi}{10} \\ 0 \end{pmatrix}_V,$$

$$\mathbf{a}_2^{\mathrm{av}} = \pi^{\|}(\mathbf{d}_4 - \mathbf{d}_2) = \frac{2}{\sqrt{5}a^*} \begin{pmatrix} \sin\frac{\pi}{10} - 1 \\ \cos\frac{\pi}{10} \\ 0 \end{pmatrix}_V,$$

$$\mathbf{a}_3^{\mathrm{av}} = \pi^{\|}(\mathbf{d}_5) = \frac{1}{a_5^*} \begin{pmatrix} 0 \\ 0 \\ 1 \end{pmatrix}_V, \qquad (3.145)$$

and $a_1^{\mathrm{av}} = a_r(3-\tau)$, $a_2^{\mathrm{av}} = a_1^{\mathrm{av}}(\sqrt{3-\tau})/\tau$, and $a_3^{\mathrm{av}} = 1/a_5$. A general lattice node $(n_1\, n_2\, n_3\, n_4\, n_5)_D$ is projected on a node $(m_1\, m_2\, m_3)_{\mathrm{av}} = (-n_3 + n_4\, n_2 - n_3\, n_5)_D$ of the PAS. Consequently, all atomic surfaces linked to nodes that differ only by vectors $(n_1\, n_2\, n_2\, n_2\, n_5)_D$ are projected onto each other (see Fig. 3.38).

With the constraint of equal densities of the QC and its average structure an occupancy factor of $(3-\tau)/\tau = 0.854$ results for the averaged atoms, i.e., the distorted pentagons (Fig. 3.37). Thus, every vertex of the PT lies within a different projected atomic surface. However, 14.6% of all projected atomic surfaces contain no vertex at all (see Fig. 3.38). This is similar to an average structure of an IMS with displacive and density modulation. The packing density of the PAS, i.e., the fraction of the unit cell covered by the projected atomic surfaces equals $2/(3\tau+1) = 0.342$.

There are overlap regions, D of each large pentagonal atomic surface, Q and K of the small ones (Fig. 3.38). These overlaps correspond to the cases where the short diagonal of a skinny unit rhomb (connecting vertices of types D and K or D and Q) lies fully inside a projected atomic surface. The overlapping regions cover a fraction of $1/(5\tau^2) = 0.076$ of the total area of the atomic surfaces. This corresponds to one fifth of the frequency of skinny rhombs in a Penrose tiling. Each doubly occupied averaged atomic surface is accompanied by two unoccupied ones. The frequency of singly occupied averaged hyperatoms is 0.7236, of doubly occupied ones 0.0652 and of unoccupied ones 0.2112. Each fat unit tile along all worms (chains of fat and skinny PT unit rhombs with parallel edges) propagating perpendicular to the aforementioned short diagonals contains one empty averaged hyperatom. Thus, we have to sum up the frequencies of the vertices connected with such configurations. The worms propagating along the four other directions contain empty averaged hyperatoms only at the crossings with the first one.

a

b

c
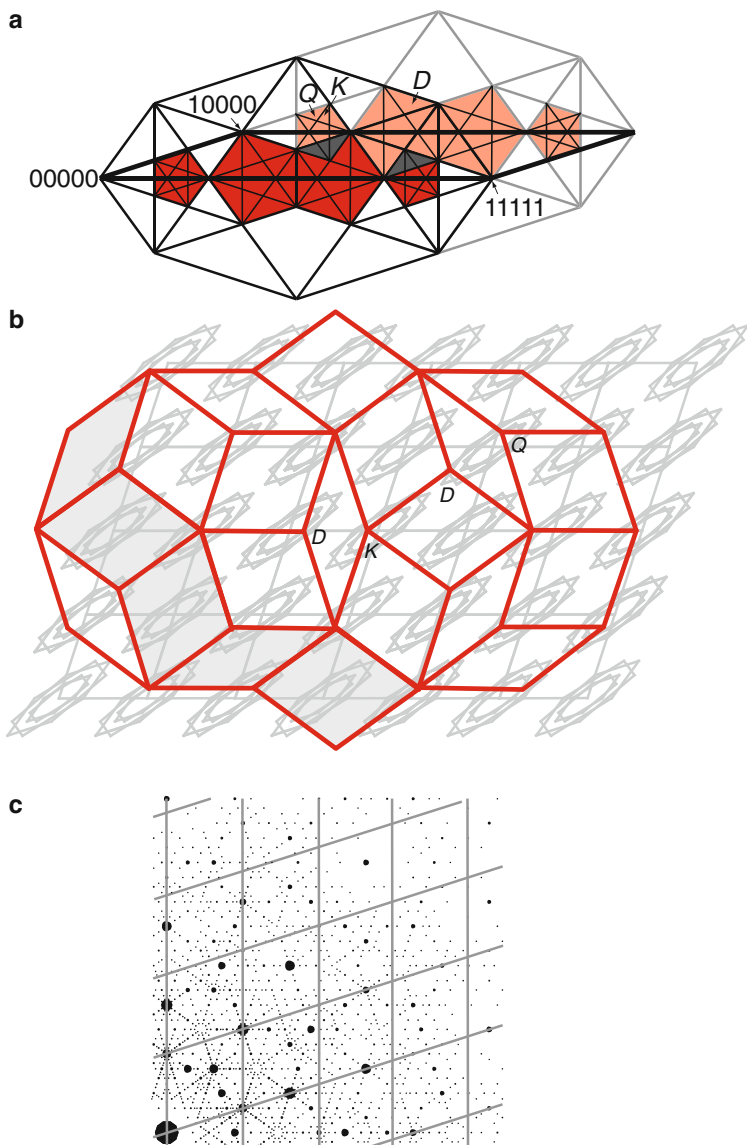
Fig. 3.38. (**a**) Perp-space projection of two unit cells of the PT related by the vector $(10000)_D$. The thick line marks one unit cell of the structure that is mapped into one averaged atomic surface by oblique projection. The overlapping regions of the atomic surfaces of type D, K, and Q are marked dark gray. (**b**) PT overlaid by its PAS. Every vertex of the PT is located inside a projected atomic surface. The vertices marked D and Q, generated from the dark gray regions in (**a**), share one projected atomic surface. Each fat unit tile along the shaded worm (lane of tiles) contains one empty projected atomic surface. (**c**) Schematical diffraction pattern of the PT with reciprocal lattice of the PAS drawn in. The main reflections are located on the lattice nodes [45]

The reciprocal lattice of the average structure is spanned by the vectors

$$
\mathbf{a}_1^{*\mathrm{av}} = a^*\sqrt{3-\tau}\begin{pmatrix} \cos\frac{\pi}{10} \\ -\sin\frac{\pi}{10} \\ 0 \end{pmatrix}_V \;,\quad
\mathbf{a}_2^{*\mathrm{av}} = a^*\sqrt{3-\tau}\begin{pmatrix} 0 \\ 1 \\ 0 \end{pmatrix}_V \;,\quad
\mathbf{a}_3^{*\mathrm{av}} = \mathbf{a}_3^*.
$$
(3.146)

In case of the monoclinic lattice, all reflections of type $\mathbf{H} = (h_1\,h_2\,h_3)_{\mathrm{av}} = (0\,h_2\,-(h_1+h_2)\,h_1\,h_3)_D$ are main reflections (all others are satellite reflections) according to

$$
\begin{pmatrix} 0 \\ h_2 \\ -(h_1+h_2) \\ h_1 \\ h_3 \end{pmatrix}_D =
\begin{pmatrix} 0 & 0 & 0 \\ 0 & 1 & 0 \\ -1 & -1 & 0 \\ 1 & 0 & 0 \\ 0 & 0 & 1 \end{pmatrix}_D
\begin{pmatrix} h_1 \\ h_2 \\ h_3 \end{pmatrix}_{\mathrm{av}} .
$$
(3.147)

The weight of the PAS relative to that of the actual QC structure can be estimated by the ratio of the integrated intensity of main reflections to all reflections (see Fig. 3.38). For realistic conditions, it amounts to 12.6% in the zero-layer with $h_5 = 0$ (X-ray diffraction, all vertices of the PT decorated with Al atoms, $a_r = 4\,\text{Å}$, isotropic ADP $B = 1\,\text{Å}^2$, $0 \le \sin\theta/\lambda \le 1\,\text{Å}^{-1}$, $-13 \le h_i \le 13, i = 0,\ldots,4$ with $h_0 = -(h_1+h_2+h_3+h_4)$; 182 972 reflections within 14 orders of magnitude). If the fact that at the same time this average structure is virtually present at five different orientations is taken into account, the weight increases to 37.5%.

Since there are always five symmetrically equivalent ways of oblique projection, each vertex of the PT must lie at the intersection point of the five projected images of the respective atomic surface where the vertex is resulting from by a par-space cut (Fig. 3.39). This intersection point is located in the barycenter of the lattice nodes $L_0\ldots L_4$ of the five monoclinic PAS lattices, the union of which we call 5-lattice in the following.

Periodic average structure (PAS) and dual-grid method Each reciprocal lattice vector $\mathbf{H}$ is perpendicular to a set of net planes (lattice planes) of the direct lattice, and its norm is inversely proportional to their distances. The intensity $I(\mathbf{H})$ of the respective Bragg reflection depends on the integrated scattering power of the atoms located on these net planes (atomic planes).

The same is true for nD hypercrystals, resulting from embedding of tilings, where the net planes of the nD lattice are occupied by hyperatoms. The traces of each set of symmetrically equivalent nD net planes, when cut by the par-space, form N-grids, with N the rotational symmetry of the nD lattice. In par-space, the tiling is dual to each N-grid. This is illustrated in Fig. 3.39, on the example of the Penrose tiling.

An N-grid is the superposition of N lattices of a particular PAS. By appropriate oblique projections, the hyperatoms are projected along each net plane giving the projected hyperatoms that form the PAS.
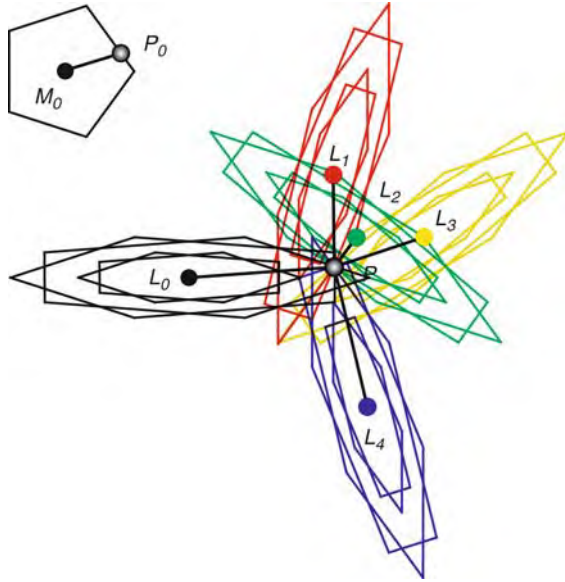
Fig. 3.39. Set of five projected atomic surfaces resulting from the five symmetrically equivalent oblique projections of one atomic surface centered in M_0 (inset upper left). The point P at the edge of the atomic surface generates the tiling vertex P where cut by par-space. P is located in the barycenter of the lattice nodes $L_0, \ldots, L_4$ of the five monoclinic PAS lattices

3.6.4.7 Approximant Structures

The symmetry and metrics of rational approximants of 2D decagonal phases with rectangular symmetry have been discussed in detail by [31], and for some concrete 3D approximants by [52] and [7]. However, the authors use different approaches. In the sequel we will derive the shear matrix on the settings and nomenclature introduced in Sect. 3.5.3.6. According to the group-subgroup symmetry relationship between a quasicrystal and its rational approximants, the approximants of the decagonal phase may exhibit orthorhombic, monoclinic or triclinic symmetry. Since only orthorhombic rational approximants of the decagonal phase have been observed so far, we will focus on that special case. Preserving two mirror planes orthogonal to each other allows only matrix coefficients A_{41} and A_{53} besides the diagonal coefficients $A_{ii} = 1, i = 1, \ldots, 5$ in the shear matrix (3.7) to differ from zero. The action of the shear matrix is to deform the 5D lattice in a way to bring two selected lattice vectors into the par-space. If we define these lattice vectors along two orthogonal directions (P- and D-direction, respectively (Fig. 3.40), according to
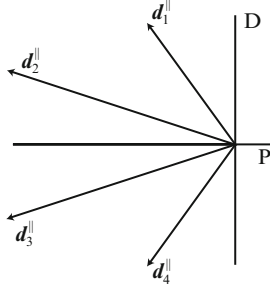
Fig. 3.40. Basis vectors in direct par-space of a decagonal QC. Pairwise combination defines the P and D direction

$$\mathbf{r}_P = -\{p(\mathbf{d}_2 + \mathbf{d}_3) + q(\mathbf{d}_1 + \mathbf{d}_4)\} = \frac{2(3-\tau)}{5a^*} \begin{pmatrix} \tau^2 p + q \\ 0 \\ 0 \\ p + \tau^2 q \\ 0 \end{pmatrix}_V \qquad (3.148)$$

and

$$\mathbf{r}_D = \{r(\mathbf{d}_1 - \mathbf{d}_4) + s(\mathbf{d}_2 - \mathbf{d}_3)\} = \frac{2\sqrt{3-\tau}}{5a^*} \begin{pmatrix} 0 \\ \tau r + s \\ 0 \\ 0 \\ -r + \tau s \end{pmatrix}_V$$

with $p, q, r, s \in Z$ the $mm2$ point group symmetry is retained.

From the condition that the perp-space components of the approximant basis vectors have to vanish

$$\pi^\perp(\mathbf{r}_P) = \pi^\perp(-\{p(\mathbf{d}_2 + \mathbf{d}_3) + q(\mathbf{d}_1 + \mathbf{d}_4)\}) = \mathbf{0} \qquad (3.149)$$

$$\pi^\perp(\mathbf{r}_D) = \pi^\perp(\{r(\mathbf{d}_1 - \mathbf{d}_4) + s(\mathbf{d}_2 - \mathbf{d}_3)\}) = \mathbf{0} \qquad (3.150)$$

we obtain with (3.123)

$$\frac{2(3-\tau)}{5a^*} \begin{pmatrix} 1 & 0 & 0 & 0 & 0 \\ 0 & 1 & 0 & 0 & 0 \\ 0 & 0 & 1 & 0 & 0 \\ A_{41} & 0 & 0 & 1 & 0 \\ 0 & A_{52} & 0 & 0 & 1 \end{pmatrix}_V \begin{pmatrix} \tau^2 p + q \\ 0 \\ 0 \\ p + \tau^2 q \\ 0 \end{pmatrix}_V =$$

$$\frac{2(3-\tau)}{5a^*} \begin{pmatrix} \tau^2 p + q \\ 0 \\ 0 \\ A_{41}(\tau^2 p + q) + p + \tau^2 q \\ 0 \end{pmatrix}_V \stackrel{!}{=} \frac{2(3-\tau)}{5a^*} \begin{pmatrix} \tau^2 p + q \\ 0 \\ 0 \\ 0 \\ 0 \end{pmatrix}_V \qquad (3.151)$$

and

$$\frac{2\sqrt{3-\tau}}{5a^*}\begin{pmatrix} 1 & 0 & 0 & 0 & 0 \\ 0 & 1 & 0 & 0 & 0 \\ 0 & 0 & 1 & 0 & 0 \\ A_{41} & 0 & 0 & 1 & 0 \\ 0 & A_{52} & 0 & 0 & 1 \end{pmatrix}_V \begin{pmatrix} 0 \\ \tau r + s \\ 0 \\ 0 \\ -r + \tau s \end{pmatrix}_V =$$

$$\frac{2\sqrt{3-\tau}}{5a^*}\begin{pmatrix} 0 \\ \tau r + s \\ 0 \\ 0 \\ A_{52}\,(\tau r + s) - r + \tau s \end{pmatrix}_V \stackrel{!}{=} \frac{2\sqrt{3-\tau}}{5a^*}\begin{pmatrix} 0 \\ \tau r + s \\ 0 \\ 0 \\ 0 \end{pmatrix}_V . \quad (3.152)$$

Therefrom, the coefficients A_{41} and A_{52} result to

$$A_{41} = -\frac{p + \tau^2 q}{\tau^2 p + q}, \quad A_{52} = \frac{r - \tau s}{\tau r + s} \quad (3.153)$$

and the basis vectors spanning the unit cell of the $\langle p/q, r/s\rangle$-approximant are given by

$$\mathbf{a}_1^{\mathrm{Ap}} = \pi^{\|}(\mathbf{r}_P) = \frac{2\,(3-\tau)}{5a^*}\begin{pmatrix} \tau^2 p + q \\ 0 \\ 0 \end{pmatrix}_V,$$

$$\mathbf{a}_2^{\mathrm{Ap}} = \pi^{\|}(\mathbf{r}_D) = \frac{2\sqrt{3-\tau}}{5a^*}\begin{pmatrix} 0 \\ \tau r + s \\ 0 \end{pmatrix}_V,$$

$$\mathbf{a}_3^{\mathrm{Ap}} = \pi^{\|}(\mathbf{d}_5) = \frac{1}{a_5^*}\begin{pmatrix} 0 \\ 0 \\ 1 \end{pmatrix}_V . \quad (3.154)$$

For the most common approximants the coefficients p, q, r, s correspond to Fibonacci numbers F_n defined as

$$F_{n+1} = F_n + F_{n-1}, \quad F_0 = 0, \; F_1 = 1 . \quad (3.155)$$

If we set $p = F_{n+2}, q = -F_n, r = F_{n'+1}, s = F_{n'}$ then we obtain the $\langle -F_{n+2}/F_n, F_{n'+1}/\,F_{n'}\rangle$- or, for short, n/n'-approximants (Fig. 3.41) with lattice parameters

$$\left|\mathbf{a}_1^{\mathrm{Ap}}\right| = \frac{2\,(3-\tau)}{5a^*}\tau^{n+2} = a_r\,(3-\tau)\,\tau^n,$$

$$\left|\mathbf{a}_2^{\mathrm{Ap}}\right| = \frac{2\sqrt{3-\tau}}{5a^*}\tau^{n'+1} = a_r\sqrt{3-\tau}\tau^{n'-1}, \quad \left|\mathbf{a}_3^{\mathrm{Ap}}\right| = \frac{1}{a_5^*} \quad (3.156)$$
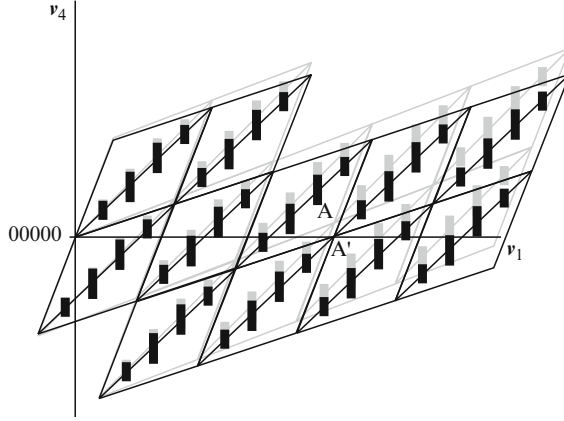
Fig. 3.41. Characteristic $[10010]_V$ section of the Penrose tiling (light gray) superimposed on its rational approximant (black) with $p = 3, q = -1$. The lattice point A is mapped upon A$'$ by shearing the 5D lattice

using the equality $\tau F_{n+1} + F_n = \tau^{n+1}$ and $a_r = 2\tau^2/(5a^*)$. The approximants of this type are centered orthorhombic if $n \bmod 3 = (n' + 1) \bmod 3$. In this case, not only $\mathbf{r}_P$ and $\mathbf{r}_D$ are lattice vectors but also $(\mathbf{r}_P + \mathbf{r}_D)/2$ as shown by [7].

All Bragg peaks are shifted according to (3.8). Projecting the 5D reciprocal space onto par-space results in a periodic reciprocal lattice. All reflections $\mathbf{H} = (h_1 h_2 h_3 h_4 h_5)$ are transformed to $\mathbf{H}^{\mathrm{Ap}} = (h_1^{\mathrm{Ap}} \, h_2^{\mathrm{Ap}} \, h_3^{\mathrm{Ap}})$ with

$$(h_1^{\mathrm{Ap}} \, h_2^{\mathrm{Ap}} \, h_3^{\mathrm{Ap}}) = ([-p(h_2 + h_3) - q(h_1 + h_4)] \; [r(h_1 - h_4) + s(h_2 - h_3)] \; h_5).$$

3.6.4.8 Example: Periodic Average Structure of a Pentagon Tiling

In the following, we derive the PAS of a 2D decagonal pentagon tiling generated from a 4D hyperlattice, which is decorated by one decagonal atomic surface at the origin of each unit cell (Fig. 3.42). The tiling as well as the size and partitioning of the atomic surface correspond to the case $\mathrm{DT}_1/\mathrm{VT}_1$ according to [30].

The 4D basis is given by

$$\mathbf{d}_i = \frac{2}{5a^*} \begin{pmatrix} \cos\frac{(2i-1)\pi}{5} - 1 \\ \sin\frac{(2i-1)\pi}{5} \\ \cos\frac{(6i-1)\pi}{5} - 1 \\ \sin\frac{(6i-1)\pi}{5} \end{pmatrix}_V, \quad i = 1, \ldots, 4. \tag{3.157}$$
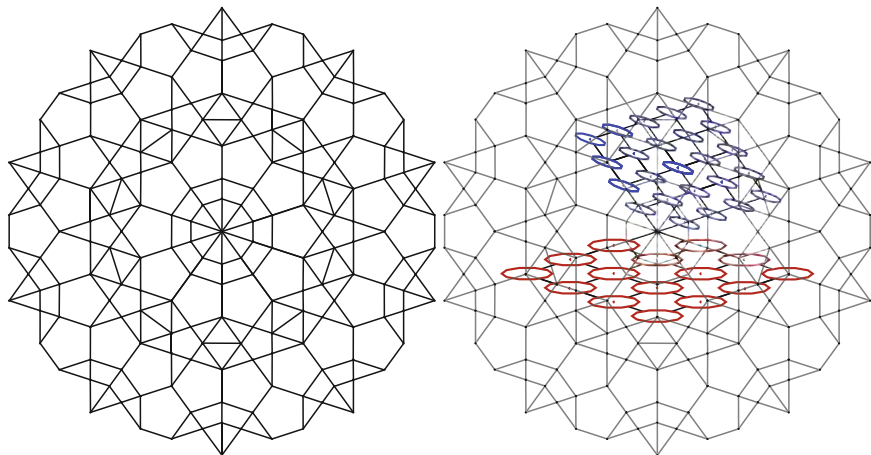
Fig. 3.42. The pentagon tiling consists of copies of five different kinds of Delone tiles. A small and a large pentagon, an equilateral and an isosceles triangle, and a trapezoid. On the right side, the tiling is overlaid with two different PAS. The decagonal atomic surfaces have been distorted in the oblique projection. The upper (online: blue) PAS has an occupancy factor of 0.9102, the lower (online: red) PAS of 1.4727

If we set for simplicity $a^* = 2/5$, then the atomic surface is defined by the vectors

$$\mathbf{a}_i^{AS} = \gamma \frac{-\sqrt{5 - \sqrt{5}} + \sqrt{5 + \sqrt{5}}}{\sqrt{2}} \begin{pmatrix} 0 \\ 0 \\ \cos \frac{i\pi}{5} \\ \sin \frac{i\pi}{5} \end{pmatrix}_V, \quad i = 1, \ldots, 10. \qquad (3.158)$$

with $1 < \gamma < \tau(\tau + 2)/5$. A tiling generated with $\gamma = 1.117$ is depicted in Fig. 3.42. It is constituted of copies of five different kinds of Delone tiles: a small and a large pentagon, an equilateral and an isosceles triangle, and a trapezoid.

Among all possible PAS resulting from strong Bragg peaks that have been investigated (denoted by the letters a–f in Fig. 3.43), the most significant one is based on the reflections $000\bar{1}$ and $00\bar{1}0$. In this PAS (black (online: blue) grid in Fig. 3.43, upper (online: blue) PAS in Fig. 3.42), only 9% or all projected atomic surfaces are not occupied by tiling vertices. The PAS resulting from other symmetrically equivalent reflections, defining the thick outlined gray (online:red) grid in Fig. 3.43, has a much large occupancy factor of 1.4727 (lower (online: red) PAS in Fig. 3.42).
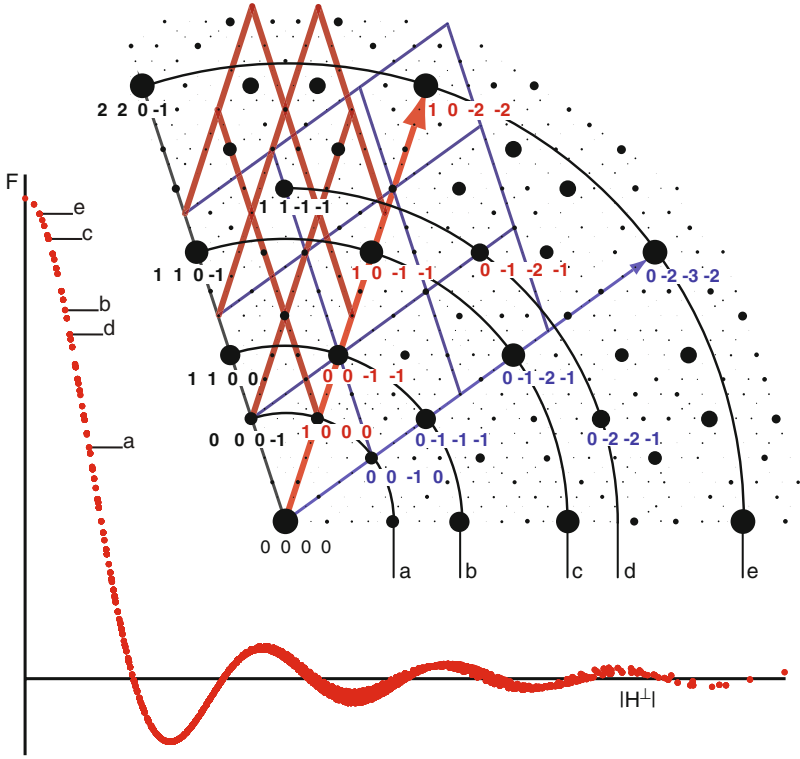
Fig. 3.43. Structure factors of the decagonal pentagon tiling as a function of $|\mathbf{H}^{\perp}|$ (*lower left part*) and diffraction pattern in par-space (*upper right part*). The absolute value of $F(|\mathbf{H}^{\perp}|)$ decreases with increasing $|\mathbf{H}^{\perp}|$ and oscillates around zero. There is only one branch as expected for a atomic surface positioned on the origin of the hypercrystal structure. On the diffraction pattern, reflections are denoted that have been chosen to create PAS. Symmetrically equivalent reflections are marked by letters a–f. For a, the linear combinations of two chosen reflections are shown as grids (online: red and blue). Reflections on these grids lie on the corresponding cut-planes in nD reciprocal space

3.6.5 Dodecagonal Structures

Axial quasicrystals with dodecagonal diffraction symmetry possess dodecagonal structures. There is only a small number of examples known, most of them are metastable. The embedding matrix can be derived from the reducible representation $\Gamma(\alpha)$ of the 12-fold rotation, $\alpha = 12$, which can be written as 5×5 matrix with integer coefficients acting on the reciprocal space vectors $\mathbf{H}$. The 5D representation can be composed from the irreducible representations Γ_5, Γ_1, and Γ_9 shown in the character table below (Table 3.15).

Table 3.15. Character table for the dodecagonal group $12mm$ (C_12v) [20]. ε denotes the identity operation, α^n the rotation around $2n\pi/12$, and β, β' the reflection on mirror planes

Elements	ε	α	α^2	α^3	α^4	α^5	α^6	β	β'
Γ_1	1	1	1	1	1	1	1	1	1
Γ_2	1	1	1	1	1	1	1	-1	-1
Γ_3	1	-1	1	-1	1	-1	1	1	-1
Γ_4	1	-1	1	-1	1	-1	1	-1	1
Γ_5	2	$\sqrt{3}$	1	0	-1	$-\sqrt{3}$	-2	0	0
Γ_6	2	1	-1	-2	-1	1	2	0	0
Γ_7	2	0	-2	0	2	0	-2	0	0
Γ_8	2	-1	-1	2	-1	-1	2	0	0
Γ_9	2	$-\sqrt{3}$	1	0	-1	$\sqrt{3}$	-2	0	0

The 12-fold rotation α can be described in its action by the reducible matrix

$$\Gamma(12) = \begin{pmatrix} 0\ 0\ 0\ \bar{1}\ 0 \\ 1\ 0\ 0\ 0\ 0 \\ 0\ 1\ 0\ 1\ 0 \\ 0\ 0\ 1\ 0\ 0 \\ 0\ 0\ 0\ 0\ 1 \end{pmatrix}_D \tag{3.159}$$

with trace 1. If we consider this rotation taking place in 5D space (D-basis) then we can also represent it on a Cartesian basis (V-basis). By this transformation the trace must not change. Since the characters correspond to the traces of the respective symmetry matrices we can identify the character $\Gamma_5(\alpha) = \sqrt{3}$ and $\Gamma_9(\alpha) = -\sqrt{3}$ as traces of the symmetry matrices

$$\begin{pmatrix} \cos\frac{2\pi}{12} & -\sin\frac{2\pi}{12} \\ \sin\frac{2\pi}{12} & \cos\frac{2\pi}{12} \end{pmatrix}_V = \frac{1}{2}\begin{pmatrix} \sqrt{3} & -1 \\ 1 & \sqrt{3} \end{pmatrix}_V, \quad \begin{pmatrix} \cos\frac{10\pi}{12} & -\sin\frac{10\pi}{12} \\ \sin\frac{10\pi}{12} & \cos\frac{10\pi}{12} \end{pmatrix}_V = \frac{1}{2}\begin{pmatrix} -\sqrt{3} & -1 \\ 1 & -\sqrt{3} \end{pmatrix}_V . \tag{3.160}$$

Consequently, in 5D space the then irreducible integer representation of $\Gamma(\alpha)$ in (3.159) can be composed of the two 2D representations $\Gamma_5(\alpha)$ and $\Gamma_9(\alpha)$ plus, for the periodic direction, $\Gamma_1(\alpha)$

$$\Gamma(12) = \begin{pmatrix} 0\ 0\ 0\ \bar{1}\ 0 \\ 1\ 0\ 0\ 0\ 0 \\ 0\ 1\ 0\ 1\ 0 \\ 0\ 0\ 1\ 0\ 0 \\ 0\ 0\ 0\ 0\ 1 \end{pmatrix}_D = \left(\begin{array}{ccc|c|cc} \frac{\sqrt{3}}{2} & -\frac{1}{2} & 0 & 0 & 0 \\ \frac{1}{2} & \frac{\sqrt{3}}{2} & 0 & 0 & 0 \\ \hline 0 & 0 & 1 & 0 & 0 \\ \hline 0 & 0 & 0 & -\frac{\sqrt{3}}{2} & -\frac{1}{2} \\ 0 & 0 & 0 & \frac{1}{2} & -\frac{\sqrt{3}}{2} \end{array}\right)_V = \left(\begin{array}{c|c|c} \Gamma_5(12) & 0 & 0 \\ \hline 0 & \Gamma_1(12) & 0 \\ \hline 0 & 0 & \Gamma_9(12) \end{array}\right)_V \tag{3.161}$$

This gives a coupling factor 5 for the components of the 12-fold rotation in perp-space and allows the definition of a suitable basis in reciprocal space.

3.6.5.1 Reciprocal Space

The electron density distribution function $\rho(\mathbf{r})$ of a 3D quasicrystal can be represented by the Fourier series given in (3.41). All Fourier coefficients, i.e., the structure factors $F(\mathbf{H})$, can be integer indexed based on four reciprocal basis vectors: $\mathbf{H} = \sum_{i=1}^{4} h_i \mathbf{a}_i^*$ with $\mathbf{a}_i^* = a^* \left(\cos 2\pi i/12, \sin 2\pi i/12, 0 \right),\ i = 1, \ldots, 4,$ $a^* = |\mathbf{a}_1^*| = |\mathbf{a}_2^*| = |\mathbf{a}_3^*| = |\mathbf{a}_4^*|, \mathbf{a}_5^* = |\mathbf{a}_5^*| (0, 0, 1)$ and $h_i \in \mathbb{Z}$ (Fig. 3.44).

The vector components refer to a Cartesian coordinate system in par-space $V^{\parallel}$. The set of all diffraction vectors $\mathbf{H}$ forms a $\mathbb{Z}$-module M^* of rank five. The vectors $\mathbf{a}_i^*,\ i = 1, \ldots, 5$ can be considered as par-space projections of the basis vectors $\mathbf{d}_i^*,\ i = 1, \ldots, 5$ of the 5D reciprocal lattice Σ^* with

$$\mathbf{d}_i^* = a^* \begin{pmatrix} \cos \frac{2\pi i}{12} \\ \sin \frac{2\pi i}{12} \\ 0 \\ c \cos \frac{10\pi i}{2} \\ c \sin \frac{10\pi i}{12} \end{pmatrix}_V , \quad i = 1, \ldots, 4; \quad \mathbf{d}_5^* = a_5^* \begin{pmatrix} 0 \\ 0 \\ 1 \\ 0 \\ 0 \end{pmatrix}_V . \quad (3.162)$$

The coupling factor between par- and perp-space rotations equals 5, c is an arbitrary constant which is usually set to 1 (as it is also done in the following). The embedding matrix W (3.4) results to
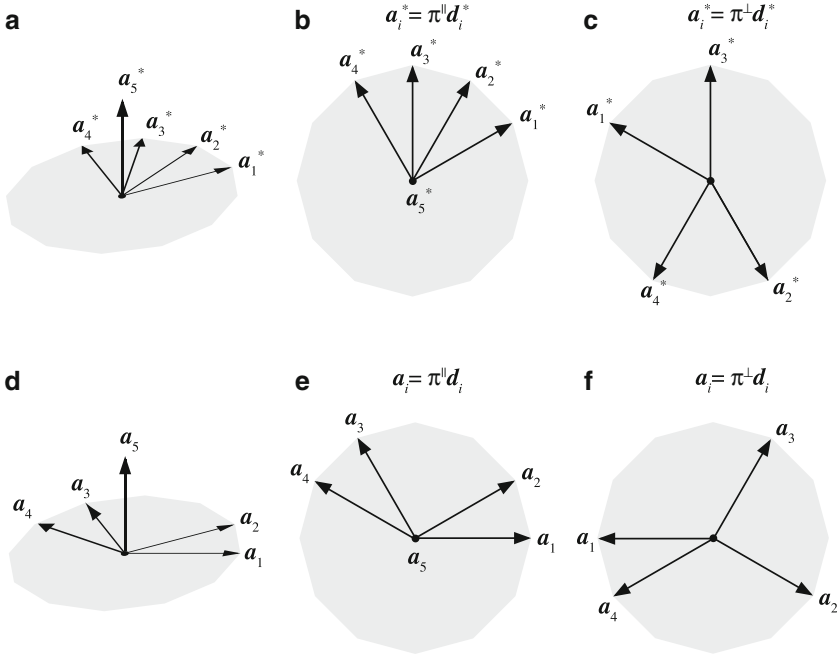
Fig. 3.44. 5D reciprocal and direct space bases $\mathbf{d}_i^*, \mathbf{d}_i, i = 1, \ldots, 5$ projected onto the (**a, b, d, e**) par- and (**c, f**) perp-space

$$
W = \begin{pmatrix}
\cos\frac{2\pi}{12} & \cos\frac{4\pi}{12} & \cos\frac{6\pi}{12} & \cos\frac{8\pi}{12} & 0 \\
\sin\frac{2\pi}{12} & \sin\frac{4\pi}{12} & \sin\frac{6\pi}{12} & \sin\frac{8\pi}{12} & 0 \\
0 & 0 & 0 & 0 & 1 \\
\cos\frac{10\pi}{12} & \cos\frac{8\pi}{12} & \cos\frac{6\pi}{12} & \cos\frac{16\pi}{12} & 0 \\
\sin\frac{10\pi}{12} & \sin\frac{8\pi}{12} & \sin\frac{6\pi}{12} & \sin\frac{16\pi}{12} & 0
\end{pmatrix}
= \begin{pmatrix}
\frac{\sqrt{3}}{2} & \frac{1}{2} & 0 & -\frac{1}{2} & 0 \\
\frac{1}{2} & \frac{\sqrt{3}}{2} & 1 & \frac{\sqrt{3}}{2} & 0 \\
0 & 0 & 0 & 0 & 1 \\
-\frac{\sqrt{3}}{2} & \frac{1}{2} & 0 & -\frac{1}{2} & 0 \\
\frac{1}{2} & -\frac{\sqrt{3}}{2} & 1 & -\frac{\sqrt{3}}{2} & 0
\end{pmatrix}.
$$

$$(3.163)$$

The direct 5D basis is obtained from the orthogonality condition (3.5)

$$
\mathbf{d}_i = \frac{1}{\sqrt{3}a_i^*}\begin{pmatrix}
\cos\frac{2\pi(i-1)}{12} \\
\sin\frac{2\pi(i-1)}{12} \\
0 \\
\cos\frac{2\pi(5i+1)}{12} \\
\sin\frac{2\pi(5i+1)}{12}
\end{pmatrix}_V, \quad i = 1,2; \quad
\mathbf{d}_i = \frac{1}{\sqrt{3}a_i^*}\begin{pmatrix}
\cos\frac{2\pi(i+1)}{12} \\
\sin\frac{2\pi(i+1)}{12} \\
0 \\
\cos\frac{2\pi(5i+11)}{12} \\
\sin\frac{2\pi(5i+11)}{12}
\end{pmatrix}_V,
$$

$$
i = 3,4, \quad \mathbf{d}_5 = \frac{1}{a_5^*}\begin{pmatrix} 0 \\ 0 \\ 1 \\ 0 \\ 0 \end{pmatrix}_V. \tag{3.164}
$$

The metric tensors G and G^* are of type

$$
\begin{pmatrix}
A & 0 & B & 0 & 0 \\
0 & A & 0 & B & 0 \\
B & 0 & A & 0 & 0 \\
0 & B & 0 & A & 0 \\
0 & 0 & 0 & 0 & C
\end{pmatrix} \tag{3.165}
$$

with $A = 2a_1^{*2}$, $B = a_1^{*2}$, $C = a_5^{*2}$ for reciprocal space and $A = 2/3a_1^{*2}$, $B = -1/3a_1^{*2}$, $C = -1/a_5^{*2}$ for direct space. Therefrom, the direct and reciprocal lattice parameters can be derived as

$$
d_i^* = \sqrt{2}a_1^*, \quad d_5^* = a_5^*, \quad \alpha_{ij} = 60°, \quad \alpha_{i5} = 90°, \ i,j = 1,\ldots,4 \tag{3.166}
$$

and

$$
d_i = \frac{\sqrt{2}}{\sqrt{3}a^*}, \ i,j = 1,\ldots,4, \quad d_5 = \frac{1}{a_5^*}, \quad \alpha_{ij} = 120°, \quad \alpha_{i5} = 90°, \ i,j = 1,\ldots,4. \tag{3.167}
$$

This means that the unit cell has hyperhexagonal symmetry and the 4D subspace orthogonal to the periodic direction is hyperrhombohedral. The volume of the 5D unit cell results to

$$
V = \sqrt{\det(\mathsf{G})} = \frac{1}{3a^{*4}a_5^*}. \tag{3.168}
$$
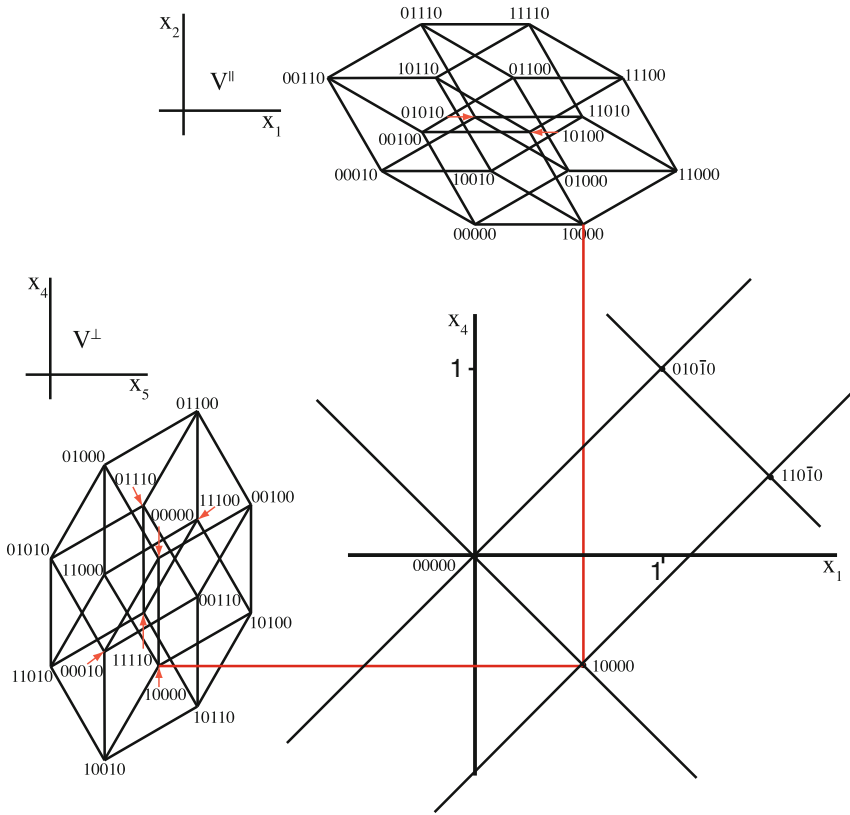
Fig. 3.45. Characteristic (x_100x_40) section through the 5D unit cell together with its projections onto par- and perp-space. The 16 corners of the unit cell are indexed on the D-basis

A characteristic section through the 5D unit cell together with its projections onto par- and perp-space is shown in Fig. 3.45.

3.6.5.2 Symmetry

The diffraction symmetry of dodecagonal phases, i.e., the point symmetry group leaving the intensity weighted Fourier module (diffraction pattern) M_I^* invariant, is one of the two Laue groups $12/mmm$ or $12/m$. The 15 space groups [36] leaving the 5D hypercrystal structure invariant are that subset of the 5D space groups, the point groups of which are isomorphous to the seven 3D dodecagonal point groups (Table 3.16).

The orientation of the symmetry elements of the 5D space groups is defined by the isomorphism of the 3D and 5D point groups. The 12-fold axis defines the unique direction $[00100]_V$ or $[00001]_D$, which is the periodic direction. There are two different orientations of mirror planes and dihedral axes possible with

Table 3.16. The seven 3D dodecagonal point groups of order k and the fifteen corresponding 5D dodecagonal space groups with reflection conditions [36]. The notation is analogous to that of hexagonal space groups. The first position in the point and space group symbols refers to generating symmetry elements oriented along the periodic direction, the second position to the symmetry elements oriented along reciprocal space basis vectors and the third position to those oriented between them

3D Point Group	k	5D Space Group	Reflection Conditions
$\dfrac{12}{m}\dfrac{2}{m}\dfrac{2}{m}$	48	$P\dfrac{12}{m}\dfrac{2}{m}\dfrac{2}{m}$	No condition
		$P\dfrac{12_6}{m}\dfrac{2}{c}\dfrac{2}{m}$	One of the two families of mirror lines in odd layers extinct
		$P\dfrac{12}{m}\dfrac{2}{c}\dfrac{2}{c}$	Both families of mirror lines in odd layers extinct
$\dfrac{12}{m}$	24	$P\dfrac{12}{m}$	No condition
		$P\dfrac{12_6}{m}$	$0000h_6 : h_6 = 2n$
$\overline{12}\,2m$	24	$P\overline{12}\,2m$	No condition
		$P\overline{12}\,2c$	Mirror lines in odd layers extinct
$12mm$	24	$P12mm$	No condition
		$P12_6cm$	One of the two families of mirror lines in odd layers extinct
		$P12cc$	Both families of mirror lines in odd layers extinct
1222	24	$P1222$	No condition
		$P12_j22$	$0000h_j : jh_6 = 12n$
$\overline{12}$	12	$P\overline{12}$	No condition
12	12	$P12$	No condition
		$P12_j$	$0000h_j : jh_6 = 12n$

respect to the phys-space star of reciprocal basis vectors. If the normal to the mirror plane, or the dihedral axis, is oriented along a reciprocal basis vector it gets the symbol m, or d, and it is denoted "along", otherwise it is "between" and the symbols get primed, m' and d'. Examples for the action of these two types of mirror planes are shown in eqs. 3.113 and 3.113. The normal to the mirror plane m_2 is along to $\mathbf{a}_2^*$, that of m_{12} is between $\mathbf{a}_1^*$ and $\mathbf{a}_2^*$.

The reflection and inversion operations are equivalent in both subspaces $V^{\parallel}$ and $V^{\perp}$. $\Gamma(12)$, a $2\pi/12$ rotation in $V^{\parallel}$ around the 12-fold axis corresponds

to a $10\pi/12$ rotation in $V^\perp$ (see Fig. 3.44):

$$\Gamma(m_2) = \begin{pmatrix} 0 & 0 & \bar{1} & 0 & 0 \\ 0 & \bar{1} & 0 & \bar{1} & 0 \\ \bar{1} & 0 & 0 & 0 & 0 \\ 0 & 0 & 0 & 1 & 0 \\ 0 & 0 & 0 & 0 & 1 \end{pmatrix}_{D^*} = \left(\begin{array}{ccc|cc} \frac{1}{2} & -\frac{\sqrt{3}}{2} & 0 & 0 & 0 \\ -\frac{\sqrt{3}}{2} & -\frac{1}{2} & 0 & 0 & 0 \\ 0 & 0 & 1 & 0 & 0 \\ \hline 0 & 0 & 0 & \frac{1}{2} & \frac{\sqrt{3}}{2} \\ 0 & 0 & 0 & \frac{\sqrt{3}}{2} & -\frac{1}{2} \end{array} \right)_V \tag{3.169}$$

$$\Gamma(m_{12}) = \begin{pmatrix} 0 & \bar{1} & 0 & 1 & 0 \\ \bar{1} & 0 & \bar{1} & 0 & 0 \\ 0 & 0 & 0 & \bar{1} & 0 \\ 0 & 0 & 1 & 0 & 0 \\ 0 & 0 & 0 & 0 & 1 \end{pmatrix}_{D^*} = \left(\begin{array}{ccc|cc} -\frac{\sqrt{3}}{2} & -\frac{1}{2} & 0 & -\frac{\sqrt{3}}{2} & -\frac{1}{2} \\ -\frac{1}{2} & -\frac{1}{2\sqrt{3}} & 0 & \frac{1}{2} & \frac{1}{2\sqrt{3}} \\ 0 & 0 & 1 & 0 & 0 \\ \hline \frac{\sqrt{3}}{2} & -\frac{1}{2} & 0 & \frac{\sqrt{3}}{2} & -\frac{1}{2} \\ \frac{1}{2} & -\frac{1}{2\sqrt{3}} & 0 & -\frac{1}{2} & \frac{1}{2\sqrt{3}} \end{array} \right)_V \tag{3.170}$$

The translation components of the 12-fold screw axis and the c-glide planes are along the periodic direction. The set of reciprocal space vectors M^* is invariant under scaling with the matrix S, $S^m M^* = s^m M^*$, with $s = 1 \pm \sqrt{3}$ (Fig. 3.46). The scaling matrix reads
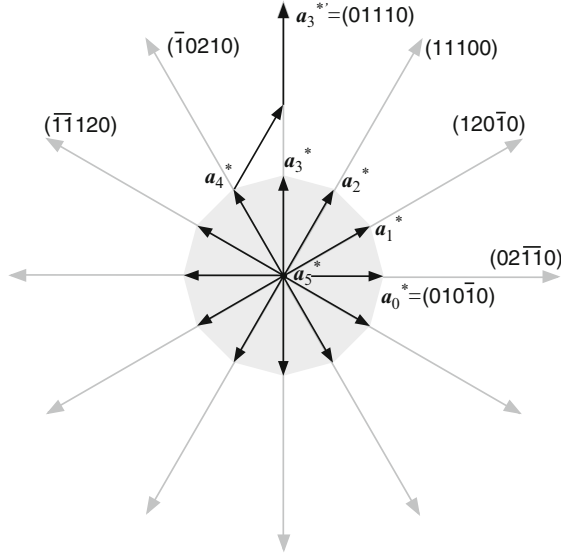
Fig. 3.46. Reciprocal space scaling of the dodecagonal structure by the matrix S. The scaled basis vectors keep their orientation and are increased in length by a factor $1 + 2\cos 2\pi/12 = 1 + \sqrt{3} = 2.7321$ (marked gray). The example shown explicitly is $\mathbf{a}_3^{*'} = \mathbf{a}_4^* + \mathbf{a}_2^* + \mathbf{a}_3^*$

$$
S = \begin{pmatrix} 1 & 1 & 0 & \bar{1} & 0 \\ 2 & 1 & 1 & 0 & 0 \\ 0 & 1 & 1 & 2 & 0 \\ \bar{1} & 0 & 1 & 1 & 0 \\ 0 & 0 & 0 & 0 & 1 \end{pmatrix}_{D^*} = \left(\begin{array}{ccc|cc} 1+\sqrt{3} & 0 & 0 & 0 & 0 \\ 0 & 1+\sqrt{3} & 0 & 0 & 0 \\ 0 & 0 & 1 & 0 & 0 \\ \hline 0 & 0 & 0 & 1-\sqrt{3} & 0 \\ 0 & 0 & 0 & 0 & 1-\sqrt{3} \end{array} \right)_V . \tag{3.171}
$$

3.6.5.3 Example: Periodic Average Structure of a Dodecagonal Tiling

In the canonical description, the V basis for a 2D dodecagonal tiling (Fig. 3.47) in respect to the D basis is given by

$$
V = a^* \frac{1}{\sqrt{3}} \begin{pmatrix} \mathbf{v}_1 \\ \mathbf{w}_1 \\ \mathbf{v}_2 \\ \mathbf{w}_2 \\ \mathbf{v}_3 \\ \mathbf{w}_3 \end{pmatrix}_D = a^* \frac{1}{\sqrt{3}} \begin{pmatrix} 1 & c_1 & -c_2 & -c_3 & c_4 & c_2 \\ 0 & s_1 & -s_2 & -s_3 & s_4 & s_2 \\ 1 & c_5 & c_4 & -c_3 & -c_2 & c_1 \\ 0 & s_5 & s_4 & -s_3 & -s_2 & s_1 \\ \frac{1}{\sqrt{2}} & -\frac{1}{\sqrt{2}} & \frac{1}{\sqrt{2}} & -\frac{1}{\sqrt{2}} & \frac{1}{\sqrt{2}} & -\frac{1}{\sqrt{2}} \\ \frac{1}{\sqrt{2}} & \frac{1}{\sqrt{2}} & \frac{1}{\sqrt{2}} & \frac{1}{\sqrt{2}} & \frac{1}{\sqrt{2}} & \frac{1}{\sqrt{2}} \end{pmatrix}_D \tag{3.172}
$$

Therein, the vectors $\mathbf{v}_1$ and $\mathbf{w}_1$ span the 2D par-space $V^\parallel$, $\mathbf{v}_2$ and $\mathbf{w}_2$ span $V_1^\perp$, and $\mathbf{v}_3$ and $\mathbf{w}_3$ span $V_2^\perp$, with $V = V^\parallel \oplus V^\perp = V^\parallel \oplus V_1^\perp \oplus V_2^\perp$, $c_k = \cos(2\pi k/12)$ and $s = \sin(2\pi k/12)$. The D basis is given by $D = V^{-1}$. The length of the basis vectors D is $1/a^*$. A tiling edge length of 1 is obtained with $a^* = 1/\sqrt{3}$. The acceptance window is given by the orthogonal projection of the hyperlattice unit cell upon perp-space.

The 2D atomic surfaces are given by six equidistant cuts of the window perpendicular to $(1\bar{1}1\bar{1}1\bar{1})_D$ and $(111111)_D$ at $i/6, 1 = 1, \ldots, 6$ along the cell diagonal in direction $\mathbf{v}_3 + \mathbf{w}_3$. For the atomic surfaces and tiling originating from an unshifted acceptance window (window origin at lattice origin), see [39]. Here, we look at a tiling which is generated by an acceptance window positioned with its center at the origin of the hyperlattice. The resulting 2D atomic surfaces are shown in Figs. 3.48 and 3.49. They have a volume in $V_1^\perp$ and are 0D in $V^\parallel$ and $V_2^\perp$.

The best PAS for the dodecagonal tiling is shown in Fig. 3.50. The corresponding reciprocal vectors are $(01\bar{2}\bar{1}00)$ and $(21000\bar{1})$. The unit cell parameter of the centered PAS is 0.9282 and only 7% of the projected atomic surfaces do not contain to tiling vertex. The distribution of vertices is homogenous in each projected atomic surface, and the deviation density adds up with the number of overlapping projected atomic surfaces within their boundaries.

A PAS without centering and with small maximal deviation of the vertices from the PAS nodes is given in Fig. 3.51. Here, all atomic surfaces project onto each other. The corresponding reciprocal vectors are $(01\bar{2}\bar{1}00)$ and $(21000\bar{1})$, the unit cell parameter of the PAS is 0.4641, and the occupancy factor is very small with 0.2679. The symmetry of the atomic surfaces is preserved by the oblique projections in both PASs.
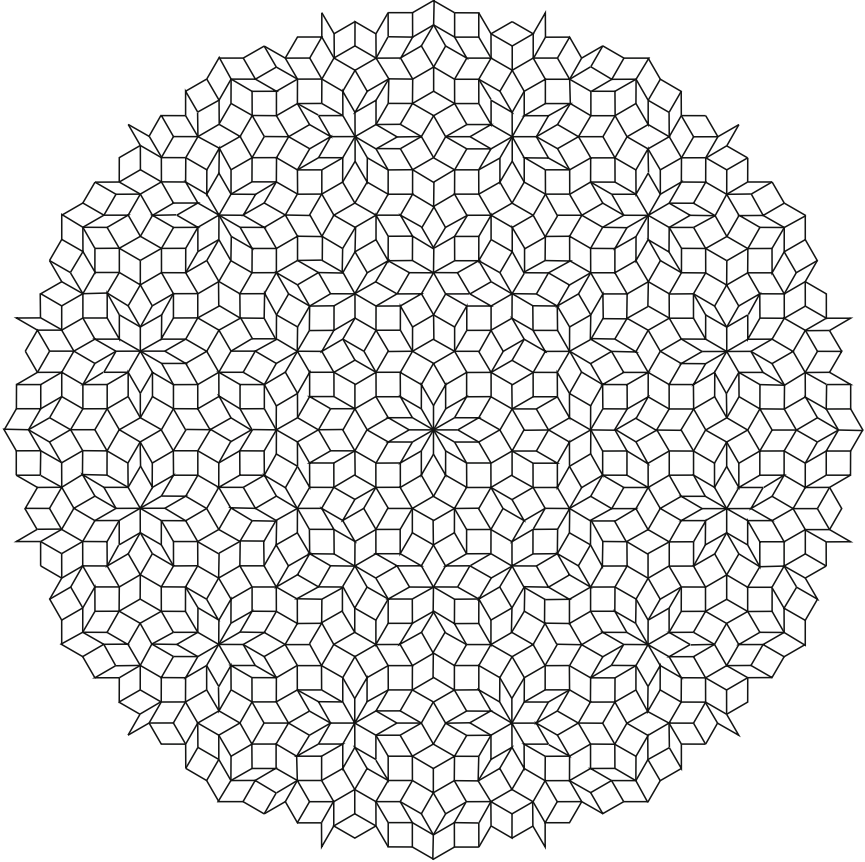
Fig. 3.47. Dodecagonal tiling, as generated by the canonical projection method, with the acceptance window centered at the origin of the nD lattice

3.6.6 Tetrakaidecagonal Structures

Axial quasicrystals with tetrakaidecagonal diffraction symmetry possess tetrakaidecagonal structures. There are only a few approximants known and no quasicrystals so far. To find the embedding matrix one has to consider the generating symmetry operations, i.e., the 14-fold rotation $\alpha = 14$, a mirror m_v and the inversion operation $\bar{1}$. These symmetry operations can be written as 7×7 matrices with integer coefficients acting on the reciprocal space vectors $\mathbf{H}$. The 7D representation is reducible to par- and perp-space components, which can be combined from the irreducible representations $\Gamma_1, \Gamma_7, \Gamma_9$ shown in the character table Table 3.17 under the condition that the trace of the 6D matrix does not change.

For instance, the 14-fold rotation α and the reflections on the mirror planes $\beta = m_2$ (with normal parallel to $\mathbf{a}_2^*$) and $\beta = m_{12}$ (with normal between $\mathbf{a}_1^*$
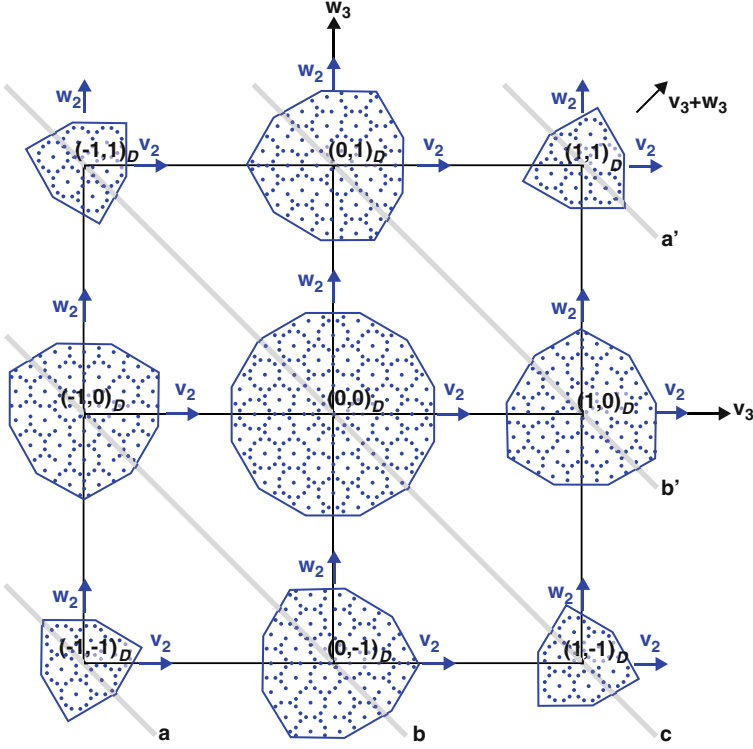
Fig. 3.48. Atomic surfaces (online: *blue*) resulting from cuts of an acceptance window centered at the origin of the hyperlattice. As they have no extension in $V_2^{\perp}$, their positions in this perpendicular subspace are plotted by their occupation of nodes on the black grid spanned by $\mathbf{v}_3$ and $\mathbf{w}_3$. Gray lines connect the atomic surfaces resulting from one cut space perpendicular to $V_2^{\perp}$. The points are lifted vertices of the dodecagonal tiling

and $\mathbf{a}_2^*$) can be described in their action in 3D reciprocal space by the reducible matrices

$$
\Gamma(14) = \begin{pmatrix} 0 & 0 & 0 & 0 & 0 & \bar{1} & 0 \\ 1 & 0 & 0 & 0 & 0 & 1 & 0 \\ 0 & 1 & 0 & 0 & 0 & \bar{1} & 0 \\ 0 & 0 & 1 & 0 & 0 & 1 & 0 \\ 0 & 0 & 0 & 1 & 0 & \bar{1} & 0 \\ 0 & 0 & 0 & 0 & 1 & 1 & 0 \\ 0 & 0 & 0 & 0 & 0 & 0 & 1 \end{pmatrix}_{D^*} \quad, \quad
\Gamma(m_2) = \begin{pmatrix} 0 & 0 & \bar{1} & \bar{1} & 0 & 0 & 0 \\ 0 & \bar{1} & 0 & 1 & 0 & 0 & 0 \\ \bar{1} & 0 & 0 & \bar{1} & 0 & 0 & 0 \\ 0 & 0 & 0 & \bar{1} & 0 & 0 & 0 \\ 0 & 0 & 0 & 1 & 0 & 1 & 0 \\ 0 & 0 & 0 & 0 & 1 & 0 & 0 \\ 0 & 0 & 0 & 0 & 0 & 0 & 1 \end{pmatrix}_{D^*} \quad,
$$

Fig. 3.49. Orthogonal 3D projections of the atomic surfaces upon the subspace spanned by $\mathbf{v}_2, \mathbf{w}_2$, and $\mathbf{v}_3$ (*middle and right part*) and upon the subspace spanned by $\mathbf{v}_2, \mathbf{w}_2$, and $\mathbf{v}_3 + \mathbf{w}_3$ (*on the left*). Each plane on the left part of the figure represents a single cut space (perpendicular to $\mathbf{v}_3$ and $\mathbf{w}_3$) and one set of resulting 2D atomic surfaces

Fig. 3.50. Centered PAS with overlapping projected atomic surfaces. The corresponding reciprocal vectors are $(01\bar{2}\bar{1}00)$ and $(21000\bar{1})$. The unit cell parameter is 0.9282. Only 7% of the PAS nodes do not correspond to a lattice vertex

$$
\Gamma(m_{12}) = \begin{pmatrix}
0 & \bar{1} & \bar{1} & 0 & 0 & 0 & 0 \\
\bar{1} & 0 & 1 & 0 & 0 & 0 & 0 \\
0 & 0 & \bar{1} & 0 & 0 & 0 & 0 \\
0 & 0 & 1 & 0 & 0 & 1 & 0 \\
0 & 0 & \bar{1} & 0 & 1 & 0 & 0 \\
0 & 0 & 1 & 1 & 0 & 0 & 0 \\
0 & 0 & 0 & 0 & 0 & 0 & 1
\end{pmatrix}_{D^*}
\tag{3.173}
$$

Fig. 3.51. PAS with complete overlap of the atomic surfaces belonging to one lattice node and small maximal deviation of the tiling vertices from the PASL. The corresponding reciprocal vectors are $(01\bar{2}\bar{1}00)$ and $(21000\bar{1})$. The unit cell parameter is 0.4641 and the occupancy factor is 0.2679

Table 3.17. Character table for the tetrakaidecagonal group $14mm$ (C_{14v}) [2]. ε denotes the identity operation, α^n the rotation around $n\pi/14$, and β the reflection on a mirror plane

Elements	ε	α, α^{13}	α^2, α^{12}	...	$\beta, \alpha^2\beta$ ...	$\alpha\beta, \alpha^3\beta$ ...
Γ_1	1	1	1		1	1
Γ_2	1	1	1		-1	-1
Γ_3	1	-1	1		1	-1
Γ_4	1	-1	1		-1	1
Γ_5	2	$2\cos 2\pi/14$	$2\cos 4\pi/14$		0	0
Γ_6	2	$2\cos 4\pi/14$	$2\cos 8\pi/14$		0	0
Γ_7	2	$2\cos 6\pi/14$	$2\cos 12\pi/14$		0	0
Γ_8	2	$2\cos 8\pi/14$	$2\cos 16\pi/14$		0	0
Γ_9	2	$2\cos 10\pi/14$	$2\cos 20\pi/14$		0	0
Γ_{10}	2	$2\cos 12\pi/14$	$2\cos 24\pi/14$		0	0

3.6.6.1 Reciprocal Space

The electron density distribution function $\rho(\mathbf{r})$ of a 3D quasicrystal can be represented by the Fourier series given in eq. 3.41. All Fourier coefficients, i.e., the structure factors $F(\mathbf{H})$, can be indexed with reciprocal space vectors $\mathbf{H} = \sum_{i=1}^{3} h_i^{\parallel} \mathbf{a}_i^*$ with $h_1^{\parallel}, h_2^{\parallel} \in \mathbb{R}$, $h_3^{\parallel} \in \mathbb{Z}$. Introducing in total seven reciprocal basis vectors, all possible reciprocal space vectors can be indexed with integer components: $\mathbf{H} = \sum_{i=1}^{7} h_i \mathbf{a}_i^*$ with $\mathbf{a}_i^* = a^* \left(\cos 2\pi i/14, \sin 2\pi i/14, 0\right)$, $i = 1, \ldots, 6, \mathbf{a}_7^* = |\mathbf{a}_7^*| \left(0, 0, 1\right)$ and $h_i \in \mathbb{Z}$ (Fig. 3.52).

a $a_i^*=\pi^{\parallel}d_i^*$ **b** $a_i^*=\pi_1^{\perp}d_i^*$ **c** $a_i^*=\pi_2^{\perp}d_i^*$

$a_i=\pi^{\parallel}d_i$ $a_i=\pi_1^{\perp}d_i$ $a_i=\pi_2^{\perp}d_i$
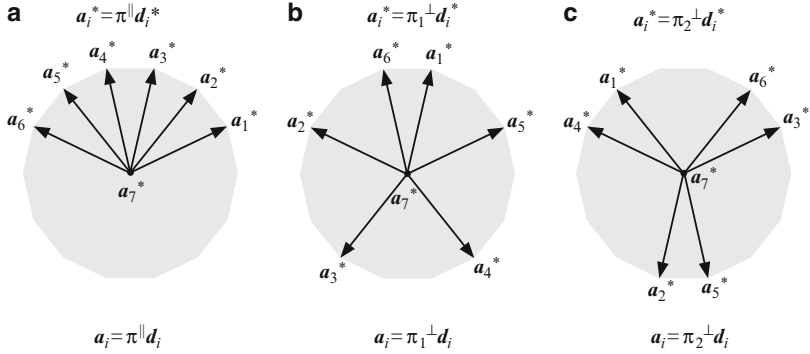
Fig. 3.52. 7D reciprocal (**a**–**c**) and direct (**d**–**f**) space bases $\mathbf{d}_i^*$ and $\mathbf{d}_i$, $i = 1, \ldots, 7$, respectively, of the tetrakaidecagonal structure projected onto the par-space (a,d) and the two 2D perp-subspaces (b,e) and (c,f). The vectors $\mathbf{a}_7^*$ and $\mathbf{a}_7$ along the periodic direction are perpendicular to the plane spanned by the vectors $\mathbf{a}_i^*$, $i = 1, \ldots, 6$ and $\mathbf{a}_i$, $i = 1, \ldots, 6$, respectively

The vector components refer to a Cartesian coordinate system in par-space $V^{\parallel}$. The set of all diffraction vectors $\mathbf{H}$ forms a $\mathbb{Z}$-module M^* of rank seven. The vectors $\mathbf{a}_i^*$, $i = 1, \ldots, 7$ can be considered as par-space projections of the basis vectors $\mathbf{d}_i^*$, $i = 1, \ldots, 7$ of the 7D reciprocal lattice Σ^* with

$$\mathbf{d}_i^* = a^* \begin{pmatrix} \cos\frac{2\pi i}{14} \\ \sin\frac{2\pi i}{14} \\ 0 \\ c\cos\frac{6\pi i}{14} \\ c\sin\frac{6\pi i}{14} \\ c\cos\frac{10\pi i}{14} \\ c\sin\frac{10\pi i}{14} \end{pmatrix}_V , \quad i = 1, \ldots, 6; \quad \mathbf{d}_7^* = a_7^* \begin{pmatrix} 0 \\ 0 \\ 1 \\ 0 \\ 0 \end{pmatrix}_V . \tag{3.174}$$

The coupling factors between par- and perp-space rotations equal 3 and 5, respectively, for the two 2D perpendicular subspaces, c is an arbitrary constant which is usually set to 1 (as it is also done in the following). The subscript V denotes components referring to a 7D Cartesian coordinate system (V-basis), while subscript D refers to the 7D crystallographic basis (D-basis). The embedding matrix W results to

$$W = \begin{pmatrix} \cos\frac{2\pi}{14} & \cos\frac{4\pi}{14} & \cos\frac{6\pi}{14} & \cos\frac{8\pi}{14} & \cos\frac{10\pi}{14} & \cos\frac{12\pi}{14} & 0 \\ \sin\frac{2\pi}{14} & \sin\frac{4\pi}{14} & \sin\frac{6\pi}{14} & \sin\frac{8\pi}{14} & \sin\frac{10\pi}{14} & \sin\frac{12\pi}{14} & 0 \\ 0 & 0 & 0 & 0 & 0 & 0 & 1 \\ \cos\frac{6\pi}{14} & \cos\frac{12\pi}{14} & \cos\frac{18\pi}{14} & \cos\frac{24\pi}{14} & \cos\frac{30\pi}{14} & \cos\frac{36\pi}{14} & 0 \\ \sin\frac{6\pi}{14} & \sin\frac{12\pi}{14} & \sin\frac{18\pi}{14} & \sin\frac{24\pi}{14} & \sin\frac{30\pi}{14} & \sin\frac{36\pi}{14} & 0 \\ \cos\frac{10\pi}{14} & \cos\frac{20\pi}{14} & \cos\frac{30\pi}{14} & \cos\frac{40\pi}{14} & \cos\frac{50\pi}{14} & \cos\frac{60\pi}{14} & 0 \\ \sin\frac{10\pi}{14} & \sin\frac{20\pi}{14} & \sin\frac{30\pi}{14} & \sin\frac{40\pi}{14} & \sin\frac{50\pi}{14} & \sin\frac{60\pi}{14} & 0 \end{pmatrix} . \tag{3.175}$$

The direct 7D basis is obtained from the orthogonality condition (3.5)

$$
\mathbf{d}_i = \frac{2}{7a_i^*}
\begin{pmatrix}
\cos\frac{2\pi i}{14} + (-1)^{i-1} \\
\sin\frac{2\pi i}{14} \\
0 \\
\cos\frac{4\pi i}{14} + (-1)^{i-1} \\
\sin\frac{4\pi i}{14} \\
\cos\frac{6\pi i}{14} + (-1)^{i-1} \\
\sin\frac{6\pi i}{14}
\end{pmatrix}_V
, \quad i = 1,\ldots,6; \quad
\mathbf{d}_7 = \frac{1}{a_7^*}
\begin{pmatrix}
0 \\ 0 \\ 1 \\ 0 \\ 0 \\ 0 \\ 0
\end{pmatrix}_V
. \quad (3.176)
$$

The metric tensors G and G^* are of type

$$
\begin{pmatrix}
A & B & -B & B & -B & B & 0 \\
B & A & B & -B & B & -B & 0 \\
-B & B & A & B & -B & B & 0 \\
B & -B & B & A & B & -B & 0 \\
-B & B & -B & B & A & B & 0 \\
B & -B & B & -B & B & A & 0 \\
0 & 0 & 0 & 0 & 0 & 0 & C
\end{pmatrix}
\quad (3.177)
$$

with $A = 3a^{*2}$, $B = 1/2a^{*2}$, $C = a_7^{*2}$, for reciprocal space and $A = 4/(7a^{*2})$, $B = -2/(7a^{*2})$, $C = 1/a_7^{*2}$ for direct space. Therefrom, the direct and reciprocal lattice parameters can be derived as

$$
d_i^* = \sqrt{3}a^*, \quad d_7^* = a_7^*, \quad \alpha_{ij} = \arccos-\frac{1}{6} = 99.59°, \ \forall i \neq j, \ i+j = 2n,
$$

$$
\alpha_{ij} = \arccos\frac{1}{6} = 80.41°, \ \forall i \neq j, \ i+j = 2n+1, \quad \alpha_{i7} = 90°, \ i,j = 1,\ldots,6
$$

and

$$
d_i = \frac{2}{\sqrt{7}a^*}, \quad d_7 = \frac{1}{a_7^*}, \quad \alpha_{ij} = 120°, \quad \forall i \neq j, \ i+j = 2n,
$$

$$
\alpha_{ij} = 60°, \quad \forall i \neq j, \quad i+j = 2n+1, \quad \alpha_{i5} = 90°, \quad i,j = 1,\ldots,6.
$$

This means that the 6D subspace orthogonal to the periodic direction has hyperrhombohedral symmetry. The volume of the 7D unit cell results to

$$
V = \sqrt{\det(\mathsf{G})} = \frac{8}{49\sqrt{7}a^{*6}a_7^*}. \quad (3.178)
$$

3.6.6.2 Symmetry

The diffraction symmetry of tetrakaidecagonal phases, i.e., the point symmetry group leaving the intensity weighted Fourier module (diffraction pattern)

Table 3.18. The seven 3D tetrakaidecagonal point groups of order k and the nine-teen corresponding 7D tetrakaidecagonal space groups with reflection conditions [36]. The notation is analogous to that of hexagonal space groups. The first position in the point and space group symbols refers to generating symmetry elements oriented along the periodic direction, the second position to the symmetry elements oriented along reciprocal space basis vectors and the third position to those oriented between them

3D Point Group	k	7D Space Group	Reflection Conditions
$\frac{14}{m}\frac{2}{m}\frac{2}{m}$	56	$P\frac{14}{m}\frac{2}{m}\frac{2}{m}$	No condition
		$P\frac{14}{m}\frac{2}{c}\frac{2}{c}$	$h_1h_2h_2h_1h_7 : h_7 = 2n$
			$h_1h_2\bar{h}_2\bar{h}_1h_7 : h_7 = 2n$
		$P\frac{14_7}{m}\frac{2}{m}\frac{2}{c}$	$h_1h_2\bar{h}_2\bar{h}_1h_7 : h_7 = 2n$
		$P\frac{14_7}{m}\frac{2}{c}\frac{2}{m}$	$h_1h_2h_2h_1h_7 : h_7 = 2n$
$\overline{14}m2$	28	$P\overline{14}m2$	No condition
		$P\overline{14}c2$	$h_1h_2h_2h_1h_7 : h_7 = 2n$
		$P\overline{14}2m$	No condition
		$P\overline{14}2c$	$h_1h_2\bar{h}_2\bar{h}_1h_7 : h_7 = 2n$
$14mm$	28	$P14mm$	No condition
		$P14cc$	$h_1h_2h_2h_1h_7 : h_7 = 2n$
			$h_1h_2\bar{h}_2\bar{h}_1h_7 : h_7 = 2n$
		$P14_7mc$	$h_1h_2\bar{h}_2\bar{h}_1h_7 : h_7 = 2n$
		$P14_7cm$	$h_1h_2h_2h_1h_7 : h_7 = 2n$
1422	28	$P1422$	No condition
		$P14_j22$	$0000h_j : jh_7 = 14n$
$\frac{14}{m}$	20	$P\frac{14}{m}$	No condition
		$P\frac{14_7}{m}$	$0000h_7 : h_7 = 2n$
$\overline{14}$	14	$P\overline{14}$	No condition
14	14	$P14$	No condition
		$P14_j$	$0000h_j : jh_7 = 14n$

M_I^* invariant, is one of the two Laue groups $14/mmm$ or $14/m$. The 19 space groups [36] leaving the 7D hypercrystal structure invariant are that subset of the 7D space groups, the point groups of which are isomorphous to the seven 3D tetrakaidecagonal point groups (Table 3.18).

The reflection and inversion operations are equivalent in both subspaces $V^{\parallel}$ and $V^{\perp}$. $\Gamma(14)$, a $2\pi/14$ rotation in $V^{\parallel}$ around the 14-fold axis has component rotations of $6\pi/14$ and $10\pi/14$ in the two 2D $V^{\perp}$ subspaces (see Fig. 3.52)

$$\Gamma(14) = \begin{pmatrix} 0\,0\,0\,0\,0\,\bar{1}\,0 \\ 1\,0\,0\,0\,0\,1\,0 \\ 0\,1\,0\,0\,0\,\bar{1}\,0 \\ 0\,0\,1\,0\,0\,1\,0 \\ 0\,0\,0\,1\,0\,\bar{1}\,0 \\ 0\,0\,0\,0\,1\,1\,0 \\ 0\,0\,0\,0\,0\,0\,1 \end{pmatrix}_{D^*} = \left(\begin{array}{c|c|c} \Gamma^{\parallel}(14) & 0 & 0 \\ \hline 0 & \Gamma_1^{\perp}(14) & 0 \\ \hline 0 & 0 & \Gamma_2^{\perp}(14) \end{array} \right)_{V} =$$

$$= \left(\begin{array}{ccc|cc|cc} \cos\frac{2\pi}{14} & -\sin\frac{2\pi}{14} & 0 & 0 & 0 & 0 & 0 \\ \sin\frac{2\pi}{14} & \cos\frac{2\pi}{14} & 0 & 0 & 0 & 0 & 0 \\ 0 & 0 & 1 & 0 & 0 & 0 & 0 \\ \hline 0 & 0 & 0 & \cos\frac{4\pi}{14} & -\sin\frac{4\pi}{14} & 0 & 0 \\ 0 & 0 & 0 & \sin\frac{4\pi}{14} & \cos\frac{4\pi}{14} & 0 & 0 \\ \hline 0 & 0 & 0 & 0 & 0 & \cos\frac{6\pi}{14} & -\sin\frac{6\pi}{14} \\ 0 & 0 & 0 & 0 & 0 & \sin\frac{6\pi}{14} & \cos\frac{6\pi}{14} \end{array} \right)_{V} \quad (3.179)$$

The scaling symmetry leaving the reciprocal space lattice invariant (Fig. 3.53) is represented by the matrix S^*

$$\mathsf{S}^* = \begin{pmatrix} 1\,1\,1\,0\,\bar{1}\,\bar{1}\,0 \\ 0\,0\,0\,1\,1\,0\,0 \\ 1\,1\,1\,0\,0\,0\,0 \\ 0\,0\,0\,1\,1\,1\,0 \\ 0\,1\,1\,0\,0\,0\,0 \\ \bar{1}\,\bar{1}\,0\,1\,1\,1\,0 \\ 0\,0\,0\,0\,0\,0\,1 \end{pmatrix}_{D^*} = \left(\begin{array}{c|c|c} \Gamma^{\parallel}(\mathsf{S}) & 0 & 0 \\ \hline 0 & \Gamma_1^{\perp}(\mathsf{S}) & 0 \\ \hline 0 & 0 & \Gamma_2^{\perp}(\mathsf{S}) \end{array} \right)_{V^*} = \quad (3.180)$$

$$\left(\begin{array}{ccc|cc|cc} 1+2\cos\frac{4\pi}{14} & 0 & 0 & 0 & 0 & 0 & 0 \\ 0 & 1+2\cos\frac{4\pi}{14} & 0 & 0 & 0 & 0 & 0 \\ 0 & 0 & 1 & 0 & 0 & 0 & 0 \\ \hline 0 & 0 & 0 & 1+2\cos\frac{12\pi}{14} & 0 & 0 & 0 \\ 0 & 0 & 0 & 0 & 1+2\cos\frac{12\pi}{14} & 0 & 0 \\ \hline 0 & 0 & 0 & 0 & 0 & 1+2\cos\frac{20\pi}{14} & 0 \\ 0 & 0 & 0 & 0 & 0 & 0 & 1+2\cos\frac{20\pi}{14} \end{array} \right)_{V^*} .$$

The eigenvalues of the scaling matrix are the cubic Pisot numbers

$$\lambda_1 = 1 + 2\cos 4\pi/14 = 2.24698, \quad \lambda_2 = 1 + 2\cos 12\pi/14 = -0.80194,$$
$$\lambda_3 = 1 + 2\cos 20\pi/14 = 0.55496. \quad (3.181)$$

which are the solutions of the characteristic polynomial $1 - 5x + 6x^2 + 4x^3 - 9x^4 + x^5 + 3x^6 - x^7 = (1-x)(1 - 2x - x^2 + x^3)^2$.

3.6.6.3 Example: Tetrakaidecagonal Quasicrystal

The lattice Σ of the tetrakaidecagonal structure possesses tetrakaidecagonal symmetry. A structure with this symmetry may be formed by heptagonal
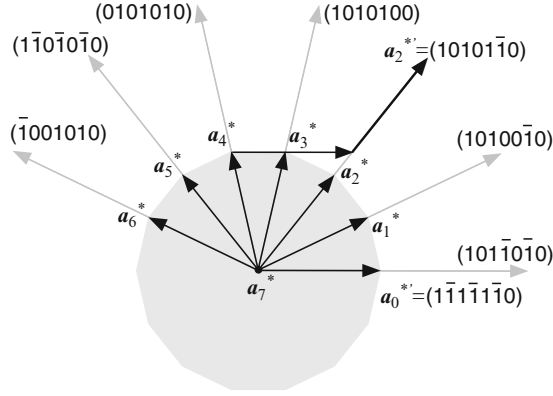
Fig. 3.53. Reciprocal space scaling of the tetrakaidecagonal structure by the matrix S. The scaled basis vectors keep their orientation and are increased in length by a factor $1 + 2\cos 2\pi/7 = 2.24698$ (marked gray). The example shown explicitly is $\mathbf{a}_2^{*'} = \mathbf{a}_4^* + \mathbf{a}_0^* + \mathbf{a}_2^*$

tilings related by a screw axis along the periodic direction. A heptagonal tiling is a 2D quasiperiodic tiling with (at least local) heptagonal symmetry and tetrakaidecagonal diffraction symmetry ($14mm$).

All reciprocal space vectors $\mathbf{H} \in M^*$ of a 2D heptagonal tiling can be represented on a 2D basis $\mathbf{a}_i^* = (\cos(2\pi i/7), \sin(2\pi i/7))$, $i = 1, .., 6$, as $\mathbf{H} = \sum_{i=1}^{6} h_i \mathbf{a}_i^*$. The vector components refer to a Cartesian coordinate system in par-space. From the number of independent reciprocal basis vectors necessary to index the Bragg reflections with integer numbers, the dimension of the embedding space has to be at least six.

The set M^* of all vectors $\mathbf{H}$ remains invariant under the action of the symmetry operations of the point group $14mm$. The symmetry-adapted matrix representations for the point group generators, the 14-fold rotation $\alpha = 14$, the reflection on the 3D mirror space $\beta = m_2$ (the vectors $(a_i^* - a_{i+5}^*)$, $(a_{i+1}^* - a_{i+4}^*)$ and $(a_{i+2}^* - a_{i+3}^*)$, $i = 1, .., 7$ are normal to the corresponding mirror spaces) and the inversion operation $\Gamma(\gamma) = \bar{1}$ can be written in the form:

$$\Gamma(\alpha) = \begin{pmatrix} 0\,0\,1\,\bar{1}\,0\,0 \\ 0\,0\,1\,0\,\bar{1}\,0 \\ 0\,0\,1\,0\,0\,\bar{1} \\ 0\,0\,1\,0\,0\,0 \\ \bar{1}\,0\,1\,0\,0\,0 \\ 0\,\bar{1}\,1\,0\,0\,0 \end{pmatrix}_D \quad , \quad \Gamma(\beta) = \begin{pmatrix} 0\,0\,0\,0\,0\,1 \\ 0\,0\,0\,0\,1\,0 \\ 0\,0\,0\,1\,0\,0 \\ 0\,0\,1\,0\,0\,0 \\ 0\,1\,0\,0\,0\,0 \\ 1\,0\,0\,0\,0\,0 \end{pmatrix}_D \quad ,$$

$$\Gamma(\gamma) = \begin{pmatrix} \bar{1}\,0\,0\,0\,0\,0 \\ 0\,\bar{1}\,0\,0\,0\,0 \\ 0\,0\,\bar{1}\,0\,0\,0 \\ 0\,0\,0\,\bar{1}\,0\,0 \\ 0\,0\,0\,0\,\bar{1}\,0 \\ 0\,0\,0\,0\,0\,\bar{1} \end{pmatrix}_D \quad . \tag{3.182}$$

By block-diagonalization, these reducible symmetry matrices can be decomposed into non-equivalent irreducible representations. These can be assigned to the two orthogonal subspaces forming the 6D embedding space $\mathbf{V} = \mathbf{V}^{\parallel} \oplus \mathbf{V}^{\perp}$, with a 2D parallel subspace $\mathbf{V}^{\parallel}$, and the perpendicular 4D subspace, $\mathbf{V}^{\perp}$. The latter consists of two orthogonal 2D subspaces $\mathbf{V}_1^{\perp}$ and $\mathbf{V}_2^{\perp}$, as will be seen later. With $\mathsf{W} \cdot \Gamma \cdot \mathsf{W}^{-1} = \Gamma_V = \Gamma^{\parallel} \oplus \Gamma^{\perp}$, we obtain

$$
\Gamma(\alpha) = \left(\begin{array}{cc|cc|cc}
\cos(\pi/7) & -\sin(\pi/7) & 0 & 0 & 0 & 0 \\
\sin(\pi/7) & \cos(\pi/7) & 0 & 0 & 0 & 0 \\
\hline
0 & 0 & \cos(5\pi/7) & -\sin(5\pi/7) & 0 & 0 \\
0 & 0 & \sin(5\pi/7) & \cos(5\pi/7) & 0 & 0 \\
0 & 0 & 0 & 0 & \cos(3\pi/7) & -\sin(3\pi/7) \\
0 & 0 & 0 & 0 & \sin(3\pi/7) & \cos(3\pi/7)
\end{array}\right)_V
$$

$$
= \left(\begin{array}{c|c}
\Gamma^{\parallel}(\alpha) & 0 \\
\hline
0 & \Gamma^{\perp}(\alpha)
\end{array}\right)_V ,
$$

$$
\Gamma(\beta) = \left(\begin{array}{cc|cccc}
1 & 0 & 0 & 0 & 0 & 0 \\
0 & \bar{1} & 0 & 0 & 0 & 0 \\
\hline
0 & 0 & 1 & 0 & 0 & 0 \\
0 & 0 & 0 & \bar{1} & 0 & 0 \\
0 & 0 & 0 & 0 & 1 & 0 \\
0 & 0 & 0 & 0 & 0 & \bar{1}
\end{array}\right)_V , \quad
\Gamma(\gamma) = \left(\begin{array}{cc|cccc}
\bar{1} & 0 & 0 & 0 & 0 & 0 \\
0 & \bar{1} & 0 & 0 & 0 & 0 \\
\hline
0 & 0 & \bar{1} & 0 & 0 & 0 \\
0 & 0 & 0 & \bar{1} & 0 & 0 \\
0 & 0 & 0 & 0 & \bar{1} & 0 \\
0 & 0 & 0 & 0 & 0 & \bar{1}
\end{array}\right)_V , \tag{3.183}
$$

where W is as defined in (3.93).

$$
W = \left(\begin{array}{cccccc}
\cos(2\pi/7) & \cos(4\pi/7) & \cos(6\pi/7) & \cos(8\pi/7) & \cos(10\pi/7) & \cos(12\pi/7) \\
sin(2\pi/7) & \sin(4\pi/7) & \sin(6\pi/7) & \sin(8\pi/7) & \sin(10\pi/7) & \sin(12\pi/7) \\
\hline
\cos(4\pi/7) & \cos(8\pi/7) & \cos(12\pi/7) & \cos(2\pi/7) & \cos(6\pi/7) & \cos(10\pi/7) \\
\sin(4\pi/7) & \sin(8\pi/7) & \sin(12\pi/7) & \sin(2\pi/7) & \sin(6\pi/7) & \sin(10\pi/7) \\
\cos(6\pi/7) & \cos(12\pi/7) & \cos(4\pi/7) & \cos(10\pi/7) & \cos(2\pi/7) & \cos(8\pi/7) \\
\sin(6\pi/7) & \sin(12\pi/7) & \sin(4\pi/7) & \sin(10\pi/7) & \sin(2\pi/7) & \sin(8\pi/7)
\end{array}\right)_V .
$$

$$\tag{3.184}$$

The column vectors of the matrix W give a reciprocal basis in V space $W = (\mathbf{d}_1^*, \mathbf{d}_2^*, \mathbf{d}_3^*, \mathbf{d}_4^*, \mathbf{d}_5^*, \mathbf{d}_6^*)$, with their par- and perp-space components above and below the partition line. The reciprocal basis of the 6D embedding space (D basis) is:

$$
\mathbf{d}_i^* = a_i^* \left(\begin{array}{c}
\cos(2\pi i/7) \\
\sin(2\pi i/7) \\
\cos(4\pi i/7) \\
\sin(4\pi i/7) \\
\cos(6\pi i/7) \\
\sin(6\pi i/7)
\end{array}\right)_V , \quad i = 1,..,6 \tag{3.185}
$$

The 6×6 symmetry matrices can each be decomposed into three 2×2 matrices. the first one, $\Gamma^{\parallel}$, acts on the parallel space component of a vector. The second two build $\Gamma^{\perp}$ and act on the perp-space component. The rotation $\Gamma(\alpha)$ can thus be interpreted as the coupling of three rotations. Each of them leave a 4D space invariant and span a 2D space. As a result, $\Gamma(\alpha)$ leaves a point invariant and generates the 6D space. The coupling factors between a rotation in parallel and perp-space are 5 and 3. Thus, a $\pi/7$ rotation in par-space is related to a $5\pi/7$ and a $3\pi/7$ rotation in perp-space.

$\Gamma(\beta)$ leaves three dimensions invariant, while changing the sign of the remaining three. It can thus be interpreted as a mirror operation on a 3D space. The fact that the 4D perp-space $V^{\perp}$ decomposes into two 2D invariant subspaces, simplifies the problem of visualizing the 4D atomic surfaces, as will be seen later. With the condition $\mathbf{d}_i \cdot \mathbf{d}_j^* = \delta_{ij}$, a basis in direct 6D space is obtained:

$$\mathbf{d}_i = \frac{2}{7a_i^*} \begin{pmatrix} \cos(2\pi i/7) - 1 \\ \sin(2\pi i/7) \\ \cos(4\pi i/7) - 1 \\ \sin(4\pi i/7) \\ \cos(6\pi i/7) - 1 \\ \sin(6\pi i/7) \end{pmatrix}_V \;, \; i = 1, .., 6 \tag{3.186}$$

The heptagonal tiling can also be embedded canonically in 7D. Canonically means that the 7D lattice is hypercubic and that the projection of one unit cell of the hypercrystal upon the 5D perp-space $V^{\perp}$ defines the window function (acceptance window). Then, the heptagonal tiling can be constructed by the strip-projection technique. The V basis in terms of the D basis is given by

$$V = a^* \sqrt{\frac{2}{7}} \begin{pmatrix} \mathbf{v}_1 \\ \mathbf{w}_1 \\ \mathbf{v}_2 \\ \mathbf{w}_2 \\ \mathbf{v}_3 \\ \mathbf{w}_3 \\ \mathbf{d} \end{pmatrix}_D = a^* \sqrt{\frac{2}{7}} \begin{pmatrix} \cos(2\pi i/7) \\ \sin(2\pi i/7) \\ \cos(4\pi i/7) \\ \sin(4\pi i/7) \\ \cos(6\pi i/7) \\ \sin(6\pi i/7) \\ \frac{1}{\sqrt{2}} \end{pmatrix}_D \;, \; i = 1, .., 7. \tag{3.187}$$

Therein, the vectors $\mathbf{v}_1$ and $\mathbf{w}_1$ span the 2D par-space $V^{\parallel}$, $\mathbf{v}_2$ and $\mathbf{w}_2$ span $V_1^{\perp}$, $\mathbf{v}_3$ and $\mathbf{w}_3$ span $V_2^{\perp}$ and $\mathbf{d}$ spans $V_3^{\perp}$, with $V = V^{\parallel} \oplus V^{\perp} = V^{\parallel} \oplus V_1^{\perp} \oplus V_2^{\perp} \oplus V_3^{\perp}$. The D basis is given by $D = V^{-1}$. The length of the basis vectors spanning the D basis is $1/a^*$, edge length of the unit tiles amounts to $a_r = \sqrt{2/7}/a^*$.

The window function cuts a 5D slab parallel to the 2D par-space from the 7D lattice. All 7D lattice points contained in the window are then orthogonally projected upon the par-space. This set of vertices defines a tetrakaidecagonal tiling, if the window function has the proper irrational orientation. For a detailed description see [22, 37]. In our case, this window is a zonohedron with heptagonal symmetry (Fig. 3.54).
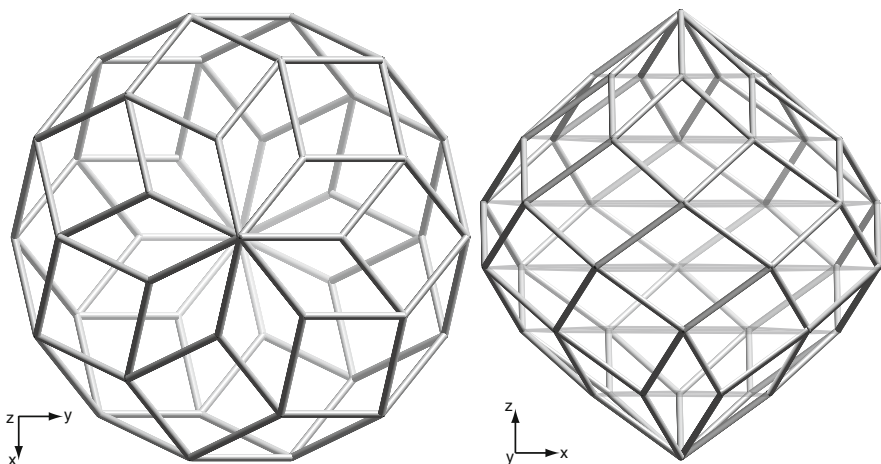
Fig. 3.54. Different views of the 7D hypercubic unit cell (orthogonal projection of the unit cell upon $V^\perp$). The convex hull of the orthogonal projection of the cell upon $V_1^\perp$ (x,y) and the body diagonal of the hypercrystal $((0000001)_V)$ as the z-direction. The atomic surfaces are cuts perpendicular to the body diagonal, as is schematically shown on the right side, for the first two atomic surfaces

The atomic surfaces are convex 4D polytopes. Every vertex of the acceptance window corresponds to a vertex of the unit cell, which is then orthogonally projected upon perp-space. A convenient way to obtain the vertices belonging to a atomic surface, is to identify the unit cell vertices creating the atomic surface after projection upon $V^\perp$. The convex hull of the ith atomic surface is then defined by the perp-space components of the unit cell vertices fulfilling $\sum_{j=1}^{7} a_{jk} = i$, with $i = 0, .., 6$ for the seven atomic surfaces and $(a_{1k}, .., a_{7k})_D$ the k-th vertex of the unit cell given in the D basis.

The atomic surfaces for the (6D) cut-and-project formalism are then obtained by projection of the atomic surfaces in the canonical description along the vector interconnecting the diagonal of the 7D basis with the diagonal of the 6D basis (with a seventh coordinate set to zero) upon the 6D basis given above. The seven atomic surfaces are located on the $(i/7)(111111)_D$, $i = 0, .., 6$ on the diagonal of the hyperrhombohedral unit cell in the 6D description. The 0D atomic surface is located at the origin $(i = 0)$. Neighboring atomic surfaces are in *anti*-position to each other, as can be seen in Fig. 3.55. The six atomic surfaces within the zonohedron are related by an inversion center at one half of the body diagonal of the zonohedron. We, thus, have three independent, non-zero atomic surfaces. By proper projection upon the 6D basis described before, we reduce the dimension of the canonical description by the redundant one (the parallel space image of the seven basis vectors is not linearly independent), and obtain the atomic surfaces for the cut-and-project formalism.
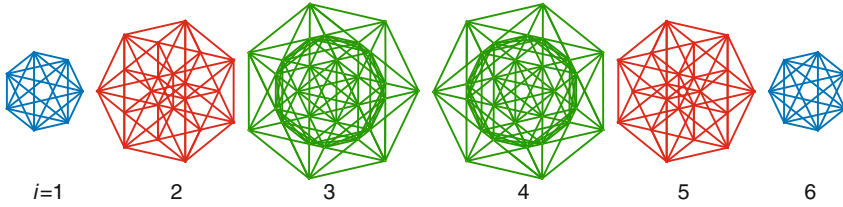
Fig. 3.55. The six atomic surfaces of the tetrakaidecagonal tiling with a non-zero volume are located at $i/7(1111111)_D$, $i = 1, .., 6$ in the canonical description, and at $i/7(111111)_D$, $i = 1, .., 6$ in the cut-and-project method. They are related by an inversion center in the origin and at $1/2(1111111)_D$. The atomic surfaces are 4D polytopes, and have only a volume in $V^\perp$. We see here an orthogonal projection of the atomic surfaces upon one of the two invariant subspaces of $V^\perp$. Projection upon the second subspace would lead to the same image, but the order of the projected vertices would change

3.6.6.4 Periodic Average Structure

The periodic average structures of heptagonal tilings will be generated using the canonical projection method with a 7D basis, as described in the previous section. 5D projections are then necessary to generate a PAS. Thereby, the dimension of the atomic surfaces is reduced from 4D to 2D. This has direct implications on the distribution function of the vertices in the projected atomic surfaces.

In the following, we will discuss all symmetrically non-equivalent PAS resulting from two types of reflections, which give PAS with the most reasonable occupancy factors. For that purpose, the two strongest Bragg reflections are chosen related to PAS lattice parameters close to the tiling edge length. The resulting PAS unit cells correspond to the three different unit tiles of the heptagonal tiling.

In these PAS (Figs. 3.56 and 3.58), the symmetry of the atomic surfaces is not preserved in the oblique projections, and atomic surfaces are projected upon each other and, in some cases, they are additionally overlapping with projected atomic surfaces located at other lattice nodes (Fig. 3.56). The decomposition of heavily overlapping projected atomic surfaces ("Christmas tree" of Fig. 3.56) in the individual projected atomic surfaces is shown in Fig. 3.57.

The best PAS with regard to the occupancy (Fig. 3.56, "Christmas tree") has an occupancy factor close to one, (only 4% of all projected atomic surfaces are not occupied), but its unit cell is almost completely covered with the projected atomic surfaces. On the other hand, the best PAS with a reasonable maximal deviation of the tiling vertices from the lattice nodes (Fig. 3.58, left) has only an occupancy factor of 0.5663. Almost half of the projected atomic surfaces are not occupied. The heptagonal case shows, therefore, a high "degree of quasiperiodicity."
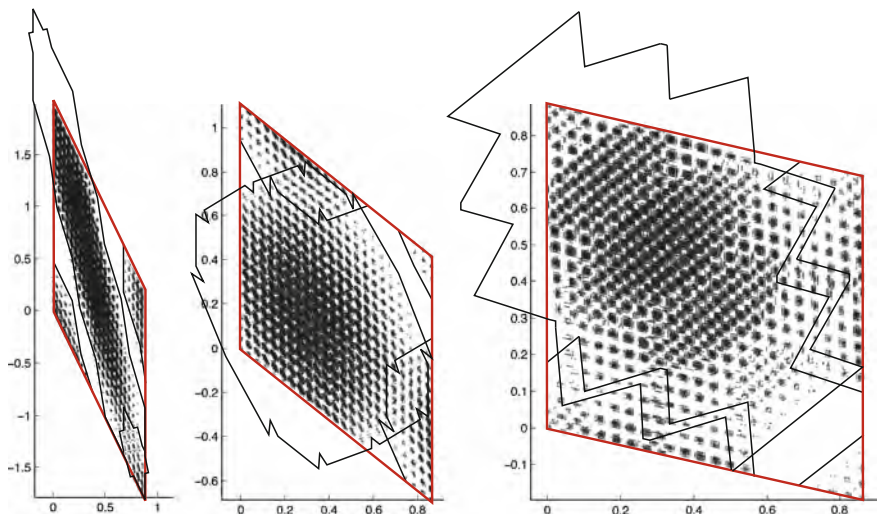
Fig. 3.56. Projected average structures with overlapping projected atomic surfaces. Depicted are all symmetrically nonequivalent PAS that correspond to $(10\bar{1}\bar{1}011)_D$ and one symmetry equivalent reflection. The second reflection is either $(10\bar{1}\bar{1}\bar{1}01)_D$ (*left*), $(110\bar{1}\bar{1}01)_D$ (*center*) or $(110\bar{1}\bar{1}\bar{1}0)_D$ (*right*). In all cases, the projected atomic surfaces fill almost the whole unit cell of the PAS lattice. They have the lattice parameters/occupancy factors (*from left to right*): 1.9924/2.1529; 1.1057/1.1948; 0.8867/0.9581. Black lines mark the outer boundary of the projected atomic surfaces, points result from the heptagonal tiling modulo one unit cell of the PAS
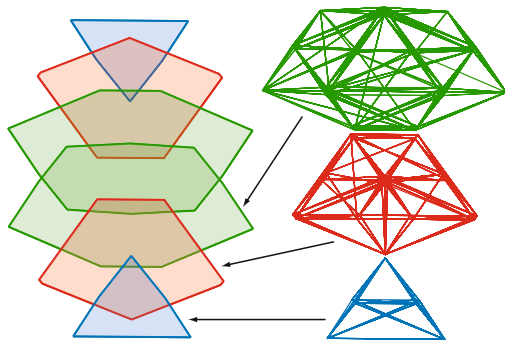
Fig. 3.57. Projected atomic surfaces for the periodic average structure defined by the reflections $(10\bar{1}\bar{1}011)_D$ and $(110\bar{1}\bar{1}\bar{1}0)_D$ (Fig. 3.56, *right*). The individual, symmetry independent, projected atomic surfaces
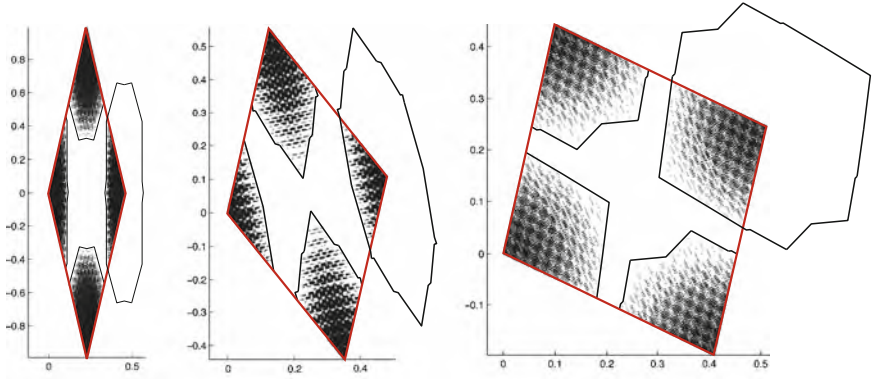
Fig. 3.58. Projected average structures with overlapping projected atomic surfaces. Shown are all symmetrically nonequivalent PAS that correspond to $(1\bar{1}\bar{2}\bar{2}022)_D$ and one symmetry equivalent reflection. The second reflection is either $(20\bar{2}\bar{2}\bar{1}12)_D$ (*left*), $(21\bar{1}\bar{2}\bar{2}02)_D$ (*center*) or $(220\bar{2}\bar{2}\bar{1}1)_D$ (*right*). Their lattice parameters/occupancy factors are (*from left to right*): 1.0218/0.5663; 0.5671/0.3142; 0.4547/0.2520. *Black lines* mark the outer boundary of the projected atomic surfaces, points result from the heptagonal tiling modulo one unit cell of the PAS

3.6.6.5 General Comment on the Periodic Average Structure

The PAS of 2D tilings with symmetries 5, 7, 8, 10, 12, and 14 strongly differ in the size of the projected atomic surfaces relative to the unit cell dimensions. Since the boundaries of a projected atomic surface defines the maximum deviation of a tiling vertex from the closest PAS lattice node, this size is an important indicator for the "degree of quasiperiodicity" of a tiling. The smaller the "degree of quasiperiodicity," the closer the tiling is to periodicity and the better can some of its properties be approximated by its PAS (compare Figs. 3.22, 3.23, 3.50, 3.51, 3.56, and 3.58) [47].

The tiling modulo the unit cell of its PAS corresponds to the projection of the atomic surfaces. Since the vertex distribution in an atomic surface is homogenous, so is the projection of one single atomic surface, if its dimension is not reduced by the projection. This is the case, for instance, for the octagonal and decagonal tilings that are generated by one single 2D atomic surface at the origin of the nD unit-cell.

In the case of heptagonal and dodecagonal tilings, these originate from several unconnected atomic surfaces, which overlap in their projection for all PAS of physical relevance (those generated by strong Bragg reflections). For the dodecagonal tiling, the atomic surfaces and their projections are 2D and homogenous. However, parts of the atomic surfaces are projected upon each other. The resulting density distribution in the PAS can then be described by a simple step function following the boundaries of the single projected atomic surfaces and their overlaps.

The heptagonal case is the most complicated one, since it not only shows more then one atomic surface but also a reduction in the dimension of the 4D atomic surfaces during projection to 2D. The projected density distribution resulting from a single atomic surface is therefore not homogenous.

Although the density distribution of the PAS can be interpreted as a measure for the "degree of quasiperiodicity," this concept has to be treated carefully. It is only reliable if the total diffraction intensity represented by a PAS is large, and if the occupancy factor of the projected atomic surfaces is close to one. The 1D Fibonacci sequence and the 2D octagonal tiling, for instance, can be described quite nicely by a PAS, contrary to the heptagonal tiling that eludes a reasonable description by a PAS. It is interesting, that the heptagonal case, which seems to be the "most quasiperiodic" case among the examples discussed, is also the system with the highest dimensionality. The generalization of this result might seem quite intuitive on a first glance, but has to be verified by the study of tilings with atomic surfaces of dimensionality higher than four. However, the diversity of the "degree of quasiperiodicity" within the range of tilings of equal dimensions but different symmetries shows that this problem cannot be reduced to one of dimensions only.

3.7 3D Quasiperiodic Structures with Icosahedral Symmetry

For finding the embedding matrix one has, as usual, to consider the generating symmetry operations, the 5-fold rotation $\Gamma(\alpha)$, reflection on a mirror $\Gamma(\beta)$ and the inversion operation $\Gamma(i)$. These symmetry operations can be written as 6×6 matrices with integer coefficients acting on the reciprocal space vectors $\mathbf{H}$. The 6D representation is reducible to a par- and perp-space component. It can be combined from the irreducible representations shown in the character table (Table 3.19) under the condition that the trace of the 6D matrix does not change with the similarity transformation.

Table 3.19. Character table for the icosahedral group $\bar{3}\bar{5}m$ (I_h) [20]. ε denotes the identity operation, α^n the rotation around $2n\pi/5$, and β the reflection on a mirror plane

Elements	ε	α	α^2	β	β'
Γ_1	1	1	1	1	1
Γ_2	3	$-\tau$	$1+\tau$	0	-1
Γ_3	3	$1+\tau$	$-\tau$	0	-1
Γ_4	4	-1	-1	1	0
Γ_5	5	0	0	-1	1

Fig. 3.59. Stereographic projection of the icosahedral point group $m\,\bar{3}\,\bar{5}$ of order 120. The six $\bar{5}$ axes include angles of $\arctan 2 = 63.43°$. Each 5-fold axis is surrounded by five 3-fold $(37.38°)$ and five 2-fold axes $(31.72°)$ and is perpendicular to five more 2-fold axes. The angles between neighboring 3-fold axes are $41.81°$, between neighboring 2-fold axes $36°$. The smallest angle between a 3- and a 2-fold axis is $20.90°$. The letters P, D and $\bar{P}$, used frequently in electron microscopy, mark special directions

3.7.1 Reciprocal Space

Quasicrystals exhibiting icosahedral diffraction symmetry (Fig. 3.59) are called icosahedral quasicrystals. The most perfect quasiperiodic phases known belong to this class ([43] and references therein). The Ammann or 3D Penrose tiling will be used as example of a 3D quasiperiodic structure.

The set of diffraction vectors M^* forms a Z-module of rank six. Sextuplets of integers are needed, therefore, to describe the diffraction vectors $\mathbf{H} = \sum_{i=1}^{6} h_i \mathbf{a}_i^*$, $h_i \in Z$. Since there are several different indexing schemes in use, one has to keep in mind that the indices may refer to different reciprocal bases.

The generic indexing scheme (*setting 1*) uses six reciprocal basis vectors $\mathbf{a}_i^*$ directed towards the corners of an icosahedron:

$$\mathbf{a}_1^* = a^* \left(0, 0, 1\right), \ \ \mathbf{a}_i^* = a^* \left(\sin\theta\,\cos 2\pi i/5, \ \sin\theta\,\sin 2\pi i/5, \cos\theta\right), \ \ i = 2, \ldots, 6,$$

with $\tan\theta = 2$. θ is the angle between two adjacent 5-fold axes, $a^* = |\mathbf{a}_i^*|$ and $h_i \in Z$ (Fig. 3.60).

The vectors $\mathbf{a}_i^*$, $i = 1, \ldots, 6$ can be considered as par-space projections of the basis vectors $\mathbf{d}_i^*$, $i = 1, \ldots, 6$ of the 6D reciprocal lattice Σ^* with

a   **b**
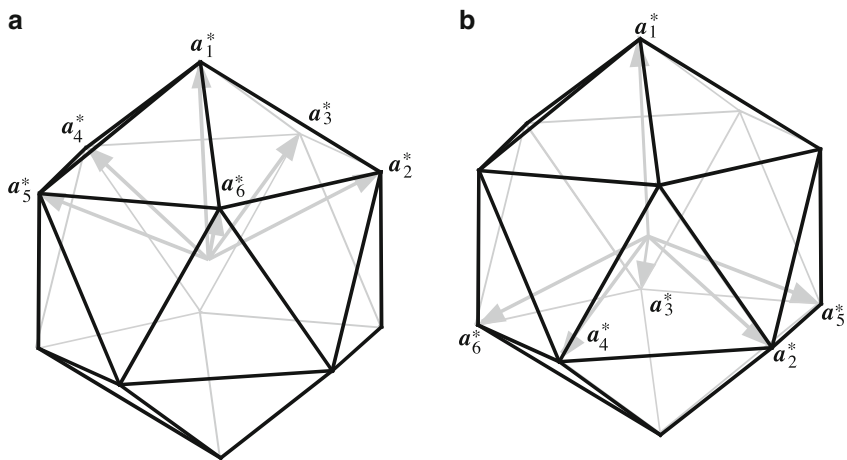
Fig. 3.60. Perspective view of the reciprocal basis of the icosahedral phase: (**a**) parallel and (**b**) perp-space components

$$\mathbf{d}_1^* = a^* \begin{pmatrix} 0 \\ 0 \\ 1 \\ 0 \\ 0 \\ c \end{pmatrix}_V \quad , \quad \mathbf{d}_i^* = a^* \begin{pmatrix} \sin\theta\cos\frac{2\pi i}{5} \\ \sin\theta\sin\frac{2\pi i}{5} \\ 1 \\ -c\sin\theta\cos\frac{4\pi i}{5} \\ -c\sin\theta\sin\frac{4\pi i}{5} \\ -c\cos\theta \end{pmatrix}_V \quad , \quad i = 2,\ldots,6 \ . \quad (3.188)$$

c is an arbitrary constant usually set equal to one. The direct 6D basis results from the orthogonality condition (3.5) and we obtain

$$\mathbf{d}_1 = \frac{1}{2ca^*} \begin{pmatrix} 0 \\ 0 \\ c \\ 0 \\ 0 \\ 1 \end{pmatrix}_V \quad , \quad \mathbf{d}_i = \frac{1}{2ca^*} \begin{pmatrix} c\sin\theta\cos\frac{2\pi i}{5} \\ c\sin\theta\sin\frac{2\pi i}{5} \\ c \\ -\sin\theta\cos\frac{4\pi i}{5} \\ -\sin\theta\sin\frac{4\pi i}{5} \\ -\cos\theta \end{pmatrix}_V \quad , \quad (3.189)$$

$$i = 2,\ldots,6 \ .$$

The metric tensors G and G^* are of type

$$\begin{pmatrix} A & B & B & B & B & B \\ B & A & B & -B & -B & B \\ B & B & A & B & -B & -B \\ B & -B & B & A & B & -B \\ B & -B & -B & B & A & B \\ B & B & -B & -B & B & A \end{pmatrix} \quad (3.190)$$

with $A = \left(1 + c^2\right) a^{*2}$, $B = \left(\sqrt{5}/5\right)\left(1 - c^2\right) a^{*2}$ for reciprocal space and $A = \left(1 + c^2\right)/4 \left(ca^*\right)^2$, $B = \sqrt{5}\left(c^2 - 1\right)/20 \left(ca^*\right)^2$ for direct space. Thus, for $c = 1$ hypercubic lattices result. The direct and reciprocal lattice parameters are

$$|\mathbf{d}_i^*| = a^*\sqrt{2}, \quad \alpha_{ij}^* = 90°, \; i, j = 1, \ldots, 6 \tag{3.191}$$

and

$$|\mathbf{d}_i| = \frac{1}{a^*\sqrt{2}}, \quad \alpha_{ij} = 90°, \; i, j = 1, \ldots, 6 . \tag{3.192}$$

The volume of the 6D direct lattice unit cell results to

$$V = \sqrt{\det\left(\mathsf{G}\right)} = \left(\frac{1}{a^*\sqrt{2}}\right)^6 = |\mathbf{d}_i|^6 . \tag{3.193}$$

Alternatively, there exists another common setting for the reciprocal basis of icosahedral QC. The same six-star of reciprocal basis vectors in different orientation (*setting* $1'$) is referred to a Cartesian coordinate system (*C*-basis) oriented along 2-fold axes [1]

$$\begin{pmatrix} \mathbf{a}_1^* \\ \mathbf{a}_2^* \\ \mathbf{a}_3^* \\ \mathbf{a}_4^* \\ \mathbf{a}_5^* \\ \mathbf{a}_6^* \end{pmatrix} = \frac{a^*}{\sqrt{2 + \tau}} \begin{pmatrix} 0 & 1 & \tau \\ -1 & \tau & 0 \\ -\tau & 0 & 1 \\ 0 & -1 & \tau \\ \tau & 0 & 1 \\ 1 & \tau & 0 \end{pmatrix} \begin{pmatrix} \mathbf{c}_1 \\ \mathbf{c}_2 \\ \mathbf{c}_3 \end{pmatrix} . \tag{3.194}$$

The *C*-basis is related to the *V*-basis by the rotation

$$\begin{pmatrix} \mathbf{c}_1 \\ \mathbf{c}_2 \\ \mathbf{c}_3 \end{pmatrix} = \begin{pmatrix} \cos\frac{\pi}{10} & \sin\frac{\pi}{10} & 0 \\ -\cos\frac{\theta}{2}\sin\frac{\pi}{10} & \cos\frac{\theta}{2}\cos\frac{\pi}{10} & \sin\frac{\theta}{2} \\ \sin\frac{\theta}{2}\sin\frac{\pi}{10} & -\sin\frac{\theta}{2}\cos\frac{\pi}{10} & \cos\frac{\theta}{2} \end{pmatrix} \begin{pmatrix} \mathbf{v}_1 \\ \mathbf{v}_2 \\ \mathbf{v}_3 \end{pmatrix} . \tag{3.195}$$

Though both bases are represented on different Cartesian bases, the 6D description is equivalent and the 6D indices are identical.

A different way of indexing is based on a cubic basis (*setting 2*) (Fig. 3.61)

$$\begin{pmatrix} \mathbf{b}_1^* \\ \mathbf{b}_2^* \\ \mathbf{b}_3^* \end{pmatrix} = \frac{1}{2} \begin{pmatrix} 0 & \bar{1} & 0 & 0 & 0 & 1 \\ 1 & 0 & 0 & \bar{1} & 0 & 0 \\ 0 & 0 & 1 & 0 & 1 & 0 \end{pmatrix} \begin{pmatrix} \mathbf{a}_1^* \\ \mathbf{a}_2^* \\ \mathbf{a}_3^* \\ \mathbf{a}_4^* \\ \mathbf{a}_5^* \\ \mathbf{a}_6^* \end{pmatrix} = \frac{a^*}{\sqrt{2 + \tau}} \begin{pmatrix} \mathbf{c}_1 \\ \mathbf{c}_2 \\ \mathbf{c}_3 \end{pmatrix} . \tag{3.196}$$

The indices $h_1 h_2 h_3 h_4 h_5 h_6$ of *setting 1* are related to those of *setting 2* $h/h'\; k/k'\; l/l'$ by the transformation
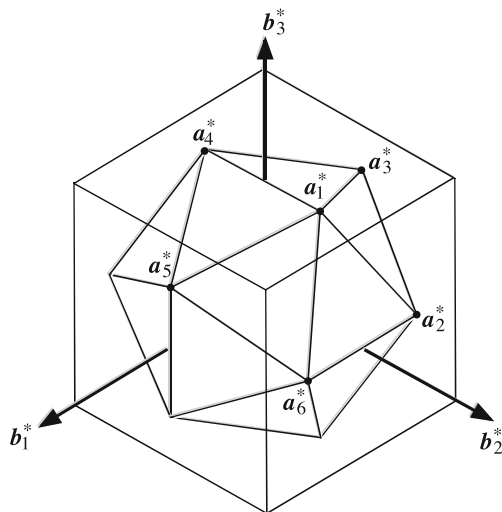
Fig. 3.61. Perspective parallel space view of the two alternative reciprocal bases of the icosahedral phase: the cubic and the icosahedral setting, represented by the bases $\mathbf{b}_i^*, i = 1, \ldots, 3$ and $\mathbf{a}_i^*, i = 1, \ldots, 6$, respectively

$$
\begin{pmatrix} h \\ h' \\ k \\ k' \\ l \\ l' \end{pmatrix}_C = \begin{pmatrix} 0 & \bar{1} & 0 & 0 & 0 & 1 \\ 0 & 0 & \bar{1} & 0 & 1 & 0 \\ 1 & 0 & 0 & \bar{1} & 0 & 0 \\ 0 & 1 & 0 & 0 & 0 & 1 \\ 0 & 0 & 1 & 0 & 1 & 0 \\ 1 & 0 & 0 & 1 & 0 & 0 \end{pmatrix} \begin{pmatrix} h_1 \\ h_2 \\ h_3 \\ h_4 \\ h_5 \\ h_6 \end{pmatrix}_D = \begin{pmatrix} h_6 - h_2 \\ h_5 - h_3 \\ h_1 - h_4 \\ h_6 + h_2 \\ h_5 + h_3 \\ h_1 + h_4 \end{pmatrix}_D . \qquad (3.197)
$$

The primed indices refer to τ-times enlarged basis vectors $\mathbf{b}_i^*$.

3.7.2 Symmetry

The diffraction symmetry of icosahedral phases, i.e., the point symmetry group of the intensity weighted Fourier module (diffraction pattern) M_I^* can be described by the Laue group $m\bar{3}\bar{5}$. The 11 symmetry groups leaving the 6D hypercrystal structure invariant are that subset of the 6D space groups, the point groups of which are isomorphous to the two possible 3D icosahedral point groups (Table 3.20). Besides primitive 6D Bravais lattice symmetry (P, primitive hypercubic) also body centered (I, body centered hypercubic) and all-face centered (F, all-face centered hypercubic) Bravais lattices occur.

The orientation of the symmetry elements of the 6D space groups is fixed by the isomorphism of the 3D and 6D point groups. The reducible matrix representations of the generating symmetry operations are

Table 3.20. 3D point groups of order k and corresponding 6D hypercubic space groups with their reflection conditions [28, 38]

3D Point Group	k	6D Space Group	Reflection Conditions
$\dfrac{2}{m}\bar{3}\bar{5}$	120	$P\dfrac{2}{m}\bar{3}\bar{5}$	No condition
		$P\dfrac{2}{n}\bar{3}\bar{5}$	$h_1 h_2 \bar{h}_1 \bar{h}_2 h_5 h_6 : h_5 - h_6 = 2n$
		$I\dfrac{2}{m}\bar{3}\bar{5}$	$h_1 h_2 h_3 h_4 h_5 h_6 : \sum_{i=1}^{6} h_i = 2n$
		$F\dfrac{2}{m}\bar{3}\bar{5}$	$h_1 h_2 h_3 h_4 h_5 h_6 : \sum_{i\neq j=1}^{6} h_i + hj = 2n$
		$F\dfrac{2}{n}\bar{3}\bar{5}$	$h_1 h_2 h_3 h_4 h_5 h_6 : \sum_{i\neq j=1}^{6} h_i + hj = 2n$
			$h_1 h_2 \bar{h}_1 \bar{h}_2 h_5 h_6 : h_5 - h_6 = 2n$
235	60	$P235$	No condition
		$P235_1$	$h_1 h_2 h_2 h_2 h_2 h_2 : h_1 = 5n$
		$I235$	$h_1 h_2 h_3 h_4 h_5 h_6 : \sum_{i=1}^{6} h_i = 2n$
		$I235_1$	$h_1 h_2 h_3 h_4 h_5 h_6 : \sum_{i=1}^{6} h_i = 2n$
			$h_1 h_2 h_2 h_2 h_2 h_2 : h_1 = 5n$
		$F235$	$h_1 h_2 h_3 h_4 h_5 h_6 : \sum_{i\neq j=1}^{6} h_i + hj = 2n$
		$F235_1$	$h_1 h_2 h_3 h_4 h_5 h_6 : \sum_{i\neq j=1}^{6} h_i + hj = 2n$
			$h_1 h_2 h_2 h_2 h_2 h_2 : h_1 = 5n$

$$\Gamma_D(5) = \begin{pmatrix} 1&0&0&0&0&0 \\ 0&0&0&0&0&1 \\ 0&1&0&0&0&0 \\ 0&0&1&0&0&0 \\ 0&0&0&1&0&0 \\ 0&0&0&0&1&0 \end{pmatrix}_D \,,\quad \Gamma_D(3) = \begin{pmatrix} 0&1&0&0&0&0 \\ 0&0&0&0&0&1 \\ 0&0&0&\bar{1}&0&0 \\ 0&0&0&0&\bar{1}&0 \\ 0&0&1&0&0&0 \\ 1&0&0&0&0&0 \end{pmatrix}_D \,,\quad \Gamma_D(2) = \begin{pmatrix} 0&0&0&0&1&0 \\ 0&\bar{1}&0&0&0&0 \\ 0&0&\bar{1}&0&0&0 \\ 0&0&0&0&0&1 \\ 1&0&0&0&0&0 \\ 0&0&0&1&0&0 \end{pmatrix}_D \,,$$

$$\Gamma_D(\bar{1}) = \begin{pmatrix} \bar{1}&0&0&0&0&0 \\ 0&\bar{1}&0&0&0&0 \\ 0&0&\bar{1}&0&0&0 \\ 0&0&0&\bar{1}&0&0 \\ 0&0&0&0&\bar{1}&0 \\ 0&0&0&0&0&\bar{1} \end{pmatrix}_D \,,\quad \Gamma_D(m) = \begin{pmatrix} 1&0&0&0&0&0 \\ 0&0&0&0&0&1 \\ 0&0&0&0&1&0 \\ 0&0&0&1&0&0 \\ 0&0&1&0&0&0 \\ 0&1&0&0&0&0 \end{pmatrix}_D \,. \qquad (3.198)$$

The block-diagonalisation of these matrices by the matrix

$$
\mathsf{W} = a^* \begin{pmatrix}
0 & s\cos\frac{4\pi}{5} & s\cos\frac{6\pi}{5} & s\cos\frac{8\pi}{5} & s & s\cos\frac{2\pi}{5} \\
0 & s\sin\frac{4\pi}{5} & s\sin\frac{6\pi}{5} & s\sin\frac{8\pi}{5} & 0 & s\sin\frac{2\pi}{5} \\
1 & c & c & c & c & c \\
0 & -s\cos\frac{8\pi}{5} & -s\cos\frac{2\pi}{5} & -s\cos\frac{6\pi}{5} & -s & -s\cos\frac{4\pi}{5} \\
0 & -s\sin\frac{8\pi}{5} & -s\sin\frac{2\pi}{5} & -s\sin\frac{6\pi}{5} & 0 & -s\sin\frac{4\pi}{5} \\
1 & -c & -c & -c & -c & -c
\end{pmatrix}
\tag{3.199}
$$

with $s = \sin\theta$ and $c = \cos\theta$ gives the irreducible representations of the symmetry operations in the orthogonal subspaces.

The reflection and inversion operations $\Gamma_V\,(m)$ and $\Gamma_V\,(\bar{1})$ are equivalent in both subspaces $V^{\parallel}$ and $V^{\perp}$. $\Gamma_V\,(5)$, a $2\pi/5$ rotation in $V^{\parallel}$ around the 5-fold axis, however, corresponds to a $4\pi/5$ rotation in $V^{\perp}$

$$
\Gamma\,(5) = \left(\begin{array}{ccc|ccc}
\cos\frac{2\pi}{5} & -\sin\frac{2\pi}{5} & 0 & 0 & 0 & 0 \\
\sin\frac{2\pi}{5} & \cos\frac{2\pi}{5} & 0 & 0 & 0 & 0 \\
0 & 0 & 1 & 0 & 0 & 0 \\
\hline
0 & 0 & 0 & \cos\frac{4\pi}{5} & -\sin\frac{4\pi}{5} & 0 \\
0 & 0 & 0 & \sin\frac{4\pi}{5} & \cos\frac{4\pi}{5} & 0 \\
0 & 0 & 0 & 0 & 0 & 1
\end{array}\right)_V = \left(\begin{array}{c|c}
\Gamma^{\parallel}\,(5) & 0 \\
\hline
0 & \Gamma^{\perp}\,(5)
\end{array}\right)_V .
\tag{3.200}
$$

The same holds for the 3-fold rotation operation. The Fourier module in physical reciprocal space M^* of icosahedral quasicrystals with primitive Bravais hyperlattice is invariant under the action of the scaling matrix S^3

$$
S = \frac{1}{2}\begin{pmatrix}
1 & 1 & 1 & 1 & 1 & 1 \\
1 & 1 & 1 & \bar{1} & \bar{1} & 1 \\
1 & 1 & 1 & 1 & \bar{1} & \bar{1} \\
1 & \bar{1} & 1 & 1 & 1 & \bar{1} \\
1 & \bar{1} & \bar{1} & 1 & 1 & 1 \\
1 & 1 & \bar{1} & \bar{1} & 1 & 1
\end{pmatrix}_D , \qquad
S^3 = 8\begin{pmatrix}
2 & 1 & 1 & 1 & 1 & 1 \\
1 & 2 & 1 & \bar{1} & \bar{1} & 1 \\
1 & 1 & 2 & 1 & \bar{1} & \bar{1} \\
1 & \bar{1} & 1 & 2 & 1 & \bar{1} \\
1 & \bar{1} & \bar{1} & 1 & 2 & 1 \\
1 & 1 & \bar{1} & \bar{1} & 1 & 2
\end{pmatrix}_D
\tag{3.201}
$$

and we obtain $S^3 M^* = \tau^3 M^*$. In the case of centered Bravais hyperlattices the respective scaling operations correspond to the matrix S. By similarity transformation with the matrix W the components of the scaling operation in the two subspaces can be obtained

$$
S = \left(\begin{array}{ccc|ccc}
\tau & 0 & 0 & 0 & 0 & 0 \\
0 & \tau & 0 & 0 & 0 & 0 \\
0 & 0 & \tau & 0 & 0 & 0 \\
\hline
0 & 0 & 0 & -\frac{1}{\tau} & 0 & 0 \\
0 & 0 & 0 & 0 & -\frac{1}{\tau} & 0 \\
0 & 0 & 0 & 0 & 0 & -\frac{1}{\tau}
\end{array}\right)_V = \left(\begin{array}{c|c}
S^{\parallel} & 0 \\
\hline
0 & S^{\perp}
\end{array}\right)_V .
\tag{3.202}
$$

Centered 6D Bravais lattices with icosahedral point group symmetry   A 6D hypercube has 64 corners, 192 edges, 240 2D faces, 160 3D faces (cells), 60 4D faces (hypercells) and 12 5D faces. Centering the 6D hypercube itself, leads to I centering with translation vector $1/2(111111)$.

The 5D faces can be seen in analogy to the 2D faces of a 3D cube, i.e., for each face there is only one dimension of the cube were it has no extension. In 3D, the centers of the six 2D faces are at $1/2(110)$, $1/2(112)$ and all permutations. In 6D, the centers of the twelve 5D faces are at $1/2(111110)$, $1/2(111112)$ and all permutations. A hyperatom at such a position belongs to one halve to the unit cell, in total contributing 6 hyperatoms.

Analogously, the centers of the 60 4D faces are given by $1/2(111100)$, $1/2(111120)$, $1/2(111122)$ and all permutations. A hyperatom at such a position belongs to one quarter to the unit cell, in total contributing 15 hyperatoms. The 160 3D faces are centered at $1/2(111000)$, $1/2(111200)$, $1/2(111220)$, $1/2(111222)$, and all permutations. A hyperatom at such a position belongs to one eight to the unit cell, in total contributing 20 hyperatoms. The 240 2D faces are centered by $1/2(110000)$, $1/2(112000)$, $1/2(112200)$, $1/2(112220)$, $1/2(112222)$, and all permutations. A hyperatom at such a position belongs to one sixteenth to the 6D unit cell, in total contributing 15 hyperatoms.

The F centering of quasiperiodic structures with icosahedral symmetry, can best be described by the set of translation vectors to all even nodes of a sublattice with half the lattice constant of the 6D F-centered lattice. This corresponds to centerings of all 2D and 4D faces and of the 6D hypercube itself. I centering is, therefore, part of F centering. This is true for nD hypercubic lattices with n an even number.

3.7.3 Example: Ammann Tiling (AT)

In the 6D description, the Ammann Tiling is obtained by an irrational cut of a hypercubic lattice decorated with triacontahedral atomic surfaces (Fig. 3.62) at the hyperlattice nodes. The AT is a canonical tiling, i.e., the shape of the atomic surfaces corresponds to a perp-space projection of the 6D unit cell. Thus, the edge length of the rhombs covering the atomic surface is equal to the perp-space component of the basis vectors $\pi^{\perp}(\mathbf{d}_i) = 1/2a^*$.

3.7.3.1 Structure Factor

The structure factor of the AT can be calculated according to the general formula (3.12). The geometrical form factor g_k for the AT corresponds to the Fourier transform of one triacontahedral atomic surface at the origin of the 6D unit cell. The volumes of the projected unit cell and of the atomic surface are in the case of the canonical AT equal and amount to

$$A_{\mathrm{UC}}^{\perp} = 8a_r^3 \left(\sin \frac{2\pi}{5} + \sin \frac{\pi}{5} \right) . \tag{3.203}$$
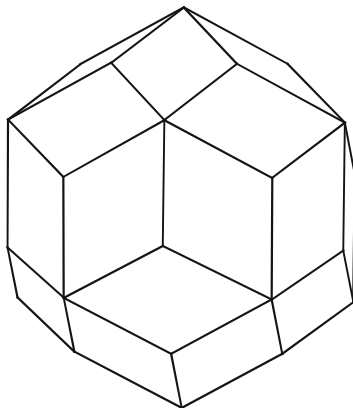
Fig. 3.62. Atomic surface of the AT in the 6D description. It results from the projection of one 6D unit cell upon $V^\perp$

Integrating the triacontahedron by decomposition into trigonal pyramids (directed from the center of the triacontahedron to three of its corners with the vectors $\mathbf{e}_i, i = 1, \ldots, 3$) yields

$$g\left(\mathbf{H}^\perp\right) = \frac{1}{A_{\mathrm{UC}}^\perp} \sum_R g_k\left(R^T \mathbf{H}^\perp\right) \tag{3.204}$$

with $k = 1, \ldots, 60$ running over all symmetry operations R of the icosahedral point group,

$$g_k\left(\mathbf{H}^\perp\right) = -\mathrm{i}V_r \frac{A_2 A_3 A_4 \mathrm{e}^{\mathrm{i}A_1} + A_1 A_3 A_5 \mathrm{e}^{\mathrm{i}A_2} + A_1 A_2 A_6 \mathrm{e}^{\mathrm{i}A_3} + A_4 A_5 A_6}{A_1 A_2 A_3 A_4 A_5 A_6}$$

$$\tag{3.205}$$

with $A_j = 2\pi \mathbf{H}^\perp \mathbf{e}_j, j = 1, \ldots, 3, A_4 = A_2 - A_3, A_5 = A_3 - A_1, A_6 = A_1 - A_2$, and $V_r = \mathbf{e}_1 \cdot (\mathbf{e}_2 \times \mathbf{e}_3)$ the volume of the parallelepiped defined by the vectors $\mathbf{e}_j, j = 1, \ldots, 3$ [51].

The radial structure factor distribution of the centrosymmetric AT decorated with point scatterers is shown in Fig. 3.63 as a function of the par- and perp-space components of the diffraction vectors.

The number of weak reflections, i.e., those with large values of $H^\perp$, increases with the power of 6, that of strong reflections, i.e., those that are from 6D reciprocal lattice points close to $V^\parallel$, only with the power of three. Now we define a lattice with doubled unit cell parameters, and call the lattice we used for the AT the sublattice. If we decorate the origin and the center of the new unit cell with the atomic surface of the AT, we get an I-centered structure, by decoration of all even nodes of the sublattice we get F-centering. The radial distribution functions of a 6D I-centered and a 6D F-centered AT are shown in Fig. 3.64.

A more realistic distribution function is illustrated in Fig. 3.65. Here the extinct reflections are not plotted. If we designate the contributions from the
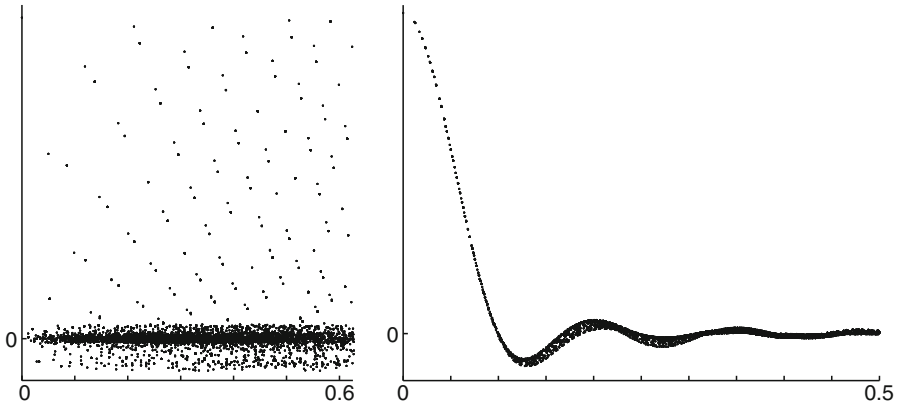
Fig. 3.63. Radial distribution function of the structure factors $F(\mathbf{H})$ of the Ammann tiling, decorated with point atoms, as a function of $H^\parallel$ and $H^\perp$ ($a_r = 5.0$ Å). All reflections are shown within $-6 \le h_i \le 6$, $i = 1, \ldots, 6$, units of the axes are Å^{-1}
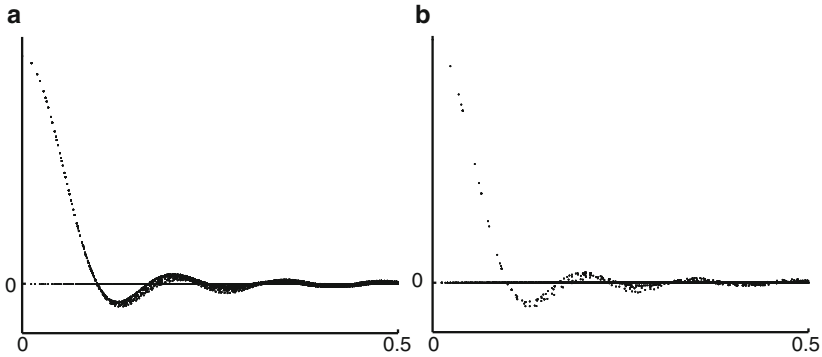
Fig. 3.64. Radial distribution function of the structure factors $F(\mathbf{H})$ of an I-centered (**a**) and an F-centered (**b**) Ammann tiling, decorated with point atoms, as a function of $H^\perp$ ($a_r = 5.0$ Å). In both cases, the branch of extinct reflections are shown as horizontal line. All reflections are shown within $-6 \le h_i \le 6$, $i = 1, \ldots, 6$, units of the axes are Å^{-1}

three hyperatoms, Pn and Pn' at the odd and even sublattice nodes and Pbc in the body center (see Sect. 9.4), as A, B, and C, then the four branches can be explained in the following way: A+B+C gives the topmost branch, A+B−C the second, A−B+C the third and A−B−C the negative branch. The sign of B and C depends on the parity of reflections. Note that all strong reflections have positive signs, which allows a straightforward determination of a first rough structure model, without partitioning of the atomic surfaces.

The Bragg intensity distribution of P and F centered 6D Bravais lattices with equal 6D lattice parameters is shown in Fig. 3.66. The primitive structure is obtained from the F centered by occupying all atomic surfaces on the even

a

b
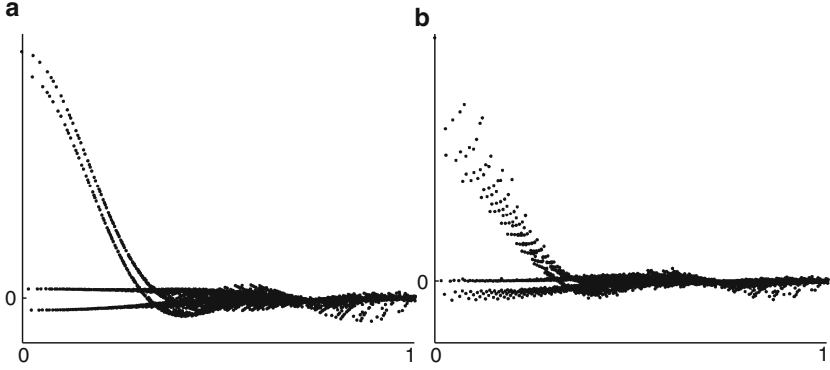
Fig. 3.65. Radial distribution function of the structure factors $F(\mathbf{H})$ of the QG model [35] for i-Al-Cu-Fe (see Sect. 9.4) as function of $H^\perp$. The structure factors have been calculated for neutron scattering in (**a**) and for X-ray diffraction in (**b**). All reflections are shown within $10^{-4}I(\mathbf{0}) < I(\mathbf{H}) < I(\mathbf{0})$, $-6 \le h_i \le 6$, $i = 1, \ldots, 6$, units of axes are Å^{-1}

sublattice nodes except the origin with Cu, while the atomic surface at the origin is occupied by Al. In the F centered case all atomic surfaces are occupied by Al. In this way, the underlying structures only differ in their chemical site occupancies.

3.7.3.2 Periodic Average Structure

An all-face centered periodic cubic average structure of the AT can be obtained by oblique projection of the 6D hypercrystal structure along $[\bar{1}11010]_D$, $[01\bar{1}10\bar{1}]_D$ and $[\bar{1}001\bar{1}1]_D$ onto $V^\parallel$ (Fig. 3.67) with the projector

$$
\pi^\parallel = \begin{pmatrix} 1\ 0\ 0 & 0 & 0 & -(2\tau-3) \\ 0\ 1\ 0 & 0 & 2\tau-3 & 0 \\ 0\ 0\ 1 & 2\tau-3 & 0 & 0 \end{pmatrix}_V = \frac{1}{2a^*} \times
$$

$$
\begin{pmatrix} -(2\tau-3) & -(\tau-1) & -(\tau-1) & 2-\tau & 1 & 2-\tau \\ 0 & \tan\frac{\pi}{5} & -\tan\frac{\pi}{5} & -\tan\frac{\pi}{5} & 0 & \tan\frac{\pi}{5} \\ 1 & 2-\tau & 2-\tau & \tau-1 & 2\tau-3 & \tau-1 \end{pmatrix}_D . \quad (3.206)
$$

The lattice parameter results to

$$
|\mathbf{a}^{av}| = \left| \pi^\parallel \begin{pmatrix} 0 \\ 0 \\ 0 \\ \bar{1} \\ 0 \\ 1 \end{pmatrix}_D \right| = \left| \frac{1}{a^*} \begin{pmatrix} 0 \\ \tan\frac{\pi}{5} \\ 0 \end{pmatrix}_V \right| = \frac{\tan\frac{\pi}{5}}{a^*} = 2a_r \tan\frac{\pi}{5}. \quad (3.207)
$$
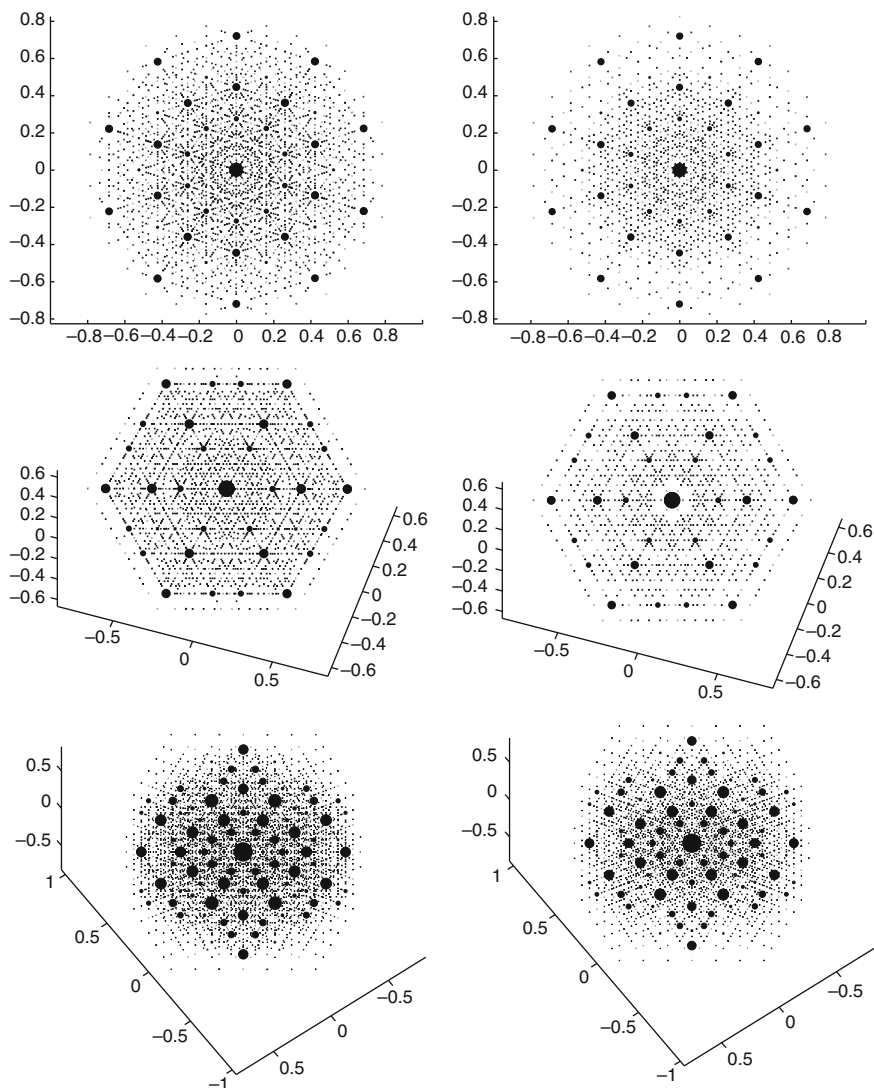
Fig. 3.66. Diffraction patterns of a P (*left side*) and an F centered (*right side*) Ammann tiling decorated with Al and Cu atoms (P), or only Al atoms (F). From top to bottom, sections with 5-, 3- and 2-fold symmetry are shown. All reflections are plotted within $10^{-4}I(\mathbf{0}), < I(\mathbf{H}) < I(\mathbf{0}), -6 \leq h_i \leq 6, i = 1, \ldots, 6$, units of axes are Å^{-1}

The projected atomic surfaces are still of regular triacontahedral shape and by a factor $\cos\phi = 0.230$, $\phi = \arctan(\tau^3)$ smaller than the original ones (Fig. 3.68). The topology of the AT allows only an occupancy factor of
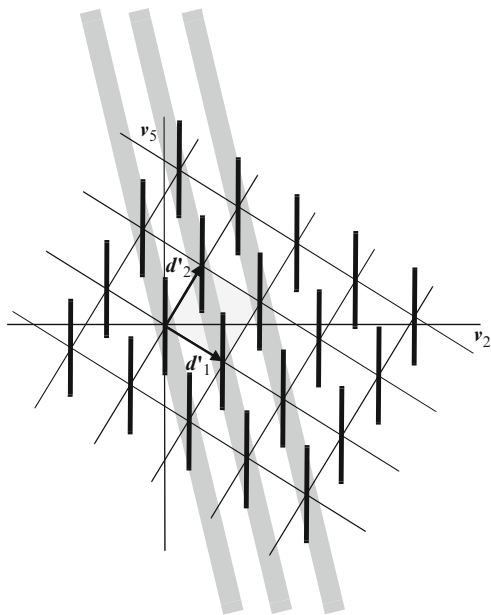
Fig. 3.67. Characteristic 2-fold section of the Ammann tiling in the 6D description. The vectors $\mathbf{d}'_1$ and $\mathbf{d}'_2$ correspond to the vectors $(000\bar{1}01)_D$ and $(01\bar{1}000)_D$. The oblique projection is indicated by gray strips
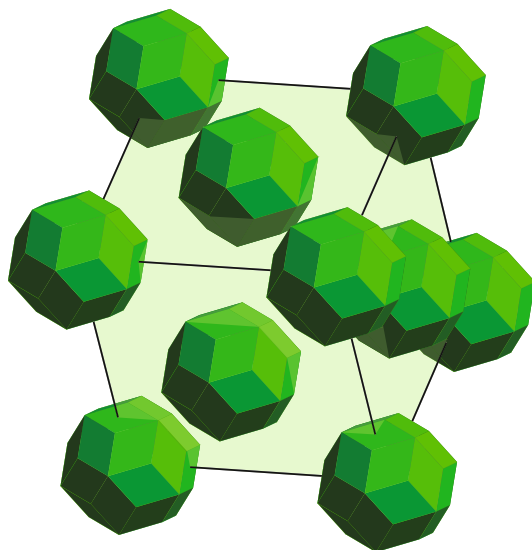
Fig. 3.68. Perspective view of one 3D unit cell of the periodic average structure of the Ammann tiling. The F-centered unit cell is decorated by undistorted but shrunk triacontahedra resulting from the oblique projection

$2\tau + 1/5 = 0.847$. This means that every vertex of the AT lies inside a different projected atomic surface. 15.3% of all projected atomic surfaces contain no vertex at all. This is comparable to the average structure of an IMS with both displacive and substitutional modulation.

The volume fraction occupied by the projected atomic surfaces in the average structure amounts to

$$\frac{4\tau \cos \phi \sin \frac{2\pi}{5}}{\left(\tan \frac{\pi}{5}\right)^3} = 0.195 \ . \tag{3.208}$$

The reciprocal lattice Λ^* corresponding to the average structure is spanned by the vectors

$$\mathbf{a}_1^{*\mathrm{av}} = a^* \tan \frac{3\pi}{10} \begin{pmatrix} \cos \frac{\theta}{2} \\ 0 \\ \sin \frac{\theta}{2} \end{pmatrix}_V \ , \quad \mathbf{a}_2^{*\mathrm{av}} = a^* \tan \frac{3\pi}{10} \begin{pmatrix} 0 \\ 1 \\ 0 \end{pmatrix}_V \ ,$$

$$\mathbf{a}_3^{*\mathrm{av}} = a^* \tan \frac{3\pi}{10} \begin{pmatrix} \sin \frac{\theta}{2} \\ 0 \\ \cos \frac{\theta}{2} \end{pmatrix}_V \ . \tag{3.209}$$

They are enlarged by a factor τ^2 compared with the reciprocal basis vectors of the setting 2 discussed above. Thus, all reflections of the type

$$\mathbf{H} = \frac{1}{2} \left((-h_1 + h_3)\,(-h_1 + h_2)\,(-h_1 - h_2)\,(-h_2 + h_3)\,(h_1 + h_3)\,(h_2 + h_3)\right)_D$$

are main reflections.

3.7.3.3 Approximant Structures

The symmetry and metrics of rational approximants of 3D icosahedral phases with pentagonal, cubic and trigonal symmetry have been discussed in detail by [10] and for orthorhombic approximants by [32]. In the following we will demonstrate the derivation of shear matrix and lattice parameters on the example of cubic rational approximants consistent with our settings and nomenclature.

Preserving a particular subset of 3-fold axis of the icosahedral point group results in cubic approximants. The action of the shear matrix is to deform the 6D lattice Σ defined by the basis matrix

$$(\mathbf{d}_1 \mathbf{d}_2 \mathbf{d}_3 \mathbf{d}_4 \mathbf{d}_5 \mathbf{d}_6) = \frac{1}{a^* 2\sqrt{2 + \tau}} \begin{pmatrix} 0 & -1 & -\tau & 0 & \tau & 1 \\ 1 & \tau & 0 & -1 & 0 & \tau \\ \tau & 0 & 1 & \tau & 1 & 0 \\ 0 & 0 & -1 & \tau & -\tau & 1 \\ 1 & 1 & -\tau & 0 & 0 & -\tau \\ \tau & -\tau & 0 & -1 & -1 & 0 \end{pmatrix}_C \tag{3.210}$$

in a way to bring three selected lattice vectors into the par-space. If we define these lattice vectors along the cubic axes of setting 2 according to

$$\mathbf{r}_1 = \{p\,(\mathbf{d}_6 - \mathbf{d}_2) + q\,(\mathbf{d}_5 - \mathbf{d}_3)\} = \frac{1}{a^*2\sqrt{2+\tau}} \begin{pmatrix} 2\,(p+\tau q) \\ 0 \\ 0 \\ p - (\tau - 1)\,q \\ -\tau^2 p + \tau q \\ \tau p - q \end{pmatrix}_C$$

$$\mathbf{r}_2 = \{r\,(\mathbf{d}_1 - \mathbf{d}_4) + s\,(\mathbf{d}_2 + \mathbf{d}_6)\} = \frac{1}{a^*2\sqrt{2+\tau}} \begin{pmatrix} 0 \\ 2\,(r+\tau s) \\ 0 \\ -\tau r + s \\ r - (\tau - 1)\,s \\ \tau^2 r - \tau s \end{pmatrix}_C$$

$$\mathbf{r}_3 = \{t\,(\mathbf{d}_3 + \mathbf{d}_5) + u\,(\mathbf{d}_1 + \mathbf{d}_4)\} = \frac{1}{a^*2\sqrt{2+\tau}} \begin{pmatrix} 0 \\ 0 \\ 2\,(t+\tau u) \\ -\tau^2 t + \tau u \\ -\tau t + u \\ -t + (\tau - 1)\,u \end{pmatrix}_C \qquad (3.211)$$

with $p, q, r, s, t, u \in \mathbb{Z}$ the $m\bar{3}$ point group symmetry is retained. From the condition that the perp-space components of the approximant basis vectors have to vanish we obtain

$$A\frac{1}{a^*2\sqrt{2+\tau}} \begin{pmatrix} 2\,(p+\tau q) \\ 0 \\ 0 \\ p - (\tau - 1)\,q \\ -\tau^2 p + \tau q \\ \tau p - q \end{pmatrix}_C =$$

$$= \frac{1}{a^*2\sqrt{2+\tau}} \begin{pmatrix} 2\,(p+\tau q) \\ 0 \\ 0 \\ A_{41}2\,(p+\tau q) + p - (\tau - 1)\,q \\ A_{51}2\,(p+\tau q) - \tau^2 p + \tau q \\ A_{61}2\,(p+\tau q) + \tau p - q \end{pmatrix}_C \overset{!}{=} \frac{2(p+\tau q)}{a^*2\sqrt{2+\tau}} \begin{pmatrix} 1 \\ 0 \\ 0 \\ 0 \\ 0 \\ 0 \end{pmatrix}_C , \qquad (3.212)$$

$$A\frac{1}{a^*2\sqrt{2+\tau}} \begin{pmatrix} 0 \\ 2\,(r+\tau s) \\ 0 \\ -\tau r + s \\ r - (\tau - 1)\,s \\ \tau^2 r - \tau s \end{pmatrix}_C =$$

$$= \frac{1}{a^*2\sqrt{2+\tau}} \begin{pmatrix} 0 \\ 2(r+\tau s) \\ 0 \\ A_{42}2(r+\tau s) - \tau r + s \\ A_{52}2(r+\tau s) + r - (\tau - 1)s \\ A_{62}2(r+\tau s) + \tau^2 r - \tau s \end{pmatrix}_C \stackrel{!}{=} \frac{1}{a^*2\sqrt{2+\tau}} \begin{pmatrix} 0 \\ 2(r+\tau s) \\ 0 \\ 0 \\ 0 \\ 0 \end{pmatrix}_C, \quad (3.213)$$

$$A\frac{1}{a^*2\sqrt{2+\tau}} \begin{pmatrix} 0 \\ 0 \\ 2(t+\tau u) \\ -\tau^2 t + \tau u \\ -\tau t + u \\ -t + (\tau - 1)u \end{pmatrix}_C =$$

$$= \frac{1}{a^*2\sqrt{2+\tau}} \begin{pmatrix} 0 \\ 0 \\ 2(t+\tau u) \\ A_{43}2(t+\tau u) - \tau^2 t + \tau u \\ A_{53}2(t+\tau u) - \tau t + u \\ A_{63}2(t+\tau u) - t + (\tau - 1)u \end{pmatrix}_C \stackrel{!}{=} \frac{1}{a^*2\sqrt{2+\tau}} \begin{pmatrix} 0 \\ 0 \\ 2(t+\tau u) \\ 0 \\ 0 \\ 0 \end{pmatrix}_C. \quad (3.214)$$

In the case of cubic symmetry we have the equalities $p = r = t$ and $q = s = u$. Therewith, the submatrix $(\tilde{A}^{-1})^T$ is

$$(\tilde{A}^{-1})^T = \frac{q - \tau p}{2(p + \tau q)} \begin{pmatrix} \frac{1}{\tau} & 1 & \tau \\ \tau & \frac{1}{\tau} & 1 \\ 1 & \tau & \frac{1}{\tau} \end{pmatrix}_C . \quad (3.215)$$

The basis vectors spanning the unit cell of the cubic $\langle q, p \rangle$-approximant are given by

$$\mathbf{a}_1^{\mathrm{Ap}} = \left| \pi^\parallel (\mathbf{r}_1) \right| = \frac{p + \tau q}{a^*\sqrt{2+\tau}} \begin{pmatrix} 1 \\ 0 \\ 0 \end{pmatrix}_C ,$$

$$\mathbf{a}_2^{\mathrm{Ap}} = \left| \pi^\parallel (\mathbf{r}_2) \right| = \frac{p + \tau q}{a^*\sqrt{2+\tau}} \begin{pmatrix} 0 \\ 1 \\ 0 \end{pmatrix}_C ,$$

$$\mathbf{a}_3^{\mathrm{Ap}} = \left| \pi^\parallel (\mathbf{r}_3) \right| = \frac{p + \tau q}{a^*\sqrt{2+\tau}} \begin{pmatrix} 0 \\ 0 \\ 1 \end{pmatrix}_C . \quad (3.216)$$

For the most common approximants the coefficients p, q, r, s, t, u correspond to Fibonacci numbers F_n. Setting $p = r = t = F_n, q = s = u = F_{n+1}$ we obtain the $\langle F_{n+1}, F_n \rangle$-approximants with lattice parameters

$$\left| \mathbf{a}_1^{\mathrm{Ap}} \right| = \frac{\tau^{n+1}}{a^*\sqrt{2+\tau}} = \left| \mathbf{a}_2^{\mathrm{Ap}} \right| = \left| \mathbf{a}_3^{\mathrm{Ap}} \right| \quad (3.217)$$

by using the equality $\tau F_{n+1} + F_n = \tau^{n+1}$.

All Bragg peaks are shifted according to (3.8). Projecting the 6D reciprocal space onto par-space results in a periodic reciprocal lattice. All reflections $\mathbf{H} = h_1 h_2 h_3 h_4 h_5 h_6$ are transformed to

$$\begin{aligned}
\mathbf{H}^{\mathrm{Ap}} = \ & [p(h_6 - h_2) + q(h_5 - h_3)] \ [r(h_1 - h_4) + s(h_2 + h_6)] \\
& [t(h_3 + h_5) + u(h_1 + h_4)] \ .
\end{aligned}$$

References

1. P.A. Bancel, P.A. Heiney, P.W. Stephens, A.I. Goldman, P.M. Horn, Structure of Rapidly Quenched Al-Mn. Phys. Rev. Lett. **54**, 2422–2425 (1985)
2. S. Bhagavantam, T. Venkatarayudu, Theory of Groups and its Application to Physical Problems. Academic Press: New York London (1969)
3. A. Cervellino, W. Steurer, General periodic average structures of decagonal quasicrystals. Acta Crystallogr A **58**, 180–184 (2002)
4. A. Cervellino, T. Haibach, W. Steurer, Derivation of the Proper Basis of Quasicrystals. Phys. Rev. B **57**, 11223–11231 (1998)
5. N.G. de Bruijn, Algebraic theory of Penrose's nonperiodic tilings of the plane, I, II. Proc. Kon. Nederl. Akad. Wetenschap. A **84**, 39–52, 53–66 (1981)
6. P.M. de Wolff, The Pseudo-symmetry of Modulated Crystal Structures. Acta Crystallogr. A **30**, 777–785 (1974)
7. K. Edagawa, K. Suzuki, M. Ichihara, S. Takeuchi, T. Shibuya, High-order Periodic Approximants of Decagonal Quasicrystal in $Al_{70}Ni_{15}Co_{15}$. Phil. Mag. B **64**, 629–638 (1991)
8. V. Elser, Indexing Problems in Quasicrystal Diffraction. Phys. Rev. B **32**, 4892–4898 (1985)
9. A.I. Goldman, R.F. Kelton, Quasicrystals and Crystalline Approximants. Rev. Mod.Phys. **65**, 213–230 (1993)
10. D. Gratias, A. Katz, M. Quiquandon, Geometry of Approximant Structures in Quasicrystals. J. Phys.: Condens. Matter **7**, 9101–9125 (1995)
11. C.L. Henley, Sphere Packings and Local Environments in Penrose Tilings. Phys. Rev. B **34**, 797–816 (1986)
12. C. Hermann, Kristallographie in Räumen beliebiger Dimensionszahl. I. Die Symmetrieoperationen. Acta Crystallogr. **2**, 139–145 (1949)
13. C.S. Herz, Fourier Transforms Related to Convex Sets. Ann. Math. **75**, 81–92 (1962)
14. H. Hiller, The Crystallographic Restriction in Higher Dimensions. Acta Crystallogr. A **41**, 541–544 (1985)
15. A. Janner, Decagrammal Symmetry of Decagonal $Al_{78}Mn_{22}$ Quasicrystal. Acta Crystallogr. A **48**, 884–901 (1992)
16. T. Janssen, Crystallography of Quasi-Crystals. Acta Crystallogr. A **42**, 261–271(1986)
17. T. Janssen, Aperiodic Crystals: a Contradictio in Terminis? Phys. Rep. **168**, 55–113 (1988)
18. T. Janssen, The Symmetry Operations for N-dimensional Periodic and Quasiperiodic Structures. Z. Kristallogr. **198**, 17–32 (1992)
19. T. Janssen, Crystallographic Scale Transformations. Phil. Mag. B **66**, 125–134 (1992)

20. T. Janssen, Tensors in quasiperiodic structures. In: International Tables for Crystallography, vol. D) Kluwer Academic Publisher, Dordrecht, pp. 243–264, (2003)

21. T. Janssen, A. Janner, A, Looijenga-Vos, P.M. Wolff, de: Incommensurate and Commensurate Modulated Crystal Structures. In: International Tables for Crystallography, vol. C, Kluwer Academic Publisher, Dordrecht, pp. 797–844 (1992)

22. M.V. Jaric, Diffraction from Quasi-Crystals - Geometric Structure Factor. Phys. Rev. B **34**, 4685–4698 (1986)

23. M.A. Kaliteevski, V.V. Nikolaev, R.A. Abram, S. Brand, Bandgap structure of optical Fibonacci lattices after light diffraction. Opt. Spectr. **91**, 109–118 (2001)

24. M. Kalning, S. Kek, H.G. Krane, V. Dorna, W. Press, W. Steurer, Phason-strain Analysis of the Twinned Approximant to Decagonal Quasicrystal $Al_{70}Co_{15}Ni_{15}$: Evidence for a One-dimensional Quasicrystal. Phys. Rev. B **55**, 187–192 (1997)

25. E. Koch, Twinning. (International Tables for Crystallography, vol. C, Kluwer Academic Publisher, Dordrecht, pp. 10–14 (1992)

26. P. Kramer, M. Schlottmann, Dualization of Voronoi Domains and Klotz Construction - a General-Method for the Generation of Proper Space Fillings. J. Phys. A: Math. Gen. **22**, L1097–L1102 (1989)

27. D. Levine, P.J. Steinhardt, Quasicrystals. I. Definition and Structure. Phys. Rev. B **34**, 596–616 (1986)

28. L.S. Levitov, J. Rhyner, Crystallography of Quasicrystals; Application to Icosahedral Symmetry. J. Phys. France **49**, 1835–1849 (1988)

29. J.M. Luck, C. Godrèche, A. Janner, T. Janssen, The Nature of the Atomic Surfaces of Quasiperiodic Self-similar Structures. J. Phys. A: Math. Gen. **26**, 1951–1999 (1993)

30. Z. Masakova, J. Patera, J. Zich, Classification of Voronoi and Delone tiles of quasicrystals: III. Decagonal acceptance window of any size. J. Phys A - Math. Gen. **38**, 1947–1960 (2005)

31. K. Niizeki, A Classification of the Space Groups of Approximant Lattices to a Decagonal Quasilattice. J. Phys. A: Math. Gen. **24**, 3641–3654 (1991)

32. K. Niizeki, The Space Groups of Orthorhombic Approximants to the Icosahedral Quasilattice. J. Phys. A: Math. Gen. **25**, 1843–1854 (1992)

33. A. Pavlovitch, M. Kléman, Generalized 2D Penrose Tilings: Structural Properties. J. Phys. A: Math. Gen. **20**, 687–702 (1987)

34. R. Penrose, The Rôle of Aesthetics in Pure and Applied Mathematical Research. Bull. Inst. Math, Appl. **10**, 266–271 (1974)

35. M. Quiquandon, D. Gratias, Unique six-dimensional structural model for Al-Pd-Mn and Al-Cu-Fe icosahedral phases. Phys. Rev. B **74**, - art. no. 214205 (2006)

36. D.A. Rabson, N.D. Mermin, D.S. Rokhsar, D.C. Wright, The Space Groups of Axial Crystals and Quasicrystals. Rev. Mod. Phys. **63**, 699–733 (1991)

37. P. Repetowicz, J. Wolny, Diffraction pattern calculations for a certain class of N-fold quasilattices. Journal of Physics a-Mathematical and General **31**, 6873–6886 (1998)

38. D.S. Rokshar, N.D. Mermin, D.C. Wright, The Two-dimensional Quasicrystallographic Space Groups less than 23–fold. Acta Crystallogr. A **44**, 197–211 (1988)

39. J.E.S. Socolar, Simple Octagonal and Dodecagonal Quasicrystals. Phys. Rev. B **39**, 10519–10551 (1989)

40. J.E.S. Socolar, P.J. Steinhardt, Quasicrystals. II., Unit Cell Configurations. Phys. Rev. B **34**, 617–647 (1986)
41. B. Souvignier, Enantiomorphism of crystallographic groups in higher dimensions with results in dimensions up to 6. Acta Crystallogr. A **59**, 2003
42. W. Steurer, Experimental aspects of the structure analysis of aperiodic materials. In: Axel, F., Gratias, D. (eds.): Beyond Quasicrystals. Les Edition de Physique, Les Ulis, Springer, Berlin (1995)
43. W. Steurer, The Structure of Quasicrystals. Physical Metallurgy, vol. 1, Elsevier Science North Holland, Amsterdam, pp. 371–411 (1996)
44. W. Steurer, Twenty years of structure research on quasicrystals. Part 1. Pentagonal, octagonal, decagonal and dodecagonal quasicrystals. Z. Kristall. **219**, 391–446 (2004)
45. W. Steurer, T. Haibach, The Periodic Average Structure of Particular Quasicrystals. Acta Crystallogr. A **55**, 48–57 (1999)
46. W. Steurer, T. Haibach, Reciprocal Space Images of Aperiodic Crystals. International Tables for Crystallography, vol. B, Kluwer Academic Publishers: Dordrecht, pp. 486–518, (2001)
47. D. Sutter-Widmer, S. Deloudi, W. Steurer, Prediction of Bragg-scattering-induced band gaps in phononic quasicrystals. Phys. Rev. B **75**, art. no. 094304 (2007)
48. S. van Smaalen, Incommensurate Crystallography. International Series of Monographs in Physics. Oxford University Press: Oxford, UK (2007)
49. R. Wang, Y. Wenge, C. Hu, D. Ding, Point and Space Groups and Elastic Behaviours of One-dimensional Quasicrystals. J. Phys.: Condens. Matter **9**, 2411–2422 (1997)
50. B.T.M. Willis, A.W. Pryor, Thermal vibrations in Crystallography. Cambridge University Press, Cambridge (1975)
51. A. Yamamoto, Ideal Structure of Icosahedral Al-Cu-Li Quasicrystals. Phys. Rev. B **45**, 5217–5227 (1992)
52. H. Zhang, K.H. Kuo, Giant Al-M (M=Transitional Metal) Crystals as Penrose-tiling Approximants of theDecagonal Quasicrystal. Phys. Rev. B **42**, 8907–8914 (1990)

4

Experimental Techniques

Structure analysis aims at deriving structure models on atomic level, which explain the experimental observations quantitatively. The full description of the *real structure*; this is what can be obtained at best based on experimental observations. It includes a model of the underlying ideal structure and of the deviations from it. Such a model can serve as the basis for further modeling and for the derivation of physical properties.

In case of the analysis of crystal structures with 3D periodicity, the determination of the average structure, and, based thereupon, of the ideal structure, comprises just the determination of the structure of a single unit cell. Even though it may be difficult to determine the atomic distribution for structures with giant unit cells containing thousands of atoms, there is at least certainty about the long-range order, there is no need to prove that the structure is periodic. This is different for quasicrystals, where both the local as well as, particularly, the global structure have to be determined.

In the 3D tiling description, the local structure mainly refers to the atomic arrangement inside a unit tile or cluster, i.e. the recurrent structural building units. Global structure means the ordering of the unit tiles or clusters themselves on a higher hierarchy level. The global ordering of 3D periodic structures can be described by one of the 14 Bravais lattice types. In case of QC, however, there are infinitely many different 3D quasilattices, i.e. tilings underlying a quasiperiodic structure, not to speak about other types of aperiodic structures (see for instance [2]).

In case of the nD description of QC structures, the situation seems to be much simpler because there are only a few relevant nD Bravais lattice types. However, while there is no reason to doubt the on-average 3D periodicity of regular crystal structures, the nD periodicity of real QC had to be proved before employing the nD approach, it had to be checked whether it is applicable anyway. The usage of the nD approach actually implies that the QC structure is strictly quasiperiodic, at least on average.

Another challenge for structure determination is disorder. In 3D periodic structures, disorder means the deviation from the ideal order of atoms within one or more unit cells. Already thermal vibrations of atoms, impurities, or thermal vacancies, for instance, destroy ideal order. However, since there is only one kind of unit cell building the structure, there cannot exist disorder in the arrangement of unit cells.

Polytypic structures with stacking disorder or twinned structures may be seen as special cases where this description, i.e. disorder of unit cells of a kind of basic structure, could be applied somehow. In case of QC, where at least two different quasi unit cells (unit tiles) make up the structure, disorder in the quasilattice can occur and is entropically favored. In the limit, a structure strongly disordered in this way, can be described by a random tiling. Consequently, in the case of QC structure analysis, the analysis of disorder is crucial.

How to get the full picture, i.e. the structure of a real QC? A satisfactory QC structure solution is based on experimental data from complimentary methods such as electron microscopy, spectroscopy, surface imaging, and diffraction; it will include quantum-mechanical calculations as well.

Some methods and the information that they can provide

Electron microscopy Local structure averaged over the sample thickness ($\approx 100\,\text{Å}$); lateral ordering of clusters on the scale of up to several hundred nanometers; best possible lateral resolution with spherical aberration corrected microscopes $\approx 0.8\,\text{Å}$ at $300\,\text{kV}$, allowing the determination of atomic distances with an accuracy of $\approx 0.05\,\text{Å}$ [28].

Diffraction Local and global structure averaged into one nD unit cell, if only Bragg reflections are included in the analysis; correlation length; thermal parameters (atomic displacement parameters, ADP); if diffuse scattering is used as well, then information about the kind of disorder can be obtained; best possible 3D resolution $\approx 0.0001\,\text{Å}$.

Spectroscopy Globally averaged local structural information; best possible 3D resolution $\approx 0.0001\,\text{Å}$, depending on the technique.

Surface imaging Local surface structure over ranges of up to several hundred nanometers; best possible lateral resolution $\approx 0.05\,\text{Å}$, depending on the method.

Quantum-mechanical calculations Information on the stability of *periodic* structure models and on chemical bonding; calculations can only be performed in 3D and for approximants; the origin of the higher stability of QC compared with high-order approximants cannot be satisfactorily studied in this way.

What kind of information can we get about the structure of quasicrystals applying the full power of state-of-the-art methods? Before entering this

discussion, we should be aware of what we would like to know about a QC structure, why do we want to know it, and what do we want to do with this information.

Any *real crystal*, be it periodic or aperiodic, is finite and has equilibrium defects such as thermal vacancies, and may as well have nonequilibrium defects like dislocations or chemical heterogeneities. A real crystal with only equilibrium defects is called *perfect crystal* otherwise *imperfect crystal*. The structure of a perfect crystal differs from that of an ideal crystal as well by the existence of dynamical excitations such as phonons and phasons. Additionally, equilibrated chemical and structural disorder of other origin may be present. Consequently, in order to be able to fully describe the real structure of a crystal, one needs a model for the ideal structure as well as a model describing the deviations from it (dynamics, disorder, and defects).

This would be the ideal situation. Unfortunately, a real crystal is rarely in thermodynamic equilibrium. Usually crystallized from the melt, the actual quasicrystal at ambient conditions is always in a kind of quenched metastable state. Thermodynamic equilibrium at ambient temperature cannot be reached due to sluggish kinetics (low diffusion rates) at temperatures less than $\approx 2/3$ of the melting temperature, T_{m}. For most QC T_{m} is between 1000 and 1500 K.

It is typical for X-ray diffraction patterns of QC that they show sharp Bragg reflections even if strong (phason) diffuse scattering is present. This indicates long correlation lengths (micrometers) of the space and time averaged structure. Thus, QC show on average long-range order accompanied by short-range disorder. This is preferentially random phason disorder and, in particular for (pseudo-)ternary QC, in addition chemical disorder.

There are many other factors making QC structure analysis extremely challenging. The most serious problem beside sample quality is that only very limited data sets are experimentally accessible, be it diffraction data or microscopic data. This makes it impossible to determine the "absolute order" of a macroscopic QC. A good fit to experimental data of a model is no proof that the global minimum was found and that the proposed model is the best possible one. Thus it is very difficult to find out whether a QC is quasiperiodic in the strict meaning of the word, only on average, or not at all; or to prove that a QC is energy or entropy stabilized, whether its structure can be described by an ordered tiling or rather by a random tiling.

It is also difficult to prove that QC modeling can be accurately done by the nD approach. Probably, final modeling has to be performed in 3D space to properly account for atomic relaxation and disorder. Therefore, it is essential to know the maximum error one can make by using the one or the other method. There is a couple of publications on the potential and limits of QC structure analysis (cf. [3, 9, 20]). In the following, the tools, techniques, and methods most frequently employed in QC structure analysis are given briefly.

4.1 Electron Microscopy

General overviews of the application of electron microscopic methods to QC are given by [3, 10, 20]. The recent developments such as spherical aberration (C_s) corrected electron microscopy are reviewed by [28]. There are several ways to use an electron microscope either in the imaging mode or in the diffraction mode:

Scanning electron microscopy (SEM) has been used for imaging QC on the micro- and nano-scale, for investigating the shape of micro- and nanocrystals as well as of voids ("negative crystals"); the chemical composition has been studied by energy- or wave-length-dispersive X-ray spectroscopy (EDX or WDX).

Transmission electron microscopy (TEM) is based on mass (absorption) contrast and has been employed for the study of the micro- and defect-structure of QC, for instance, after plastic deformation. It does not have atomic resolution.

High-resolution transmission electron microscopy (HRTEM) or phase contrast method. The electrons, scattered up to higher Bragg angles, are recombined for imaging (Fig. 4.1). The contrasts visible on electron micrographs are related to the projected structure (potential). They strongly depend on sample thickness (≈ 100 Å) and defocus value of the objective lens. The interpretation of HRTEM images is not straightforward and contrast simulations should confirm the models derived. For instance, it was demonstrated by computer simulations that a pentagonal cluster model can produce HRTEM images with local pentagonal as well as decagonal symmetry, depending on the accelerating voltage, 200 and 300 kV, respectively [26].

The lateral resolution of standard HRTEM experiments is 1–2 Å, depending on the acceleration voltage for the electrons. However, it is not always possible to work at highest resolution, i.e. highest voltages, because even metallic samples may undergo structural changes under irradiation, in particular for voltages U > 400 kV (sometimes already for U > 250 kV [18]). Electron microscopes that are C_s-corrected decrease the probability of sample damage, since they have already sub-ångström resolution at lower voltages. An automated approach for the analysis of HRTEM images of QC was developed [12, 21] to match tilings to the observed contrasts in an unbiased way.

High-angle annular detector dark-field scanning transmission electron microscopy (HAADF-STEM) or Z-contrast method. The image is formed by electrons scattered incoherently at high angles (≈ 100 mrad) in an STEM (Fig. 4.1). Dynamical effects and the influence of specimen thickness are less significant compared with SAED and HRTEM. By a finely focused electron beam (≈ 2 Å diameter) as probe, the specimen is scanned illuminating atomic column by atomic column. The annular detector generates an intensity map of incoherently scattered electrons with atomic number (Z) contrast. Therefore, this method is also called Z-contrast method (see [16, 20] and references therein). Thus, in case of transition-metal aluminides it allows an easy differentiation

between contrasts originating from transition metal atoms or from aluminum atoms. Usually the contrast is reversed compared with HRTEM micrographs. Image deformation is possible due to sample drift, obscuring the symmetry (distortion of decagonal clusters, for instance). A comparison of both methods is illustrated in Fig. 4.1.

Recently, the resolution that can be reached by HRTEM and HAADF-STEM has been greatly improved by a novel electron optics corrected for spherical aberration. This not only makes sub-ångström resolution possible it also improves the contrast. Atomic distances can be determined with an accuracy of the order of 0.05 Å and even atomic site occupancies can be derived due to the negligible point spread function [28]. The power of aberration-corrected HAADF-STEM with subsequent enhancing of the contrasts by the maximum-entropy method has been recently demonstrated in a study of decagonal Al–Co–Cu [25] (Fig. 4.2). However, simulations of HRTEM images, calculated for microscopes even without any spherical aberration, show the limits in distinguishing between structure models with different shapes of the atomic surfaces [17].

4.2 Diffraction Methods

While X-ray diffraction is the standard method for structure analysis, electron diffraction is mainly performed in combination with electron microscopic imaging. Neutron scattering is mainly used for investigating the dynamical properties and has the disadvantage that rather large samples are needed, cubic millimeters on a high-flux source compared with cubic microns in case of synchrotron radiation. Electron diffraction works with very small and thin samples, however, multiple diffraction makes a quantitative evaluation difficult.

Selected area electron diffraction (SAED). Due to multiple scattering and other interaction potentials, SAED patterns significantly differ from X-ray diffraction (XRD) images. The reflection intensities are not proportional to the squares of the structure amplitudes as it is the case if the kinematical theory applies. For the calculation of SAED patterns, dynamical theory is needed, the powerful tools of X-ray structure analysis (direct methods, e.g.) do not work. However, the rapid progress in electron crystallography is going to change this situation (see, e.g., [6]). Multiple scattering generally leads to a relative enhancement of weak reflections and of diffuse scattering.

Compared to X-ray diffraction, the SAED exposure time is usually much shorter, the intrinsic background much higher and the dynamical range much smaller (just 2–3 orders of magnitude) (Fig. 4.1a). X-ray intensities may be quantitatively collected within a dynamical range of ten orders of magnitude. Diffraction symmetry (Laue class) as well as systematic extinctions are imaged in the same way as in the case of X-ray and neutron diffraction. Due to the small penetration depth of the electron beam in the sample ($<1,000$ Å)
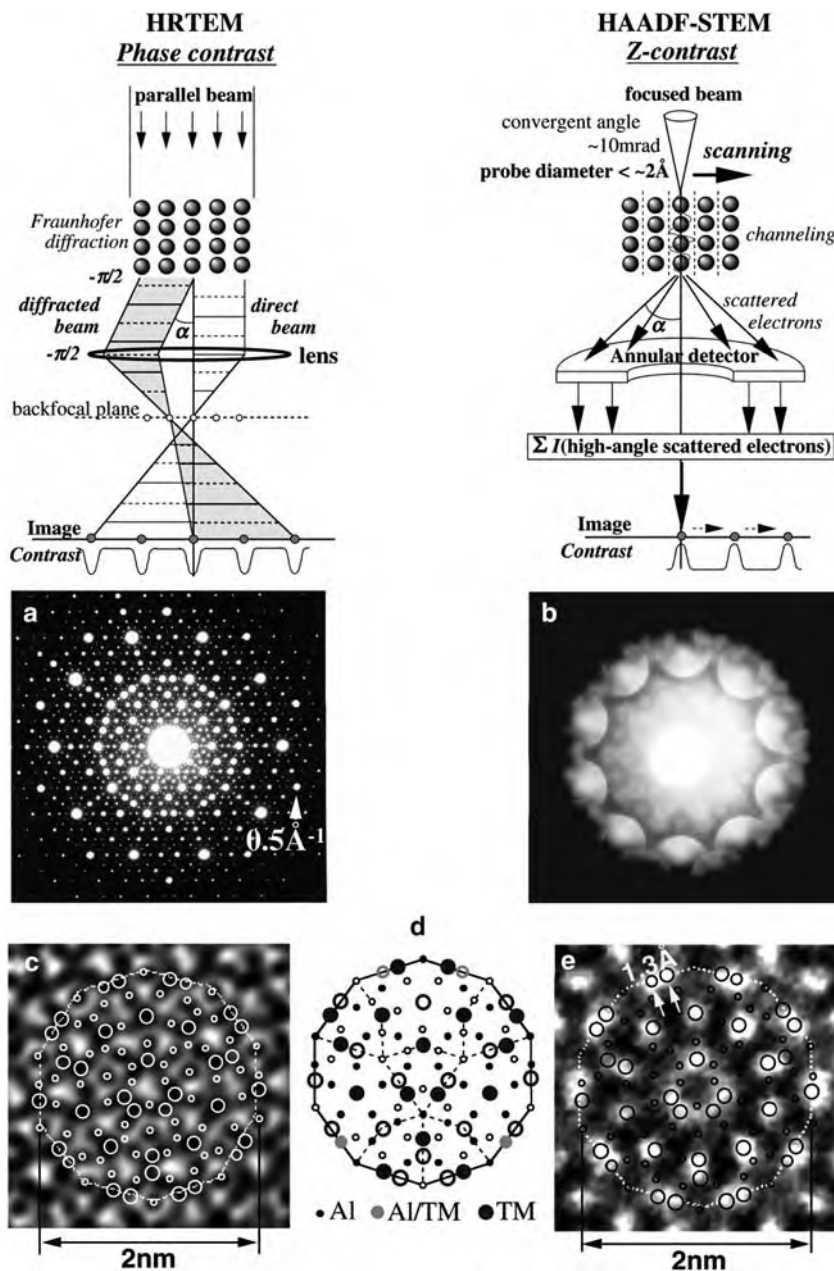
Fig. 4.1. *Top*: Imaging principles of HRTEM and HAADF. (**a**) SAED and (**b**) CBED images taken along the 10-fold axis of decagonal $Al_{72}Co_8Ni_{20}$. (**c**) HRTEM micrograph of an atomic cluster from a very thin region ($<50\,\text{Å}$) of the sample; (**e**) HAADF image from a region with thickness of $\approx 100\,\text{Å}$; (**d**) structure model of the cluster imaged in (**c**) and (**e**). Note that contrasts for atomic columns are just opposite in the two cases (with permission from [1])
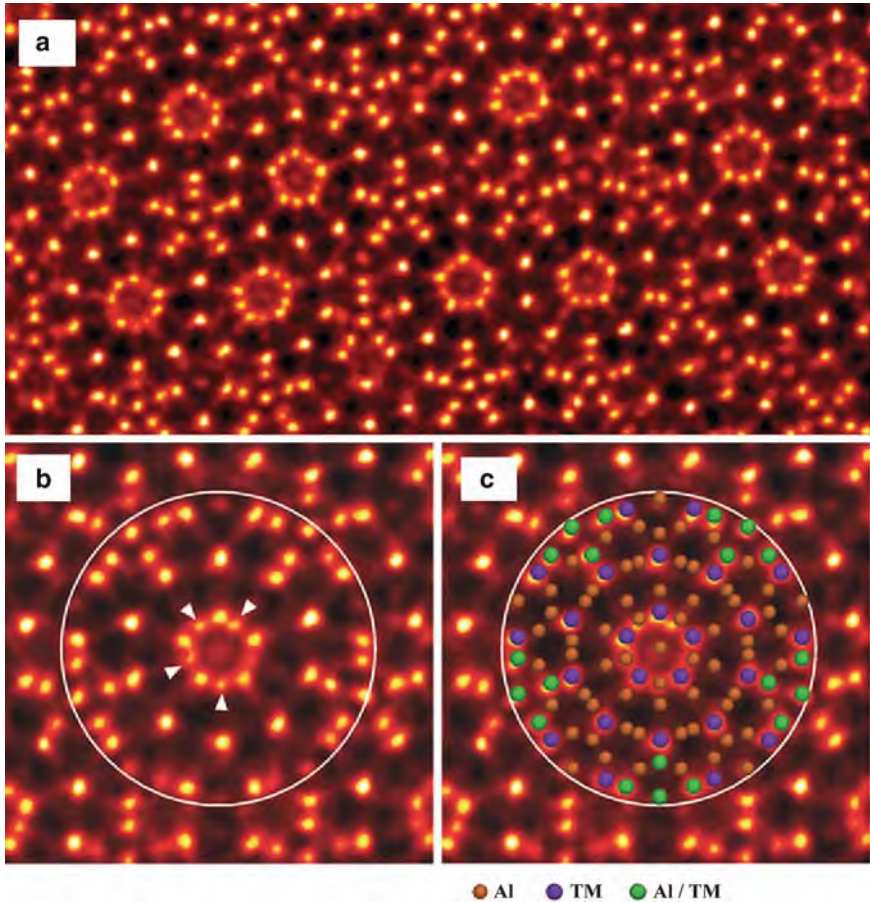
Fig. 4.2. Ultrahigh-resolution Z-contrast STEM image of decagonal $Al_{64}Cu_{22}Co_{14}$, taken along the periodic axis with an accelerating voltage of $200\,kV$ and deconvoluted by maximum-entropy method. In (**b**) and (**c**) enlarged parts are shown of the image in (**a**). A $\approx 20\,\text{Å}$ cluster, derived for the W–Al–Co–Ni approximant is superimposed (with permission from [25])

and its usually small diameter (500–5,000 Å) [26], scattering information of submicroscopic parts of a sample can be obtained only (the volume of a sample for XRD is larger by about nine orders of magnitude).

Convergent beam electron diffraction (CBED). By this method a very small area of the thinned ($\approx 100\,\text{Å}$ thickness) sample with 10–100 Å diameter is probed by the convergent electron beam (Fig. 4.1b). This method allows, for instance, deriving the full point group symmetry of the sample [24] instead of just the Laue class as in the case of X-ray diffraction. One can even quantitatively refine the parameters of a trial structure model by fitting the line profiles of the high-order Laue-zone (HOLZ) reflections (see, for instance [8, 27]).

Low energy electron diffraction (LEED). This method is used for the analysis of surface structures. Due to the low energy of electrons (a few eV), only the uppermost 5–10 atomic layers contribute to the diffraction pattern. Due to strong multiple scattering effects, the diffraction pattern has to be calculated fully dynamically. Usually, the profiles of reciprocal lattice rods are calculated at different electron energies. The resolution is of the order of 0.01 Å.

X-ray diffraction (XRD) and Neutron diffraction (ND). In both cases, the kinematical theory can be applied to describe the correspondence between structure and diffraction pattern of a sample. A very powerful toolbox of structure determination techniques has been developed during the past 80 years, which allows solving even virus structures in a more or less straightforward way. Some of these tools such as Patterson analysis, least-squares structure refinement, method of entropy maximization (MEM) etc. have been modified for higher-dimensional structure analysis (Fig. 4.3).
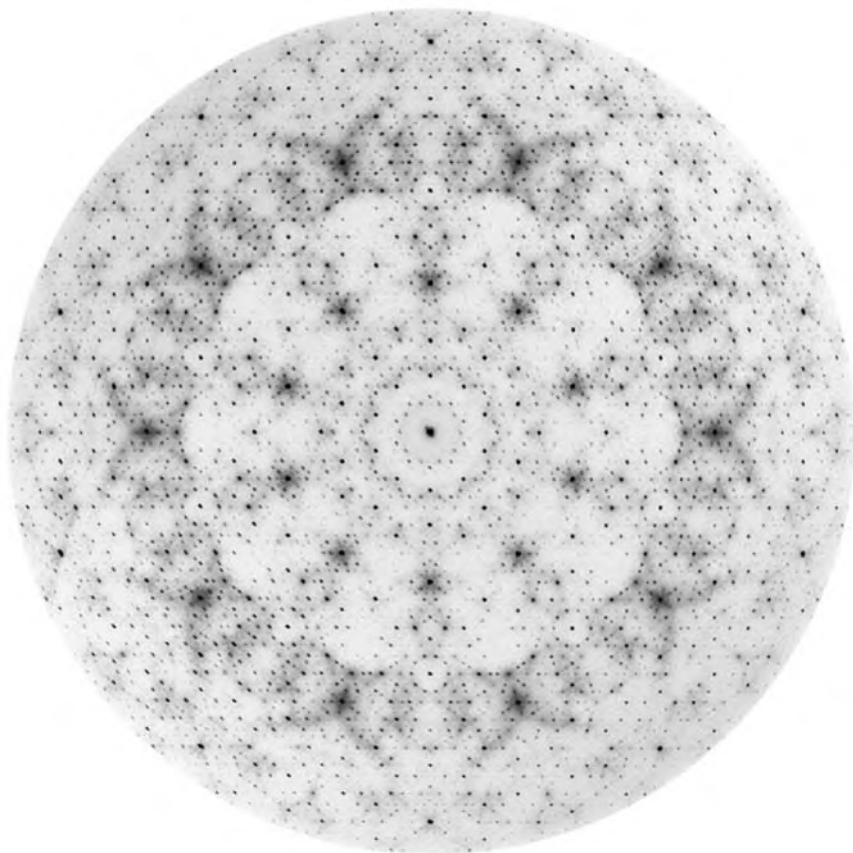
Fig. 4.3. X-ray diffraction pattern of d-$Al_{71}Co_{13}Ni_{16}$ reconstructed from 720 image plate frames taken at SNBL/ESRF, Grenoble [7]. The second Bragg layer is shown. Sharp Bragg reflections are accompanied by significant diffuse scattering

XRD on polycrystalline materials is often used to characterize quasicrystalline samples and to check their quality. It has to be kept in mind, however, that a powder XRD pattern is just a projection of the full 3D reciprocal space information upon 1D. Superposition of Bragg peaks and leveling out of structured diffuse scattering is the consequence. High-resolution powder XRD can be useful as a fingerprint of a known QC or for the accurate determination of lattice parameters. It must not be used as the sole proof for quasiperiodicity or perfection of a QC, however.

Single-crystal XRD or elastic ND are the diffraction methods of choice for structure analysis. The Bragg reflections carry information about the globally averaged structure, the diffuse intensities about the pair correlation functions of local structural deviations from this average structure. A 3D resolution better than $0.001\,\text{Å}$ can easily be obtained. XRD and ND are for many elements complementary in scattering power. This can be used to distinguish, for instance, the ordering of Co and Ni, what is almost impossible for XRD since their scattering factors differ by just one electron. The different scattering power of different isotopes of an element can be used to calculate partial structure factors. The potentialities and limits of XRD on QC have been discussed by [9] with the focus on Bragg scattering and by [7] focusing on diffuse scattering. Those of ND have been outlined by [5], for instance.

Some beam-lines at third generation synchrotron sources already offer (partly) coherent X-ray radiation (for a review see, e.g., [14]). It can be particularly useful for the interpretation of diffuse scattering (speckle patterns). For instance, the study of the phason dynamics may profit from this technique [13].

Inelastic and quasielastic neutron scattering. The study of the dynamical properties of QC, i.e. the phonon and phason dynamics, can be performed in the usual way by inelastic and quasielastic NS, respectively (see, e.g. [4, 5], and references therein).

4.3 Spectroscopy

Spectroscopical techniques are not suited for identifying the long-range order of QC structures but they can be very powerful in distinguishing structure models which differ in their local structure. Since quasicrystals consist of the same structure motifs as their crystalline approximants, the differences between both structure types, if any, may be directly or indirectly (electronic band structure) caused by their different long-range order.

Most frequently used in the course of structural studies on QC are the *Extended X-ray absorption fine structure spectroscopy (EXAFS)*, *Mössbauer effect (ME) spectroscopy*, and *Nuclear magnetic resonance (NMR)*. All three of them can give very accurate information on the local configuration and chemical composition of structural units (clusters). However, this information is globally averaged over the whole sample. Examples for the application of

these techniques are the study of the local order in icosahedral AlCu(Ru,Fe) at ambient conditions [15] and at high pressure [19] by EXAFS, in icosahedral $Ag_{50}In_{36}Gd_{14}$ by ME spectroscopy [22], in decagonal Al–Co–Ni by NMR [11], and the study of the vacancy concentration in $Cd_{17}Ca_3$ and its 1/1 approximant Cd_6Ca by positron annihilation [23].

References

1. E. Abe, A.P. Tsai, Structure of quasicrystals studied by atomic-resolution electron microscopy. JEOL News **36**E, 18–21 (2001)
2. F. Axel, D. Gratias (eds.), *Beyond Quasicrystals*, Les Edition de Physique, Les Ulis, (Springer, Berlin, 1995)
3. Beeli, C. Quasicrystal structures studied by high-resolution transmission electron microscopy. Z. Kristallogr. **215**, 606–617 (2000)
4. G. Coddens, S. Lyonnard, B. Hennion, Y. Calvayrac, Triple-axis neutron-scattering study of phason dynamics in Al-Mn-Pd quasicrystals. Phys. Rev. B **62**, 6268–6295 (2000)
5. M. De Boissieu, Structure determination of quasicrystals and neutron scattering. Z. Kristallogr. **215**, 597–605 (2000)
6. D.L. Dorset, C.J. Gilmore, (eds.), Special Issue on Electron Crystallography. Z. Kristallogr. **218**, 237–319 (2003)
7. M.A. Estermann, K. Lemster, T. Haibach, W. Steurer, Towards the real structure of quasicrystals and approximants by analysing diffuse scattering and deconvolving the Patterson. Z. Kristallogr. **215**, 584–596 (2000)
8. A.H. Fang, H.M. Zou, F.M. Yu, R.H. Wang, X.F. Duan, Structure refinement of the icosahedral AlPdMn quasicrystal using quantitative convergent beam electron diffraction and symmetry-adapted parameters. J. Phys. Cond. Matt. **15**, 4947–4960 (2003)
9. T. Haibach, A. Cervellino, M.A. Estermann, W. Steurer, X-ray structure determination of quasicrystals - Limits and potentiality. Z. Kristallogr. **215**, 569–583 (2000)
10. K. Hiraga, The structure of quasicrystals studied by atomic-scale observations of transmission electron microscopy. Adv. Imag. Electr. Phys. **122**, 1–86 (2002)
11. P. Jeglic, J. Dolinsek, NMR features of a decagonal $Al_{72.6}Ni_{10.5}Co_{16.9}$ quasicrystal. Phys. Rev. B **71**, art. no. 014204 (2005)
12. D. Joseph, S. Ritsch, C. Beeli, Distinguishing quasiperiodic from random order in high- resolution TEM images. Phys. Rev. B **55**, 8175–8183 (1997)
13. A. Letoublon, F. Yakhou, F. Livet, F. Bley, M. de Boissieu, L. Mancini, R. Caudron, C. Vettier, J. Gastaldi, Coherent X-ray diffraction and phason fluctuations in quasicrystals. Europhys. Lett. **54**, 753–759 (2001)
14. F. Livet, Diffraction with a coherent X-ray beam: dynamics and imaging. Acta Crystallogr. A **63**, 87–107 (2007)
15. A.P. Menushenkov, Y.V. Rakshun, EXAFS spectroscopy of quasicrystals. Crystallogr. Rep. **52**, 1006–1013 (2007)
16. S.J. Pennycook, Structure determination through Z-contrast microscopy. Adv. Imag. Electr. Phys. **123**, 173–206 (2002)

17. M. Quiquandon, J.T. Beauchesne, D. Gratias, Simulations of high-resolution electron microscopy images of icosahedral quasicrystals. Philos. Mag. **88**, 1941–1948 (2008)
18. S. Ritsch, C. Beeli, H.U. Nissen, R. Lück, Two Different Superstructures of the Decagonal Al-Co-Ni Quasi-Crystal. Philos. Mag. A **71**, 671–685 (1995)
19. A. Sadoc, J.P. Itie, A. Polian, In situ high pressure X-ray diffraction and EXAFS spectroscopy of icosahedral Al-Cu-Ru quasicrystals. Philos. Mag. A **80**, 2057–2071 (2000)
20. K. Saitoh, K. Tsuda, M. Tanaka, A.P. Tsai, Structural studies on decagonal quasicrystals using the HAADF- STEM and CBED methods. Z. Kristallogr. **215**, 618–626 (2000)
21. C. Soltmann, C. Beeli, Structure analysis of two-dimensional quasicrystals. Philos. Mag. Lett. **81**, 877–884 (2001)
22. Z.M. Stadnik, K. Al-Qadi, P. Wang, Magnetic properties and Gd-155 Mössbauer spectroscopy of the icosahedral quasicrystal $Ag_{50}In_{36}Gd_{14}$. J. Phys. Cond. Matt. **19**, art. no. 326208 (2007)
23. Y. Takagiwa, T. Akiyama, I. Kanazawa, K. Sato, H. Murakami, Y. Kobayashi, R. Tamura, S. Takeuchi, The study of the binary quasicrystal $Cd_{17}Ca_3$ and its 1/1 approximant Cd_6Ca by positron annihilation spectroscopy. Philos. Mag. **86**, 513–517 (2006)
24. M. Tanaka, Convergent-Beam Electron Diffraction. Acta Crystallogr. A **50**, 261–286 (1994)
25. S. Taniguchi, E. Abe, Highly-perfect decagonal quasicrystalline $Al_{64}Cu_{22}Co_{14}$ with non-centrosymmetry. Philos. Mag. **88**, 1949–1958 (2008)
26. K. Tsuda, Y. Nishida, M. Tanaka, A.P. Tsai, A. Inoue, T. Masumoto, Convergent-beam electron diffraction and electron microscopy study of decagonal quasicrystals of Al-Ni-Rh and Al-Ni-Ir. Philos. Mag. Lett. **73**, 271–278 (1996)
27. K. Tsuda, M. Tanaka, Refinement of Crystal-Structure Parameters Using Convergent- Beam Electron-Diffraction - the Low-Temperature Phase of $SrTiO_3$. Acta Crystallogr. A **51**, 7–19 (1995)
28. K.W. Urban, The new paradigm of transmission electron microscopy. MRS Bull. **32**, 946–952 (2007)

5

Structure Analysis

Quantitative structure analysis still means structure analysis based on methods such as X-ray, neutron and, to some extent, electron diffraction. A structure analysis consists of three main parts, data collection, structure solution, and structure refinement. Even if crystal growth may be cumbersome, it pays off preparing crystals of highest quality and collecting as many diffraction data as possible. The better the data the higher the chance to obtain a reliable structure model.

Once a complete data set has been measured, the structure has to be solved, i.e. phases, $\phi(\mathbf{H})$ have to be derived for the structure amplitudes $|F(\mathbf{H})| = \sqrt{I(\mathbf{H})}$, with $I(\mathbf{H})$ the reduced intensity. Reduced intensity means, the experimental intensity corrected for absorption, polarization, peak scanning geometry (Lorentz factor) etc. Fourier transforming the structure factors, $F(\mathbf{H}) = |F(\mathbf{H})| \exp[2\pi i \phi(\mathbf{H})]$, derived by the phasing methods discussed below, yields the electron density distribution function $\rho(\mathbf{r})$. Knowing the chemical composition, atoms can be assigned to the peaks in the electron density maps leading to a structure model.

The analysis of structures being periodic in 3D or in nD ($n > 3$) has some common features and some fundamentally different ones. The experimental techniques and methods which can be used, are essentially the same as well as the final goal, a detailed 3D structure model. The crucial difference is in the model to be refined: an easily enumerable and localizable amount of well defined atoms in the 3D case compared with arbitrarily complex occupation domains, each representing an infinite number of atoms, in the nD case.

Structure analysis of 3D periodic structures means just the determination of the structure of a single 3D unit cell, i.e. only the short-range order since the periodic long-range order is taken for granted. On the contrary, the determination of the content of a nD unit cell, particularly the complex shape of the occupation domains, includes the determination of long-range order up to infinity. Analyzing a quasicrystal structure fully in 3D space means determining with atomic resolution a macroscopic structure with $> 10^{12}$ atoms, finding the correct quasilattice out of infinitely many possible ones and decorating it properly.

The prerequisite of nD QC structure analysis is the existence of a Fourier module, i.e. a diffraction pattern with Bragg reflections. Indeed, there are good reasons, such as distribution, sharpness, and shape of experimentally observed reflections, to assume that they are Bragg reflections. Otherwise, the nD approach would not be applicable. This would be the case for structure models based on random tilings. Due to severe geometrical and electronic constraints, diffraction patterns of 3D random tilings would contain Bragg-like peaks but perhaps no real Bragg peaks, depending on the kind of random tiling. For a more detailed discussion of this case see [16].

The different temperature dependence of diffraction data taken on QC with strictly quasiperiodic structures and those based on random tilings is a better measure for distinguishing these two cases than trying to differentiate between Bragg and Bragg-like reflections. With increasing temperature, strictly quasiperiodic structures would become more and more disordered due to an increasing amount of random phason fluctuations. The same is true for random-tiling based structures. While at low temperature the latter structures would be locally unstable against the formation of small approximant domains, these fluctuations would disappear at high temperature. Intensities of Bragg reflections and diffuse scattering would differently change with temperature in these two cases.

If structure analysis (in any dimension) is solely based on Bragg diffraction data, only structure models averaged over the whole crystal can be obtained. If, additionally, diffuse diffraction intensities are included, an idealized structure model can be derived together with a model for the kind of structural disorder present.

For instance, very large structures of biological macromolecules can be solved because some a priori information can be used such as the limited number of amino acids as building units and their sequences in polypeptide chains. In case of QC, useful a priori information can be the existence of clusters, the structure of which is known from approximants, and their distribution that can be unraveled by electron-microscopic methods. The existence of recurring atomic clusters constrains the complexity of atomic surfaces. The big question is whether *strictly quasiperiodic* models are appropriate for describing the structures of real quasicrystals, even if made more realistic by applying disorder models.

In the following a few methods for quasicrystal structure analysis are reviewed. The method of choice for phasing structure amplitudes is the nD low-density-elimination (LDE) method. One of the reasons why LDE or related methods work so well is because the hyperatoms are located on special positions in the nD unit cell, leading to simple phase assignments for stronger reflections, particularly in case of icosahedral phases (see Figs. 3.63 and 3.65, for instance). The rather straightforward solution of the structure, i.e. the determination of the locations and approximate shapes of the hyperatoms, has to be followed by a rather tedious derivation of the partitioning of the atomic surfaces, however.

The calculation of the 3D or nD Patterson function, which yields vector maps of a structure in a straightforward way, can be useful if one wants to study the changes in inter- or intra-cluster order as a function of temperature, for instance. Particularly useful can be the difference Patterson function in case of superstructure ordering, because it allows to check structure models in the least biased way.

The refinement of a structure model against the observed diffraction data is the necessary last step for obtaining quantitative structural information as well as a measure for its reliability. A side effect is that it assigns improved phases to all reflections. This is a prerequisite for the calculation of the electron density distribution function, a valuable tool for analyzing chemical bonding. The nD entropy-maximization method (MEM) is the best technique to compute the electron density distribution function free of series truncation ripples known from Fourier maps due to limited data sets.

5.1 Data Collection Strategy

The number of unique reflections to be included in a structure analysis of a periodic crystal depends on its lattice parameters. It may range from a few hundred in case of simple cubic structures to a few hundred thousand in case of a virus crystal. There is no ambiguity in the selection of Bragg reflections to be collected, observed and unobserved ones. The data set has to be complete, i.e. has to contain all reflections within a given limiting sphere in reciprocal space, otherwise the results may be biased. One has to keep in mind that also unobserved reflections contain important information. Only those structure models that reproduce both observed intensities and those that are too weak to be observed can be reliable.

How many reflections have to be collected for a reliable structure model? If not only the structure but also the electron density distribution function is to be studied, one needs a resolution of at least ≈ 0.4 Å, otherwise ≈ 0.7 Å can be sufficient (this corresponds to maximum diffraction angles of $\theta = 60°$ and $\theta = 30°$, respectively, for MoKα radiation with $\lambda = 0.70926$ Å).

In the case of quasicrystals, it is not possible to collect the infinite number of densely distributed observed and unobserved Bragg reflections within a given θ range. The number of observable reflections within this limiting sphere only depends on the spatial and intensity resolution (see Fig. 5.8). How many reflections are needed for a reliable quasicrystal structure model meeting the same high standards as those of periodic crystals? In par-space we should have the same resolution as for periodic crystals. In perp-space, the resolution has to be the highest possible, since the detailed size, shape, and partition of the atomic surfaces is crucial for a model structure reflecting properly both short- and long-range-order of a quasicrystal.

The best strategy is collecting all data within a sphere in reciprocal par-space as usual (radius at least $r^{\parallel} = 1.5$ Å^{-1}). The radius $r^{\perp}$ of the perp-space

sphere depends on the still observable reflections with largest perp-space component, $|H^\perp|$, of its diffraction vector. This depends, of course, on the experimental conditions. All observed and unobserved reflections inside this 6D hyperellipsoid with radius $r = (r^\parallel, r^\perp)$ should be collected.

State of the art of data collection is employing synchrotron radiation and an area detector with large dynamic range and low intrinsic background. The crucial factor is the maximum peak/background ratio that can be achieved. In the best cases so far, reflections have been measured within an intensity range of 10^9 [44]. An example is shown in Fig. 5.1, where reconstructed reciprocal space sections are depicted based on diffraction patterns taken with synchrotron radiation (SLS/PSI, Villigen) and the pixel detector PILATUS 6M. This detector is free of read-out noise, has a dynamic range of 10^6, and allows suppressing fluorescence radiation by energy discrimination. The images demonstrate that an increase of exposure time by almost three orders of magnitude does not show more Bragg reflections. One observes strong TDS and PDS around some Bragg reflections as well as diffuse scattering.

5.2 Multiple Diffraction (*Umweganregung*)

Experimental data of high quality are the *sine qua non* of reliable structure models. The corrections for crystal shape, absorption, and other experimental parameters are standard for quasicrystals. However, *Umweganregung* (multiple diffraction) can be a problem severely biasing a part of diffraction data. This is a general well-known problem for electron diffraction but not for standard X-ray diffraction structure analysis.

Due to its dense set of Bragg reflections, *Umweganregung* is omnipresent during a diffraction experiment on QC, at least theoretically. Indeed, the poor fit of weak reflections in some QC structure analyses is frequently attributed to the enhancement of weak reflections by *Umweganregung*.

Multiple diffraction means that at least two Bragg reflections $I(\mathbf{H})$ and $I(\mathbf{G})$ are simultaneously excited by the primary beam with wave vector $\mathbf{k_0}$ (Fig. 5.2). Then, the coupling reflection $I(\mathbf{H} - \mathbf{G})$ is excited as well, with the reflected beam $\mathbf{k_G}$ acting as the (usually much weaker) primary beam. The reflected beams $\mathbf{k_H}$ and $\mathbf{k_{H-G}}$ point into the same direction and the resulting interference wave with intensity $I = |F(\mathbf{H}) + F(\mathbf{H} - \mathbf{G})|^2$ is detected instead of $I(\mathbf{H})$.

Fortunately, multiple diffraction only plays a role if $I(\mathbf{G})$ and/or $I(\mathbf{H} - \mathbf{G}) \gg I(\mathbf{H})$. Strong reflections must have rather small values for the perp-space component of the diffraction vectors. If $\mathbf{G}^\perp$ and $\mathbf{H}^\perp - \mathbf{G}^\perp$ are both small, then $\mathbf{H}^\perp$ is small as well and $I(\mathbf{H}^\perp)$ strong, consequently. On the other hand, if $I(\mathbf{H}^\perp)$ is weak and the coupling reflection $I(\mathbf{H} - \mathbf{G}) \gg I(\mathbf{H})$ strong, then $I(\mathbf{G})$ must be weak as well. Therefore, the majority of very weak unobservable reflections, i.e. those with large values of $\mathbf{H}^\perp$, could not be enhanced sufficiently by multiple diffraction to become observable.
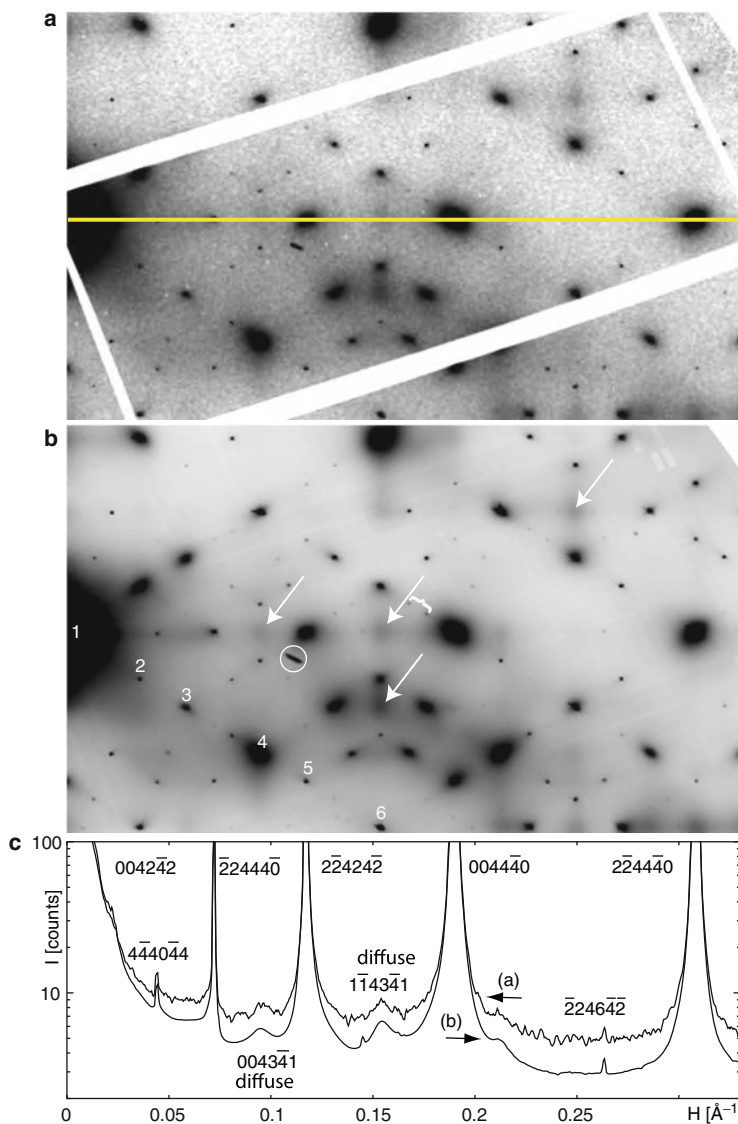
Fig. 5.1. Reconstructed twofold reciprocal space sections of i-Al$_{64}$Cu$_{23}$Fe$_{13}$ (horizontally 0–0.33 Å^{-1}, vertically 0.4–0.6 Å^{-1} from the origin) based on (**a**) a single exposure and (**b**) on 753 exposures. The white stripes in (**a**) result from the gaps between the detector modules, which are filled by multiple exposures at shifted detector positions in (**b**). Arrows indicate diffuse maxima breaking 6D *F*-lattice symmetry, the circle marks a contribution from a second grain, and brace the shortest distance between Bragg reflections. Indices and perp-space components (Å^{-1}) of numbered reflections: 1 $004\overline{2}\overline{4}2$ 0.046, 2 $\overline{1}151\overline{5}\overline{1}$ 0.342, 3 $1\overline{1}33\overline{3}3$ 0.149, 4 $004\overline{2}\overline{4}0$ 0.157, 5 $2\overline{2}2\overline{4}2\overline{4}$ 0.335, 6 $1\overline{1}33\overline{3}1$ 0.040. Line scans through (**a**) and (**b**) along the thin line in (**a**) are shown in (**c**). For clarity, the upper curve is shifted upward by two counts (from [44])
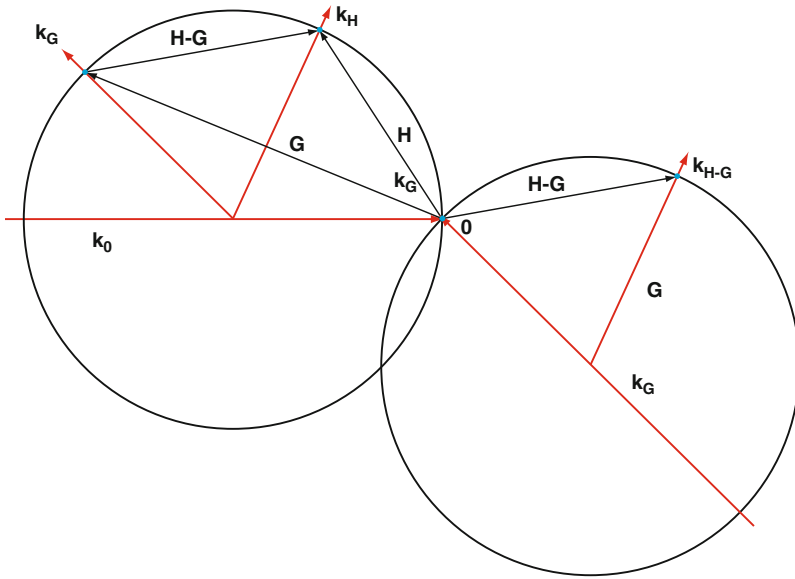
Fig. 5.2. *Umweganregung* in the Ewald construction. The primary beam $\mathbf{k_0}$ creates the two reflected beams $\mathbf{k_H}$ and $\mathbf{k_G}$ at the same time. In the right lower construction is shown how the reflected beam $\mathbf{k_G}$ acts now as primary beam and that the beam is reflected now into the direction $\mathbf{k_{(H-G)}}$. $\mathbf{0}$ denotes the origin of the reciprocal lattice and the wave vector $\mathbf{k}$ has the modulus $1/\lambda$, with λ the wave length of the X-ray beam

Generally, the situation for QC is comparable to that of complex intermetallic phases with large unit cells where *Umweganregung* is usually no problem at all for structure analysis. Significant *Umweganregung* in QC mainly takes place for special diffraction geometries such as rotation around particular diffraction vectors (see, e.g., [22, 23]).

5.3 Patterson Methods

The Patterson (auto- or pair correlation) function (PF) is the Fourier transform of the reduced diffraction intensities, i.e. the squared moduli (amplitudes) of the structure factors, $I(\mathbf{H}) = |F(\mathbf{H})|^2$. Reduced data means that all corrections, for absorption, polarization, extinction, etc., have been applied. Since structure amplitudes can be directly derived from observed X-ray or neutron diffraction data, the PF can be calculated in a straightforward way. It has first been used within the higher-dimensional approach for incommensurately modulated structures [36] and shortly later for the first quasicrystal, i-Al–Mn–Si [12]. The nD Patterson function

$$P(\mathbf{u}) = \frac{1}{V_{\mathrm{uc}}} \sum_{\mathbf{H}} I(\mathbf{H}) \cos(2\pi\mathbf{H} \cdot \mathbf{u}) = V_{\mathrm{uc}} \int_V \rho(\mathbf{r})\rho(\mathbf{r} + \mathbf{u})d\mathbf{r} \qquad (5.1)$$

has maxima at all interatomic vectors $\mathbf{u}$ within the nD unit cell with volume V_{uc} and electron density distribution function $\rho(\mathbf{r})$ (in case of XRD). The heights of Patterson peaks (electrons squared per unit volume) are proportional to the product of scattering factors of the atoms contributing to the peaks and to the multiplicity of these Patterson vectors.

In par-space the Patterson peaks are very sharp, with their widths corresponding to the convolution of 3D almost spherical atoms. In perp-space, on the contrary, the Patterson maxima are extended since they result as convolution of extended atomic surfaces. Due to the different shapes of atomic surfaces along par- and perp-space the resolution of the PF is intrinsically anisotropic.

The symmetry of the PF, i.e. of the vector set of the structure, always corresponds to a centrosymmetric symmorphic supergroup of the space group of the structure. This means that glide planes and screw axes are replaced by mirror planes and rotation axes, and that an inversion center is added. This results in 7 different Patterson symmetries for 2D structures, to 24 in case of 3D structures, and to 3 in case of icosahedral quasicrystals ($P2/m\overline{3}5$, $I2/m\overline{3}5$, $F2/m\overline{3}5$), for instance. The point-group part of the space group symbol corresponds to the Laue class (centrosymmetric point group) to which the space group belongs. Enantiomorphous and, in general, homometric structures have exactly the same PF.

Many methods have been developed for the derivation of structure models from Patterson maps in the case of periodic structures. The simplest method, trial and error, may have a better chance for the solution of nD quasicrystal structures than for complex 3D intermetallic phases, because there are usually only very few atomic surfaces in a nD unit cell. These are in most cases even sitting at special positions. Patterson methods in conjunction with isomorphous replacements (heavy atom or isotopic substitution methods) or anomalous dispersion may be useful for the identification of the chemical composition of the atomic surfaces.

A very efficient way of unraveling Patterson maps of complex structures by the symmetry-minimum function (SMF) does not only consider peak maxima but evaluates voxelwise the entire Patterson map [9]. According to a known nD space group $\mathsf{G}_{n\mathrm{D}}$, all unique Harker vectors, i.e. the vectors between atoms generated by the symmetry elements S_i, with multiplicities m_i are examined on a Patterson map $P(\mathbf{u})$. Taking the minimum over all symmetry-equivalent vectors [34]

$$smf(\mathbf{r}) = \min\left[\frac{1}{m_i}P(\mathbf{r} - \mathsf{S}_i\mathbf{r})|\mathsf{S}_i \in G_{n\mathrm{D}}\right] \qquad (5.2)$$

will result in all possible atomic positions $\mathbf{r}$ compatible with the nD Cheshire group [17], i.e. all possible atomic positions including origin shifts and enantiomorphs.

Careful inspection of the SMF usually allows one or more positions of hyperatoms to be fixed by assigning an atomic surface to the highest peak. Choosing these trial positions as pivot elements $\mathbf{r}^P$, the PF can be further deconvoluted. Trial atomic positions can be selected voxelwise and the corresponding interatomic cross vectors $\mathbf{r} - \mathbf{r}^P$ can be searched in the Patterson map. Taking the minimum over all symmetry equivalent vectors within the Patterson function

$$imf(\mathbf{r}) = \min \left[P(\mathbf{r} - \mathsf{S}_i \mathbf{r}^P) | \mathsf{S}_i \in G_{nD} \right] \tag{5.3}$$

will now result in an unambiguous structure solution. Including more than one pivot element enlarges the set of vectors checked in the image seeking minimum function (IMF). If structure elements (e.g., clusters) were known they could be included. Usually two pivot elements are enough to obtain a reliable solution in noncentrosymmetric structures. Again, the resulting trial electron density distribution only allows the parallel space components to be retrieved reliably. A detailed deconvolution of the hyperatoms fails because of the low resolution along these dimensions.

The results of the IMF can directly be used as starting probability density function for MEM calculations, for instance. Furthermore, the positions of the hyperatoms can directly be used to fix the phases of reflections with small perp-space components. As they are not sensitive to the shape of the atomic surfaces their phases (at least in centrosymmetric structures) can be assumed to be correct. The larger the set of these reflections is, the better the convergence of the MEM algorithms will be.

In the following, the deconvolution of a PF via SMF and IMF is shown on the example of basic Ni-rich decagonal Al–Co–Ni (Fig. 5.3). Its 5D space group is $P10_5/mmc$ with the four generators: $\bar{1}$ in $(0, 0, 0, 0, 0), 10_5$ in $(0, 0, 0, 0, x_5), m$ in $(x_1, x_2, x_2, x_1, x_5)$ and m in $(x_1, x_2, x_3, x_4, 1/4)$. The symmetry of the characteristic section $(10110)_V$ in this space group can be described by the plane group $p2mg$. Therefrom the symmetry of the PF and the SMF is derived to $p2mm$. Comparing the SMF with the IMF, which is already the electron density distribution of the actual structure in Fig. 5.3, one sees that the SMF results from the superposition of permitted origin shifts by $(0, 0, 1/2, 0, 0)_V$ and $(1/2, 0, 0, 1/2, 0)_V$.

The most important of the 32 unique Harker vectors $\mathbf{u} = (u_1\, u_2\, u_3\, u_4\, u_5)_D$ and their multiplicities related to a general position $\mathbf{r} = (x_1\, x_2\, x_3\, x_4\, x_5)_D$ are listed in Table 5.1. PF peak positions $\mathbf{r}$ are only significant if the corresponding Harker vectors $\mathbf{u}$ are all significantly above the background level. In our example, all three hyperatoms, which are located at $(x, x, x, x, 0.25)_D = (2x, 0, 1/4, 2x, 0)_V$ with $x = 0, 1/5, 3/5$ (Fig. 5.3c), and their Harker vectors $(2u, 0, 1/2, 2u, 0)_V$, with $u = 2x$, and $(0, 0, 2u, 0, 0)_V$, with $u = 2x_5$, are in the section shown in Fig. 5.3a.
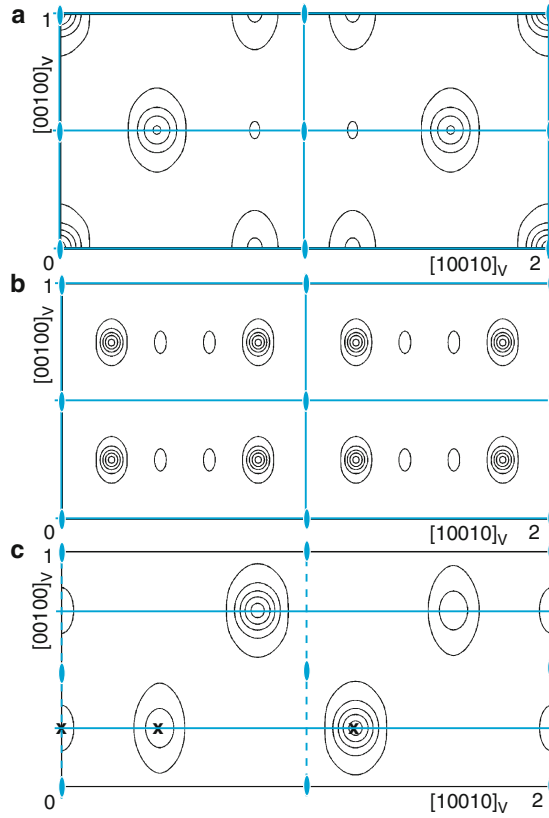
Fig. 5.3. Characteristic $(10110)_V$ sections through the 5D unit cell of basic Ni-rich decagonal Al–Co–Ni [15] with symmetry elements drawn in. Shown are sections of the Patterson function (PF) in (**a**), the symmetry-minimum function (SMF) in (**b**) and the image-seeking minimum function (IMF) in (**c**). The maps were calculated on a 200×100 grid, corresponding to 0.04 Å resolution. The positions of the atomic surfaces in the asymmetric unit are marked by crosses in (**c**) [15]

Table 5.1. The four most important Harker vectors $\mathbf{u} = (u_1\,u_2\,u_3\,u_4\,u_5)_D$ and their multiplicities m_i for the 5D space group $P10_5/mmc$ [15]

u_1	u_2	u_3	u_4	u_5	m_i
0	0	0	0	$2x_5$	20
$x_1 + x_4$	$-x_1 - x_3 - x_4$	$x_1 + x_3$	$x_2 + x_4$	$1/2$	4
$2x_1$	$2x_2$	$2x_3$	$2x_4$	$1/2$	2
$2x_1$	$2x_2$	$2x_3$	$2x_4$	$2x_5$	1

5.4 Statistical Direct Methods

The term *direct methods* has been introduced for reciprocal space techniques that directly determine the phases of experimentally obtained structure amplitudes, based on algebraic and/or statistical phase relationships (for a review see, e.g., [13]). Prerequisite for a successful application of such methods is the use of normalized structure factors

$$|E(\mathbf{H})|^2 = \frac{|F(\mathbf{H})|^2}{\langle |F(\mathbf{H})|^2 \rangle}, \tag{5.4}$$

which needs an appropriate estimate of $\langle |F(\mathbf{H})|^2 \rangle$ based on a priori information such as structural distribution functions. In most cases, atomic positions are just considered as random variables, which does not work in case of nD structure analysis. The nD unit cell of quasiperiodic structures is usually populated by just a few atomic surfaces with strongly anisotropic shape, which are rather easy to locate by Patterson methods. This is certainly the main reason, why, contrary to classical structure analysis, only the beginnings of such methods have been developed for QC structure solution.

There has been only one attempt to overcome the problem of the anisotropic scattering density distribution of hyperatoms [11, 46]. Thereby, the structure factor is written as

$$F(\mathbf{H}) = S(\mathbf{H}^\perp)G(\mathbf{H}), \tag{5.5}$$

where $S(\mathbf{H}^\perp)$, denotes shape factor, $F(\mathbf{H})$ is the Fourier transform of the atomic surface, $G(\mathbf{H})$ is the structure factor of the nD lattice decorated with hyperatoms with point-like perp-space components and regular atoms for par-space components. After the shape factor has been determined from the nD Patterson function, normalized structure factors can be calculated in the usual way.

$$|E(\mathbf{H})| = \frac{|G(\mathbf{H})|}{\left(\sum_j f_j^2 \right)^{1/2}}, \tag{5.6}$$

where f_j is the conventional atomic scattering factor for the jth atom. The crucial point is to find a good shape function. If the peaks in the nD PF calculated from normalized structure factor amplitudes $|E(\mathbf{H})|$ are close to point-like, than the shape function have been derived properly.

If the nD unit cell contains several hyperatoms, which significantly differ in their shape and chemical composition, the derivation of the shape function would be more or less equivalent to the determination of the nD structure. In other words, the main part of structure solution is performed via PF and not by statistical direct methods.

5.5 Charge Flipping Method (CF)

The charge flipping (CF) method is an iterative algorithm for the ab initio reconstruction of the electron density distribution function of a structure based on diffraction data [24, 25]. As input only the unit cell parameters and observed structure amplitudes (intensities) are needed. Neither chemical information nor symmetry is explicitly used in the structure solution process.

First, a starting set of structure factors $F^{(0)}(\mathbf{H})$ is created by assigning random phases to the experimental structure amplitudes $|F_{\mathrm{obs}}(\mathbf{H})|$. Then each iteration involves four steps in the following way [27]:

1. A trial electron density $\rho^{(n)}$, sampled on voxels with values $\rho_i, i = 1, \ldots, N_p$, is obtained by inverse Fourier transform of the structure factors $F^{(n)(\mathbf{H})}$:

$$\rho^{(n)} = \mathrm{FT}^{-1}\left[F^{(n)}(\mathbf{H})\right]. \tag{5.7}$$

2. A modified density $\sigma_i^{(n)}$ is obtained from $\rho_i^{(n)}$ by reversing the sign (charge flipping) of all pixels i with density below a certain positive threshold δ:

$$\sigma_i^{(n)} = \begin{cases} +\rho_i^{(n)} & \text{if} \quad \rho_i^{(n)} > \delta \\ -\rho_i^{(n)} & \text{if} \quad \rho_i^{(n)} \le \delta. \end{cases} \tag{5.8}$$

3. The structure factors $G^{(n)}(\mathbf{H})$ of this modified density are obtained by Fourier transform of $\sigma^{(n)}$

$$G^{(n)}(\mathbf{H}) = \mathrm{FT}\left[\sigma^{(n)}\right]. \tag{5.9}$$

4. The structure factors $F^{(n+1)}(\mathbf{H})$ are obtained from $F_{\mathrm{obs}}(\mathbf{H})$ and $G^{(n)}(\mathbf{H}) = |G^{(n)}(\mathbf{H})|\exp[2\pi\mathrm{i}\phi_G(\mathbf{H})]$ according to the following scheme:

$$F^{(n+1)}(\mathbf{H}) = |F_{\mathrm{obs}}(\mathbf{H})|\exp[2\pi\mathrm{i}\phi_G(\mathbf{H})] \tag{5.10}$$

for F(H) observed and strong,

$$F^{(n+1)}(\mathbf{H}) = |G^{(n)}(\mathbf{H})|\exp\{2\pi\mathrm{i}[\phi_G(\mathbf{H}) + 1/4]\} \tag{5.11}$$

for F(H) observed and weak,

$$F^{(n+1)}(\mathbf{H}) = 0 \tag{5.12}$$

for F(H) unobserved, and

$$F^{(n+1)}(\mathbf{H}) = G^{(n)}(\mathbf{H}) \tag{5.13}$$

for $\mathbf{H} = 0$.
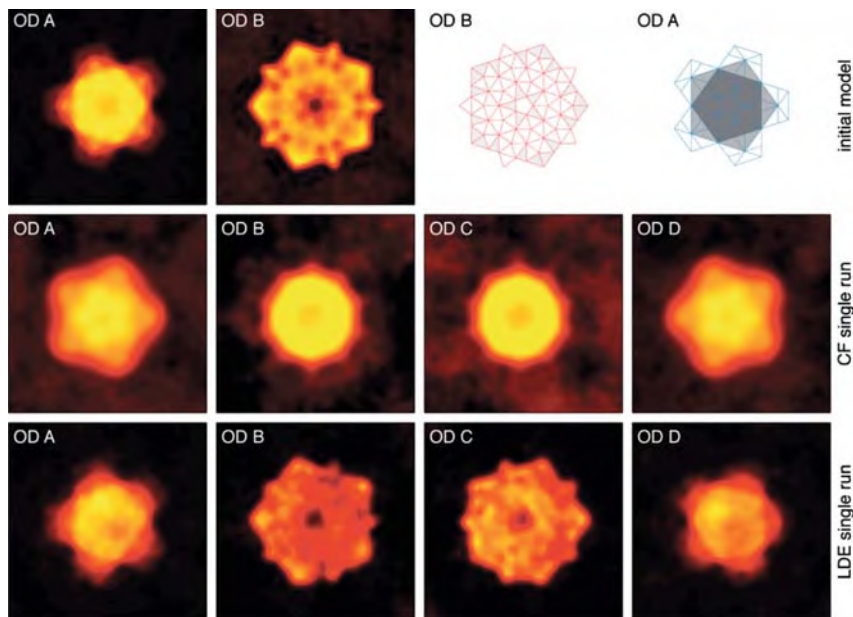
Fig. 5.4. Map of reconstructed occupation domains (OD) of d-$Al_{72}Co_8Ni_{20}$ [42] based on single CF and LDE runs phasing 32,521 reflections in $P1$ ($\approx$1,600 unique reflections). The pentagonal-shaped OD A, B and C, D related by an inversion operation. No symmetry averaging was performed [10]

The iteration cycles are repeated until convergence. The threshold value δ determines how fast the iterations converge, if at all. It can be determined by trial and error in an automated way. Another crucial parameter is the number of reflections considered weak in the fourth step of the iteration cycle. Shifting the phases of the weak reflections can significantly improve the performance of the algorithm in cases of more complex structures [25]. The algorithm seeks a Fourier map that is stable against repeated flipping of all density regions below. Obviously, a large number of missing reflections, which cause termination ripples, will make the algorithm less efficient. A method for a better performance of CF for incomplete data sets has been developed by Palatinus [27]. A computer program for using CF in nD space, SUPERFLIP, is publicly available [26]. An example for CF calculations on a QC model structure is shown in Fig. 5.4.

5.6 Low-Density Elimination

The LDE is a direct-space method like CF. It has been developed in 1992 [33] for the solution of complex periodic structures such as proteins. In 2001 it was modified for nD structure analysis of QC [41, 42]. The principle behind this

iterative approach is that all (electron) density values below a given threshold δ are set to zero. The value of δ is a crucial parameter and was originally set to one fifth of the peak height of the lightest atom in the structure [33].

First, a starting set of structure factors $F^{(0)}(\mathbf{H}) = |F_{\text{obs}}(\mathbf{H})| \exp(2\pi i\phi_{\text{rand}})$ is created by assigning random phases ϕ_{rand} to the experimentally derived structure amplitudes $|F_{\text{obs}}(\mathbf{H})|$ and a trial electron density $\rho^{(0)}$ is obtained by inverse Fourier transform of the structure factors $F^{(0)}$:

$$\rho^{(0)} = \text{FT}^{-1}\left[w(\mathbf{H})F^{(0)}(\mathbf{H})\right]. \tag{5.14}$$

Then each iteration cycle n involves the following steps:

1. The density $\rho_i^{(n)}$ in the ith voxel is modified to $\sigma_i^{(n)}$ according to:

$$\sigma_i^{(n)} = \begin{cases} \rho_i^{(n)}\{1 - \exp[-\frac{1}{2}(\frac{\rho_i^{(n)}}{0.2\rho_c})^2]\} & \text{if } \rho_i^{(n)} > \delta \\ 0 & \text{if } \rho_i^{(n)} \leq \delta. \end{cases} \tag{5.15}$$

ρ_c is the expected average peak height in the unit cell. It can be estimated by determining the average of the maximum peak height $\rho_{\text{max}}^{(j)}$ in each of the M sections:

$$\rho_c = \frac{1}{M}\left(\sum_{j+1}^{M} \rho_{\text{max}}^{(j)}\right). \tag{5.16}$$

2. The structure factors $G^{(n)}(\mathbf{H})$ of this modified density are obtained by Fourier transform of $\sigma^{(n)}$

$$G^{(n)}(\mathbf{H}) = \text{FT}\left[\sigma^{(n)}\right]. \tag{5.17}$$

3. The structure factors $F^{(n+1)}(\mathbf{H})$ are obtained from $F_{\text{obs}}(\mathbf{H})$ and $G^{(n)}(\mathbf{H}) = |G^{(n)}(\mathbf{H})| \exp[2\pi i\phi_G(\mathbf{H})]$ as

$$F^{(n+1)}(\mathbf{H}) = |F_{\text{obs}}(\mathbf{H})| \exp[2\pi i\phi_G(\mathbf{H})]. \tag{5.18}$$

4. The new electron density $\rho^{(n+1)}$ is obtained by inverse Fourier transform of the weighted structure factors $w(\mathbf{H})F^{(n+1)}$:

$$\rho^{(n+1)} = \text{FT}^{-1}\left[w(\mathbf{H})F^{(n+1)}(\mathbf{H})\right] \tag{5.19}$$

with

$$w(\mathbf{H}) = \tanh\left[\frac{|G^{(n+1)}(\mathbf{H})F^{n+1}(\mathbf{H})|}{\langle G^{(n+1)}(\mathbf{H})\rangle\langle F^{n+1}(\mathbf{H})\rangle}\right]. \tag{5.20}$$

Then the iteration cycles are repeated until convergence, which can be defined in a way that phase changes in each cycle are smaller than $0.5°$, for instance. Subsequently, the weight is set to one and several cycles more are calculated to obtain the final electron density maps.

A performance test of CF versus LDE shows that LDE is superior to CF for nD structure solution (Fig. 5.4) [10].

5.7 Maximum Entropy Method

MEM play an important role everywhere where weak signals have to be filtered out of a noisy background, for instance, for image processing in astronomy. Entropy maximization was introduced already in 1948 by Shannon [32], who formulated an optimization algorithm for telegraphic data transmission. Around 10 years later, the method was further developed by Jaynes [18], who connected the methods of discrete information theory with continuous physical observations. It took two more decades until MEM was first used in the course of the solution of crystallographic problems [5]. By the usual Fourier transform of structure factors, highly accurate electron density maps can only be obtained from large and complete diffraction data sets. MEM allows to improve these data sets since it does not produce artifacts such as truncation ripples. Furthermore, by MEM well-resolved electron density maps can be obtained even from incomplete or very noisy data sets.

MEM can also be used as direct method for structure solution [2]. Driving forces have been protein crystallography [1] and powder diffraction [3, 31]. Most of the MEM algorithms are based on exponential modeling [6]. Whereas direct methods solve the structure in reciprocal space, the principle of exponential modeling is based on direct space. A trial electron density distribution is varied and its diffraction pattern is compared with the intensity data. Based on the residuals a new trial electron density distribution can be derived, which finally converges to the most probable one.

After it was suggested to use MEM in the course of structure analyses of aperiodic crystals [7, 28, 37], it was first applied to increase the resolution of atomic surface density maps of decagonal Al–Co–Ni [39]. Later, it was employed as direct method in combination with Patterson deconvolution techniques, for the structure solution of d-Al–Mn–Pd [15, 40, 45] and i-Zn–Mg–Y [47]. MEM has also been used to get accurate charge density distribution data for the study of chemical bonding in Al-based quasicrystal approximants for powder diffraction data [19–21].

Based on Bayes' theorem it can be shown that the most probable solution of a problem that can be described by an additive and positive probability distribution function (pdf) is given by [35]

$$\underbrace{-\sum_{i=1}^{N_{\mathrm{P}}} p_i \ln \frac{p_i}{q_i}}_{\text{entropy S}} + \underbrace{\lambda_0 \left(\sum_{i=1}^{N_{\mathrm{P}}} p_i - 1 \right)}_{\text{normalization}} + \underbrace{\sum_{j=1}^{N_{\mathrm{c}}} \lambda_j C_j(p)}_{\text{set of } N_{\mathrm{c}} \text{ constraints}} = \max! \qquad (5.21)$$

Here, the electron density distribution $\rho(r_i)$ can be associated with the probabilities p_i on a regular grid of N_{p} points, and the N_{c} constraints C_j will include the set of known structure factors $F(\mathbf{H})$ and the set of structure amplitudes $|F(\mathbf{H})|$ with their Lagrangian multipliers λ_j. Furthermore, bond distances, density, and any known structural properties might be included. q_i are the

prior probabilities, which can all be set equal as starting pdf. Differentiation of (5.21) leads to the fundamental maximum entropy equations [2]

$$p_i = \frac{q_i}{Z(\lambda_1, \ldots, \lambda_{N_c})} \exp\left(\sum_{j=1}^{N_c} \lambda_j \frac{\partial C_j}{\partial p_i}\right); \quad Z(\lambda_1, \ldots, \lambda_{N_c})$$

$$= \sum_{i=1}^{N_P} q_i \exp\left(\sum_{j=1}^{N_c} \lambda_j \frac{\partial C_j}{\partial p_i}\right). \tag{5.22}$$

$Z(\lambda_1, \ldots, \lambda_{N_c})$ directly follows from the normalization of the a posteriori pdf p_i. The result exclusively depends on the constraint equations supplied. However, in the case of multimodal pdf as in the case of 'phaseless' Fourier transforms, a reliable solution can be obtained only if a set of sufficient constraints and a good estimate of the starting pdf are provided.

The electron density $\rho(r_i)$ in the ith voxel and the probability density p_i are related in the following way

$$p_i = \frac{\rho(r_i)}{\sum_{i=1}^{N_P} \rho(r_i)}. \tag{5.23}$$

The fundamental MEM equations can always be solved in the case of linear problems such as the calculation of electron density maps for known structure factors. The results would not depend on the starting pdf. However, in the case of unknown phases the problem gets more complicated as several local maxima exist. Consequently, reliable results depend on proper algorithms as well as on the set of constraints. Even the starting pdf will influence the maximum finally found [8].

A combination of PF, CF, or LDE with MEM can be used for ab initio phase determination of quasicrystal structures. Two main constraint equations are necessary to take all structure factors $F_{clc}(\mathbf{H})$ derived from either PF deconvolution techniques, CF or LDE, and all the observed structure amplitudes $|F_{obs}(\mathbf{H})|$ into account. Assuming Gaussian noise all known structure factors can be constrained by

$$C_1 = \sum_{\mathbf{H}} \frac{1}{\sigma^2} |F_{obs}(\mathbf{H}) - F_{clc}(\mathbf{H})|^2 = \chi^2 \tag{5.24}$$

with their corresponding standard deviation σ. Enforcing all calculated structure factors F_{clc} to be exactly equal to F_{obs} would put statistical errors of the data set into the MEM solution. The corresponding constraint equation for structure amplitudes [30] is

$$C_2 = \sum_{\mathbf{H}} \frac{1}{\sigma^2} \left||F_{obs}(\mathbf{H})| - |F_{clc}(\mathbf{H})|\right|^2 = \chi^2. \tag{5.25}$$

Substituting (5.24) and (5.25) into (2) results in the general nD equation to be solved

$$p_i = \frac{q_i}{Z(\lambda_1, \lambda_2)} \exp\Big[-2\lambda_1 \sum_{\mathbf{H}} \frac{1}{\sigma^2} |F_{\mathrm{obs}}(\mathbf{H}) - F_{\mathrm{clc}}(\mathbf{H})| \cos(2\pi\mathbf{H} \cdot \mathbf{x}_i - \phi_\Delta)$$

$$-2\lambda_2 \sum_{\mathbf{H}} \frac{1}{\sigma^2} \big||F_{\mathrm{obs}}(\mathbf{H})| - |F_{\mathrm{clc}}(\mathbf{H})|\big| \cos(2\pi\mathbf{H} \cdot \mathbf{x}_i - \phi_{\mathrm{clc}})\Big] \quad (5.26)$$

with $\phi_\Delta = \arctan\{Im[F_{\mathrm{obs}}(\mathbf{H}) - F_{\mathrm{clc}}(\mathbf{H})]/Re[F_{\mathrm{obs}}(\mathbf{H}) - F_{\mathrm{clc}}(\mathbf{H})]\}$, the phase of the residual. The corresponding Lagrangians can be solved by Newton's method [2] or iteratively, using the exponential modeling technique [6].

Example: decagonal structure

The reliability and efficacy of MEM is demonstrated on the example of a decagonal model structure with composition $Al_{53}Ni_{15}Ru_{32}$, 5D space group $P10_5/mmc$, and two layers along the periodic direction [14]. The atomic surfaces correspond to those of the PT, the decoration with Al, Ni, Ru is shown in Fig. 5.5.

The influence of the perp-space resolution on the resolution of the electron density maps of the atomic surfaces calculated by MEM and, for comparison, by Fourier transformation, is shown in Fig. 5.6. The MEM calculations have been performed on a 3D model of $760 \times 760 \times 4\,\text{Å}^3$ size, which has been subsequently lifted.

Whereas a perpendicular resolution of $|H^\perp| \leq 2\,\text{Å}^{-1}$ leads to good results (Fig. 5.6a,d) even with the Fourier transform, the more realistic threshold of $|H^\perp| \leq 1\,\text{Å}^{-1}$ clearly shows the advantage of the MEM density (Fig. 5.6b,e). At $|H^\perp| \leq 0.5\,\text{Å}^{-1}$ still the shape of the atomic surface is represented correctly by the MEM, the absolute values of the electron density distribution, however,
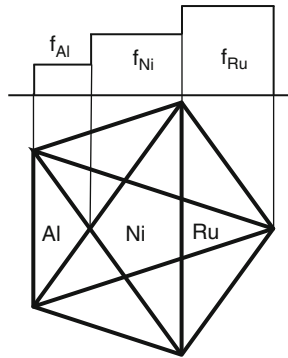
Fig. 5.5. One of the atomic surfaces of the model structure of decagonal $Al_{53}Ni_{15}Ru_{32}$, with scattering factor along the horizontal line shown schematically [14]
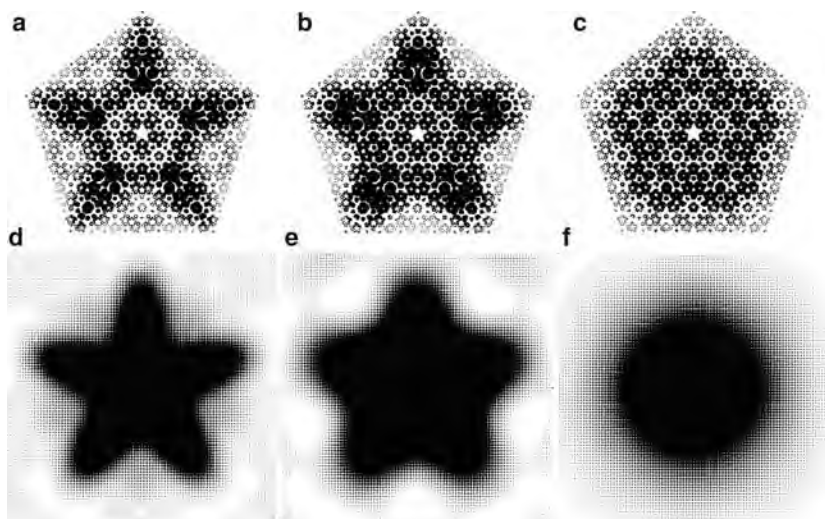
Fig. 5.6. Atomic surfaces of the model structure of decagonal $Al_{53}Ni_{15}Ru_{32}$ reconstructed with different perp-space resolution by 5D MEM (**a**–**c**) compared to 5D FF (**d**–**f**). Perp-space thresholds are $|H^{\perp}| \leq 2\,\text{Å}^{-1}$ for (**a**, **d**), $|H^{\perp}| \leq 1\,\text{Å}^{-1}$ for (**b**,**e**) and $|H^{\perp}| \leq 0.5\,\text{Å}^{-1}$ for (**c**, **f**). Dot size corresponds to peak intensity [14]
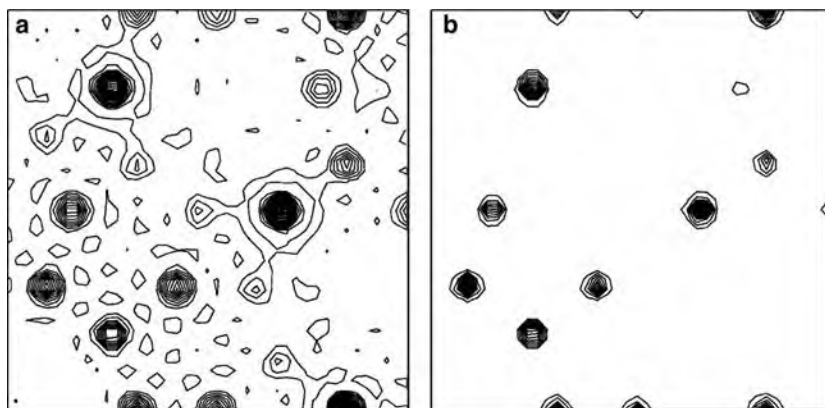
Fig. 5.7. Electron density distribution ($7.6\,\text{Å} \times 7.6\,\text{Å}$) the model structure of decagonal $Al_{53}Ni_{15}Ru_{32}$ reconstructed from a data set with perpendicular space threshold of $|H^{\perp}| \leq 0.5\,\text{Å}^{-1}$. (**a**) Fourier transform, (**b**) MEM [14]

are not reliable anymore. This can even better be seen in the enlarged physical space section. The influence of perp-space resolution on the par-space electron density distribution is depicted in Fig. 5.7. One clearly sees artifacts, which could be misinterpreted as real atoms, due to truncation in Fig. 5.7a, while the MEM density is reliable up to the lowest contour line of 1% of $\rho_{\max}$.

5.8 Structure Refinement

The last step of a structure analysis is the structure refinement. For reviews on the best ways to refine 3D periodic structures see, e.g., [43], and for nD structure analysis of QC see [38]. Structures are refined against the observed intensities usually by the least-squares method. The function to be minimized is

$$\sum_{\mathbf{H}} w(\mathbf{H})[|F_{\mathrm{obs}}|^2 - |F_{\mathrm{clc}}|^2]^2 \tag{5.27}$$

with the weights $w(\mathbf{H})$ inversely proportional to the standard deviation $\sigma(I(\mathbf{H})$ of the observed intensity. In case of the validity of Poisson statistics, the estimated standard deviation is calculated as $\sigma^2(I(\mathbf{H})) = I(\mathbf{H})$. It is crucial to include all data into a structure refinement, not only those above a certain threshold value (usually intensities with $I(\mathbf{H}) \geq 2\sigma(I(\mathbf{H}))$). This has already be discussed in Sect. 5.1.

During a refinement, the structure model is modified so that it fits best to the observed diffraction data. Refineable 3D model parameters are usually atomic coordinates, occupancy factors, and atomic displacement parameters (ADP). Additionally, structure model independent parameters can be refined taking into account dynamical effects such as extinction or twinning. In case of nD structure refinement, things are much more complicated. Here, the crucial parameters are positions, occupancies, and par-space displacements of the hyperatoms as well as size and shape of their perp-space components, the atomic surfaces.

There are constraints concerning the minimum distance between fully occupied positions as well as the closeness condition. While the first constraint has to be strictly obeyed, the second is a hard constraint only for ideally quasiperiodic structures. The closeness condition takes care that no atom disappears, is created or changes its species by moving the par-space section along the perp-space as it is the case for phasonic excitations (phason modes). Whether the structures of real QC strictly obeys the closeness condition is not proven yet. The stability of real QC against a transformation to approximants may be caused by a kind of lock-in state of the structure due to local violations of the closeness condition pinning the par-space locally.

Another peculiarity for nD structure refinements is the phason Debye–Waller (DW) factor. It has been defined in analogy to the standard phonon DW factor and describes the influence of phasons on the structure amplitude. It describes phason flips (atomic jumps in a double-well potential) caused by phason modes as well as by random phason fluctuations.

Phonons and phasons break the (hyper)lattice symmetry and lead to diffuse scattering beneath and around Bragg reflections, to thermal diffuse scattering (TDS) and phason diffuse scattering (PDS). Hyperatoms related by the closeness condition have to have the same phason DW factor, otherwise the closeness condition will not be obeyed. The phason DW factor has a strong
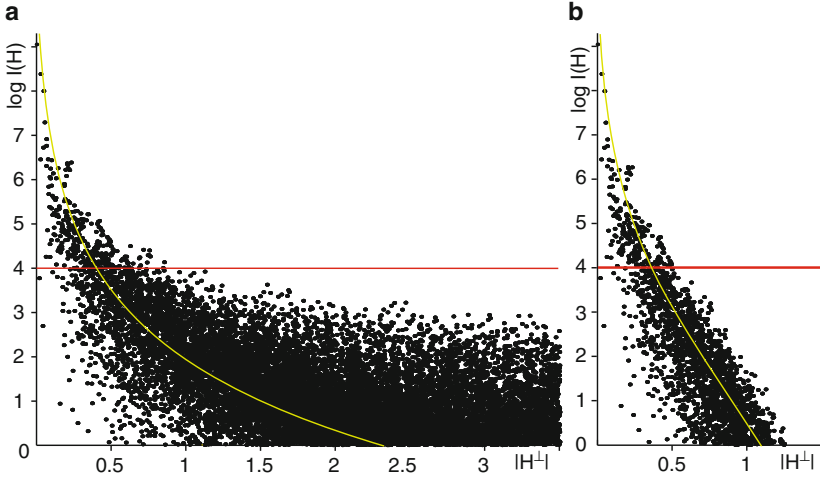
Fig. 5.8. $\log I(\mathbf{H})$ *versus* $|\mathbf{H}^{\perp}|$ calculated for (**a**) the ideal QG structure model of i-Al$_{64}$Cu$_{23}$Fe$_{13}$ [29] and (**b**) after applying a phason DW factor with $<u^2> = 0.12$ Å^2. Only Bragg reflections within a 2D par-space section with $|\mathbf{H}^{||}| \leq 0.8$ Å^{-1} and $|h_i| \leq 40$, $i = 1 \cdots 6$, are shown. The reflections above the gray (online: red) horizontal line are observable by standard synchrotron area detector experiments. The light-gray (online: yellow) curve, $I(\mathbf{H}) \propto |\mathbf{H}^{\perp}|^{-4}$, marks the general decrease of intensities with $|\mathbf{H}^{\perp}|$ without (**a**) and with (**b**) the phason DW applied (from [44])

influence on the number of reflections that can be measured. This is illustrated on the example of the diffraction pattern of the QG structure model of i-Al$_{64}$Cu$_{23}$Fe$_{13}$ (Fig. 5.8) [29, 44].

In case of the ideal QG model we expect 74,725 reflections within a 2D par-space section with $|\mathbf{H}^{||}| \leq 0.8$ Å^{-1}, $|h_i| \leq 40$, $i = 1 \cdots 6$, and a dynamic range of nine orders of magnitude, which is the detection range of that experiment. The number of expected observable reflections is drastically reduced to 8,357 when we apply an experimentally derived single isotropic phason DW factor of $<u^2> = 0.12$ Å^2. The phason DW factor was determined by fitting the calculated reflection density to the observed one under the constraint that all observed reflections must also have calculated counterparts of comparable intensity. Within the dynamic range of $\approx 10^5$ for a standard area-detector based synchrotron data collection, only the reflections above the line in Fig. 5.8 would be strong enough to be detected. The determination of a reliable phason DW factor from a structure refinement would be difficult based alone on such a small set of reflections. Strong correlations between the phason DW factor and occupancy factors would bias the results.

The quality of a structure refinement is usually indicated by different reliability (R) factors. The most common used R factors are the unweighted R factors R_1 and R_2 related to unweighted structure amplitudes and their squares, respectively, and the weighted R factor wR_2 and the goodness of fit (GoF, S, χ^2):

$$R_1 = \frac{\sum_{\mathbf{H}} |F_{\text{obs}}(\mathbf{H})| - |F_{\text{clc}}(\mathbf{H})|}{\sum_{\mathbf{H}} |F_{\text{obs}}(\mathbf{H})|}$$

$$R_2 = \left\{ \frac{\sum_{\mathbf{H}} \left[|F_{\text{obs}}(\mathbf{H})|^2 - |F_{\text{clc}}(\mathbf{H})|^2 \right]^2}{\sum_{\mathbf{H}} |F_{\text{obs}}(\mathbf{H})|^2} \right\}^{1/2}$$

$$wR_2 = \left\{ \frac{\sum_{\mathbf{H}} w(\mathbf{H}) \left[|F_{\text{obs}}(\mathbf{H})|^2 - |F_{\text{clc}}(\mathbf{H})|^2 \right]^2}{\sum_{\mathbf{H}} w(\mathbf{H}) |F_{\text{obs}}(\mathbf{H})|^2} \right\}^{1/2}$$

$$GoF = \frac{\sum_{\mathbf{H}} w(\mathbf{H}) \left[|F_{\text{obs}}(\mathbf{H})|^2 - |F_{\text{clc}}(\mathbf{H})|^2 \right]^2}{n - m} \tag{5.28}$$

for n reflections and m refined parameters. The *GoF* should amount to one in case of proper weights and a perfect refinement.

In case of a QC structure refinement these quality factors are not sufficient. Due to the high fraction of weak reflections and the importance of reflections with large perp-space components of the diffraction vectors, a more detailed statistical analysis is needed. An example is shown in Fig. 5.9 for the refinement of the structure of decagonal Al–Co–Ni [4].
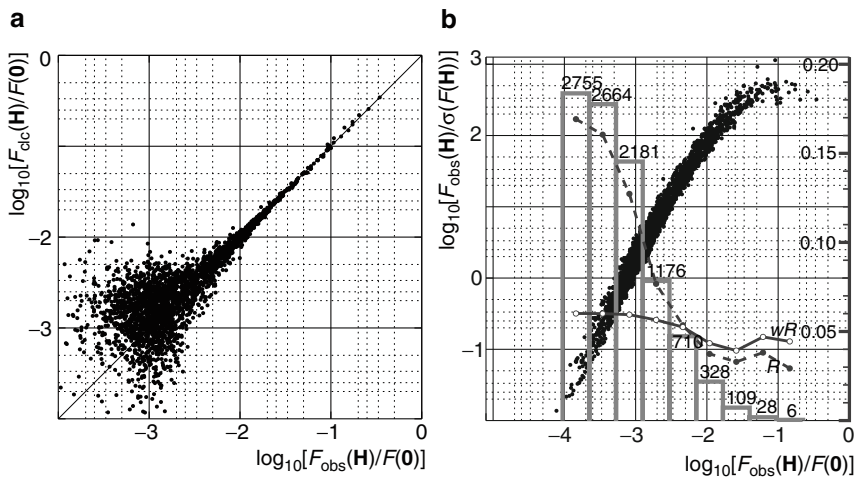
Fig. 5.9. (a) Logarithmic $F_{\text{clc}}(\mathbf{H})$ versus $F_{\text{obs}}(\mathbf{H})$ plot for the refinement of decagonal Al–Co–Ni. $F_{\text{clc}}(\mathbf{0})$ has been taken as unity. (b) Illustration of the weighting scheme and the final error distribution. *Black dots:* logarithmic $F_{\text{obs}}(\mathbf{H})/\sigma(F_{\text{obs}}(\mathbf{H})$ versus $F_{\text{obs}}(\mathbf{H})/F_{\text{clc}}(\mathbf{0})$ plot for showing the distribution of errors on the measured intensity. *Columns with numbers:* number of reflections over a given $F(\mathbf{H})$ threshold. Every column has a height proportional to the number of reflections with $F_{\text{obs}}(\mathbf{H}) > kF_{\text{clc}}(\mathbf{0})$, where k is the center of the column base (logarithmic scale). *Full circles, dashed line, right scale:* the unweighted reliability factor R calculated for each of the reflection subsets indicated by the corresponding column. *Empty circles, continuous line, right scale:* the weighted agreement factor wR calculated for the same reflection subsets (from [4])

Statistical indicators are not in all cases sufficient to distinguish between models differing in parameters which are either highly correlated in the refinement algorithm or not properly represented in the observed data set. Strongly correlated can be, for instance, phason DW factors and occupancy factors of individual subdomains of the atomic surfaces. Parameters describing the partitioning, occupancy, and detailed chemical composition of the subdomains of atomic surfaces can only be properly refined if the data set includes a sufficient amount of reflections with large perp-space component of the diffraction vectors.

Complementary methods for structural characterization such as electron microscopy and/or spectroscopical techniques can help to resolve ambiguities between different structure models by extending the experimental evidence. Structural modeling based on quantum-mechanical calculations can further add information to remove ambiguities.

For example, in the presence of disorder it is not easy to distinguish between disorder in the arrangement of well-ordered clusters and disorder within long-range well-ordered clusters. This can be easily seen by HRTEM but is difficult to derive from Bragg diffraction data. The way short- and long-range order is coded in the atomic surfaces is not easily separable. The long-range order of clusters is defined by the general shape of atomic surface and that of the cluster content by its partitioning. A phason DW factor applied to the whole atomic surface for describing phasonic disorder of the clusters, e.g., would act on the cluster atoms in a way which is not appropriate if the cluster content itself remains fully ordered. From diffuse intensity data, the disorder on different length scales could be discriminated, fortunately.

5.9 Crystallographic Data for Publication

The quality standards of 3D structure analyses by X-ray or neutron diffraction methods and the information required for publication have been clearly defined by the International Union of Crystallography (IUCr).[1] Unfortunately, no such standards do yet exist for the publication of QC structures. The few groups worldwide which have been involved in QC structure analysis had also to invent the analysis methods and the ways of representing the structures in nD as well as in 3D. Since their focus is not always crystallographic, the information is sometimes incomplete or insufficient from the crystallographic point of view. This makes it difficult even for the expert to extract the needed information out of the respective publications and in most cases not the fully required information is given. The following guidelines lists the kind of information a paper on a QC structure analysis should contain.

---

[1] See, for instance, the *Author services* of Acta Crystallogr. C at http://www.iucr.org/

Guidelines for the publication of structural quasicrystal data
All experimental and refined parameters should be given together with their
estimated standard deviations (esds).

Crystal data
Chemical formula
nD space group
nD lattice parameters
Quasilattice parameter
Mass density, point density
Linear absorption coefficient
Crystal shape and dimensions
Thermal history of the sample
*Crystal 'finger print' (Single crystal XRD to show the crystal quality, amount
and distribution of diffuse scattering and way of indexing)*
Crystal quality (FWHM, random and linear phason strain)

Data collection
Type and source of radiation
Type of diffractometer and detector
*Kind of absorption correction applied (minimum and maximum transmission
factors)*
Number of measured, observed, unobserved and unique reflections
Internal R factor, R_{int} (resulting from merging redundant reflections)
Range of reflections measured

Structure solution and Refinement
Structure solution method
Refinement on $|F(\mathbf{H})|$ or on $|F(\mathbf{H})|^2$
R factors, goodness of fit and R-factor statistics
Number of reflections used in the refinement
Number of parameters
Weighting scheme
Extinction parameter
Parameters defining position, shape, size and partitioning of atomic surfaces

Structure model
Graphical representation of the structure model in 3D and nD

References

1. G. Bricogne, Direct Phase Determination by Entropy Maximization and Likelihood Ranking: Status Report and Perspectives. Acta Crystallogr. D **49**, 37–60 (1993)
2. G. Bricogne, Maximum Entropy and the Foundations of Direct Methods. Acta Crystallogr. A **40**, 410–445 (1984)

3. K. Burger, Enhanced versions of the maximum entropy program MEED for X-ray and neutron diffraction. Powder Diff. **13**, 117–120 (1998)
4. A. Cervellino, T. Haibach, W. Steurer, Structure solution of the basic decagonal Al-Co-Ni phase by the atomic surfaces modelling method. Acta Crystallogr. B **58**, 8–33 (2002)
5. D.M. Collins, Electron Density Images from Imperfect Data by Iterative Entropy Maximization. Nature **298**, 49–51 (1982)
6. D.M. Collins, M.C. Mahar, Electron Density: An Exponential Model. Acta Crystallogr. A **39**, 252–256 (1983)
7. M. De Boissieu, R.J. Papoular, C. Janot, Maximum-Entropy Method as Applied in Quasi-Crystallography. Europhys. Lett. **16**, 343–347 (1991)
8. R.Y. DeVries, W.J. Briels, D. Feils, Critical analysis of non-nuclear electron-density maxima and the maximum entropy method. Phys. Rev. Lett. **77**, 1719–1722 (1996)
9. M.A. Estermann, Solving Crystal Structures with the Symmetry Minimum Function. Nucl. Instrum. Methods **354**, 126–133 (1995)
10. F. Fleischer, Personal communication (2009)
11. Z.Q. Fu, F.H. Li, H.F. Fan, Solving a 3-Dimensional Quasicrystal Structure in 6-Dimensional Space Using the Direct Method. Z. Kristallogr. **206**, 57–68 (1993)
12. D. Gratias, J.W. Cahn, B. Mozer, 6-Dimensional Fourier-Analysis of the Icosahedral $Al_{73}Mn_{21}Si_6$ Alloy. Phys. Rev. B **38**, 1643–1646 (1988)
13. C. Giacovazzo, *Direct Methods*. (International Tables for Crystallography, vol. B (Kluwer Academic Publishers, Dordrecht, pp. 210–234 (2001)
14. T. Haibach, Methoden der hherdimensionalen Strukturanalyse dekagonaler Quasikristalle. Thesis No. 10885 ETH Zurich (1994)
15. T. Haibach, W. Steurer, Five-dimensional symmetry minimum function and maximum-entropy method for ab initio solution of decagonal structures. Acta Crystallogr. A **52**, 277–286 (1996)
16. C.L. Henley, V. Elser, M. Mihalkovic, Structure determinations for random-tiling quasicrystals. Z. Kristallogr. **215**, 553–568 (2000)
17. F.L. Hirshfeld, Symmetry in the Generation of Trial Structures. Acta Crystallogr. A **24**, 301–311 (1968)
18. E.T. Jaynes, Information Theory and Statistical Methods. Phys. Rev. **106**, 620–630 (1957)
19. K. Kirihara, T. Nakata, M. Takata, Y. Kubota, E. Nishibori, K. Kimura, M. Sakata, Covalent bonds in AlMnSi icosahedral quasicrystalline approximant. Phys. Rev. Lett. **85** 3468–3471 (2000)
20. K. Kirihara, T. Nakata, K. Kimura, K. Kato, M. Takata, E. Nishibori, M. Sakata, Covalent bonds and their crucial effects on pseudogap formation in alpha-Al(Mn,Re)Si icosahedral quasicrystalline approximant.Phys. Rev. B **68**, art. no. 014205 (2003)
21. K. Kirihara, T. Nakata, M. Takata, Y. Kubota, E. Nishibori, K. Kimura, M. Sakata, Electron-density distribution of approximants of the icosahedral Al-based alloys by the maximum-entropy method and the Rietveld refinement. Mater. Sci. Eng. A **294**, 492–495 (2000)
22. H. Lee, R. Colella, L.D. Chapman, Phase Determination of X-Ray Reflections in a Quasicrystal. Acta Crystallogr. A **49**, 600–605 (1993)
23. H. Lee, R. Colella, Q. Shen, Multiple Bragg diffraction in quasicrystals: The issue of centrosymmetry in Al-Pd-Mn. Phys. Rev. B **54**, 214–221 (1996)

24. G. Oszlányi, A. Sütő, Ab initio structure solution by charge flipping. Acta Crystallogr. A **60**, 134141 (2004)
25. G. Oszlányi, A. Sütő, Ab initio structure solution by charge flipping. II. Use of weak reflections. Acta Crystallogr. A **61**, 147–152 (2005)
26. L. Palatinus, G. Chapuis, SUPERFLIP – a computer program for the solution of crystal structures by charge flipping in arbitrary dimensions. J. Appl. Crystallogr. **40**, 786–790 (2007)
27. L. Palatinus, W. Steurer, G. Chapuis, Extending the charge-flipping method towards structure solution from incomplete data sets. J. Appl. Crystallogr. **40**, 456–462 (2007)
28. R.J. Papoular, M. de Boissieu, C. Janot, The Maximum Entropy Method in Quasicrystallography. In: Methods of Structural Analysis of Modulated Structures and Quasicrystals. Perez-Mato, J.M.; Zuniga, F.J.; Madariaga, G. (Eds.) Singapore: World Scientific pp. 333–343 (1991)
29. M. Quiquandon, D. Gratias, Unique six-dimensional structural model for Al-Pd-Mn and Al-Cu-Fe icosahedral phases. Phys. Rev. B **74**, - art. no. 214205 (2006)
30. M. Sakata, M. Sato, Accurate Structure Analysis by the Maximum-Entropy Method. Acta Crystallogr. A **46**, (1990) 263–270.
31. K. Shankland, C.J. Gilmore, G. Bricogne, H. Hashizume, A Multisolution Method of Phase Determination by Combined Maximization of Entropy and Likelihood. VI. Automatic Likelihood Analysis via Student t Test with an Application to the Powder Structure of Magnesium Boron Nitride, Mg_3BN_3. Acta Crystallogr. A **49**, 493–501 (1993)
32. C.E. Shannon, A Mathematical Theory of Communication. Bell System Tech. J. **27**, 379–656 (1948)
33. M. Shiono, M.M. Woolfson, Direct-space methods in phase extensions and phase determination. I. Low-density elimination. Acta Cryst. A **48**, 451–456 (1992)
34. P.G. Simpson, R.D. Dobrott, W.N. Lipscomb, The Symmetry Minimum Function: High Order Image Seeking Functions in X-ray Crystallography. Acta Crystallogr. **18**, 169–179 (1965)
35. D.S. Sivia, Data Analysis-A Bayesian Tutorial. Oxford: Clarendon Press (1996)
36. W. Steurer, (3+1)-Dimensional Patterson and Fourier Methods for the Determination of One-Dimensionally Modulated Structures. Acta Crystallogr. A **43**, 36–42 (1987)
37. W. Steurer, The N-Dim Maximum - Entropy Method. Methods of Structural Analysis of Modulated Structures and Quasicrystals. In: Methods of Structural Analysis of Modulated Structures and Quasicrystals. Perez-Mato, J.M.; Zuniga, F.J.; Madariaga, G. (Eds.) Singapore: World Scientific, pp. 344–349 (1991)
38. W. Steurer, Quasicrystal structure analysis, a never-ending story? J. Non-Cryst. Solids 334, 137–142 (2004)
39. W. Steurer, T. Haibach, B. Zhang, S. Kek, R. Lück, The Structure of Decagonal $Al_{70}Ni_{15}Co_{15}$. Acta Crystallogr. B **49**, 661–675 (1993)
40. W. Steurer, T. Haibach, B. Zhang, S. Kek, R. Lück, The Structure of Decagonal $Al_{70.5}Mn_{16.5}Pd_{13}$. J. Phys. Cond. Matt. **6**, 613–632 (1994)
41. H. Takakura, M. Shiono, T.J. Sato, A. Yamamoto, A.P. Tsai, Ab initio structure determination of icosahedral Zn-Mg-Ho quasicrystals by density modification method. Phys. Rev. Lett. **86**, 236–239 (2001)

42. H. Takakura, A. Yamamoto, M. Shiono, T.J. Sato, A.P. Tsai, Ab initio structure determination of quasicrystals by density modification method. J. Alloys Comp. **342**, 72–76 (2002)

43. D. Watkin, Structure refinement: some background theory and practical strategies. J. Appl. Crystallogr. **41**, 491–522 (2008)

44. T. Weber, S. Deloudi, M. Kobas, Y. Yokoyama, A. Inoue, W. Steurer, Reciprocal-space imaging of a real quasicrystal. A feasibility study with PILATUS 6M. J. Appl. Crystallogr. **41** 669–674 (2008)

45. S. Weber, A. Yamamoto, Application of the five-dimensional maximum-entropy method to the structure refinement of decagonal $Al_{70}Mn_{17}Pd_{13}$. Philos. Mag. A **76** 85–106 (1997)

46. S. Xiang, F. Li, H. Fan, On the Determination of Quasicrystal Structures. Acta Crystallogr. A **46**, 473–478 (1990)

47. A. Yamamoto, S. Weber, A. Sato, K. Kato, K. Ohshima, A.P. Tsai, A. Niikura, K. Hiraga, A. Inoue, T. Masumoto, Electron density of icosahedral Zn-Mg-Y quasicrystals determined by a six-dimensional maximum entropy method. Philos. Mag. Lett. **73**, 247–254 (1996)

6

Diffuse Scattering and Disorder

Ideal order is just a mathematical concept and cannot exist in real crystals, be they periodic or quasiperiodic. Consequently, in diffraction experiments on real crystals of any kind, structural diffuse scattering will always be observed additionally to Bragg peaks. Thus, structural diffuse scattering (diffuse scattering of other origin will not be discussed here) indicates nonperiodic deviations from nD translational symmetry of a structure.[1]

The diffraction pattern of a disordered structure, $\rho_{\mathrm{dis}}(\mathbf{r})$, consists of a Bragg part, I_{Bragg}, which is related to the average structure, $\rho_{\mathrm{aver}}(\mathbf{r})$, and an absolute continuous (diffuse) one, I_{diff},

$$I_{\mathrm{total}} = I_{\mathrm{Bragg}} + I_{\mathrm{diff}} \tag{6.1}$$

with

$$I_{\mathrm{diff}} = |FT\,[\rho_{\mathrm{dis}}(\mathbf{r})] - FT\,[\rho_{\mathrm{aver}}(\mathbf{r})]\,|^2 = |FT\,[\Delta\rho(\mathbf{r})]\,|^2 \tag{6.2}$$

and $\Delta\rho(\mathbf{r})$, the difference structure between ideally ordered and disordered structure. In thermodynamic equilibrium these deviations can be, for instance:

- Point defects such as thermal vacancies and impurities
- Dynamic excitations such as phonons and phasons
- Structural disorder

Here, we will only consider the last item, structural disorder, and not the defect structure. As an example for equilibrium (as far as experimentally achievable due to sluggish kinetics) diffuse scattering, which does not disappear even after annealing more than hundred days 90°C below the incongruent melting point, is shown on diffraction patterns of i-Al–Mn–Pd (Fig. 6.1a). Besides TDS and PDS, significant diffuse scattering is observed between and beneath the Bragg reflections indicating a substantial amount of structural disorder on the scale of 5–100 Å.

---

[1] Periodic derivations would lead to modulated structures, which, in the ideal case, possess nD translational symmetry and a pure point Fourier spectrum.
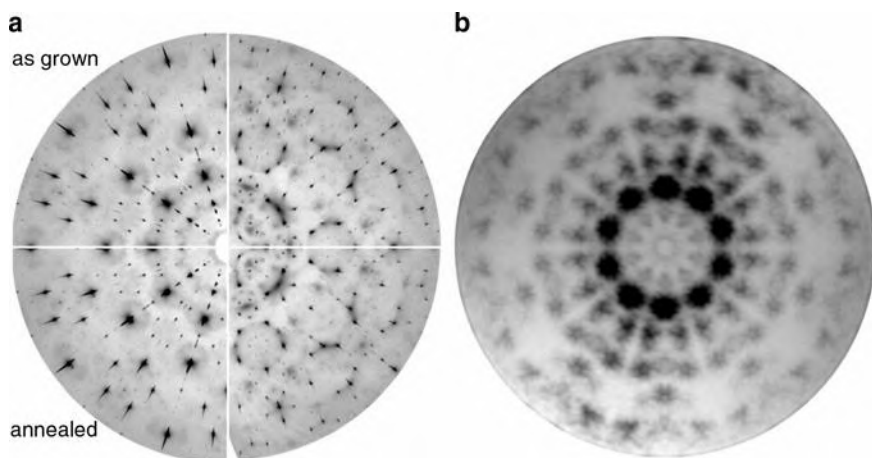
Fig. 6.1. Reconstructed five-fold X-ray diffraction patterns of (**a**) Czochralski grown i-$Al_{70.1}Pd_{21.4}Mn_{8.5}$. The images in the left two quadrants are zero-layer reciprocal space sections, those in the right ones correspond to a higher layer; the images in the upper two quadrants are taken on an as grown sample, those in the lower two quadrants on a crystal annealed for 2,445 hs at 800 °C (samples courtesy of B. Grushko). Long-time annealing does not change the order/disorder in the quasicrystal within the frame of the experiment. (**b**) Reconstructed 10-fold X-ray diffraction pattern of d-$Al_{65}Cu_{20}Co_{15}$ showing the third diffuse inter-layer. The diffuse diffraction pattern obeys the extinction rules of a 5D c-glide plane (space group $P10_5/mmc$) with glide component along the periodic direction. Diffraction data were collected at room temperature (**a**) in-house and (**b**) at SNBL/ESRF, Grenoble, France (courtesy of Th. Weber)

Quenched nonequilibrium deviations can be, for instance:

- Excess vacancies and dislocations
- Domains and domain boundaries
- Chemical inhomogeneities
- Strains and disorder

Diffuse scattering due to nonequilibrium deviations usually breaks the diffraction symmetry defined by the Bragg reflections (Laue class), while equilibrium disorder scattering can obey the full diffraction symmetry of the average structure (Laue class and systematic extinctions) (see Fig. 6.1b).

Structural disorder usually increases the energy of a crystal structure. At finite temperature, this can be compensated by the increase of the configurational entropy, which can decrease the free energy of a crystal sufficiently to stabilize the disordered structure. Disorder is favorable if the energy landscape allows alternative structural arrangements at low energy costs, particularly at elevated temperatures where entropic contributions to the free energy weigh stronger. Those QC which have a broad compositional stability range, i.e. form a more or less extended solid solution at least for a substructure, can

have large entropic contributions from site occupancy disorder (chemical disorder and/or structural-vacancy disorder). The study of equilibrium disorder, therefore, can give valuable insight into the structural factors governing the stability of a crystal.

In the following, we discuss all diffraction phenomena based on the *kinematical theory*. This theory connects direct space and reciprocal space by Fourier transformation and applies within some limits to X-ray and neutron diffraction, but not to electron diffraction. Selected area electron diffraction (SAED) patterns significantly differ from X-ray diffraction (XRD) patterns due to multiple scattering and, of course, due to the different interaction potential. While Bragg reflections and diffuse scattering are at the same reciprocal space positions, their intensities can strongly differ. In most cases, weak diffraction phenomena are enhanced by multiple scattering.

Any nonperiodic deviation from an ideal QC structure which breaks the translational symmetry of the corresponding nD hypercrystal leads to a continuous contribution to its Fourier spectrum (diffuse scattering). These deviations can be time dependent (dynamic) or time independent (static) regarding the time scale of a diffraction experiment, giving rise to inelastic or elastic diffuse scattering, respectively. High-temperature dynamic disorder can often be quenched and observed as static disorder at low temperatures.

One has to keep in mind, however, that structural diffuse scattering is not always a sign of disorder. Ideal deterministically ordered structures without any disorder may even exhibit diffraction patterns (Fourier spectra) with only diffuse scattering, without any Bragg reflections [2]. Generally, a Fourier spectrum, $I(\mathbf{H})$, can consist of three parts [1],

$$I(\mathbf{H})_{\text{total}} = I_{\text{Bragg}}(\mathbf{H}) + I_{\text{diff}}^{\text{sc}}(\mathbf{H}) + I_{\text{diff}}^{\text{ac}}(\mathbf{H}). \tag{6.3}$$

$I_{\text{Bragg}}(\mathbf{H})$, the pure point part, refers to the Bragg reflections (Dirac δ-peaks) resulting from the translationally periodic part of a structure, which is its average structure for a disordered structure. $I_{\text{diff}}^{\text{ac}}(\mathbf{H})$, the absolute continuous part, is a differentiable continuous function, i.e. what we mean by structural diffuse scattering. $I_{\text{diff}}^{\text{sc}}(\mathbf{H})$, the singular continuous part, is neither continuous nor does it have Bragg peaks. It has broad peaks, which are never isolated. They split again and again into further broad peaks if one is looking at them with increasing resolution, and the integrated diffracted intensity behaves like a Cantor function (devil's staircase). The Thue-Morse sequence, for instance, has a singular continuous Fourier spectrum while the Rudin-Shapiro sequence shows an absolute continuous one [5]. Depending on the decoration, however, the Thue-Morse sequence will show Bragg peaks besides the singular continuous spectrum (Fig. 6.2).

The interpretation of disorder diffuse scattering and its quantitative modeling is still not as straightforward as the solution of the average structure based on Bragg reflections. For a general introduction into the field of disorder diffuse scattering and the different methods to analyze it, see, e.g. [16].
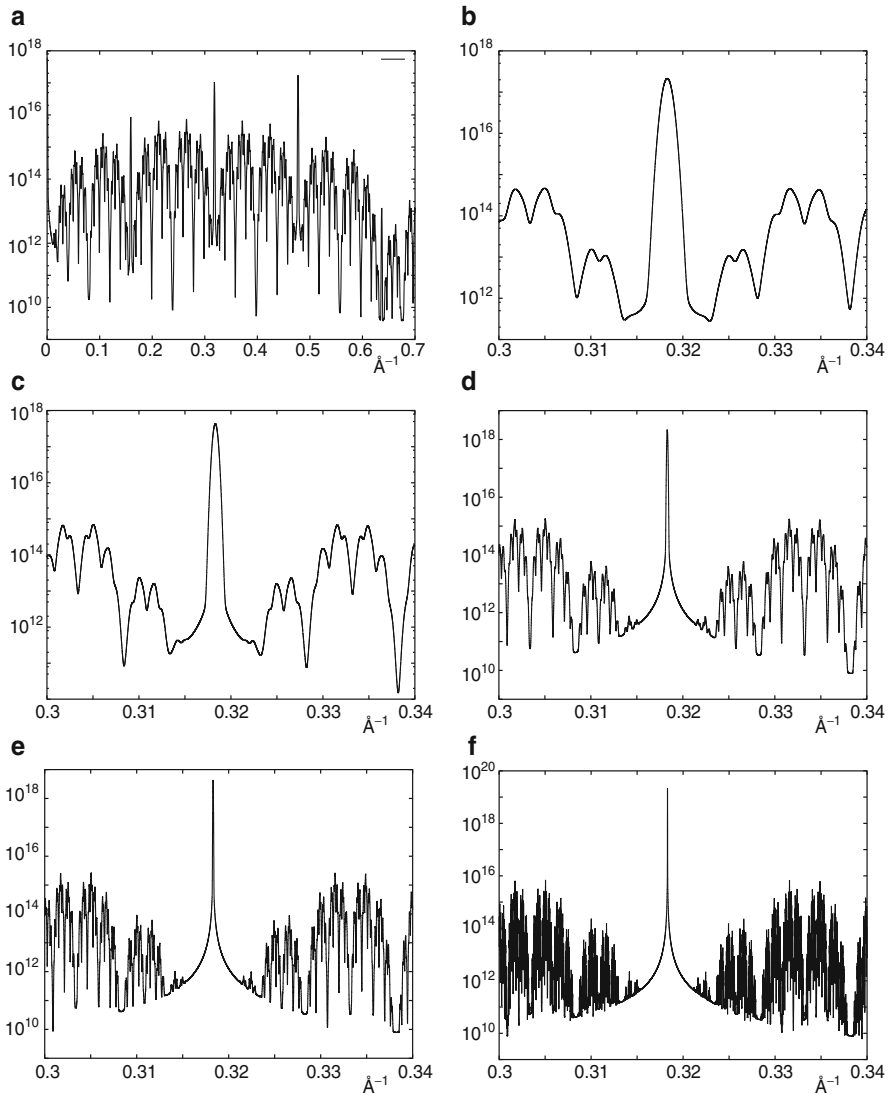
Fig. 6.2. Fourier spectrum (intensities on a logarithmic scale) of a Thue-Morse sequence (see Sect. 1.1.4) for realistic conditions: 10^6 Al atoms with distances A $= 2.4\,\text{Å}$, B $= \tau$A, corresponding to a "crystal" size of $\approx 300\,\mu$m. The typical reciprocal-space range of an in-house diffraction experiment with resolution $0.001\,\text{Å}^{-1}$ is shown in (**a**), and an enlarged part in (**b**). The other images are calculated for resolutions of (**c**) $0.0005\,\text{Å}^{-1}$, (**d**) $0.0001\,\text{Å}^{-1}$, (**e**) $0.00005\,\text{Å}^{-1}$, and (**f**) $0.00001\,\text{Å}^{-1}$. The sharp peak at $\approx 0.318\,\text{Å}^{-1}$ is a Bragg reflection that does not split with increasing resolution, while all other peaks in (**b**)–(**f**) bifurcate with increasing resolution into more and more diffuse maxima (courtesy of Th. Weber)

In the following, we will shortly discuss the application of one particular method, the pair distribution function (PDF), which is for diffuse scattering what the Patterson function is for Bragg scattering. It is simply the Fourier transform of the total diffracted reduced intensity. Frequently, in order to enhance the disorder phenomena, the difference PDF is used, which is based on diffuse intensities alone.

6.1 Phasonic Diffuse Scattering (PDS) on the Example of the Penrose Rhomb Tiling

Phonons (lattice vibrations) dynamically disturb the lattice periodicity of crystals and give rise to thermal diffuse scattering (TDS). In the average structure, the resulting thermal vibrations of the atoms are described by the Debye–Waller (DW) factor. In quasicrystals, additionally a different kind of excitations is possible, phasons, which cause phason diffuse scattering (PDS). In the nD approach, phasons (phason modes) correspond to periodic distortions of the nD hyperlattice with polarization parallel to perp-space while phonons have a polarization parallel to par-space. In 3D physical space, phasons lead to correlated jumps (phason flips) of atoms in double-well potentials. In the average structure, this can be described by a phason DW factor.

The quantitative description of PDS is based on the hydrodynamic theory using the elastic properties of a fictitious nD hypercrystal [8, 11, 14, 15]. For the Laue class 10/mmm, for instance, five elastic constants are associated with the phonon field, three with the phason field and one with the phonon–phason coupling [6, 17]. The phason elastic constants can be experimentally determined based on phason diffuse scattering (see, e.g., [4] and references therein).

According to the hydrodynamic theory for quasicrystals, the phonon displacement field relaxes rapidly via phonon-modes, whereas the phason displacement field relaxes diffusively with much longer relaxation times [12]. At higher temperatures, phasons can be treated analogous to phonons as thermal excitations and described in a unified way. At lower temperatures, however, atomic diffusion is very sluggish and phonons will equilibrate in the presence of a quenched phason displacement field [7, 11, 15]. In this case phonons and phasons have to be treated separately.

For the calculation of PDS and TDS of a 2D diffraction pattern such as that of the Penrose rhomb tiling, one has to solve the following expression for each Bragg reflection [11, 14, 15]:

$$I(\mathbf{H}^\parallel + \mathbf{o}^\parallel) = \frac{k_B T}{(2\pi)^3} I_{\text{Bragg}}(\mathbf{H}^\parallel) \cdot (\mathbf{H}^\parallel, \mathbf{H}^\perp)_V \cdot \mathbf{A}^{-1}(\mathbf{o}^\parallel) \cdot (\mathbf{H}^\parallel, \mathbf{H}^\perp)_V. \quad (6.4)$$

$I(\mathbf{H}^\parallel + \mathbf{o}^\parallel)$ is the diffuse intensity at an offset $\mathbf{o}^\parallel$ from a particular Bragg reflection with nD diffraction vector $(\mathbf{H}^\parallel, \mathbf{H}^\perp)_V$ (subscripts D and V denote D- and V-basis, respectively), k_B is the Boltzmann constant, and T the temperature,

$I_{\mathrm{Bragg}}(\mathbf{H}^{\parallel})$ is the Bragg scattering intensity of a particular reflection, and $A^{-1}(\mathbf{o}^{\parallel})$ is the hydrodynamic matrix. $A^{-1}(\mathbf{o}^{\parallel})$ includes information on the elastic properties of the quasicrystal and, therefore, it is also a function of the phononic elastic constants C_{ijkl}, the phasonic elastic constants K_{ijkl}, and the phonon–phason coupling constants R_{ijkl}.

Equation (6.4) is valid in the case of simultaneously thermalized phonons and phasons ($T \geq T_{\mathrm{q}}$, with the phason-quenching temperature T_{q}). In the case of quenched phasons ($T \leq T_{\mathrm{q}}$), (6.4) can still be written in the same form but $A(\mathbf{o}^{\parallel})$ has to be replaced by an effective hydrodynamic matrix $A_{\mathrm{eff}}(\mathbf{o}^{\parallel})$. $A_{\mathrm{eff}}(\mathbf{o}^{\parallel})$ is not only associated with C_{ijkl}, K_{ijkl}, and R_{ijkl} at temperature T, but also with those at temperature T_{q}. Thus, the effectively needed input for the calculation of PDS and TDS are the elastic constants and the Bragg intensities.

The influence of a variation of the elastic properties of a Penrose rhomb tiling on PDS and TDS is illustrated in Fig. 6.3. As shown in Sect. 3.6.4, the Penrose rhomb tiling can be described as 4D hypercrystal structure with four pentagonal atomic surfaces. In our model structure, the two small pentagonal atomic surfaces are decorated with Ni atoms, the two τ times larger ones with Al atoms. The reciprocal space images are shown together with the resulting PDF for five cases with different elastic parameters (Table 6.1). The cases of pure TDS and PDS are realized by stiffening the Penrose rhomb tiling in par- and perp-space, respectively. The overall distribution of diffuse scattering looks very similar in the cases (a)–(d) but differs from the case of pure TDS in (e).

Taking a look at the PDF maps (Fig. 6.3(f–j)) one can hardly see any difference for the first four cases (f–i). This is not surprising since the diffuse intensities in (a–d) change only in their fine structure, which predominantly contributes to longer PDF vectors ($>100\,\text{Å}$) which are out of range. In contrast, the PDF of the pure TDS diffraction pattern (Fig. 6.3j) shows uniformly distributed positive peaks, each with a negative halo around it. The absence of certain vectors in the PDF maps of the first four cases (see arrows in Fig. 6.3(f–i)) means that the structure at these vectors corresponds to the average structure, i.e. that these vectors are not influenced by phasonic disorder. Consequently, the Penrose rhomb tiling is not uniformly disordered by phasons such as it is in the case of TDS. Note that the integrated diffuse intensity from the pure TDS case is at least one order of magnitude smaller than that for the other cases.

6.2 Diffuse Scattering as a Function of Temperature on the Example of d-Al–Co–Ni

The structural ordering phenomena of quasicrystals as reflected in the variation of Bragg and diffuse scattering with temperature (illustrated on the example of d-Al–Co–Ni, Fig. 6.4) can give some insight into the stabilization
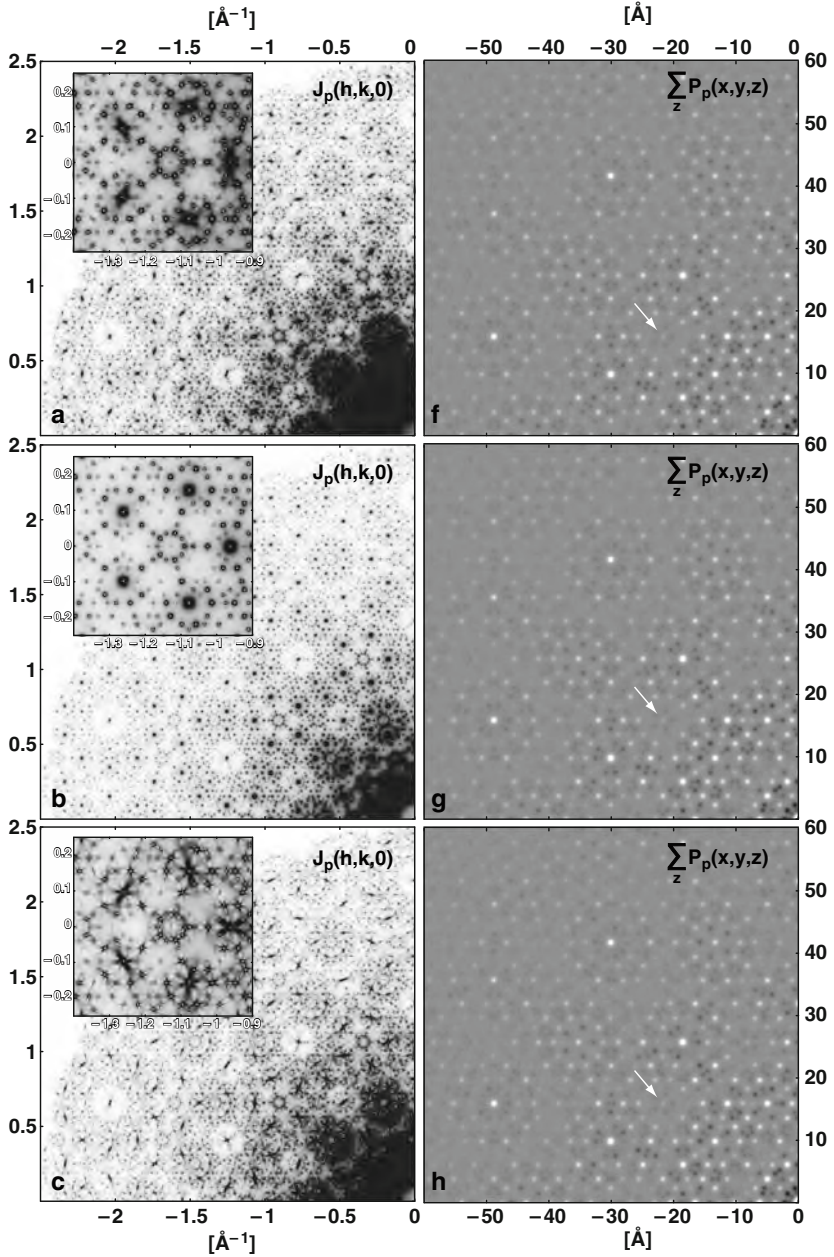
Fig. 6.3. Influence of a variation of the elastic parameters on the PDS and TDS calculations of a Penrose rhomb tiling in reciprocal- and vector-space (PDF) (see Table 6.1). Zoomed sections of the diffraction patterns of the five cases examined are shown as inserts in (**a**–**e**), the corresponding PDF maps in (**f**–**j**). The Bragg peaks have been punched out and do not contribute to the calculation of the PDF maps. The overall distribution of diffuse scattering
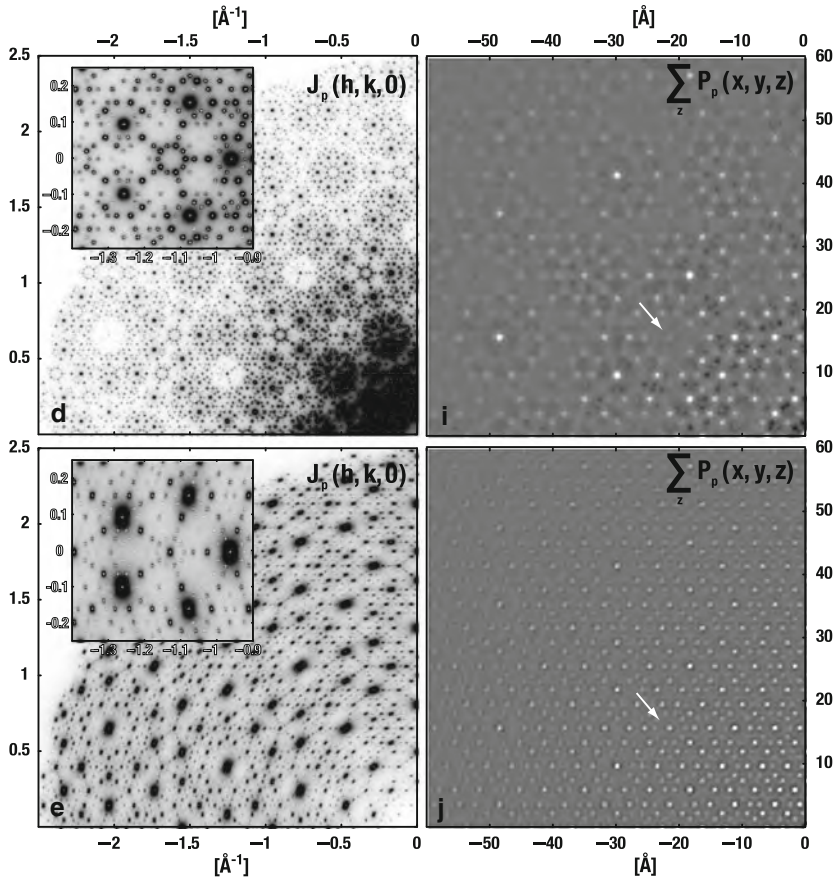
Fig. 6.3. (continued) looks very similar in the cases (**a**–**d**) but the fine structure changes significantly. Hardly any differences can be observed in the PDF maps of the first four cases (**f**–**i**). *Arrows* indicate one example of a PDF vector that is absent in (**f**–**i**) and present in (**j**). Relative scaling of the patterns in (**f**)–(**j**) is 80:40:160:40:1 [9]

mechanism of the quasicrystalline phase. There are three scenarios:

- If quasicrystals were perfectly quasiperiodic at zero K (i.e., energy stabilized) then phasonic disorder should increase with temperature. Since the phason Debye–Waller factor strongly depends on the perp-space norm of scattering vectors, the intensities of reflections with high perp-space norm should faster decrease with increasing temperature.
- In case of entropy stabilization, the ground state was a periodic structure (approximant). With increasing temperature the structure would approach more and more, on average quasiperiodic, random tiling. The increasing configurational entropy would drive the stabilization of the quasiperiodic

Table 6.1. Elastic constants for the PDS and TDS calculations on the Penrose rhomb tiling shown in Fig. 6.3. Units are in 10^{12} dyn/cm^2 [10]

	$R > 0$ Figs. 6.3a,f	$R = 0$ Figs. 6.3b,g	$R < 0$ Figs. 6.3c,h	pure PDS Figs. 6.3d,i	pure TDS Figs. 6.3e,j
C_{11}	2.34315	2.34315	2.34315	1.10^6	2.34315
C_{13}	0.66625	0.66625	0.66625	1.10^6	0.66625
C_{33}	2.32215	2.32215	2.32215	1.10^6	2.32215
C_{44}	0.70190	0.70190	0.70190	1.10^6	0.70190
C_{66}	0.88455	0.88455	0.88455	1.10^6	0.88455
K_1	0.02	0.0189	0.0189	0.0189	1.10^6
K_4	0.4	0.4	0.4	0.4	1.10^6
R	0.1	0.0	-0.12	0.0	0.0

structure. In the nD description, the atomic surfaces would start to condense with increasing temperature indicating the increase in on-average quasiperiodic order of the random tiling compared with that of the approximant. This causes the intensities of reflections with high perp-space norm to increase at higher temperature.

- Both stabilization mechanisms can be combined solving some contradictory or implausible features of both approaches. Let us assume an ideally ordered quasiperiodic structure based on one or more clusters as its basic elements. The ideal quasiperiodic order of the clusters would be counterbalanced by strong disorder in the cluster interior. Enough configurational entropy (close to the values of metallic glasses) could be generated in this way to explain the quasicrystal's thermodynamic stability at high temperature. Long-range-correlation terms in the total energy (explaining and reinforcing the observed Hume-Rothery effect) can be easily introduced in this way. In this frame, at high temperatures the ground state would be the quasicrystal, as the structural and energetic limit of approximants with increasingly large unit cell. Small-unit-cell approximants, with more ordered clusters, would be the ground state at lower temperatures. The high-temperature behavior of the main Bragg reflections can also be easily justified, without the need to introduce random tilings in the strict sense, which have never been proven to have Bragg peaks in their diffraction pattern.

The diffraction patterns shown in Fig. 6.4 have been taken from a crystal with nominal composition $Al_{70}Co_{12}Ni_{18}$, quenched from $900°C$ by switching off the high-vacuum furnace. Consequently, the room temperature diffraction patterns reflect the structure of the quenched crystal, while those taken from the same crystal but now in situ at $800°C$ and $850°C$, respectively, correspond to equilibrated structures. Going from top to bottom of Fig. 6.4, we see that only every other layer (Bragg layers) contains sharp Bragg reflections. This sequence of Bragg layers corresponds to a period of two quasiperiodic atomic
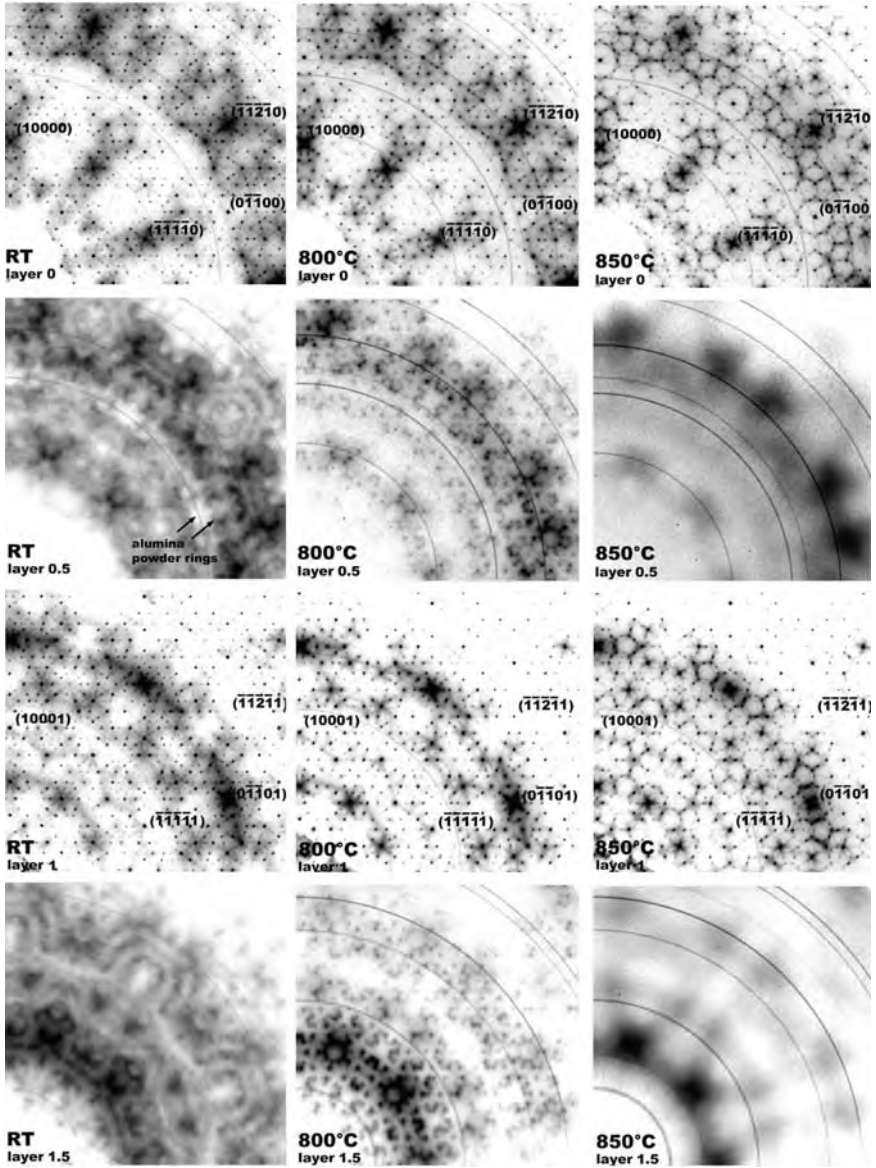
Fig. 6.4. Reciprocal space sections of d-$Al_{70}Co_{12}Ni_{18}$ reconstructed from 360 image plate scanner frames at each temperature (marresearch 345, wave length $\lambda = 0.7\,\text{Å}$, oscillation angle $\Delta\phi = 0.5°$, Swiss-Norwegian Beam Lines/ESRF, Grenoble). In the first column, sections of the reciprocal space layers $h_1 h_2 h_3 h_4 h_5$ with $h_5 = 0, 0.5, 1, 1.5$, all taken at room temperature, are shown. The second and third column contain the sections collected at 800 and 850 °C, respectively. The thin rings originate from the alumina sample holder [13]

layers along the tenfold axis. The diffuse interlayers indicate a two-fold superstructure with long correlation length along the tenfold axis and a much shorter one within the quasiperiodic layers. The correlation length changes, however, with temperature. Going from room temperature to 800°C, surprisingly, the extended diffuse scattering phenomena condense into almost Bragg reflection like diffuse maxima. This means, the correlation length of some ordering phenomena increases drastically with temperature while the widths of Bragg reflections do not change within the experimental resolution.

How can these phenomena be interpreted? We know from many experimental studies that decagonal Al–Co–Ni phases are build from columnar clusters with approximately 20 Å diameter. According to the small width of the diffraction phenomena parallel to the periodic direction, these columns must have rather perfect four-layer periodicity along the tenfold axis. The narrow width of the Bragg reflections indicates almost perfect quasiperiodic long-range order of the columns on a two-layer scale. On the four-layer scale, the correlation length is of the order of a few cluster diameters for the quenched sample at room temperature. It increases by one or two orders of magnitude at 800°C and breaks down almost completely at 850°C. At this temperature also the four-layer correlation length along the ten-fold axis decreases. This indicates, that, at least for this composition, the decagonal phase is better ordered at high temperature.

References

1. M. Baake, In *Quasicrystals: Introduction to Structure, Physical Properties, and Applications*, ed. by J.B. Suck, M. Schreiber, P. Hussler, (Springer Berlin, 2002), pp. 17
2. M. Baake, U. Grimm, Kinematic diffraction is insufficient to distinguish order from disorder. Phys. Rev. B **79**, art. no. 020203(R) (2009)
3. V. Cowley, Diffraction Physics, 3rd edition, Elsevier Science B.V., Amsterdam (1995)
4. M. De Boissieu, S. Francoual, Diffuse scattering and phason modes in the i-AlPdMn quasicrystalline phase. Z. Kristall. **220**, 1043–1051 (2005)
5. C. Godreche, J.M. Luck, F. Vallet, Quasiperiodicity and Types of Order. A Study in One Dimension. J. Phys., A (London). Math. Gen. **20**, 4483–4499 (1987)
6. C.Z. Hu, R.H. Wang, W.G. Yang, D.H. Ding, Point groups and elastic properties of two-dimensional quasicrystals. Acta Crystallogr. A **52**, 251–256 (1996)
7. Y. Ishii, Phason Softening and Structural Transitions in Icosahedral Quasi-Crystals. Phys. Rev. B **45**, 5228–5239 (1992)
8. M.V. Jaric, D.R. Nelson, Diffuse-Scattering from Quasicrystals. Phys. Rev. B **37**, 4458–4472 (1988)
9. M. Kobas, Modelling disorder in quasicrystals. Decagonal Al-Co-Ni. Thesis ETH No. 15819 (2004)
10. M. Kobas, T. Weber, W. Steurer, Structural disorder in the decagonal Al-Co-Ni. II. Modeling. Phys. Rev. B **71**, art. no. 224206 (2005)

11. J.L. Lei, R.H. Wang, C.Z. Hu, D.H. Ding, Diffuse scattering from decagonal quasicrystals. Phys. Rev. B **59**, 822–828 (1999)
12. T.C. Lubensky, S. Ramaswamy, J. Toner, Hydrodynamics of Icosahedral Quasicrystals. Phys. Rev. B **32**, 7444–7452 (1985)
13. W. Steurer, A. Cervellino, K. Lemster, S. Ortelli, M.A. Estermann, Ordering principles in decagonal Al-Co-Ni quasicrystals. Chimia **55**, 528–533 (2001)
14. R.H. Wang, C.Z. Hu, J.L. Lei, D.H. Ding, Theoretical aspects of thermal diffuse scattering from quasicrystals. Phys. Rev. B **61**, 5843–5845 (2000)
15. R.H. Wang, C.Z. Hu, J.L. Lei, Theory of diffuse scattering of quasicrystals due to fluctuations of thermalised phonons and phasons. Phys. Stat. Sol. B **225**, 21–34 (2001)
16. T.R. Welberry, Diffuse X-ray scattering and models of disorder. Oxford University Press, Oxford (2004)
17. W. Yang, C.Z. Hu, D.H. Ding, R.H. Wang, Differences in Elastic Behavior between Pentagonal and Decagonal Quasi-Crystals. Phys. Rev. B **51**, 3906–3909 (1995)

Structures with 1D Quasiperiodicity

Basically, 1D quasicrystals can be equally well described in the framework of quasiperiodic structures and in the one of incommensurately modulated structures. However, in the cases where τ-scaling symmetry applies to the diffraction pattern, the QC-setting may be more appropriate. This is also true for 1D quasicrystals resulting from phase transformations of axial or icosahedral quasicrystals. Structural relationships between initial and final phases can be better described within the same approach.

One class of 1D quasicrystals comprises vacancy-ordered phases, i.e. series of superstructures of the CsCl type, in systems such as Al-Pd, Al-Ni, Al-Cu-Ni. They are characterized by stackings of (111) layers, either fully occupied or containing vacancies, related to the Fibonacci sequence [1].

Stable 1D quasicrystals have been found in annealed samples with compositions $Al_{75}Fe_{10}Pd_{15}$ [4] and $Al_{65}Cu_{20}Fe_{10}Mn_5$ [5]. Some characteristic parameters are listed in Table 7.1. The lattice parameter a is along a two-fold direction ($A2P^1$) and c the period along the ten-fold axis of the related decagonal phase.

Another class includes metastable 1D quasicrystals resulting as intermediate states during the transformation from a decagonal phase to an approximant. Examples are rapidly solidified $Al_{80}Ni_{14}Si_6$, $Al_{65}Cu_{20}Mn_{15}$ and $Al_{65}Cu_{20}Co_{15}$ alloys [3] as well as slowly solidified $Al_{70}Co_{15}Ni_{15}$. The phase transformation can be described by the application of linear phason strain, which also leads to a domain structure.

---

[1] A2P marks directions along a twofold axis in case of icosahedral symmetry; for the decagonal phase this direction is characterized by a hexagonal appearance of six strong reflections in the diffraction pattern [2].

Table 7.1. Lattice parameters of 1D quasicrystals, with $a = m \times 2.3\,\text{Å}$ and $c = n \times 2.0\,\text{Å}$ [6]

m	$a\,[\text{Å}]$	n	$c\,[\text{Å}]$	Composition	References
3	6.9	8	16	$Al_{80}Ni_{14}Si_6$	[3]
5	11.5	6	12	$Al_{65}Cu_{20}Mn_{15}$	[3]
5	11.5	8	16	$Al_{75}Fe_{10}Pd_{15}$	[4]
8	18.4	6	12	$Al_{65}Cu_{20}Fe_{10}Mn_5$	[5, 6]
8	18.4	8	16	$Al_{75}Fe_{10}Pd_{15}$	[4]
13	29.9	2	4	$Al_{65}Cu_{20}Co_{15}$	[3]
13	29.9	6	12	$Al_{65}Cu_{20}Fe_{10}Mn_5$	[6]
18	41.4	6	12	$Al_{65}Cu_{20}Fe_{10}Mn_5$	[6]

References

1. K. Chattopadhyay, S. Lele, N. Thangaraj, S. Ranganathan, Vacancy Ordered Phases and One-Dimensional Quasiperiodicity. Acta Metall. **35**, 727–733 (1987)
2. K.K. Fung, C.Y. Yang, Y.Q. Zhou, J.G. Zhao, W.S. Zhan, B.G. Shen, Icosahedrally Related Decagonal Quasi-Crystal in Rapidly Cooled Al-14-at.%-Fe Alloy. Phys. Rev. Lett. **56**, 2060–2063 (1986)
3. L.X. He, X.Z. Li, Z. Zhang, K.H. Kuo, One-Dimensional Quasicrystal in Rapidly Solidified Alloys. Phys. Rev. Lett. **61**, 1116–1118 (1988)
4. A.P. Tsai, T. Masumoto, A. Yamamoto, Stable One-Dimensional Quasi-Crystals in Al-Pd-Fe Alloys. Philos. Mag. Lett. **66**, 203–208 (1992)
5. A.P. Tsai, A. Sato, A. Yamamoto, A. Inoue, T. Masumoto, Stable One-Dimensional Quasi Crystal in a Al-Cu-Fe-Mn System. Jap. J. Appl. Phys. Lett. **31**, L970–L973 (1992)
6. W.G. Yang, J.N. Gui, R.H. Wang, Some new stable one-dimensional quasicrystals in an $Al_{65}Cu_{20}Fe_{10}Mn_5$ alloy. Philos. Mag. Lett. **74**, 357–366 (1996)

Structures with 2D Quasiperiodicity

Axial quasicrystals have just one special axis N with multiplicity n larger than two. Along this axis they show a periodic sequence of atomic layers, which are ordered quasiperiodically in two dimensions. Theoretically, n could be any integer and there are no principal geometrical restrictions. However, all stable axial quasicrystals known so far show five- or ten-fold symmetry only (cf. [99] and references therein). This is not too surprising since icosahedral coordination is the most frequent atomic environment type (AET) in intermetallic phases [26]. However, since polyhedra with icosahedral symmetry cannot be packed without gaps, they are distorted and/or mixed with other AET. There are a few reports on quasicrystals with 8- or 12-fold symmetry. However, these quasiperiodic phases are either metastable or of poor quality. Not a single quasicrystal with any other noncrystallographic symmetry has ever been reported.

For the hypothetical case of 2D structures, it has been argued that only quasicrystals based on quadratic irrationalities, $a + b\sqrt{c}$ ($a, b, c \ldots$ rational numbers), could be energetically stable [71]. Consequently, only quasicrystals with 5-, 8-, 10-, and 12-fold symmetries would be allowed. In the more realistic case of 3D QC, however, symmetries based on cubic irrationalities, such as 7-, 9-, 14- and 18-fold could also be possible according to this approach [84, 98].

It was also shown that weak matching rules, based on the alternation condition, exist for tilings with n-fold symmetry, where n is either a prime number or the double of a prime number. This means that a ground state could exist for structures based on such tilings. Generally, in case of n-fold rotational symmetry the irrationality would be of order $\phi(n)/2$, i.e. a root of the algebraic equation $a_n x^n + a_{n-1} x^{n-1} + \cdots + a_1 x + a_0 = 0$, where a_i are integers. $\phi(n)$ is Euler's totient function, i.e. the number of all positive integers k that are relatively prime to (do not contain any factor with) n, $\gcd(k, n) = 1$ and $k \leq n$ (see Table 8.1). The number $\phi(n)$ is also equal to the number of possible generators of the cyclic group C_n.

In 1985, the discovery of the first (metastable) axial quasicrystals, decagonal Al–Mn [11, 20], and dodecagonal Ni–Cr [53] was reported. The first stable

Table 8.1. Values of Euler's totient function for n-fold symmetry

n	1	2	3	4	5	6	7	8	9	10	11	12	13	14	15	16	17	18
$\phi(n)$	1	1	2	2	4	2	6	4	6	4	10	4	12	6	8	8	16	6

decagonal quasicrystal, $Al_{10}FeNi_3$, was actually discovered in 1982 [61], but not identified as quasiperiodic before 1994 [70]. The first report on a stable decagonal phase, $Al_{65}Cu_{20}Co_{15}$, was published in 1988 [46]. There are no stable heptagonal and octagonal phases known so far, and only one, rather poorly ordered, dodecagonal phase, $Ta_{1.6}Te$, has been reported in 1998 [25]. It should be mentioned here that the local axial symmetry and scaling properties in some proteins show rotational orders $n = 5, 7, 8, 9, 11$ [54–56].

8.1 Heptagonal Phases

No regular or semiregular polyhedra (Platonic or Archimedian solids) exist with rotational symmetry larger than five-fold. However, polyhedra with only axial n-fold symmetry (e.g. prisms or pyramids) are possible for arbitrary n. Indeed, (distorted) seven-membered rings are very common in the structures of ternary borides and borocarbides (see later). These structures can be seen as approximants of heptagonal quasicrystals. If approximants exist, why are no heptagonal quasicrystals known so far?

A tiling with seven-fold (or any other) symmetry can be constructed by the dual-grid method as easily as one with 5-fold symmetry (see also Sect. 1.2.4). It gets more complicated, however, if one tries to construct a structure based on a cluster with seven-fold symmetry. We demonstrate this by the example of local polysynthetic twinning of pentagonal and heptagonal clusters (e.g., pentagonal and heptagonal bipyramids, respectively) (Fig. 8.1).

The first pentagon P (nucleus) is twinned along its edges: P + 5P → P5P. The twinning is repeated at the edges of the τ^2-times larger (in diameter) aggregates: P5P + 5P 5P → (P5P)5(P5P) and so forth. The local twinning procedure applied to heptagons, already leads in the first shell of neighbors to overlaps, which may cause problems in the case of real atomic clusters. This problem can be overcome if one does not try to build the quasiperiodic structure by overlapping heptagonal clusters but build the structure based on at least three different unit tiles.

The heptagonal tiling consists of three different rhombic prototiles (Fig. 8.2). The prototiles have a different frequency in the heptagonal tiling and the approximant, respectively. In the tiling the frequency of the three prototiles is proportional to their areas [119], while in the approximant it depends on the order of the approximant.
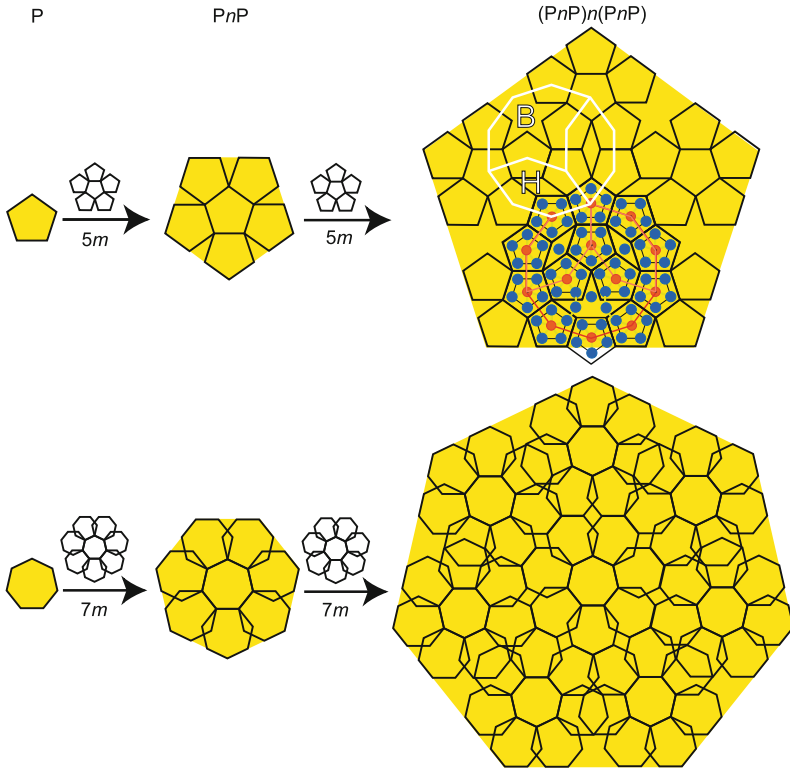
Fig. 8.1. Fractal n-grammal growth model for $n = 5$ and 7, respectively. The growth takes place by twinning along the free edges of the n-gons and clusters of n-gons. In case of pentagon-twinning, decagons (*white*) appear after the second twinning cycle. These decagons consist of two hexagonal (H) and one boat tile (B) that are typical for decagonal quasicrystals. A decagon of the type found in decagonal Al–Co–Ni, decorated with Al (dark-gray, online: *blue*) and TM (light-gray, online: *red*) atoms, is shown. In case of heptagons, even the first twinning cycle leads to overlapping problems

Socolar [98] found that weak matching rules (alternation condition) can exist for heptagonal tilings. This means that quasicrystals with this symmetry could grow with bounded perpendicular-space fluctuations, just based on local matching rules. However, there are some more complications. The 2D quasiperiodic part of a QC with axial n-fold symmetry can be described as a section of a 4D hypercrystal in case of quadratic irrationalities and of a 6D hypercrystal in case of cubic irrationalities. Consequently, in the case of 7-fold symmetry we need a 6D embedding space. Then the dimension of the perpendicular space (4D) is higher than that of the physical space (2D). Consequently, that there are two types of 2D phason fields instead of just one for the known QC [51]. It is not known what consequences these degrees of freedom may have for QC growth.
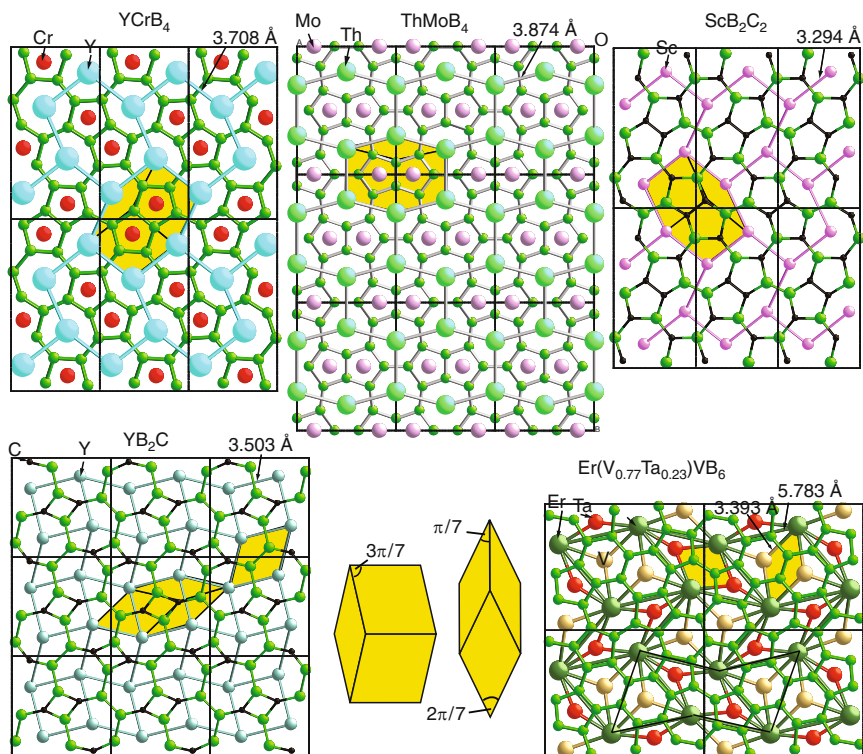
Fig. 8.2. Structure types of borides and borocarbides with seven-membered rings. The close relationship of structure motifs to the unit tiles (gray, online: *yellow* rhombs and heptagons) of the heptagonal tiling is shown

8.1.1 Approximants: Borides, Borocarbides, and Carbides

Pentagonal symmetry is not only the dominating symmetry in quasicrystals but also quite common in nature, particularly in living organisms [43]. By contrast, heptagonal symmetry is rarely observed in nature, a few examples are some representatives of sea weeds and ascidians [32]. More frequently observed are seven-membered rings in organic heterocyclic molecules [80] and in inorganic borides and borocarbides. Recently, the occurrence of heptagrammal symmetry in proteins was reported [54–56].

There are several known structure types, such as borides, borocarbides and carbides, which contain seven-membered rings. In all cases, the structures consist of 2D nets with intercalated metal atoms. Since a packing of regular heptagons does not cover the plane without gaps and overlaps, at least one other type of polygonal tile is needed. In Fig. 8.2 representatives of structure types (see also Table 8.2) are shown, which are built from one or two of the three unit tiles of the heptagonal tiling.

Table 8.2. Crystallographic data of structure types containing seven-membered rings

Nominal composition	Pearson Symbol	Space Group	a (Å)	b (Å)	c (Å)	References
$YCrB_4$	$oP24$	$Pbam$	5.972	11.460	3.461	[69]
ThB_4	$tP20$	$P4/mbm$	7.256	7.256	4.113	[124]
$ThMoB_4$	$oP24$	$Cmmm$	7.481	9.658	3.771	[86]
Y_2ReB_6	$oP36$	$Pbam$	9.175	11.550	3.673	[68]
Na_3B_{20}	$oC46$	$Cmmm$	18.695	5.701	4.151	[2]
ScB_2C_2	$oP20$	$Pbam$	5.175	10.075	3.440	[97]
YB_2C	$tP32$	$P4_2mbc$	6.793	6.793	7.438	[7]
$DyCoC_2$	$oP8$	$Amm2$	3.544	4.515	6.036	[57]

The most common structure types are $YCrB_4$ and Y_2ReB_6 with $\approx$90 and 39 representatives, respectively. As can be seen in Fig. 8.2, the most regular heptagons are obtained in a tiling together with pentagons and hexagons such as in $YCrB_4$. They are more strongly distorted in case of accompanying rhombic or triangular tiles such as in YB_2C.

The $YCrB_4$ structure type [69], with more than 90 known representatives, consists of vertically stacked, planar three-connected boron nets containing five- and seven-membered boron rings (Fig. 8.2a). The metal atoms are located halfway between the nets. The atomic distances indicate that the metal atoms donate their valence electrons to the covalently bonded boron net. However, there is no pure ionic bonding between metal cations and the anionic boron net. Covalent bonding between metal and boron atoms also plays a significant role. Geometrically, the structure can be seen as built from heptagonal bipyramids decorating the vertices of a tiling of squashed hexagons (Fig. 8.2). The heptagonal bipyramids consist of a heptagonal boron ring capped by the large rare earth (RE) ions. The voids left by the heptagonal bipyramids correspond to pentagonal bipyramids capped by the smaller transition metal (TM) ions. The structure of Y_2ReB_6 (B_5, B_6, and B_7 rings) can be seen as intermediate between the structure of YB_2 (AlB_2-type; only B_6 rings) and that of $YReB_4$ ($YCrB_4$-type; B_5 and B_7 rings) [68]. Rare-earth metal borocarbides with ScB_2C_2- and YB_2C-type, respectively, are crystal-chemically very similar to the borides [8]. However, with the way of ordering B and C atoms in the B–C network ('coloring problem'), borocarbides possess additional degrees of freedom.

The electronic structures of $YCrB_4$, Y_2ReB_6 and MgC_2B_2, with a structure closely related to superconducting MgB_2, were studied by [79]. $YCrB_4$, becomes a narrow-gap semiconductor, which could be transformed to the metallic state by hole or electronic dopants. Boron σ-bands are responsible for the superconductivity in MgB_2. Doping of $YCrB_4$ would change the occupancy of Cr 3d states rather than those of boron. Therefore, a transition to a superconducting state not would be very probable. More promising could be

doping of Y_2ReB_6 that already has metallic properties. The creation of holes could be achieved by partial substitution of Re by W, for instance.

8.1.2 Approximants: γ-Gallium

Another example of a structure with local heptagonal symmetry is metastable γ-gallium, which can be obtained from supercooled liquid gallium at atmospheric pressure [13]. The structure consists of heptagonal antiprisms centered by a chain of Ga atoms parallel to the c-direction (Fig. 8.3). Between the antiprisms there are ladders of Ga atoms running along c as well.

8.2 Octagonal Phases

The first octagonal phase was discovered in 1987 in rapidly solidified samples of V–Ni–Si and Cr–Ni–Si alloys [115]. It is amazing that all other (metastable) octagonal phases known so far have been discovered within two years 1987/1988 (Table 8.3).
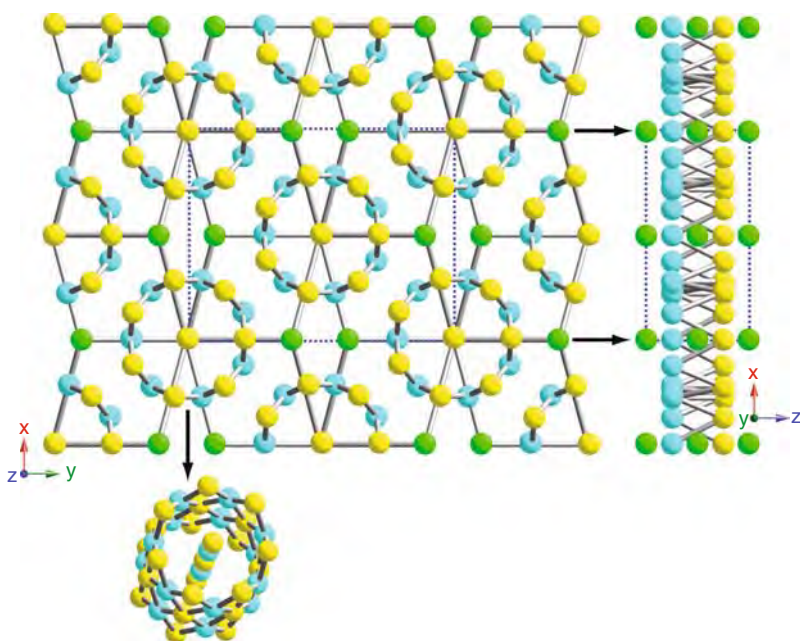
Fig. 8.3. Structure of γ-gallium projected along the c-direction (*left* drawing) and along the a-direction (*right* drawing). The crystallographic data are: $oC40$, *Cmcm*, $a = 10.593$, $b = 13.523$, $c = 5.203$ Å [13]. Different colors (online) mark Ga atoms belonging to different structural subunits: single chains, double chains, and heptagonal antiprisms

Table 8.3. Octagonal quasicrystals known so far. All phases have been obtained by rapid solidification and are metastable

Nominal composition	Period (Å)	5D space group	References
$Cr_5Ni_3Si_2$	6.3		[115]
Mn_4Si	6.2		[16]
$Mn_{82}Si_{15}Al_3$	6.2	$I8_4/mcm$	[10, 116]
Mn-Fe-Si			[117]
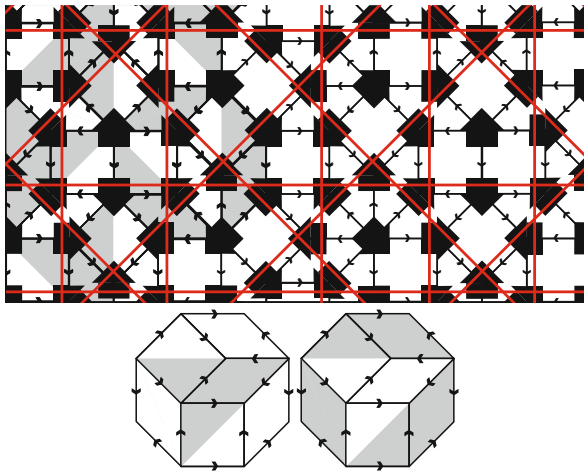
Fig. 8.4. Octagonal Ammann–Beenker tiling with Ammann lines drawn in. The *left part* of the tiling is covered with the two octagon patches shown below [10]

A detailed structure model of o-$Mn_{80}Si_{15}Al_5$ was derived from HRTEM images based on the structure of β-Mn [52, 58]. The structure model consists of stackings of four quasiperiodic layers with sequence ... ABAB'... and a period of 6.3 Å. The layer A shows eight-fold symmetry while the layers B and B' are four-fold symmetric only. B' results by rotating layer B by 45°. Each layer corresponds to a quasiperiodic tiling built from 45° rhombs and squares with edge length $a_r = 8.2$ Å. These unit tiles can be further decomposed to tiles with an edge length $a'_r = 3.4$ Å, smaller by a factor $\sqrt{2} - 1$. The local symmetry is $8_4/mmc$. Based on this model, a covering cluster description was derived (Fig. 8.4) and shown that this octagonal QC has the highest density of octagonal prismatic clusters [10].

A continuous change from metastable o-Cr–Ni–Si and o-Mn–Si–Al to the cubic phase with β-Mn type structure was observed by moving the SAED aperture successively from the octagonal to the cubic area of the samples [118]. An orientational relationship, $[001]_{\beta-Mn}\|[00001]_{oct}$ and $[100]_{\beta-Mn}\|[11000]_{oct}$,

between coexisting cubic β-Mn and the octagonal phases o-Cr–Ni–Si and o–Mn–Si–Al was observed [118] and the structural relationship is described in [72]. This transformation was explained by gradual introduction of a phason strain field [76] and a theoretical model based on the Schur rotation, i.e. a one-parameter rotation in the nD description [5].

8.3 Decagonal Phases

Decagonal quasicrystals are characterized by their decagonal diffraction symmetry $10/m$ or $10/mmm$. The period along the tenfold axis is an even number of atomic layers. There are examples of two-, four-, six-, and eight-layer periodicity (Tables 8.4, 8.5, 8.6). The stability ranges of decagonal phases are schematically shown in Fig. 8.5.

Although decagonal QC can be described as periodic stackings of quasiperiodic layers, this is only a geometrical picture. Indeed bonding does not differ between layers and within layers. Typical structural building units, such as pentagonal bipyramids or icosahedral clusters, extend over more than one atomic layer. This is also reflected in the kind of disorder observed. One never sees stacking disorder in stable QC, which could be observed as diffuse streaks parallel to the periodic axis. Diffuse scattering is exclusively within the layers perpendicular to this axis. Consequently, decagonal QC could rather be seen as packings of columnar clusters.

Decagonal quasicrystals with six-layer periodicity show icosahedral pseudosymmetry. This means, they are more closely related to icosahedral quasicrystals than those with other periodicities.

8.3.1 Two-Layer and Four-Layer Periodicity

The stable decagonal quasicrystals with a period of two or four atomic layers along the tenfold axis as well as some of their approximants are listed in Table 8.4. There is a close structural relationship between the different modifications of decagonal Al-based phases including their approximants. This will be discussed with reference to selected models of d-Al–Co–Cu and d-Al–Co–Ni in the following section.

We want to recall here that by 'cluster' we mean just structural building units without implying any crystal-chemically relevant properties that are different from their environment. It is rather assumed, that the clusters used here are ensembles of crystal-chemically favorable local AET in a preferred constellation to each other. When two clusters overlap, most atomic positions that are favored by the two contributing clusters do match. If two atomic positions do not coincide, they will generate split positions, corresponding to phason flips in the nD description. Both generated positions are crystal-chemically equivalent, as they belong to both clusters at the same time.

Table 8.4. Stable decagonal quasicrystals with two- or four-layer period and some of their approximants (listed below the line). The pseudodecagonal axis is underlined (SG... space group, PS... Pearson symbol)

Nominal composition	Layers/period	Lattice parameters (Å)	SG/PS	References
$Zn_{58}Mg_{40}Dy_2$	2			[90]
$Zn_{58}Mg_{40}RE_2$	2			[91]
(RE = Dy, Er, Ho, Lu, Tm, Y)				
$Al_{70+x}Ni_{15+y}Co_{15+z}{}^a$	2 or 4			[99, 107]
$Al_{70}Ni_{15}Fe_{15}$	2 or 4			[107]
$Al_{65}Cu_{15}Rh_{20}$	2 or 4 or 6			[109]
$Al_{70}Ni_{20}Rh_{10}$	2 or 4			[111]
$Al_{65}Cu_{20}Co_{15}$	4			[46, 102]
$Al_{65}Cu_{20}Ir_{15}$				[4]
Co_4Al_{11}	2	$a = 24.661(5)$	$P2$	[73]
$\quad Al_{73.2}Co_{26.8}$		$\underline{b = 4.056(9)}$	$mP52$	
		$c = 7.569(2)$		
		$\beta = 107.88(3)°$		
$(Co_{1-y},Ni_y)_4Al_{13-x}$	2	$a = 17.071(2)$	$C2/m$	[126]
$\quad Al_{75.2}(Co,Ni)_{24.8}$		$\underline{b = 4.0993(6)}$	$mC34\text{-}1.8$	
		$c = 7.4910(9)$		
		$\beta = 116.17(1)°$		
Co_2Al_5	4	$a = 7.6717(4)$	$P6_3/mmc$	[15]
$\quad Al_{71.5}Co_{28.5}$		$c = 7.6052(5)$	$hP28$	
$Co_4(Al,Cu)_{13}$	4	$\underline{a = 15.2215(4)}$	Cm	[33]
$\quad Al_{71.5}Co_{23.6}Cu_{4.9}$		$b = 8.0849(2)$	$mC102$	
		$c = 12.3908(3)$		
		$\beta = 108.081(1)°$		
Co_4Al_{13}	4	$a = 8.158(1)$	$Pmn2_1$	[37]
$\quad Al_{76}Co_{24}$		$\underline{b = 12.342(1)}$	$oP102$	
		$c = 14.452(2)$		
Co_2NiAl_9	6	$a = 12.0646(7)$	$Immm$	[36]
$\quad Al_{74.8}Co_{17.0}Ni_{8.2}$		$\underline{b = 7.5553(7)}$	$oI96$	
		$c = 15.353(1)$		
$Co_{21.1}Ni_{7.1}Al_{71.8}$	4	$a = 39.668(3)$	Cm	[44, 103]
$\quad Al_{71.8}Co_{21.1}Ni_{7.1}$		$b = 8.158(1)$	$mC530$	
		$\underline{c = 23.392(1)}$		
		$\beta = 90.05(1)°$		

^{a} Broad stability range with eight quasiperiodic modifications

This feature is of importance for the understanding and development of growth models, more specifically for the geometrical aspects that can lead to quasiperiodicity. Two overlapping clusters are the geometrical equivalent of one cluster, that already contains in itself a part of the next neighboring
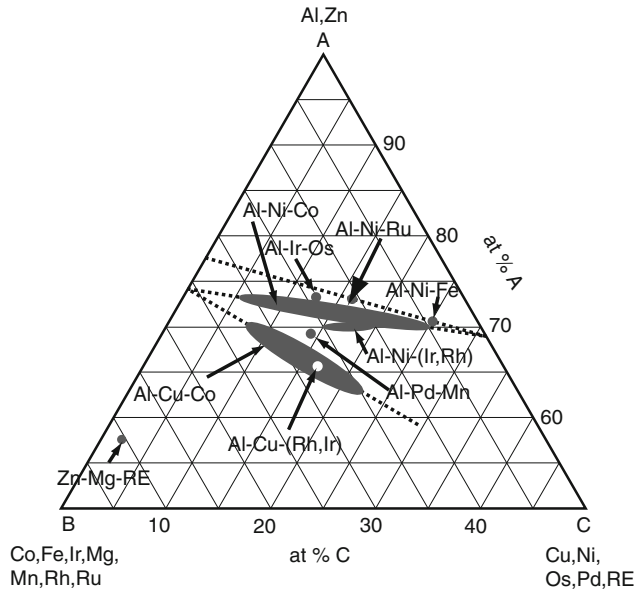
Fig. 8.5. Stability regions of decagonal quasicrystals. RE denotes the rare earth metals Y, Dy, Ho, Er, Tm, Lu in case of d-Zn–Mg–RE. Note that only the A-rich parts ($50 \leqslant A \leqslant 100$ at.%) of the concentration diagrams are shown (based on [42])

cluster. By having one cluster, we therefore have also the germ from which the next cluster can grow. Besides this ansatz for the development of a growth model, we will not go into this field as it is beyond the scope of this book. Here, we will focus on the geometrical aspects of the models for Al-based decagonal QC with four-layer periodicity.

In Fig. 8.6, we illustrate how structure models can be derived for the d-phases in the systems Al–Co–Ni, Al–Co–Cu, and Al–Fe–Ni. They are built by decorating particular tilings with clusters of diameter ≈ 20 Å and symmetry $\overline{10}2m$. Two different clusters (cluster 1 and 2) are needed as building units in all cases but two, the approximant τ^2-Al$_{13}$Co$_4$ [88, 89] and d-Al$_{64}$Co$_{14}$Cu$_{22}$ [106]. Their structures are drawn in gray (online: red) boxes in Fig. 8.6.

All clusters have a four-layer structure with ≈ 8 Å periodicity. The periodic direction is oriented along the 10-fold axis (z-direction). The layers are denoted A ($z = 0$), B ($z = 1/4$), C ($z = 1/2$), and D ($z = 3/4$) Fig. 8.6. Layers A and C are flat (all atoms have the same z-coordinates) and lie on mirror planes. Layers B and D are puckered (atoms have different z-coordinates) and are related to each other by the mirror planes at $z = 0$ (A) and $z = 1/2$ (C). This means, that the structures of B and D are equal if projected along the periodic direction. Therefore, only the structure of layer B is depicted in Fig. 8.6.

The differences in the structures of layers A and C are small in every case and affect only a part of the Al positions. For most of the phases, the
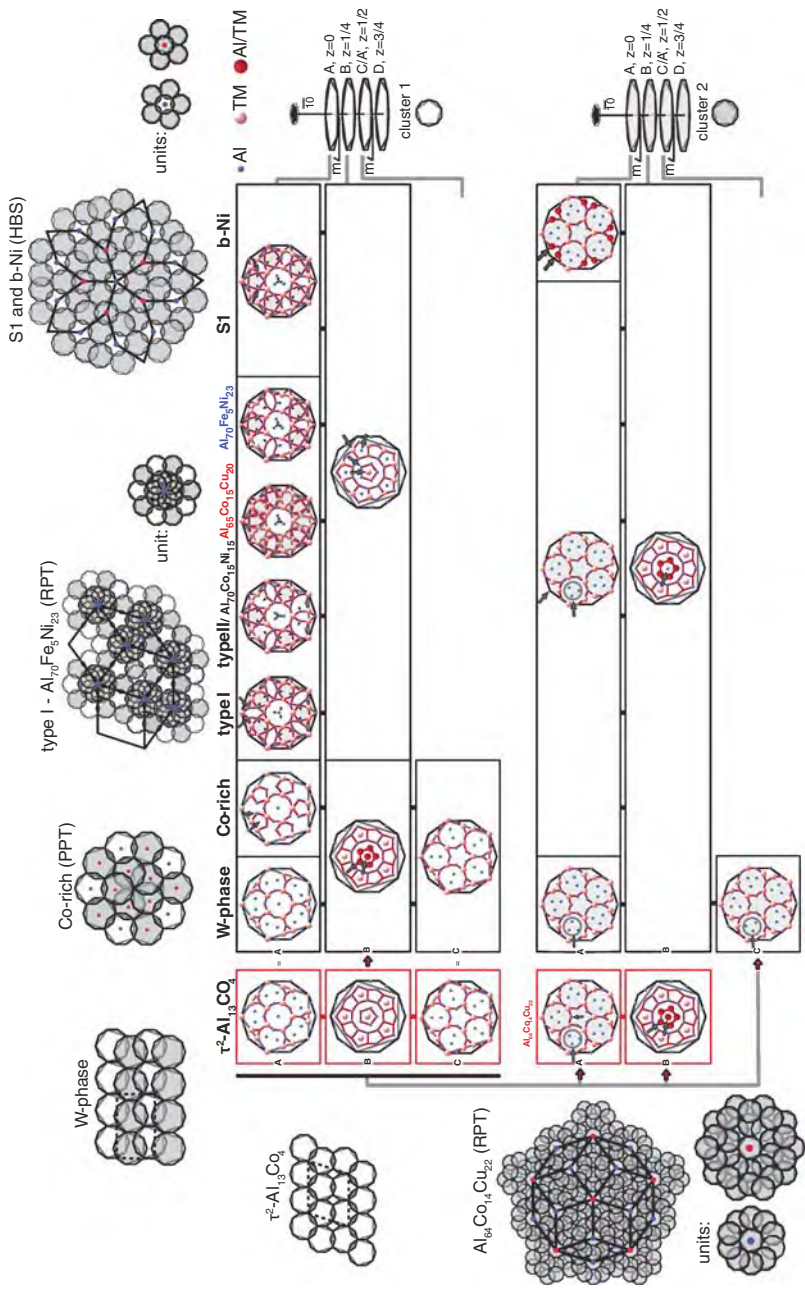
Fig. 8.6. Derivation chart of the models for the systems Al–Co–Ni (*black fonts*), Al–Co–Cu (online: *red fonts*), and Al–Fe–Ni (online: *blue fonts*). The atomic decoration of each cluster-layer is given, as well as the underlying tilings (*see text for details*)

experimental resolution does not allow to identify them. Then, we denote C = A′, and only layer A is given. For the Co-rich phase, layer C in cluster 1 is derived from the structure of the W-phase. For cluster 2 of the d-phases it is assumed that layer C shows the same structure as layer A. The fivefold symmetry of cluster 1 ($\overline{10} = 5/m$) can be broken in some cases by the preferred occupancy of split positions in layer A. In these cases, five different orientations of cluster 1 can be distinguished within the structure.

The structure of the W-phase shows a shift of $1/2$ in z-direction of neighboring clusters. Therefore, each layer perpendicular to the z-direction contains A and C, or B and D of different clusters. We assume that such shifts are also essential in the decagonal phases. However, we will not include shifts of clusters along the periodic direction or accurate z-coordinates of the puckered layers in the modeling. As can be seen in Fig. 8.6, several phases have layers of clusters in common. The most prominent example is layer B of cluster 2 that has the same structure for every two-cluster-phase. Figure 8.6 can also be read as a derivation chart of the models, as the small structural changes interconnecting the different phases are denoted with arrows in each layer. The cluster of τ^2-Al$_{13}$Co$_4$, the only binary phase here, is derived from the W-phase and used as a starting point. We refer to this cluster as the fundamental cluster.

The tilings underlying the model structures are also given in Fig. 8.6 for all phases. In every case, except for the approximants and the Co-rich phase, superclusters can be defined (referred to as 'units' in the figure). The tilings are either rhomb PT or HBS tilings that can be decorated with the superclusters. The Co-rich phase results from decorating a pentagon PT with clusters 1 and 2. Of course, all tilings refer to idealized, averaged structures obtained from electron density maps based on single crystal XRD. HAADF-STEM (Z-contrast) images give access to their local structures, i.e. the projected clusters and their local arrangements. The data suggest that the structures are not strictly quasiperiodic, but show some random fluctuations.

8.3.1.1 *d*-Al–Co–Cu

In 1988, the first stable decagonal phase was discovered in a sample with a composition Al$_{65}$Co$_{15}$Cu$_{20}$ [46]. Of the identified *d*-phases with two-, four-, six-, and eight-layer periodicities, only the one with four-layer periodicity was later proved to be stable [38–41, 108]. The mass density of d-Al$_{62}$Co$_{20}$Cu$_{15}$Si$_3$ ($a_{1-4} = 3.776(8), a_5 = 4.1441(5)$ Å) has been determined to $\rho_m = 4.53(3)$ Mgm^{-3} [63]. The d-phase as well as the monoclinic approximant m-(Al,Cu)$_{13}$Co$_4$ and the τ-phases lie on the connecting line between Al$_3$Co and the vacancy-ordered phase AlCu.

The first quantitative single-crystal X-ray structure analysis of the *d*-phase in the system Al–Co–Cu was performed on *d*-Al$_{65}$Co$_{15}$Cu$_{20}$ [102]. The structure was solved by the 5D Patterson method, 11 parameters were refined against 259 reflections to $R = 0.098$ in the 5D space group $P10_5/mmc$. The

structure was discussed in terms of pentagon tilings, one of the TM atoms with 4.7 Å edge length and another one of Al atoms with 2.9 Å edge length. The close resemblance to m-$Al_{13}Co_4$ was pointed out.

A ternary model of d-$Al_{64.8}Co_{19.6}Cu_{15.6}$, an HBS-tiling (edge length ≈ 6.38 Å) decorated with pentagonal 11-atom clusters, all in the same orientation in a given layer, was studied by total energy calculations [22]. The formation of Co–Cu zigzag chains (corresponding to a matching rule) was energetically more favorable than Co–Co or Cu–Cu chains. Remarkably, some Cu atoms and off-plane atoms in the tile interior as well as the cluster position along the z-direction exhibited fluctuations down to very low temperatures <100 K. A further study based on these results employed tile Hamiltonians with effective interactions between and within tiles [3]. The preferred Co-Cu interaction was confirmed. It was also shown that pure HB-tilings are lower in energy than HBS-tilings. At 1,000 K, 72° angle interactions (i.e. tile edges meet in a vertex withy 72° angle) are dominant compared to 144° ones.

Example: Structure Model of d-$Al_{64}Co_{14}Cu_{22}$

According to its electron micrographs, d-$Al_{64}Co_{14}Cu_{22}$ [106] is the only d-phase in the investigated systems that can be modeled by just one cluster type. Although SAED patterns indicate the existence of a disordered four-layer period, we present here only the two layer model of the basic structure [27]. The electron micrographs used for modeling do not contain enough information for identifying the disordered four-layer superstructure. The structures of the layers and their projection along the periodic direction are shown in Fig. 8.7.
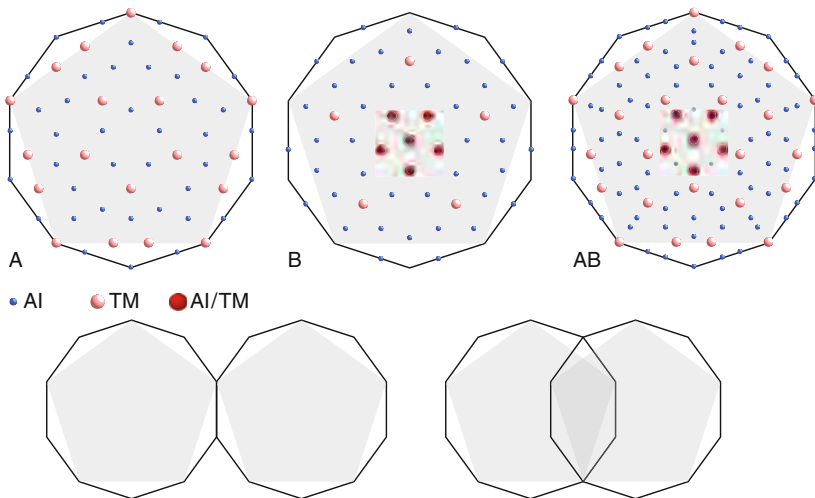
Fig. 8.7. Structure of the basic cluster of d-$Al_{64}Co_{14}Cu_{22}$. Layers A, B and their projection along the periodic direction are shown. The *lower* part of the figure shows the allowed arrangements of two clusters

Layer A of the cluster corresponds to layer A of cluster 2 in the phases with structure type from Co-rich to S1 (Fig. 8.6). Layer B shows additional mixed occupation of Al and TM in the center, and therefore corresponds to the layer B of cluster 1 in the Co-rich phase. For an overview of the structure of d-Al$_{64}$Co$_{14}$Cu$_{22}$ compared to the other phases, see Fig. 8.6.

An important feature of the model is that all the clusters have the same orientation in the structure. There is only one permitted way of overlapping (Fig. 8.7), which is the same as the one between clusters of the same kind in the phases from type Co-rich to AlFeNi (Fig. 8.6). The overlap region of the two clusters is of hexagonal shape. One cluster can overlap with maximal three clusters (see Fig. 8.9 or 8.10). The other allowed cluster configuration is realized when two of them have one decagon edge in common.

In Fig. 8.8, the ideal structures are shown of two overlapping clusters. Within the overlap region, one can see what split positions and chemically mixed sites are created. On the right side of the figure, only the overlap region of the clusters is shown, where all split positions were eliminated in favor of an idealized structure, which will be used from now on.

There are two superclusters needed for the decoration of the tiling. In Fig. 8.9, one of them is shown in projection along the periodic direction. The second supercluster is a subset of the first and consists of the cluster in the center, surrounded by ten more clusters. Those clusters have each one edge in common with the central cluster, and each one of them overlaps with two of its neighbors. Figure 8.10 shows a pentagon PT decorated with the superclusters. Dark-gray (online: red) vertices of the tiling are decorated with the large supercluster, light-gray (online: yellow) with the smaller one.

Figure 8.11 shows an C_s-corrected HAADF-STEM image [106] of d-Al$_{64}$Co$_{14}$ Cu$_{22}$ in comparison with the model. Since the resolution of the image is very high, even the Al positions of the model can be compared with the experimental data.
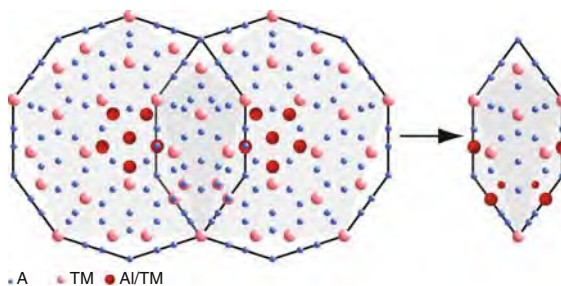
Fig. 8.8. The overlap of two clusters is shown in projection along the periodic direction. At *left*, we see the generated split positions and introduced chemical disorder. At *right*, the overlap region is shown with the preferred occupation of split positions in the structure
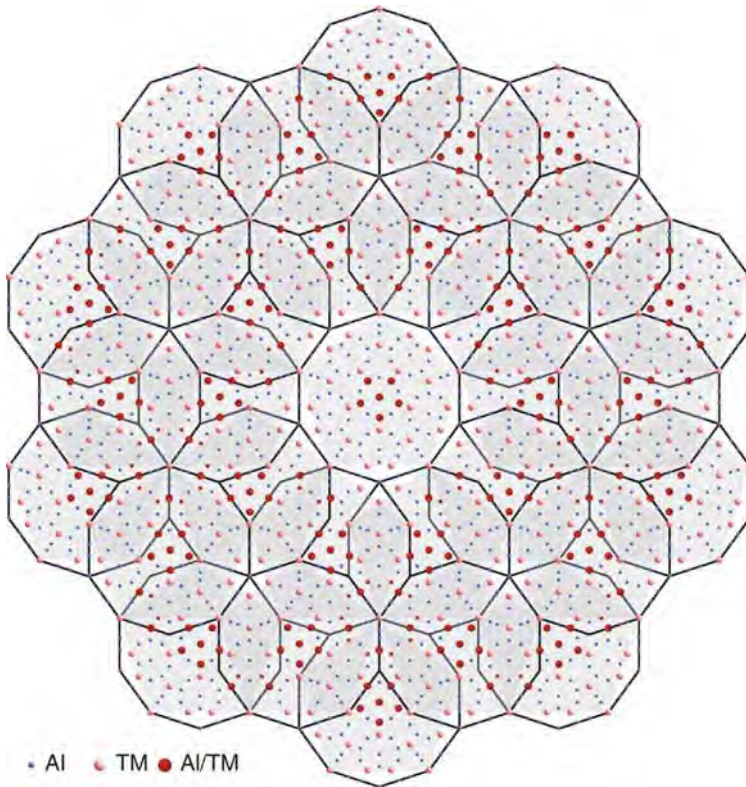
Fig. 8.9. A supercluster of d-Al$_{64}$Co$_{14}$Cu$_{22}$ is shown in projection along the periodic direction. It consists of 31 clusters which have only one allowed orientation and one kind of overlap. A second supercluster is needed for the decoration of the rhomb PT shown in Fig. 8.10. It is a subset of the cluster shown here, and consists of the cluster in the center and the ten neighboring clusters. They have each one decagon edge in common with the cluster in the center

Example: Structure Model of d-Al–Co–Ni

The system Al–Co–Ni, its d-phases and approximants have been in the focus of decagonal QC research of the last 20 years. It is an excellent model system: the phase diagram is quite well known (Fig. 8.12); large and rather perfect single crystals can be easily (and cheaply) grown; several ordering variants (modifications) of the decagonal phase have been found as a function of temperature and/or composition; the full power of electron-microscopic and surface-imaging methods can be used due to the short translation period (2–4 atomic layers) along the tenfold axis.

In the Co-rich corner of the stability region of d-Al–Co–Ni, a 'basic Co-rich' pentagonal phase ('5f') with a HT and an LT modification was found. Increasing the Ni-content, at HT a 1D quasiperiodic phase was identified, at LT an approximant; at even higher Ni concentrations, two LT modifications
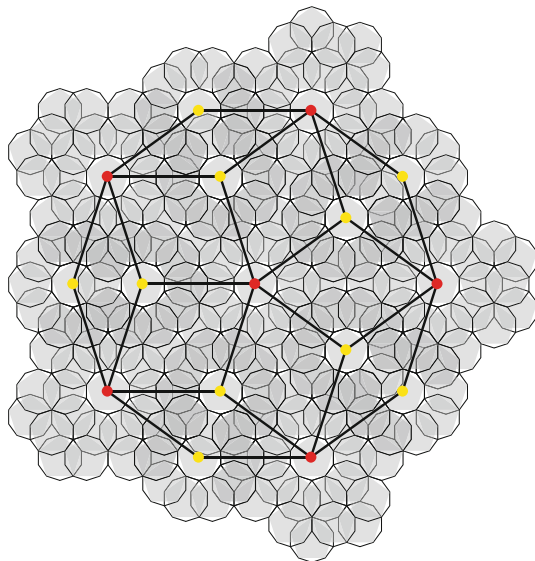
Fig. 8.10. Rhomb PT decorated with the two types of superclusters. *Yellow/red* vertices are decorated with the small/large supercluster
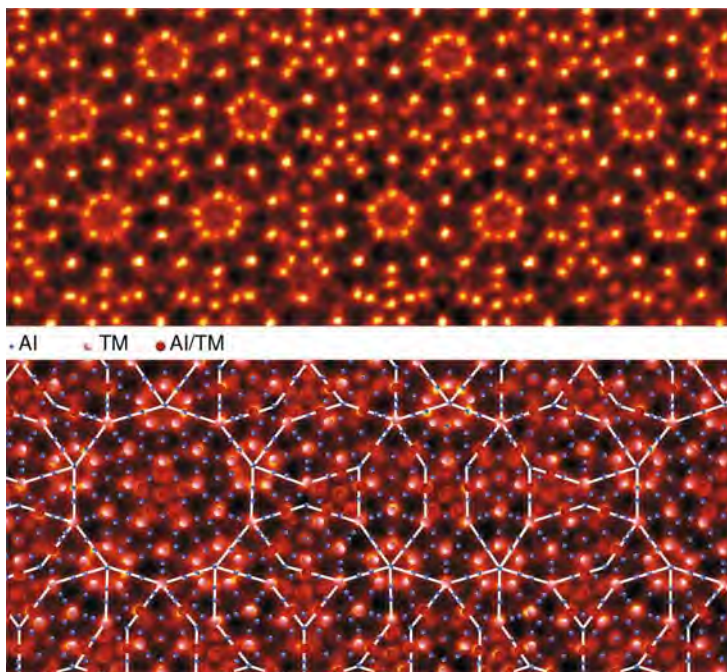
Fig. 8.11. C_s-corrected HAADF-STEM image of d-$Al_{64}Co_{14}Cu_{22}$ [106] shown without and with overlaid structure model. This high-resolution image even allows to verify most of the Al-sites in the model additionally to the TM sites
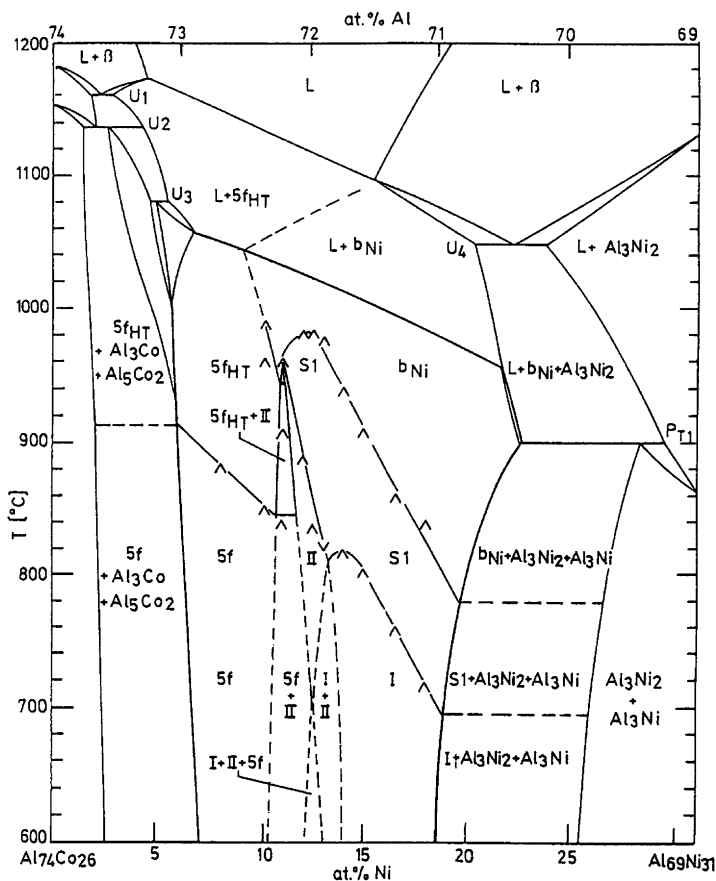
Fig. 8.12. Temperature concentration section $Al_{74}Co_{26}$–$Al_{69}Ni_{31}$. The transformations within the d-phase are determined by dilatometric measurements. The phase diagram is delineated assuming second-order transformations between the d-phase modifications (from [75]). $5f$ basic Co-rich pentagonal phase with HT and LT modification I, II superstructures type I, II, $S1$ superstructure type I with only first-order superstructure reflections, b_{Ni} ... basic Ni-rich d-phase

('superstructure type I' and 'S1') and a HT decagonal phase ('basic Ni-rich') were discovered.

It is still not fully clear whether all these modifications are stable and how large the stability ranges of the stable phases are, in particular at low temperatures ($T < 500°C$). There is some experimental evidence that the 'superstructure type II' is a metastable, orientationally five-fold twinned nanodomain state [28], for instance, and the superstructure S1 may be just an intermediate HT state of the superstructure type I (second-order satellites usually disappear faster with temperature then first order ones). The reciprocal basis of the superstructure type I is related to that of the 'basic Ni-rich'

d-phase by rotoscaling (rotation by $\pi/10$ and scaling by a factor $\sqrt{3-\tau}$). The determinant of the transformation matrix equals five. The d-phases in the binary boundary systems Al–Co and Al–Ni are metastable.

The structure of the basic Ni-rich phase, with two-layer period, can be described by a somewhat disordered cluster decorating a highly perfect pentagonal Penrose tiling. In the superstructures of types I and II, the pentagonal clusters are ordered anti-parallel along the $\approx 20\,\text{Å}$ linkages. The basic Co-rich phase is seen to be more related to the superstructures than to the basic Ni-rich phase. The structure contains domains of equally oriented pentagonal clusters. The pentagonal phase is characterized by a parallel orientation of all pentagonal clusters. The 1D quasicrystal, with periods $\approx 30.7\,\text{Å}$ and $\approx 4.1\,\text{Å}$, also contains the pentagonal clusters in parallel orientation.

Several quantitative single-crystal X-ray diffraction structure analyses of the basic Ni-rich modification have been performed so far (see, e.g., [19, 105] and references therein). As example, the projected electron density function of d-$Al_{70.6}Co_{6.7}Ni_{22.7}$ is shown in Fig. 8.13 in comparison with a HAADF (Z-contrast) image.

In the following, structure models of some of the different modifications are discussed (for a more detailed discussion see [27]). In Fig. 8.14 the structure of the W-phase is shown, with clusters 1 and 2 drawn in (cluster 1 with an empty pentagon inside, cluster 2 with a filled gray pentagon). Neighboring clusters
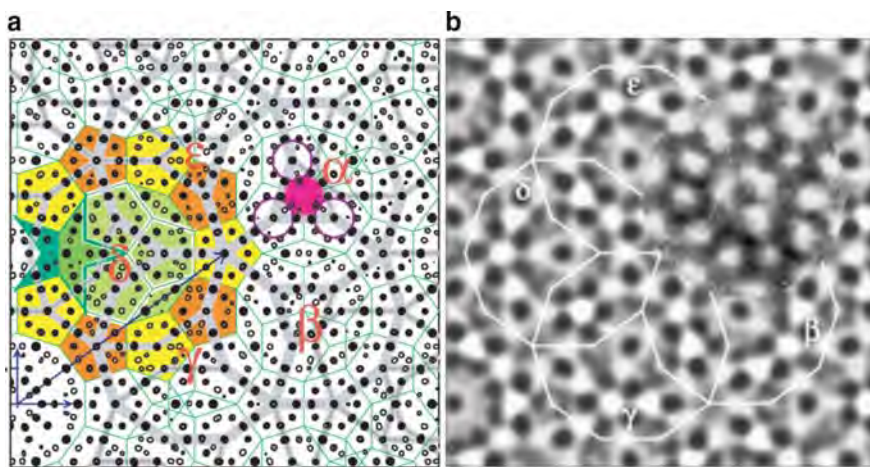
Fig. 8.13. (**a**) The projected electron density of d-$Al_{70.6}Co_{6.7}Ni_{22.7}$ is shown in a $45\,\text{Å} \times 45\,\text{Å}$ contour plot. A pentagonal Penrose tiling is drawn in (online: *green lines*) (edge length $a_r = 4.625\,\text{Å}$). A group of five Gummelt decagonal clusters with $20.600\,\text{Å}$ diameters is labeled by *Greek letters*. The centers of the Gummelt decagons are located on a τ^2-inflated version of the pentagon tiling. (**b**) The projected electron density on a resolution comparable to that of the HAADF image (from [1]) copied upon the place of Gummelt decagon α. *Black* corresponds to zero density, *white* to maximum density
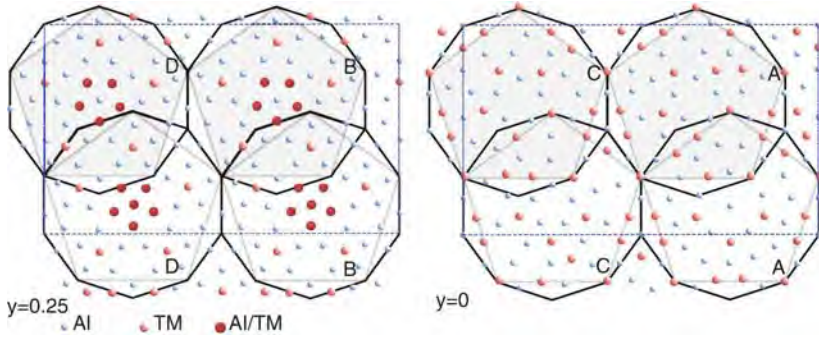
Fig. 8.14. Structure model of the W-phase, a monoclinic approximant to d-Al–Co–Ni. Cluster 1 is drawn with an empty pentagon inside, cluster 2 with a gray-shaded pentagon. Two layers of the W-phase are shown, at $y = 0$ layers A and C and at $y = 1/4$ layers B and D. This is due to the $1/2$ **b** shift of neighboring clusters
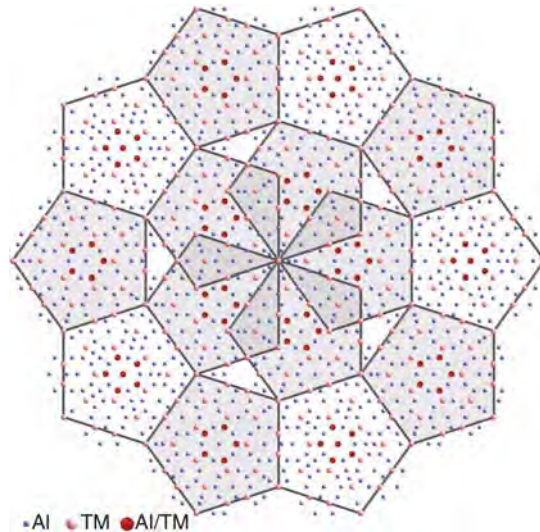
Fig. 8.15. Structure model of Co-rich d-Al–Co–Ni. Cluster 1 is denoted by a non-shaded pentagon, cluster 2 by a *shaded* pentagon. The decagonal borders of the clusters are not shown here. All clusters of one kind have the same orientation. Clusters 1 and 2 are in *anti*-orientation to each other

are shifted by $1/2$ **b**. The notation of the axes follows here the monoclinic setting of the W-phase (space group Cm, lattice parameters $a = 39.668$ Å, $b = 8.158$ Å, $c = 23.392$ Å, and $\beta = 90.1°$). Therefore, the y-direction corresponds to the periodic direction of the decagonal phases, and is referred to as z-direction in Sect. 8.3.1.1.

A part of the structure model of the Co-rich phase is shown in Fig. 8.15. Clusters 1 and 2 are marked by white and gray-shaded pentagons. The

decagonal borders of the clusters are not drawn in (compare Fig. 8.18). Two clusters of the same kind can have one pentagon corner in common, while the pentagon edges form a straight line. Clusters 1 and 2 can coincide on one edge of the pentagons and have a very small overlap region. One can see how the local structure of the clusters changes within an overlapping region.

All clusters of the same kind have the same orientation. Clusters 1 and 2 are in *anti*-orientation to each other. Most related *d*-phases show this structural feature. Exceptions are the S1 and basic-Ni phase (see tilings in Fig. 8.6). *d*-$Al_{64}Co_{14}Cu_{22}$ is single clustered and shows only one cluster orientation.

An important difference of the W-phase lies in the orientation of the clusters. In contrast to the Co-rich *d*-phase, clusters of different kind have the same orientation in the W-phase. While in the Co-rich d-phase only overlaps of clusters of the same kind are allowed, in the W-phase overlaps are allowed only between clusters of different kind. One can see in this example, how different overlapping rules can result in a periodic, or in a quasiperiodic arrangement of clusters. The overlaps in the W-phase seem to distort the ideal cluster structure more than that in the Co-rich *d*-phase (compare Figs. 8.14 and 8.18). Structural and chemical disorder certainly contributes significantly to the stabilization of the periodic arrangement of the clusters in the W-phase, which is a HT phase. All ideal atomic positions in a cluster can be derived in accordance with its decagrammal symmetry. This is demonstrated in Fig. 8.16 for the clusters of the type I phase.

Layers A and B are shown for both kinds of clusters. All atoms lie in intersecting points within a certain decagram, or between two decagrams. Some Al atoms lie on decagrams in scaled decagons on the borders of the clusters (layer B, cluster 1, and both layers cluster 2). In this case, the construction of the ideal positions is only shown for one of the scaled decagons (drawn in yellow in Fig. 8.16). The rest of the construction is symmetrically related to the one that is given in the figure.

The *d*-phases of type I, type II ($Al_{70}Co_{15}Ni_{15}$), $Al_{65}Co_{15}Cu_{20}$, $Al_{72}Fe_5Ni_{23}$, S1, and basic-Ni are closely related to each other in their cluster structures (see overview in Fig. 8.6). With the exception of the S1 and basic-Ni phase, they also have in common the tiling underlying their average structure. This can be seen in the electron density maps obtained by single crystal XRD. A characteristic difference between those phases can be found in their preferred occupation of radial split positions in layer A, cluster 1 (see Fig. 8.17).

There are two possible occupations of the split positions in the structures which maintain the fivefold symmetry of cluster 1. They correspond to the preferred occupations in the *d*-phases of type I and S1/basic-Ni. These two configurations are connected by a flip of all involved atoms. If only a subset of the atoms occupies different split positions, the symmetry of the clusters is broken. These clusters can occur in five different orientations in the structure, and build superstructures. For comparison with experiment, see Fig. 8.19 for the type I d-phase, and Fig. 8.20 for the type II *d*-phase. One of these clusters
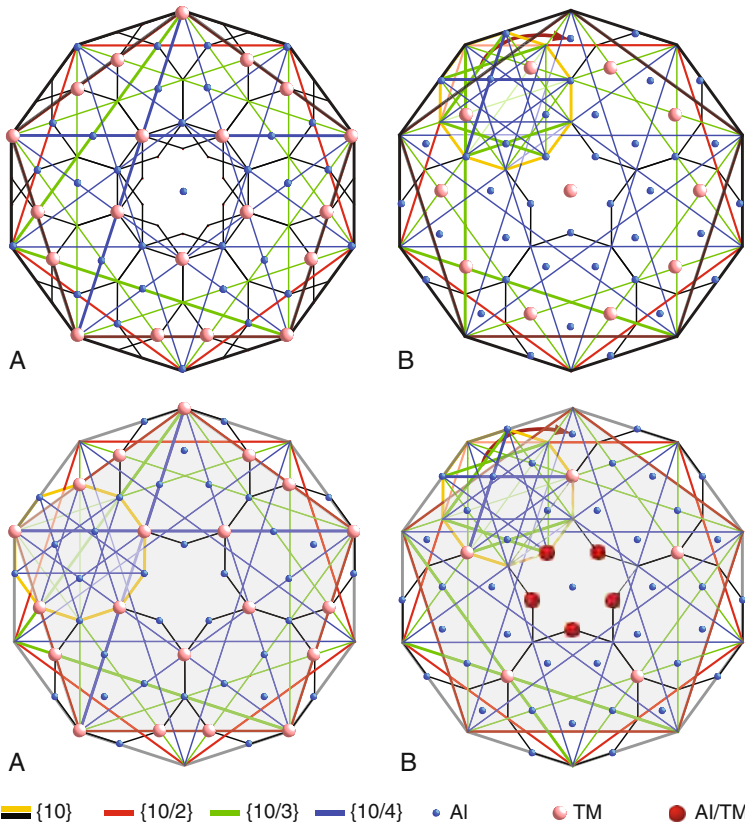
Fig. 8.16. Clusters of the type I phase of *d*-Al-Co-Ni. Clusters 1 and 2 are denoted with *white* and *gray filled pentagons*. Layers A and B are given in both cases. All ideal atomic positions can be derived as intersections of decagrams within the clusters. The *Schläfli symbols* of the decagrams are given at the *bottom* of the figure with the corresponding *color* of the decagrams

is denoted in red in each figure. The five different orientations of the clusters can also be seen where the fivefold symmetry is broken.

In the following, the model structures are compared with experimental data. In the upper part of Fig. 8.18, the local arrangement of clusters in Co-rich *d*-Al-Co-Ni is shown. It does not correspond to an ideal quasiperiodic tiling, but rather to an arrangement based on crystal-chemically favorable AET resulting from allowed overlaps. Experimentally caused distortions of the image are taken into account in the overlaid model. One sees how the small pentagons are generated by atoms at the cluster borders in one of their possible arrangements. The regions of the structure which cannot be explained with the usual cluster [103] correspond to a cluster, the neighbors of which are not overlapping in the immediate region of this cluster, and to a center where five clusters coincide. Both regions are indicated by (online: red) stars in the upper part of
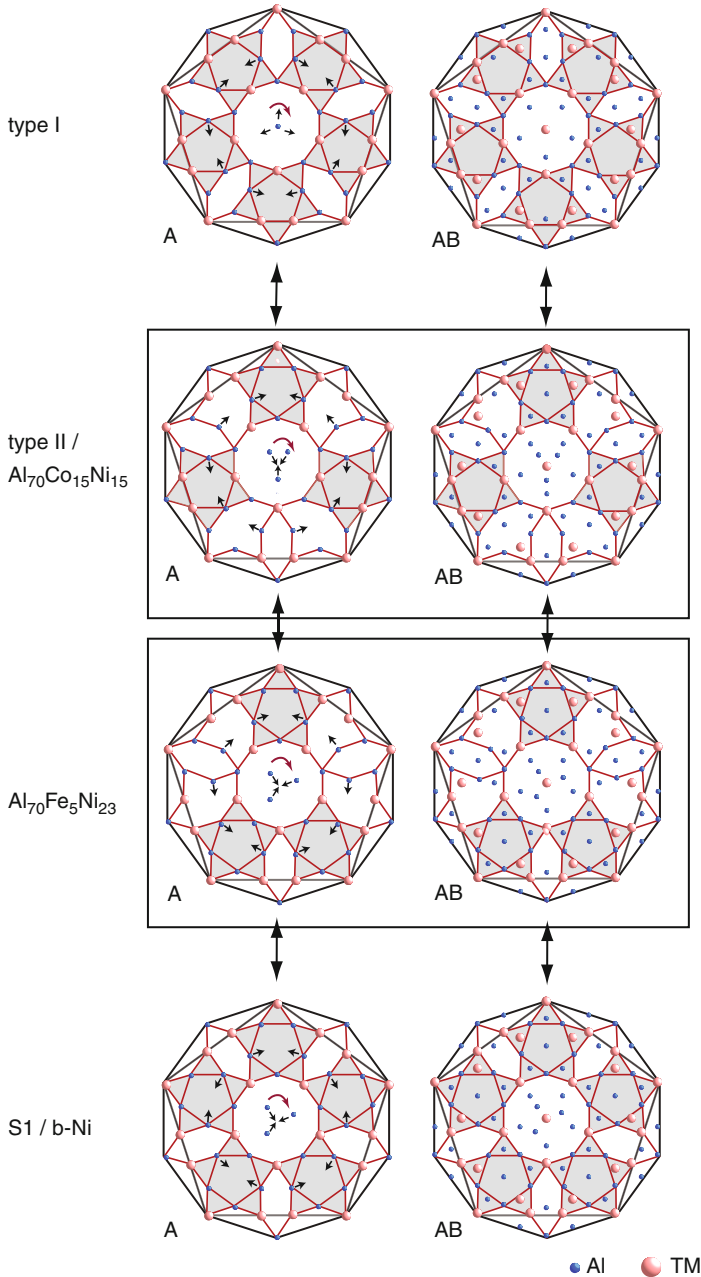
Fig. 8.17. Occupancy of radial split positions in layer A, cluster 1 of the *d*-phases of type I, type II ($Al_{70}Co_{15}Ni_{15}$), $Al_{72}Fe_5Ni_{23}$, S1, and basic-Ni. Split positions are denoted with small *black arrows* in the A layers of each cluster. The atomic decorations correspond to the preferred (not an absolute) occupation in the phases. We can see symmetry breaking in the clusters framed by the *black boxes*. The projection (AB) of each cluster is shown in the *lower part* of the figure
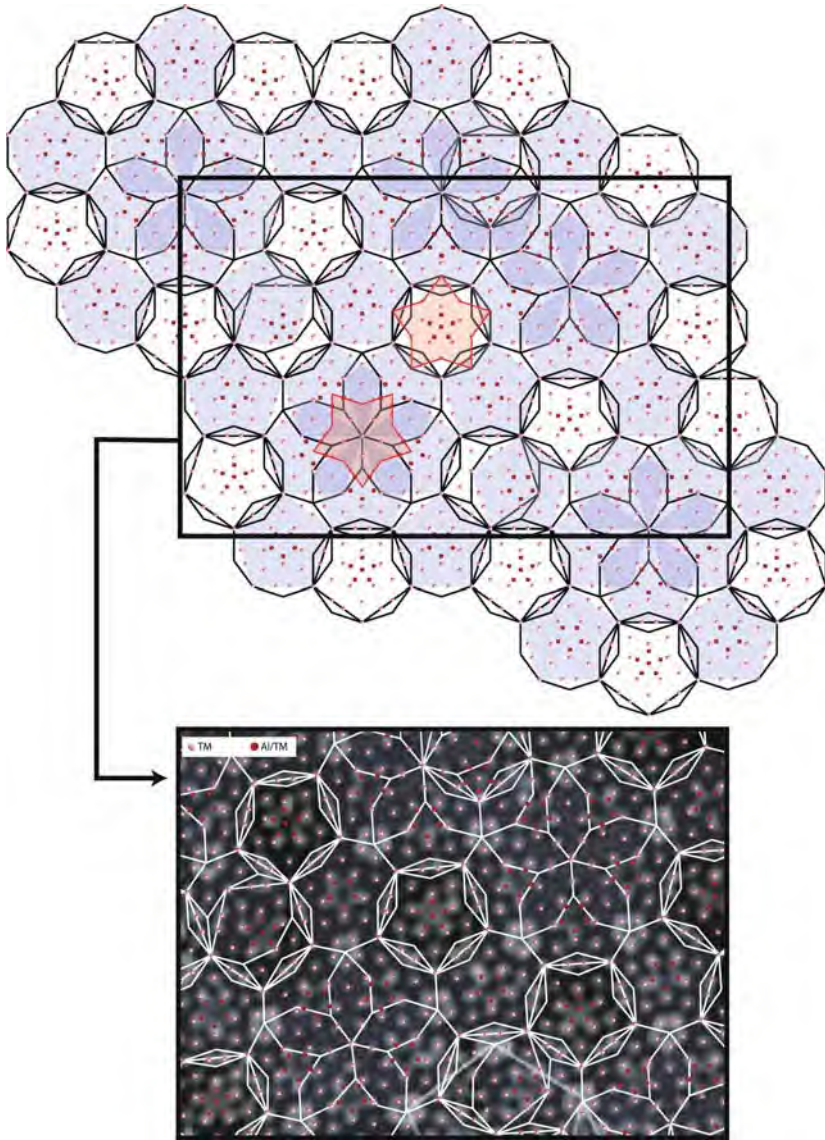
Fig. 8.18. In the *upper part* of the figure, a local arrangement of clusters in Co-rich *d*-Al–Co–Ni is depicted. In the *lower part*, the structure model is compared to a HAADF-STEM image [50]. One sees how the small pentagons (black dots, online: pink dots) are generated by the atoms at the cluster borders in one of their possible arrangements

Fig. 8.18. The (online: red) stars have opposite orientation and correspond to the two structural motives that cannot be generated with the usual cluster. Each structure motif appears only in one orientation within the structure.
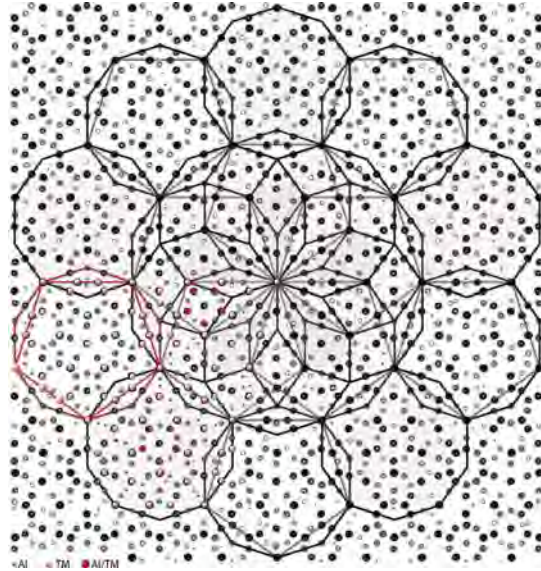
Fig. 8.19. Projected electron density map of the type I phase obtained from single crystal XRD [30] with structure model superimposed. Clusters 1 and 2 are drawn with *white* and *gray shaded* pentagons
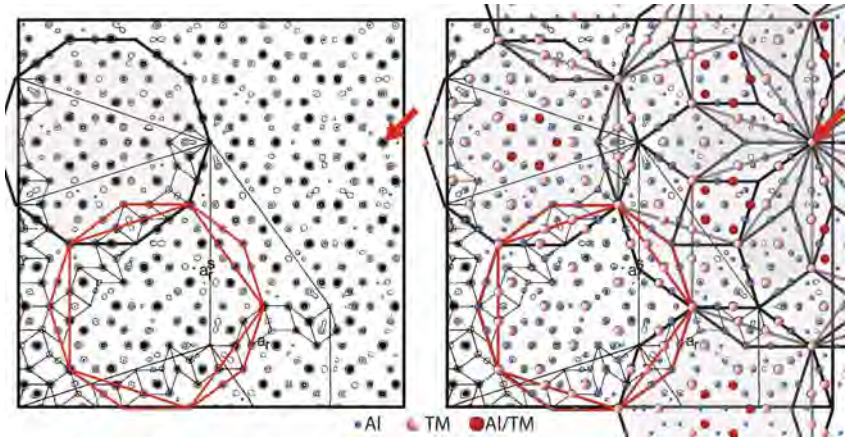
Fig. 8.20. Projected electron density map of the type II phase [100] without and with overlaid structure model. Clusters 1 and 2 are drawn with *empty* and *gray shaded   pentagons*. The black (online: red)   *arrow* on the right denotes the center of the supercluster. One cluster of type 1 is highlighted in gray (online: *red*)

Figure 8.19 shows an electron density map of the type I phase obtained from single crystal XRD [30] in projection along the periodic direction.

Similarly, the electron density map of the type II phase and the comparison with the model is shown in Fig. 8.20. One supercluster is plotted and

compared to experiment. The preferred occupation of Al-split positions previously discussed is visible. Here, we compare with a cluster for which we decided on the preferred occupation of split positions in general, to get the best agreement for an idealized model. However, all split positions visible in the electron density map are generated through overlaps between clusters. They can be explained (and predicted) within the model, as atomic positions which are most favorable for the participating clusters.

8.3.2 Six-Layer Periodicity

The first decagonal phase identified as such was metastable d-Al–Mn with six-layer periodicity along the ten-fold axis. d-Al–Mn can be stabilized by substituting mainly Al by Pd (Table 8.5). Close to the composition of d-Al–Mn, several stable approximants are known (Table 8.5). These are $Al_{11}Mn_4$ (a rational 3/2-approximant according to [127]), hexagonal μ-$MnAl_{4.12}$ [96] and λ-Al_4Mn [66], and orthorhombic Y–Al_3Mn [83, 95]. The structure of Y–Al_3Mn can be seen as a squashed-hexagon (H) tiling decorated with edge-sharing pentagons. Each pentagon is filled with a pentagonal columnar cluster.

The only stable decagonal phase with six-layer period studied so far in several semi-quantitative structure analyses is d-Al–Mn–Pd. We present one of the structure models for d-$Al_{70.5}Mn_{16.5}Pd_{13}$ [101] (Fig. 8.21). It can be described as periodic stacking of two different quasiperiodic layers A (puckered ± 0.3 Å) and B (flat) with sequence ABAaba (a, b correspond to layers A, B rotated by $\pi/5$). In terms of the physically more reasonable cluster model, it can be described by ≈ 20 Å columnar clusters decorating the vertices of a disordered Robinson triangle tiling. From the similarities in the respective projected 3D Patterson functions of the d-phase and Al_3Mn [47], the similarity of their projected local structures (at least for interatomic distances <12 Å) can be concluded.

Table 8.5. Stable decagonal quasicrystals with six-layer period and some of their approximants (listed below the line). The pseudodecagonal axis is underlined (SG space group, PS Pearson symbol)

Nominal composition	Lattice parameters (Å)	SG/PS	References
$Al_{70.5}Mn_{16.5}Pd_{13}$	$a_{1-4} = 3.891(1)$ $a_5 = 12.557(4)$	$P10_5/mmc$	[9, 101]
$Al_{40}Mn_{25}Fe_{15}Ge_{20}$			[121]
$Ga_{33}Fe_{46}Cu_3Si_{18}$			[34]
$Ga_{43}Co_{47}Cu_{10}$			[34]
$Ga_{35}V_{45}Ni_6Si_{14}$			[34]
$Al_{75}Mn_{20}Pd_5$ (Al$_3$Mn-type)	$a = 14.727(3)$ $b = 12.509(3)$ $c = 12.600(3)$	$Pnma$ $oP156$	[78]
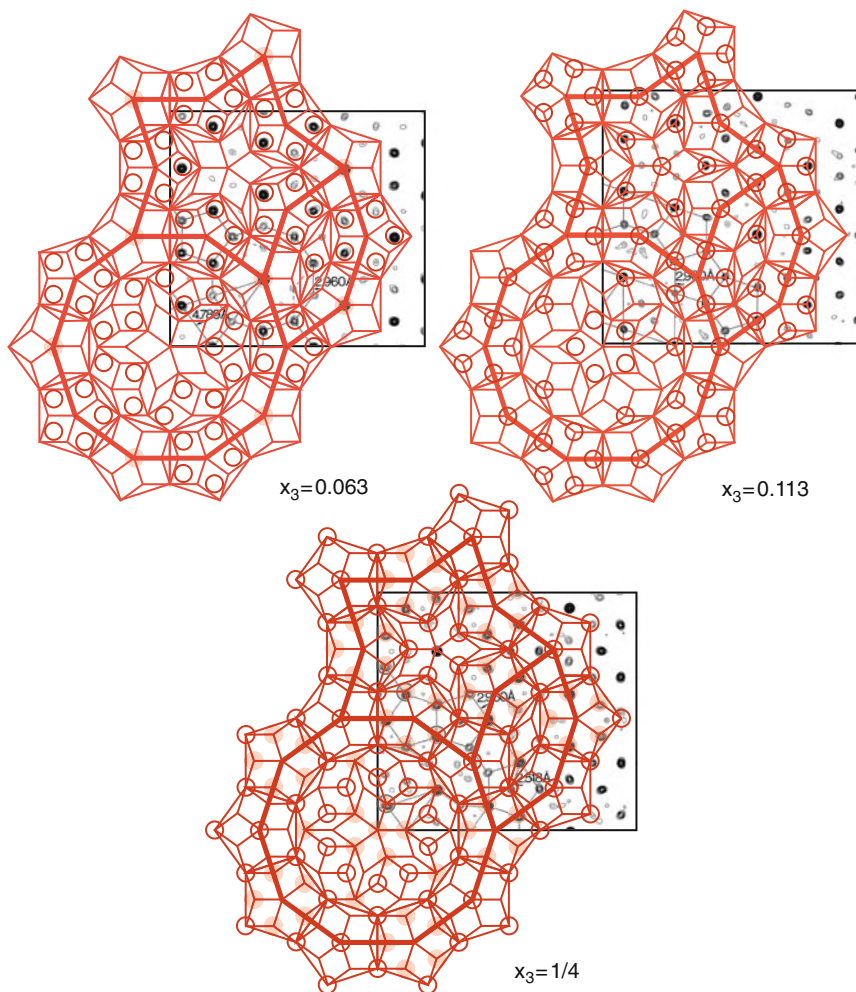
Fig. 8.21. 23.4 Å by 23.4 Å parallel space (11000) electron density maps of d-Al$_{70.5}$ Mn$_{16.5}$Pd$_{13}$ [101] with a model derived from electron-microscopic images [48] model (gray, online: *red drawing*; *Al empty circles, Mn/Pd full circles*) superposed. Sections correspond to (**a**) $x_3 = 0.063$, (**b**) $x_3 = 0.113$ (*puckered layers*), (**c**) $x_3 = 0.25$ (*flat layer on mirror plane*)

It is remarkable that the projected electron densities of d-Al$_{70.5}$Mn$_{16.5}$Pd$_{13}$ and i-Al$_{68.7}$Mn$_{9.6}$Pd$_{21.7}$ [14] agree quite well. Even the atomic sites on the layers A, B have their counterparts in the icosahedral phase. Thus the d-phase, which has pseudoicosahedral symmetry like other d-phases with 12 Å period, is an approximant of the i-phase. Of course, there is also a close resemblance between the structures of d-Al–Mn–Pd and d-Al–Mn.

8.3.3 Eight-Layer Periodicity

There are a couple of metastable and a few possibly stable d-phases known with eight-layer periodicity (Table 8.6). The stable phases d-Al–Pd–TM (TM = Ru, Os) can be seen as transition-metal stabilized d-Al–Pd. Metastable d-Al–Pd was discovered by rapid solidification in the year 1986 by different groups independently from each other [6, 12, 87]. Its structure was derived based on electron-microscopic images and the structure of the orthorhombic $(2/1,1/1)$-approximant Al_3Pd [77]. The latter one can be seen as a squashed-hexagon (H) tiling decorated with edge-sharing decagons. The decagons are each filled with one pentagonal columnar cluster. The phase diagram of Al–Pd was recently revised [123].

Besides some qualitative models based on electron microscopic images of metastable d-Al–Pd and its approximants, semiquantitative single-crystal X-ray diffraction studies of almost isostructural d-Al–Os–Pd, d-Al–Ir–Os, and d-Al–Ni–Ru were performed [18, 60, 92]. The evaluation of the large-scale electron density maps resulted in a first structure model. A pentagonal Penrose tiling with edge length $a_r = 4.799$ Å is the basis for a dual HBS-supertiling (edge length $a_r^s = 6.605$ Å) decorated appropriately by decagonal clusters with 21.378 Å diameter (Fig. 8.22). The atomic surfaces have been reconstructed by fitting the MEM electron density maxima to 3D Gaussians and lifting to 5D space (Fig. 8.22e).

Table 8.6. Stable decagonal quasicrystals with 8-layer periodicity and some of their approximants (listed below the line). The pseudo-decagonal axis is underlined (SG... space group, PS... Pearson symbol)

Nominal composition	Lattice parameters [Å]	SG/PS	References
$Al_{75}Os_{10}Pd_{15}$	$a_{1-4} = 3.8986(3)$	$P10_5/mmc$	[18, 110]
	$a_5 = 16.750(3)$		
$Al_{75}Ru_{10}Pd_{15}$			[110]
$Al_{73}Ir_{14.5}Os_{12.5}$	$a_{1-4} = 3.864(3)$	$P10_5mc$	[60]
	$a_5 = 16.821(8)$		
$Al_{70}Ni_{20}Ru_{10}$	$a_{1-4} = 3.8361(5)$	$P10_5/mmc$	[92, 104]
	$a_5 = 16.539(3)$		
$PdAl_3{}^a$	$a = 23.36$	$Pna2_1$	[77]
$Al_{72.5}Pd_{27.5}$	$b = 12.32$	$oP280$	
	$\underline{c = 16.59}$		
$Pd_{13}Ru_{12}Al_{75}{}^b$	$a = 23.889(3)$	$Pna2_1$	[128]
$Al_{75}Pd_{13}Ru_{12}$	$b = 32.802(3)$	oC	
	$\underline{c = 16.692(1)}$		

^{a} 2/1,1/1-approximant; ^{b} 3/2,2/1-approximant
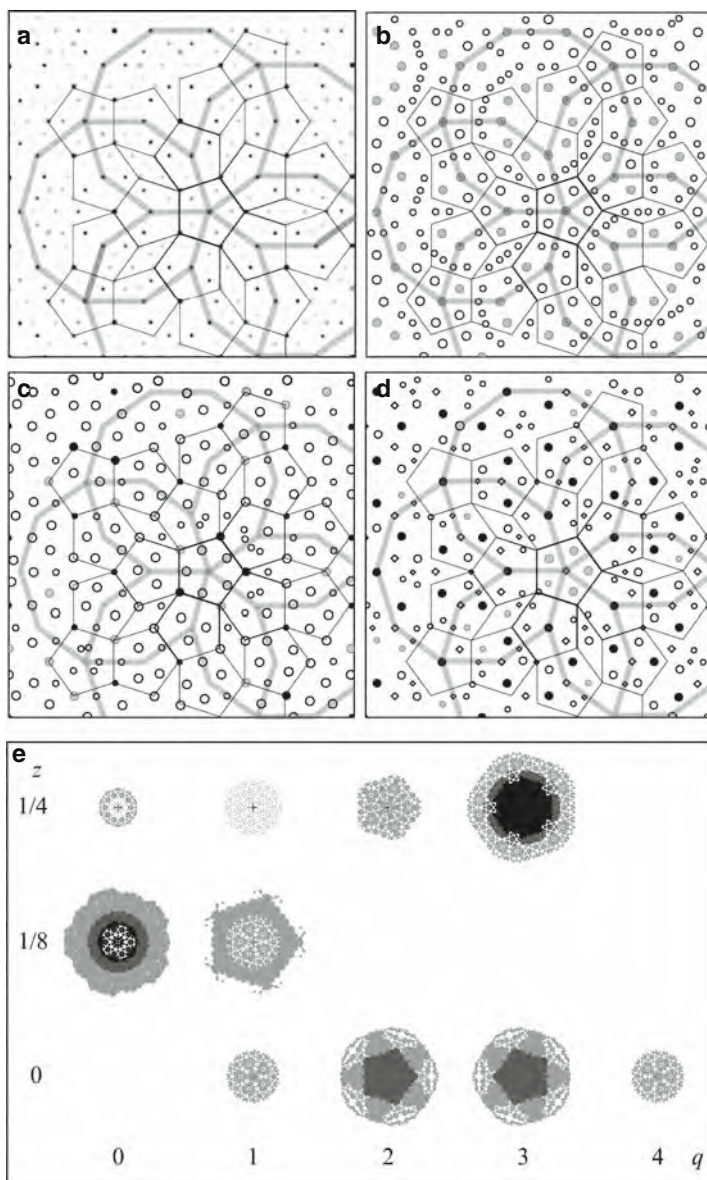
Fig. 8.22. (**a**) Projected MEM electron density map $(39 \times 39 \text{Å}^2)$ of $d\text{-Al}_{75}\text{Os}_{10}\text{Pd}_{15}$ $(0 \leqslant z \leqslant 1/4)$. The reconstructed structures of the layers are shown for (**b**) $z = 0$, (**c**) $z = 1/8$, (**d**) $z = 1/4$ with pentagon tiling and HBS-supertiling drawn in (*empty circles* Al, *full grey circles* Pd, *black full circles* Os; circle size is proportional to the occupancy of the site; *diamonds* Al atoms shifted from the mirror plane). (**e**) Reconstructed atomic surfaces for layers at $z = 0$, $z = 1/8$ and $z = 1/4$. The surfaces show displacements along z. The numbers q refer to the positions of the atomic surfaces, $1/5(p\,p\,p\,p\,5z)$ on the diagonal in the 5D unit cell (*black dots* Os, *dark grey* Pd, *light grey* Al; *dot* size is proportional to occupancy of the site) [18]

8.3.4 Surface Structures of Decagonal Phases

Surface studies have merely been performed on d-Al–Co–Cu and d-Al–Co–Ni since these are the only decagonal quasicrystals which can be grown in the size needed for experiments. One of the main results is that the surface structures of these quasicrystals are not reconstructed and that each atomic layer can be a termination layer. For a review on the structure of quasicrystal surfaces and overlayers see, e.g., [94]. In the following section a few examples are shortly discussed for illustration.

The first study of a QC surface was performed by scanning tunneling microscopy (STM) on d-$Al_{65}Co_{20}Cu_{15}$ [64]. The terraced structure was found similar to a decorated pentagon Penrose tiling and there were no indications of a reconstruction. Similar conclusions were drawn for d-$Al_{72.1}Co_{16.4}Ni_{11.5}$, which was investigated by spot-profile analysis low-energy electron diffraction (SPA-LEED) [35].

The first STM study of both the ten- and two-fold surface of d-$Al_{72}Co_{16}Ni_{12}$ revealed atomically flat terraces with a step height of 2.2(4) Å in the quasiperiodic layers [62]. Characteristic pentagonal-star shaped motifs were identified, all of which have the same orientation within a terrace layer and the opposite orientation in adjacent terraces in agreement with bulk structure models. The step heights of the terraces parallel to the twofold surface amount to 8.0(4) and 5.0(4) Å. Two-, four- and six-layer periodicities of the columnar clusters along the periodic direction were found indicating some disorder. An example of a twofold surface is shown in Fig. 8.23.

By a LEED and STM study on d-$Al_{73}Co_{17}Ni_{10}$, the contraction of the outermost layer spacing was quantified to 0.2 Å (10% of 2.04 Å average bulk structure spacing) and the expansion of the next spacing to 0.1 Å (5%) [31]. This is comparable to the findings for relatively open metal surfaces such as cP2-NiAl(110). The size of terraces was of the order of 1000 Å. A structure model [19], refined against LEED data, was shown to be in full agreement with the STM images, indicating that the surface structure does not significantly differ from the bulk structure (Fig. 8.24).

An investigation of the twofold surface of d-$Al_{71.8}Ni_{14.8}Co_{13.4}$ by SPA-LEED and He diffraction revealed a very short correlation length of only 80 Å for the four-layer period [93]. This agrees well with the findings for the bulk structure, i.e. the width of the maxima in diffuse scattering (see, e.g. [59]). There were also indications of an eight-layer period from faint scattering phenomena.

An ab initio study of the surface of an W-phase based Al–Co–Ni model structure confirmed that there are no reconstructions and only atomic displacements <0.15 Å due to relaxation [65]. The two different atomic layers in the model structure, a flat one and a puckered one with slightly different composition, both can be terminating layers and hardly distinguished by STM.

While cut and annealed surfaces always show flat terraces, cleavage surfaces are characterized by a corrugated, cobblestone-like topography as shown
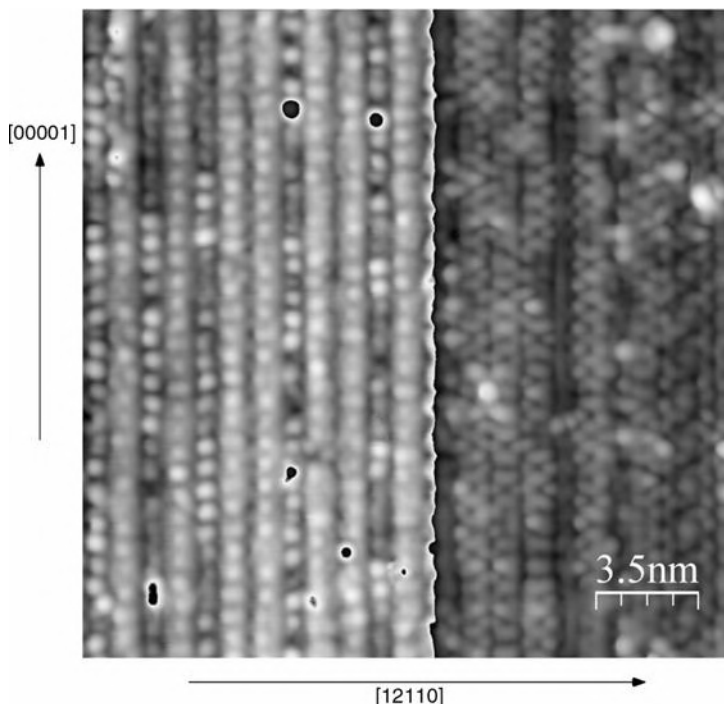
Fig. 8.23. STM image of the twofold surface of d-$Al_{72.9}Co_{16.7}Ni_{10.4}$. Two terraces with different terminations are shown, separated by a step height of 2.45 Å. The smallest periodicity observable is 8 Å (courtesy of R. Mäder)

in the example of d-$Al_{72.4}Co_{11.8}Ni_{15.8}$ by scanning electron microscopy (SEM) as well as by STM [29]. The surface showed a rather high roughness of 4–8 Å. According to the authors, the "cluster-subcluster" structure directly reflects the architecture of the d-phase, which is considered a quasiperiodic packing of 10–20 Å columnar clusters.

One shortcoming of this interpretation is, however, that the distribution of features in the STM images is not quasiperiodic. This has been shown in another study by the calculation of the autocorrelation function [17]. The cleavage surface is rather a random cut through the cluster structure, i.e. there are no particularly preferred crack propagation directions through such a cluster or an arrangement of clusters. There is no difference in the strength of bonds within a cluster or between clusters. The picture of strongly bonded low energy clusters in a matrix with weaker bonds does not apply to decagonal quasicrystals. First, there are no matrix atoms at all. All atoms of the structure are part of at least one cluster. Second, all clusters are partially overlapping each other. Thirdly, by flipping a small subset of atoms clusters can flip. Consequently, cluster boundaries do not have a particular meaning for the mechanical stability of a decagonal quasicrystal.
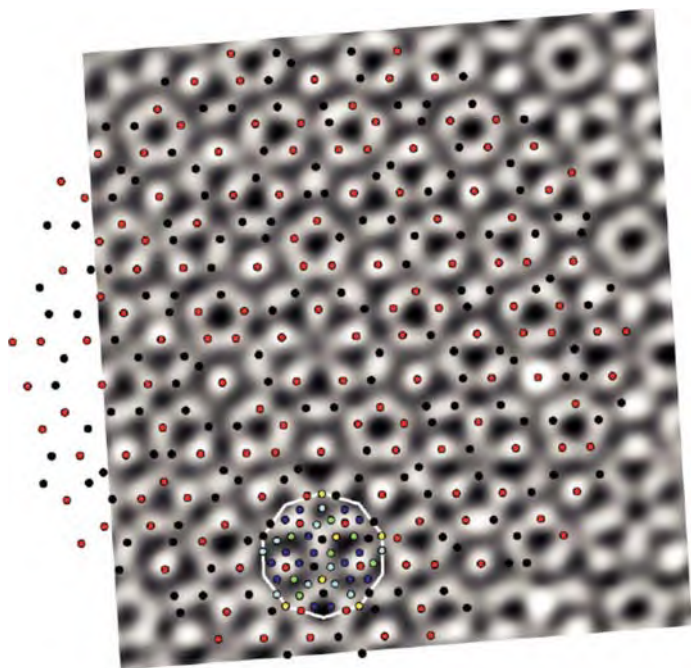
Fig. 8.24. Superposition of the structure model, refined against LEED data, onto the STM image of the tenfold surface of d-Al$_{73}$Co$_{17}$Ni$_{10}$ (from [31]) (online: *black, red* TM atoms, *other colors* Al atoms)

8.4 Dodecagonal Phases

The first (metastable) dodecagonal phase has been discovered in the year 1985 [53] in the system Ni–Cr (Table 8.7). Only in 1994, the first stable dodecagonal phase, dd-Ta$_{1.6}$Te, was discovered [25, 67] (Fig. 8.25). Ta can be partially substituted by V yielding dd-(Ta$_{1-x}$V$_x$)$_{1.6}$Te, $0 \leqslant x \leqslant 0.28$ [85]. With increasing V content the quasilattice parameter shrinks due to the smaller diameter of V compared to that of Ta, and the period along the twelvefold axis is halved.

dd-Ta$_{62}$Te$_{38}$ and its approximants can be as well described as incommensurately modulated structures with slightly different modulation vectors [112–114]. The structures of both phases are composed of two incommensurate layers rotated by 30° against each other. The origin of the modulation was suggested to be the same as for the well-known TaTe$_4$, resulting from periodic lattice distortions and vacancy ordering due to charge-density waves.

Due to the low quality of the dd-phase, probably because it possesses a real layer structure contrary to all other axial QC, no accurate structure analysis could be performed so far. However, a 5D model with pinwheel-shaped and fractal occupation domains was proposed, which can also describe the structure of the pseudotetragonal approximant Ta$_{181}$Te$_{112}$ by applying linear

Table 8.7. Dodecagonal quasicrystals and approximants known so far. Stable phases are marked by *

Nominal composition	Period along 12-fold axis/lattice parameters (Å)	Space group	References
$Ni_{70.6}Cr_{29.4}$			[53]
V_3Ni_2	4.5 Å		[21]
$V_{15}Ni_{10}Si$	4.5 Å		[21]
Bi-Mn			[122]
*$Ta_{1.6}Te$	$a_{1...4} = 3.8171(6)$	$P\overline{1}2m2$	[67]
	$a_5 = 20.79(9)$		
*$Ta_{97}Te_{60}$	$a = 27.672(2)$	$P2_12_12_1$	[23]
	$b = 27.672(2)$		
	$c = 20.613(2)$		
*$Ta_{181}Te_{112}$	$a = 37.58$	$P2_12_12_1$	[23]
	$b = 37.58$		
	$c = 20.66$		
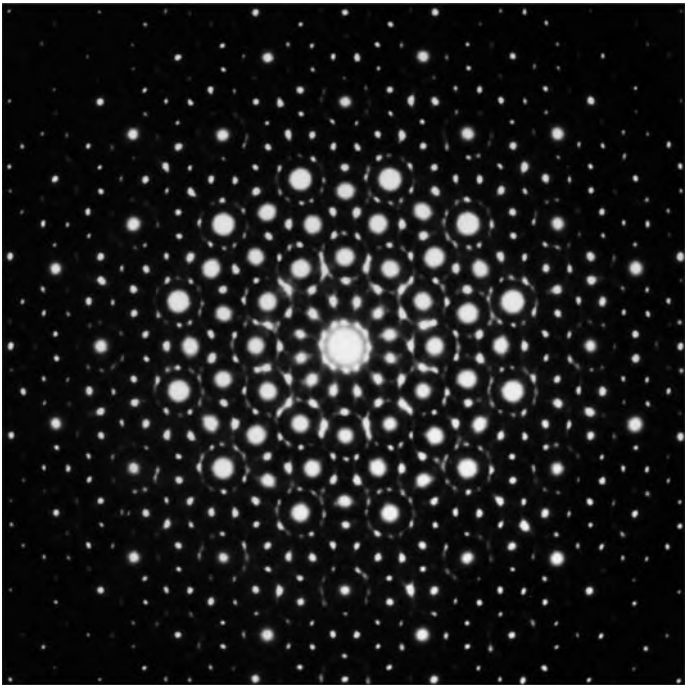
Fig. 8.25. Electron diffraction pattern of dd-$Ta_{1.6}Te$ (courtesy of B. Harbrecht/F. Krumeich)

phason strain [120]. According to this model, the structure is built from two ≈ 20 Å unit clusters decorating a square-triangle tiling.

Contrary to the dodecagonal phase its approximants $oP628$-$Ta_{97}Te_{60}$ and $Ta_{83}V_{14}Te_{60}$ are quite well ordered. The basic building unit of $Ta_{97}Te_{60}$ is a Ta-centered and Te-capped hexagonal antiprismatic $TaTa-12Te_2$ cluster ($d_{Ta-Te} \approx 3.05$ Å, $d_{Ta-Ta} \approx 2.95$ Å) [24]. Nineteen condensed basic clusters of this kind form a vaulted $Ta_{151}Te_{74}$-supercluster with dodecagonal shape and ≈ 25 Å diameter (Fig. 8.26).
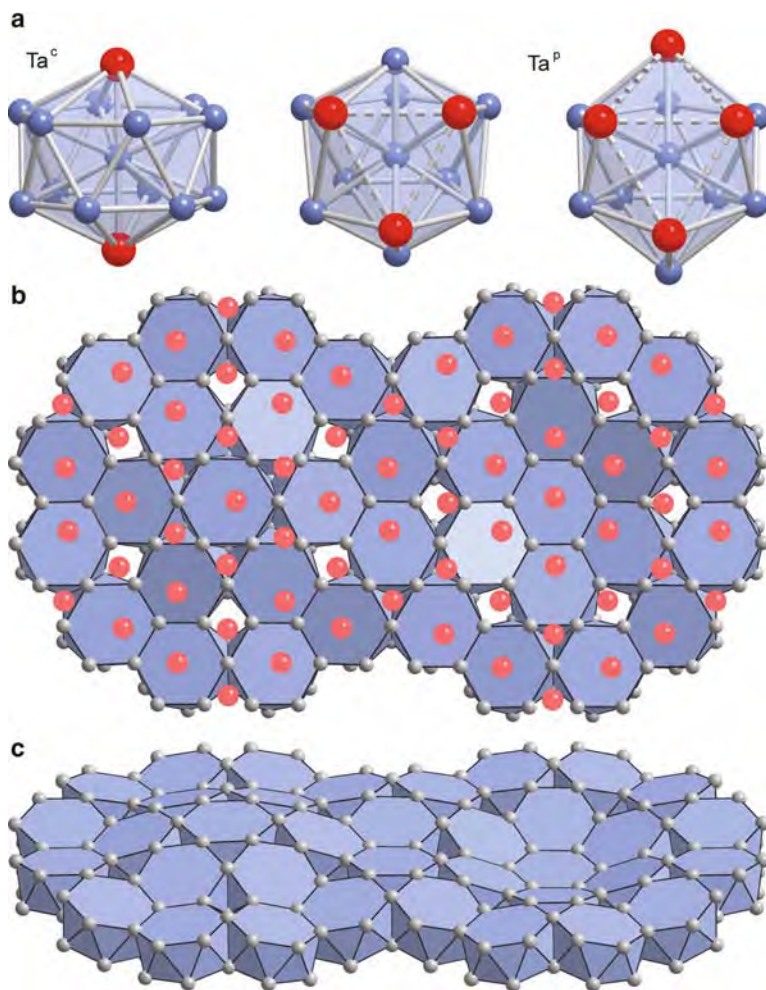
Fig. 8.26. (**a**) The three chemically distinct coordination types for Ta in the dd-phase approximant $oP628$-$Ta_{97}Te_{60}$. (**b**) Projection onto (001) and (**c**) side view of two partially overlapping vaulted Ta_{151} units composed of 19 concentrically fused hexagonal antiprismatic $TaTa_{12}$ clusters covered by Te atoms (*red circles*) in (**b**) (Fig. 3 of [24])

Along the pseudo-dodecagonal c-axis ≈ 10 Å thick slabs of this supercluster are stacked with a period of two slabs and related by a 2_1-screw axis. Each slab consists of five corrugated atomic layers, the outer ones are just Te layers ...Te–Ta–Ta–Ta–Te.... Consequently, the slabs are bonded just by weak Te–Te interactions ($d_{Te-Te} \geqslant 3.34$ Å), which are responsible for the lubricant-like properties of this material. The superclusters occupy the vertices of a square tiling with edge length 19.52 AA (same edge length as found for dd-$Ta_{1.6}Te$ from HRTEM images) (Fig. 8.27). The ideal stoichiometry of a dd-quasicrystal based on this supercluster results in $Ta_{3+2\sqrt{3}}Te_4$.

Quasiperiodic structures with 12-fold rotational symmetry have also been identified in nonmetallic systems showing that (at least dodecagonal) quasiperiodicity is not restricted to intermetallic phases and does not
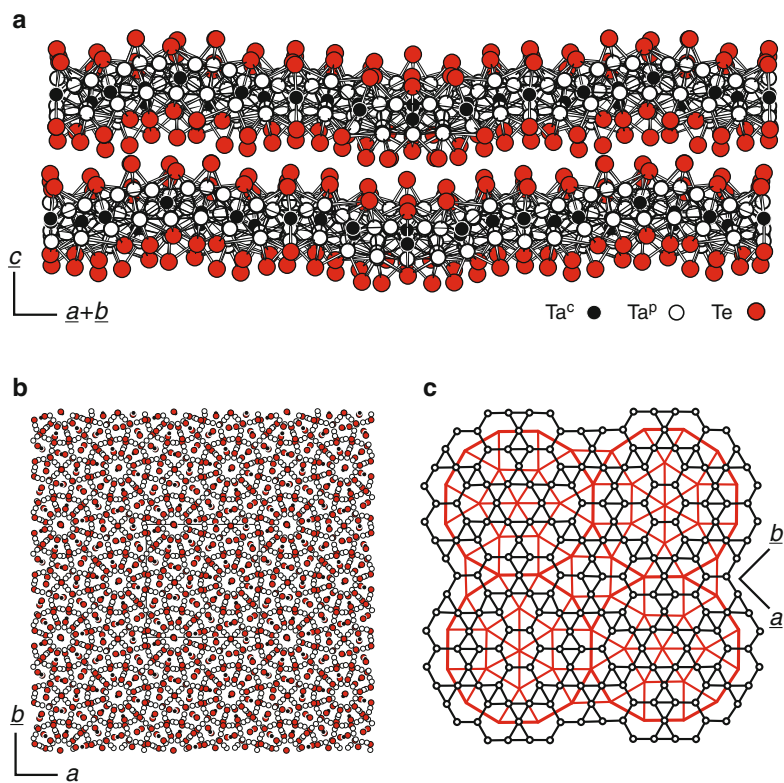
Fig. 8.27. (**a**) Projection of a suitable section of the crystal structure of the dd-phase approximant $Ta_{97}Te_{60}$ onto $(1\bar{1}0)$ with emphasis on the corrugation of the lamellae. (**b**) Projection of the lamella onto (001). (**c**) Network presentation of the Ta partial structure. The Ta^p atoms are arranged in layers corresponding to an irregular hexagon/traingle net (*black*). The Ta^c atoms form an irregular square triangle net (*red*). (Fig. 2 of [24])

necessarily require electronic stabilization. The first example is a dendrimer-based liquid quasicrystal [125]. This quasiperiodic phase transforms into a cubic phase upon heating, indicating that the quasiperiodic state is energetically favored at low temperature. The second example is a three-component polymer system composed of polyisoprene, polystyrene, and poly(2-vinylpyridine) which forms a star-shaped terpolymer [45]. A model explaining the particular stability of dodecagonal soft quasicrystals has been suggested by Lifshitz & Diamant [74]. They impose two requirements for quasiperiodicity: two different natural length scales and the existence of effective three-body interactions. See also Sect. 11.1.

References

1. E. Abe, A.P. Tsai, Stucture of quasicrystals studied by atomic-resolution electron microscopy. JEOL News 36E, 18–21 (2001)
2. B. Albert, K. Hofmann, Synthesis, Characterization, and crystal structure of Na_3B_{20}, determined and refined from X-ray and neutron powder data. Z. Anorg. Allgem. Chem. **625**, 709–713 (1999)
3. I. Al-Lehyani, M. Widom, Tile Hamiltonian for decagonal AlCoCu derived from first principles. Phys. Rev. B **67**, art. no. 014204 (2003)
4. N.S. Athanasiou, Formation, characterization and magnetic properties of some ternary Al-Cu-M (M equals transition metal) quasicrystals prepared by conventional solidification. Intern. J. Mod. Phys. B **11**, 2443–2464 (1997)
5. M. Baake, D. Joseph, P. Kramer, The Schur rotation as a simple approach to the transition between Quasi-periodic and periodic phases. J. Phys. A **24**, L961–L967 (1991)
6. P. A. Bancel, P. A. Heiney, Icosahedral aluminum-transition-metal alloys. Phys. Rev. B **33**, 7917–7922 (1986)
7. J. Bauer, J. Debuigne, The rare earth borocarbides with formula REB_2C (in French). J. Inorg. Nucl. Chem. **37**, 2473–2476 (1975)
8. J. Bauer, J.F. Halet, J.Y. Saillard, Rare earth metal borocarbides – Examples of coordination compounds in solid-state chemistry. Coord. Chem. Rev. **178**, 723–753 (1998)
9. C. Beeli, H.U. Nissen, J. Robadey, Stable Al–Mn–Pd quasi-crystals. Philos. Mag. Lett. **63**, 87–95 (1991)
10. S.I. Ben Abraham, F. Gaehler, Covering cluster description of octagonal Mn-SiAl quasicrystals. Phys. Rev. B **60**, 860–864 (1999)
11. L. Bendersky, Quasicrystal with One-dimensional translational symmetry and a tenfold rotation axis. Phys. Rev. Lett. **55**, 1461–1463 (1985)
12. L. Bendersky, Decagonal phase. J. De Phys. **47**, C3-457–464 (1986)
13. L. Bosio, H. Curien, M. Dupont, A. Rimsky, Structure cristalline de Ga γ. Acta Cryst. B **28**, 1974–1975 (1972)
14. M. Boudard, M. de Boissieu, C. Janot, G. Heger, C. Beeli, H. U. Nissen, H. Vincent, R. Ibberson, M. Audier, J.M. Dubois, Neutron and X-ray single-crystal study of the AlPdMn icosahedral phase. J. Phys.: Condens. Matter **4**, 10149–10168 (1992)

15. U. Burkhardt, M. Ellner, Grin Yu, B. Baumgartner, Powder diffraction refinement of the Co_2Al_5 structure. Pow. Diffr. **13**, 159–162 (1998)

16. W. Cao, H.Q. Ye, K.H. Kuo, A New octagonal quasicrystal and related crystalline phases in rapidly solidified Mn_4Si. Phys. Stat. Solidi A **107**, 511–519 (1988)

17. C. Cecco, C. Barth, P. Gille, M. Feuerbacher, G. Krausch, M. Reichling, Cleaved surfaces of d-AlNiCo and ξ'-AlPdMn. J. Non-Cryst. Solids **334**, 491–494 (2004)

18. A. Cervellino, Higher-dimensional modelling of decagonal quasicrystal structures. ETH Zurich Thesis No. 14023 (2002)

19. A. Cervellino, T. Haibach, W. Steurer, Structure solution of the basic decagonal Al–Co–Ni phase by the atomic surfaces modelling method. Acta Crystallogr. B **58**, 8–33 (2002)

20. K. Chattopadhyay, S. Ranganathan, G.N. Subbanna, N. Thangaraj, Electron-microscopy of quasi-crystals in rapidly solidified Al-14-Percent Mn alloys. Scr. Met. **19**, 767–771 (1985)

21. H. Chen, D.X. Li, K.H. Kuo, New Type of two-dimensional quasicrystal with twelvefold rotational symmetry. Phys. Rev. Lett. **60**, 1645–1648 (1988)

22. E. Cockayne, M. Widom, Ternary model of an Al–Cu–Co decagonal quasicrystal. Phys. Rev. Lett. **81**, 598–601 (1998)

23. M. Conrad, B. Harbrecht, Structural Properties of $Ta_{97}Te_{60}$ and $Ta_{181}Te_{112}$, Two approximants of a dodecagonal tantalum telluride In M. DeBoissieu, J.L. Verger-Gaugry, R. Currat, Aperiodic'97 : *Proceedings of the International Conference on Aperiodic Crystals*, 27–31 August 1997, p. 205–209. World Scientific, Alpe d'Huez, France (1998)

24. M. Conrad, B. Harbrecht, $Ta_{97}Te_{60}$: A crystalline approximant of a tantalum telluride quasicrystal with twelvefold rotational symmetry. Chem. Eur. J. **8**, 3094–3102 (2002)

25. M. Conrad, F. Krumeich, B. Harbrecht, A dodecagonal quasicrystalline chalcogenide. Angew. Chem. Int. Ed. **37**, 1384–1386 (1998)

26. J. Daams, P. Villars, Atomic environments in relation to compound prediction. Eng. Appl. Artif. Intell. **13**, 507–511 (2000)

27. S. Deloudi, Modeling of quasiperiodic systems. Thesis ETH Zurich No. 18107 (2008)

28. M. Doblinger, R. Wittmann, B. Grushko, Metastable transformation states of decagonal Al-Co-Ni due to inhibited decomposition. Phys. Rev. B **13**, art. no.-134208 (2001)

29. P. Ebert, F. Kluge, M. Yurechko, B. Grushko, K. Urban, Structure and composition of cleaved and heat-treated tenfold surfaces of decagonal Al–Ni–Co quasicrystals. Surf. Sci. **523**, 298–306 (2003)

30. F. Fleischer, W. Steurer, Solution of the average structure of decagonal $Al_{71.5}Co_{14.6}Ni_{13.9}$ by the 'charge-flipping method'. Philos. Mag. **87**, 2753–2758 (2007)

31. N. Ferralis, K. Pussi, E.J. Cox, M. Gierer, J. Ledieu, I.R. Fisher, C.J. Jenks, M. Lindroos, R. Mcgrath, R.D. Diehl, Structure of the tenfold d-Al–Ni–Co quasicrystal surface. Phys. Rev. B **69**, art. no. 153404 (2004)

32. B.J.O. Franco, 3rd-Order Fibonacci sequence associated to a heptagonal quasiperiodic tiling of the plane. Phys. Lett. A **178**, 119–122 (1993)

33. C. Freiburg, B. Grushko, R. Wittenberg, W. Reichert, Once more about monoclinic $Al_{13}Co_4$. Proc. Europ. Pow. Diffr. Conf., EPDIC 4, TransTech Publ., Switzerland, 583–585 (1996)

34. S.P. Ge, K.H. Kuo, Icosahedral and stable decagonal quasicrystals in $Ga_{46}Fe_{23}Cu_{23}Si_8$, $Ga_{50}Co_{25}Cu25$ and $Ga_{46}V_{23}Ni_{23}Si_8$. Philos. Mag. Lett. **75**, 245–253 (1997)

35. M. Gierer, A. Mikkelsen, M. Graber, P. Gille, W. Moritz, Quasi-crystalline surface order on decagonal $Al_{72.1}Ni_{11.5}Co_{16.4}$: An in-vestigation with spot profile analysis LEED. Surf. Sci. **463**, L654–L660 (2000)

36. Yu. Grin, K. Peters, U. Burkhardt, K. Gotzmann, M. Ellner, The structure of the ternary phase Co2NiAl9 (Y2). Z. Kristallogr. **213**, 364–368 (1998)

37. J. Grin, U. Burkhardt, M. Ellner, K. Peters, Crystal-structure of orthorhombic Co_4Al_{13}. J. Alloys Comp. **206**, 243–247(1994)

38. B. Grushko, The composition of the decagonal quasicrystalline phase in the Al–Cu–Co alloy system. Philos. Mag. Lett. **66**, 151–157 (1992)

39. B. Grushko, Phase equilibrium and transformation of stable quasicrystals – Decagonal Al–Cu–Co phase. Mater. Trans. JIM. **34**, 116–121 (1993)

40. B. Grushko, A study of the Al–Cu–Co phase diagram and the solidification of alloys containing decagonal phase. Phase Trans. **44**, 99–110 (1993)

41. B. Grushko, A study of the high-Cu Al–Cu–Co decagonal phase. J. Mater. Res. **8**, 1473–1476 (1993)

42. B. Grushko, T.Y. Velikanova, Stable and metastable quasicrystals in Al-based alloy systems with transition metals. J. Alloy. Compd. **367**, 58–63 (2004)

43. I. Hargittai (ed.), *Fivefold symmetry*. (World Scientific, Singapore, 1992)

44. K.H. Hassdenteufel, A.R. Oganov, S. Katrych, W. Steurer, Ab initio study of W-Al-Co-Ni: An approximant of the decagonal Al-Co-Ni quasicrystal. Phys. Rev. B **75**, art. No. 144115 (2007)

45. K. Hayashida, T. Dotera, A. Takano, Y. Matsushita, Polymeric quasicrystal: Mesoscopic quasicrystalline tiling in ABC star polymers. Phys. Rev. Lett. **98**, art. no. 1955025502–5502 (2007)

46. L.X. He, Z. Zhang, Y.K. Wu, K.H. Kuo, Stable decagonal quasi-crystals with different periodicities along the tenfold axis in $Al_{65}Cu_{20}Co_{15}$. Inst. Phys. Conf. Ser. No. **93**: Vol. 2, Chapter 13, Conf. EUREM 501–502 (1988)

47. K. Hiraga, M. Kaneko, Y. Matsuo, S. Hashimoto, The Structure of Al_3Mn – Close relationship to decagonal quasi-crystals. Philos. Mag. B **67**, 193–205 (1993)

48. K. Hiraga, W. Sun, Tiling in Al–Pd–Mn decagonal quasi-crystal, studied by high-resolution electron-microscopy. J. Phys. Soc. Jpn. **62**, 1833–1836 (1993)

49. K. Hiraga, T. Ohsuna, S. Nishimura, A new crystalline phase related to an Al–Ni–Co decagonal phase. J. Alloys Compd. **325**, 145–150 (2001)

50. K. Hiraga, T. Ohsuna, W. Sun, K. Sugiyama, The structural characteristics of Al–Co–Ni decagonal quasicrystals and crystalline approximants. J. Alloys Compd. **342**, 110–114 (2002)

51. C.Z. Hu, D.H. Ding, W.G. Yang, and R.H. Wang, Possible 2-Dimensional quasicrystal Structures with a 6-dimensional embedding space. Phys. Rev. B **49**, 9423–9427 (1994)

52. Z. Huang, S. Hovmoeller, An octagonal quasicrystal structure model with 8_3 screw axes. Philos. Mag. Lett. **64**, 83–88 (1991)

53. T. Ishimasa, H.U. Nissen, Y. Fukano, New ordered state between crystalline and amorphous in Ni–Cr particles. Phys. Rev. Lett. **55**, 511–513 (1985)

54. A. Janner, The architecture of the GroEL-GroES-(ADP)(7) chaperonin complex. I. Heptagrammal molecular forms. Acta Crystallogr. D **59**, 783–794 (2003)
55. A. Janner, The architecture of the GroEL-GroES-(ADP)(7) chaperonin complex. II. Heptagrammal characterization of the folding. Acta Crystallogr. D **59**, 795–808 (2003)
56. A. Janner, Strongly correlated structure of axial-symmetric proteins. II. Pentagonal, heptagonal, octagonal, nonagonal and ondecagonal symmetries. Acta Crystallogr. D **61**, 256–268 (2005)
57. W. Jeitschko, M.H. Gerss, Ternary carbides of the reare earth and iron group metals with $CeCoC_2$- and $CeNiC_2$-type structure. J. Less Comm. Met. **116**, 147–157 (1986)
58. J.C. Jiang, S. Hovmoeller, X.D. Zou, A 3-dimensional structure model of 8-fold quasi-crystals obtained by high-resolution electron-microscopy. Philos. Mag. Lett. **71**, 123–129 (1995)
59. S. Katrych, W. Steurer, X-ray diffraction study of decagonal Al–Co–Ni as a function of composition. Z. Kristall. **219**, 606–613 (2004)
60. S. Katrych, T. Weber, A. Kobas, L. Massuger, L. Palatinus, G. Chapuis, W. Steurer, New stable decagonal quasicrystal in the system Al–Ir–Os. J. Alloy. Compd. **428**, 164–172 (2007)
61. M. Khaidar, C.H. Allibert, J. Driole, Phase-equilibria of the Fe–Ni–Al system for Al content above 50 at-percent and crystal-structures of some ternary phases. Z. Metkd. **73**, 433–438 (1982)
62. M. Kishida, Y. Kamimura, R. Tamura, K. Edagawa, S. Takeuchi, T. Sato, Y. Yokoyama, J.Q. Guo, A.P. Tsai, lScanning tunnel-ing microscopy of an Al–Ni–Co decagonal quasicrystal. Phys. Rev. B **65**, art. no. 094208 (2002)
63. G. Kloess, C. Schetelich, R. Wittmann, V. Geist, Mass density and perfection of decagonal quasicrystals with nominal composition $Al_{62}Co_{20}Cu_{15}Si_3$. Phys. Stat. Sol. A **144**, K5–K9 (1994)
64. A.R. Kortan, R.S. Becker, F.A. Thiel, H.S. Chen, Real-space atomic structure of a two-dimensional decagonal quasicrystal. Phys. Rev. Lett. **64**, 200–203 (1990)
65. M. Krajci, J. Hafner, M. Mihalkovic, Ab initio study of the surface of a decagonal Al–Co–Ni quasicrystal. Phys. Rev. B **73**, art. no. 134203 (2006)
66. G. Kreiner, H.F. Franzen, The crystal structure of λ-Al_4Mn. J. Alloys Comp. **261**, 83–104 (1997)
67. F. Krumeich, M. Conrad, B. Harbrecht, TEM Study of Decagonal Tantalum Telluride and two Tetragonal Approximants. 13. Intern. Congr. Electr. Microsc., ICEM 17.-22. Juli, Paris (1994)
68. Yu. Kuz'ma, S.I. Svarichevskaya, Crystal structure of Y_2ReB_6 and its analogs. Sov. Phys. Crystallogr. **17**, 569–571 (1972)
69. Yu. Kuz'ma, Crystal structure of the compound $YCrB_4$ and its analogs. Sov. Phys. Crystallogr. **15**, 312–14 (1970)
70. U. Lemmerz, B. Grushko, C. Freiburg, M. Jansen, Study of decagonal quasi-crystalline phase-formation in the Al–Ni–Fe alloy system. Philos. Mag. Lett. **69**, 141–146 (1994)
71. L.S. Levitov, Why only quadratic irrationalities are observed in quasi-crystals. Europhys. Lett. **6**, 517–522 (1988)
72. F.H. Li, Y.F. Cheng, Relationship between octagonal quasicrystal and β-Mn type crystal in cut description. Chin. Phys. Lett. **13**, 199–202 (1996)

73. X.Z. Li, N.C. Shi, Z.S. Ma, X.L. Ma, K.H. Kuo, Structure of $Al_{11}Co_4$, a new monoclinic approximant of the Al-Co decagonal quasicrystal. Philos. Mag. Lett. **72**, 79–86 (1995)

74. R. Lifshitz, H. Diamant, Soft quasicrystals – Why are they stable? Philos. Mag. **87**, 3021–3030 (2007)

75. R. Lück, M. Scheffer, T. Gdecke, S. Ritsch, C. Beeli, Phase diagram determination for modifications of the d-phase in the Al–AlCo–AlNi system. Mater. Res. Soc. Symp. Proc. Vol. **553**, 25–36 (1999)

76. Z.H. Mai, L. Xu, N. Wang, K.H. Kuo, Z.C. Jin, G. Cheng, Effect of phason strain on the transition of an octagonal quasi-crystal to a Beta-Mn-Type Structure. Phys. Rev. B **40**, 12183–12186 (1989)

77. Y. Matsuo, K. Hiraga, The Structure of Al_3Pd – Close relationship to decagonal quasi-crystals. Philos. Mag. Lett. **70**, 155–161 (1994)

78. Y. Matsuo, M. Kaneko, T. Yamanoi, N. Kaji, K. Sugiyama, K. Hiraga, The structure of an Al_3Mn-type $Al_3(Mn, Pd)$ crystal studied by single-crystal X-ray diffraction analysis. Philos. Mag. Lett. **76**, 357–62 (1997)

79. N.I. Medvedeva, Yu.E. Medvedeva, and A.I. Ivnovskii, Electronic structure of ternary boron-containing phases $YCrB_4$, Y_2ReB_6, and MgC_2B_2. Dokl. Phys. Chem. **383**, 75–77 (2002)

80. G.R. Newkome (ed.), Comprehensive heterocyclic chemistry II. Vol. **9**: Seven-membered and larger rings and all fused derivatives. (Elsevier (Pergamon), Oxford, 1996)

81. K. Niizeki, Self-similarity of quasilattices in two dimensions: I. The n-gonal quasilattice. J. Phys. A **22**, 193–204 (1989)

82. T. Okabe, J.I. Furihata, K. Morishita, H. Fujimori, Decagonal phase and pseudo-decagonal phase in the Al–Cu–Cr system. Philos. Mag. Lett. **66**, 259–264 (1992)

83. V.V. Pavlyuk, T.I. Yanson, O.I. Bodak, R. Cerny, R.E. Gladyshevskii, K. Yvon, Structure refinement of orthorhombic $MnAl_3$. Acta Crystallogr. C **51**, 792–794 (1995)

84. E. Pelantova, R. Twarock, Tiles in quasicrystals with cubic irrationality. J. Phys. A. Math. Gen. **36**, 4091–4111 (2003)

85. C. Reich, M. Conrad, F. Krumeich, B. Harbrecht, The dodecagonal quasicrystalline telluride $(Ta,V)_{1.6}Te$ and its crystalline approximant $(Ta,V)_{97}Te_{60}$. MRS Proc. **553**, 83–94 (1999)

86. P. Rogl, Complex borides with uranium. Monatsh. Chem. **106**, 381–387 (1975)

87. G.V.S. Sastry, C. Suryanarayana, A comparison of the decagonal phase in rapidly solidified Al–Mn and Al–Pd Alloys. Scr. Metall. **20**, 1359–1360 (1986)

88. K. Saitoh, T. Yokosawa, M. Tanaka, A. P. Tsai, Structural studies of monoclinic approximants of $Al_{13}Fe_4$ and τ^2-inflated $Al_{13}Co_4$ by the high-angle annular dark-field method. J. Electron Microsc. **48**, 105–114 (1999)

89. K. Saitoh, T. Yokosawa, M. Tanaka, A. P. Tsai, Formation of an Al-Co decagonal quasicrystal from a τ^2-inflated $Al_{13}Co_4$ approximant. J. Phys. Soc. Jpn. **68**, 2886–2889 (1999)

90. T.J. Sato, E. Abe, A.P. Tsai, A novel decagonal quasicrystal in Zn-Mg-Dy system. Jpn. J. Appl. Phys. **36**, L1038–L1039 (1997)

91. T.J. Sato, E. Abe, A.P. Tsai, Composition and stability of decagonal quasicrystals in the Zn- Mg-rare-earth systems. Philos. Mag. Lett. **77**, 213–219 (1998)

92. T. Scholpp, Dekagonale Quasikristalle und Approximanten in den Systemen Al–Ni–Co, Al-Cu-Co und Al-Ni-Ru, Thesis ETH, Zurich, Thesis No. 14292 (2002)

93. H.R. Sharma, K.J. Franke, W. Theis, A. Riemann, S. Folsch, K.H. Rieder, P. Gille, Investigation of the twofold decagonal $Al_{71.8}Ni_{14.8}Co_{13.4}$ (10000) surface by SPA-LEED and He diffraction. Surf. Sci. **561**, 121–126 (2004)

94. H.R. Sharma, M. Shimoda, A.P. Tsai, Quasicrystal surfaces: structure and growth of atomic overlayers. Adv. Phys. **56**, 403–464 (2007)

95. N.C. Shi, X.Z. Li, Z.S. Ma, K.H. Kuo, Crystalline phases related to a decagonal quasi-crystal .1. A single-crystal X-ray-diffraction study of the orthorhombic Al_3Mn phase. Acta. Crystallogr. B **50**, 22–30 (1994)

96. C.B. Shoemaker, D.A. Keszler, D.P. Shoemaker, Structure of μ-MnAl$_4$ with composition close to that of quasicrystal phases. Acta. Crystallogr. B **45**, 13–20 (1989)

97. G.S. Smith, Q. Johnson, P.C. Nordine, The crystal stgructure of ScB_2C_2. Acta. Crystallogr. **19**, 668–673 (1965)

98. J.E.S. Socolar, Weak matching rules for quasi- rystals. Comm. Math. Phys. **129**, 599–619 (1990)

99. W. Steurer, Twenty years of structure research on quasicrystals. Part 1. Pentagonal, octagonal, decagonal and dodecagonal quasicrystals. Z. Kristallogr. **219**, 391–446 (2004)

100. W. Steurer, T. Haibach, B. Zhang, S. Kek, R. Luck, The structure of decagonal $Al_{70}Ni_{15}Co_{15}$. Acta. Crystallogr. B **49**, 661–675 (1993)

101. W. Steurer, T. Haibach, B. Zhang, C. Beeli, H.U. Nissen, The structure of decagonal $Al_{70.5}Mn_{16.5}Pd_{13}$. J. Phys. Condens. Matter **6**, 613–632 (1994)

102. W. Steurer, K.H. Kuo, 5-Dimensional structure-analysis of decagonal $Al_{65}Cu_{20}Co_{15}$. Acta. Crystallogr. B **46**, 703–712 (1990)

103. K. Sugiyama, S. Nishimura, K. Hiraga, Structure of a W(AlCoNi) crystalline phase related to Al–Co–Ni decagonal quasicrystals, studied by single crystal X-ray diffraction. J. Alloys Compd. **342**, 65–71 (2002)

104. W. Sun, K. Hiraga, A new highly ordered Al-Ni-Ru decagonal quasicrystal with 1.6 nm periodicity. Philos. Mag. Lett. **80**, 157–164 (2000)

105. H. Takakura, A. Yamamoto, A.P. Tsai, The structure of a decagonal Al72Ni20Co8 quasicrystal. Acta Crystallogr. A **57**, 576–585 (2001)

106. S. Taniguchi, E. Abe, Highly-perfect decagonal quasicrystalline $Al_{64}Cu_{22}Co_{14}$ with non-centrosymmetry. Philos. Mag. **88**, 1949–1958 (2008)

107. A.P. Tsai, A. Inoue, T. Masumoto, New decagonal Al-Ni-Fe and Al-Ni-Co alloys prepared by liquid quenching. Mater. Trans. JIM **30**, 150–154 (1989)

108. A.P. Tsai, A. Inoue, T. Masumoto, A stable decagonal quasicrystal in the Al–Cu–Co system. Mater. Trans. JIM **30**, 300–304 (1989)

109. A.P. Tsai, A. Inoue, T. Masumoto, Icosahedral, decagonal and amorphous phases in Al-Cu-M (M=Transition Metal) systems. Mater. Trans. JIM **30**, 666–676 (1989)

110. A.P. Tsai, A. Inoue, T. Masumoto, Stable decagonal quasicrystals with a periodicity of 1.6 nm in Al-Pd-(Fe, Ru or Os) alloys. Philos. Mag. Lett. **64**, 163–167 (1991)

111. A.P. Tsai, A. Inoue, T. Masumoto, Chemical effects on periodicity and structure of decagonal phases in Al–Ni-based and Al-Co-based alloys. Philos. Mag. Lett. **71**, 161–167 (1995)

112. M. Uchida, S. Horiuchi, $Ta_{62}Te_{38}$ twelvefold quasicrystal synthesized by non-equilibrium solid state reactions. Jpn. J. Appl. Phys. Lett. **36**, L1523–L1524 (1997)

113. M. Uchida, S. Horiuchi, Modulated-crystal model for the twelvefold quasicrystal $Ta_{62}Te_{38}$. J. Appl. Crystallogr. **31**, 634–637 (1998)

114. M. Uchida, S. Horiuchi, Twelve-fold quasicrystal and its approximant of $Ta_{62}Te_{38}$ interpreted as modulated crystals. Micron **31**, 493–497 (2000)

115. N. Wang, H. Chen, K.H. Kuo, Two-dimensional quasicrystal with eightfold rotational symmetry. Phys. Rev. Lett. **59**, 1010–1013 (1987)

116. N. Wang, K.K. Fung, K.H. Kuo, Symmetry study of the Mn-Si-Al octagonal quasicrystal by convergent beam electron-diffraction. Appl. Phys. Lett. **52**, 2120–2121 (1988)

117. Z.M. Wang, K.H. Kuo, The octagonal quasilattice and electron-diffraction patterns of the octagonal phase. Acta. Crystallogr. A **44**, 857–863 (1988)

118. N. Wang, K.H. Kuo, Transformation of the octagonal quasi-crystal into the beta-mn-type crystalline-structure. Philos. Mag. Lett. **61**, 63–68 (1990)

119. E.J.W. Whittaker, R.M. Whittaker, Some generalized penrose patterns from projections of N-dimensional lattices. Acta. Crystallogr. A **44**, 105–112 (1988)

120. A. Yamamoto, A five-dimensional model of dodecagonal Ta-Te quasicrystals with fractal occupation domains. Acta Crystallogr. A **60**, 142–145 (2004)

121. Y. Yokoyama, Y. Yamada, K. Fukaura, H. Sunada, A. Inoue, R. Note, Stable decagonal quasicrystal in an Al-Mn-Fe-Ge system. Jpn. J. Appl. Phys. Part 1, **36**, 6470–6474 (1997)

122. K. Yoshida, T. Yamada, Non-equilibrium alloy phases in Bi-Mn thin films prepared by vacuum depositions, a metastable Mn_3Bi and other long period crystal lattices. Proc. of JIMIS-5: Non-equilibrium solid phases of metals and alloys. Suppl. Trans. JIM **29**, 135–138 (1988)

123. M. Yurechko, A. Fattah, T. Velikanova, B. Grushko, A contribution to the AlPd phase diagram. J. Alloys Comp. **329**, 173–181 (2001)

124. A. Zalkin, D.H. Templeton, The crystal structures of CeB_4, ThB_4 and UB_4. Acta Crystallogr. **6**, 269–272 (1953)

125. X.B. Zeng, G. Ungar, Y.S. Liu, V. Percec, S.E. Dulcey, J.K. Hobbs, Supramolecular dendritic liquid quasicrystals. Nature **428**, 157–160 (2004)

126. B. Zhang, V. Gramlich, W. Steurer, $Al_{13-x}(Co_{1-y}Ni_y)_4$, a new approximant of the decagonal quasicrystal in the Al-Co-Ni system. Z.Kristallogr. **210**, 498–503 (1995)

127. H. Zhang, K.H. Kuo, Giant Al-M (M = Transitional Metal) crystals as penrose-tiling approximants of the decagonal quasicrystal. Phys. Rev. B **42**, 8907–8914 (1990)

128. B. Zhang, X.Z. Li, W. Steurer, J. Schneider, F. Frey, New crystalline approximant of the decagonal quasi-crystal in Al-Pd-Ru alloy. Philos. Mag. Lett. **72**, 239–244 (1995)

129. H. Zhang, D.H. Wang, K.H. Kuo, Icosahedral and decagonal quasicrystals, crystalline phases, and multiple twins in rapidly solidified $Al_{13}Cr_4Si_4$. J. Mater. Sci. **24**, 2981–2986 (1989)

9

Structures with 3D Quasiperiodicity

Quasicrystals with icosahedral diffraction symmetry (Fig. 9.1) are called icosahedral phases (*i*-phases) or icosahedral quasicrystals. Their structures are quasiperiodic in all three dimensions, therefore they are called 3D quasicrystals. There are no 3D quasicrystals known with other than icosahedral noncrystallographic point symmetry. 3D quasiperiodic structures with crystallographic point symmetry are usually dealt with in the framework of incommensurately modulated structures. It may make sense to describe them as quasicrystals if they either result from phase transformations of icosahedral phases or if there is no clearly identifiable sublattice of main reflections. A metastable cubic quasicrystal, for instance, was found in the system Al–Mg [18]. Due to the scaling symmetry of its diffraction pattern, it has been described as quasiperiodic rather than as incommensurately modulated structure [23].

Quasicrystals were discovered by Dan Shechtman on April 8, 1982, by examining electron diffraction patterns of rapidly solidified Al–Mn alloys. This first quasicrystal, i-Al–Mn, exhibited icosahedral diffraction symmetry and was metastable as all other quasicrystalline phases prepared in the following years. In 1986, the first stable icosahedral quasicrystal was discovered in the system Al–Cu–Li [19]. The systematic application of a concept based on valence electron concentration, ratios of atomic radii, and the existence of approximants (for a review see [108]) lead to the discovery of a large number of stable quasicrystals up to date (Fig. 9.2). Unfortunately, the majority of quasicrystals and approximants has not been properly characterized yet; rarely known are their stability range, symmetry, and lattice parameters. In a few cases the structures have already been solved by diffraction methods complemented by electron microscopic studies. The knowledge of approximant structures crucially contributed to the understanding of the local cluster structures.

Several chances were missed to identify novel intermetallic phases as quasicrystals long before Dan Shechtman's discovery. As early as 1939, the aluminum rich part of the Al–Cu–Fe system was studied and a new phase,
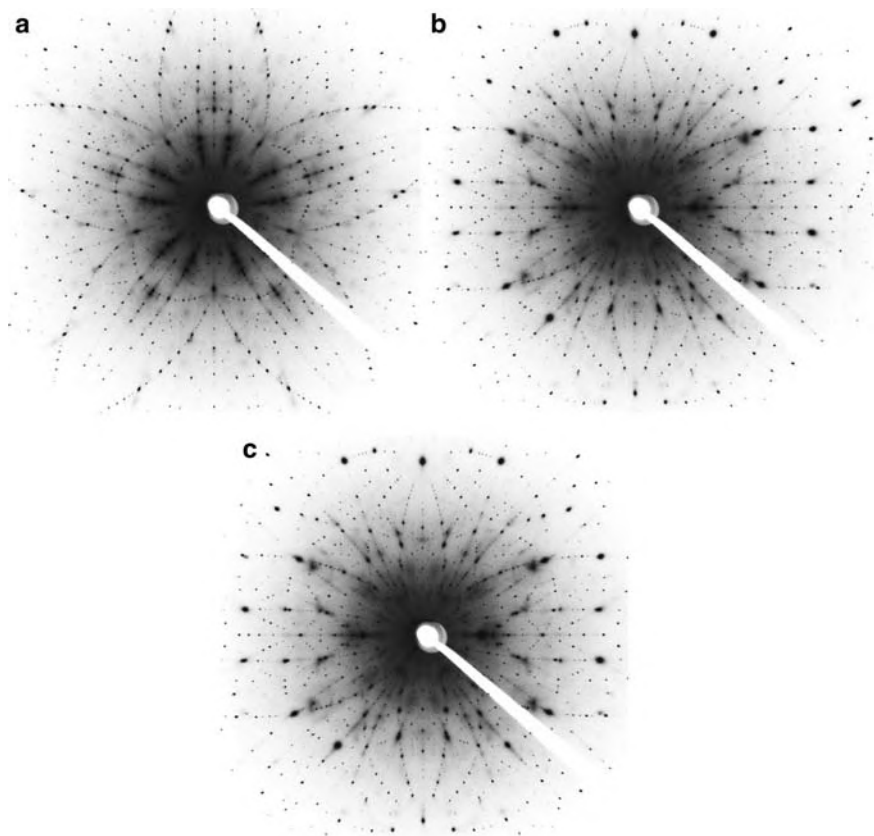
Fig. 9.1. X-ray Laue photographs of icosahedral Al-Mn-Pd in different orientations, with (**a**) 5-fold, (**b**) 3-fold and (**c**) 2-fold symmetry. The pictures were taken in-house

ψ, reported [8]. Since at that time only X-ray powder diffraction was used for phase characterization, the icosahedral symmetry of this quasicrystalline phase could not be identified. The same happened in the system Al–Cu–Li, where in 1956 Hardy and Silcock [38] found a phase, T2, with weak, "fairly simple," but not cubic powder pattern, later identified as quasicrystal [4, 81]. The Z phase in the system Mg–Zn–Y, found in 1982 by Padezhnova et al. [71] also corresponds to a quasicrystalline phase [61]. The former "unknown" compounds $Cd_{5.7}Y$, found in 1971 by Palenzona [72], and $Cd_{17}Ca_3$, discovered in 1972 by Bruzzone [10], have later been identified as quasicrystals as well [35, 109].

Employing the nD approach allows describing the structures of icosahedral quasicrystals as periodic hypercrystals in a 6D embedding space. So far, only quasicrystals have been experimentally found with point group symmetry $m\bar{3}\bar{5}$ and primitive (P) or face-centered (F) 6D Bravais lattice type. There
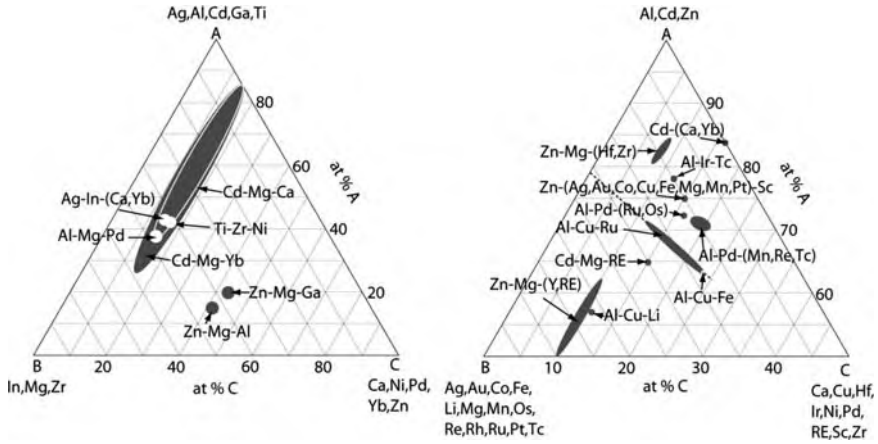
Fig. 9.2. Approximate stability regions of some classes of icosahedral quasicrystals. RE denotes the rare earth metals Y, Dy, Ho, Er, Tm, Lu in case of d-Zn-Mg-RE; Nd, Eu, Gd, Tb, Dy, Ho, Er, Tm, Yb, Lu in case of i-Cd-Mg-RE; La, Ce, Pr, Nd, Gd, Tb, Dy, Ho, Er, Yb in case of i-Zn-Mg-RE. Note that only the A-rich part ($50 \leq A \leq 100$ at.%) is shown in the right concentration diagram (figures are based on [33, 34])

are no representatives known of quasiperiodic structures with point symmetry $2\bar{3}\bar{5}$ or with body-centered (I) 6D Bravais lattice. Frequently, the iP-phases are just disordered variants of iF-phases. In these cases, the lattice parameter of the primitive 6D unit cell equals half the value of the lattice parameter of the face-centered 6D unit cell. Unfortunately, there is some confusion in literature about the terminology. Here, we just extend the conventions of 3D crystallography to 6D lattices.

The usual classification of quasicrystal structures is based on the prevalent cluster type in the structure. This can either be the Mackay or pseudo-Mackay cluster (type A) [7, 62], the Bergman cluster (type B or Frank-Kasper type) [5, 104], and the Tsai (type C) [35] cluster. It was shown, however, that this is not a very robust classification [32, 60]. F-type icosahedral quasicrystals of the type A cannot be described properly based on Mackay clusters alone. They can even be slightly better described based on Bergman clusters (type B). When only one of these two cluster types is used, only ≈75% of the structure is covered. In case of using both cluster types complementarily, ≈98% of all atoms are accounted for [60]. The remainder are so-called glue atoms.

For all three types of icosahedral quasicrystals stable approximants are known, a few 1/0- and mostly 1/1- or 2/1-approximants. Particularly helpful for structure analysis are the 2/1-approximants, because they already contain full clusters which decorate both oblate and prolate Penrose rhombohedra. Approximant structures are also used as periodic quasicrystal models for quantum-mechanical calculations, which are crucial for understanding

the chemical bonding and electronic band structure. However, the origin of quasiperiodic long-range order can hardly be revealed in this way. The lattice parameter, $a_{p/q}$, of the p/q-approximant is related to the 6D primitive lattice parameter, a_P, in the following way: $a_{p/q} = (2/(2+\tau))^{1/2}(p+q\tau)a_P$. The relationship to the edge length, a_r, of the rhombohedra of the underlying Penrose tiling is $a_P = a_r\sqrt{2}$.

Some of the cluster shells of the approximant structures are rather strongly distorted and/or disordered. The differences in the structure of experimentally observed and ideal 1/1- and 2/1-approximants can reach up to more than 1 Å, and are smallest in case of type A and largest in case of type C approximants [16, 17]. These distortions result from the rather low packing density of approximant structures derived from ideal icosahedral quasicrystal structure models. Quasicrystal structures refined against experimental diffraction data also show atomic displacements from their ideal positions of similar size. Consequently, quasiperiodic long-range order does not necessarily lead to less distorted clusters with icosahedral symmetry.

9.1 Mackay-Cluster Based Icosahedral Phases (Type A)

The Mackay-cluster based icosahedral phases known so far, all contain Al as main constituent, Cu or Pd as second component and a transition element of group 7 (Mn, Tc, Re) or group 8 (Fe, Ru, Os) as third constituent. The stable icosahedral phases of this type and their approximants are listed in Table 9.1.

Sometimes the Mackay-cluster based i-phases are called spd-quasicrystals due to the substantial hybridization between the p states of aluminum and the d states of the transition metal (TM) atoms [14]. Their stability range is related to an electron concentration (valence electrons per atom) of $1.6 \geq e/a \geq 1.9$ (Al: 3, Fe: -2.66, Os: -2.66, Pd: 0, Ru: -2.66 [80]).

The first intermetallic phase where Mackay-clusters were identified was α-Al–Mn–Si [13, 97]. Its structure, that of a 1/1-approximant of icosahedral Mackay-cluster-based quasicrystals, is shown in Fig. 9.3. A double-Mackay-cluster built from five shells (a) – (e) is located at the origin of the unit cell. A Mackay-cluster, consisting of the first three shells (a) – (c) of the double-Mackay-cluster, occupies the body center. In both cases, the innermost icosahedron shows Al/Si disorder.

The 1/1-approximant in the system Al–Cu–Fe–Si shows a rather large compositional stability range ($a = 12.312 - 12.329$ Å, $Pm\bar{3}$, [94]). This is reflected in the chemical disorder leading to mixed Al, Cu and Al, Cu, Fe sites mainly in the second shell of the cluster in the origin and the first shell of that in the body center. A slightly different structure was found for the 1/1-approximant $\alpha-\mathrm{Al}_{57.3}\mathrm{Cu}_{31.4}\mathrm{Ru}_{11.3}$ ($a = 12.377$ Å, $Pm\bar{3}$, [100]). There, the strongly disordered first cluster shells at both the origin as well as at the body center are centered by an Ru atom. The structure of the 2/1-approximant ($a = 20.211$ Å, $Pm\bar{3}$ [98]) is shown in Fig. 9.4.

Table 9.1. Stable icosahedral quasicrystals and approximants (below the line) based on packings of Mackay clusters ($a_r = a_P/\sqrt{2} = a_F/(2\sqrt{2})$). The structures are ordered with increasing (quasi)lattice parameter

Nominal composition	a_r [Å]	6D/3D-Space group	References
i-Al$_{65}$Cu$_{20}$Ru$_{15}$	4.541	$Fm\bar{3}\bar{5}$	[111]
i-Al$_{65}$Cu$_{20}$Os$_{15}$	4.524	$Fm\bar{3}\bar{5}$	[111]
i-Al$_{65}$Cu$_{20}$Fe$_{15}$	4.465	$Fm\bar{3}\bar{5}$	[110, 113]
i-Al$_{70.5}$Pd$_{21}$Mn$_{8.5}$	4.562	$Fm\bar{3}\bar{5}$	[24, 112]
i-Al$_{70}$Pd$_{20}$Re$_{10}$	4.617	$Fm\bar{3}\bar{5}$	[78, 112]
i-Al$_{70}$Pd$_{21}$Tc$_9$	4.606	$Fm\bar{3}\bar{5}$	[67]
i-Al$_{71}$Pd$_{21}$Re$_8$[a]	7.383	$Pm\bar{3}\bar{5}$	[42]
i-Al$_{72}$Pd$_{17}$Ru$_{11}$		$Fm\bar{3}\bar{5}$	[2]
i-Al$_{72}$Pd$_{17}$Os$_{11}$		$Fm\bar{3}\bar{5}$	[2]
1/0-Al$_{71.5}$Cu$_{8.5}$Ru$_{20}$	7.745	$P2_13$	[49]
γ-Al$_{55.1}$Cu$_{14.6}$Ru$_{20.2}$Si$_{10.1}$[b]	2×7.690	$Fm\bar{3}$	[101]
c-Al$_{39}$Pd$_{21}$Fe$_2$[b]	2×7.758	$Fm\bar{3}$	[22]
c-Al$_{68}$Pd$_{20}$Ru$_{12}$[b]	2×7.770	$P23$	[64]
1/1-Al$_{57.3}$Cu$_{31.4}$Ru$_{11.3}$	12.377	$Pm\bar{3}$	[91, 100]
1/1-Al$_{55}$Cu$_{25.5}$Fe$_{12.5}$Si$_7$	12.329	$Pm\bar{3}$	[94]
1/1-Al$_{40}$Mn$_{10.1}$Si$_{7.4}$	12.643	$Pm\bar{3}$	[97]
1/1-Al$_{67}$Pd$_{11}$Mn$_{14}$Si$_7$	12.281	$Pm\bar{3}$	[99]
2/1-Al$_{66.6}$Rh$_{26.1}$Si$_{7.3}$	19.935	$Pm\bar{3}$	[103]
2/1-Al$_{70}$Pd$_{23}$Mn$_6$Si	20.211	$Pm\bar{3}$	[98]

[a] perhaps metastable τ-fold superstructure of the F-centered i-phase, also called $F2$ phase
[b] 2-fold superstructure of a 1/0-approximant

9.2 Bergman-Cluster Based Icosahedral Phases (Type B)

The first Bergman-cluster based icosahedral phase was discovered in the system Al–Cu–Li [19]. Since it contains only elements with s and p valence electrons, this type of quasicrystals is also called sp-quasicrystals. The 3d electrons of Cu are considered as core electrons since they do not significantly contribute to the Fermi energy. Their stability range is related to an electron concentration (valence electrons per atom) of $2.1 \geq e/a \geq 2.4$ (Al: 3, Fe: -2.66, Os: -2.66, Pd: 0, Rh: -1.71, Ru: -2.66 [80]). Another name in use for this type of i-phases is Frank–Kasper-type quasicrystals, because their approximants belong to the Frank–Kasper phases, which form the family of tetrahedrally close-packed (tcp) structures. These structures only contain tetrahedral interstices and the coordination polyhedra are limited to essentially four with coordination numbers (CN) 12, 14, 15, and 16 [93]. The known stable icosahedral quasicrystals of this type and their approximants are listed in Table 9.2.

The 1/1-approximants of Frank–Kasper-type icosahedral quasicrystals contain a bcc packing of Bergman clusters. The structure of the Bergman
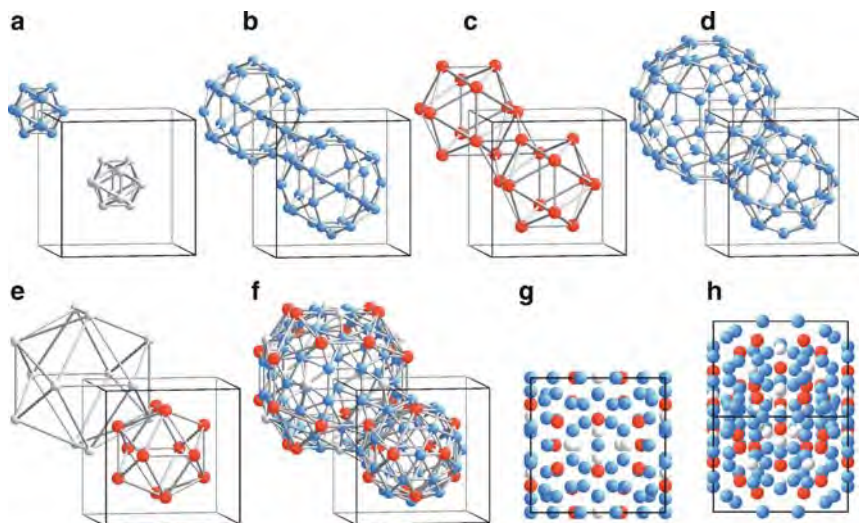
Fig. 9.3. Shells of the Mackay-cluster (at the body center) and double-Mackay-cluster (at the origin) on the example of α-Al$_{40}$Mn$_{10.1}$Si$_{7.4}$ ($a = 12.643$ Å, $Pm\bar{3}$, [97]). (**a**) (Al$_{0.65}$Si$_{0.35}$)$_{12}$ icosahedron (edge length $a_r = 2.585$ Å, diameter $\varnothing = 4.908$ Å) connected via an octahedron to the icosahedron in the body center; (**b**) Al$_{30}$ origin-centered icosidodecahedron ($a_r = 2.826 - 2.983$ Å, $\varnothing = 9.301$ Å); (**c**) Mn$_{12}$ icosahedron ($a_r = 5.091$ Å, $\varnothing = 9.648$ Å) connected via an octahedron to the one in the body center; (**d**) Al$_{60}$ distorted rhombicosidodecahedron ($a_r = 2.826 - 3.359$ Å, $\varnothing = 13.361$ Å) sharing a triangle face with the icosidodecahedron in the body-center; (**e**) (Al$_{0.01}$Si$_{0.99}$)$_{12}$ icosahedron ($a_r = 7.324 - 7.775$ Å, $\varnothing = 14.611$ Å). (**f**) Combination of cluster shells (**c**)–(**e**); Si atoms cap all 12 pentagons, Mn all squares. The projections of one unit cell along [100] and [110] are shown in (**g**) and (**h**)

cluster, first described for Mg$_{32}$(Al,Zn) [5], will be discussed as an example of R–Al$_5$CuLi$_3$ (Fig. 9.5). The *bcc* unit cell (space group $Im\bar{3}$, $a = 13.906$ Å [3]) contains 160 atoms in two overlapping clusters. By a combined X-ray and neutron scattering analysis, Al and Cu was found strongly substitutionally disordered.

The first four shells, a small (Cu,Al)$_{12}$ icosahedron, a Li$_{20}$ pentagondodecahedron, a large (Cu,Al)$_{12}$ icosahedron, and a distorted truncated Cu$_{48}$Al$_{12}$ triacontahedron, form the 104-atom Samson cluster. In a *bcc* packing of the Samson clusters, these are connected via Al pairs along the [100] directions, and by sharing 8 hexagon faces along the [111] directions. In the open space left, 12 Li atoms cap the pentagon faces. The shells in Fig. 9.5b and c can be combined to the (Cu,Al)$_{12}$Li$_{20}$ triacontahedron shown in Fig. 9.5f. A better description of the packing refers to a packing of the large triacontahedral 132-atom clusters (Pauling triacontahedra), which share one rhomb face along the [100] directions and an oblate rhombohedron along [111] (see also Fig. 2.5b). The Li atoms on the body diagonal are shared by the small (b) and large (e) triacontahedra.
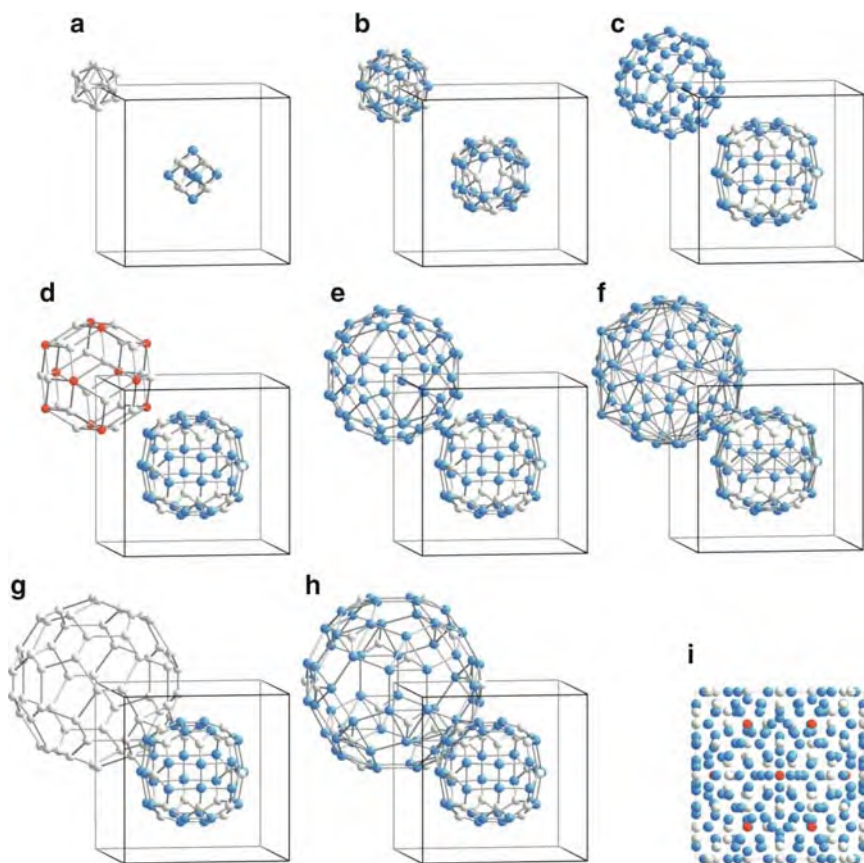
Fig. 9.4. Shells of the clusters at the origin (**a**–**h**) and body center (**a**–**c**) of an Mackay-type 2/1-approximant on the example of cubic $Al_{70}Pd_{23}Mn_6Si$ ($a = 20.211$ Å, $Pm\bar{3}$ [98]). (**a**) Pd_{12} icosahedron (edge length $a_r = 3.011$–3.058 Å, diameter $\varnothing = 5.799$ Å) in the origin and Al_6Pd_8 rhombdodecahedron ($a_r = 2.568$ Å, diameter $\varnothing = 5.898$ Å) at the body-center; (**b**) $Al_{20}Pd_{12}$ origin-centered triacontahedron ($a_r = 2.744$–2.947 Å, $\varnothing = 8.945$ Å) and $Al_{24}Pd_{12}$ cluster ($a_r = 2.580$–3.048 Å, $\varnothing = 9.579$ Å) at the body center; (**c**) Al_{30} disordered icosidodecahedron with 60 partially occupied split positions ($a_r = 1.952$–2.896 Å, $\varnothing = 12.632$ Å) and $Al_{36}Pd_{20}$ cluster ($a_r = 2.504$–3.943 Å, $\varnothing = 13.510$ Å) at the body center; (**d**) $Mn_{12}Pd_{20}$ triacontahedron ($a_r = 4.505$–4.538 Å, $\varnothing = 14.620$ Å); (**e**) distorted Al_{60} rhombicosidodecahedron ($a_r = 2.882$–4.892 Å, $\varnothing = 16.385$ Å). (**f**) cluster shell of an Al_{60} truncated dodecahedron merged with an Al_{12} icosahedron ($a_r = 2.825$–5.372 Å, $\varnothing = 19.404$ Å) linked via a joint tetrahedron (edge length 2.723 Å) to a Pd atom of the cluster in the body center; (**g**) truncated Pd_{60} icosahedron ($a_r = 3.011$–4.729 Å, $\varnothing = 20.543$ Å) capped by a Pd atom of the cluster in the body center (distance 4.123 Å); (**h**) cluster shell of an Al_{60} rhombicosidodecahedron merged with an Pd_{20} dodecahedron ($a_r = 2.744$–4.920 Å, $\varnothing = 21.691$ Å) sharing a Pd atom with the cluster in the body center; (**i**) projection of one unit cell along [100]

Table 9.2. Stable icosahedral quasicrystals and approximants (below the line) based on packings of Bergman clusters (Frank–Kasper type). a_r is the edge length of Penrose rhombohedra ($a_r = a_P/\sqrt{2} = A_F/(2\sqrt{2})$). The structures are ordered with increasing (quasi)lattice parameter

Nominal composition	a_r [Å]	6D/3D-Space group	References
i-$Zn_{76}Mg_{17}Hf_7$	5.011	$Fm\bar{3}\bar{5}$	[39]
i-$Zn_{84}Mg_7Zr_9$	5.031	$Pm\bar{3}\bar{5}$	[39]
i-Al_6CuLi_3	5.043	$Pm\bar{3}\bar{5}$	[82, 90]
i-$Mg_{43}Al_{42}Pd_{15}$	5.13	$Pm\bar{3}\bar{5}$	[50]
i-$Zn_{40}Mg_{39.5}Ga_{25}$	5.133	$Pm\bar{3}\bar{5}$	[12, 21, 70]
i-$Zn_{74}Mg_{15}Ho_{11}$	5.144	$Pm\bar{3}\bar{5}$	[9, 69]
i-$Zn_{41}Mg_{44}Al_{15}$[a]	5.17	$Pm\bar{3}\bar{5}$	[107]
i-$Zn_{56.8}Mg_{34.6}Tb_{8.7}$	5.173	$Fm\bar{3}\bar{5}$	[25, 69]
i-$Zn_{65}Mg_{26}Ho_9$	5.18	$Fm\bar{3}\bar{5}$	[9, 69]
i-$Zn_{64}Mg_{25}Y_{11}$	5.19	$Fm\bar{3}\bar{5}$	[9, 69]
i-$Zn_{55}Mg_{40}Nd_5$	5.25	$Pm\bar{3}\bar{5}$	[114]
i-$Zn_{56.8}Mg_{34.6}Dy_{8.7}$		$Fm\bar{3}\bar{5}$	[25, 69]
i-Ti-Zr-Ni			
1/1-$Zn_{77}Mg_{17.5}Ti_{5.5}$	13.554	$Pm\bar{3}$	[31]
1/1-$Zn_{77}Mg_{18}Hf_5$	13.674	$Pm\bar{3}$	[31]
1/1-$Zn_{77}Mg_{18}Zr_5$	13.709	$Pm\bar{3}$	[31]
1/1-$Al_{88.6}Cu_{19.4}Li_{50.3}$	13.906	$Im\bar{3}$	[3]
1/1-$Zn_{34.6}Mg_{40}Al_{25.4}$	14.217	$Im\bar{3}$	[5, 104]
2/1-$Zn_{61.4}Mg_{24.5}Er_{14.1}$	20.20	$F\bar{4}3m$	[51]
2/1-$Zn_{37}Mg_{46}Al_{17}$	23.064	$Pm\bar{3}$	[102]
2/1-$Zn_{47.3}Mg_{27}Al_{10.7}$	23.035	$Pa\bar{3}$	[57]
2/1-$Zn_{73.6}Mg_{2.5}Sc_{11.2}$		$Pa\bar{3}$	[57]
3/2-2/1-2/1-$Zn_{40}Mg_{39.5}Ga_{16.4}Al_{4.1}$	$a = 36.840$ $b = 22.782$ $c = 22.931$	$Cmc2_1$	[21, 53]

[a] Perhaps metastable

The structure of a 2/1-approximant of a Bergman-type icosahedral quasicrystal is discussed on the example of cubic $Zn_{47.3}Mg_{27}Al_{10.7}$ ($a = 23.035$ Å, $Pa\bar{3}$, [57]) (Fig. 9.6). The triacontahedral cluster has a structure similar to that of the 1/1-approximant. The main difference is in the packing of the clusters.

In case of the 1/1-approximant, the triacontahedral clusters occupy the lattice nodes of a *bcc* unit cell, with lattice parameter $a_{1/1}$. It has been shown [40] that the structure can as well be described by a vertex-decorated packing of oblate rhombohedra with edge length $a_r = a\sqrt{3}/2$ (Fig. 9.7a). Compared with the oblate rhombohedron ($\alpha_r = 63.44°$), which is one of the two prototiles of the Amman tiling, it appears slightly distorted ($\alpha_r = 70.53°$). Along the short diagonal (length $= a_{1/1}$) of the rhombic faces, the clusters share one of
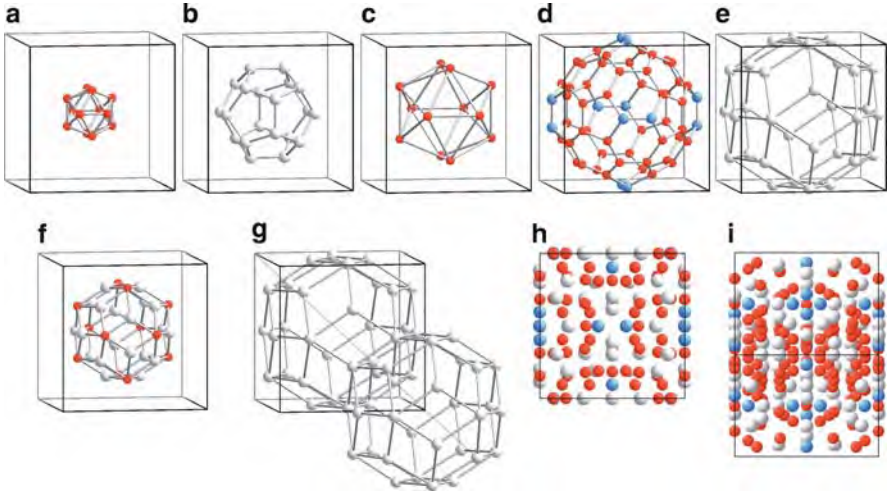
Fig. 9.5. Shells of the Bergman cluster as an example of *bcc* R–Al₅CuLi₃, a 1/1-approximant of *i*-Al₆CuLi₃ [3]. (**a**) $(Al_{0.89}Cu_{0.11})_{12}$ icosahedron (edge length $a_r = 2.651$ Å, diameter $\varnothing = 5.033$ Å); (**b**) Li_{20} pentagondodecahedron ($a_r = 3.226$ Å, $\varnothing = 9.078$ Å); (**c**) $(Al_{0.54}Cu_{0.46})_{12}$ icosahedron ($a_r = 5.383$ Å, $\varnothing = 10.093$ Å); (**d**) $(Al_{0.89}Cu_{0.11})_{48}Al_{12}$ distorted truncated triacontahedron ($a_r = 2.658$–2.861 Å, $\varnothing = 14.161$ Å); (**e**) Li_{32} triacontahedron ($a_r = 5.020$–5.071 Å, $\varnothing = 16.238$ Å). The shells in (**b**) and (**c**) can be combined to the $(Cu,Al)_{12}Li_{20}$ triacontahedron shown in (**f**). The ratio of the diameters of the large and the small triacontahedra depicted in (**e**) and (**f**) amounts to τ. The large triacontahedra are face-connected along the [100] directions and (**g**) share an oblate rhombohedron along [111] (see also Fig. 2.5b). The projections of one unit cell along [100] and [110] are shown in (**h**) and (**i**)

its rhombs. The neighboring clusters along the edges and the short body diagonal (length $a_r = a\sqrt{3}/2$) have an oblate rhombohedron as common volume.

In case of the cubic 2/1-approximant, with lattice parameter $a_{2/1}$, essentially the same triacontahedral clusters occupy the points of the lattice complex generated by Wyckoff position 8*c* *x x x* in space group $Pa\bar{3}$. This point set can also be described as the set of vertices of a 1:1 packing of oblate and prolate rhombohedra with edge length $a_r = a\sqrt{3}/(2\tau)$. The distortion of these rhombohedra, compared with the Amman prototiles, is smaller than in case of the 1/1-approximant as indicated by $\alpha_r = 69.83°$.

Based on the commonly used 6D lattice parameter $a_P = \sqrt{2}a_r$, the edge length of the Ammann rhombohedra in the approximants is larger by a factor τ^2. For example, the edge lengths of the rhombohedra in the structure of 2/1-$Zn_{47.3}Mg_{27}Al_{10.7}$ are 13.646 Å compared with $\tau^2 a_r = 13.535$ Å calculated from the icosahedral phase with $a_r = 5.17$ Å.
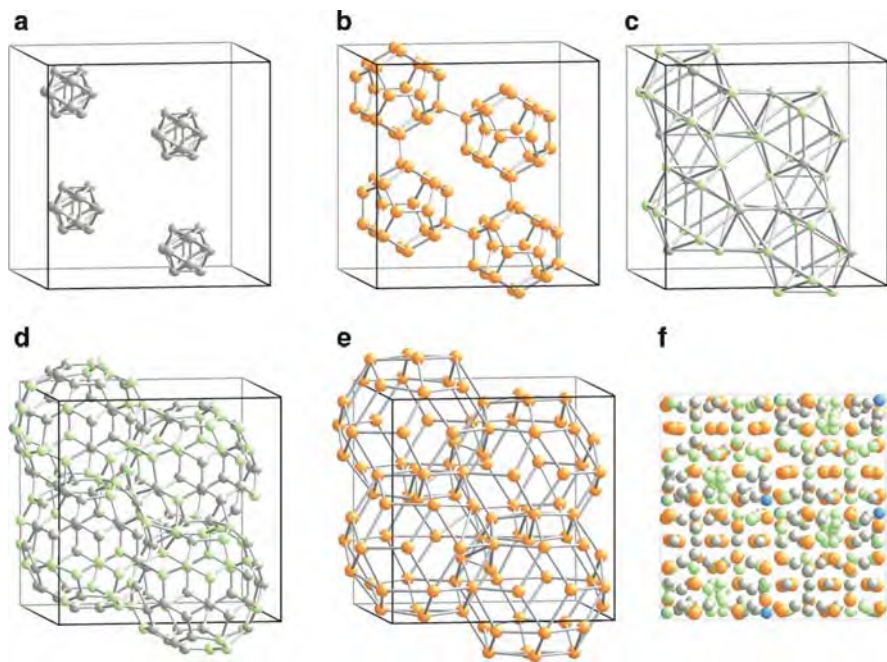
Fig. 9.6. Shells of the characteristic cluster in a 2/1-approximant as an example of cubic $Zn_{47.3}Mg_{27}Al_{10.7}$ ($a = 23.035\,\text{Å}$, $Pa\bar{3}$, [57]). (**a**) Zn_{12} icosahedron (edge length $a_r = 2.633$–$2.700\,\text{Å}$, $\varnothing = 5.083\,\text{Å}$); (**b**) Mg_{20} dodecahedron ($a_r = 3.254$–$3.322\,\text{Å}$, diameter $\varnothing = 9.235\,\text{Å}$) linked to the neighboring cluster via two atoms with a distance of $3.176\,\text{Å}$; (**c**) $(Zn_{0.75}, Al_{0.25})_{12}$ icosahedron ($a_r = 5.187$–$5.573\,\text{Å}$, $\varnothing = 10.191\,\text{Å}$) linked to the neighboring cluster via an octahedron ($a_r = 5.310$–$5.573\,\text{Å}$); (**d**) distorted $(Zn_{0.768}, Al_{208})_{60}$ fullerene shell ($a_r = 2.648$–$3.225\,\text{Å}$, $\varnothing = 13.960\,\text{Å}$) connected via a hexagon face to the neighboring cluster; (**e**) distorted Mg_{32} triacontahedron ($a_r = 4.692$–$5.616\,\text{Å}$, $\varnothing = 16.553\,\text{Å}$) sharing oblate rhombohedra with the overlapping other clusters; (**f**) projection of one unit cell along [100]

9.3 Tsai-Cluster-Based Icosahedral Phases (Type C)

The Tsai-cluster-based icosahedral quasicrystals are the latest class of quasicrystals discovered so far [35]. The peculiarity of these quasicrystals is that they can exist as stable binary phases in the systems Cd–Ca and Cd–Yb. This not only has the advantage that its chemical order can be more easily determined by X-ray structure analysis than in the case of ternary systems. It also means that chemical disorder, and the entropy gain related to it, is not a necessary ingredient of quasiperiodicity. A list of stable icosahedral phases of this type and their approximants is given in Tables. 9.3 and 9.4.

The 1/1-approximants of Tsai-type icosahedral quasicrystals contain a *bcc* packing of Tsai clusters. The structure of the Tsai cluster will be discussed as
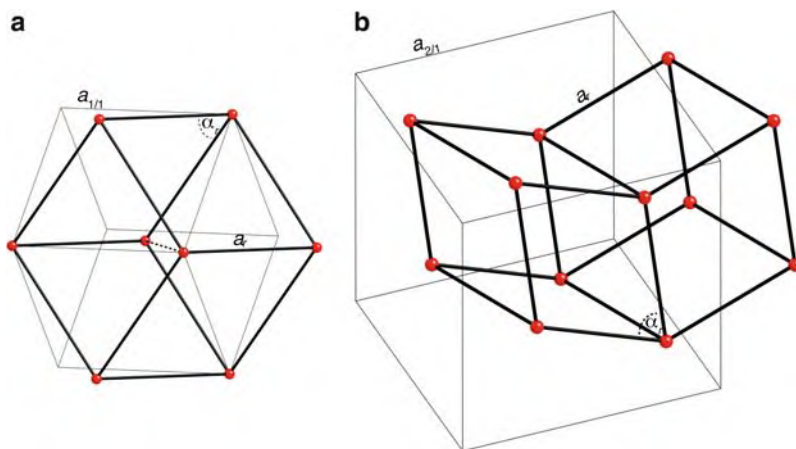
Fig. 9.7. Positions of the cluster centers in the cubic 1/1- and 2/1-approximants (marked by red spheres) forming the vertices of oblate and prolate rhombohedra. The cluster centers form a tiling of oblate rhombohedra in case of the 1/1-approximant (**a**), and one of alternating oblate and prolate rhombohedra in the case of the 2/1-approximant (**b**). The cluster centers occupy the sites 0 0 0 and 1/2 1/2 1/2 in the unit cell shown in (**a**) and 0.15 0.15 0.15, 0.35 0.85 0.65, 0.65 0.35 0.85, 0.85 0.65 0.35, 0.85 0.85 0.85, 0.65 0.15 0.35, 0.35 0.65 0.15, 0.15 0.35 0.65, in (**b**)

an example of Cd_6Yb [29, 72] (Fig. 9.8). The *bcc* unit cell (space group $Im\bar{3}$, $a = 15.661$ Å) contains 168 atoms. The structure can be described as packing of 158-atom triacontahedral clusters, which share one rhomb face along the [100] directions and an oblate rhombohedron along [111] (see also Fig. 2.5b).

The first cluster shell is an orientationally disordered Cd tetrahedron. The electron density is distributed along the edges of a truncated cube (Fig. 9.8a). It is surrounded by a Cd dodecahedron, followed by an Yb icosahedron. The triangle faces of the Yb icosahedra form octahedra along [111] directions. The fourth cluster shell is a Cd icosidodecahedron, which is surrounded by a unit-cell filling distorted edge-centered triacontahedron (Fig. 9.8e). Of the 92 Cd atoms of the triacontahedral shell, 8 atoms are also part of the dodecahedral shell and 24 of the icosidodecahedral shell. The 48 atoms located on the unit cell faces contribute only one half, i.e. 24 atoms, to the unit cell. This means that the triacontahedral shell only contributes 36 atoms to the 168 atom unit cell. The kind of disorder of the central tetrahedron depends on the chemical composition [29].

The cluster structure of the 2/1-approximant of the Tsai-type icosahedral phase is shown on the example of cubic $Cd_{76}Cd_{13}$ (Fig. 9.9) [28]. The triacontahedral clusters decorate the vertices of a rhombohedron ($a_r = 13.646$ Å, $\alpha = 69.83°$), which is close to the obtuse rhombohedron, one of the two prototiles of the Ammann tiling. Along the edges of the rhombohedra, the clusters overlap forming oblate rhombohedra. Along the short body diagonal

Table 9.3. Stable Tsai-type icosahedral quasicrystals as a function of the Penrose rhombohedron edge length a_r. The structures are ordered with increasing quasilattice parameter

Nominal composition	a_r [Å]	6D/3D-Space group	References
$Cu_{48}Sc_{15}Ga_{34}Mg_3$	4.906		[45]
$Cu_{46}Sc_{16}Al_{38}$	4.921		[41]
$Zn_{84}Ti_8Mg_8$	4.966		[43]
$Zn_{75}Sc_{15}Ni_{10}$	4.981		[63]
$Zn_{72}Sc_{16}Cu_{12}$	4.996		[56]
$Zn_{75}Sc_{15}Co_{10}$	4.994		[63]
$Zn_{75}Sc_{15}Fe_{10}$	5.008		[63]
$Zn_{75}Sc_{15}Mn_{10}$	5.025		[63]
$Zn_{80}Sc_{15}Mg_5$	5.028	$Pm\bar{3}\bar{5}$	[44]
$Zn_{75}Sc_{15}Pt_{10}$	5.029		[47]
$Zn_{75}Sc_{15}Pd_{10}$	5.030		[47]
$Zn_{75}Sc_{15}Au_{10}$	5.057		[47]
$Zn_{75}Sc_{15}Ag_{10}$	5.054		[47]
$Zn_{77}Sc_8Ho_8Fe_7$	5.066		[47]
$Zn_{77}Sc_8Er_8Fe_7$	5.070		[47]
$Zn_{77}Sc_7Tm_9Fe_7$	5.067		[47]
$Zn_{56.8}Er_{8.7}Mg_{34.6}$	5.18	$Fm\bar{3}\bar{5}$	[25, 69, 96]
$Zn_{76}Yb_{14}Mg_{10}$	5.211		[63]
$Cd_{65}Mg_{20}Lu_{15}$	5.571		[36]
$Ag_{42}In_{42}Yb_{16}$	5.590	$Pm\bar{3}\bar{5}$	[37]
$Cd_{65}Mg_{20}Tm_{15}$	5.602		[36]
$Ag_{42}In_{42}Ca_{16}$	5.606	$Pm\bar{3}\bar{5}$	[37]
$Au_{44.2}In_{41.7}Ca_{14.1}$		$Pm\bar{3}\bar{5}$	[58]
$Cd_{65}Mg_{20}Y_{15}$	5.606	$Pm\bar{3}\bar{5}$	[36]
$Cd_{65}Mg_{20}Er_{15}$	5.622	$Fm\bar{3}\bar{5}$	[36]
$Cd_{65}Mg_{20}Ho_{15}$	5.625	$Fm\bar{3}\bar{5}$	[36]
$Cd_{65}Mg_{20}Tb_{15}$	5.628	$Fm\bar{3}\bar{5}$	[36]
$Cd_{65}Mg_{20}Dy_{15}$	5.628	$Fm\bar{3}\bar{5}$	[36]
$Cd_{65}Mg_{20}Gd_{15}$	5.648		[36]
$Cd_{84}Yb_{16}$	5.689	$Pm\bar{3}\bar{5}$	[106]
$Cd_{65}Mg_{20}Yb_{15}$	5.727		[35, 36]
$Cd_{85}Ca_{15}$	5.731		[35]
$Cd_{65}Mg_{20}Ca_{15}$	5.731	$Pm\bar{3}\bar{5}$	[35, 36]

they share a rhombohedron face. The rhombohedra are packed in a zigzag manner. The Cd atoms around the center of such a rhombohedron leave a space in the form of a double Friauf polyhedron occupied by two Ca atoms along the long body diagonal, 3.567 Å apart.

The structure of i-$Cd_{5.7}Yb$ can be described as 3D Penrose rhomb tiling decorated by triacontahedral clusters as depicted in Fig. 9.9d [106]. This decoration covers 93.8% of all atoms. The remaining gaps are filled by different

Table 9.4. Stable approximants based on the Tsai-cluster. All compounds not explicitly marked 2/1- are 1/1-approximants. The structures are ordered with increasing lattice parameter

Nominal composition	Lattice parameter [Å]	Space group	References
$Be_{17}Ru_3$	11.337		[83]
$Ga_{3.85}Ni_{2.15}Hf$	13.319		[65]
$Ga_{3.22}Ni_{2.78}Zr$	13.374		[65]
$Ga_{3.64}Ni_{2.36}Sc$	13.440		[65]
$Ga_{2.3}Cu_{3.7}Sc$	13.472		[65]
$Ga_{2.6}Cu_{3.4}Lu$	13.745		[66]
$Zn_{17}Sc_3$	13.843		[1]
$Zn_{17}Yb_3$	14.291		[11]
$Ag_{42.5}Ga_{42.5}Yb_{15}$	14.707		[46]
$Au_{50.5}Ga_{35.9}Ca_{13.6}$	14.731	$Im\bar{3}$	[59]
$Au_{61.2}Sn_{23.9}Dy_{15.2}$	14.90		[68]
Au-Sn-Tb	14.91		[68]
$Au_{62.3}Sn_{23.1}Gd_{14.6}$	14.97		[68]
$Ag_{42.2}In_{42.6}Tm_{15.2}$	15.05		[68]
$Au_{47.2}In_{37.2}Gd_{15.6}$	15.07		[68]
$Au_{12.2}In_{6.3}Ca_3$	15.152	$Im\bar{3}$	[58]
$Au_{64.2}Sn_{21.3}Pr_{14.5}$	15.16		[68]
$Au_{65}Sn_{20}Ce_{15}$	15.190	$Im\bar{3}$	[48]
$Ag_{46.4}In_{39.7}Gd_{13.9}$	15.21		[68]
$Au_{49.7}In_{35.4}Ce_{14.9}$	15.28		[68]
$Au_{60.7}Sn_{25.2}Eu_{14.1}$	15.35		[68]
Ag_2In_4Yb	15.362	$Im\bar{3}$	[105]
$Ag_{46.9}In_{38.7}Pr_{14.4}$	15.39		[68]
$Au_{42}In_{42}Yb_{16}$	15.4	$Ia\bar{3}$	[95]
Cd_6Gd	15.441	$Im\bar{3}$	[29]
Ag_2In_4Ca	15.454	$Im\bar{3}$	[105]
$Ag_{47.7}In_{38.7}Ce_{14.2}$	15.46		[68]
Cd_6Dy	15.462	$Im\bar{3}$	[29]
Cd_6Y	15.482		[29, 54]
Cd_6Sm	15.589	$Im\bar{3}$	[29]
Cd_6Nd	15.605	$Im\bar{3}$	[29]
Cd_6Yb	15.661	$Im\bar{3}$	[29, 72]
$Ag_{42.9}In_{43.6}Eu_{13.5}$	15.69		[68]
Cd_6Ca	15.702	$Im\bar{3}$	[10, 29]
$Cd_{25}Eu$[a]	2×15.936	$Fd\bar{3}$	[30]
$Cd_{19}Pr_3$	15.955	$Im\bar{3}$	[29]
Cd_6Sr	16.044		[10]
$2/1\text{-}Au_{61.1}Ga_{25.0}Ca_{13.9}$	23.938	$Pa\bar{3}$	[59]
$2/1\text{-}Au_{60.3}Sn_{24.6}Yb_{15.1}$	24.28		[68]
$2/1\text{-}Au_{61.2}Sn_{24.3}Ca_{14.5}$	24.37		[68]
$2/1\text{-}Au_{42.9}In_{41.9}Yb_{15.2}$	24.63	$Pa\bar{3}$	[68]
$2/1\text{-}Au_{37}In_{39.6}Ca_{12.6}$	24.632	$Pa\bar{3}$	[58]
$2/1\text{-}Ag_{41.7}In_{43.2}Yb_{15.1}$	24.869	$Pa\bar{3}$	[55]

(continued)

Table 9.4. (continued)

Nominal composition	Lattice parameter [Å]	Space group	References
2/1-$Au_{61.2}Sn_{24.5}Eu_{14.3}$	24.87		[68]
2/1-$Ag_{41}In_{44}Yb_{15}$	24.88		[68]
2/1-$Ag_{42}In_{45}Ca_{13}$	24.96	$Pa\bar{3}$	[15]
2/1-$Cd_{76}Ca_{13}$	25.339	$Pa\bar{3}$	[28]
2/1-$Ag_{43.4}In_{42.8}Eu_{13.8}$	25.35	$Pa\bar{3}$	[68]

[a] $2 \times 2 \times 2$ Superstructure of a 1/1-approximant
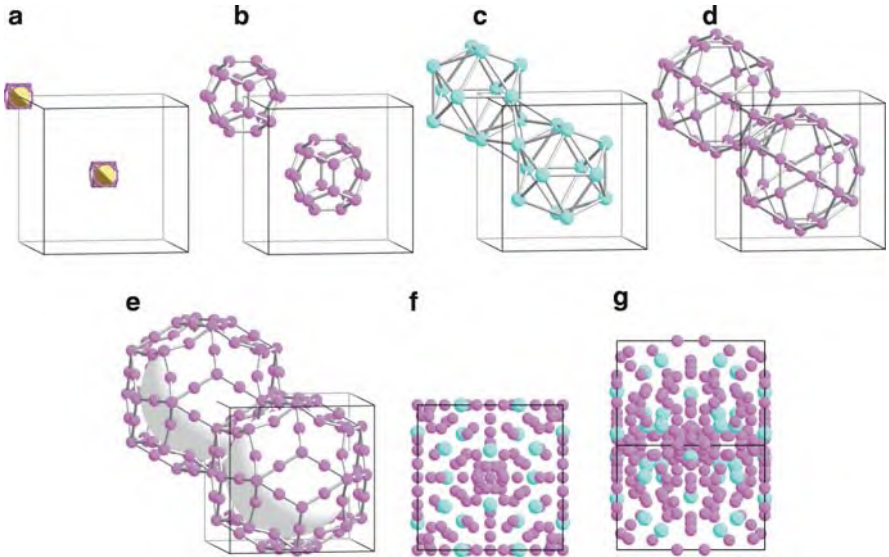
Fig. 9.8. Shells of the Tsai cluster as an example of *bcc* Cd_6Yb, a 1/1-approximant of *i*-$Cd_{5.7}Yb$ [29]. (**a**) Cd_4 tetrahedron (edge length $a_r = 3.229$ Å, diameter $\emptyset = 3.954$ Å), which is orientationally disordered. The averaged electron density is smeared along the edges of an truncated cube; (**b**) Cd_{20} pentagondodecahedron ($a_r = 2.90$–3.027 Å, $\emptyset = 8.049$ Å); (**c**) Yb_{12} icosahedron ($a_r = 5.817$–5.875 Å, $\emptyset = 11.087$ Å); (**d**) Cd_{30} icosidodecahedron ($a_r = 3.644$–4.384 Å, $\emptyset = 12.765$ Å); (**e**) Cd_{92} distorted, edge-centered triacontahedron ($a_r = 2.836 - 3.075$ Å, $\emptyset = 18.473$ Å). The triacontahedra are face-connected along the [100] directions and share an oblate rhombohedron along [111] (see also Fig. 2.5(b)). The projections of one unit cell along [100] and [110] are shown in (**f**) and (**g**)

arrangements of acute and oblate rhombohedral tiles. The acute rhombohedron corresponds to a double Friauf polyhedron with two Yb along its long diagonal and Cd on the vertices. The oblate rhombohedron is decorated by Cd on the vertices and edge centers. The distortion of the cluster shells,
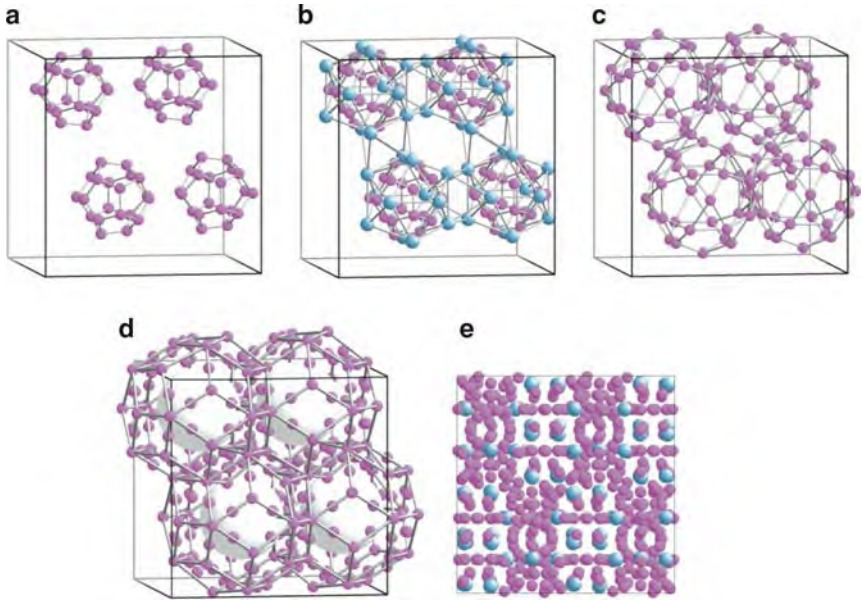
Fig. 9.9. Shells of the Tsai-cluster in a 2/1-approximant as an example of cubic $Cd_{76}Ca_{13}$ (a = 25.339 Å, $Pa\bar{3}$, [28]). (**a**) Cd_{20} dodecahedron (edge length a_r = 2.928–3.076 Å, diameter Ø = 8.541 Å) enclosing an orientationally disordered Cd_4 tetrahedron similar to the 1/1-approximant; (**b**) Ca_{12} icosahedron (a_r = 5.800–5.861 Å, Ø = 11.131 Å); (**c**) distorted Cd_{30} icosidodecahedron (a_r = 3.567–4.461 Å, Ø = 12.899 Å) connected via a trigonal antiprism octahedron to the neighboring cluster; (**d**) Cd_{80} decorated triacontahedron (a_r = 2.815–3.094 Å, Ø = 18.508 Å) sharing oblate rhombohedra with the overlapping other clusters; (**e**) Projection of one unit cell along [100]

particularly of the icosidodecahedral one, is comparable to that of the 2/1-approximant. The structure shows τ^3 scaling symmetry. It is noteworthy that the structure cannot be described as a 3D Penrose tiling with uniquely decorated unit tiles while the decorating clusters have a unique structure.

9.4 Example: Icosahedral Al–Cu–Fe

In the following, the structure of an icosahedral quasicrystal will be discussed as an example of an ideal model (QG model) suggested by Quiquandon and Gratias [79] for the type A quasicrystal in the system Al–Cu–Fe. Its 6D space group is $Fm\bar{3}\bar{5}$. A section of the structure is shown in Fig. 9.10.

The fundamental B, B', and M clusters are indicated by one of their cluster shells in each case. These clusters are defined as follows [79]:
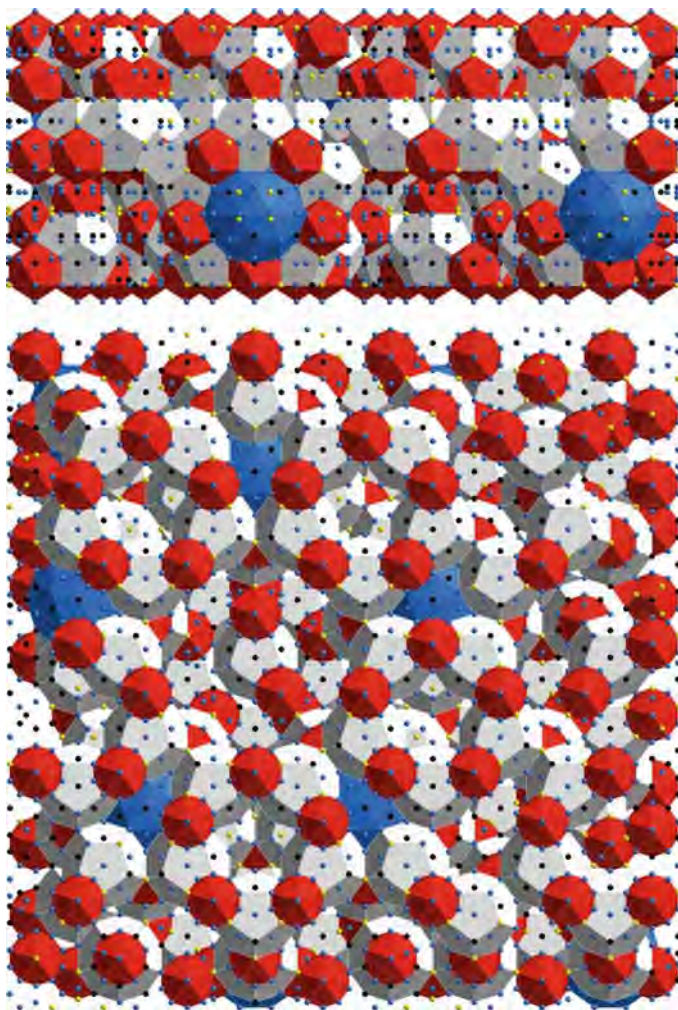
Fig. 9.10. Approximately $63 \times 63 \times 28$ Å^3 large section of i-Al–Cu–Fe according to the QG model [79]. Projections along a twofold (*top*) and a fivefold (*bottom*) direction are shown. The dark-gray (online: *red*) icosahedra are part of the B clusters, the *light-gray* dodecahedra of the B' clusters, and the (online: *blue*) icosidodecahedra of the M clusters. Atoms: Al...*dark-gray*, (online: *blue*), Cu...*black*, Fe...*light-gray*, (online: *yellow*)

M **cluster** A central Al atom is surrounded by a partially occupied dodeca-
hedron, $r = 2.513$ Å, (7 Fe atoms on 20 sites), then by a an icosahedron,
$r = 4.465$ Å, of Cu, followed by an Al icosidodecahedron, $r = 4.695$ Å.
The cluster consists of 50 atoms in total.

B **cluster** A central Cu atom is surrounded by an icosahedron, $r = 2.760$ Å, of Fe/Al, followed by an dodecahedron, $r = 4.066$ Å, of Cu/Fe. The cluster consists of 33 atoms in total.

B′ **cluster** Around an empty center, there is a first partially occupied icosahedron, $r = 1.706$ Å, (3 Al atoms on 12 sites) completed by a second partially occupied icosahedron, $r = 2.760$ Å, (9 Al/Cu atoms on 12 sites) followed by an Al/Cu/Fe dodecahedron, $r = 4.066$ Å. The cluster consists of 33 atoms in total.

The chemical composition of the cluster shells is complex and is described in detail in [79].

The 6D hypercrystal structure can be best visualized with characteristic sections along the rotation planes. In case of a rotation in 6D, not only a line (rotation axis) as in 3D, but a 2D plane (rotation plane) remains invariant as can be seen from the block-diagonalized rotation matrix (3.200). A 6D hypercubic structure shows 6 fivefold, 10 threefold and 15 twofold rotation planes. 6D space sections of the structure of icosahedral Al–Cu–Fe along the three different rotation planes are shown in Fig. 9.11.

The vectors **N** spanning these planes remain invariant under the action of the respective symmetry matrices given in (3.198). The section inside one unit cell is shaded gray. Note that the unit cell and the indices refer to the 6D *F*-centered hyperlattice ($a^{6D} = 12.6292$ Å) and not, as frequently done, to the subcell (sublattice) with half the edge length. With reference to this sublattice, frequently the sublattice nodes are classified as even or odd. This refers to the sum of the six corresponding coordinates of the respective sublattice nodes [7]. The basis that spans the 6D lattice is given by

$$
D = \frac{A}{\sqrt{5 + \sqrt{5}}}
\begin{pmatrix}
1 & \tau & 0 & -\tau & 1 & 0 \\
\tau & 0 & 1 & 1 & 0 & -\tau \\
0 & 1 & \tau & 0 & -\tau & 1 \\
-1 & \tau & 0 & \tau & 1 & 0 \\
\tau & 0 & -1 & 1 & 0 & \tau \\
0 & -1 & \tau & 0 & \tau & 1
\end{pmatrix}_V ,
\tag{9.1}
$$

where A is the unit cell edge length of the hyperlattice.

The atomic surfaces (Fig. 9.13) are 3D polyhedra in perp-space and appear as lines in the sections shown in (Fig. 9.11). These sections are spanned by one par- and one perp-space basis vector, $\mathbf{N}^{\parallel}$ and $\mathbf{N}^{\perp}$, respectively. N stands for an N-fold rotation axis, $\mathbf{N}^{\parallel}$ and $\mathbf{N}^{\perp}$ means their par- and perp-space components. The atomic surfaces occupy (a) corners plus face centers, also denoted as even nodes n of the sublattice, (b) edge centers, also called odd nodes n, (c) body centers of half of the eight cubes, also called odd body centers bc. The structure can be seen as 6D analog of the 3D cF-12 LiAlSi-structure type (Fig. 9.12). The differently shaded areas (bounded by horizontal lines) between the atomic surfaces mark neighboring atomic positions.
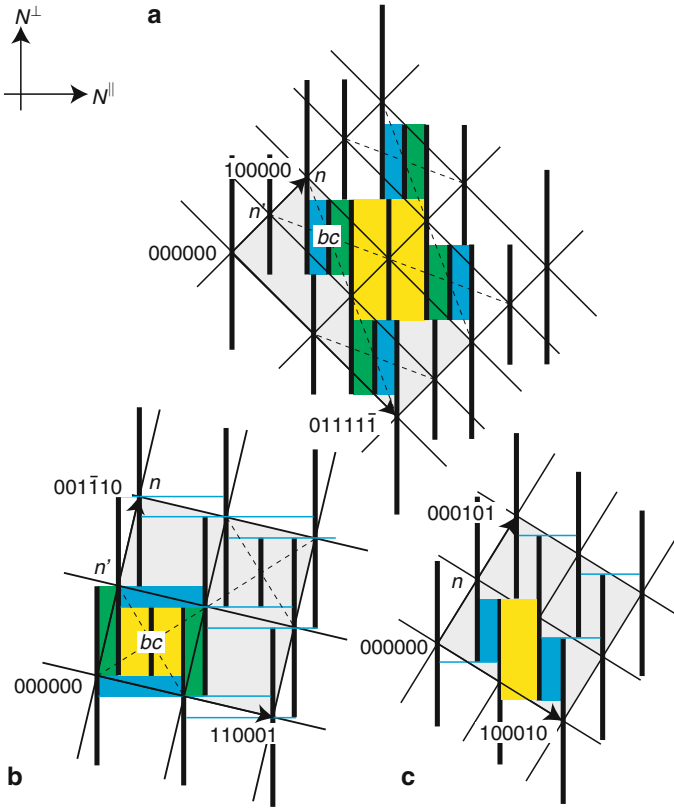
Fig. 9.11. 2D sections of the 6D unit cell of icosahedral Al–Cu–Fe/Al–Mn–Pd according to the QG model [79]. (**a**) Fivefold section spanned by one fivefold axis along par-space (horizontally) and one along perp-space (vertically). In (**b**) and (**c**) the threefold and twofold sections are shown correspondingly. The par-space components of the rotation axes run horizontally, the perp-space ones vertically. Indices refer to the 6D F-centered lattice with lattice parameter $a^{6D} = 12.6292$ Å
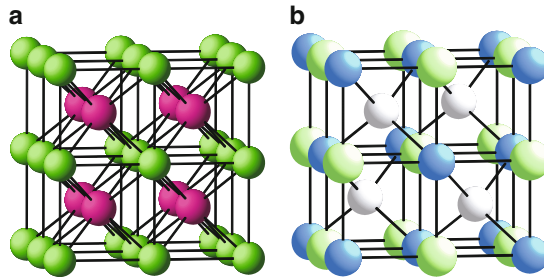
Fig. 9.12. (**a**) CsCl and (**b**) LiAlSi structure. The latter can be seen as superstructure of the former. This is the 3D analog to the 6D Al–Cu–Fe-type structure, where the sites n, n', and half of the body centers bc are occupied by the atomic surfaces shown in Fig. 9.13
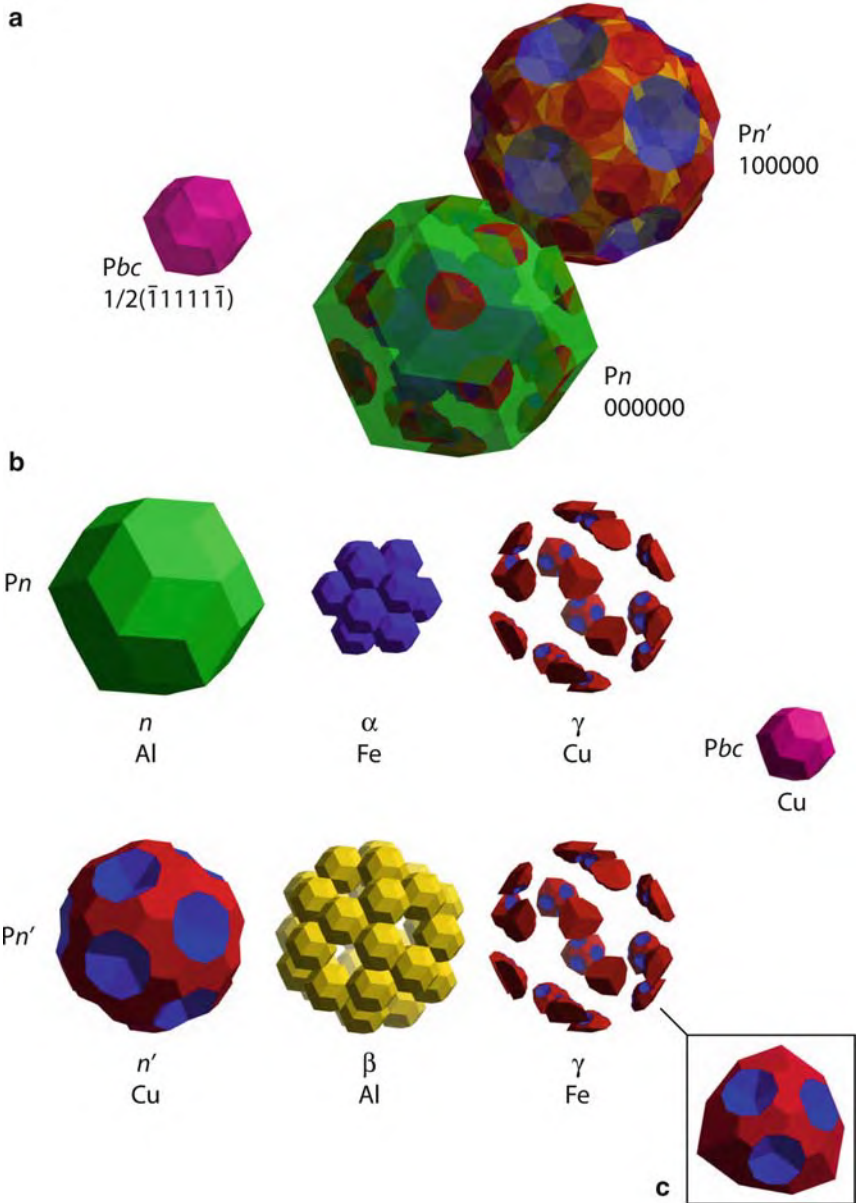
Fig. 9.13. Atomic surfaces and their substructure according to the QG model [79] of i-Al–Cu–Fe. (**a**) shows the atomic surfaces with their chemical decoration in relation to each other. Indices refer to the sublattice nodes. The original basis with 6D lattice parameter $a^{6D} = 6.3146$ Å has been scaled by a factor τ^{-3} and the atomic surfaces by a factor τ^{-6}. The resulting quasiperiodic structure is invariant under this scaling, which has the advantage that the truncation of Pn' by Pn can be visualized within one unit cell. (**b**) shows the decomposition of the atomic surfaces in chemical occupation domains. One of the polyhedra from γ is shown enlarged in (**c**)

The polyhedral atomic surfaces and their chemical decoration are shown in Fig. 9.13. In order to visualize the closeness condition on neighboring polyhedra, a basis is chosen scaled by a factor τ^{-3}, which corresponds to a scaling of the atomic surfaces by a factor τ^{-6}. The atomic coordinates, generated by a cut of the hypercrystal with par-space remain unchanged thereby.

The polytope, Pn, occupying the even nodes of the sublattice is a triacontahedron. It can be defined by one triangular facet, given by the orthogonal projection of a, b, and c upon perp-space. $a = (-1\ -1\ 1\ 1\ 3\ 1)/2$, $b = (0\ -2\ 1\ 0\ 2\ 1)/2$, and $c = (0\ -1\ 1\ 0\ 1\ 0)$ refer to the sublattice. Pn' is a truncated triacontahedron of the same size and the truncation is given by the cut with Pn (see Fig. 9.13(a)). Pbc is a triacontahedron with an outer radius, which is by a factor τ^2 smaller than Pn. Pbc is fully occupied by Cu.

The chemical decoration of all three atomic surfaces can be seen in Fig. 9.13 as well. Pn is occupied by Al except for the regions within Pn which are denoted α (Fe) and γ (Cu) in Fig. 9.13(b). α consists of 12 triacontahedra with an outer radius by a factor τ^3 smaller than Pn. The 12 triacontahedra, with their centers on the vertices of an icosahedron, are touching each other. One of these positions is at the perp-space projection of $\tau^{-4}(-1\ 1\ 1\ 1\ 1\ -1)/2$. They are located on the fivefold axes of Pn.

β consists of 30 triacontahedra of the same size as in α. They are also touching each other and their centers build an icosidodecahedron. If β is constructed with its barycenter at the origin of the lattice before shifting it to the position of Pn', one of the centers is given by the perp-space projection of $\tau^{-2}(1\ 1\ 0\ 0\ 0\ 0)$.

γ consists of 20 more complex polyhedra, which result by the cut of triacontahedra of the same size as in α with Pn' (or Pn) and β. The centers of the triacontahedra lie on the corners of Pn' along the threefold axes and they build a dodecahedron. After the cut with Pn' the centers become therefore corners of the new polyhedra, which are truncated by β. An enlarged view of one of the polyhedra, where the truncation can be seen, is given in Fig. 9.13c.

The periodic average structure can be obtained by oblique projection of the 6D hypercrystal structure onto the physical space (Fig. 9.14). It is congruent to the infinite 3D quasiperiodic structure module of the unit cell of the periodic average structure.

9.5 Surface Structures of Icosahedral Phases

Surface studies have been performed so far on i-Al–Cu–Fe, i-Al–Cu–Ru, i-Al–Mn–Pd and its approximant, ξ'-Al–Mn–Pd [27], as well as on i-Ag–In–Yb [86]. These are the only icosahedral quasicrystals which could be grown in the size needed and do not have a too high vapor pressure in ultra-high vacuum (UHV). The main result is that the surface structures of these quasicrystals are essentially unreconstructed and that termination takes place where atomic
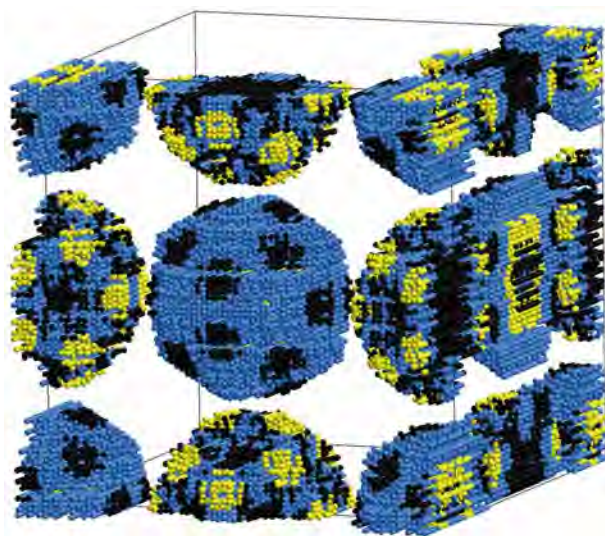
Fig. 9.14. One unit cell of the *fcc* periodic average structure of the QG model [79], which is of the NaCl-type. The chemical decoration of the atomic surfaces is still visible after the oblique projection (Al ... *gray*, online: *blue*, Cu ... *black*, Fe ... *light-gray*, online: *yellow*)

layers are separated by larger gaps. For a review of the structure of quasicrystal surfaces and overlayers see [88]. In the following, a few examples are briefly discussed for illustration.

The first i-phase studied by high-resolution STM was i-$Al_{68}Mn_{23}Pd_9$ [84], since this was the first quasicrystal for which large and high-quality single-crystals were available. A terraced surface structure was found in agreement with 3D quasiperiodic long-range order. A quantitative LEED study of the fivefold surface found that terminating layers are Al rich and that the spacing between the two topmost layers (Al/Mn-Al/Pd double-layer) is contracted by 0.1 Å to 0.38 Å [26] (Fig. 9.15). The 2D density of these double-layers, which could also be seen as a single puckered layer, amounts to 0.136 atoms/$Å^2$ compared with 0.141 atoms/$Å^2$ for one layer of the close packed Al(111) surface.

The first surface study of i-Al–Cu–Fe appeared shortly after the first large single crystals could be grown [89]. The fivefold surfaces of i-Al–Cu–Ru, i-Al–Cu–Fe, and i-Al–Mn–Pd are essentially isostructural like the bulk structures [85, 87, 92].

Ab initio calculations on a 2/1 approximant confirm that the fivefold surface of i-Al–Mn–Pd is essentially stable in its unreconstructed form [52]. While the skeleton of the underlying pentagon tiling formed by Pd atoms was found to be stable, Al atoms undergo partially substantial displacements. It is remarkable that the surface seems to have a much more metallic character than the bulk, which shows a significant degree of covalent Al–TM bonding.
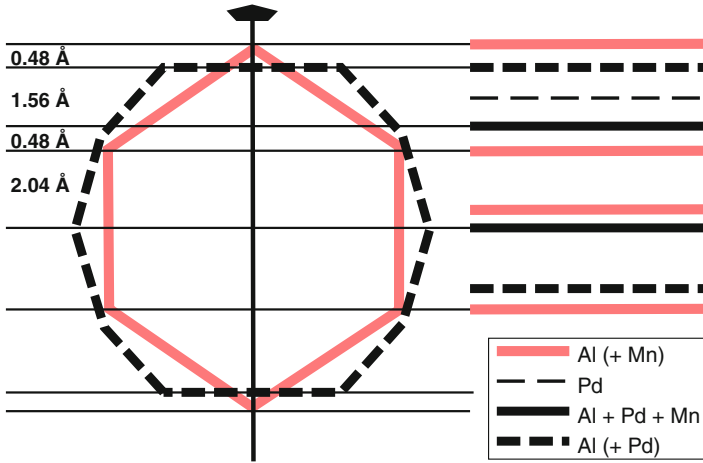
Fig. 9.15. Pseudo-Mackay-icosahedron (PMI) and the layer structure of i-Al–Mn–Pd. The topmost layer is one of the terminating planes (after [26])
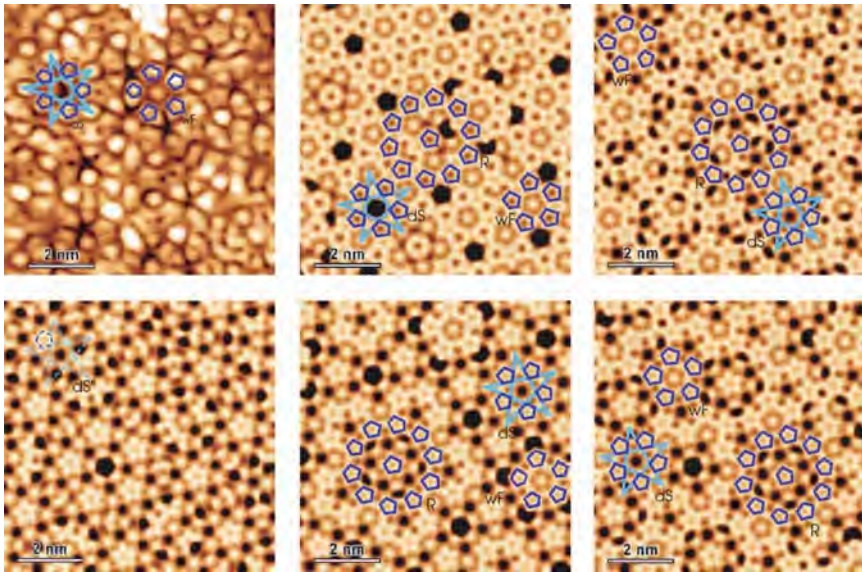
Fig. 9.16. (*upper left*) STM image of the fivefold surface of i-AlPdMn, with the marked representative fivefold symmetric local configurations 'dark star' (dS) and the 'white flower' (wF). The other images present STM simulations performed on different candidates for the terminations. The same local configurations were observed on the STM images of the fivefold surface of i-AlCuFe as well (from [76])

However, one must keep in mind that the ab initio calculations have been performed on a rather small approximant and a rather thin slab simulating a surface and do not necessarily reflect the influence of quasiperiodic long-range order.

Attempts to identify the termination planes by relating experimental STM images to atomic layers of bulk structure models (Fig. 9.16) have been only partially successful [73–76]. The bulk structure models used do not seem to be good enough to describe the local surface structure in all its details, atomic positions, and chemistry. One of the essential findings is that Bravais' rule, saying that the densest atomic layers in the bulk are the stablest surface terminations, applies to quasicrystals as well. It only has to be extended to "thick layers of atomic planes" in case of not densely packed single atomic layers. This is, of course, not only true for quasicrystals but also for intermetallics with open structures in general.

The corrugation of a cleaved surface of i-$Al_{70.5}Mn_{8.5}Pd_{21}$ was first explained resulting from crack propagation around mechanically stable clusters [20]. Later, the images from the underlying experiments have been reinterpreted. The observed roughness was shown to "follow scaling invariance properties similar to those of disordered materials, irrespective of the cleavage plane" [77].

References

1. R.I. Andrusyak, B.Y. Kotur, V.E. Zavodnik, Crystal-structure of Sc_3Zn_{17}. Kristallografiya **34**, 996–998 (1989)
2. T. Asao, R. Tamura, S. Takeuchi, New stable icosahedral phases in Al-Pd-Ru and Al-Pd-Os systems. Philos. Mag. Lett. **82**, 217–223 (2002)
3. M. Audier, J. Pannetier, C. Janot, M. Leblanc, J.M. Lang, B. Dubost, An Approach to the Structure of Quasicrystals. A Single Crystal X-Ray and Neutron Diffraction Study of the R-Al_5CuLi_3 Phase. Physica B **153**, 136–142 (1988)
4. M.D. Ball, D.J. Lloyd, Particles apparently exhibiting fivefold symmetry in Al-Li-Cu-Mg alloys. Scr. Metall. **19**, 1065–1068 (1985)
5. G. Bergman, J.L.T. Waugh, L. Pauling, The Crystal Structure of the Metallic Phase $Mg_{32}(Al, Zn)$. Acta Crystallogr. **10**, 254–259 (1957)
6. M. Boudard, M. Deboissieu, C. Janot, J.M. Dubois, C. Dong, The Structure of the Icosahedral AlPdMn Quasi-Crystal. Philos. Mag. Lett. **64**, 197–206 (1991)
7. M. Boudard, M. Deboissieu, C. Janot, G. Heger, C. Beeli, H.U. Nissen, H. Vincent, R. Ibberson, M. Audier, J.M. Dubois, Neutron and X-Ray Single-Crystal Study of the Alpdmn Icosahedral Phase. J. Phys.-Condens. Matter **4**, 10149–10168 (1992)
8. A.J. Bradley, H.J. Goldschmidt, An X-ray study of slowly-cooled iron-copper-aluminium alloys. Part II.-Alloys rich in aluminium. J. Inst. Met. **65**, 195–210 (1939)
9. S. Brühne, E. Uhrig, G. Kreiner, W. Assmus: Local atomic three-dimensional real-space structural analysis of icosahedral Mg-Zn-RE (RE = Y or Ho) alloys: Strategy, method and models. Philos. Mag. **86**, 463–468 (2006)

10. G. Bruzzone, Ca-Cd and Ba-Cd Systems. Gaz. Chim. Ital. **102**, 234–242 (1972)
11. G. Bruzzone, M.L. Fornasini, F. Merlo, Rare-earth intermediate phases with zinc. J. Less-Comm. Met. **22**, 253–264 (1970)
12. H.S. Chen, A. Inoue, Formation and Structure of New Quasi-Crystals of $Ga_{16}Mg_{32}Zn_{52}$ and $Al_{60}Si_{20}Cr_{20}$. Scr. Met. **21**, 527–530 (1987)
13. M. Cooper, K. Robinson, Crystal Structure of Ternary Alloy α(AlMnSi). Acta Crystallogr. **20**, 614–617 (1966)
14. G.T. De Laissardiere, D. Nguyen-Manh, D. Mayou, Electronic structure of complex Hume-Rothery phases and quasicrystals in transition metal aluminides. Progress in Materials Science **50**, 679–788 (2005)
15. B.B. Deng, K.H. Kuo, The 2/1 cubic approximant of the $Ag_{42}In_{42}Ca_{16}$ icosahedral quasicrystal. J. Alloy. Compd. **366**, L1–L5 (2004)
16. V.E. Dmitrienko, V.A. Chizhikov, Approximants of icosahedral quasicrystals: Atomic structure, inherent defects, and superstructural ordering. Crystallogr. Rep. **51**, 552–558 (2006)
17. V.E. Dmitrienko, V.A. Chizhikov, Distortions of the atomic structure of 2/1 approximants of icosahedral quasicrystals. Crystallogr. Rep. **52**, 1040–1047 (2007)
18. P. Donnadieu, M. Harmelin, H.L. Su, H.J. Seifert, G. Effenberg, F. Aldinger, A quasicrystal with inflation symmetry and no forbidden symmetry axes in a rapidly solidified Mg-Al alloy. Z. Metallkunde **88**, 33–37 (1997)
19. B. Dubost, J.M. Lang, M. Tanaka, P. Sainfort, M. Audier, Large AlCuLi Single Quasi-Crystals with Triacontahedral Solidification Morphology. Nature **324**, 48–50 (1986)
20. P. Ebert, M. Feuerbacher, N. Tamura, M. Wollgarten, K. Urban, Evidence for a cluster-based structure of AlPdMn single quasicrystals. Phys. Rev. Lett. **77**, 3827–3830 (1996)
21. K. Edagawa, Phonon-phason coupling in a Mg-Ga-Al-Zn icosahedral quasicrystal. Philos. Mag. Lett. **85**, 455–462 (2005)
22. F.J. Edler, V. Gramlich, W. Steurer, Structure and disorder phenomena of cubic $Al_{39}Fe_2Pd_{21}$ in comparison with related structures. J. Alloy. Compd. **269**, 7–12 (1998)
23. L. Elcoro, J.M. Perez-Mato, Cubic superspace symmetry and inflation rules in metastable MgAl alloy. Eur. Phys. J. B **7**, 85–89 (1999)
24. A.H. Fang, H.M. Zou, F.M. Yu, R.H. Wang, X.F. Duan, Structure refinement of the icosahedral AlPdMn quasicrystal using quantitative convergent beam electron diffraction and symmetry-adapted parameters. J. Phys.-Condes. Matter **15**, 4947–4960 (2003)
25. I.R. Fisher, Z. Islam, A.F. Panchula, K.O. Cheon, M.J. Kramer, P.C. Canfield, A.I. Goldman, Growth of large-grain R-Mg-Zn quasicrystals from the ternary melt (R = Y, Er, Ho, Dy, Tb). Philos. Mag. B **77**, 1601–1615 (1998)
26. M. Gierer, M.A. Vanhove, A.I. Goldman, Z. Shen, S.L. Chang, P.J. Pinhero, C.J. Jenks, J.W. Anderegg, C.M. Zhang, P.A. Thiel, Fivefold surface of quasicrystalline AlPdMn: Structure determination using low-energy-electron diffraction. Phys. Rev. B **57**, 7628–7641 (1998)
27. V. Fournee, A.R. Ross, T.A. Lograsso, J.W. Anderegg, C. Dong, M. Kramer, I.R. Fisher, P.C. Canfield, P.A. Thiel, Surface structures of approximant phases in the Al-Pd-Mn system. Phys. Rev. B **66**, art. no. 165423 (2002)

28. C.P. Gomez, S. Lidin, Structure of $Ca_{13}Cd_{76}$: A novel approximant to the $MCd_{5.7}$ quasicrystals (M = Ca, Yb). Angew. Chem. Int. Ed. **40**, 4037–4039 (2001)

29. C.P. Gomez, S. Lidin, Comparative structural study of the disordered MCd_6 quasicrystal approximants. Phys. Rev. B **68**, art. no. 024203 (2003)

30. C.P. Gomez, S. Lidin, Superstructure of Eu_4Cd_{25}: A quasicrystal approximant. Chem. Eur. J. **10**, 3279–3285 (2004)

31. C.P. Gomez, S. Ohhashi, A. Yamamoto, A.P. Tsai, Disordered structures of the TM-Mg-Zn 1/1 quasicrystal approximants (TM = Hf, Zr, or Ti) and chemical intergrowth. Inorg. Chem. **47**, 8258–8266 (2008)

32. D. Gratias, F. Puyraimond, M. Quiquandon, A. Katz, Atomic clusters in icosahedral F-type quasicrystals. Phys. Rev. B **63**, art. no. 024202 (2001)

33. B. Grushko, T.Y. Velikanova, Formation of quasicrystals and related structures in systems of aluminum with transition metals. II. Binary systems formed by aluminum with 4d and 5d metals. Powder Metall. Met. Ceram. **43**, 72–86 (2004)

34. B. Grushko, T.Y. Velikanova, Formation of quasicrystals and related structures in systems of aluminum with transition metals. II. Binary systems formed by aluminum with 4d and 5d metals. Powder Metall. Met. Ceram. **43**, 311–322 (2004)

35. J.Q. Guo, E. Abe, A.P. Tsai, Stable icosahedral quasicrystals in binary Cd-Ca and Cd-Yb systems. Phys. Rev. B **62**, R14605–R14608 (2000)

36. J.Q. Guo, E. Abe, A.P. Tsai, Stable quasicrystals in the Cd-based alloys. In: Quasicrystals–Preparation, Properties and Applications (eds. E. Belin-Ferre, P.A. Thiel, A-P. Tsai, K. Urban). MRS Proceedings Vol. 643, paper K2.7.1, Materials Research Society: Warrendale PA (2001)

37. J.Q. Guo, A.P. Tsai, Stable icosahedral quasicrystals in the Ag-In-Ca, Ag-In-Yb, Ag- In-Ca-Mg and Ag-In-Yb-Mg systems. Philos. Mag. Lett. **82**, 349–352 (2002)

38. H.K. Hardy, J.M. Silcock, The phase sections at 500C and 350C of aluminium-rich aluminium-copper-lithium alloys. J. Inst. Met. **84**, 423–428 (1956)

39. J. Hasegawa, S. Takeuchi, A.P. Tsai, Stable quasicrystals and approximants in Zn-Mg-Zr and Zn-Mg-Hf alloys. Philos. Mag. Lett. **85**, 289–297 (2005)

40. K. Hiraga, K. Sugiyama, Y. Ishii, Arrangement of atomic clusters in a 2/1 cubic approximant in the Al-Zn-Mg alloy system. Philos. Mag. Lett. **82**, 341–347 (2002)

41. T. Honma, T. Ishimasa, New icosahedral quasicrystals formed in Cu-based ternary alloys. Philos. Mag. **87**, 2721–2726 (2007)

42. T. Ishimasa, Superlattice Ordering in the Low-Temperature Icosahedral Phase of Al-Pd-Mn. Philos. Mag. Lett. **71**, 65–73 (1995)

43. T. Ishimasa, Y. Kaneko, H. Kaneko, A Zn-based icosahedral quasicrystal classified into the same structure type as Cd-based icosahedral quasicrystals? J. Alloy. Compd. **342**, 13–17 (2002)

44. Y. Kaneko, Y. Arichika, T. Ishimasa, Icosahedral quasicrystal in annealed Zn-Mg-Sc alloys. Philos. Mag. Lett. **81**, 777–787 (2001)

45. Y. Kaneko, R. Maezawa, H. Kaneko, T. Ishimasa, Cu-based icosahedral quasicrystal formed in Cu-Ga-Mg-Sc alloys. Philos. Mag. Lett. **82**, 483–493 (2002)

46. S. Kashimoto, R. Maezawa, Y. Kaneko, T. Ishimasa, Formation and structure of the icosahedral phase in the Ag-Ga-Yb alloy system. Meeting abstracts of the Physical Society of Japan **58**, 716 (2003)

47. S. Kashimoto, C. Masuda, S. Motomura, S. Matsuo, T. Ishimasa, Formation and magnetic properties of p-type icosahedral quasicrystals in Zn-Fe-Sc-L (L = Ho, Er, Tm) alloys. Philos. Mag. **87**, 2929–2937 (2007)

48. S. Kenzari, V. Demange, P. Boulet, M.C. De Weerd, J. Ledieu, J.M. Dubois, V. Fournee, Complex metallic alloys in the Ce-Au-Sn system: a study of the atomic and electronic structures. J. Phys.-Condes. Matter **20**, art. no. 095218 (2008)

49. K. Kirihara, K. Kimura, H. Ino, V.E. Dmitrienko, Structural analysis of Al-CuRu 1/0-cubic approximant, In *Proceedings of the 6th International Conference on Quasicrystals*, Tokyo, ed. by S. Takeuchi, T. Fujiwara, pp. 243–246, World Scientific Singapore (1998)

50. N. Koshikawa, S. Sakamoto, K. Edagawa, S. Takeuchi, New Stable Icosahedral Quasi-Crystal in Mg-Pd-Al System. Jap. J. Appl. Phys. Part 2-Lett. **31**, L966–L969 (1992)

51. A. Kounis, G. Miehe, K. Saitoh, H. Fuess, R. Sterzel, W. Assmus, Structure of a Zn-Mg-Er cubic phase and its relation to icosahedral phases. Philos. Mag. Lett. **81**, 395–403 (2001)

52. M. Krajci, J. Hafner, Structure, stability, and electronic properties of the i-AlPdMn quasicrystalline surface. Phys. Rev. B **71**, art. no. 054202 (2005)

53. G. Kreiner, Towards realistic quasiperiodic structures: modelling, synthesis and structure of $(Ga,Zn)_{175-\delta}Mg_{97+\delta}$ - a large 3/2-2/1-2/1 Fibonacci approximant. J. Alloy. Compd. **338**, 261–273 (2002)

54. A.C. Larson, D.T. Cromer, Crystal structure of YCd_6. Acta Crystallogr. B **27**, 1875–1879 (1971)

55. M.R. Li, S. Hovmoller, J.L. Sun, X.D. Zou, K.H. Kuo, Crystal structure of the 2/1 cubic approximant $Ag_{42}In_{42}Yb_{16}$. J. Alloy. Compd. **465**, 132–138 (2008)

56. Q.S. Lin, J.D. Corbett, New stable icosahedral quasicrystalline phase in the Sc-Cu-Zn system. Philos. Mag. Lett. **83**, 755–762 (2003)

57. Q.S. Lin, J.D.Corbett, New building blocks in the 2/1 crystalline approximant of a Bergman-type icosahedral quasicrystal. Proc. Natl. Acad. Sci. USA **103**, 13589–13594 (2006)

58. Q.S. Lin, J.D. Corbett, Development of the Ca-Au-In icosahedral quasicrystal and two crystalline approximants: Practice via pseudogap electronic tuning. J. Amer. Chem. Soc. **129**, 6789–6797 (2007)

59. Q.S. Lin, J.D. Corbett, Approximant phases and an icosahedral quasicrystal in the Ca-Au-Ga system: The influence of size of gallium versus indium. Inorg. Chem. **47**, 7651–7659 (2008)

60. L. Loreto, R. Farinato, S. Catallo, C. Janot, G. Gerbasi, Deangelis: Polyhedral, and chemical orders in icosahedral Al-Pd-Mn quasicrystals. Physica B **328**, 193–203 (2003)

61. Z. Luo, S. Zhang, Y. Tang, D. Zhao, Quasicrystals in as-cast Mg-Zn-RE alloys. Scr. Met. Mater. **28**, 1513–1518 (1993)

62. A.L. Mackay, A Dense Non-Crystallographic Packing of Equal Spheres. Acta Crystallogr. **15**, 916–918 (1962)

63. R. Maezawa, S. Kashimoto, T. Ishimasa, Icosahedral quasicrystals in Zn-T-Sc (T = Mn, Fe, Co or Ni) alloys. Philos. Mag. Lett. **84**, 215–223 (2004)

64. S. Mahne, W. Steurer, The crystal structure of the ternary alloy c-$Al_{68}Pd_{20}Ru_{12}$. Z. Kristallogr. **211**, 17–24 (1996)

65. V.Y. Markiv, N.N. Belyavina, New representatives of $YbCd_6$ and $MgCuAl_2$ structure types. Dop. Akad. Nauk. Ukr. RSR Ser. B **12**, 30–33 (1983)

66. V.Y. Markiv, I.P. Shevchenko, N.N. Belyavina, Phase-equilibria and crystalline structure of a compound in the Lu-Cu-Ga SYSTEM. Russ. Metall. **2**, 201–206 (1989)

67. M.N. Mikheeva, G.K. Panova, A.A. Teplov, M.N. Khlopin, N.A. Chernoplekov, A.A. Shikov, Thermodynamic and kinetic properties of an icosahedral quasicrystalline phase in the Al-Pd-Tc system. Phys. Sol. State **42**, 2177–2183 (2000)

68. Y. Morita, A.P. Tsai, Approximants in the Ag-In-M and Au-Sn-M (M = Ca or Rare Earth Metals) Systems. Jap. J. Appl. Phys. **47**, 7975–7979 (2008)

69. A. Niikura, A.P. Tsai, A. Inoue, T. Masumoto, Stable Zn-Mg-Rare-Earth Face-Centered Icosahedral Alloys with Pentagonal Dodecahedral Solidification Morphology. Philos. Mag. Lett. **69**, 351–355 (1994)

70. W. Ohashi, F. Spaepen, Stable Ga-Mg-Zn Quasi-Periodic Crystals With Pentagonal Dodecahedral Solidification Morphology. Nature **330**, 555–556 (1987)

71. E.M. Padezhnova, E.V. Melnik, R.A. Miliyevskiy, T.V. Dobatkina, V.V. Kinzhibalo, Investigation of the Zn-Mg-Y system. Russ. Metall. (Engl. Transl.) **3**, 185–188 (1982)

72. A. Palenzona, Ytterbium-Cadmium System. J. Less-Comm. Met. **25**, 367–372 (1971)

73. Z. Papadopolos, G. Kasner, Thick atomic layers of maximum density as bulk terminations of quasicrystals . Phys. Rev. B **72**, art. no. 094206 (2005)

74. Z. Papadopolos, G. Kasner, J. Ledieu, E.J. Cox, N.V. Richardson, Q. Chen, R.D. Diehl, T.A. Lograsso, A.R. Ross, R. McGrath, Bulk termination of the quasicrystalline fivefold surface of $Al_{70}Pd_{21}Mn_9$. Phys. Rev. B **66**, art. no. 184207 (2002)

75. Z. Papadopolos, P. Pleasants, G. Kasner, V. Fournee, C.J. Jenks, J. Ledieu, R. Mcgrath, Maximum density rule for bulk terminations of quasicrystals. Phys. Rev. B **69**, art. no. 224201 (2004)

76. Z. Papadopolos, R. Widmer, O. Groning, Testing bulk models of icosahedral quasicrystals with STM images of clean surfaces. Philos. Mag. **88**, 2083–2093 (2008)

77. L. Ponson, D. Bonamy, L. Barbier, Cleaved surface of i-AlPdMn quasicrystals: Influence of the local temperature elevation at the crack tip on the fracture surface roughness. Phys. Rev. B **74**, art. no. 184205 (2006)

78. J.J. Prejean, J.C. Lasjaunias, C. Berger, A. Sulpice, Resistive and calorimetric investigations of an insulating quasicrystal i-AlPdRe. Phys. Rev. B **61**, 9356–9364 (2000)

79. M. Quiquandon, D. Gratias, Unique six-dimensional structural model for Al-Pd-Mn and Al-Cu-Fe icosahedral phases. Phys. Rev. B **74**, art. no. 214205 (2006)

80. G.V. Raynor, Progress in the theory of metals. Prog. Met. Phys. **1**, 1–76 (1949)

81. P. Saintfort, B. Dubost, A. Dubus, "Quasi-Crystalline" Precipitation From Solid Solutions of the Al-Li-Cu-Mg System. Precipitation De "quasi-Cristaux" Par Decomposition De Solutions Solides Du Systeme Al-Li-Cu-Mg. C. R. Seances Acad. Sci., Ser. 2. **301**, 689–692 (1985)

82. P. Sainfort, B. Dubost, The T2 Compound - a Stable Quasi-Crystal in the System Al-Li- Cu-(Mg). J. Phys. (France) **47**, 321–330 (1986)

83. D.E. Sands, Q.C. Johnson, O.H. Krikorian, K.L. Kromholtz, Crystal structure of RU_3Be_{17}. Acta Crystallogr. **15**, 1191–1195 (1962)

84. T.M. Schaub, D.E. Burgler, H.J. Guntherodt, J.B. Suck, Quasi-Crystalline Structure of Icosahedral $Al_{68}Pd_{23}Mn_9$ Resolved by Scanning-Tunneling-Microscopy. Phys. Rev. Lett. **73**, 1255–1258 (1994)

85. H.R. Sharma, V. Fournee, M. Shimoda, A.R. Ross, T.A. Lograsso, A.P. Tsai, A. Yamamoto, Structure of the fivefold surface of the icosahedral Al-Cu-Fe quasicrystal: Experimental evidence of bulk truncations at larger interlayer spacings. Phys. Rev. Lett. **93**, art. no. 165502 (2004)

86. H.R. Sharma, M. Shimoda, S. Ohhashi, A.P. Tsai, First UHV surface studies of single-grain icosahedral Ag-In-Yb quasicrystal. Philos. Mag. **87**, 2989–2994 (2007).

87. Sharma, H.R., Shimoda, M., A.P. Tsai, Comparison of surface structure of icosahedral Al-Pd-Mn family quasi-crystals. Jpn. J. Appl. Phys. Part 1 **45**, 2208–2211 (2006)

88. H.R. Sharma, M. Shimoda, A.P. Tsai, Quasicrystal surfaces: structure and growth of atomic overlayers. Adv. Phys. **56**, 403–464 (2007)

89. Z. Shen, P.J. Pinhero, T.A. Lograsso, D.W. Delaney, C.J. Jenks, P.A. Thiel, The five-fold surface of quasicrystalline AlCuFe: preparation and characterization with LEED and AES. Surf. Sci. **385**, L923–L929 (1997)

90. Y. Shen, S.J. Poon, W. Dmowski, T. Egami, G.J. Shiflet, Structure of Al-Li-Cu Icosahedral Crystals and Penrose Tiling. Phys. Rev. Lett. **58**, 1440–1443 (1987)

91. J.E. Shield, L.S. Chumbley, R.W. Mccallum, A.I. Goldman, An Approximant to the Al-Cu-Ru Icosahedral Phase. J. Mater. Res. **8**, 44–48 (1993)

92. M. Shimoda, H.R. Sharma, A.P. Tsai, Scanning tunneling microscopy study of the fivefold surface of icosahedral Al-Cu-Ru quasicrystal. Surf. Sci. **598**, 88–95 (2005)

93. D.P. Shoemaker, C.B. Shoemaker, Concerning the relative numbers of atomic coordination types in tetrahedrally close packed metal structures. Acta Crystallogr. B **42**, 3–11 (1986)

94. V. Simonet, F. Hippert, R.A. Brand, Y. Calvayrac, J. Rodriguez-Carvajal, A. Sadoc, Chemical order in 1/1 Al(Si)-Cu-Fe approximant phases. Phys. Rev. B **72**, art. no. 024214 (2005)

95. A. Singh, J.Q. Guo, A.P. Tsai, Stability and diffraction features of quasicrystal and 2/1 approximant phase in an $Au_{42}In_{42}Yb_{16}$ alloy. Mater. Sci. Eng. A **449**, 991–994 (2007)

96. R. Sterzel, C. Gross, A. Kounis, G. Miehe, H. Fuess, S. Reutzel, D. Holland-Moritz, W. Assmus, A new well-ordered simple icosahedral quasicrystalline phase in the Zn-Mg-Er system. Philos. Mag. Lett. **82**, 443–450 (2002)

97. K. Sugiyama, N. Kaji, K. Hiraga, Re-refinement of $\alpha-$(AlMnSi). Acta Crystallogr. C **54**, 445–447 (1998)

98. K. Sugiyama, N. Kaji, K. Hiraga, T. Ishimasa, Crystal structure of a cubic $Al_{70}Pd_{23}Mn_6Si$; a 2/1 rational approximant of an icosahedral phase. Z. Kristallogr. **213**, 90–95 (1998)

99. K. Sugiyama, N. Kaji, K. Hiraga, T. Ishimasa, Crystal structure of a cubic $Al_{67}Pd_{11}Mn_{14}Si_7$; a new 1/1 rational approximant for the Al-Pd-Mn icosahedral phase. Z. Kristallogr. **213**, 168–173 (1998)

100. K. Sugiyama, T. Kato, T. Ogawa, K. Hiraga, K. Saito, Crystal structure of a new 1/1-rational approximant for the Al-Cu-Ru icosahedral phase. J. Alloy. Compd. **299**, 169–174 (2000)

101. K. Sugiyama, T. Kato, K. Saito, K. Hiraga, The crystal structure of a gamma-(Al-Cu-Ru-Si) cubic phase: a new approximant phase for the Al-Cu-Ru icosahedral quasicrystal. Philos. Mag. Lett. **77**, 165–171 (1998)

102. K. Sugiyama, W. Sun, K. Hiraga, Crystal structure of a cubic Al17Zn37Mg46; a 2/1 rational approximant structure for the AI-Zn-Mg icosahedral phase. J. Alloy. Compd. **342**, 139–142 (2002)

103. K. Sugiyama, W. Sun, K. Hiraga, Crystal structure of a 2/1 cubic approximant in an Al-Rh-Si alloy. J. Non-Cryst. Solids **334**, 156–160 (2004)

104. W. Sun, F.J. Lincoln, K. Sugiyama, K. Hiraga, Structure refinement of (Al, Zn)(49)Mg-32-type phases by single-crystal X-ray diffraction. Mater. Sci. Eng. A **294**, 327–330 (2000)

105. L.V. Sysa, Y.M. Kalychak, Y.V. Galadzhun, V.I. Zaremba, L.G. Akselrud, R.V. Skolozdra, Crystal structure and properties of $YbAg_2In_4$ and $CaAg_2In_4$ compounds. J. Alloys. Comp. **266**, 17–21 (1998)

106. H. Takakura, C.P. Gomez, A. Yamamoto, M. De Boissieu, A.P. Tsai, Atomic structure of the binary icosahedral Yb-Cd quasicrystal. Nature Materials **6**, 58–63 (2007)

107. T. Takeuchi, U. Mizutani, Electronic-Structure, Electron-Transport Properties, and Relative Stability of Icosahedral Quasi-Crystals and Their 1/1 and 2/1 Approximants in the Al-Mg-Zn Alloy System. Phys. Rev. B **52**, 9300–9309 (1995)

108. A.P. Tsai, "Back to the future" - An account discovery of stable ouasicrystals. Acc. Chem. Res. **36**, 31–38 (2003)

109. A.P. Tsai, J.Q. Guo, E. Abe, H. Takakura, T.J. Sato, A stable binary quasicrystal. Nature **408**, 537–538 (2000)

110. A.P. Tsai, A. Inoue, T. Masumoto, A Stable Quasi-Crystal in Al-Cu-Fe System. Jap. J. App. Phys. Lett. **26**, L1505–L1507 (1987)

111. A.P. Tsai, A. Inoue, T. Masumoto, New Stable Icosahedral Al-Cu-Ru and Al-Cu-Os Alloys. Jap. J. Appl. Phys. Lett. **27**, L1587–L1590 (1988)

112. A.P. Tsai, A. Inoue, Y. Yokoyama, T. Masumoto, Stable Icosahedral Al-Pd-Mn and Al-Pd-Re Alloys. Mater. Trans. JIM **31**, 98–103 (1990)

113. T. Weber, S. Deloudi, M. Kobas, Y. Yokoyama, A. Inoue, W. Steurer, Reciprocal-space imaging of a real quasicrystal. A feasibility study with PILATUS 6M. J. Appl. Crystallogr. **41**, 669–674 (2008)

114. J.S. Zhang, J. Yan, W. Liang, C.X. Xu, C.L. Zhou, Icosahedral quasicrystal phase in Mg-Zn-Nd ternary system. Mater. Lett. **62**, 4489–4491 (2008)

10

Phase Formation and Stability

Why is matter in thermodynamic equilibrium crystalline, either periodic or quasiperiodic?[1] Why has not any other strictly deterministic ordering principle ever been observed, for instance, the one realized in the almost periodic Thue-Morse chain? Why does the existence of a pure point spectrum (Bragg reflections only) seem so important for stability? What are the local driving forces for the formation and growth of quasiperiodic crystals, how do they differ from those leading to approximants, i.e. complex periodic intermetallic structures with giant unit cells?

The dimensionality seems to play a role in the thermodynamic stability of nonperiodic structures. Most of the icosahedral quasicrystalline phases found so far are thermodynamically stable. This is in contrast to decagonal quasicrystals, where the majority of known phases is metastable. All octagonal and, with one exception, all dodecagonal phases are metastable as well.

In some systems, however, during rapid solidification first metastable quasicrystals form instead of stable periodic crystals with lower free energy. If the formation of quasicrystals is kinetically favored, then the nucleation barrier must be lower for quasiperiodic phases. This has been explained by local icosahedral or polytetrahedral order in liquid alloys close to the solidification temperature.

The stability range of quasicrystals as a function of temperature reaches from only a few up to several hundred degrees. For instance, congruently melting i-Cd$_{84}$Yb$_{16}$ is (experimentally) stable from ambient temperature to the melting point [78] while d-Al–Fe–Ni exists only between 1120 and 1200 K [48]. The compositional stability field ranges from less than 1% for i-Cd–Yb [50] up to 60% for i-Cd–Mg–Yb [50], for instance.

---

[1] Quasiperiodicity in the general definition also includes incommensurately modulated crystals as well as composite crystals. Here, we will not discuss these cases, which either can be seen as periodic modification of an underlying basic structure or as a kind of intergrowth of periodic structures. For a detailed discussion see, e.g., [66, 134] and references therein.

10.1 Formation of Quasicrystals

Quasiperiodic structural order seems to be much more complex than periodic order. While local interactions are sufficient to generate periodicity, this does not seem to be the case for quasiperiodicity. Consequently, one would expect the formation and growth of quasicrystals to be a rather slow, diffusion dominated process, which is controlled by the electronic structure. The experimental observations, however, indicate just the opposite. Quasicrystalline phases can be easily obtained by rapid solidification such as melt spinning or splat cooling, with cooling rates of $>10^6 \, \mathrm{K \, sec^{-1}}$. At highest cooling rates metallic glasses form, at intermediate cooling rates quasicrystals, while the nucleation of periodic crystals takes longest. Some of the quasicrystals obtained by rapid solidification techniques are stable, however, most of them are metastable and transform into crystalline phases during thermal annealing.

Electron diffraction patterns indicate good quasiperiodic order in rapidly solidified samples, on a scale of several hundred ångströms. This raises the question of how quasiperiodic long-range order is achieved on that timescale. The easy formation of metastable icosahedral QC has been explained by their preferred nucleation from undercooled melts due to the icosahedral short-range order already present in liquid alloys of particular composition [73, 112]. This view is also supported by the frequently observed nucleation of icosahedral QC in metallic glasses during devitrification. Sometimes nucleation is eased by epitaxial growth. For instance, for less rapidly solidified Al–Mn, a metastable decagonal phase grows epitaxially on the nuclei of icosahedral Al–Mn and replaces it during further growth [116]. At higher Mn concentrations, d-Al–Mn directly nucleates from the melt. This is no contradiction to the hypothesis that preformed icosahedral clusters in the melt are responsible for the easy and rapid nucleation of icosahedral QC because d-Al–Mn consists of almost the same kind of icosahedral clusters as icosahedral Al–Mn.

Icosahedral short-range order in liquid alloys, however, could not make easier the formation of the experimentally observed metastable octagonal and dodecagonal quasicrystalline phases. The solidification behavior has also been found different, for instance, for congruently melting stable i-$\mathrm{Cd_{84}Yb_{16}}$, where no indications for icosahedral short-range order were found at all [78]. However, close to the melting temperature it can be generally expected that the different atom types in an alloy are chemically rather homogenously distributed. Furthermore, they will locally form atomic arrangements matching their size ratios and attractive or repulsive interactions, which are not too different from the short-range order (AET) in the crystal. Solidification then does not need large diffusion paths and complex reordering of atoms, it just rearranges slightly preexisting AET. Of course, tetrahedral or polytetrahedral order is preferred compared to more open structure motifs such as octahedral or cuboid ones.

In terms of the higher-dimensional approach, the nuclei correspond to different patches from the physical-space cut of the nD hypercrystal. The driving

force fitting them together into a tiling, like pieces into a puzzle, is the maximization of the number of favorable clusters and the energy minimization of the domain boundaries. Local rebuilding of clusters and cluster flips correspond to considerable par-space fluctuations (phason fluctuations) in the nD description. This means that during the growth process these fluctuations probe the full nD unit cell. Thereby all possible vertex coordinations are explored. Those which are in accordance with the constraints of symmetry and the formation of "thick atomic layers" survive (TAL) (see below, Sect. 10.2).

Locally, similar structural ordering of parent phase and nucleating phase lowers the energy barrier for the nucleation of icosahedral QC from undercooled liquid alloys. It does not explain, however, how quasiperiodic long-range order is obtained. Which parameters favor the growth of quasicrystals against the formation of high-order approximants that do not differ locally from quasicrystals?

Scenario   A hypothetical scenario for the formation of icosahedral quasicrystals by rapid solidification could be the following. In a fully miscible liquid alloy, the atoms will be chemically, rather homogenously distributed at high temperature. Due to the high mobility of atoms, the structural configuration space is explored within the given free energy range. Approaching the solidification temperature, the strongly reduced mobility of atoms will locally stabilize AET similar to those in the solid [19, 54, 55]. During solidification, there is only a small volume change and long-range order is mainly established by narrowing down the angular distribution of atomic distances. Thus, even complex structures have dynamically varying precursors in the liquid state close to the freezing temperature. Precursor is meant to be a configuration of atoms, which is locally similar to that of the solid compound. In simple monoatomic liquids, the formation of icosahedral clusters during solidification will be in competition with the formation of an as dense as possible packing of atoms.

By molecular dynamics simulations, the cluster structure of liquid aluminum under cooling conditions was shown to be near cubic close packed with some icosahedral cluster elements [87, 130]. Taking into account that the periodic average structure of icosahedral quasicrystals is closely related to the structure of *fcc* aluminum, we can conclude that on-average cubic close packing and local icosahedral order are not necessarily a contradiction. Quasiperiodic order can evolve from an on-average cubic close packing by local relaxations (<1 Å) due to chemical order. The correlation between clusters, over several hundred ångströms in rapidly solidified metastable quasicrystals, is carried by the underlying periodic average structure.

The geometrical constraints for the formation of icosahedral quasicrystals seem to be much stronger than those of decagonal quasicrystals. However, d-QC must not be seen as stackings of $2D$ quasiperiodic atomic layers similar to polytypic structures [14]. The chemical bonding is equally parallel and perpendicular to the quasiperiodic atomic layers. This is reflected, to some

extent, in the growth morphology of crystals of the decagonal phase. As it was shown in the examples of d-Al–Co–Ni and d-Al–Co–Cu [126], the decaprismatic crystals not only show prism faces but also facets inclined to the 10-fold axis (Fig. 10.1). This means that there are low-energy net planes (atomic layers) connecting quasiperiodic axes with the periodic one, which can be easily explained in the framework of the periodic average structure (PAS) of quasicrystals. Since the inclined net planes, which are net planes of the PAS, link periodic with quasiperiodic directions, they may play a crucial role in establishing quasiperiodic long-range order. Any local deviation from quasiperiodicity would locally destroy the corresponding net planes. A decagonal quasicrystal with stacking disorder would not show any inclined net planes at all. Consequently, the periodic growth along the tenfold axis forces the quasiperiodic growth in the planes perpendicular to it.

10.2 Stabilization of Quasicrystals

Depending on their unit cell size, rational approximants can be arbitrarily close to quasicrystal structures. Beside their "advantage" of being periodic, high approximants can accommodate clusters with noncrystallographic symmetry basically as well as QC. Some distortions and disorder are present in quasicrystals likewise [28]. So, what is the reason behind the formation of quasicrystals that can be more favorable than that of arbitrarily high approximants? Why does this big gap exist between experimentally observed low-order approximants and quasicrystals, why is there no devil's staircase of arbitrarily high-order approximants during phase transitions? Obviously, the free energy of quasicrystals can be significantly lower than that of any medium- or high-order approximant.

Everywhere in an ideal QC, portions of approximants of any order exist locally. The strict order of the QC is related to the stability of all this local realizations of approximants. The structure can be phason-strained if one of the approximants wins the stability race.

Moving the cutting space along the perp-space, in terms of the nD approach, infinitely many different locally isomorphous noncongruent structures form. Since they are all created from the same nD hypercrystal, their Fourier transforms are the same, except for a phase factor, as well as the Patterson functions and diffraction patterns. In other words, there is an infinite number of homometric structures, each one of them with the same total free energy.

In the case of finite real quasicrystals, there will be no infinite but a large number of configurationally different but energetically (almost) equal structures contributing to the entropy of the system. This is peculiar for quasiperiodic structures. Other factors increasing the entropy besides thermal vibrations and chemical disorder are random phason fluctuations. Random phason fluctuations lead to atomic jumps (phason flips) in double-well potentials. In the first approximation the two wells have the same shape and depth. Taking atomic interactions on a larger scale into account this is no
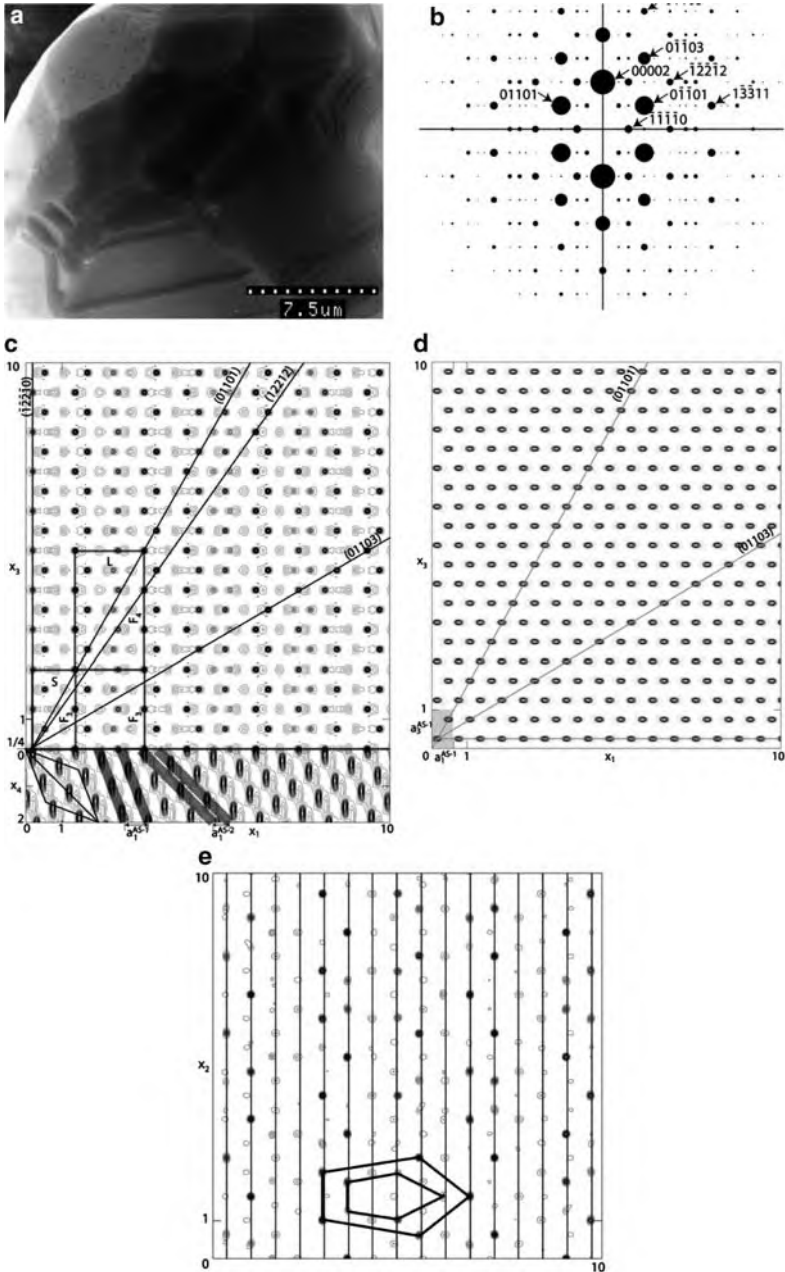
Fig. 10.1. (**a**) Growth morphology of a decaprismatic crystal of decagonal Al-Co-Ni exhibiting facets inclined to the 10-fold axis (courtesy of A. P. Tsai). (**b**) (h_10h_300) reciprocal space section of d-Al–Co–Ni. (x_10x_200) sections of (**c**) the structure and (**d**) (x_10x_3) section the PAS of d-Al–Co–Ni. (**e**) Structure of the (01100) net plane. Pictures are taken from [126]

more true. Phason flips can occur in high-order approximants as well and may not be the crucial parameters stabilizing quasicrystals against a transformation into approximants. Generally, it is still not clear whether entropy plays a decisive role for the stabilization of quasicrystals.

In case the Hume-Rothery mechanism applies, QC are favored over approximants, because Brillouin zones with icosahedral symmetry allow a better Fermi surface nesting. The energy balance can be further improved if a maximum density of low-energy clusters with noncrystallographic symmetry is compatible with a maximum number of energetically favorable flat atomic layers (decorated net planes) (Fig. 10.2). It is amazing that almost all atoms are arranged on flat atomic layers (Ammann planes). This is best visible in the projection along the 5-fold axis (Fig. 10.2a). The approximant structure shows flat atomic layers mainly along the 2-fold direction (Fig. 10.2f), however, much less atoms are covered by them.

The facets bounding a crystal are always flat, densely occupied by atoms and, therefore, parallel to netplanes, which are related to strong Bragg reflections. Analogously, these flat atomic layers can be seen as a kind of internal surfaces, forming interfaces between particular structural regions. Due to their planarity they can act as mirror planes or glide reflection planes. One should always keep in mind that the space or point group symmetry of a structure is a consequence of the optimum structural ordering and not an a priori existing ordering principle.

Ammann lines of the Penrose tiling are an example of the traces of such netplanes in a 2D section of a quasicrystal. The netplanes are decorated by atoms and can have a certain thickness, if a few neighboring loosely packed atomic layers are combined to "thick atomic layers" (TAL). These TAL frequently form the terminating layers at quasicrystal surfaces (see Sect. 9.5). In the bulk, they can be seen as low-energy internal surfaces (interfaces). Only in a quasiperiodic arrangement, clusters with non-crystallographic symmetry and TAL are fully compatible with each other (see Fig. 10.2a and b). This stabilizes QC topologically against phase transitions. Thus, noncrystallographic symmetry is a strong constraint for QC structure formation and stability. This may be one of the reasons why octagonal and most dodecagonal phases are not stable. Tetragonal and hexagonal arrangements of octagonal and dodecagonal clusters seem to be an energetically reasonable compromise between periodic packing and noncrystallographic symmetry.

According to the definition, reciprocal space images of quasiperiodic structures are purely point diffractive (Bragg reflections only). Reciprocal space vectors of Bragg peaks (diffraction vectors) are perpendicular to sets of parallel net planes. In terms of the nD approach, these net planes are lattice planes of the nD hyperlattice and their intersections with par-space are the net planes of one of the periodic average structures (PAS). For each set of Bragg reflections (harmonics), a different PAS and corresponding set of net planes exists. These net planes are as relevant for the propagation of electrons as those of periodic crystals.
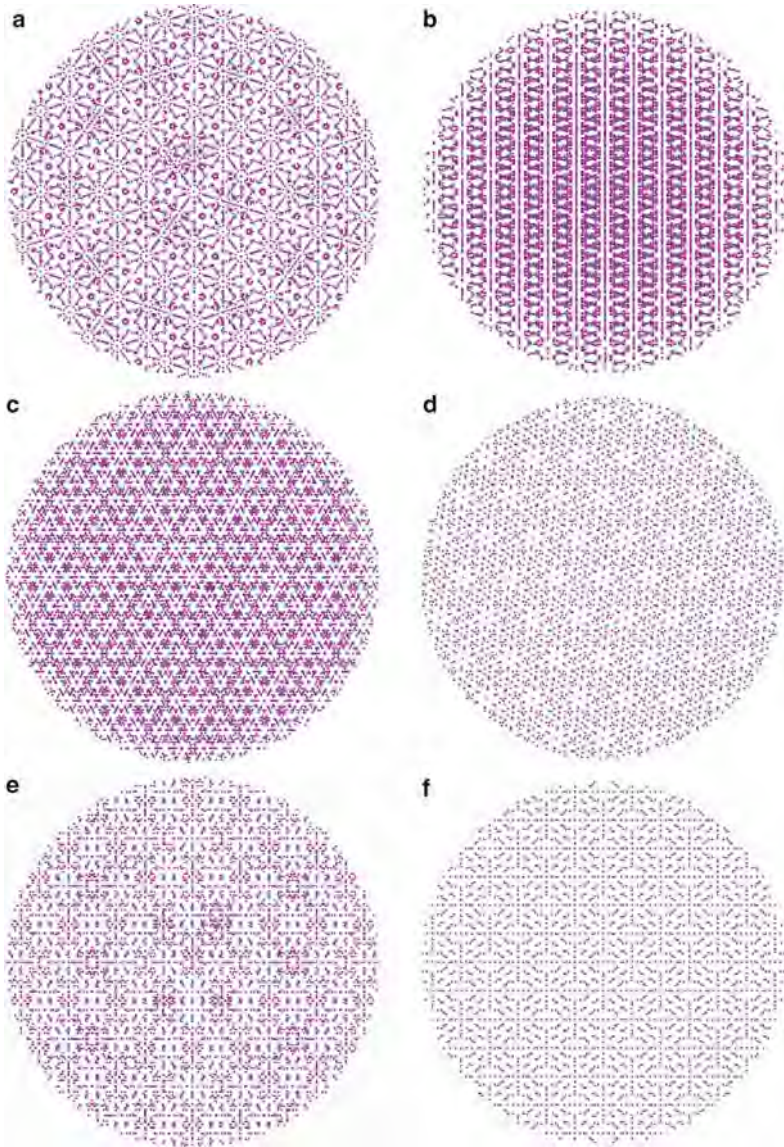
Fig. 10.2. Projections of the structure of *i*-Cd–Yb (courtesy of H. Takakura) along (**a**) a fivefold axis, (**c**) a threefold axis and (**e**) a twofold axis. In (**b**), (**d**) and (**f**), the corresponding projections of 1/1-Cd–Yb are depicted, i.e. along the pseudo-5-fold and the 3- and 2-fold directions, respectively. The atomic layers form a network compatible with 5-fold symmetry only in (**a**) and not in (**b**). On top of it, almost all atoms are arranged in flat atomic layers (internal surfaces or interfaces), a kind of Ammann planes, which interpenetrate each other in a way, which is only possible in quasiperiodic structures. In all cases projection of a spherical section (diameter 100 Å) of the structures are shown

Consequently, quasiperiodic structures are the union of an infinite number of PAS. The "thickness" of the net planes (atomic layers) of the PAS leads to rapid decrease of the intensities of higher harmonics. The smaller the occupation domains and the simpler the nD unit cell, the better defined the PAS and the more and stronger the higher harmonics and the more distinct the band gaps (see QPNC in Sect. 11.2). This property disfavors random-tiling based structures.

Factors Stabilizing Quasicrystals

- Existence of two or more incommensurate length scales, i.e. that of the PAS and those of the clusters.
- Noncrystallographic symmetry of clusters and the existence of internal surfaces, "thick atomic layers (TAL)," crisscrossing them.
- Particular chemical composition favoring an irrational stoichiometry.
- Particular valence electron concentration favoring the Hume-Rothery mechanism.
- High configurational entropy due to phasonic disorder.

Symmetries Other than 5-, 8-, 10-, 12-Fold Are Disfavored Due to

- poor PAS (see example of 7-fold symmetry 3.6.2).
- geometrical reasons, for instance, no AET with those symmetries are known in periodic intermetallics.

10.3 Clusters

The structures of quasicrystals, as of many other complex intermetallic compounds, can be well described based on polyhedral recurring structure motifs, commonly called clusters. In case of icosahedral phases, these are typically Mackay-, Bergmann- or Tsai-clusters, in case of decagonal phase columnar Gummelt-clusters. This cluster-based analysis of quasicrystal structures has been a powerful tool to get the big picture of the complex arrangement of atoms and to identify the underlying structural ordering principles.

However, there are some open questions concerning the role of clusters for the stability and physical properties of quasicrystals. Are these clusters more than just geometrical structure motifs, more than coordination polyhedra? As already shortly discussed clusters do not necessarily need to be crystal-chemically well-defined entities. Well defined means, for instance, that the chemical bonding between the atoms within the cluster differ from the bonds to atoms outside of the cluster. This is shown in the simple example of *fcc* aluminum (Fig. 10.3). The "cluster shells" look quite convincing. However, the crucial point is that every single Al atom in the structure is surrounded

r = 2.863 Å   4.049 Å   4.960 Å   5.727 Å   6.403 Å
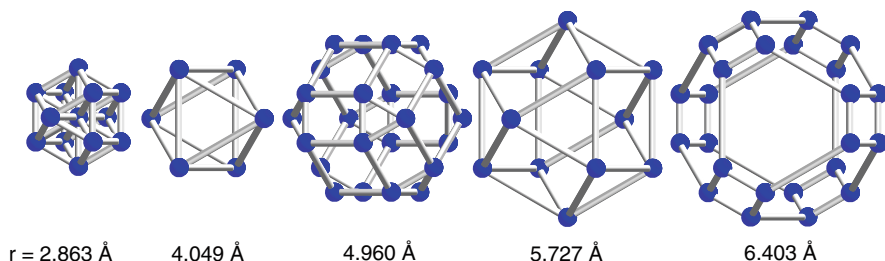
Fig. 10.3. The first five "cluster shells" around any Al atom in *fcc* aluminium. The radii of these coordination polyhedra (cluster shells) have a ratio of 1: $\sqrt{2}$: $\sqrt{3}$: $\sqrt{4}$: $\sqrt{5}$ (from [125])

by exactly the same coordination polyhedra and that the bond distances between neighboring atoms are always exactly the same. Consequently, there is no crystal-chemical meaning at all in this kind of "cluster." In this case, a meaningful description is that of a cubic close packing.

Using the cluster approach for the description of complex structures, it is necessary to define in what meaning the term *cluster* is used. Depending on the context, the term cluster may denote a recurrent structure motif (purely geometrical pattern), a structural building block or unit (perhaps with some physical justification), a quasi-unit cell (stable entity in the meaning given by Jeong and Steinhardt [67]) or a complex coordination polyhedron with some chemical stability, particularly in case of covalent or ionic bonding. In some cases, clusters can be considered as electronically stabilized entities, and according to the jellium model [62] as a kind of soft superatom. In case of strong covalent intra-cluster bonds and weak inter-cluster interactions, they may even have a significant mechanical stability [37]. The nanometer-sized particles obtained, for instance, by laser ablation and investigated in mass spectrometers, are called free (bare, naked) clusters [90, 135]. If a bare cluster sits on a surface [68] or in a matrix [94], it is called a supported cluster. One gets embedded clusters if the matrix is formed by organic ligands, as in metal-organic compounds [106]. There, the clusters correspond to a polyhedral arrangement of up to more than 100 metal atoms. In all these cases, it is clearly defined by the character of chemical bonding that is, it depends on which atom belongs to a cluster and which one does not.

What the Term Cluster May Mean

226	*Structure motif*	Coordination polyhedra in *fcc* Al shown in Fig. 10.3.
227	*Structural*	SiO$_4$-tetrahedra in silicate structures (rather stable entities
228	*building unit*	existing in differently connected ways and also in isolated
229		form, e.g. [SiO$_4$]$^{-4}$ complex-ions in nesosilicates).
230	*Coordination*	NaCl$_6$-octahedra in the sodium chloride structure (just

231	*polyhedron*	geometrical visualization).
232	*Covering cluster*	A structural unit is a covering cluster if a quasiperiodic
233		structure can be completely covered by partly overlapping
234		copies of it (see, for instance, [49]).
235	*Quasi-unit cell*	Columnar covering clusters (Gummelt decagons) in
236		decagonal Al–Co–Ni [67].
237	*Free cluster*	*fcc* Ni–Al clusters up to 55 atoms [30]; *fcc* NaI clusters [90].
238	*Supported cluster*	nanoparticles of Au on SiO_2 [30].
239	*Embedded cluster*	Icosahedral Tl_{13}^{-10} cluster in $Na_4K_6Tl_{13}$ (electronically
240		stabilized) [23]; pentagonal bipyramidal Ga_7-cluster in
241		$[Li(thf)_4][\{(Me_3Si)_3Si\}_4\{(\mu_2\text{-}Me_3Si)_3SiGa\}_2Ga_7]$ [75].

For instance, a 9(12)-shell cluster with a 20.21 Å diameter was derived from cubic 2/1-$Al_{70}Mn_6Pd_{23}Si$ [129], which was used in the structural description of the icosahedral phase [144]. Taking a closer look at this cluster (Fig. 10.4), one finds that it consists of fully occupied shells and of disordered/distorted or partially occupied shells breaking the icosahedral symmetry. The pentagon-dodecahedral Al-shell (2a) is fully occupied with a rather long Al–Al distances of 2.947–3.015 Å. The icosahedral shells (1) and (2b) are separated by mere 1.573 Å and the 24 sites can be occupied by 12 Pd atoms only. The 60 split sites of the third shell can be occupied by 30 atoms only. At high temperature, there can be a high mobility of the atoms between the split positions. Consequently, it will be really difficult to define the 'stable part' of this cluster, which looks like a kind of spherical 'roller bearing'.
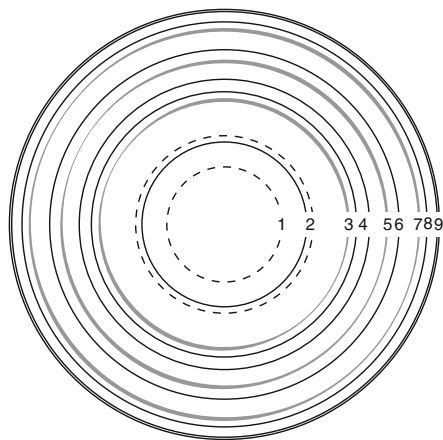
Fig. 10.4. Schematic representation of the cluster at the origin in the cubic 2/1-approximant structure $Al_{70}Mn_6Pd_{23}Si$ [144]. Each circle represents a shell or part of a double shell. The sites in the shells 1 and 3 (*dashed circles*) can be occupied by atoms alternatingly only. Shells 3, 5 and 7 (asymmetrically broadened, *grey*) contain up to 50% split positions. (from [125])

Cluster-based structures may have very interesting physical properties provided that clusters and matrix behave differently with respect to electrons [26, 76], phonons [64], propagation of defects (dislocations, cracks) [93] or diffusion. In the limit, structures of this type can be considered as a kind of single-phase nanocomposites with components (atoms, clusters and matrix) interacting on different scales. Quasicrystals are certainly not typical representatives of such a material class, however, clusters certainly play a larger role than being just structure motifs. Metallic bonding is a collective phenomenon resulting from interactions of atoms inside and outside a cluster. Significant differences in intra- and inter-cluster bonding may be restricted to those cases where covalent bonding contributions exist. It is not clear whether the Al-TM sp-d hybridization, which contributes to a pseudo-gap at the Fermi energy, plays a role in the stabilization of the clusters. It has been shown that the electronic density of states exhibits narrow peaks, which have been assigned to TM-cluster resonance states [26].

There are some indications that clusters, stabilized by covalent bonding, for instance, are much smaller than the features seen on electron microscopic images. The stable part of the Al–Mn–Pd cluster may just end at shell 2, resulting in a cluster diameter of 8–9 Å (Fig. 10.4). Only a rather small cluster has also been identified in a thorough theoretical analysis of possible atomic clusters in F-type quasicrystals [31]. The 8.12 Å diameter 33-atom B-cluster (centered icosahedron + dodecahedron) is the best choice for a well-ordered quasicrystal, such as Al-Cu-Fe. Larger clusters automatically introduce disorder. However, since only 78.83% of the total number of sites is covered by the B-clusters, additional partially disordered clusters (M, M′) are needed to fill the gaps. According to a charge-density study [76], indications of covalent bonding in the first two shells of the Mackay cluster in α-Al(Mn,Re)Si corroborate the possible larger stability of very small clusters. Therefore, the important factor is whether the center of the innermost icosahedral cluster is empty or filled. According to [74], empty Al_{12}-cluster shells (e.g. in Mackay clusters) have a covalent-bonding nature, while the centered Al_{13}-ones (e.g. in Mg–Al–Zn quasicrystals) are metallic. Typical of Al_{12}-clusters are very short nearest-neighbour distances below 2.55 Å (in fcc Al $\approx$ 2.86 Å), which are indicative of strong bonding. In Al_6 clusters, the atomic distances can even reach 2.435 Å [68]. Clusters forming in undercooled liquids [29], certainly have a kind of stability as well as free clusters with a magic number of atoms (electrons).

In case of d-Al–Co–Ni, a large ($\approx$20 or even $\approx$32 Å diameter) covering cluster (Gummelt decagon, quasi-unit cell approach) has been used for the explanation of structure and stability [2, 49, 53, 103]. Taking into account the studies on free Ni–Al [30] or transition metal clusters [135], as well as the structure of the approximants in the system Al–Co–Ni, the 'stable clusters' seem to be the pentagonal-bipyramidal ones. The $\approx$20 Å clusters, consequently, are constituted by small stable subclusters (e.g. S and P subclusters [114]). Most Al atoms are just glue atoms with a rather high mobility. In a Monte Carlo

simulation, even some 40% of all Al atoms have been found to be rather delocalized [51].

How mechanically stable are clusters in quasicrystals? There are some observations that have been interpreted as proof for the existence of clusters in quasicrystals with a rather high mechanical stability: on one hand, cleavage and annealing experiments on i-Al–Mn–Pd [36–39, 41] and d-Al–Co–Ni [40]; on the other hand, molecular-dynamics-based modelling of crack and dislocation propagation in simple quasiperiodic model structures [93, 93, 111].

A cleavage surface results from crack propagation, which avoids cutting strong bonds. Consequently, the cleavage surface should be parallel to the network of strongest bonds. This is also true for equilibrium surfaces, which usually are parallel to net planes of atoms, connected by the strongest bonds. Annealed surfaces obtained after the usual surface preparation procedures are always atomically flat, or show atomically flat terraces (see, e.g. [145]). Since surface atoms always have incomplete coordination, the energy-weighted surface has to be minimum. This minimum-energy surface does not a priori have to be flat. If there are strong covalent bonds only within the cluster shells and not perpendicular to them, a kind of 'cobblestone' surface could be energetically more favorable. However, if the hollows are filled by glue atoms (i.e. the matrix between the clusters), the energy balance of the flattened surface would become even better. The energy costs for moving glue atoms has been shown to be one-order of magnitude smaller than that for cluster atoms [47]. Even if after annealing the 'cobblestone' surface were maintained, there were obviously no mobile glue atoms. This means that the chemical bonding does not differ very much between atoms belonging to different cluster shells or to glue atoms. An analysis of gas-phase clusters made from laser-vaporized i-Al–Mn–Pd did not identify any cluster occurring in the bulk structure [15].

If one looks at the distribution of strong bonds, as indicated by short nearest-neighbor distances, in the 2/1-approximant of i-Al–Mn–Pd, one would expect a very puckered cleavage plane indeed (Fig. 10.5). However, since the crystal is expected to break along the strongest bond chains, these do not
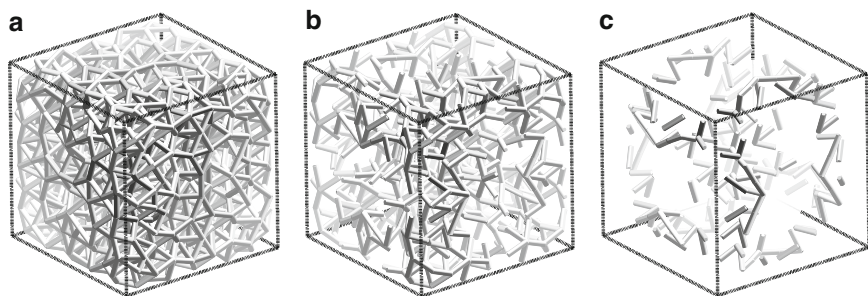
Fig. 10.5. One unit cell of the cubic 2/1-approximant $Al_{70}Mn_6Pd_{23}Si$ [144]. The bonds between all atoms are shown, the distances of which are smaller than the sum of (**a**) the atomic radii, (**b**) the covalent radii plus 0.05 Å , and (**c**) the covalent radii (from [125])

seem to be along the shells of the known geometrical clusters. An ab initio study of the five fold surface of a 3/2-approximant of icosahedral Al–Mn–Pd revealed, even after relaxation, a flat surface cutting through the Bergman and pseudo-Mackay (M) clusters [77]. A high mobility of Al atoms in the M clusters was observed. It is remarkable that the metallic character of the electronic structure is enhanced at the surface.

The effective size of a cluster may depend on the kind of property considered. We may identify rather large clusters for geometrical repetition units (structural building blocks) [53]. Medium sized clusters may be relevant to electronic [26, 76] or vibrational properties [64]. A particular mechanical stability against crack propagation [93, 111] due to strong bonds may be restricted to the smallest clusters.

To conclude, one should keep in mind, that the most prominent recurring structural unit in periodic structures is the unit cell. And, as it is well known from nanoparticles, the unit cell is not a necessary stable unit per se. Its properties always have to be considered in the context of all other unit cells and of its periodic arrangement. The same seems to be true for the 'unit cells' of quasicrystals, the clusters.

10.4 Phase Transformations of Quasicrystals

In this section we will focus on the microscopic (geometrical) mechanisms of quasicrystal transformations. A few scenarios about how the atoms could move in such transitions will be discussed. Concerning the mechanism of phase transitions of QC, is there anything peculiar? Do they differ in any way from those of translationally periodic crystals (PC) or those of incommensurately modulated structures (IMS), or the much better understood large class of aperiodic crystals [24]? Is it possible to use the same phenomenological approaches such as the Landau theory? IMS can be described by a 1D, 2D or 3D displacive and/or substitutional modulation of an underlying periodic basic structure. The projection of the IMS into one unit cell of the basic structure gives the periodic average structure (PAS). The periods of the modulation wave and of the basic structure are incommensurate to each other. The modulation wave vector may continuously vary with temperature or pressure running through all rational and irrational multiples of the lattice parameters. In case of rational multiples commensurately modulated phases can be formed by a lock-in transformation. If the amplitude of the modulation wave approaches zero the PAS of the IMS turns into the basic structure without any variation in the equilibrium positions of the atoms. This occurs, for instance, if the IMS transforms by a second order phase transition into a HT high-symmetry periodic structure. The phase transition can be well described in terms of the phenomenological Landau theory with the amplitude of the modulation wave as order parameter (see, for instance, [11]). At low temperature, IMS can undergo a soft-mode driven lock-in transition to a periodic phase (the irrational

wave vector locks in a rational value), which can be described as a commensurately modulated phase (superstructure).

Geometrically, QC can be described in different ways (QC- and IMS-setting) depending on what property is to be discussed. Based on its Fourier coefficients, a QC can be considered as a composite structure of mass density waves with wave vectors locked by the constraints of noncrystallographic symmetry [12]. Phenomenologically, infinitesimal distortions (linear phason strain) of the wave vectors (reciprocal lattice) could create a devil's staircase of phase transitions running through all orders of rational approximants as it is known from IMS [11]. This has never been experimentally observed for QC transitions, however. Contrary to purely displacive IMS, one-to-one mapping of atomic positions of the QC structure onto atomic positions in any periodic structure is not possible. The only exceptions are 1D quasicrystal structures and all those with crystallographic diffraction symmetry.

Despite some similarities between QC and IMS (cf. [123] and references therein) such as the (lock-in) transformation to rational approximants there are also major differences: the wave vectors of the mass density waves do not continuously vary with temperature; QC do not transform to periodic HT high-symmetry phases in second order transitions; purely displacive QC $\Rightarrow$ AC transitions are not possible due to topological incompatibilities [33], equilibrium can be easily achieved during IMS transitions contrary to the much more sluggish QC transitions. For a more recent comprehensive general review on phase transitions of quasicrystals see [124].

In the following section, we first discuss examples of quasicrystal $\Leftrightarrow$ quasicrystal transitions then of quasicrystal $\Leftrightarrow$ crystal transformations. The examples are taken from [124].

10.4.1 Quasicrystal $\Leftrightarrow$ Quasicrystal Transition

Several examples of ordering transitions have been experimentally observed for icosahedral and decagonal QC. The structures transform either as a function of composition (*morphotropic transitions*) (Fig. 10.6) or as a function of temperature or pressure (*polymorphic transitions*) (Fig. 10.7). An ordered quasiperiodic superstructure at low temperature can become disordered at high-temperature driven by the increase of entropy. In most cases, the superstructures are caused by chemical order (distribution of atomic species on structural sites).

In the following lines, experimental observations of phase transformations of quasicrystals of different kind are shortly reviewed.

i-**Al$_6$Li$_3$Cu**   QC $\overset{10\ \mathrm{GPa}}{\Longrightarrow}$ amorphous $\overset{28\ \mathrm{GPa}}{\Longrightarrow}$ QC(?)
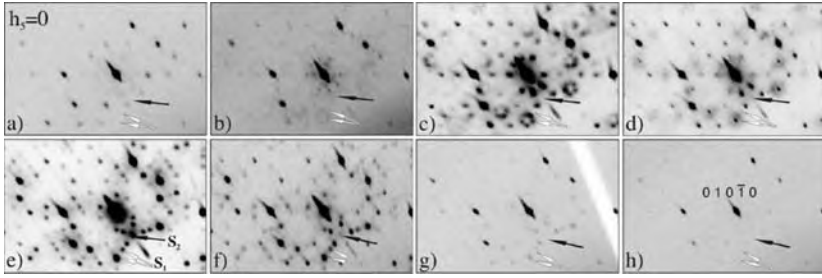
Fig. 10.6. Example of morphotropic phase transitions in the stability range of d-Al–Co–Ni as reflected in its X-ray diffraction patterns. The enlarged area around the strong $010\overline{1}0$ reflection is shown. Positions of S1 and S2 superstructure reflections of the type I phase are marked by *white and black arrows*, respectively. (**a**) 'basic Co-rich' $Al_{72.5}Co_{19.5}Ni_8$, (**b**) $Al_{71.5}Co_{18}Ni_{10.5}$, (**c**) $Al_{71.5}Co_{16}Ni_{12.5}$, (**d**) $Al_{71.5}Co_{15}Ni_{13.5}$, (**e**) 'superstructure type I (S1+S2)' $Al_{71.5}Co_{14}Ni_{14.5}$, (**f**) 'superstructure type I (S1)' $Al_{71.5}Co_{10.5}Ni_{18}$, (**g**) $Al_{71.5}Co_{10}Ni_{18.5}$, (**h**) 'basic Ni-rich' $Al_{71.5}Co_{8.5}Ni_{20}$ [124]
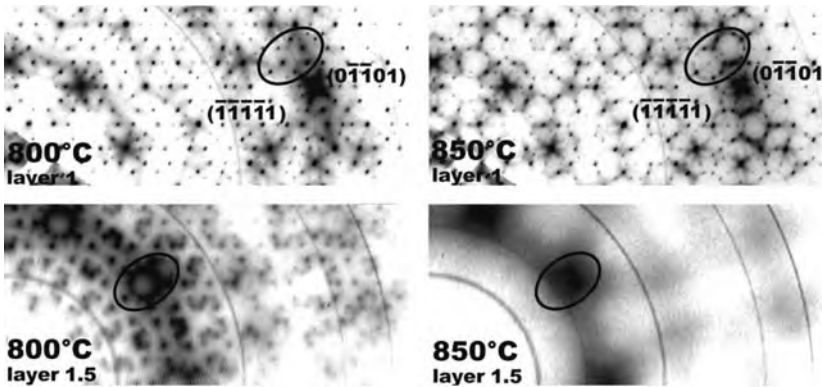
Fig. 10.7. Example of a polymorphic phase transition, superstructure type I (S1+S2) to superstructure type I (S1), for d-$Al_{70}Co_{12}Ni_{18}$. Reciprocal space sections $h_1h_2h_3h_4h_5$ are shown, with $h_5 = 1$ and 1.5 based on $a_5^* = 4.08$ Å, collected at $800°$C and $850°$C, respectively (marresearch 345, wave length $\lambda = 0.7$ Å, oscillation angle $\Delta\phi = 0.5°$, Swiss–Norwegian Beam Lines/ESRF, Grenoble). Regions that show typical changes in the intensities of S1 and S2 satellite reflections and diffuse scattering phenomena are *encircled* [124]

After pressure induced amorphisation of i-Al_6Li_3Cu above ≈ 10 GPa, a quasicrystalline (?) phase forms again above ≈ 28 GPa [3]. The transition was interpreted in terms of a change from Bergman- to Mackay-type clusters.

The first coordination shell of Cu decreases up to 12 GPa, remains constant up to 20 GPa and then increases again up to the highest studied pressure of 33 GPa [113].

R-**Al$_5$Li$_3$Cu**   AC $\overset{18.6-23.2 \text{ GPa}}{\Longrightarrow}$ amorphous
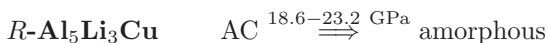
The cubic approximant R-Al$_5$Li$_3$Cu was found to transform into the amorphous state between 18.6 and 23.2 GPa [141]. Pressure-induced, largely isoconfigurational, amorphization indicates a locally close structural (topological) relationship of the two ordering states such as polytetrahedral packing.

There are no other pressure-dependent phase transitions of QC known so far (for an overview see [79]).

i-**Al$_{71}$Mn$_8$Pd$_{21}$** $F \overset{1021 \text{ K}}{\Longrightarrow} F2 \overset{1011 \text{ K}}{\Longrightarrow} F2M$
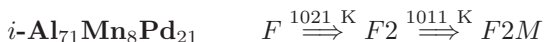
Several reversible phase transitions have been observed as function of temperature [25, 52, 82]. Above 1021 K, an ordered icosahedral phase is stable, with F-centerd 6D hypercubic structure ($a_F = 12.901$ Å). Annealing a few minutes at 1000 K yields the $F2$-phase, a superstructure of the F-phase, which can be described in terms of a 6D diamond structure [61]. This phase is a metastable transient state between the HT F-phase and the LT $F2M$-phase [82]. The $F2$-to-$F2M$-phase transition takes place around after annealing 10 h at 1011 K indicating a diffusion-controlled mechanism (see also [25]). The $F2M$-phase is a modulated quasicrystalline phase with cubic diffraction symmetry representing a superstructure of the $F2$-phase [7].

i-**Al$_{63.5}$Cu$_{24}$Fe$_{12.5}$** i-Al–Cu–Fe transforms to a rhombohedral approximant via an intermediate modulated quasicrystalline phase, with the wave vector varying with temperature [5, 6, 63]. The transition from the i-QC to the modulated intermediate state was modeled by a mechanism based on fractional shears of the 6D hypercrystal [32, 35]. A characteristic network of domains bounded by planar defects results from bounded transformations mapping the 6D QC lattice onto a lattice for which the physical space is rational. A detailed model with a periodic phason mode was suggested, which finally locks into the crystalline approximant [6]. Such a type of second order transition, driven by a soft phason mode instability was discussed by several groups [13, 59, 60, 65]. However, a chemical composition variation could drive such a transition as well [92]. Indeed, in an experimental study of i-Al$_{63.5}$Cu$_{24}$Fe$_{12.5}$, it was qualitatively verified that the modulation is thermally activated, and that atomic diffusion should be involved in the phase transition. A compositional variation was found for the Al and Fe concentration of approximately 1.5%.

d-**Al–Co–Ni** Besides morphotropic (Fig. 10.6) also polymorphic transitions have been observed for d-Al–Co–Ni (Fig. 10.7). There is an ordering transition from the LT 'superstructure type I (S1+S2),' with main reflections and first and second-order satellite reflections, via the superstructure type I (S1) to the HT phase without any satellite reflections [42, 127].

The 'type I' $\Rightarrow$ 'S1' phase transition is of second order with an onset temperature of 1007 K and a finishing temperature of 1042 K [119]. It is accompanied by an elongation of coordination polyhedra along the tenfold axis and a contraction perpendicular to it. Thermal expansion was found to be isotropic at temperatures up to 900 K. The mobility of atoms was estimated based on diffusion coefficient data. Within 100 s, Co and Al move $\approx$0.8 and $\approx$20 Å at 670 K, $\approx$18 and $\approx$350 Å at 770 K, respectively.

The transition from the 'basic Ni-rich' to the 'S1-type' structure has been studied by in-situ HRTEM on d-$Al_{72}Co_8Ni_{20}$. Already at 723 K the 12 Å intercluster distance disappears and the cluster symmetry changes from m, as present in samples quenched from 1173 K, to 5 [115]. The 'S1-type' super-order seems to be caused by the orientational order of the clusters with 5-fold symmetry.

10.4.2 Quasicrystal $\Leftrightarrow$ Crystal Transformation

Only a few fully reversible structural phase transitions of QC as a function of temperature or pressure have been reported so far. Most of them are transitions between different quasiperiodic ordering states. Quite common, however, are QC$\Rightarrow$PC transformations taking place under irradiation or during high-energy ball milling. These transitions are usually accompanied or rather a consequence of an induced change in chemical composition (morphotropic transition). Remarkably, even in these cases, characteristic orientation relationships between special directions in the QC and the transformation product are found. The formation of mostly metastable QC during devitrification of amorphous alloys (a-alloys) are also frequently observed. These a-alloys have been found to undergo a two-stage phase transition during annealing. First, in the LT regime a metastable quasicrystalline phase nucleates. Later on, at HT, this QC phase is transformed into a crystalline phase.

This kind of transition requires an extensive reconstruction of the structure, which needs diffusion of atoms. At temperatures $T < T_{m/2}$, i.e. well below the melting temperature T_m, this can only be achieved if the sluggish phase transition kinetics is enhanced by ballistic diffusion associated with a high defect density. This is the case during high-energy electron or ion irradiation as well as during high-energy ball milling, respectively. In these cases, it is probable, however, that due to induced changes in chemical composition the transitions are morphotropic rather than polymorphic.

Phase transitions of rational approximants are of interest since they are built from the same fundamental clusters as the QC they are related with. A phenomenological study in terms of the Landau theory was performed on the possible phase transitions in cubic approximants of i-phases [21] and on decagonal phases [16]. It was therefore assumed that the number of atoms in the unit cell does not change during the transition. Only, order/disorder transitions were considered and the results demonstrated transitions in the 0/1-approximant (FeSi-type structure) based on sublattice ordering.

10.4.2.1 Transitions as a Function of Temperature

i-Al–Cu–Fe(Si)

Several transitions of the *i*-phase have been observed depending on sample composition and annealing conditions: QC to cubic 1/1- [102] and rhombohedral 2/2- [6], 3/2- [86] or 5/3-approximants [85]. In some cases an intermediate linear-phason strained quasicrystalline phase or a transient modulated *i*-phase with satellite reflections along the fivefold directions was observed [9]. According to [8], the transition *i*-phase (stable at $T > 948$ K) to rhombohedral approximant (stable at $T < 948$ K) is reversible. Heating up as-quenched samples of the *i*-phase leads first to the formation of the modulated *i*-phase ($673 < T < 923$ K, in some experiments up to 1023 K) with the modulation period (≈ 200 Å) increasing with temperature. For longer annealing times ($873 < T < 923$ K), the system transforms into a two-phase system with chemical composition fluctuations [91] as well as with phason and phonon disorder [92]. Longer annealing at $943 < T < 953$ K recovers well-defined *i*-phase and rhombohedral approximant in coexistence.

This behavior was successfully modeled by free-energy analysis in terms of composition and phason strain [139]. In agreement with the experimental evidence, the calculated phase diagram shows the HT *i*-phase and the LT approximant separated by a two-phase region with both phases coexisting. By taking into account the energy associated with the phason strain gradient, spatially fluctuating phason strain should be present in the two-phase region (i.e. a modulated transient phase). In previous experimental work [138] was found that at the composition $Al_{63}Cu_{24}Fe_{13}$ the *i*-phase has its largest stability range as a function of temperature (730 K $< T < T_m$). A hypothetical order/disorder transition temperature of 1590 K (melting temperature $T_m \approx 1100$ K) was calculated, based on the intensity evolution with temperature of the superstructure reflections (related to *F*-centering of the 6D Bravais lattice). The rhombohedral 2/1-approximant was obtained for compositions $Al_{64}Cu_{24}Fe_{12}$ - $Al_{63}Cu_{26}Fe_{11}$, the rhombohedral 3/2-approximant for slightly lower Al concentration such as $Al_{62}Cu_{26}Fe_{12}$. The intermediate state ($Al_{63}Cu_{25}Fe_{12}$, 670°C) was interpreted by a slope of the strip in the 6D approach equal to 1.70–1.75 (in the ideal QC it amounts to $\tau = 1.618\dots$).

The transition from the as-quenched icosahedral phase to the cubic 1/1-approximant, α-$Al_{55}Cu_{25.5}Fe_{12.5}Si_7$, takes place within 2 h at 750°C almost without any change in chemical composition [81]. A theoretical model for the transition mechanism based on the domain structure observed was suggested. The domains, each one containing a few cubic approximant unit cells, are assumed already existing in the parent *i*-phase. They act as nuclei for the formation of the cubic α-phase. The translation vectors connecting them are therefore still vectors of the i-phase and the extension of the periodic structure needs a partial reconstruction between joining domains. The authors point out that this occurs by small rearrangements of atoms rather than by a reconstructive transformation [34, 81].

i-Ti–Zr–Ni

i-Ti$_{41.5}$Zr$_{41.5}$Ni$_{17}$, produced by melt spinning and subsequent annealing, transforms above 565°C to the body-centerd cubic W-phase, an 1/1-approximant [147]. By cooling the reverse transformation it could not be observed probably due to the sluggish kinetics.

i-Mg–Zn–Al

After heating a mechanically alloyed sample of i-Mg$_{44}$Zn$_{41}$Al$_{15}$ to temperatures above 613 K, it transformed topotactically to the metastable cubic 2/1-approximant. Cooling the sample down yielded the icosahedral phase again [17]. It should be kept in mind that mechanical alloying leads to highly defective samples.

i-Zn–Mg–Y

A reversible phase transition between i-Zn$_{64}$Mg$_{27}$Y$_9$ (20 h at 873 K) and hexagonal h-Zn$_{66}$Mg$_{27}$Y$_7$ (72 h at 773 K) was observed during annealing experiments [1]. The hexagonal phase was found being structurally related but not a rational approximant. At 750 K both phases exist adjacent to each other in the phase diagram.

cI 168-Cd$_6$Me (Me = Ca, Y, Yb)

c-Cd$_6$Y, a 1/1-approximant of icosahedral i-Cd$_{5.7}$Yb and i-Cd$_{17}$Ca$_3$, shows a LT phase transition at 164 K. The transition is believed to be due to the ordering of the innermost shell of the basic 66-atom icosahedral cluster occupying the vertices and body center of the cubic unit cell. The innermost cluster, a Cd$_4$-tetrahedron in the center of a Cd$_{20}$ dodecahedron is orientationally disordered above 164 K. At lower temperatures, the ordering is accompanied by a very small tetragonal distortion and the formation of a $2 \times 2 \times 1$ orthorhombic (?) superstructure [131]. A similar order/disorder transition was found for isotypic c-Cd$_6$Yb at about 110 K [132, 133]. The LT ordering transition was also found for the 2/1-approximants Cd$_{84.8}$Ca$_{14.2}$ and Cd$_{85.1}$Yb$_{14.9}$ below 110 K [99]. Under pressure, the ordering transitions start at higher temperatures [140]. No phase transformation for temperatures down to 20 K have been found for the corresponding i-phases.

i-Au$_{42}$In$_{42}$Yb$_{16}$

This stable i-phase, isostructural to i-Cd$_{5.7}$Yb, transforms below 524 K to the 1/1-approximant [117].

d-Al–Co–Cu–Si

In a synchrotron radiation diffraction study, it was shown that a slowly cooled sample with composition $Al_{63}Co_{17.5}Cu_{17.5}Si_2$ was actually a twinned approximant, with lattice parameters a = b = 51.515 Å, c = 4.13 Å, $\gamma = 108°$ [43]. In an in situ high-temperature study on samples with the same composition, a reversible QC⇔PC transformation was found taking place at $\approx 750°C$ [44]. The observed hysteresis indicates a first order transition [27] identified as-grown (Bridgman technique) samples as orientationally-twinned 1D QC. The transformation of this state to the decagonal phase took place at $\approx 830°C$. In neither study, transient states (such as in a 'devil's stair case' known from IMS) have been observed.

d-Al–Co–Ni

A 'continuous' transformation between the decagonal quasicrystalline and the crystalline state was observed by electron-microscopic investigations of differently long annealed (1120–1370 K, 40–1370 h) samples with composition $Al_{72.7}Co_{19}Ni_{8.3}$ [29]. After homogenization, the *d*-phase with S1 superstructure was identified as a minority phase beside a disordered quasiperiodic phase with pseudo-fivefold symmetry and without superstructure reflections. By prolonged annealing these phases were transformed into a 1D QC and finally to a "non-Fibonacci-type approximant" (for a definition of this term see [29]) with lattice parameters $a \approx 50.8$ Å, $b \approx 8.25$ Å, $c \approx 32.2$ Å.

d-Al–Ni–Fe

A sample with composition $Al_{70}Fe_{7.5}Ni_{22.5}$ has been shown to transform below 1120 K into $Al_3Ni_2(Fe)$, $Al_3Ni(Fe)$, and $Al_{13}(Fe,Ni)_4$ [48].

Metastable i-$Al_{85}Mn_{14}Si_1$, i-$Al_{85}(Mn_{0.72}Fe_{0.28})_{14}Si_1$

Metastable QC show rather short correlation lengths of a few 100 Å at most, i.e. a few cluster diameters only. Additionally, they contain many defects and may not be fully chemically ordered. Consequently, diffusive transitions to the crystalline phases will be easier than that of perfectly ordered stable quasicrystals.

By heating the rapidly quenched samples directly up to 700 K, both samples were transformed into their orthorhombic modifications, *o*-Al_6Mn and *o*-$Al_6(Mn_{0.72}Fe_{0.28})$. In the in situ experiment, the first step starts at ≈ 620 K and is the completed at 690 K with the formation of the orthorhombic phase. The second step starts at ≈ 710 K with the formation of the cubic α-Al–Mn–Si phase and ends at ≈ 750 K. Based on contrast variation data, the authors conclude that the Al subnetwork of the *i*-phase transforms smoothly into that of the orthorhombic phase without deep modification of the subset average structure. On the contrary, the Mn subnetwork is completely reconstructed, and it destabilizes when the Al subnetwork has absorbed too much external aluminium.

Metastable d-Al_5Pd

On heating to 600°C for several hours, the *d*-phase gradually transforms into decagonally-twinned orthorhombic Al_3Pd and into τ-phases [88].

Metastable Octagonal-Phases

Phase transitions of *o*-$Mn_{82}Si_{15}Al_3$ to either cubic micro-twinned $Mn_3Si(Al)$ (slow heating) or a β-Mn-type (rapid heating) structure have been observed [142]. The transitions are described phenomenologically as being of the phason-type and resulting from two different phason fields.

A continuous change from metastable *o*-Cr–Ni–Si and *o*-Mn–Si–Al to the cubic phase with β-Mn structure type was observed by moving the SAED aperture successively from the octagonal to the cubic area of the samples [136]. The orientational relationship between the cubic and the octagonal phase resulted in $[001]_{\beta-Mn}||[00001]_{oct}$ and $[100]_{\beta-Mn}||[11000]_{oct}$ [83]. The transformation was explained by gradual introduction of a phason strain field [89]. A theoretical model based on the Schur rotation (i.e. a one-parameter rotation in the *n*D description) for this transition was published by [10].

10.4.2.2 Transitions as Function of Irradiation

By fast particle (electrons, ions) irradiation of a sample above a specific energy threshold (20–30 eV) radiolytic (ionization and bond breaking) or knock-on (collision and knocking out of atoms from their sites) damage can take place. Radiolytic effects predominantly occur at low energies, knock-on effects only at high-energies. The induced defects accelerate atomic diffusion considerably [46, 118]. This may help to overcome the sluggish kinetics of low-temperature QC $\Rightarrow$ PC transformations.

i-$Al_{62}Cu_{25.5}Fe_{12.5}$

The irradiation-induced (120 keV Ar^+ ions) dose-dependent transition of the *i*- to the $B2$ phase was studied at room temperature (RT) [137] and at liquid-nitrogen temperature [146]. Between the 5-fold ($A5$) and 2-fold ($A2$) directions of the QC and the corresponding directions of the $B2$-phase the following orientation relationships were observed: $A5||[110]_{B2}, [113]_{B2}, A2||[11\bar{1}]_{B2}$. Only heating the sample above 880 K transformed it back again into the *i*-phase. This was taken as evidence for the stability of the $B2$ phase at RT.

i-$Al62Cu25.5Fe12.5$, α-$Al_{55}Cu_{27}Fe_{11}Si_7$

Both phases remain stable under irradiation with 900 MeV Pb and 780 MeV Xe ions at 80 K and at RT [22]. This experiment was complementary to the above mentioned one due to the different energy deposition by the ions in the target, i.e. mainly by high electronic excitations instead by nuclear

collisions. The relaxation of the energy deposited in the excited electrons is assumed to generate shock waves with pressures of several tens of GPa. Since quasicrystals are remarkably stable under pressure, it is not surprising that no phase transition has been induced in this experiment.

d-Al–Co–Cu(–Si,Ge)

Irradiation of d-$Al_{65}Co_{15}Cu_{20}$ with a 400 kV electron beam induced a structural transformation to the β-phase, which cannot be observed for beams with 100 kV [105]. In a similar experiment [148], it was shown that d-$Al_{65}Co_{20}Cu_{15}$ and d-$Al_{62}Co_{15}Cu_{20}Si_3$ first transform into the β-phase (disordered CsCl-type), which then orders to a CsCl-type phase within 15 min. The authors concluded that the transformation was not induced by electron beam heating ($\Delta T < 323\,K$) but by radiation damage, and that the major effect consisted in an enhancement of the rate at which the transformation occurred. The stable phase at room temperature should be the CsCl-type one, consequently. The orientation relationship between the d-phase and the cubic phase was as follows: $A10||[110], A2D||[1\bar{1}0] or [1\bar{1}1], A2P||[001]$ ($A2P$ and $A2D$ denote the two symmetrically inequivalent 2-fold directions).

A QC $\Rightarrow$ PC transformation was observed during electron beam irradiation of a microcrystalline sample with composition $Al_{63}Co_{17.5}Cu_{17.5}Si_2$ [9]. The back-transformation from the microcrystalline to the quasiperiodic state takes place shortly before the sample begins to melt. Irradiation experiments carried out later on microcrystalline $Al_{62}Co_{15}Cu_{20}Si_3$ with a 400 keV electron beam confirmed this phase transformation [104].

The orientation relationship between the d-phase and the β-phase was explained in terms of the PAS common to both phases [122]. The $[\bar{1}10]_\beta$ direction of the β-phase is parallel to the 10-fold axis of the decagonal QC, $[110]_\beta$ and $[110]_\beta$ are parallel to the two different 2-fold axes of the d-phase. From this it follows for the average structure: $\mathbf{a}_1^{PAS}||[001]_\beta, \mathbf{a}_2^{PAS}||[110]_\beta$ and $\mathbf{a}_3^{PAS}||[\bar{1}10]_\beta$. The translation period along $[001]_\beta$ ranges from 2.88 to 2.92 Å, along $[110]_\beta$ and $[\bar{1}10]_\beta$ from 4.08 to 4.13 Å, respectively, and for lattice parameters of the β-phase from $a_\beta = 2.88\,\text{Å}$ in case of AlCo to $a_\beta = 2.92\,\text{Å}$ in case of Al(Co,Cu). This fits nicely to the periods in the respective directions of the periodic average structure of the d-phase (Al–Co–Cu: $a_r = 2.436, a_1^{PAS} = 2.88, a_2^{PAS} = 3.96, a_3^{PAS} = 4.15$ Å; Al–Co–Ni: $a_r = 2.456, a_1^{PAS} = 2.90, a_2^{PAS} = 3.99, a_3^{PAS} = 4.08$ Å).

Under irradiation with 1.5 MeV Xe$^+$ ions d-Al–Co–Cu–Ge transformed via an Al depleted *bcc* phase (β-phase?) to an amorphous phase [20]. Annealing at 873 K restored the d-phase again.

d-Al–Co–Ni

Phase transformations of annealed $Al_{70}Co_{15}Ni_{15}$ under irradiation with a 120 keV Ar$^+$ ion beam were studied by electron diffraction [100]. The following transformation sequence was observed as a function of increasing dose: ordered

d-phase $\Rightarrow$ disordered *d*-phase $\Rightarrow$ bcc phase (?) $\Rightarrow$ CsCl-type phase $\Rightarrow$ bcc phase (β-phase?). First, the increasing number of defects leads to an increase in disorder accompanied by diffusion of atoms to approach the equilibrium structure. Then, due to the high concentration of defects thermal diffusion leads to an ordered (close to equilibrium) state. Finally, further irradiation destroys the ordered equilibrium phase again.

i-$Al_{70}Pd_{20}Mn_{10}$

Under 1.5 keV-Ar^+-irradiation, the pentagonal surface of icosahedral $Al_{70}Pd_{20}Mn_{10}$ transforms into the cubic β-phase [18]. Annealing at 700 K restores the icosahedral symmetry again. Both phases are in an orientation relationship with a high degree of structural registry. The authors find "most remarkable the long-range orientational coherence across the entire macro-scopic surface of both the bcc and annealed quasicrystalline structures." The five fold axis of the *i*-phase perpendicular to the surface is parallel to the [110]-direction of the β-phase. This case is very similar to the example discussed above since the pentagonal surface of the *i*-phase is similar to that of a *d*-phase.

10.4.2.3 Transitions by High-Energy Ball Milling

d-$Al_{65}Co_{15}Cu_{20}$

The *d*-phase transforms to a rather disordered nanocrystalline $B2$-phase after 30 h high-energy ball milling. Annealing up to 150 min at 873 K resulted in an increased ordering of the $B2$-phase rather than in the back-transformation to the decagonal phase [95, 96]. It is unclear whether this is due to the different resulting chemical composition of the $B2$-phase compared to that of the original *d*-phase or to a potential LT instability of the *d*-phase.

i-$Al_{63}Cu_{26}Fe_{11}$

After 1 h high-energy ball milling in air, the *i*-phase was partly transformed to $B2$-phase [97]. Further milling for 10 h yielded nanocrystalline $B2$-phase in an amorphous matrix. Subsequent heating/cooling cycles in a DTA experiment lead to a partial restoration of the *i*-phase while annealing at 1123 K for 10–20 h yields just well ordered $B2$-phase. Ball milling under argon of *i*-$Al_{65}Cu_{20}Fe_{15}$ lead to purely amorphous phase [98]. No $B2$-phase was observed at any time of this experiment.

$Al_{70}Fe_{7.5}Ni_{22.5}$

The *d*-phase transforms after 8 h ball milling into the $B2$ phase [143].

10.4.2.4 Amorphous $\Rightarrow$ Transient QC $\Rightarrow$ PC

Finally, transformations from the liquid or amorphous state to the crystalline state via an quasiperiodic intermediate state are briefly discussed.

l-$Ti_{39.5}Zr_{39.5}Ni_{21}$

The nucleation rate of the i-phase in undercooled liquid alloys is extremely high (cf. [56, 71] and references therein). This indicates a very low interfacial energy between the quasicrystalline nuclei and the liquid and, consequently, a locally similar structural ordering. Since an icosahedron consists of 20 slightly distorted tetrahedra and has locally a higher packing density than the cubic and hexagonal close sphere packings, the existence of local icosahedral (polytetrahedral) ordering in undercooled liquids was already suggested by Frank [45].

Recently, some more experimental evidence for Frank's hypothesis was found in an undercooling experiment on liquid $Ti_{39.5}Zr_{39.5}Ni_{21}$. At 953 K, first a metastable i-phase formed, which a few seconds later transformed into the Laves phase that is stable at this temperature [72]. Since the i-phase is stable only below 843 K, the nucleation barrier for the i-phase must be significantly lower than for the Laves phase, which also shows local polytetrahedral order. This small interfacial energy seems to also play an important role in the frequently observed QC nucleation in amorphous alloys.

Undercooling experiments on binary Ti–Zr and ternary Ti–Zr–Ni alloys showed that icosahedral short-range-order is best developed for the ternary alloys with a Ni content of 21%, which is the composition of the i-phase [80].

a-$Zr_{65}Ni_{10}Cu_{7.5}Al_{7.5}Ag_{10}$

The phase transitions of the bulk metallic glass were studied by continuous heating and isothermal annealing [84]. Activation energies for QC nucleation were found with 280 kJ mol^{-1} significantly smaller than the 366 kJ mol^{-1} reported for rapidly quenched amorphous ribbons. This indicates a local structure that is closer to icosahedral order in the bulk metallic glass than in the amorphous ribbon. The Avrami exponent varied from 3 to 2 as a function of the already transformed volume fraction of the sample. This was interpreted by a mechanism of 3D interfacial-controlled growth with zero-nucleation rate followed by diffusion-controlled growth with changing nucleation rate and, finally, a 2D interfacial-controlled growth with grain-edge nucleation. At higher temperatures, the quasicrystalline phase transformed into a crystalline Zr_2Cu-like phase.

The influence of pressure on the amorphous-to-quasicrystal transition was investigated on a material with the same composition by in situ high-pressure (0.68 GPa) and HT (663–693 K) X-ray diffraction as a function of annealing time [69]. The Avrami exponent was determined by the very low value of 1

indicating that atomic diffusion may play an important role in this phase transition. Indeed, the main effect of pressure was to enhance the onset temperature for the formation of QC with a rate of $9.4\,\mathrm{K\,GPa^{-1}}$ while the temperature interval for the stability of QC and their grain size decrease.

a-$Al_{75}\,Cu_{15}\,V_{10}$

The amorphous phase, obtained by high-energy ball milling, transforms at 727 K into an i-phase and subsequently, at 794 K, to crystalline Al_3V and Al_2Cu [4].

10.4.3 Microscopic Models

Several kinds of geometrical models have been developed to describe the transitions from and to the quasicrystalline state. The simplest and least realistic one is just based on a perp-space shear of a nD hypercrystal structure in terms of the higher-dimensional approach. This corresponds to the action of linear phason strain. In 3D reciprocal space, increasing linear phason strain manifests itself in a continuous displacement of the Bragg reflections from their original high-symmetry positions on a $\mathbb{Z}$-module of rank n. In direct space, linear phason strain causes atomic jumps (phason flips) in a correlated way. The number of flips increases linearly with the distance between the origin and the transformation front. This is illustrated in Fig. 10.8, where the transformation is shown as cutting space rotation in the IMS setting (see also Fig. 3.1).

The atoms can only run through this series of phason flips without strong local distortions if this is done in the whole quasicrystal in a fully correlated way. The practical problems related to this mechanism have been discussed by Steurer ([121, 123] and references therein). A more realistic scenario is the one shown by the stepped blue line (modulated cutting space) in Fig. 10.8. This course of the curve resembles that of a flattened phason mode. The transition can start locally everywhere in the quasicrystal, preferentially where patches of the quasiperiodic structure are actually similar to the approximant structure. In this case the quasicrystal would transform into an approximant nano-domain structure (Fig. 10.9).

Close to the transition temperature, AC nuclei begin to grow everywhere in the QC matrix where locally the structures of the QC and its n/m-approximant are already very similar (Fig. 10.10). These regions are around the origin (0,0) and all hyperlattice points of the type (F_{k+1}, F_k). For special values of k where $F_{k+2} = l(n + m)$, with $l \in \mathbb{Z}$, all those n/m-AC unit cells are in-phase (i.e. on the same AC-lattice) that have their origin at hyperlattice points (F_{k+1}, F_k). This condition is fulfilled for multiples of k as a consequence of the fact that $F_{lk} = LF_k$, with integer L and $l = 1, 2, \ldots$ [58]. Since n, m correspond to subsequent Fibonacci numbers $n = F_{k'+1}, m = F_{k'}$, the period of the rational n/m-AC along $V^{\parallel}$ corresponds to $(n+m)a_{PAS} = F_{k'+2}a_{PAS}$, with a_{PAS} the lattice parameter of the PAS of

the Fibonacci chain. Thus, all approximant domains growing from nuclei located at positions of that kind are in phase. This explains why domains being far away from each other can be in phase as observed in decagonal Al–Co–Ni transformation products [70].

The nuclei, consisting of a few AC unit cells, are chemically well ordered and their PAS coincides with that of the QC (Fig. 10.9(a)). With increasing size of the AC domains, however, the interatomic distances of the AC have to be slightly modified to keep the point density constant over the whole sample (Fig. 10.9(b)). Thus, the AC domains are strained. The strain can be partly released by the formation of $(n+1)/(m+1)$-AC domain walls. Further grain coarsening allows the strain to be released and to relax the interatomic distances to their former values (Fig. 10.9(c)).

The registry of AC unit cells on the lattice of the PAS forces the formation of low-energy domain boundaries or even a smooth transition from one domain to the other. The AC domains themselves, however, show a kind of chemically modulated structure (antiphase subdomains, see also Fig. 10.8). This is a result of the superposition of a completed positional QC $\Rightarrow$ AC transformation with the chemical order of the original QC. A well-ordered AC could be obtained from this transition state only by diffusion processes during long-time annealing. The diffraction pattern of the transient shown schematically in Fig. 10.9(a), would be very similar to that of the QC plus,
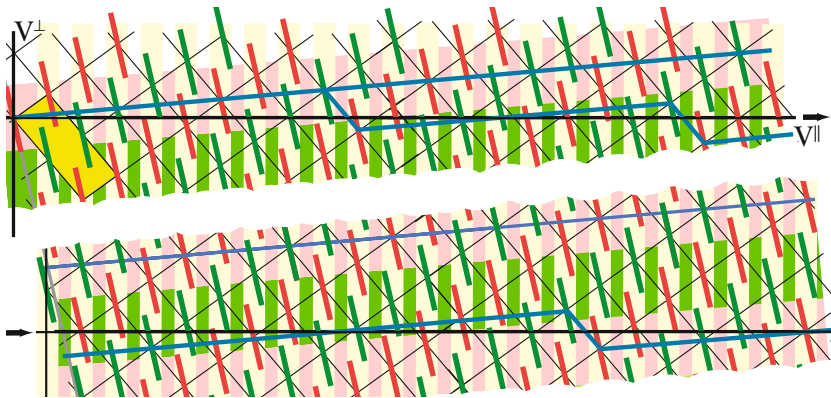
Fig. 10.8. The phase transition from the two-color Fibonacci sequence to the 2/1-approximant in the IMS-setting. The vertices of the 1D quasiperioidc structures are generated where the physical space (*black horizontal line*) cuts the 2D hypercrystal. The *blue lines* mark the cutting spaces generating a 2/1-approximant. While the distance between the *straight blue line* and $V^{\parallel}$ increases with increasing distance from the origin, the *stepped blue line* fluctuates closely around $V^{\parallel}$. In the first case, a single crystalline 2/1-approximant is formed by an increasing number of local phason flips. In the second case, nano-domains of 2/1-approximants are created by a few phason flips, separated by discommensurations. The *red* and *green areas* in the background illustrate the resulting nano-domains (from [123])
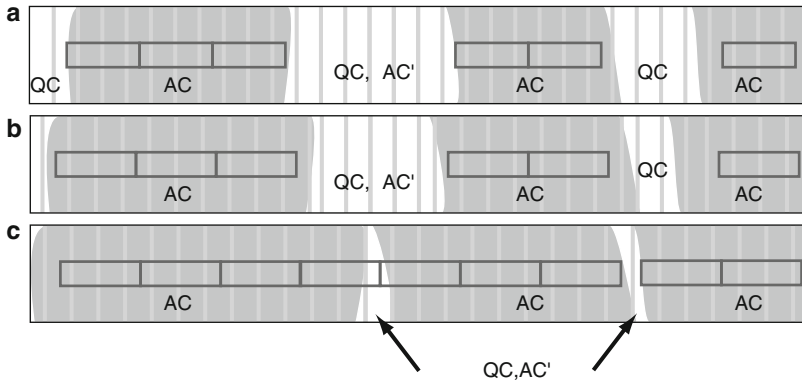
Fig. 10.9. Scenario of a QC ⇒ AC transformation. The AC domains are *shadowed*, the AC unit cells are schematically *outlined*, and the lattice of the PAS is shown by *vertical gray lines*. The different stages of the transition are shown from *top to bottom*: In (**a**) the PAS (and therewith the point densities) of QC and AC regions are equal, in (**b**) the AC domains relax their PAS, and the remaining QC or AC' matrix acts as discommensuration with respect to the AC lattice. In (**c**) the final fully relaxed state with low-energy domain boundaries is shown. The *arrows* indicate a unit cell misfit of one period of the PAS [121]
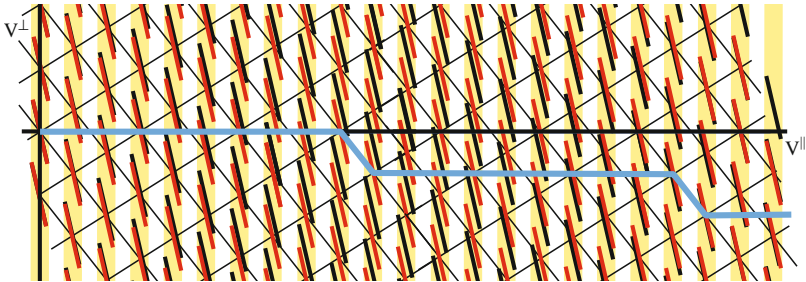
Fig. 10.10. Fibonacci sequence (*black*) superposed by its 2/1-approximant (*gray*, online: *red*) showing locally close agreement. Both have the same PAS. The *stepped gray* (online: *blue*) line connects the same vertices of the approximant hyperlattice as in Fig. 10.8. The distance between the $V_{||}$ cuts of a *gray* and its neighbouring *black* hyperatom corresponds to the displacement remaining after a series of phason flips necessary for a transformation from the Fibonacci sequence to the 2/1-approximant. This illustrates how a longitudinal phonon mode could drive the QC⇔AC transformation [123]

additionally, some diffuse scattering. With larger AC domains (Fig. 10.9(b)) broad AC reflections would replace more and more QC reflections and the diffuse scattering would become more structured. Finally (Fig. 10.9(c)), sharp AC reflections accompanied by (diffuse) satellite reflections plus some less structured diffuse scattering would be observed.
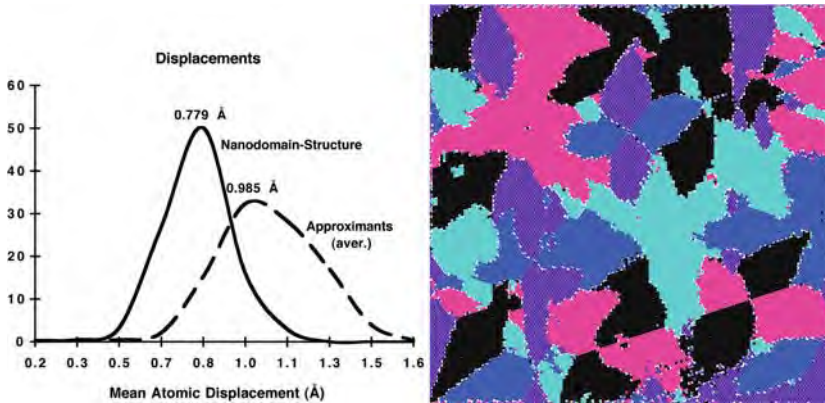
Fig. 10.11. (*at left*) Distribution functions of the atomic displacements necessary for the transformation of d-Al–Co–Ni to a single crystalline 4/6-approximant (*broken line*) and to an orientationally twinned nanodomain structure (*solid line*) as calculated from the simulations. (*at right*) Nanodomain structure, consisting of 22,151 unit cells of the 4/6-approximant, calculated in an area of $0\,\text{Å} \leqslant x, y \leqslant 8000\,\text{Å}$. The orientation of each approximant unit cell is selected according to the minimum sum of displacements necessary for transforming the QC into the approximant. The different domain orientations are indicated by *different* shades of gray (online: *colors*) [57]

The results obtained for a 1D QC, however, cannot be simply transferred to decagonal or icosahedral QC. For them such simple one-to-one mappings of all atoms of the PAS of QC and AC are not possible. Consequently, the first step in a QC to AC transformation in this model would yield a much more disordered and vacancy rich intermediate state and in the second step, diffusion would play an important role to reach the thermodynamic equilibrium state. This was demonstrated in the case of a model structure for d-Al–Co–Ni, where the specific properties of its PAS cause inherent disorder and the need of diffusion of approximately 40% of all atoms in course of the second stage of the QC-to-AC transformation [57] (Fig. 10.11).

Here, the 4/6-approximant was constructed with the lattice parameters $a_0 \approx 60.89\,\text{Å}$, $b_0 \approx 83.81\,\text{Å}$ in the orthorhombic C-centered setting, i.e. $a_m = b_m \approx 51.80\,\text{Å}$, $\gamma = 108°$ in the monoclinic one. The periodicity in the c-direction is $\approx 4.08\,\text{Å}$ for both the quasicrystal and the approximant, the stacking sequence is the same. This specific approximant was found in the systems Al–Cu–Co(–Si) and Al–Co–Ni by HRTEM, SAED and high resolution X-ray diffraction [43, 44, 70, 120]. The structure is built from the pentagonal clusters (diameter $\approx 20\,\text{Å}$) that decorate the quasiperiodic tiling. As a result of lowering the symmetry from $P10_5/mmc$ to $Ccmm$ the approximant structure is generated in five possible orientations, each one rotated relative to each other by $2\pi i/5$ $(i = 1, \ldots, 4)$.

However, at least in the case of decagonal phases, 1D quasicrystals have been observed as intermediate states of the QC $\Rightarrow$ AC transition. Probably, they generally play a role as intermediate state in the QC $\Rightarrow$ AC transitions. Rochal [110] proposed an interesting two-step mechanism for a "continuous

defect-free structural transformation of long-range order" of the infinite pentagonal Penrose tiling to one of its orthorhombic approximants through a series of intermediate structures, one of them a 1D quasicrystal. It essentially works by applying 1D linear phason strain in combination with a simultaneous variation of the shape of the atomic surfaces in the higher-dimensional description. This is done twice in two mutually orthogonal directions. In case of finite samples the result cannot be free of defects since insufficient or excess vertices have to come from or go to infinity. Nothing is said about how chemical ordering is achieved.

Another quasicontinuous mechanism is based on the so-called T-lattice (incommensurate to the AC lattice), of which at least a subset is left invariant during the transition QC to AC [107–109]. The order parameters are related to the amplitudes of the QC and AC basic mass density waves. The local structure of the QC and AC is similar close to the T-lattice points allowing a continuous QC-to-AC transformation by small displacements of atoms. Farther away from the T-lattice points, atomic diffusion is necessary. If no relaxation takes place during the diffusion process, the quasiperiodic long-range order would be preserved. This means that in an X-ray experiment no reflection splitting would be seen after the QC-to-AC transition in contradiction to what has been already observed.

References

1. E. Abe, A.P. Tsai, Quasicrystal-crystal transformation in Zn-Mg-rare-earth alloys. Phys. Rev. Lett. **83**, 753–756 (1999)
2. E. Abe, K. Saitoh, H. Takakura, A.P. Tsai, P.J. Steinhardt, H.C. Jeong, Quasi-unit-cell model for an Al-Ni-Co ideal quasicrystal based on clusters with broken tenfold symmetry. Phys. Rev. Lett. **84**, 4609–4612 (2000)
3. Y. Akahama, Y. Mori, M. Kobayashi, H. Kawamura, K. Kimura, S. Takeuchi, Pressure-induced amorphization of quasi crystals. J. Phys. Soc. Jpn. **58**, 2231–2234 (1989)
4. N. Asahi, S. Noguchi, K. Matsumura, The amorphous to icosahedral phase-transformation in mechanically alloyed $Al_{75}Cu_{15}V_{10}$ powder. Mater. Sci. Eng. A **181/182**, 819–822 (1994)
5. M. Audier, Y. Bréchet, P. Guyot, High-temperature stability and faceting of the icosahedral Al-Fe-Cu phase. Phil. Mag. Lett. **61**, 55–62 (1990)
6. M. Audier, Y. Bréchet, M. De Boissieu, P. Guyot, C. Janot, J.M. Dubois, Perfect and modulated quasi-crystals in the system Al-Fe-Cu. Phil. Mag. B **63**, 1375–1393 (1991)
7. M. Audier, M. Duneau, M. De Boissieu, M. Boudard, A. Letoublon, Superlattice ordering of cubic symmetry in an icosahedral Al- Pd-Mn phase. Phil. Mag. A **79**, 255–270 (1999)
8. M. Audier, P. Guyot, M. De Boissieu, N. Menguy, Crystal-to-quasi-crystal transformations. J. Non-Cryst. Sol. **153/154**, 591–594 (1993)
9. M. Audier, B. Robertson, Crystalline to quasi-crystalline transformation in an AlCoCuSi alloy – characteristics of the observed decagonal quasi-lattice. Philos. Mag. Lett. **64**, 401–409 (1991)

10. M. Baake, D. Joseph, P.Kramer, The schur rotation as a simple approach to the transition between quasi-periodic and periodic phases. J. Phys. (London). A **24**, L961–L967 (1991)

11. P. Bak, Commensurate phases, incommensurate phases and the complete devil's staircase. Rep. Prog. Phys. **45**, 587–629 (1982)

12. P. Bak, Symmetry, stability, and elastic properties of icosahedral incommensurate crystals. Phys. Rev. B **32**, 5764–5772 (1985)

13. P.A. Bancel, Dynamical phasons in a perfect quasicrysta. Phys. Rev. Lett. **63**, 2741–2744l (1989)

14. A. Baronnet, Polytypism and stacking disorder. Rev. Min. **27**, 231–288 (1992)

15. J.A. Barrow, D.J. Sordelet, M.F. Besser, C.J. Jenks, P.A. Thiel, E.F. Rexer, S.J. Riley, Analysis of gas-phase clusters made from laser-vaporized icosahedral Al-Pd-Mn. J. Phys. Chem. A **106**, 9204–9208 (2002)

16. L. Beraha, W. Steurer, J.M. Perez-Mato, The quasicrystal-to-crystal transformation. II. Landau theory. Z. Kristallogr. **216**, 573–585 (2001)

17. B.B. Bokhonov, E.Y. Ivanov, B.P. Tolochko, M.P. Sharaphutdinov, In situ study of structural transformations of $Mg_{44}Al_{15}Zn_{41}$ quasicrystals under heating. Mater. Sci. Eng. A **278**, 236–241 (2000)

18. B. Bolliger, M. Erbudak, D.D. Vvedensky, M. Zurkirch, Surface structural transitions on the icosahedral quasicrystal $Al_{70}Pd_{20}Mn_{10}$. Phys. Rev. Lett. **80**, 5369–5372 (1998)

19. J. Brillo, A. Bytchkov, I. Egry, L. Hennet, G. Mathiak, I. Pozdnyakova, D.L. Price, D. Thiaudiere, D. Zanghi, Local structure in liquid binary Al-Cu and Al-Ni alloys. J. Non-Cryst. Sol. **352**, 4008–40012 (2006)

20. L.F. Chen, L.M. Wang, Y.X. Guo, R.C. Ewing, Ion irradiation-induced phase transformation in Al-Cu-Co-Ge decagonal quasicrystal. Nucl. Instr. Meth. Phys. Res. B **127**, 127–131 (1997)

21. V.A. Chizhikov, Phase transitions in cubic approximants of icosahedral quasicrystals occurring without changes of the translation symmetry. Crystallogr. Rep. **44**, 1024–1029 (1999)

22. G. Coddens, A. Dunlop, H. Dammak, R. Chatterjee, Y. Calvayrac, M. Quiquandon, E. Elkaim, M. Gailhanou, S. Rouziere, Study of the effect of high electronic excitations in quasicrystals irradiated with heavy ions. Nucl. Instr. Meth. Phys. Res. B **211**, 122–132 (2003)

23. J.D. Corbett, Polyanionic clusters and networks of the early p-element metals in the solid state: Beyond the zintl boundary. Angew. Chem. Int. Ed. **39**, 670–690 (2000)

24. H.Z. Cummins, Experimental studies of structurally incommensurate crystal phases. Phys. Rep. **185**, 211–409 (1990)

25. M. De Boissieu, M. Boudard, T. Ishimasa, E. Elkaim, J.P. Lauriat, A. Letoublon, M. Audier, M. Duneau, A. Davroski, Reversible transformation between an icosahedral Al-Pd-Mn phase and a modulated structure of cubic symmetry. Philos. Mag. A **78**, 305–326 (1998)

26. G.T. Delaissardiere, D. Mayou, Clusters and localization of electrons in quasicrystals. Phys. Rev. B **55**, 2890–2893 (1997)

27. F. Denoyer, P. Launois, T. Motsch, M. Lambert, On the phase-transition mechanism in Al-Cu-Fe - structural-analysis the modulated quasi-crystalline and of the microcrystalline states. J. Non-Cryst. Sol. **153/154**, 595–599 (1993)

28. V.E. Dmitrienko, V.A. Chizhikov, Distortions of the atomic structure of 2/1 approximants of icosahedral quasicrystals. Crystallogr. Rep. **52**, 1040–1047 (2007)

29. M. Döblinger, R. Wittmann, D. Gerthsen, B. Grushko, Continuous transition between decagonal quasicrystal and approximant by formation and ordering of out-of-phase domains. Phys. Rev. B **65**, art. no. 224201 (2002)

30. N. Doraiswamy, L.D. Marks: Preferred structures in small particles. Phil. Mag. B **71** 291–310 (1995)

31. M. Duneau, D. Gratias, Covering clusters in icosahedral quasicrystals. In *Coverings of Discrete Quasiperiodic Sets: Theory and Applications to Quasicrystals*, ed. by P. Kramer, Z. Papadopolos. Springer Tracts in Modern Physics, vol **180**, (Springer, Berlin, 2003), pp. 23–62

32. M. Duneau, Modulated quasi-crystals – a mechanism induced by 6d shears. J. Phys. I France **2**, 1731–1740 (1992)

33. M. Duneau, C. Oguey, Displacive transformations and quasi-crystalline symmetries. J. Phys. France **51**, 5–19 (1990)

34. M. Duneau, C. Oguey, Icosahedral twins can be produced by simple modulations. Europhys. Lett. **13**, 67–72 (1990)

35. M. Duneau, C. Oguey, Bounded interpolations between lattices. J. Phys. A **24**, 461–475 (1991)

36. P. Ebert, Importance of bulk properties in the structure and evolution of cleavage surfaces of quasicrystals. Prog. Surf. Sci. **75**, 109–130 (2004)

37. P. Ebert, M. Feuerbacher, N. Tamura, Urban, K, Wollgarten, M., Evidence for a cluster-based structure of AlPdMn single quasicrystals. Phys. Rev. Lett. **77**, 3827–3830 (1996)

38. P. Ebert, F. Kluge, B. Grushko, K. Urban, Evolution of the composition and structure of cleaved and heat- treated icosahedral Al-Pd-Mn quasicrystal surfaces. Phys. Rev. B **60**, 874–880 (1999)

39. P. Ebert, F. Kluge, K. Urban, Evidence for a two-step evolution of the surface structure during heat treatment of cleaved icosahedral Al-Pd-Mn single quasicrystals. Surf. Sci. **435**, 312–316 (1999)

40. P. Ebert, F. Kluge, M. Yurechko, B. Grushko, K. Urban, Structure and composition of cleaved and heat-treated tenfold surfaces of decagonal Al-Ni-Co quasicrystals. Surf. Sci. **523**, 298–306 (2003)

41. P. Ebert, F. Yue, K. Urban, Surface structures of cleaved icosahedral Al-Pd-Mn single quasicrystals after heat treatment. Phys. Rev. B **57**, 2821–2825 (1998)

42. K. Edagawa, H. Sawa, S. Takeuchi, Order-disorder transformation in an Al-Ni-Co decagonal quasi-crystal. Philos. Mag. Lett. **69**, 227–234 (1994)

43. M. Fettweis, P. Launois, F. Denoyer, R. Reich, M. Lambert, Decagonal quasi-crystalline or microcrystalline structures – the specific case of Al-Cu-Co(-Si). Phys. Rev. B. **49**, 15573–15587 (1994)

44. M. Fettweis, P. Launois, R. Reich, R. Wittmann, F. Denoyer, Evidence of a reversible microcrystal quasi-crystal phase-transition in decagonal Al-Cu-Co (-Si). Phys. Rev. B **51**, 6700–6703 (1995)

45. F.C. Frank, Supercooling of liquids. Proc. R. Soc. London A **215**, 43–46 (1952)

46. J. Gittus, Irradiation effects in crystalline solids. Appl. Sci. London (1978)

47. B.K. Godwal, R.S. Rao, R. Chidambaram, Cluster-disordered glue model and role of glue atoms in the icosahedral quasicrystalline structure. J. Non-Cryst. Solids **334**, 117–120 (2004)

48. B. Grushko, U. Lemmerz, K. Fischer, C. Freiburg, The low-temperature instability of the decagonal phase in Al- Ni-Fe. Phys. Stat. Sol. (a) **155**, 17–30 (1996)

49. P. Gummelt, Penrose tilings as coverings of congruent decagons. Geom. Dedicata **62**, 1–17 (1996)

50. J.Q. Guo, E. Abe, A.P. Tsai, Stable Cd-Mg-Yb and Cd-Mg-Ca icosahedral quasicrystals with wide composition ranges. Philos. Mag. Lett. **82**, 27–35 (2002)

51. C.L. Henley, M. Mihalkovic, M. Widom, Total-energy-based structure prediction for d(AlNiCo). J. Alloys. Comp. **342**, 221–227 (2002)

52. I. Hirai, T. Ishimasa, A. Ltoublon, M. Boudard, M. De Boissieu, Formation conditions of two quasiperiodic modifications of Al-Pd-Mn icosahedral phase studied by annealing method. Mater. Sci. Eng. A **294–296**, 33–36 (2000)

53. K. Hiraga, T. Ohsuna, W. Sun, K. Sugiyama, Structural characteristics of Al-Co-Ni decagonal quasicrystals and crystalline approximants. Mater. Trans. JIM **42**, 2354–2367 (2001)

54. V.V. Hoang, T. Odagaki, Glasses of simple liquids with double-well interaction potential. Physica B **403**, 3910–3915 (2008)

55. D. Holland-Moritz, T. Schenk, V. Simonet, R. Bellissent, Short-range order in undercooled and stable melts forming quasicrystals and approximants and its influence on nucleation. Philos. Mag. **86**, 255–262 (2006)

56. J.C. Holzer, K.F. Kelton, The structural relations between amorphous, icosahedral, and crystalline phases. Al-Cu-V; Al-Mn-Si, in *Crystal-Quasicrystal Transitions*, ed. by M.J. Yacaman, M. Torres (North-Holland, Amsterdam, 1993), pp. 103–142

57. M. Honal, T. Haibach, W. Steurer, Geometrical model of the phase transformation of decagonal Al-Co-Ni to its periodic approximant. Acta. Crystallogr. A **54**, 374–387 (1998)

58. X. Huang, C. Gong, Property of Fibonacci numbers and the periodiclike perfectly transparent electronic states in Fibonacci chains. Phys. Rev. B **58**, 739–744 (1998)

59. Y. Ishi, Soft phason modes inducing rhombohedral-icosahedral transformation. Philos. Mag. Lett. **62**, 393–397 (1990)

60. Y. Ishi, Phason softening and structural transitions in icosahedral quasicrystals. Phys. Rev. B **45**, 5228–5239 (1992)

61. T. Ishimasa, Superlattice ordering in the low-temperature icosahedral phase of Al-Pd-Mn. Philos. Mag. Lett. **71**, 65–73 (1995)

62. C. Janot, Atomic clusters, local isomorphism, and recurrently localized states in quasicrystals. J. Phys. Condens. Matter. **9**, 1493–1508 (1997)

63. C. Janot, M. Audier, M. De Boissieu, J.M. Dubois, Al-Cu-Fe quasi-crystals – low-temperature unstability via a modulation mechanism. Europhys. Lett. **14**, 355–360 (1991)

64. C. Janot, A. Magerl, B. Frick, M. De boissieu, Localized vibrations from clusters in quasi-crystals. Phys. Rev. Lett. **71**, 871–874 (1993)

65. T. Janssen, Commensurate approximants of icosahedral quasi-crystals. Europhys. Lett. **14**, 131–136 (1991)

66. T. Janssen, G. Chapuis, M. De Boissieu, *Aperiodic Crystals*. From modulated phases to quasicrystals. IUCr monographs on Crystallography 20. (Oxford University Press, Oxford 2007)

67. H.C. Jeong, P.J. Steinhardt, Cluster approach for quasi-crystals. Phys. Rev. Lett. **73**, 1943–1946 (1994)

68. J. Jia, J.Z. Wang, X. Liu, Q.K. Xue, Z.Q. Li, Y. Kawazoe, S.B. Zhang, Artificial nanocluster crystal: Lattice of identical Al clusters. Appl. Phys. Lett. **80**, 3186–3188 (2002)

69. J.Z. Jiang, Y.X. Zhuang, H. Rasmussen, J. Saida, A. Inoue, Formation of quasicrystals and amorphous-to-quasicrystalline phase transformation kinetics in $Zr_{65}Al_{7.5}$ $Ni_{10}Cu_{7.5}Ag_{10}$ metallic glass under pressure. Phys. Rev. B **64**, art. no. 094208 (2001)

70. M. Kalning, S. Kek, H.G. Krane, V. Dorna, W. Press, W. Steurer, Phason-strain analysis of the twinned approximant to the decagonal quasicrystal $Al_{70}Co_{15}Ni_{15}$: Evidence for a one-dimensional quasicrystal. Phys. Rev. B **55**, 187–192 (1997)

71. K.F. Kelton, Crystallization of liquids and glasses to quasicrystals. J. Non-Cryst. Sol. **334**, 253–258 (2004)

72. K.F. Kelton, G.W. Lee, A.K. Gangopadhyay, R.W. Hyers, T.J. Rathz, J.R. Rogers, M.B. Robinson, D.S. Robinson, First x-ray scattering studies on electrostatically levitated metallic liquids: Demonstrated influence of local icosahedral order on the nucleation barrier. Phys. Rev. Lett. **90**, art. no. 195504 (2003)

73. K.F. Kelton, G.W. Lee, A.K. Gangopadhyay, R.W. Hyers, T.J. Rathz, J.R. Rogers, M.B. Robinson, D.S. Robinson, First x-ray scattering studies on electrostatically levitated metallic liquids: Demonstrated influence of local icosahedral order on the nucleation barrier. Phys. Rev. Lett. **90**, art. no. 195504 (2003)

74. K. Kimura, M. Takeda, M. Fujimori, R. Tamura, H. Matsuda, R. Schmechel, H. Werheit, A unified picture for icosahedral cluster solids in boron-based and aluminum-based compounds. J. Solid. State. Chem. **133**, 302–309 (1997)

75. R.B. King, G.H. Robinson, Analogies between Group 13 metal clusters in organometallic and intermetallic structures. J. Organomet. Chem. **597**, 54–60 (2000)

76. K. Kirihara, T. Nagata, K. Kimura, K. Kato, M. Takata, E. Nishibori, M. Sakata, Covalent bonds and their crucial effects on pseudogap formation in alpha-Al(Mn,Re)Si icosahedral quasicrystalline approximant. Phys. Rev. B **68**, art. no. 014205 (2003)

77. M. Krajci, J. Hafner, Structure, stability, and electronic properties of the i-AlPdMn quasicrystalline surface. Phys. Rev. B **71**, art. no. 054202 (2005)

78. M.J. Kramer, T.A. Lograsso, D.J. Sordelet, Solid and liquid thermal expansion and structural observations in the quasicrystalline $Cd_{84}Yb_{16}$ compound. Philos. Mag. Lett. **85**, 151–162 (2005)

79. G. Krauss, Q.F. Gu, S. Katrych, W. Steurer, In situ study of icosahedral Zn-Mg-Dy and Co-rich decagonal Al-Co-Ni at high pressures and high temperatures. J. Phys. Condens. Matter **19**, art. no. 116203 (2007)

80. G.W. Lee, A.K. Gangopadhyay, R.W. Hyers, T.J. Rathz, J.R. Rogers, D.S. Robinson, A.I. Goldman, K.F. Kelton, Local structure of equilibrium and supercooled Ti-Zr-Ni liquids. Phys. Rev. B **77**, art. no. 184102 (2008)

81. A. Le Lann, J. Devaud, Structural transformation from the AlCuFe icosahedral phase to the 1/1 cubic $\alpha-$(AlSi)CuFe approximant phase; three dimensional models of translation defects. Eur. Phys. J. B **15**, 235–246 (2000)

82. A. Letoublon, T. Ishimasa, M. De Boissieu, M. Boudard, B. Hennion, M. Mori, Stability of the F2–(Al-Pd-Mn) phase. Phil. Mag. Lett. **80**, 205–213 (2000)

83. F.H. Li, Y.F. Cheng, Relationscip between octagonal quasicrystal and beta-Mn type crystal in cut description. Chin. Phys. Lett. **13**, 199–202 (1996)

84. L. Liu, K.C. Chan, Amorphous-to-quasicrystalline transformation in $Zr_{65}Ni_{10}Cu_{7.5}Al_{7.5}Ag_{10}$ bulk metallic glass. J. Alloys. Comp. **364**, 146–155 (2004)

85. W. Liu, U. Köster, Continuous transformation of Al-Cu-Fe quasi-crystals by structural modulations. J. Non-Cryst. Sol. **153/154**, 615–619 (1993)

86. W. Liu, U. Köster, A. Zaluska, Continuous decomposition of icosahedral quasi-crystals in Al- Cu-Fe alloys. Phys. Stat. Sol. (a) **126**, K9–K14 (1991)

87. H. Li, G.H. Wang, J.J. Zhao, X.F. Bian, Cluster structure and dynamics of liquid aluminum under cooling conditions. J. Chem. Phys. **116**, 10809–10815 (2002)

88. L. Ma, R. Wang, K.H. Kuo, Quasi-Crystals in rapidly solidified alloys of Al-Pt group-metals .4. Quasi-crystals in rapidly solidified Al-Pd and Al-Pt alloys. J. Less-Common. Met. **163**, 37–49 (1990)

89. Z.H.I. Mai, L. Xu, N. Wang, K.H. Kuo, Z.C. Jin, G. Cheng, Effect of phason strain on the transition of an octagonal quasi-crystal to a $\beta-$Mn-type structure. Phys. Rev. B **40**, 12183–12186 (1989)

90. T.P. Martin, Shells of atoms. Phys. Rep. **273**, 199–241 (1996)

91. N. Menguy, M. Audier, P. Guyot, Transient modulated chemical order during the quasi-crystal-to- crystal phase-transition of Al-Fe-Cu. Phil. Mag. Lett. **65**, 7–14 (1992)

92. N. Menguy, M. De Boissieu, P. Guyot, M. Audier, E. Elkaim, J.P. Lauriat, Single crystal X-ray study of a modulated icosahedral AlCuFe phase. J. Phys. I France **3**, 1953–1968 (1993)

93. R. Mikulla, J. Stadler, F. Krul, H.R. Trebin, P. Gumbsch, Crack propagation in quasicrystals. Phys. Rev. Lett. **81**, 3163–3166 (1998)

94. S. Mitani, H. Fujimori, K. Takanashi, K. Yakushiji, J.-G. Ha, S. Takahashi, S. Maekawa, S. Ohnuma, N. Kobayashi, T. Masumoto, M. Ohnuma, K. Hono, J. Magn. Magn. Mater. **198–199**, 179–184 (1999)

95. N.K. Mukhopadhyay, G.V.S. Murthy, B.S. Murty, G.C. Weatherly, Transformation of the decagonal quasicrystalline phase to a B2 crystalline phase in the Al-Cu-Co system by high-energy ball milling. Phil. Mag. Lett. **82**, 383–392 (2002)

96. N.K. Mukhopadhyay, G.V.S. Murthy, B.S. Murty, G.C. Weatherly, An investigation on the transformation of the decagonal phase to a B2 phase in Al-Cu-Co alloy during mechanical milling. J. Alloys. Comp. **342**, 38–41 (2002)

97. N.K. Mukhopadhyay, T.P. Yadav, O.N. Srivastava, An investigation on the transformation of the icosahedral phase in the Al-Fe-Cu system during mechanical milling and subsequent annealing. Phil. Mag. A. **82**, 2979–2993 (2002)

98. S. Nasu, M. Miglierini, K.N. Ishihara, P.H. Shingu, Transformation from icosahedral quasi-crystalline to amorphous structure in $Al_{65}Cu_{20}Fe_{15}$. J. Phys. Soc. Jpn. **61**, 3766–3772 (1992)

99. K. Nishimoto, R. Tamura, S. Takeuchi, K. Edagawa, M. Ichihara, Low-temperature transmission electron microscopy studies of Cd-based 2/1 approximants and quasicrystals. Philos. Mag. **86**, 499–503 (2006)

100. Y.L. Qin, R.H. Wang, Q.L. Wang, Y.M. Zhang, C.X. Pan, Ar^+-Ion-irradiation-induced phase transformations in an $Al_{70}Co_{15}Ni_{15}$ decagonal quasicrystal. Phil. Mag. Lett. **71**, 83–90 (1995)

101. M. Quiquandon, D. Gratias, Unique six-dimensional structural model for Al-Pd-Mn and Al-Cu-Fe icosahedral phases. Phys. Rev. B **74**, art. no. 214205 (2006)

102. A. Quivy, M. Quiquandon, Y. Calvayrac, F. Faudot, D. Gratias, C. Berger, R.A. Brand, V. Simonet, F. Hippert, A cubic approximant of the icosahedral phase in the (Al-Si)-Cu- Fe system. J. Phys. Condens. Matt. **8**, 4223–4234 (1996)

103. M. Reichert, F. Gähler, Cluster model of decagonal tilings. Phys. Rev. B **68**, art. no. 214202 (2003)

104. J. Reyes-Gasga, R. Garcia, M. Jose-Yacaman, Electron-beam-induced structure transformation of the quasi-crystalline phases of the $Al_{62}Cu_{20}Co_{15}Si_3$ alloy. Radiat. Phys. Chem. **45**, 283–291 (1995)

105. J. Reyes-Gasga, A. Lara, H. Riveros, M. Jose-Yacaman, Characterization of the decagonal quasi-crystalline phase of the $Al_{62}Cu_{20}Co_{15}Si_3$ alloy by TEM. Mater. Sci. Eng. A **150**, 87–99 (1992)

106. M.G. Richmond, Annual survey of organometallic metal cluster chemistry for the year 2002. Coord. Chem. Rev. **248**, 881–901 (2004)

107. S.B. Rochal, Theory of the crystal-quasicrystal phase transition and its applications to particular structures. Crystallogr. Rep. **42**, 714–723 (1997)

108. S.B. Rochal, Quasicontinuous mechanism of the quasicrystal-to-crystal phase transition. Phys. Lett. A **253**, 327–332 (1999)

109. S.B. Rochal, V.P. Dmitriev, V.L. Lorman, P. Toledano, Local mechanism for crystal-quasicrystal transformations. Phys. Lett. A **220**, 111–116 (1996)

110. S.B. Rochal, V.L. Lorman, Continuous defect-free structural transformation of long-range order from quasiperiodic to translational. Phys. Rev. B **68**, art. no. 144203 (2003)

111. F. Rosch, C. Rudhart, J. Roth, H.R. Trebin, P. Gumbsch, Dynamic fracture of icosahedral model quasicrystals: A molecular dynamics study. Phys. Rev. B **72**, art. no. 014128 (2005)

112. S. Sachdev, D.R. Nelson, Order in metallic glasses and icosahedral crystals. Phys. Rev. B **32**, 4592–4606 (1985)

113. A. Sadoc, J.P. Itie, A. Polian, S. Lefebvre, Pressure-induced phase transition in icosahedral Al-Li-Cu quasicrystals. Phil. Mag. A. **74**, 629–639 (1996)

114. K. Saitoh, K. Tsuda, M. Tanaka, New structural model of an $Al_7Ni_20Co_8$ decagonal quasicrystal. J. Phys. Soc. Jpn. **67**, 2578–2581 (1998)

115. K. Saitoh, T. Yokosawa, M. Tanaka, A.P. Tsai, Formation of a superlattice order from a fundamental-lattice decagonal quasierystal of $Al_{72}Ni_{20}Co_8$. J. Phys. Soc. Jpn. **73**, 1786–1792 (2004)

116. R.J. Schaefer, L.A. Bendersky, D. Shechtman, W.J. Boettinger, F.S. Biancaniello, Icosahedral and decagonal phase formation in Al-Mn alloys. Metall. Trans. A **17**, 2117–2125 (1986)

117. A. Singh, J.Q. Guo, A.P. Tsai, Stability and diffraction features of quasicrystal and 2/1 approximant phase in an $Au_{42}In_{42}Yb_{16}$ alloy. Mater. Sci. Eng. A **449**, 991–994 (2007)

118. D.J. Smith, The realization of atomic resolution with the electron microscope. Rep. Prog. Phys. **60**, 1513–1580 (1997)

119. C. Soltmann, C. Beeli, R. Lück, W. Gander, In situ high-temperature powder diffraction study of reversible phase transitions in decagonal $Al_{71.2}Co_{12.8}Ni_{16}$. J. Appl. Crystallogr. **36**, 1030–1039 (2003)

120. S.H. Song, L. Wang, E.R. Ryba, Observation of lattice fringes in an approximant to the Al-Co-Cu decagonal phase. J. Mater. Sci. Lett. **12**, 80–83 (1993)
121. W. Steurer, Structural phase transitions of decagonal quasicrystals. MRS Proc. **553**, 159–170 (1999)
122. W. Steurer, Geometry of quasicrystal-to-crystal transformations. Mater. Sci. Eng. A **294**, 268–271 (2000)
123. W. Steurer, The quasicrystal-to-crystal transformation. I. Geometrical principles. Z. Kristallogr. **215**, 323–334 (2000)
124. W. Steurer, Structural phase transitions from and to the quasicrystalline state. Acta. Crystallogr. A **61**, 28–38 (2005)
125. W. Steurer, Stable clusters in quasicrystals: Fact or fiction? Philos. Mag. **86**, 1105–1113 (2006)
126. W. Steurer, A. Cervellino, Quasiperiodicity in decagonal phases forced by inclined net planes? Acta. Crystallogr. A **57**, 333–340 (2001)
127. W. Steurer, A. Cervellino, K. Lemster, S. Ortelli, M.A. Estermann, Ordering principles in decagonal Al-Co-Ni quasicrystals. Chimia **55**, 528–33 (2001)
128. W. Steurer, T. Haibach, Reciprocal-space images of aperiodic crystals, in International Tables for Crystallography, vol. B, ed. by U. Shmueli, (Kluwer Academic Publishers, Dordrecht, 2001), 486–518
129. K. Sugiyama, N. Kaji, K. Hiraga, T. Ishimasa, Crystal structure of a cubic $Al_70Pd_23Mn_6Si$; a 2/1 rational approximant of an icosahedral phase. Z. Kristallogr. **213**, 90–95 (1998)
130. S. Takeda, S. Harada, S. Tamaki, Y. Waseda, Electron-ion correlation in liquid aluminum. J. Phys. Soc. Jpn. **60**, 2241–2247 (1991)
131. R. Tamura, K. Edagawa, C. Aoki, S. Takeuchi, K. Suzuki, Low-temperature structural phase transition in a Cd6Y 1/1 approximant. Phys. Rev., B **68**, art. no. 174105 (2003)
132. R. Tamura, K. Nishimoto, S. Takeuchi, K. Edagawa, M. Isobe, Y. Ueda, Universal low-temperature phase transition in Zn- and Cd-based crystalline approximants. Phys. Rev. B **71**, art. no. 092203 (2005)
133. R. Tamura, Y. Murao, S. Takeuchi, M. Ichihara, M. Isobe, Y. Ueda, A low-temperature order-disorder transition in a cubic Cd_6Yb crystalline approximant. Jpn. J. Appl. Phys. **41**, L524–L526 (2002)
134. S. Van Smaalen, *Incommensurate Crystallography*. IUCr monographs on Crystallography 21. (Oxford University Press, Oxford 2007)
135. D.J. Wales, L.J. Munro, J.P.K. Doye, What can calculations employing empirical potentials teach us about bare transition metal clusters? J. Chem. Soc. Dalton. Trans. **5**, 611–623 (1996)
136. N. Wang, K.H. Kuo, Transformation of the octagonal quasi-crystal into the $\beta-Mn$-type crystalline-structure. Phil. Mag. Lett. **61**, 63–68 (1990)
137. Z. Wang, X. Yang, R. Wang, Ar^+-Ion-irradiation-induced phase-transformation in an $Al_{62}Cu_{25.5}Fe12.5$ icosahedral quasi-crystal. J. Phys. Condens. Matt. **5**, 7569–7576 (1993)
138. A. Waseda, K. Kimura, H. Ino, Phase-transitions of Al-Cu-Fe face-centered icosahedral quasi-crystals. Mater. Trans. JIM **34**, 169–177 (1993)
139. A. Waseda, K. Kimura, H. Ino, Free-energy analysis for the phase-transition of quasi-crystals and phase-diagram of the Al-Cu-Fe system. Mater. Sci. Eng. A **182**, 762–765 (1994)

140. T. Watanuki, A. Machida, T. Ikeda, K. Aoki, H. Kaneko, T. Shobu, T.J. Sato, A.P. Tsai, Pressure-induced phase transitions in the Cd-Yb periodic approximant to a quasicrystal. Phys. Rev. Lett. **96**, art. no. 105702 (2006)

141. R. Winters, W.S. Hammack, Pressure-induced amorphization of R-Al_5Li_3Cu – a structural relation among amorphous metals, quasi-crystals, and curved space. Science **260**, 202–204 (1993)

142. L. Xu, N. Wang, S.T. Lee, K.K. Fung, Electron diffraction study of octagonal-cubic phase transitions in Mn-Si-Al. Phys. Rev. B **62**, 3078–3082 (2000)

143. T.P. Yadav, N.K. Mukhopadhyay, M.A. Shaz, R.S. Tiwari, O.N. Srivastava, Phase transformations in $Al_{70}Ni_{24}Fe_6$ decagonal system during high energy ball milling. Philos. Mag. **86**, 397–404 (2006)

144. A. Yamamoto, H. Takakura, A.P. Tsai, Six-dimensional model of icosahedral Al-Pd-Mn quasicrystals. Phys. Rev. B **68**, art. no. 094201 (2003)

145. W.G. Yang, M. Feuerbacher, K. Urban, Cluster structure and low-energy planes in icosahedral Al-Pd-Mn quasicrystals. J. Alloys. Comp. **342**, 164–168 (2002)

146. X.X. Yang, R.H. Wang, X.J. Fan, Phase transitions in $Al_{62}Cu_{25.5}Fe_{12.5}$ quasicrystal induced by low-temperature Ar^{2+} irradiation. Phil. Mag. Lett. **73**, 121–127 (1996)

147. S. Yi, D.H. Kim, Stability and phase transformation of icosahedral phase in a 41.5Zr 41.5Ti 17Ni alloy. J. Mater. Res. **15**, 892–897 (2000)

148. H. Zhang, K. Urban, Radiation-induced transformation from the decagonal quasi-crystalline phase to a CsCl-type phase in Al-Cu-Co(-Si). Phil. Mag. Lett. **66**, 209–215 (1992)

11

Generalized Quasiperiodic Structures

Intermetallic quasicrystals. Locally, their structures do not differ essentially from other complex intermetallics and the same is true for most of their physical properties. Fundamentally different, however, is the quasiperiodic long-range order of their structures and peculiar are the physical properties that depend on the kind of long-range order. These are, in the first place, properties based on the propagation of electrons, phonons, and, to some extent, also of dislocations. Fundamentally different is also their noncrystallographic point-group symmetry with its implications on physical properties. For instance, icosahedral quasicrystals have fully isotropic elastic properties such as amorphous materials. The elasticity tensor of i-QC has only two independent coefficients while one of the cubic crystals has three. However, despite these new options, their are no real unique applications for quasicrystals up to date.

Soft quasicrystals. Recently, quasiperiodic ordering on a mesoscopic scale has been observed in several nonmetallic materials such as micellar liquid crystals and star block copolymers. The building blocks, on the scale of a few nanometers to tenths of nanometers, order to quasicrystalline domains up to micrometers. The symmetry of these soft quasicrystals is, at least on average, dodecagonal. A short overview will be given in Sect. 11.1, for a review see [7].

Artificial quasicrystals. The peculiar propagation of waves in quasiperiodic structures can lead to band gaps in a similar way as it is known for periodic structures. Combined with arbitrarily high rotational symmetry, fully isotropic band gaps can result. Materials of this kind would easily find application in all kinds of devices for the manipulation of electromagnetic waves, from microwaves to light waves. The same is true of the manipulation of elastic waves, from acoustic to ultrasonic waves. This is the reason for the recent boom in the development of quasiperiodic photonic and phononic crystals (for a review see [15]). A short introduction into the basics will be given in Sect. 11.2.

11.1 Soft Quasicrystals

The factors governing the formation of soft quasicrystals are largely different from those controlling formation and stability of intermetallic quasicrystals. In the latter case, electrons play a decisive role although this may not apply in the same way to the dodecagonal tantalum tellurides (see Sect. 8.4). Remarkably, self-organized soft quasicrystals have been observed with dodecagonal symmetry only. The origin of this behavior has been ascribed to the existence of two different length scales and three-body interactions[1] [7].

Particular micellar systems, where the supramolecular micelles are built up of wedge- or cone-shaped mesomorphic dendrons, can form solvent-free liquid dodecagonal quasicrystals [24] (Fig. 11.1). As a function of temperature, the originally columnar hexagonal close packed structure transforms into the dodecagonal liquid quasicrystal (d-LQC). A further increase in temperature leads to the phase sequence d-LQC$\Rightarrow Pm\bar{3}n \Rightarrow P4_2/mnm \Rightarrow$ bcc.

The other class of soft quasicrystals known so far are three-component polymeric quasicrystals. ABC star-shaped terpolymers, consisting of polyisoprene (I), polystyrene (S) and poly(2-vinylpyridine) (P), form cylinder
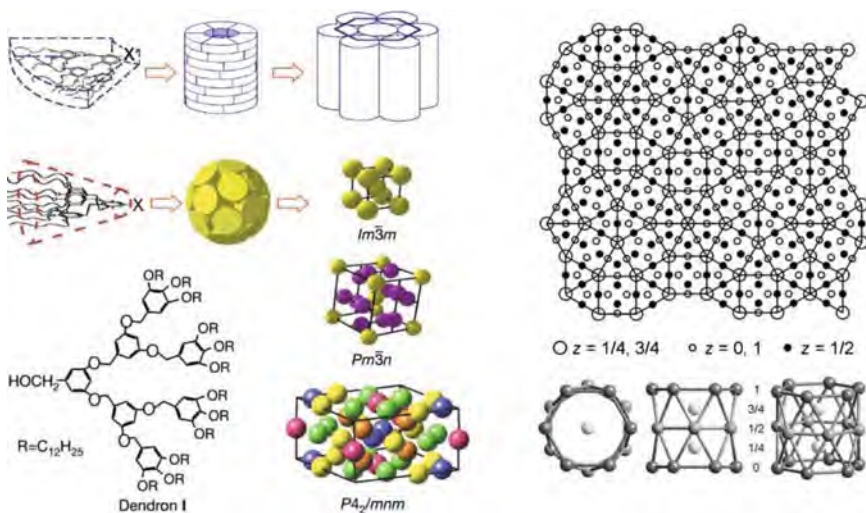
Fig. 11.1. Self-assembly of wedge- or cone-shaped tree-like molecules (dendrimers). The wedge-shape leads to cylindrical columns, which mostly assemble to hexagonal cylinder packings. If the chains need more space at higher temperature, the now cone-shaped molecules assemble to sphere-like micelles. These can adopt different structures as a function of temperature. In case of the molecule named dendron I, the dodecagonal liquid quasicrystal forms. The edge length and periodicity along the 12-fold axis of the structure model shown amounts to 81.4 Å [24]

---

[1] The ultra-soft repulsion of the building blocks and the resulting strong overlapping of their coronas lead to significant triplet interactions [19].
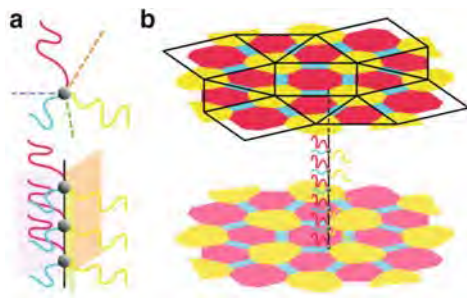
Fig. 11.2. Schematic drawing of *ABC* star-shaped terpolymer chains in bulk (**a**) and their nano-domain assembly (**b**) [5]
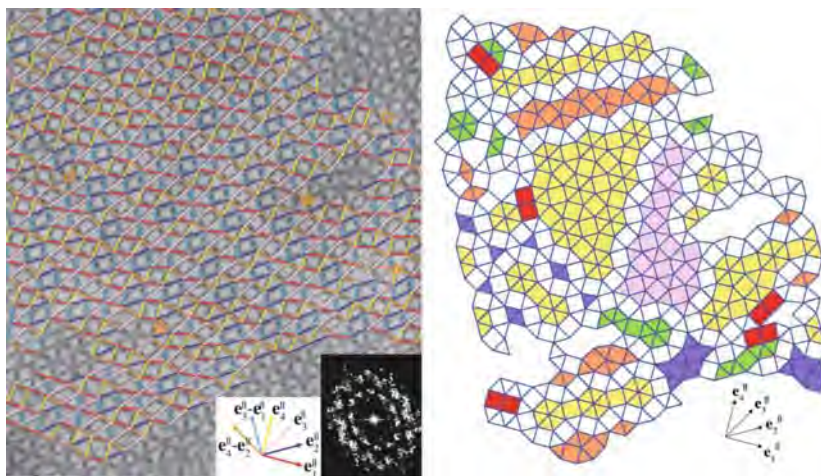
Fig. 11.3. (*left*) TEM image of a star-polymer with composition $I_{1.0}S_{2.7}P_{2.5}$ with superimposed tiling. (*right*) Idealized tiling showing patches of approximants of a quasiperiodic square–triangle decagonal tiling. The edge length of the tiles amounts to ≈470 Å[5]

packings with structures of Archimedean and dodecagonal tilings (see Sects. 1.2.1 and 1.2.6) [5, 18]. The shape of such a columnar star-polymer is shown in Fig. 11.2. If the three components are immiscible, the molecules have junction points along a line forming star-shaped columns. These columns then assemble themselves according to Archimedean or dodecagonal tilings (Fig. 11.3), depending on the composition of the components.

The triangle/square ratio of the tiling shown in Fig. 11.3 amounts to 2.305 compared to the value of 2.309 for an ideal square–triangle decagonal tiling. The experimentally observed, on-average, dodecagonal tiling consists of domains with the structure of a tetragonal Archimedean tiling (online: brown, pink, violet shaded) and of the 8/3 rational approximant (online: yellow, green shaded).

11.2 Photonic and Phononic Quasicrystals

Metacrystals (MC) such as photonic and phononic crystals (PTC and PNC) are artificial periodic heterostructures (composites), which consist of at least two materials differing in their dielectric or elastic properties, respectively. To some extent, PTC are to electromagnetic waves what PNC are to elastic (sonic, acoustic) waves and crystals to electrons. The Maxwell equations describe the interactions of electromagnetic waves in PTC, the elastic wave equations the propagation of elastic waves in PNC and the Schrödinger equation the behavior of electrons in a crystal.

Research into PNC [12] started five years after the seminal work of Yablonovitch [23] on PTC. The first phononic QC (PNQC), however, a quasiperiodic GaAs/AlAs multilayer structure was already studied in 1985 [9], only one year after the discovery of quasicrystals [11]. From the very beginning, research in this field was application driven. PTC allow the full control of light for optical computers or communication devices; they can be used for frequency filters, absorption-free wave-guides and mirrors, optical microcavities, or aberration-free negative-refraction-index lenses. PNC can be used as thermal barriers, elastic/acoustic filters, acoustic lenses, nonabsorbing mirrors and wave-guides, as sound-protection devices, and even as earthquake shields. Prerequisite for all of these applications is that the wave length is of the order of the lattice period of the PTC or PNC and the existence of well defined, omnidirectional and polarization independent band gaps (stop bands), and transmission (pass) bands. Introduction of appropriate defects can lead to localized defect states and narrow pass bands inside of band gaps.

In PTC, the existence of a band gap depends on a periodic distribution of the dielectric constant in a composite heterostructure and an optimum index contrast. In PNC, it is based on both the periodic spatial variation of the speed of elastic or acoustic waves and the mass density. A very important property of MC is the scalability of the effects. In case of PTC the scale ranges from from microwaves to light waves, in case of PNC from seismic waves to phonons. The wave propagation is governed by multiple scattering, constructive and destructive interferences in cases where the dimensions of the objects and the wavelength are of the same order, and refraction, due to different wave velocities of objects and surrounding medium. If there are strong density and velocity contrasts in a PNC, Bragg scattering leads to broad attenuation bands. If the contrasts are weak, resonance modes of single scatterers may occur in the frequency range of interest and by hybridization with the continuum bands determine the position of gaps in transmission spectra.

Now what is the difference between periodic and quasiperiodic MC (MQC), what are the peculiarities of quasiperiodic order? The arbitrarily high rotational symmetry of quasiperiodic systems favors omnidirectional band gaps; higher harmonics in quasiperiodic systems are significantly weaker than harmonics in periodic systems; the dense set of Bragg reflections makes multiple

scattering dominating; in quasiperiodic structures, there is a mixture of light propagation and localization (critical states), Bloch-wave like propagation is not possible. Covering clusters and smaller subclusters (ringlike and polyhedral arrangements) can act as resonant scatterers at lower frequencies than its component scatterers.

For a recent review on PTQC and PNQC see [15] and for a general introduction into the field for PTC and PNC see [8, 13].

11.2.1 Interactions with Classical Waves

Two mechanisms are relevant for band gap formation in MC, the Bragg-scattering and the resonance mechanism. The Bragg-scattering mechanism is related to the description of a nearly free electron system in a crystal, where band gaps open at Brillouin-zone boundaries. The resonance mechanism is best viewed in the framework of a tight-binding system. Bragg scattering takes place on net planes, with incident and back-scattered waves, with wave vector $\mathbf{k}$, interfering to standing waves $\psi(\mathbf{k})_1 = \psi(\mathbf{k})_{\mathbf{inc}} + \psi(\mathbf{k})_{\mathbf{scatt}}$, $\psi(\mathbf{k})_2 = \psi(\mathbf{k})_{\mathbf{inc}} - \psi(\mathbf{k})_{\mathbf{scatt}}$, and a splitting of the dispersion relation results (Fig. 11.4). Bragg gaps only form at Brillouin-zone boundaries at frequencies, ω, close to $\omega_{\mathrm{G}} = \pi c_{\mathrm{matrix}}/a_0$, with a_0 the lattice period and c_{matrix} the wave velocity in the matrix material.

The resonance mechanism is based on strong Mie resonances of the scattering objects [10]. If the resonators in a structure are independent from each other, they all have the same resonance frequency ω_{res}. Only the coupling medium, i.e. the matrix material, hosts additional wave states. The continuum band of the surrounding matrix material interacts with the resonance states by hybridization. In the dispersion relation, this interaction takes place
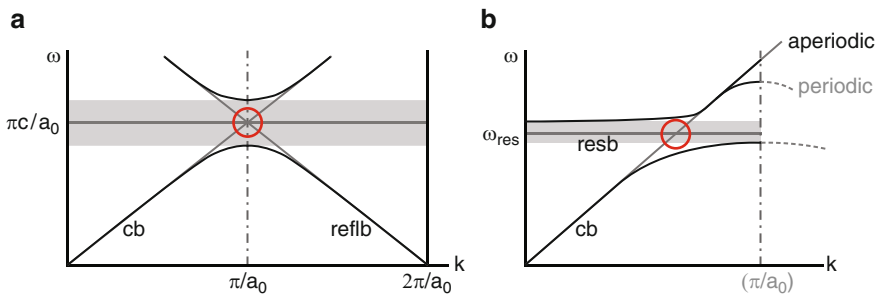
Fig. 11.4. (**a**) Dispersion relation in a periodic MC. In periodic structures the interaction of continuum waves (cb) with waves reflected at the Brillouin zone boundaries (reflb) cause the formation of gaps at the zone boundaries. If there are resonance states of the single scattering objects (**b**), a gap can be formed due to the interaction of resonance modes (resb) with modes of the continuum band (cb). Contrary to Bragg gaps, resonance gaps can be formed in periodic structures with or in aperiodic structures without zone boundaries [15]

at frequencies close to ω_{res}, at the intersection of the flat resonance band (resb) with the linear continuum band (cb) (Fig. 11.4). This frequency is structure-independent, only a minimum distance between the scatterers is required. Consequently, the position of the gaps does neither depend on the lattice parameters nor on the Bragg condition. This has the advantage of allowing band gaps with structures smaller than the wavelength. The disadvantage is that resonance implies energy dissipation by absorption.

In general, both regimes will be present in MC to some extent. Mie scattering in the same frequency range as Bragg scattering favors broad band gaps which can be easier engineered into omnidirectional ones.

Waves in an index-modulated heterostructure undergo multiple diffraction and refraction processes. By interference wave fields are formed which can either propagate and transport energy or are localized. Electromagnetic waves propagate in PTC as Bloch waves, i.e. with wavelengths related to the lattice period a_0. For dielectric PTC, there extends a large transmission band from zero frequency to the first band gap. That opens for a frequency $\nu \sim c/(2n_{\text{eff}}a_0)$, i.e. at a wavelength $\lambda \sim 2n_{\text{eff}}a_0$, with a_0 the period along the direction of wave propagation, $n_{\text{eff}} = \sqrt{\varepsilon_{\text{eff}}}$ the effective composite refractive index (effective index), ε the effective dielectric permittivity and $\varepsilon_{\text{eff}} = (1 - f) + f\varepsilon$, with the filing factor f of the dielectric. Accordingly, this gap is related to the first Bragg peak and its width depends on its intensity. The symmetrically equivalent MC directions along which such band gaps appear are the same at which the related Bragg peaks show up.

Consequently, the diffraction symmetry is the relevant symmetry for the orientation dependence of the band structure. The higher the rotational symmetry the closer to a circle is the Brillouin zone and the more overlapping are the band gaps in the different directions. An overlap of gaps for all directions can therefore be achieved even when the gaps are narrow. Therewith, constituent materials can be used with lower index contrast than for the best PTC with crystallographic symmetry. This is particularly important in the cases of self-organized colloidal MC, because usually only low index contrast can be achieved in such systems.

In case of metallic PTC, the low frequency spectrum is characterized by strong attenuation, the plasmon photonic band gap, followed by a first transmission band for $\lambda \sim 2n_{\text{eff}}a_0$. Up to this frequency, metallic PTC behave just in the opposite way to dielectric PTC, at higher frequencies the spectra are similar.

What are the mechanisms of wave propagation and band gap formation in case of MQC, are there still a kind of Bloch waves existing? The Borrmann effect, i.e. anomalous (easy) transmission of X-rays through a perfect crystal, has been observed in icosahedral Al–Mn–Pd quasicrystals [4], 15 years after its prediction [1]. For anomalous X-ray transmission, a standing wave must exist with its nodes at the planes of highest electron densities. This is easy to fulfil in case of a periodic structure. For quasiperiodic structures these planes of highest electron densities are the thick atomic layers related to the net planes

(lattice planes) of their PAS [2, 14]. This is also true for MQC, and we can assume that the Bloch waves in quasiperiodic structures are related to their respective PAS. The broader distribution of averaged scattering densities of a PAS compared to that of an MC may be one reason for the slower evolution with increasing thickness of Bragg gaps in the transmission spectra of MQC.

What else is typical for MQC? In the absence of strong resonances of the single scatterers, the scaling symmetry as well as the self-similarity of the structure are reflected both in the transmission spectra and the band structure (Fig. 11.5).

Further typical for MQC is the coexistence of extended and localized (or confined) as well as critically localized modes. While in simple periodic structures all modes are extended, simple quasiperiodic order seems to get well
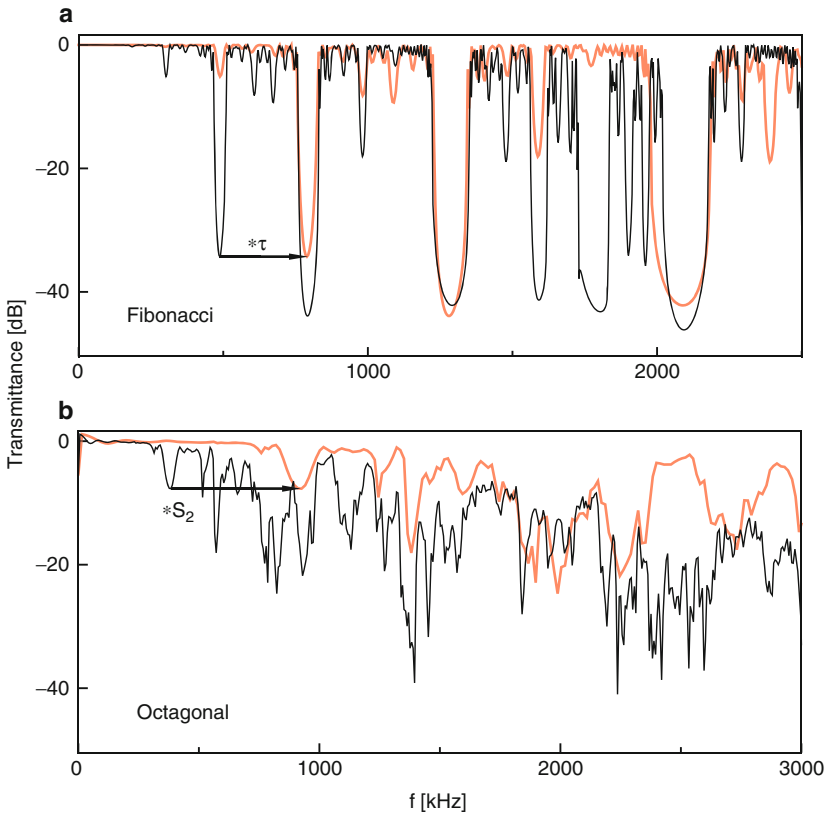
Fig. 11.5. The transmission spectrum through a Fibonacci sequence of thin epoxy sheets in water (**a**) and the same spectrum with τ-scaled frequency axes (gray, online: *red*) reveal the scaling symmetry of the most prominent gap positions. Transmittance through an octagonal PNQC (**b**) with its same spectrum scaled by $1 + \sqrt{2}$ (gray, online: *red*). A correlation between the spectra can be seen up to about 2.4 MHz [16]

along with localization. This is usually explained by the conflict between aperiodicity, which drives for localization, and self-similarity, which drives for extended wave functions [3]. The intermediate, weaker form of localization is reflected in the critical wave functions, usually decaying not exponentially but by a power law.

The type of the spectrum strictly determines the nature of the wave functions and critical waves are intrinsic to systems with singular continuous spectra ([6], and references therein). High-symmetry patches (clusters) with a high local index variation can act as centers hosting localized resonance modes (coupled single object resonances). Due to the repetitive properties of some quasiperiodic structures, such clusters will occur everywhere in the structure, again and again. For instance, in case of the regular Penrose tiling any patch with diameter d will be found again within a distance of $2d$. Overlapping wave functions localized at adjacent clusters then allow the exchange of energy and therewith propagation. Consequently, if these clusters are distributed sparsely (e.g., singular tilings with just one high-symmetry cluster in the center) the modes are trapped. This has been demonstrated for 8-, 10-, and 12-PTQC [20, 21].

Band gap engineering benefits from the many different vertex configurations that are possible in quasiperiodic structures since this allows a large variety of different defects to be created. A similar flexibility for periodic structures is only possible in complex, large-unit-cell structures such as high-order rational approximants. It is also advantageous that band gaps of MQC can be optimized without affecting other gaps too much. For instance, knowing the wave field distribution in the QMC, one can modify the structure exactly where the field amplitude is highest for the gap-edge frequency. Contrary to periodic MC, the spatial distribution of these maxima need not be the same for different gaps. This has been demonstrated on the example of a 12-PTQC, consisting of dielectric cylinders in air [22]. The introduction of further scattering objects at these sites allows to specifically modify band-edge states and also widen the band gaps thereby.

11.2.2 Examples: 1D, 2D and 3D Phononic Quasicrystals

The calculated transmission spectrum for a Fibonacci-sequence-based structure of epoxy sheets embedded in water (FS-PNQC) is shown in Fig. 11.6. One clearly sees that each peak in the Fourier spectrum corresponds to a dip in the transmission spectrum. Consequently, the band gaps are caused by Bragg scattering, resonances do not play a significant role since the volume fraction of the scattering objects is rather small.

Due to the close correspondence between Fourier and transmission spectrum, the scaling symmetry of the Fourier spectrum is well reflected in the transmission spectrum. The original and scaled spectra are shown superimposed in Fig. 11.6.
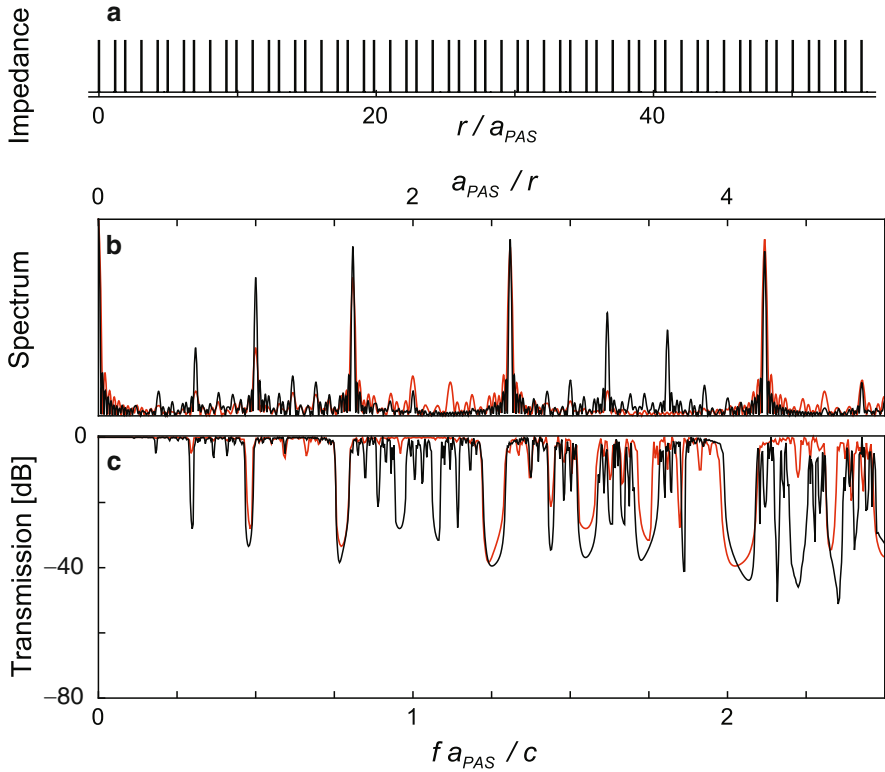
Fig. 11.6. Characteristics of the FS-PNQC. (**a**) The structure consists of 55 thin epoxy sheets in water arranged like a Fibonacci sequence; the distance from the origin, r, is normalized by the period of the PAS, a_{PAS}. (**b**) Fourier spectrum with normalized structure amplitudes with τ-scaled spectrum superimposed (gray, online: *red*); the peak related to the PAS, consequently, appears at $a_{PAS}/r = 1$. (**c**) Transmittance spectrum with τ-scaled spectrum superimposed (gray, online: *red*); the gap related to the PAS appears at $fa_{PAS}/c = 1/2$. In the *inset*, the enlarged section is shown of the band around $fa_{PAS}/c = 1$ after scaling with τ (*red*). Note the close correspondence of the Fourier spectrum and the transmission spectrum [15]

On the example of an octagonal PNQC (8-PNQC), we show the difference in the transmission spectra for the case of strongly resonant scattering as well as for the case of dominant Bragg scattering (Fig. 11.7). In the first case, the 8-PNQC consists of thick soft polymeric rods in water, in the second of steel rods in water. One sees that the maxima in the scattering cross section of the polymeric rods determine the dips in the transmission spectrum. The superimposed spectra for the two directions marked in Fig. 11.7(a) coincide to a large extent. This illustrates the direction independence of resonance spectra.
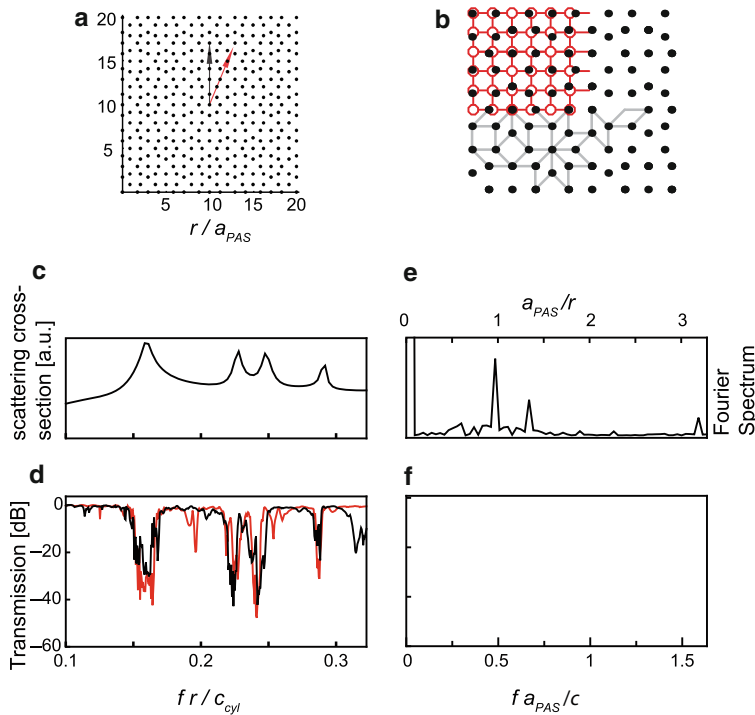
Fig. 11.7. Characteristics of the 8-PNQC. (**a**) Section of the underlying octagonal tiling with its PAS (**b**). (**d**) In case of an 8-PNQC based on soft polymeric cylinders in water, the positions of the band gaps (for the directions of transmission marked in (**a**)) are directly determined by the resonances in the scattering cross section of the single rods (**c**). (**f**) In the Bragg scattering 8-PNQC (steel rods in water), the band gaps (*black*) open at the same frequencies as do the gaps of periodic PNC with the square PAS (gray, online: *red*). Compared to other tilings the octagonal tiling possesses a strong PAS (**e**) [15]

For the 8-PNQC with hard scattering contrast, we see again the corre-spondence of the strong Bragg peak and the first deep minimum in the trans-mittance (Fig. 11.7e, f). One also sees the coincidence of the first minima of the 8-PNQC and its PAS, which is depicted in Fig. 11.7b. The lattice period of the PAS amounts to $a_{PAS} = 2a_r/(\sqrt{2}+1)$, with a_r the edge length of the tiles. Due to topological incompatibilities, the PAS of the octagonal tiling has only an occupancy factor of 0.83 compared to 1 for the Fibonacci sequence (see Sect. 3.6.3.4).

The situation is similar for PNQC with 10-, 12-, and 14-fold rotational symmetry. For 10- and 14-PNQC, the transmission spectra are getting more and more spiky with poorly defined first minimum.

Quasicrystals with icosahedral symmetry are closest to 3D isotropy. *i*-PTQC can be manufactured rather simply by optical interference lithography
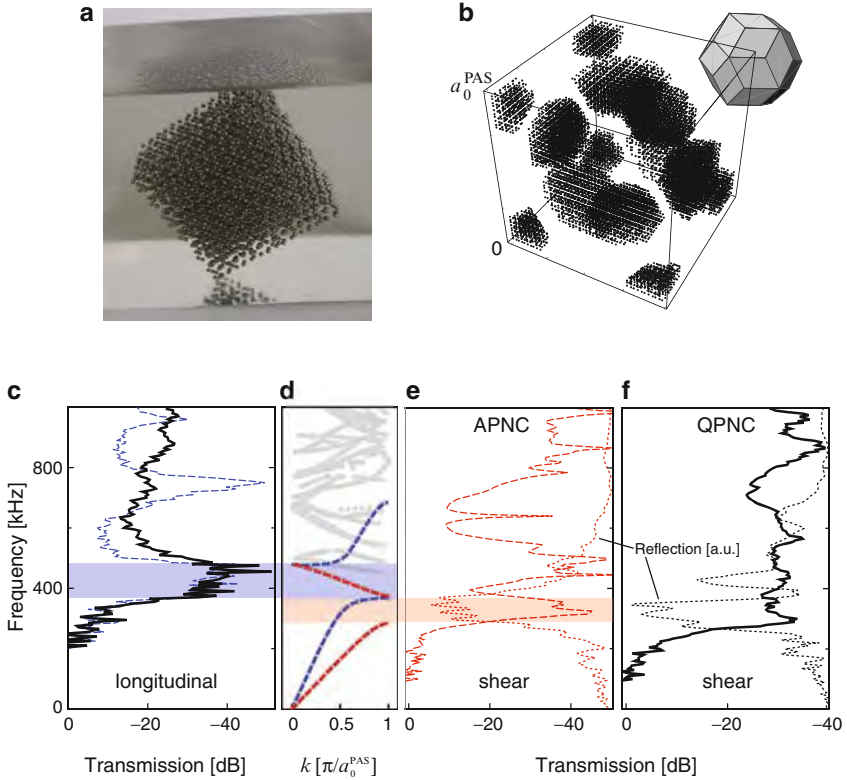
Fig. 11.8. (**a**) Photograph of the icosahedral PNQC used for the measurements is shown. It consists 3,438 steel spheres in polyester. (**b**) The icosahedral tiling underlying the *i*-PNQC modulo the unit cell of the PAS results in point sets circumscribed by triacontahedra on an fcc lattice. (**c**) Experimental longitudinal wave transmission spectra of the *i*-PNQC along a twofold axis (*solid line*) and its fcc PAS-PNC for the [100] direction (*dashed line*). (**d**) Calculated band structure of the PAS-PNC along the [100] direction. Transmission (*dashed line*) and reflection (*dotted line*) spectra for shear waves for the PAS-PNC (**e**) and QPNC (**f**) for the same directions as in (**c**). The shaded regions in (**c**–**e**) denote the frequency ranges of the longitudinal hybridization and the shear Bragg gaps [17]

(multibeam hololithography or holographic lithography) since PTC should have connected framework structures. In contrast, assembling 3D PNC is much more tricky because the scattering objects have to be disconnected. An example of an *i*-PNQC is shown in Fig. 11.8a. It has been fabricated layerwise by embedding, totally 3,438 steel balls (1 mm diameter, 1.25 mm shortest distance, filling fraction 0.074) in polyester [17]. For comparison, an *fcc* PNC (PAS-PNC) with the unit cell parameter of the PAS, $a_0^{PAS} = 3.227$ mm was used (1,458 steel balls, filling fraction 0.062).

In the following, we compare the spectral properties of the *i*-PNQC and its periodic average structure, PAS-PNC. The calculated band structure of the PAS-PNC for wave propagation along [100] shows a hybridization band gap for longitudinal and a Bragg gap for transverse polarized waves (Fig. 11.8d). The resulting stop bands are well visible in the transmission spectra. For longitudinal waves, the transmission curves of both QPNC and PAS-PNC indicate a deep and large band gap (Fig. 11.8c). This hybridization-induced gap opens up as a result of interaction between a narrow band originating from resonant dipole states of the individual steel balls with the band resulting from the propagation of the elastic waves in a homogeneous effective medium. Since QPNC and PAS-PNC contain the same kind of steel balls with similar filling fraction, the resulting gaps coincide perfectly.

This is different for the first shear wave band gaps (Figs. 11.8e and f). These Bragg gaps are orientation dependent, with an overlap of $\approx 50\%$ for the [100] and [111] directions of the PAS-PNC. The Bragg gaps of the PNQC are much more isotropic due to its higher symmetry (order 120 of $m\bar{3}\bar{5}$ compared to 48 of $m\bar{3}m$). While the bands and gaps of the PAS-PNC are well visible in both transmission and reflection (Fig. 11.8e), the Bragg gap formation of the PNQC is indicated only in the reflection spectrum (Fig. 11.8f). Around 350 kHz, a well-resolved reflection band can be observed in the transmission spectra of both the the PAS-PNC and the PNQC. The central frequencies are equal because so are the boundaries of the Jones-zone for the PNQC and of the Brillouin-zone for the PAS-PNC inducing the gap.

References

1. R. Berenson, J.L. Birman, Anomalous transmission of X-rays through a quasi-crystal. Phys. Rev. B **34**, 8926–8928 (1986)
2. A. Cervellino, W. Steurer, General periodic average structures of decagonal quasicrystals. Acta Crystallogr. A **58**, 180–184 (2002)
3. Y.S. Chan, C.T. Chan, Z.Y. Liu, Photonic band gaps in two dimensional photonic quasicrystals. Phys. Rev. Lett. **80**, 956–959 (1998)
4. J. Hartwig, S. Agliozzo, J. Baruchel, R. Colella, M. Deboissieu, J. Gastaldi, H. Klein, L. Mancini, J. Wang, Anomalous transmission of X-rays in quasicrystals. J. Phys. D **34**, A103–A108 (2001)
5. K. Hayashida, T. Dotera, A. Takano, Y. Matsushita, Polymeric quasicrystal: Mesoscopic quasicrystalline tiling in ABC star polymers. Phys. Rev. Lett. **98**, art. no. 195502 (2007)
6. M. Kohmoto, B. Sutherland, K. Iguchi, Localization in optics – quasi-periodic media. Phys. Rev. Lett. **58**, 2436–2438 (1987)
7. R. Lifshitz, H. Diamant, Soft quasicrystals – Why are they stable? Philos. Mag. **87**, 3021–3030 (2007)
8. J.-M. Lourtioz, H. Benistry, V. Berger, J.-M. Gerard, D. Maystre, A. Tchelnokov, Photonic Crystals. Towards Nanoscale Photonic Devices. (Springer Berlin, 2005)

9. R. Merlin, K. Bajema, R. Clarke, F.Y. Juang, P.K. Bhattacharya, Quasiperiodic GaAs/AlAs Heterostructures. Phys. Rev. Lett. **55**, 1768–1770 (1985)

10. G. Mie, Beiträge zur Optik trüber Medien, speziell kolloidaler Metallösungen. Ann. Phys. Lpz. **25**, 377–445 (1908)

11. D. Shechtman, I. Blech, D. Gratias, J.W. Cahn, Metallic phase with long-range orientational order and no translational symmetry. Phys. Rev. Lett. **53**, 1951–1953 (1984)

12. M.M. Sigalas, E.N. Economou, Elastic and acoustic-wave band-structure. J. Sound Vibr. **158**, 377–382 (1992)

13. M. Sigalas, M.S. Kushwaha, E.N. Economou, M. Kafesaki, I.E. Psarobas, W. Steurer, Classical vibrational modes in phononic lattices: theory and experiment. Z. Kristallogr. **220**, 765–809 (2005)

14. W. Steurer, T. Haibach, The periodic average structure of particular quasicrystals. Acta Crystallogr. A **55**, 48–57 (1999)

15. W. Steurer, D. Sutter-Widmer, Photonic and phononic quasicrystals. J. Phys. D **40** R229–R247 (2007)

16. D. Sutter-Widmer, S. Deloudi, W. Steurer, Prediction of Bragg-scattering-induced band gaps in phononic quasicrystals. Phys. Rev. B **75**, art. no. 094304 (2007)

17. D. Sutter-Widmer, P. Neves, P. Itten, R. Sainidou, W. Steurer, Distinct band gaps and isotropy combined in icosahedral band gap materials. Appl. Phys. Lett. **92**, art. no. 073308 (2008)

18. A. Takano, W. Kawashima, A. Noro, Y. Isono, N. Tanaka, T. Dotera, Y. Matsushita, A mesoscopic Archimedean tiling having a new complexity in an ABC star polymer. J. Polym. Sci. B **43**, 2427–2432 (2005)

19. C. von Ferber, A. Jusufi, C.N. Likos, H. Lowen, M. Watzlawek, Triplet interactions in star polymer solutions. Eur. Phys. J. E **2**, 311–318 (2000)

20. Y.Q. Wang, B.Y. Cheng, D.Z. Zhang, The density of states in quasiperiodic photonic crystals. J. Phys.-Condens. Matter **15**, 7675–7680 (2003)

21. Y.Q. Wang, X.Y. Hu, X.S. Xu, B.Y. Cheng, D.Z. Zhang, Localized modes in defect-free dodecagonal quasiperiodic photonic crystals. Phys. Rev. B **68**, art. no. 165106 (2003)

22. Y.Q. Wang, S.S. Jian, S.Z. Han, S. Feng, Z.F. Feng, B.Y. Cheng, D.Z. Zhang, Photonic band-gap engineering of quasiperiodic photonic crystals. J. Appl. Phys. **97**, art. no. 106112 (2005)

23. E. Yablonovitch, Inhibited spontaneous emission in solid-state physics and electronics. Phys. Rev. Lett. **58** 2059–2062 (1987)

24. X.B. Zeng, G. Ungar, Y.S. Liu, V. Percec, S.E. Dulcey, J.K. Hobbs, Supramolecular dendritic liquid quasicrystals. Nature **428**, 157–160 (2004)

Glossary

Alternation condition The alternation condition is a weak → *matching rule*, valid at least for all tilings with N-fold symmetry, where N is a prime or twice a prime, as well as for the canonical icosahedral tiling. It requires that tiles, which are related by mirror symmetry, have to alternate along each lane of tiles (→ *worm*). There can be any number of other types of tiles between such pairs of tiles. The alternation condition can be enforced by arrowing the tiles.

Ammann lines Tilings of the → *PLI* class have the property that, if their unit tiles are properly decorated by line segments, these join together in the tiling and form sets of continuous lines (Ammann lines). According to the orientational symmetry, N sets form of parallel quasiperiodically spaced lines, which are called Amman N-grid or Ammann quasilattice. Contrary to a periodic N-grid with noncrystallographic symmetry, it has a finite number of Voronoi cell shapes.

Ammann planes Analogously to Ammann lines, Ammann planes form in a particular LI class of 3D Penrose tilings.

Aperiodic tiles Set of tiles with local matching rules forcing nonperiodicity.

Atomic surface Perp-space component of an nD hyperatom, also called occupation domain, which corresponds to a probability density function of finding an atom.

Cluster In case of quasicrystals and complex intermetallic alloys, typical recurrent structure motifs are frequently called clusters. It can be, but it does not need to be, that these clusters differ from the matrix part of the structure in chemical composition, bonding, and physical properties.

Covering Patch of tiles covering a tile with overlaps but without gaps.

Enantiomorph Objects which are mirror-symmetric to each other, without having mirror symmetry themselves, are called enantiomorphs. They are said to be enantiomorphic.

Fibonacci numbers Numbers, 0, 1, 1, 2, 3, 5, 8, 13, ..., generated by the recurrence relation $F_{n+2} = F_{n+1} + F_n$, with $F_0 = 0$ and $F_1 = 1$. The limit of the ratio $(F_{n+1}/F_n$ approximates $\tau = (1 + \sqrt{5})/2$.

Hyperatom nD object decorating the unit cells of an nD hyperlattice in the frame of the higher-dimensional approach. The par-space component of a hyperatom describes a real atom, its perp-space component is called → *atomic surface* or → *occupation domain*

Hypercrystal nD generalization of a crystal.

Ideal crystal Infinite mathematical object with an idealized crystal structure. An ideal crystal can be ordered or disordered. If it is disordered, it is not periodic anymore, however, it has a periodic average structure.

Imperfect crystal Real crystal containing defects that are not in thermodynamic equilibrium (e.g., dislocations) in addition to equilibrium defects.

IMS-setting Embedding of a quasiperiodic structure analogous to that of an incommensurately modulated structure. This can be achieved by a par-space shear of the hypercrystal structure. The standard embedding is the → *QC-setting*.

Klotz construction Special tiling of the space within the nD approach.

Lane of tiles → *worm*

Local isomorphism Two tilings are locally isomorphic if and only if *every* finite region contained in either tiling can also be found, in the same orientation, in the other. In other words, locally isomorphic tilings have the same R-atlases for all R, where the R-Atlas of a tiling consists of all its tile patches of radius R.

The LI class of a tiling is the set of all locally isomorphous tilings. Locally isomorphic structures have the same autocorrelation function, i.e. they are homometric. This means they also have the same diffraction pattern. Tilings which are self-similar and which have matching rules and an Ammann quasi-lattice are said to belong to the → *Penrose local isomorphism* (PLI) class.

Metacrystal Crystal consisting of building units other than atoms (ions, molecules), such as photonic or phononic crystals.

Matching rules Matching rules rather allow to check whether a tiling is quasiperiodic than to be used as a *growth rule*, which can be derived either from substitution (deflation) rules or based on the higher-dimensional approach. Matching rules can be coded either in the decoration of the tiles or in their shape.

A tiling is said to admit *perfect* matching rules of radius R, if all tilings with the same R-atlas are locally isomorphic to it. Perfect matching rules are known for tilings with 5-, 8-, 10-, 12-fold and icosahedral symmetry.

A set of matching rules is said to be *strong*, if all tilings admitted are quasiperiodic, but not in a single LI class.

Weak matching rules are the least restrictive ones which guarantee quasiperiodicity. They allow bounded departures from a perfect quasiperiodic tiling and the diffraction pattern will show diffuse scattering besides Bragg diffraction.

Non-local matching rules need some global information on the tiling.

Nanocrystal Real crystal with dimensions on the scale of nanometers; its structure may fundamentally differ from that of larger crystals with the same composition.

Occupation domain $\rightarrow$ *atomic surface*

Packing An arrangement of an infinite number of copies of a set of 3D proto-tiles, face to face, without any gaps and overlaps.

Paracrystal Crystal showing string correlated lattice disorder, which is not necessarily bounded.

Parallelepiped A solid with six faces, each a parallelogram and each being parallel and congruent to the opposite face.

Parallelotope A generalization of a $\rightarrow$ *parallelepiped* to n dimensions.

Pell numbers Numbers, 0, 1, 2, 5, 12, 29, 70, 169, . . ., generated by the recurrence relation $P_{n+2} = 2P_{n+1} + P_n$, with $P_0 = 0$ and $P_1 = 1$. The limit of the ratio $(P_{n+1} + P_n)/P_{(n + 1)}$ approximates $\sqrt{2}$.

Penrose local isomorphism (PLI) class Tilings, which are self-similar, have matching rules and an Ammann quasilattice are said to belong to the Penrose local isomorphism (PLI) class $\rightarrow$ *Local isomorphism*

Penrose tiling Three variants of the Penrose tiling are known. P1: pentagon–rhomb tiling, P2: kite-and-dart tiling, P3: rhomb tiling. All three of them are mutually locally derivable and belong to the Penrose local isomorphism ($\rightarrow$ *PLI*) class.

Perfect crystal Real crystal in thermodynamic equilibrium (only point defects are possible such as thermal vacancies, impurities).

PLI class $\rightarrow$ *Penrose local isomorphism class.*

Point group A point group is a set of symmetry operations (symmetry group) of an object which leave at least one common point invariant. Point group operations are rotations, reflections, inversions, and rotoinversions.

Quasicrystal By the term *quasicrystal* we denote real crystals, the diffraction patterns of which show noncrystallographic symmetry. We do not use the terms *quasicrystal* and *quasiperiodic structure* synonymously. Quasicrystals may have strictly quasiperiodic structures. However, their structure may also be quasiperiodic on average only; or, even only somehow related to quasiperiodic structures. While quasiperiodic structures must obey the closeness condition in the nD description, this may not be the case for the structure of *quasicrystals* leading to a kind of lock-in state.

QC-setting Standard embedding of quasiperiodic structures as opposed to the → *IMS setting*.

R-atlas The R-atlas of a tiling consists of all tile configurations within a circle of radius R.

Real crystal Single-phase material which can be described refering to an ideal crystal.

Reflection conditions Conditions of occurrence for Bragg reflections that define when the structure factors are not systematically zero.

Row of tiles → *worm*

Self-similarity There exists a mapping of the tiling onto itself, generating a tiling with larger tiles. This mapping is called *inflation* operation since the size of the tiles is distended. The inverse operation is *deflation* which shrinks the tiling in a way that each old tile of a given shape is decorated in the same way by a patch of the new smaller tiles. Self-similarity operations must respect the matching rules. Sometimes the terms *inflation* (*deflation*) are used just in the opposite way referring to the increased (decreased) number of tiles generated.

Space group An nD space group is the set of symmetry operations (symmetry group) of an nD crystal pattern. Space group symmetry operations are translations, screw rotations and glide reflections in addition to point group operations such as rotations, reflections, inversion and rotoinversions. The set of all translations form the translation subgroup of the space group, which is an Abelian group.

Supertile Larger tile decorated by smaller tiles.

Symmorphic space group A space group is called symmorphic if, apart from the translations, the generating symmetry operations are all point group operations. The Hermann–Mauguin symbols of symmorphic space groups do not contain any glide or screw operations.

Tiling Pattern consisting of a gapless, edge-to-edge arrangement of an infinite number of copies of a set of proto-tiles.

Worm A *worm* (*row*, *lane*) is an infinite set of tiles joined along their parallel edges. It consists of all tiles that are duals of all the intersections lying on a single grid line of an n-grid.

Index